Simulation and Testing of Wave-Adaptive Modular Vessels

Andrew W. Peterson

Dissertation submitted to the Faculty of the Virginia Polytechnic Institute and State University

in partial fulfillment of the requirements for the degree of

Doctor of Philosophy

in

Mechanical Engineering

Mehdi Ahmadian, Chair

Leigh S. McCue-Weil

Saied Taheri

Steve C. Southward

Daniel J. Stilwell

December 20, 2013

Blacksburg, Virginia

Keywords: Suspension, Shock Mitigation, Vehicle Dynamics, Quarter-Boat, Catamaran

Simulation and Testing of Wave-Adaptive Modular Vessels

Andrew W. Peterson

Abstract

This study provides a comprehensive performance analysis of Wave-Adaptive Modular Vessels (WAM-V) using simulations and testing data. WAM-Vs are a new class of marine technology that build upon the advantages of lightweight, low-draft, catamaran construction. Independent suspensions above the hulls isolate the passengers and equipment from the harsh sea environment. Enhanced understanding of the relationship between suspension and vehicle performance is critical for future missions of interest to the U.S. Navy.

Throughout this study, the dynamic properties of three different WAM-Vs were evaluated. A multi-body dynamics simulation was developed for the 100-ft WAM-V 'Proteus' based on an automotive 4-post shaker rig. The model was used to characterize the sensitivities of different suspension parameters and as a platform for future models. A 12-ft unmanned surface vessel (USV) was instrumented and sea trials were conducted in the San Francisco Bay. A dynamic 4-post simulation was created for the USV using displacement inputs calculated from acceleration data via a custom integration scheme. The data was used to validate the models by comparing the model outputs to sensor data from the USV.

A vertical hydrodynamics testing rig was developed to investigate the interaction between the pontoons and the water surface to improve the understanding of how hydrodynamic forces affect suspension performance. A model was created to accurately simulate the hydrodynamic forces that result from vertical pontoon motion. The model was then scaled to fit a 33-ft WAM-V prototype. The 33-ft WAM-V was instrumented and sea trials were conducted in Norfolk, VA. The WAM-V's suspension was upgraded based on the testing results. A 2-post rig was also built for evaluating the 33-ft WAM-V's dynamics. Two dynamic models were made for the 33-ft WAM-V to evaluate different suspension designs.

The results from this study have numerous impacts on the naval community and on the development of WAM-Vs. The methodology for testing and evaluation will allow for future WAM-V designs to be compared under controlled circumstances. The performance of WAM-Vs can then be compared against conventional platforms to determine their suitability for future missions. Simulation development will enable future WAM-Vs to be evaluated prior to undergoing sea trials. The hydrodynamic models become a powerful design tool that can be easily scaled and combined with the 4-post models. By providing the simulations and test data to future vessel designers, the designers will be able to intelligently evaluate numerous iterations early in the design phase, improving performance and safety.

Table of Contents

List of Figures

List of Tables

Acknowledgements

I would like to thank my advisor, Dr. Mehdi Ahmadian, for his guidance, advice and encouragement throughout my research and doctoral studies in Mechanical Engineering with the Center for Vehicle Systems and Safety. Special thanks are also in order to the members of CVeSS for their support and knowledge that helped me overcome many obstacles during this research. I would also like to thank Dr. Leigh McCue-Weil, Dr. Saied Taheri, Dr. Steve Southward, and Dr. Daniel Stilwell for serving on my doctoral advisory committee.

Thanks are also in order to Marine Advanced Research, Inc. for their technical support during various portions of this study, as well as the Office of Naval Research, NAVSEA, and NSWCCD for their support during testing.

I would like to especially thank my parents for all their support throughout my entire engineering career. Not many kids get a Harbor Freight milling machine for Christmas, I am very blessed.

I would also like to thank Titanium Joe for helping me get my start, and for helping me win a few battles along the way.

Chapter 1 Introduction

1.1 Motivation

The constantly changing nature of the marine environment poses a difficult design challenge for designers of marine vessels, who have to balance vehicle performance and seakeeping against passenger comfort and vehicle longevity, all while operating in one of the harshest operating environments of any mode of transportation. With enhancements in propulsion technology and hull design continuing to bring ever increasing speeds at sea, innovations directed at mitigating oceanic inputs and improving seakeeping and passenger comfort in rough seas are becoming less of a luxury and more of a necessity for operating in the marine environment.

Proposed solutions for improving ride quality at sea have varied greatly in their approach and technological complexity. At the beginning of the design cycle, a multitude of different hull designs have been trialed that balance the inherent tradeoff between seakeeping performance and ultimate efficiency. Further into the design cycle, more advanced solutions such as hydrofoils designed to elevate the vessel out of the water at speed or gyroscopes designed to counter the wave inputs have also been developed. Once the design cycle is complete, a final piece of technology often retrofitted to existing crafts for improving ride quality has come in the form of shock mitigating seat technology, which prevents some of the motions of the craft from being transferred to the occupants.

A similar problem exists in the automotive domain. In an automobile, varying terrain conditions transmit vibration from the surface through the vehicle structure, into the cabin and to its occupants. Ever more advanced technological solutions are being developed, such as Magnetorheological Dampers and Interconnected Hydraulic Suspensions, to improve passenger comfort and road holding capability. However, the fundamental solution to the problem was converged upon long ago by the automotive community. An independent suspension system at each corner of the vehicle for vibration isolation is a well-established solution and nearly all advanced technologies are based on improving small aspects of the same basic design principles.

Wave-Adaptive Modular Vessels (WAM-V) are a new and novel solution for improving marine environment performance that borrows solutions from the automotive environment to improve

both passenger comfort and vehicle performance. While still early in their development, these novel catamaran-based concepts retain the inherent speed and range advantages afforded to traditional catamarans, while simultaneously incorporating aspects of automotive technology in their design to improve performance. The first design feature found on WAM-Vs for shock mitigation is the use of parallel spring-damper units as a suspension system connecting the pontoons to the superstructure. By incorporating the suspension into the design from the beginning of the design cycle, sufficient force capacities and travel capabilities are able to be packaged to handle large wave inputs.

The second area of similarity between WAM-Vs and automotive technology comes in the WAM-V's two inflatable hull structures. These hulls are able to deform under heavy loading in a similar manner to a tire rolling across an uneven road surface, flexing to absorb and dissipate energy. Like an automobile, the suspension motion is designed to attenuate large amplitude, low frequency vibration; while the flexible pontoon is designed to attenuate low amplitude, high frequency vibration. Due to the similarities Wave-Adaptive Modular Vessels share with their road-going counterparts, throughout this study a mix of automotive approaches to simulation and testing (such as 4-post shaker rig modeling and damper dynamometer testing) will be incorporated and adapted for use in the marine environment. Wave-Adaptive Modular Vessels are a new class of technology and to this point have not been extensively studied. The applicability of advanced technological solutions for improving performance will be a subject for investigation once baselines for performance and methods for simulation and testing have been established.

1.2 Objectives

The primary objectives of this study are:

- Develop a set of dynamic, multi-body simulation tools for the analysis of Wave-Adaptive Modular Vessels.
- Generate a set of data for evaluating existing WAM-V designs and to compare with future design iterations.
- Characterize existing WAM-V designs through testing and simulation
- Validate the tools used for simulation through comparisons between the simulations and the dynamic testing data analysis.
- Use the simulation tools and testing results to provide recommendations and possible directions for improvement to current and future WAM-V designs.

1.3 Approach

The following approach is used to address the issues presented in this study:

1) Develop a 4-post simulation model based on the 100-ft WAM-V prototype 'Proteus' to develop an initial understanding of how to set a simulation environment specific to WAM-Vs.
2) Perform testing and evaluation of a 12-ft USV prototype WAM-V. Use the data collected to improve the understanding of WAM-V dynamics.
3) Develop a 4-post model for the 12-ft USV using testing data as inputs to the model. Validate the modeling approach based on comparisons between the model and test data.
4) Design a testing setup to collect data on the interaction between a pontoon and suspension system to facilitate the incorporation of vertical hydrodynamics into the 4-post models to improve the simulation results.
5) Perform testing and evaluation of a 33-ft WAM-V prototype. Use the testing results from the 33-ft WAM-V to direct improvements to the models as well as future WAM-V designs.
6) Use the models and simulation tools to design an improved suspension system for the 33-ft WAM-V that is evaluated in a rough water testing environment. Incorporate existing standards from vessel and ride quality analysis to evaluating suspension performance.
7) Develop a 2-post test rig for testing the 33-ft WAM-V in a laboratory setting. Compare the testing with the virtual models and the on-water testing data.

During the course of this research, dynamic simulation models were created in four distinct phases. The first model developed was based on the 100-ft WAM-V Proteus and was used to characterize parametric sensitivities of the Proteus and serve to improve modeling capabilities. The second model developed was used to mimic the prevalent characteristics of the 12-ft USV and was employed as a validation tool for the dynamic simulations as a supplement to on-water testing. The third developed was made to relate vertical pontoon motion to hydrodynamic forces, based on the Quarter-Boat Test Rig. Finally, a fourth dynamic simulation environment was created for the 33-ft WAM-V to test configuration changes and drive future developments.

1.4 Contributions

The potential contributions of the research presented in this study to WAM-Vs, as well as the fields of, naval research, advanced catamaran design, suspension technology, hydrodynamics, and multi-body simulation are:

- Establishing a method of on-water testing and evaluation specific to Wave-Adaptive Modular Vessels.
- Establishing a baseline data set for acceleration levels and loadings in a sea state which data from other vessels as well as future WAM-Vs can be compared.
- Develop a modeling approach capable of evaluating both WAM-V current designs and future iterations.
- Apply standards for Whole-Body Vibration to WAM-Vs as a method for relating marine suspension performance to comfort.
- Provide a new and novel extension to the hydrodynamic literature of drop tests, with the premier two degree of freedom cylindrical drop test.
- Development of a novel method of incorporating vertical hydrodynamics into WAM-V analysis using mechanical simulation components.
- Provide a nondimensionalization of the component of a marine suspension system so the findings from this study can be applied to vessels of any size.
- Provide a comparison between differences in suspension system design parameters in the automotive and marine environments relevant to noise, vibration and harshness.
- Provide the first application of multi-post shaker rigs to the marine environment for evaluating vessel performance in the laboratory setting.

1.5 Outline

- Chapter 1 introduces the study and provides the objectives, approach, potential contributions from the research, and an outline of the dissertation.
- Chapter 2 provides the technical background for the study. The characteristics of various displacement hull forms, the effects of sea motion on the human body, and methods for performance comparison between crafts are presented.
- Chapter 3 details the principle characteristics of WAM-V designs beginning with the 100-ft WAM-V Proteus, as well as the development of an initial multi-body dynamic simulation tool and the results from a parametric suspension analysis.
- Chapter 4 details the instrumentation and testing of a 12-ft USV prototype and presents the results of modeling and simulation of the 12-ft USV.
- Chapter 5 details the efforts made in hydro-mechanical modeling made through the design, construction and testing of the Quarter-Boat Testing Rig.
- Chapter 6 introduces the 33-ft WAM-V prototype and its instrumentation and testing.
- Chapter 7 discusses the data analysis from the on-water testing of the 33-ft WAM-V.
- Chapter 8 applies the properties of the Quarter-Boat model to analyzing the 33-ft WAM-V and improving its suspension system.
- Chapter 9 applies Human Factors and Whole-Body Vibration standards to on-water testing with the 33-ft WAM-V.
- Chapter 10 provides the details of 2-post rig design, testing and data analysis.
- Chapter 11 details the simulation of the 6-post virtual rig based of the 2-post testing rig.
- Chapter 12 provides a direction for further investigation into WAM-Vs beyond the scope of this dissertation.

Chapter 2 Background and Technical Review

The following chapter provides the technical background necessary for understanding the research into advanced modeling of marine vessels equipped with suspension systems. An overview of hull form characteristics of different types of ships is presented, along with the characteristics of ship motions in an elevated sea state. The human and operator response to different motions seen in a sea state is reviewed, as well as methods of comparing the ride quality of a vessel or the relative ride quality between two vessels. The chapter is concluded with a discussion on the current standards for evaluating acceleration data as well as Whole-Body Vibration.

2.1 Chapter Overview

- Section 2.1 provides an overview of the chapter.
- Section 2.2 discusses the properties of different hull forms.
- Section 2.3 provides an overview of ship motion and sea state characteristics.
- Section 2.4 discusses Human Factors in the naval environment.
- Section 2.5 discusses common methods of quantifying acceleration data.
- Section 2.6 discusses the current standards for Whole-Body Vibration.

2.2 Hull Form Characteristics

The traditional monohull design is the dominant design in the marine industry for a variety of reasons. Due to an inherently large level of displacement for a relatively small wetted surface area, monohull designs provide high load carrying capacities as well as allowing for more simplified construction techniques, both of which lower costs [1]. Furthermore, as the dominant design in the naval community, the knowledgebase for hull form design far exceeds other more novel hull form types. When it comes to choosing a vessel type for a given task, there is always an inherent tradeoff between a number of factors. Figure 2.1 illustrates the tradeoffs for alternative crafts types compared to a monohull vessel.

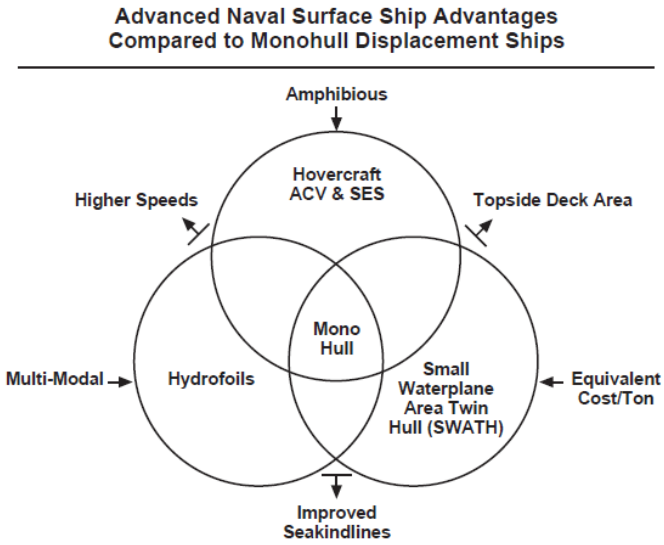

Figure 2.1 Fundamental tradeoffs between modes of transportation in the marine environment [2]

While the traditional monohull is the most common hull form, many other designs have been developed for different applications. As an example, Figure 2.2 shows the relative stability of different hull forms.

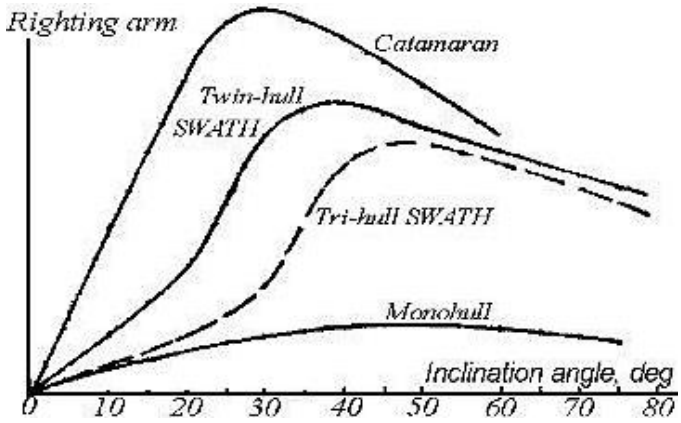

Figure 2.2 Intact stability of different hull forms [3]

Choosing a hull type with consideration to the intact stability plots shown in Figure 2.2 comes with an inherent cost, usually in the efficiency of the vessel. For quantifying the efficiency of a hull form, two common metrics used by naval architects are the Transport Factor and/or the Admiral Coefficient. The Transport Factor is defined by the formula below, where W is the ship's total weight, SHP is the ship's horsepower, V is the speed in knots, and K is a constant.

$$TF = K\left(\frac{W}{SHP/Vk}\right) \quad [4]$$

The Admiral Coefficient is another measurement of the same fundamental parameters as the Transport Factor. In the equation for the Admiral Coefficient (C) below, D is the displacement in tons, V is the speed in knots, P in the installed horsepower, and Fn is the Froude Number.

$$C = \frac{D^{2/3}V^3}{P} \text{ [3]}$$

Fundamentally, both formulas are a measure of the weight of the ship multiplied by the ship's velocity, then divided by the ship's power. Even within a given hull form, the transport factor is often a tradeoff between payload and speed, as shown in Figure 2.3. Figure 2.4 shows the change in admiral coefficient for three different hull forms at different speeds, indicated by a change in Froude number.

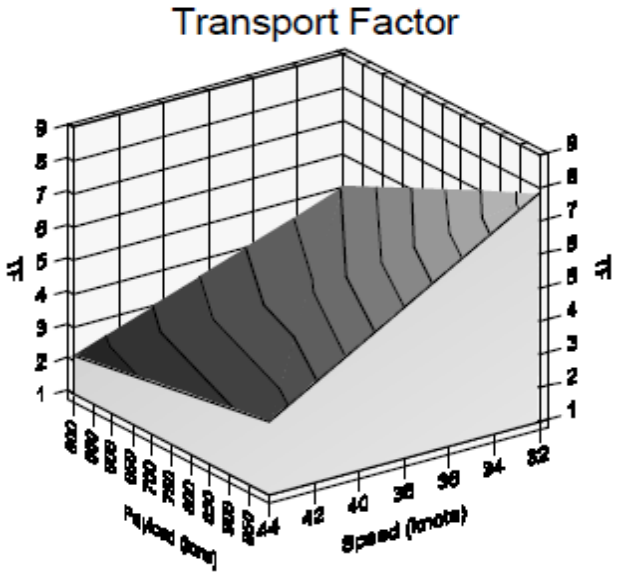

Figure 2.3 Transport factor tradeoff between parameters [4]

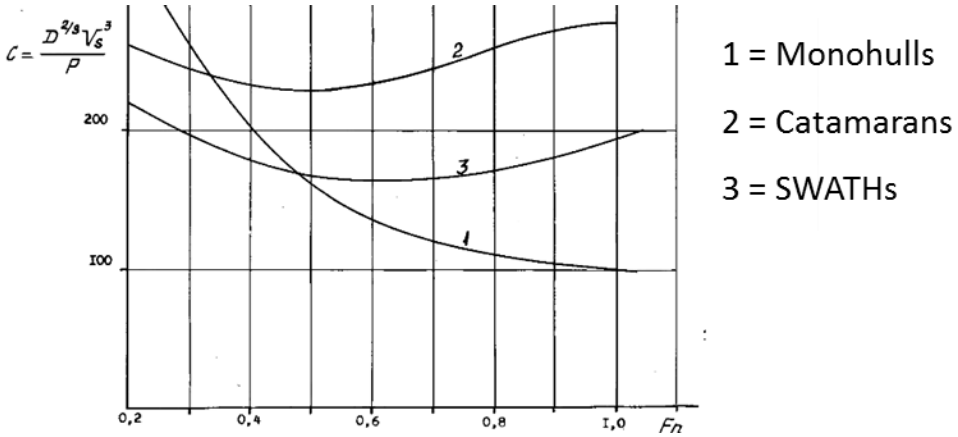

Figure 2.4 Admiral coefficients for three different hull forms (annotated from [3])

2.2.1 Characteristics of Catamarans

Multi-hulled ships have several distinct advantages over monohulls. These advantages include: a larger available deck area, excellent transverse stability, and lower power consumption for a given speed [2]. Through variation of the hull shape and the number of hulls, multi-hulled vessels can be tailored to produce vastly different performance characteristics. Catamarans are twin-hulled vessels where the superstructure rests at or above the static waterline, as shown Figure 2.5.

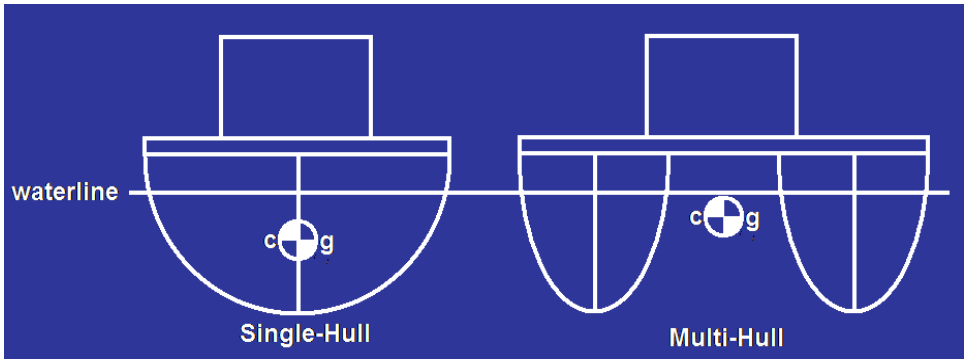

Figure 2.5 Single vs. multi-hull design overview

While catamarans have several advantages over standard monohull designs, their application in seaways can be limited. The geometry of catamarans allows for a larger deck area, and catamaran geometry has much better roll resistance than monohulls of comparable capacity. The increased stability of catamarans comes from a higher roll stiffness, meaning that roll motions occur at higher frequencies, so accelerations in roll are higher for the same roll angle experienced. Properly designed catamarans are able to see the same roll accelerations as monohulls, while experiencing 40% of the roll displacement [5].

Compared to monohulled designs, catamarans have a larger wetted surface area leading to increased parasitic drag [6]. However, they generally require less total propulsive power because the hulls can have a higher aspect ratio and thus are less wave-resistive and more efficient. The effect of wave resistance becomes more pronounced at higher speeds, this explains why catamaran designs have been commonly employed in high speed ferries. A twin-hulled vessel with a minimal wetted surface at the waterline is shown in Figure 2.6 [7].

Figure 2.6 High speed twin-hulled vessel 'Seafighter' [7]

Most catamarans are equipped with two individually operated propulsion systems, one in each of the hulls. Catamarans with this design offer a maneuverability advantage since the two propulsion systems can be independently operated to provide differential thrust [1], operating like the skid steering design found on tanks. This also adds complexity and cost to the design as two power sources must be operated and maintained; however, it also provides a fault tolerance should an engine fail at sea. Wet deck slamming also must be considered for large impacts, where the level of submersion exceeds the height of the two demi-hulls and the superstructure comes into contact with the water surface [8]. The majority of the technical background presented in this section will focus on twin-hulled catamarans, as they provide an excellent layout for pairing with advanced suspension technologies for shock and motion mitigation. The following section overviews a few other alternative hull types.

2.2.2 Other Hull-Types: SWATHs and Trimarans

Like catamarans, Small Waterplane Area Twin Hulls (SWATHs) are also marine vessels with two separate hulls. SWATHs utilize two fully submerged hulls attached to the superstructure by a thin strut area [9]. By both submerging the hulls and elevating the superstructure, the ability of oceanic inputs to influence the cabin is greatly reduced. Cargo capacity for SWATHs is reduced significantly, because the submersion of the hulls is very sensitive to the total weight of the vessel [5]. Swath vessels can offer improved passenger comfort at higher sea states where the

stability of catamarans may become problematic. At extreme sea states, the righting forces from the catamaran's hulls become very strong. The vessel shown in Figure 2.6 is actually a SWATH vessel, with most of its buoyancy coming from farther below the water surface than the picture seems to indicate.

Trimarans are vessels with three distinct hulls. Trimarans often represent an intermediate between mono-hulled and twin-hulled vessels, with intermediate transverse stability achieved by outriggers mounted away from the central hull. Some Triamarans can be considered to be like stabilized monohulls, with the primary buoyancy coming from the central hull, with double outrigger stabilizers. Stabilizer designs with low drafts are prone to nonlinearities in roll moments due to unladen outriggers lifting from the water at moderate roll angles [3].

Both SWATHs and Trimarans tend to have increased wetted surface areas compared to catamarans. However, often are able to have more slender demi-hulls, providing some compensation. By nature of their design, SWATHs run a deeper draft resulting in slower top speeds than a comparable catamaran. For comparing resistance between different hull forms, the residual resistance coefficient is often given because it is identical for a model ship and a full scale ship. Residual resistance coefficient is defined as the total resistance coefficient minus the friction resistance coefficient [3]. Figure 2.7 shows a comparison of residual resistance coefficients for monohulls, catamarans, and SWATHs of the same displacement and length for different speeds.

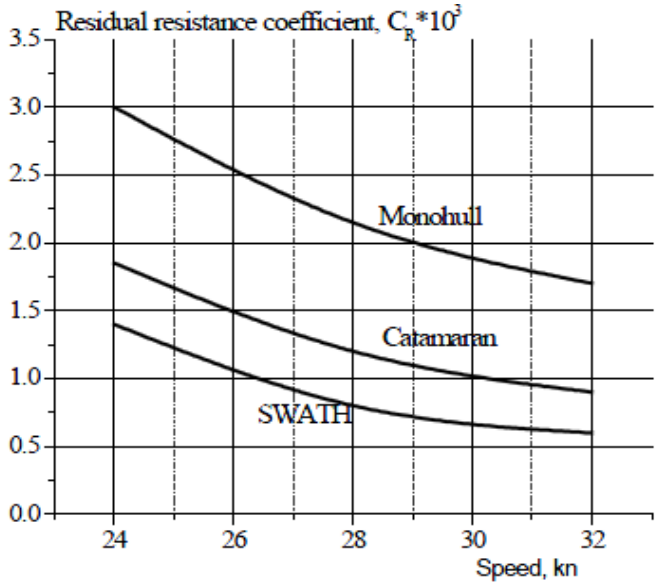

Figure 2.7 Comparison of residual resistance coefficient between different hull forms [3]

2.3 Ship Motion Characteristics

The motion of vessels in a marine environment can generally be placed into one of two categories:

- Periodic Motion
- Repeated Shocks

The first input type occurs in mild to moderate sea states and is characterized by inputs of a sinusoidal nature which still may contain, but is not dominated by transient behavior. The second type is caused by multiple wave impacts often occurring in higher sea states and is predominantly characterized by repeated impacts and transient vibrations [10]. In relation to their effect on human performance, repeated shocks are most likely to cause injury to human operators, while periodic motion is more likely to cause instances of interruption and motion sickness to occupants.

2.3.1 Periodic Motion

The difference between a periodic motion environment and a shock environment occurs when individual impact events define the perception of ride quality over the cumulative vibration effects. When characterizing the difference between a periodic or shock environment, there is a need to relate the levels of acceleration recorded to existing standards to determine a measure of ride quality. Using acceleration data, a shock environment can be distinguished from a periodic vibration environment by calculating the ratio between the RMS acceleration and the peak acceleration, known as the crest factor [11], shown by the formula below. It was found by Payne (1976) that for datasets with crest factors exceeding three, Root Mean Squared (RMS) acceleration has little correlation to perceived crew comfort and ride quality [12]. Whole-Body vibration researchers have since used a crest factor limit of nine for analyzing the effects of vibration using frequency-weighted RMS acceleration [13].

$$CF = \frac{a_{peak}}{a_{rms}} \quad [12]$$

Vibration can induce a broad and varying spectrum of sensations in the human body depending on the type of vibration. Further confounding factors for researchers include the differing physical characteristics between different individuals and the effects of the duration of exposure

to a given vibration. What a person defines as comfortable does not always correlate to what will reduce fatigue or what will reduce rates of injury. Fatigue induced by vibration is caused by increased muscular activity as the body attempts to counter the vibration. An example of this would be strain in the neck muscles when the head and neck are shaken at their resonant frequencies. Muscle activity may be voluntary or involuntary. Fatigue is greatest when the vibration reaches a resonant frequency of the human body. Research has shown that humans reach a certain level of fatigue much quicker when subjected to 4 to 8 Hz vibrations in the vertical direction [14].

The motion a person experiences onboard a ship varies greatly with the person's location on the ship. Figure 2.8 shows an example of the change in power spectral density in the vertical direction at different locations between the bow to the stern of a ship [15].

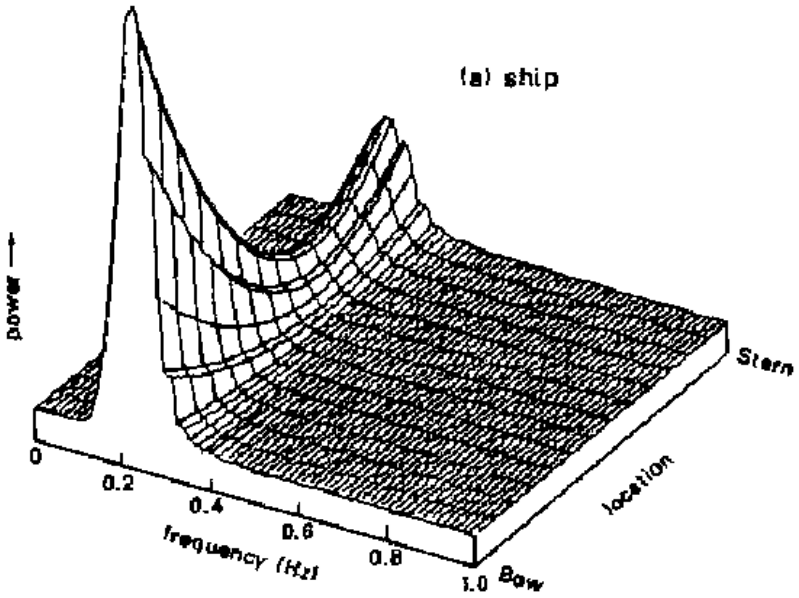

Figure 2.8 Change in power spectral density at different locations on a ship [15]

2.3.2 Shock Environment

The most damaging type of motion to operators is severe shock, which is the combination of multiple stochastic forces which often are large in magnitude and short in duration. These events often involve the craft leaving the water during a wave crest event and falling back to the water in a violent manner. Acceleration levels can reach as high as 10g's over 30 to 75ms for these events [10]. Injuries range from sprains/strains to chronic pain and more severe stress fractures.

Most injuries are fatigue induced. Fatigue induced injuries are defined as the result from exposure to dynamics for a long period of time. Fatigue is caused by the human body's reaction to the motion of the craft, this is referred to as Motion-Induced Fatigue (MIF). MIF is caused by the physical work the body must do to mitigate shocks [16].

2.3.2.1 Damage Potential in a Shock Environment

Similar to the operator response to a shock environment, the potential for damage to components on a vessel during shock events can be quantified using acceleration data as well. Of the three states of motion often used to quantify a shock environment (displacement, velocity and acceleration) velocity, or more specifically the change in velocity, is the parameter of greatest interest when it comes to evaluating the potential for damage [17]. However, peaks in acceleration data are still useful for evaluating impacts events with roughly the same duration time (such as the same impact event at different points on the craft). For crafts less than 15.85m (52ft), such as the 11-meter RIB craft shown in Figure 2.9, impact periods are on the order of 0.1 to 0.3 seconds depending upon craft displacement, average speed and wave height [11].

Figure 2.9 Eleven-meter RIB craft [18]

2.3.3 Wave Slam Sequence

The sequence of events for a single impact event in a shock environment can be broken down into small sections of data for detailed study of the vessel's response. Figure 2.10 shows an example response to a wave slam event measured at the longitudinal center of gravity of an 11m RIB craft like the one shown in Figure 2.9.

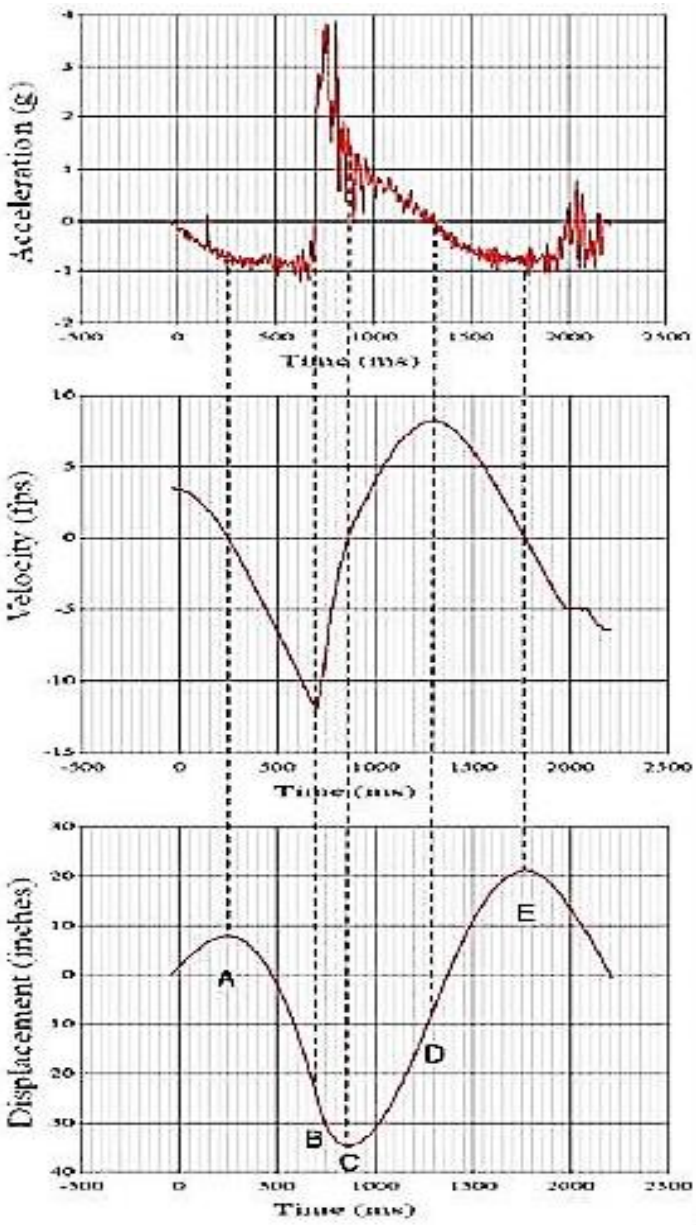

Figure 2.10 Sequence of events for a wave slam impact [11]

During the period between time A and B shown in Figure 2.10, the craft is dropping from its maximum height and at time B it impacts the water with its maximum negative velocity. The force from the wave impact, beginning at time B, brings a nearly instantaneous jump to maximum acceleration between time B and C, as the craft continues to move downward in the water, until the velocity reaches zero at time C. The craft is pushed upward by hydrodynamic and buoyant forces from time C to D, and both the net force and the acceleration approach zero. From time D to E the velocity approaches zero as the hull rises vertically [11].

It has been shown that the peak acceleration due to a wave slamming event has a proportional relationship to average acceleration experienced during the wave impact event. Therefore the ratio of the peak accelerations for two different wave slam events can be approximated using the following equation:

$$\frac{A_1}{A_2} = \frac{\Delta V_1 / \Delta t}{\Delta V_2 / \Delta t_2} \text{ [11]}$$

For impact events with duration times of the same order of magnitude, the peak vertical acceleration of each wave slam event is proportional to the ratio of the velocity change that was produced by that wave slam event. This also means that there is proportionality in the damage potential, which in some instances is used as a measure of ride quality [11].

2.3.4 Sea State Classification

When trying to classify the type of sea conditions, a common scale used is the World Meteorological Organization Sea State Code, also known as the Douglas Scale [19]. The sea state classification system is an increasing scale from 0 to 9. The rating for a particular sea state is based on variables including significant wave height, wind speed, and significant wave period. The criterion for classification under the WMO scale is shown in Table 2.1. A more detailed version of the WMO scale is the Wilbur Marks Wind and Sea Scale, shown in Table 2.2, which contains additional criteria about the sea conditions and wind predictions for a given sea state.

Table 2.1 WMO sea state classifications [19]

WMO Sea State Code	Wave Height (meters)	Sea Characteristics
0	0	Calm (glassy)
1	0 to 0.1	Calm (rippled)
2	0.1 to 0.5	Smooth (wavelets)
3	0.5 to 1.25	Slight
4	1.25 to 2.5	Moderate
5	2.5 to 4	Rough
6	4 to 6	Very rough
7	6 to 9	High
8	9 to 14	Very high
9	Over 14	Phenomenal

Table 2.2 Wilbur-Marks wind and sea scale for fully risen seas [20]

FULLY RISEN SEAS[1]											WIND			
SEA STATE[1]	WAVE HEIGHT (feet) AVERAGE	SIGNIFICANT (avg. of 1/3 highest)	AVG. OF 1/10 HIGHEST	SIGNIFICANT RANGE OF PERIODS (seconds)	T, mean period of maximum energy	T, (average period, sec.)	L, (avg. wave length, ft.)	WIND[2] SPEED (knots)	MINIMUM FETCH (nmi)	MINIMUM DURATION (hrs)	BEAUFORT No.[4]	WIND DESCRIPTION	WIND SPEED (knots)	APPEARANCE OF THE SEA[6]
0	0	0	0	–	–	–	–	–	–	–	0	CALM	<1	Sea like a mirror.
	0.05	0.08	0.10	up to 1.2 sec.	0.7	0.5	0.83	2	5	0.3	1	LIGHT AIRS	1-3	Ripples with the appearance of scales are formed, but without foam crests.
1	0.18	0.29	0.37	0.4-2.8	2.0	1.4	6.7	5	8	0.7	2	LIGHT BREEZE	4-6	Small wavelets, still short but more pronounced; crests have glassy appearance and do not break.
	0.6	1.0	1.2	0.8-5.0	3.4	2.4	20	8.5	9.8	1.7	3	GENTLE BREEZE	7-10	Large wavelets. Crests begin to break. Foam of glassy appearance. Perhaps scattered white horses.
2	0.88	1.4	1.8	1.0-6.0	4.0	2.8	27	10	10	2.4				
	1.4	2.2	2.8	1.0-7.0	4.8	3.4	40	12	18	3.8	4	MODERATE BREEZE	11-16	Small waves, becoming longer; fairly frequent white horses.
3	1.8	2.9	3.7	1.4-7.6	5.4	3.9	52	13.5	24	4.8				
	2.0	3.3	4.2	1.5-7.8	5.6	4.0	59	14	28	5.2				
	2.9	4.6	5.8	2.0-8.0	6.5	4.6	71	16	40	6.5				
4	3.8	6.1	7.6	2.5-10.0	7.2	5.1	90	18	55	8.3	5	FRESH BREEZE	17-21	Moderate waves, taking a more pronounced long form; many white horses are formed. (Chance of some spray.)
	4.3	6.9	8.7	2.5-10.6	7.7	5.4	99	19	65	9.2				
	5.0	8.0	10	3.0-11.1	8.1	5.7	111	20	75	10				
5	6.4	10	13	3.4-12.2	8.8	6.3	134	22	100	12	6	STRONG BREEZE	22-27	Large waves begin to form; the white foam crests are more extensive everywhere. (Probably some spray.)
	7.9	12	16	3.7-13.5	9.7	6.8	160	24	130	14				
6	8.2	13	17	3.8-13.6	9.9	7.0	164	24.5	140	15				
	9.6	15	20	4.0-14.5	10.5	7.4	188	26	180	17				
	11	18	23	4.5-15.5	11.3	7.8	212	28	230	20				
7	14	22	28	4.7-16.7	12.1	8.9	250	30	280	23	7	MODERATE GALE	28-33	Sea heaps up and white foam from breaking waves begins to be blown in streaks along the direction of the wind. Spindrift begins.
	14	23	29	4.8-17.0	12.4	8.7	258	30.5	290	24				
	16	26	33	5.0-17.5	12.9	9.1	285	32	340	27				
	19	30	38	5.5-18.5	13.6	9.7	322	34	420	30				
	21	35	44	5.8-19.7	14.5	10.3	363	36	500	34				
	23	37	46.7	6.0-20.5	14.9	10.5	376	37	530	37	8	FRESH GALE	34-40	Moderately high waves of greater length; edges of crests break into spindrift. The foam is blown in well-marked streaks along the direction of the wind.
	25	40	50	6.2-20.8	15.4	10.7	392	38	600	38				
	28	46	58	6.5-21.7	16.1	11.4	444	40	710	42				
8	31	50	64	7.0-23.0	17.0	12.0	492	42	830	47				
	36	58	73	7.0-24.2	17.7	12.5	534	44	960	52	9	STRONG GALE	41-47	High waves. Dense streaks of foam along the direction of the wind. Sea begins to roll. Spray may affect visibility
9	40	64	81	7.0-25.0	18.5	13.1	590	46	1110	57				
	44	71	90	7.5-25.0	19.4	13.8	650	48	1250	63				
	49	78	99	7.5-27.0	20.2	14.3	700	50	1420	69	10	WHOLE[5] GALE	48-55	Very high waves with long overhanging crests. The resulting foam in great patches is blown in dense white streaks along the direction of the wind. On the whole the surface of the sea takes a white appearance. The rolling of the sea becomes heavy and shock like. Visibility is affected.
	52	83	106	8.0-28.2	20.8	14.7	736	51.5	1580	73				
	54	87	110	8.0-28.5	21.0	14.8	750	52	1610	75				
	59	96	121	8.0-29.5	21.8	15.4	810	54	1800	81				
	64	103	130	8.5-31.0	22.8	16.3	910	56	2100	85	11	STORM[5]	56-63	Exceptionally high waves. (Small and medium-sized ships might for a long time be lost to view behind the waves.) The sea is completely covered with long white patches of foam lying along the direction of the wind. Everywhere the edges of the wave crests are blown into froth. Visibility affected.
	73	116	148	10.0-32.0	24	17.0	985	59.5	2500	101				
	>80[7]	>128[7]	>164[7]	10-(36)[7]	(26)[7]	(18)[7]	–	>64	–	–	12	HURRICANE[8]	64-71	The air filled with foam and spray. Sea completely white with driving spray; visibility very seriously affected.

From a table compiled by Wilbur Marks, David Taylor Model Basin

[1] Sea states refer only to wind waves. Swells from distant or old storms are often superimposed on the wind wave pattern.

[2] Practical Methods of Observing and Forecasting Ocean Waves, Pierson, Neuman, James, H.O.Pub. 603, 1955.

[3] Wind required to create a fully risen sea. To attain a fully risen sea for a certain wind speed, the wind must blow at that speed over a minimum distance (fetch) for a minimum time (duration).

[4] The Beaufort Number is a wind force scale. While wind and seas are causally related, Beaufort Number and sea state are not the same. For example, it is common to have force 7 winds, but because of limited fetch or duration, a sea state of only 2.

[5] Manual of Seamanship, Vol. II, Admiralty, H.M. Stationary Office, 1952.

[6] For whole gale, storm, and hurricane winds (50 knots or more) the required durations and fetches are rarely attained. Seas are therefore not fully arisen.

[7] For such high winds the seas are confused. The wave crests are blown off, and the water and air mix.

2.4 Human Factors in the Naval Environment

All marine vessels, and High Speed Craft (HSC) in particular, are capable of subjecting the crew and passengers to one of the harshest operating environments of any mode of transportation. With this in mind, the limits of a vessel's performance are often not simply the limits of the machinery itself, but the functional limits of the operator and crew. Furthermore, the enhanced speed potential of small High Speed Craft is continually increasing due to improvements in propulsion capabilities. This has consequently increased the levels of exposure of the crew. It is at this point that Human Factors and Human Factors Engineering become an integral component of the design process for improving performance, as much as or more so than improved propulsion or structural integrity. The means by which craft motion can affect human performance have been developed in a model made up of four factors, shown graphically in Figure 2.11.

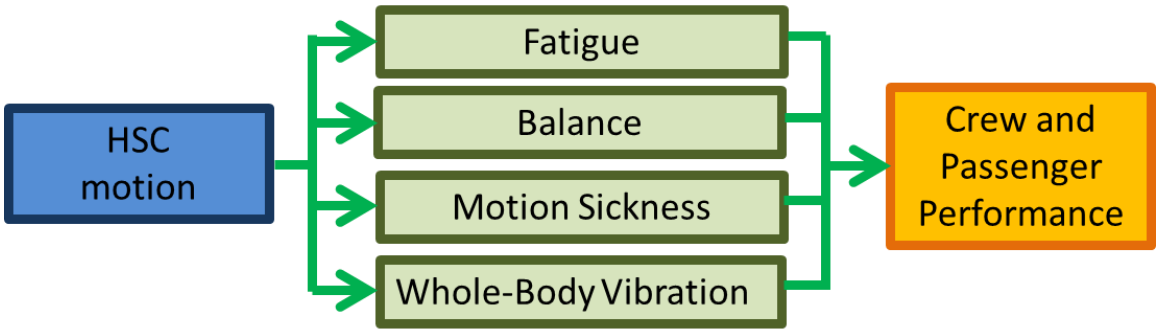

Figure 2.11 Flowchart for determining high speed craft performance (adapted from [21] and [22])

The four parameters that affect human performance, shown in green in Figure 2.11, can be defined by the following characteristics:

Fatigue: The motion of the craft causes fatigue, which degrades the work capacity (physical & cognitive) of the individual. This is known as Motion Induced Fatigue (MIF). See sections 2.3.1 & 2.3.2. Motion Induced Fatigue is characterized by low frequency, large amplitude, long term exposure [21]. Exposure can also lead to reduced situational awareness.

Balance: The motion experienced on HSC can cause individuals to lose their balance and therefore it takes longer to complete tasks. This increase in task time has to be factored into the operation of the HSC system, or solutions devised to make the task simpler. This is known as

Motion Induced Interruptions (MII). Motion Induced Interruptions are characterized by low frequency, large amplitude, short-term events [21].

Motion Sickness: Motion sickness can cause people to become incapacitated and unable to operate effectively. This is known as Motion Sickness Incidence (MSI). Motion sickness is characterized by low-frequencies, with short or long term exposure time [21]. Generally MSI is not as prevalent on HSC, although it can become prevalent during periods of long loitering.

Whole-Body Vibration (WBV): Whole-Body Vibration environment is characterized by medium/high frequency content; tolerable exposure is determined by the severity of motion [21]. Exposure can also lead to acute injuries. Prolonged expose may lead to health risks as well [22].

Many methods are available for measuring human performance, such as oxygen uptake to determine energy expenditure. Studies have been conducted on suspension seats relating oxygen consumption and heart rate to comfort. This study will focus on the Whole-Body Vibration on the operator, and the existing standards that are available. Existing standards are mainly related to discomfort and not physical injury.

2.4.1 HSC Environment:

HSC rarely expose occupants to regular, sinusoidal vibration; however, this is the mode for which the majority of WBV research exists. In benign conditions HSC may experience sinusoidal motion; otherwise motion tends to be erratic and stochastic in nature, formed from repeated impacts at irregular intervals. To date, the majority of WBV research has been sinusoidal in nature with limited consideration of impacts, and stochastic vibration has not been comprehensively assessed. Early attempts at defining ride quality were used as a measure of vehicle mobility linking vehicle speed and terrain roughness. Figure 2.12 given shows an early attempt to correlate the human sensitivity to different acceleration levels and frequencies in qualitative terms.

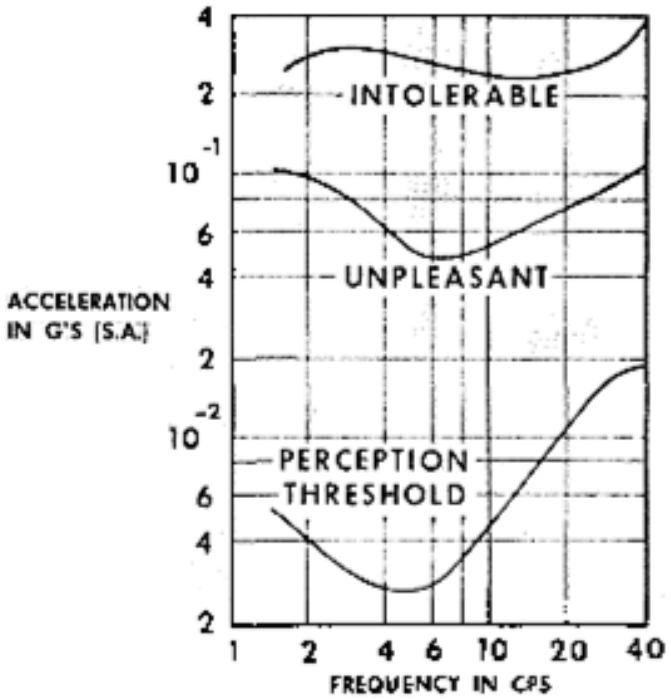

Figure 2.12 Human sensitivity to vibration [23]

At the lower limits of the vibration spectrum, the perception thresholds for continuous Whole-Body Vibration vary widely between individuals. Approximately 50% of the people in a typical population can perceive a vertical weighted peak acceleration of 0.015 m/s^2. The weighting method is discussed in Section 2.6.5.3 for different frequencies. 25% on the population are able to perceive an acceleration of 0.01 m/s^2, while another 25% of the population are only able to detect 0.02m/s^2 or greater. For other regions of discomfort, similar variance occurs between individuals [24].

2.4.2 Frequency Effects of Vibration

Different frequencies of vibration affect the human body in different ways. Injuries can come from a single event (such as a 20g impact) or the cumulative effect of long-term exposure to a large quantity of smaller energy events. The motion of HSC in a periodic motion environment may be characterized as a low level of Whole-Body Vibration (WBV) interspersed with repeated stochastic impact events. Table 2.3 gives an overview of some of the possible effects of different vibrations frequencies on the human body.

Table 2.3 Effect of different frequencies on the human body [25]

Frequency (Hz):	Effect:
0.05-2	Motion sickness, peak incidence occurs at 0.17 Hz
1-3	Side-to-side and fore-aft-bending resonances of the unsupported spine
2.5-5	Strong vertical resonance in the vertebra of the trunk and the lower lumbar spine
4-6	Resonance in the trunk
20-30	Resonances between the head and shoulders
Up to 80 Hz	Localized resonances of tissues and smaller bones

2.4.3 Modeling of Human Body-Dynamics

Research has been conducted into mechanical models that attempt to represent the human body as a series of masses, springs and dampers. Three models with different degrees of freedom model are shown in Figure 2.13. The range of resonant frequencies of different components of the body for different positions and vibration directions are listed in Table 2.4.

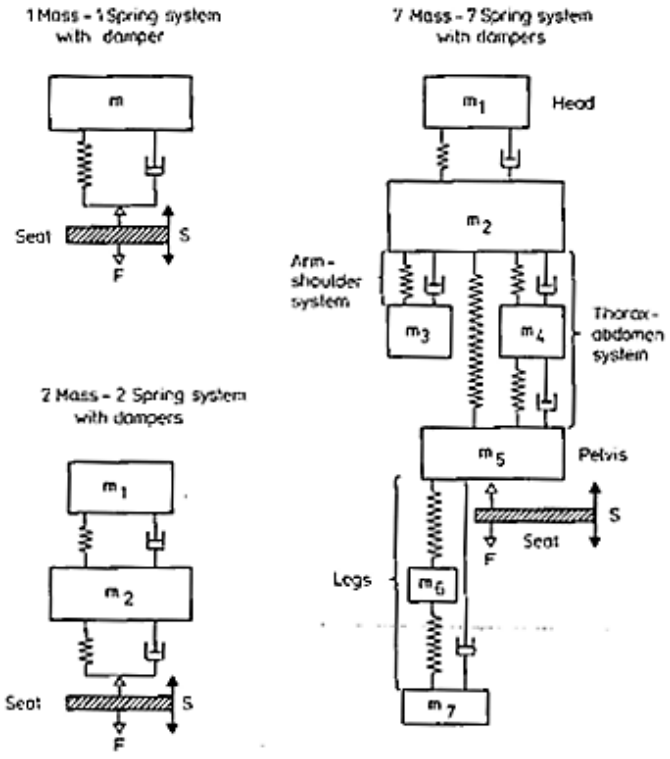

Figure 2.13 Mechanical models of the human body with different degrees of freedom [25]

Table 2.4 Range of resonant frequencies for different body parts [25]

Body Posture:	Body Part:	Vibration Direction	Range of Resonant Frequencies:
Standing	Knee	Longitudinal	1 – 3 Hz
	Shoulder	Longitudinal	1 – 2 Hz
	Head	Longitudinal	1 – 2 Hz
	Whole Body	Vertical	4– 7 Hz
Sitting	Trunk	Vertical	3– 6 Hz
	Chest	Vertical	4 – 6 Hz
	Spinal Column	Vertical	3 – 5 Hz
	Shoulder	Vertical	2 – 6 Hz
	Stomach	Vertical	4 – 5 Hz
	Eyes	Vertical	20 – 25 Hz

2.4.4 Suspension Systems in a HSC Environment

Limited research has been conducted on suspension systems for shock mitigation in the marine environment. The bulk of the research that has been conducted has focused on suspension seats retrofitted to existing marine vessels to improve rough seas performance.

The bulk of the research on suspension systems comes from ground vehicles. Conventional suspension systems for ground vehicles are customarily tuned to produce sprung mass resonance in the range of 1-2 Hz, effectively isolating the occupants from irritating vibrations in the 4 to 8 Hz range. This is no accident, as can be seen in the human vertical vibration sensitivities in Table 2.3 and Table 2.4.

2.4.5 Motion Sickness Response

Largely separate from injury response, the human response to low-frequency periodic motion is quite interesting. By simply being exposed to a repetitive motion, a sickness can occur. On a given craft, this may only happen to a certain percentage of the people onboard that are most susceptible; this is called motion sickness. However, all normal persons can be made sick by a suitable stimulus [26]. The quest to understand this phenomenon has been the subject of considerable research. Motion sickness can be defined as the uneasiness and resulting conditions associated with a repetitive movement. A sense of balance and equilibrium are disrupted causing a sense of changing spatial orientation [27].

Quantifying the occurrence of motion sickness has resulted in some important information. From experimental studies, motion sickness incidences have been found to occur based on the frequency of the periodic motion and the acceleration of the head. While other factors also influence the people who are susceptible and the severity of their sickness, metrics can be used to define with reasonable certainty the percentage of people who will become sick based of the frequency and acceleration of the motion [28]. In fact, motion sickness is almost exclusively found in the frequency range from 0.08 Hz to 0.4 Hz [28]. Human bodies exhibit a natural sway at frequencies between 0.1 and 0.3 Hz [29].

Another note worth mentioning is that motion sickness is more prevalent on ships because the 0.08 to 0.4 Hz frequency range for motion sickness is also the predominant frequency characteristic seen on most sea ships [29]. Induced optical motion at these frequencies can lead to motion sickness when standing [16]. The amplitude of some of these oscillations is so small, some subjects aren't aware that anything is moving

While there are many different ways to characterize a wave, the simple truth is that sickness is predominately based on the frequency of the wave [29]. Worsening sea conditions provide a stimulus for sickness, by changing in amplitude of the waves and not the wave frequency [29]. This will in turn increase the resulting accelerations on the body. A variety of testing has been performed to simulate different frequencies and acceleration changes. Figure 2.14 reveals how motion sickness incidences (MSI) change with different frequencies and RMS head accelerations.

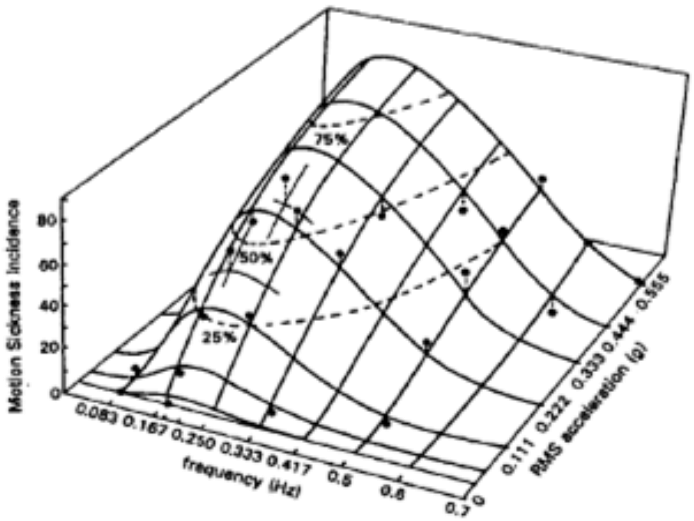

Figure 2.14 Motion sickness incidence based on frequency and acceleration [28]

It can be seen in Figure 2.14 that maximum incidences occur at roughly 0.17 Hz and increase with an increase in acceleration at the head to nearly 70% of people exhibiting motion sickness at 0.5 g's of acceleration within 2 hours of the beginning of the test. This is why ships are nauseating. Ships in deep water oscillate in roll at around 0.2 Hz [30]. Being farther from the ship's center produces increased acceleration. Therefore, those more susceptible to motion sickness are encouraged to move toward the middle of the ship.

Currently, the International Standard Organization (ISO 2631, 1997) and British Standard Organization (BS 6841, 1987) employ the Vomiting Index (VI) model for predicting Motion Sickness Incidence, or the percentage of people that will become sick [29]. With known magnitudes and duration of oscillations with frequencies ranging from 0.08 to 0.5 Hz, we can use the equation below to find the MSDV (Motion Sickness Dose Value). This is a function of the accelerations throughout time.

$$MSDV_z = \left(\int_0^T a_z^{\,2}(t)dt \right)^{1/2} \quad [24]$$

This value is then multiplied by a gain factor that is based upon the single frequency experimental data to achieve a percentage of people who may become sick. Figure 2.15 shows the acceleration levels as a function of frequency that will cause 10, 20, and 40% VI for a two hour exposure duration. Generally, incidence will double if magnitude is doubled or exposure frequency is quadrupled [24].

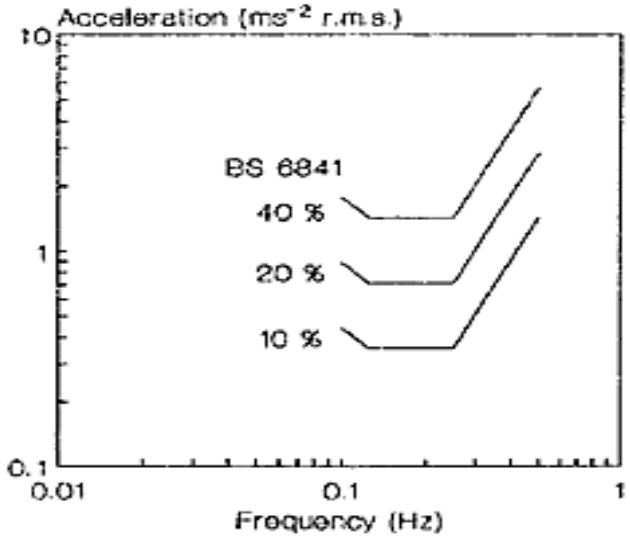

Figure 2.15 Incidence rate of sickness as a function of frequency and acceleration [24]

This gain factor is also at a maximum at 0.17 Hz, as shown in the model for MSI. The effect of reduced susceptibility to motion sickness due to long-term repeated exposure was not used in this model. The acceleration modeled in the MSDV is only in the vertical direction, because vertical motion is the most predominant motion in terms of motion sickness. Pitch and roll do not contribute much to the same extent [28].

While frequency and acceleration in periodic motion are the most significant causes of motion sickness, other factors do contribute as well. Fitness level of a person affects MSI [31]. Those who are more physically active usually have a more refined vestibular system, and any disturbance will cause a more dramatic change in the information relayed from it [29]. Females are more susceptible at a ratio of 1.7:1 to males [29]. People, on average, peak in rate of incidences between 20 to 29 years of age [31]. Also, those who are exposed to the periodic motion more often are less affected [28]. Figure 2.16 shows data on the Vomiting Index collected data from 20,000 passengers over 370 of recorded ship voyages [15]. Vomiting Index has a direct correlation with Motion Sickness Dose Value, but the effect varies greatly from person to person.

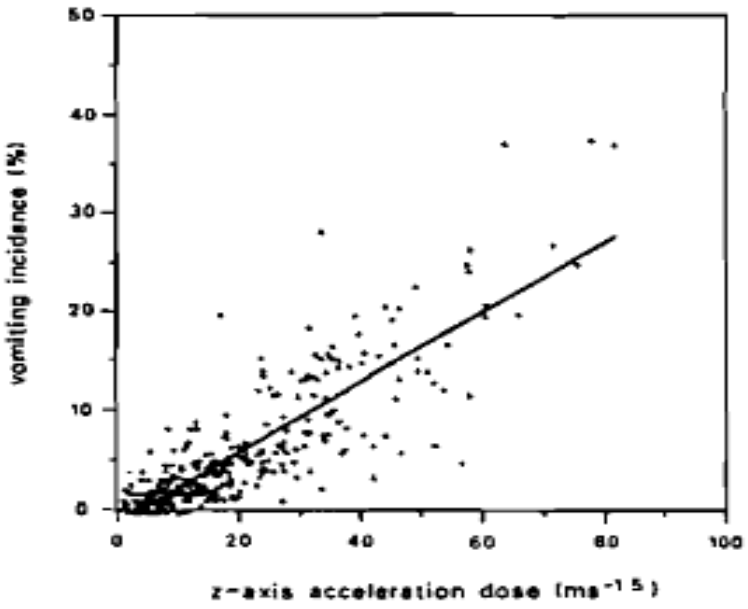

Figure 2.16 Vomiting incidence vs. acceleration dose for dataset for different voyages [15]

The research currently being done in this field can eventually contribute to boat and ship design where the structures can be designed to resist motion at specific frequencies most likely to cause injury or sickness.

2.5 Methods of Quantifying Acceleration Data

As it relates to high speed craft performance, acceleration data is one the most useful methods of inferring the performance characteristics of a vessel. The focus on acceleration data for marine vessels comes from marine vessels being treated as rigid bodies not subject to large, low frequency relative motion between portions of the ship that can be measured by displacement sensors. Sections 2.5 and 2.6 deal with acceleration reporting criteria as it applies to vessel performance and Whole-Body Vibration, respectively.

2.5.1 Root Mean Squared Analysis and Root Mean Quad Analysis

When analyzing seakeeping data on a marine vessel, the magnitude of vibration of time-series accelerometer data is often characterized by Root Mean Square (RMS) acceleration. RMS can be correlated to motion sickness and fatigue using the information in Section 2.4

RMS is one of the most basic and common techniques for quantifying acceleration. RMS acceleration, often referred to as the effective value of acceleration, represents the standard deviation of the acceleration about the mean, presented with the following formula, where a_i are the data points, and n is the total number of points of data recorded in the data set.

$$RMS = \sqrt{\frac{1}{n}\sum_{i=1}^{n} a_i^2} \quad [32]$$

In a severe dynamic environment, RMS has been shown to underestimate the effects of transient vibrations. In this case, Root Mean Quad (RMQ) tends to better emphasize the short durations shocks and their effects. Shocks are more detrimental to health and perception of ride quality. RMQ is defined by the following formula:

$$RMQ = \left[\frac{1}{n}\sum_{i=1}^{n} a_i^2\right]^{\frac{1}{4}} \quad [32]$$

Because the data points are raised to the fourth power, the peaks receive higher weighting. This means that impact events become more prevalent in the data. The RMQ values better emphasize the effects of shocks and short time duration vibration events in a sea state; this is important because impacts have been found to have a greater effect on the perceived ride quality and human comfort of a vessel.

2.5.2 Peak Acceleration Reporting

The peak values of a dataset represent the largest magnitude of the positive and negative accelerations recorded throughout the entire sample of data from a particular test. Representing the extreme values of the data, the maximum and minimum values do not necessarily provide a good characterization of the motions experienced, especially for large pieces of data. However, the peak values are helpful for completing the statistical representation of the wave environment and may be used to provide a worst case scenario for design purposes and calculations of factors of safety.

2.5.3 Average of the Highest 1/3rd, 1/10th, and 1/100th Acceleration Peaks

Often a more statistically relevant measure of the wave environment than the maximum and minimum acceleration values can be formed by the average of the highest acceleration peaks in a set of data. For the marine environment, three values often used are the averages of the $1/3^{rd}$, $1/10^{th}$, and $1/100^{th}$ highest peaks. Acceleration levels for crew tolerance and structural design are most frequently given as the average of the one-tenth highest accelerations [33]. For design purposes, the average of the one-one hundredth accelerations is often used [33]. In ship design, it is not uncommon to see the average of the one-one thousandth highest acceleration used to account for those waves of low probability [33].

A standard method for determining the peaks is presented below [34]. The number of peaks in a signal is determined by two factors:

1. Time between peaks
2. RMS value of the acceleration data

An example segment of acceleration data is shown in Figure 2.17 to demonstrate the procedure for counting the peaks from a representative piece of time-series acceleration data. Three wave impact events are shown over a 5 second time series. The dotted blue lines represent the calculated RMS values; the positive acceleration exceeds the RMS three distinct times, indicating 3 wave impact events.

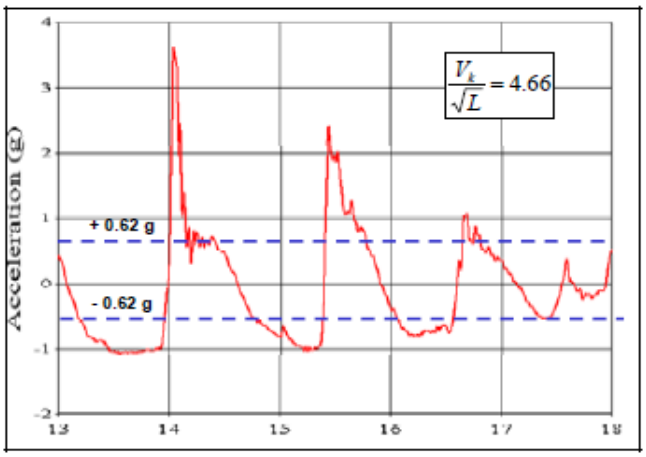

Figure 2.17 RMS acceleration for three wave impact events [11]

The average time period between wave impacts has been experimentally shown to be roughly 0.5 second or greater for speeds up to 60 knots [33]. Significant wave heights are usually greater than 0.5 meter. Since the majority of wave slam events will be greater than 0.5 second apart (wave encounter frequency of 2 Hz of less), a 0.5 second minimum distance between peaks can be used without missing separate wave events. In Figure 2.17, without these criteria, multiple wave impacts would be recorded for the first and third impact events.

Acceleration values used in a shock environment are often the averages of the 1/3rd, 1/10th, and 100th peak accelerations. The average of the one-third highest accelerations is computed using the following equation, where Ai represent the individual acceleration peaks taken from an acceleration time history sorted so the largest amplitude has i = 1 and the lowest has i = N/3, and N is the number of peaks.

$$A_{1/100} = \left(\frac{1}{N/3}\right)\sum_{i=1}^{N/3} A_i \text{ [34]}$$

2.5.4 Crest Factor Analysis

There has long been a general impression that when a vibration profile contains occasional bumps, the discomfort it produces may not be well predicted by an RMS average of the vibration magnitude [26]. Crest factor is the ratio of two magnitudes, and thus it gives no information as to the discomfort of the vibration. The crest factor is defined as the ratio of the peak and the RMS acceleration, as shown in the following formula:

$$CF = \frac{a_{peak}}{RMS} \text{ [12]}$$

Crest factor is the ratio of two magnitudes, and thus it gives no information as to the discomfort of the vibration. The crest factor is often over influenced by a single peak in the motion, thus in itself is an unsatisfactory measure of vibration. Determining the crest factor of a data set is a method of determining the type of acceleration environment. A higher crest factor does not indicate a rougher environment; however, it may indicate the presence of shocks, and may cause a modification to be made in the type of analysis that is being used for the data. A crest factor of one indicates a single square wave over a longer period of time. A crest factor equal to a square root of two indicates pure sinusoidal vibration.

2.5.5 Impact Count Analysis

Impact count analysis provides a representation of the number of impact spikes in the data as a histogram. The method for determining the peaks in the data is the same as the method for determining the $1/3^{rd}$, $1/10^{th}$, and $1/100^{th}$ highest peaks as detailed in Section 2.5.3. Using this type of analysis, the number of peaks at a given acceleration level can be compared for different sensors during a single test or between different tests for the same sensor, to see if the shape of the curve formed by the histogram is consistent throughout the comparisons.

2.5.6 Filtered Acceleration Analysis

To better understand a vessel's global response to the wave environment, it is recommended that the acceleration data be passed through a 10 Hz low pass filter and then compared with the unfiltered data. It is recommended that the filter be set up in accordance with marine standards [35]. Research has shown that filtering with a 10 Hz low-pass cutoff frequency for planing craft sufficiently removes local vibrations without severely effecting rigid body peak amplitudes. [34] The wave encounter frequency has been showed to be less than 2 Hz; it has also been shown that structural vibrations for craft are on the order of 20 Hz or greater [34]. The structural vibrations are low amplitude vibrations; however, they add significantly to the response shown in the accelerometer data. A comparison can be drawn between the filtered and the unfiltered data. More specifically, the peak, RMS and RMQ values can be compared to see the level of reduction in the acceleration due to the filter. A high level of reduction may indicate local vibrations near the sensor and/or high frequency vibration, most likely transmitted from the propulsion units. These types of accelerations are less relevant to studying the dynamics of craft motion, although localized accelerations are still important for other types of analysis.

2.5.7 Fast Fourier Transforms

In addition to computing acceleration values relative to the magnitude of the data, it is also useful to know the frequency content of the acceleration signal. The frequency content of the data contains useful properties to understanding marine vessels such as:

- The natural frequencies of the system
- The forced driving frequency of the input
- Frequencies of engine vibration (changing with engine speed)
- Medium-frequency structural vibrations
- High-frequency local vibrations

Two methods of analyzing the frequency content of an acceleration signal are a Fast Fourier Transform (FFT) and a Power Spectral Density (PSD) analysis. Both types of analysis use similar techniques and are considered applicable for acceleration and displacement data.

2.5.7.1 Fast Fourier Transforms

The Fourier transform is a fundamental component of many frequency analysis methods. A Fast Fourier Transform (FFT) is a technique for distilling a function into a series of component parts representing the content of the signal at a certain frequency. A Fast Fourier Transform is capable of transforming a signal from the time domain into the frequency domain. One problem with using FFT's for human vibration analysis comes from a characteristics of FFTs where a greater duration time signal results in a narrower frequency resolution. With vibration measurements at a minimum lasting several minutes, this makes an FFT less ideal. Despite this, FFT analysis is highly useful for interpreting vehicle sensor data [36].

2.5.7.2 Power Spectral Density

Power Spectral Density (PSD) is one of the most common techniques for analyzing the frequency content of signals for human vibration applications as it is ideally suited for the analysis of random signal types. It generates a measure of the energy contained within a frequency band. Power Spectral Density splits up the original signal into shorter segments and calculates the FFT for each section. The length of each individual segment is selected such that the FFT generates an appropriate frequency resolution. The units of Power Spectral Density are $m/\left(s^2 * Hz\right)$ [36].

2.5.8 Ride Quality Index

"When marine vehicle motions include shocks or impulsive velocity change, then RMS acceleration values have no relation to crew comfort or the potential for injury for crest factors (peak acceleration to RMS ratio) greater than three [12]."

A technique specifically developed for comparing marine environments is the Ride Quality Index. Ride Quality Index is a method for relating statistical acceleration levels from single-wave events or cumulative wave impacts to indicate potential damage to ship components or the ride quality for passengers. Ride Quality Index compares two conditions in a shock environment in the marine domain. The following section describes the methodology for computing Ride Quality Index.

2.5.8.1 Procedure for Calculating Ride Quality Index

Despite RMS acceleration having little impact on ride quality, it can still be used when looking at time-series data to identify wave impact events. The peaks from the data need to be calculated as in Section 2.5.3. Filtering with a 10 Hz low-pass cutoff frequency for planing craft sufficiently removes local vibrations without severely effecting rigid body peak amplitudes [34]. The Ride Quality Index formula shows that a ride with lower peak accelerations, as well as fewer high acceleration slams can be characterized as an improved ride. Figure 2.18 shows a flowchart for conducting a Ride Quality Index analysis. The Ride Quality Index for one condition relative to the other is defined by the formula below:

$$RQI_{2-1} = 1 - \frac{A_2}{A_1} \quad [11]$$

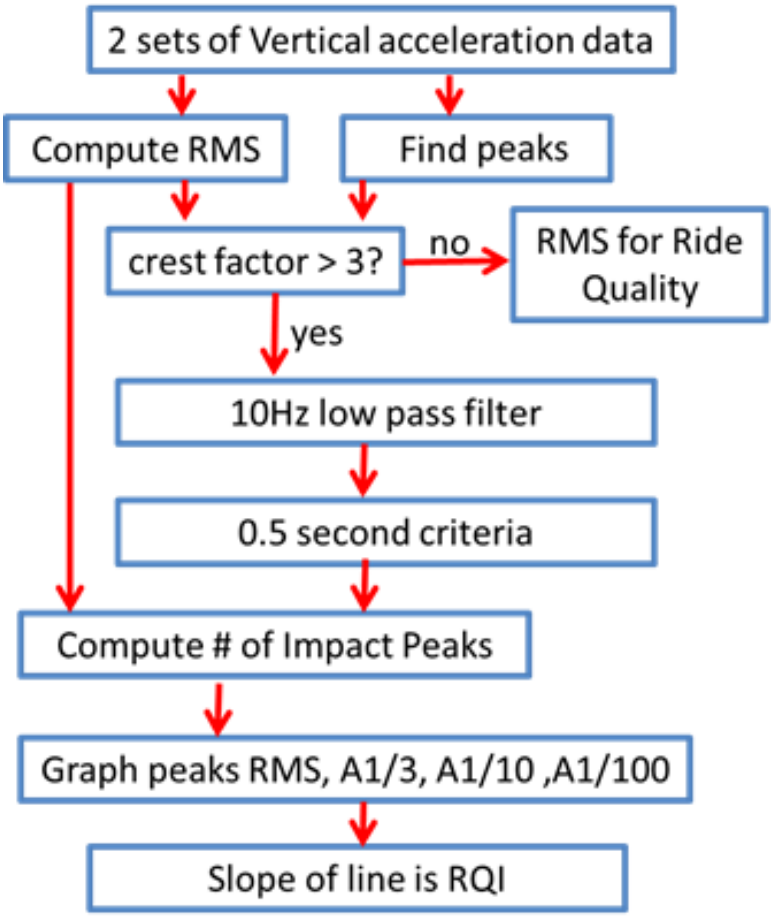

Figure 2.18 Ride Quality Index flowchart

In qualitative terms, the Ride Quality Index between two conditions can be defined as the percentage improvement or detriment between the two conditions. Positive values of RQI indicate better relative ride quality; the larger the number, the better the relative ride quality. Larger numbers indicate lower damage potential as well. Table 2.5 shows example calculations of RQI between two data sets [11].

Table 2.5 Example Ride Quality Index computations [11]

Test	Condition 1	Condition 2	Ride Quality Index
A 1/100	5.31g	3.50g	0.34
A 1/10	3.48g	2.82g	0.19
A 1/3	2.41g	1.87g	0.24
RMS	0.62g	0.54g	0.13
1-Slope	N/A	N/A	0.29

For most applications a quantitative measure of ride quality is desired for relating the passenger comfort between two relative conditions. Ride quality can be compared either between two vessels in the same conditions, between the same vessel with different configurations, or between different locations on the same vessel such as near the ride quality near the bow vs. near the stern. Figure 2.19 shows and example plot for a computed Ride Quality Index between two conditions. In this example condition II is showing a better ride quality index than condition I.

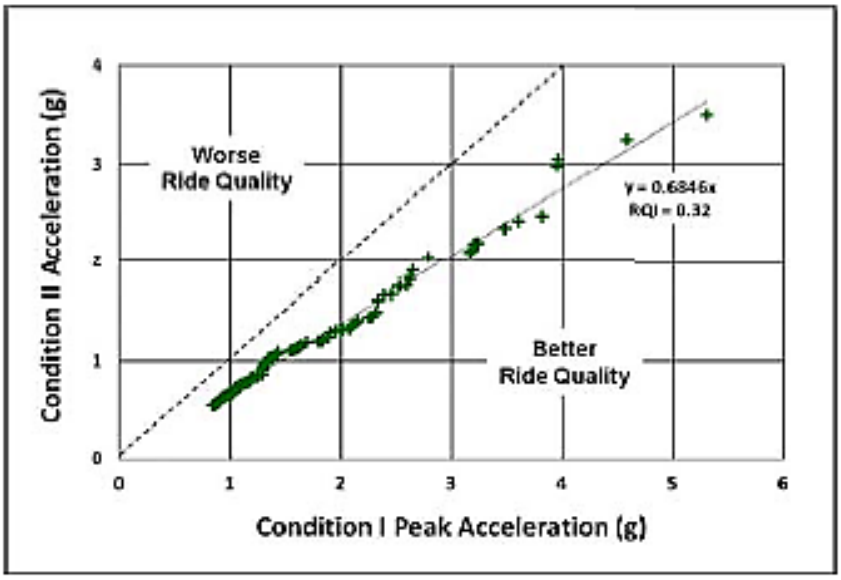

Figure 2.19 Ride Quality Index example comparison plot [11]

2.5.9 Suspension Analysis Methods

Not common in marine vessels, vehicles with suspension systems require an additional set of tools for analyzing the suspension data. However, many of the methods are the same as or similar to the methods for accelerometer data. Maximum and minimum displacement values are important to know, as well as their proximities to the limits of suspension travel to see the available capacity in the suspension before hitting the ends stops. RMS displacement can be used to characterize how the suspension travel is used during different tests. The frequency content of motion is highly important and can be used to determine the suspension's natural frequency and the dominant input frequencies. Determining damping ratios and using histograms of the damper's velocity are important as well. Bias in histogram peaks may indicate different ratios of compression and rebound damping in the suspension.

2.6 Whole-Body Vibration Standards

Whole-Body Vibration occurs when the body is supported on a surface which is vibrating. Separate standards are available for hand-transmitted vibration from machinery. The position can be standing, sitting or lying, each with a slightly different response. This section will focus on Whole-Body Vibration standards developed based on a seated person.

Standardization of vibration limits comes from the desire to relate the operating conditions to a defined operating limit. The limit may itself be a moving target that is altered by vehicle configuration changes and changes in operating speeds over the same terrain. Various standards for assessing Whole-Body Vibration have been promulgated. The standards attempt to define simplistic methods for quantifying complex vibrating conditions. The current human vibration standards all require similar sequences for their execution. The current standards can most often be broken into two sections:

- Standard vibration evaluation procedure
- Vibration limits based on standards

Defining a procedure for evaluating vibration begins with the collection of acceleration data. The International Organization for Standardization (ISO) has defined an orthogonal coordinate system, shown in Figure 2.20, for expressing the vibration magnitudes along different axes [26].

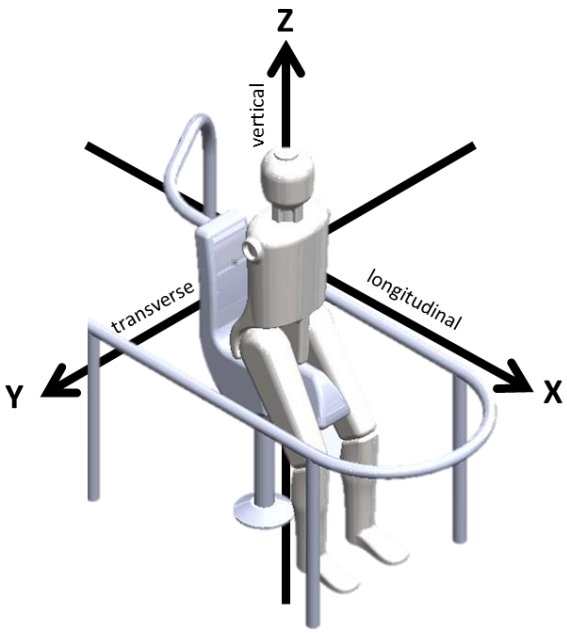

Figure 2.20 ISO coordinate system for mechanical vibration

2.6.1 Absorbed Power

The Absorbed Power method was developed to better understand oscillatory disturbances. Absorbed Power was first developed by the US Army Tank-Automotive Command (TACOM) in 1966 [23], and is the accepted measure of human tolerance to vibration for military vehicles negotiating rough terrain [37]. The principle objective of Absorbed Power was to develop a means of predicting the ride-limited speed of a vehicle, based on the vehicle's ride quality at different terrain roughnesses. This requires a measure to quantify the vehicular vibrations that were acceptable to human occupants. Pradko et al [23] describe the method by which a human being forms an impression to the vibration input as quasi-linear under the proper constraints and comparable to an elastic system, a system that can store and dissipate energy. The subjective response, however, is nonlinear and needs to be treated as such.

Absorbed Power is a measure of the rate at which energy is absorbed by a human subjected to ride vibration. Absorbed Power is a scalar-quantity that reflects the rate at which vibrational energy is absorbed by a typical human being. The advantage of absorbed power is that it has physical significance [23]. Absorbed Power places vibration severity on an absolute scale and is applicable in the time or frequency domain [23].

From years of testing a variety of vehicles at different speeds over different terrains, an upper limit of 6 watts of Absorbed Power was chosen as the limit for determining the ride-limited speed. Beyond a limit of 6 watts, the vehicle occupant can do little but hold tight. When drivers are instructed to drive as they see fit yet maintain good speeds, they rarely drive at vibration levels exceeding 6 watts other than during surprises or unexpected encounters. Drivers have been seen to tolerate 20 watts for periods up to 12 minutes in extreme conditions. In one documented test, the vehicle tests produced 24 watts for less than 1 minute. However, the driver could not tolerate the ride again, and refused to repeat the test. Absorbed Power is a nonlinear quantity, the level of absorbed power has been observed to increase tenfold when the acceleration levels were tripled [38].

2.6.1.1 Procedure for Calculating Absorbed Power

The procedure for calculating Absorbed Power begins with collecting triaxial acceleration data at the seat of the vehicle and conditions being analyzed. The data is preferably collected with a seat pad accelerometer or a triaxial accelerometer in close proximity to the seat. The data then needs to be converted into the frequency content of the signal according to the standards. A flowchart for calculating Absorbed Power is shown in Figure 2.21.

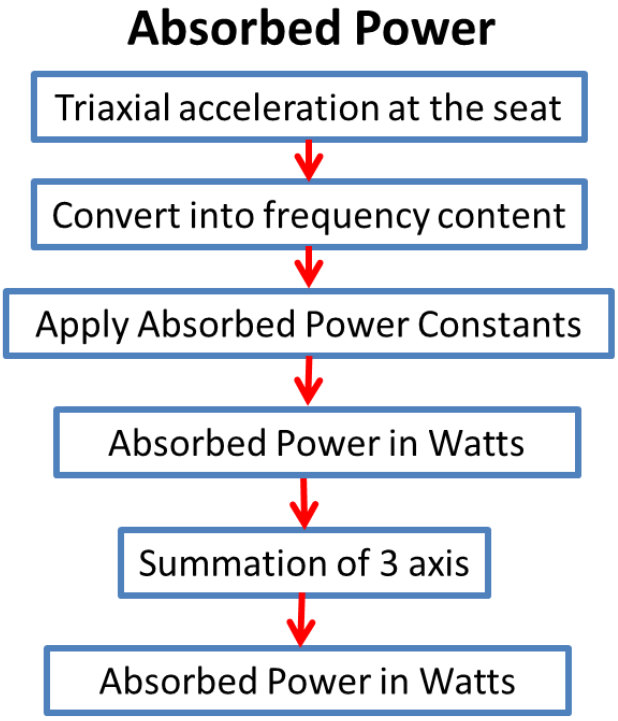

Figure 2.21 Flowchart for calculating Absorbed Power

The equations for calculating Absorbed Power for a particular axis are as follows:

$$P = \sum_{1}^{n} (C_i) A_i^{\,2} \text{ [37]}$$

Where:

P = Absorbed power in Watts

A_i = RMS acceleration (units $ft/\sec^2$) within the i^{th} spectral band

$C_i = K_1 K_0 \left(F_1 F_4 - F_2 F_3\right) / \left(F_3^2 + W_i^2 F_4^2\right)$

W_i = Frequency (units radians/second)

f_i = center frequency of the i^{th} spectral band

F and K constants calculated from Table 2.6.

Table 2.6 F and K values for Absorbed Power calculations [37]

	Vertical	Longitudinal	Transverse
K0	4.357	4.3532	4.353
K1	1.356	1.356	1.356
Wi	2*pi*fi	2*pi*fi	2*pi*fi
F1	$-0.10245*10^{-9}*Wi^6+0.17583*10^{-5}*Wi^4-0.44601*10^{-2}*Wi^2+1$	1.0	$0.24052124*10^{-3}*Wi^4-0.066974483*Wi^2+1$
F2	$0.12882*10^{-7}*Wi^4-0.93394*10^{-4}*Wi^2+0.10543$	0.219106	$0.57384538*10^{-5}*Wi^4-0.50170413*10^{-2}*Wi^2+0.33092592$
F3	$-0.45416*10^{-9}*Wi^6+0.37667*10^{-5}*Wi^4-0.56104*10^{-2}*Wi^2+1$	$0.0185309*Wi^2+1$	$-0.14979958*10^{5}*Wi^6+0.0010088882*Wi^4-0.10108617*Wi^2+11+1$
F4	$-0.21179*10^{-11}*Wi^6+0.51728*10^{-7}*Wi^4-0.17947*10^{-3}*Wi^2+0.10543$	$0.00061893*Wi^2+0.219106$	$-0.1713749*10^{-7}*Wi^6+0.53137351*10^{-4}*Wi^4-0.011096507*Wi^2+0.33092592$

Figure 2.22 shows three curves, each of the curves represents the RMS acceleration by a sinusoidal signal of a single frequency that would correspond to 6 watts of Absorbed Power. The longitudinal and transverse axes reach the 6 watt limit at their most sensitive frequencies at lower RMS acceleration levels than does the vertical axis. Longitudinal and transverse accelerations are shown to be particularly important for frequencies of less than 3 Hz.

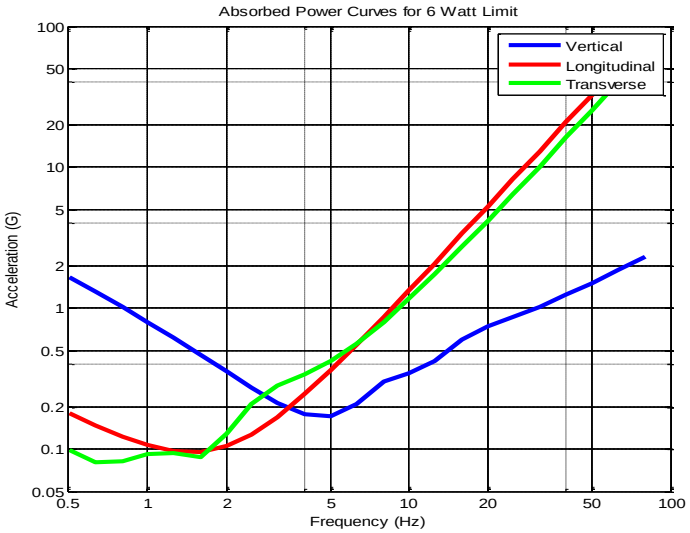

Figure 2.22 RMS acceleration curves for a constant 6 watts of Absorbed Power in each axis

It can be seen from Figure 2.22 that for Absorbed Power the body is most sensitive to the following frequency ranges:

- Vertical Acceleration: 4-8 Hz
- Longitudinal Acceleration: 1-2 Hz
- Transverse Acceleration: 0.5-1.5 Hz

2.6.2 ISO 2631-1 Frequency Weighted Acceleration

The use of frequency-weighted RMS acceleration as a standard for evaluation of Whole-Body Vibration was developed by the International Organization for Standardization (ISO) starting in 1974. The ISO standard defines numerical limits for exposure to vibrations in terms of weighted RMS accelerations in the frequency range of 0.5 to 80 Hz. There are three levels for exposure, in order of increasing severity:

- Reduced comfort boundary
- Fatigue-decreased proficiency boundary
- Exposure limit boundary

The ISO limits are based on sinusoidal acceleration, as a function of frequency and exposure time. The standard also states that frequencies between 4-15 Hz are the most important regarding injury in humans. Daily exposure limits are determined from weighted accelerations with scaling factors depending on the axis. The crest factor is used to determine whether or not the evaluation method is applicable to the particular acceleration environment. When crest factors are below or equal to 9 the evaluation method is considered valid.

2.6.2.1 Procedure for Calculating ISO 2631-1 Weighted RMS Acceleration

The weighted RMS acceleration is often computed separately in 1/3 octave band increments, and each band is evaluated to see the frequency content of the acceleration signal. To see the contributions, ISO 2631-1 specifies the center frequencies of the one-third octave frequency bands, as well as the upper and lower frequencies for each of the bands. ISO 2631-1 also specifies weighting values for each frequency band. The weighting values are multiplied by the RMS acceleration in each band and then the weighted RMS values are squared and summed over the entire frequency range. The square root of that value is the weighted RMS acceleration. A flowchart for calculating the weighted RMS acceleration as outlined in ISO 2631-1 is outlined in Figure 2.23. The equations for calculating the weighted RMS acceleration as per ISO-2631-1 for a particular axis is below, where aw(t) is the weighted acceleration as a function of time in m/s^2, and T is the duration of the test in seconds.

$$a_w = \left[\frac{1}{T} \int_0^T a_w^2(t) dt \right]^{\frac{1}{2}} \quad [13]$$

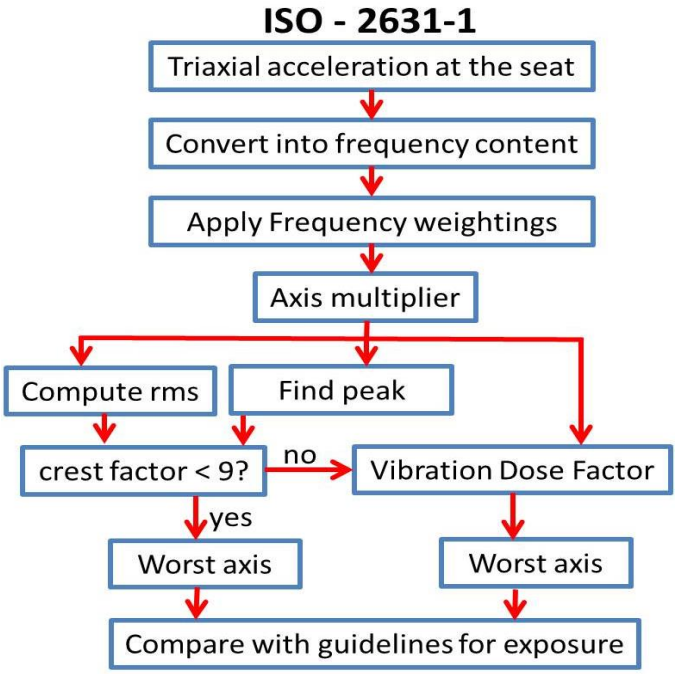

Figure 2.23 Flowchart for calculating weighted RMS acceleration per ISO-2631-1

The ISO acceleration for multiple axes is then taken as the worst of the three axes for purposes of determining comfort and fatigue boundaries. Figure 2.24 shows two curves representing the weighting factors to be applied to the acceleration bands as a function of frequency. It can be seen that for ISO 2631-1, the body is most sensitive to the following frequency ranges:

- Vertical Acceleration: 4-8 Hz
- Longitudinal/transverse Acceleration: 1-2 Hz

The values used for generating the curves are listed in Table 2.7.

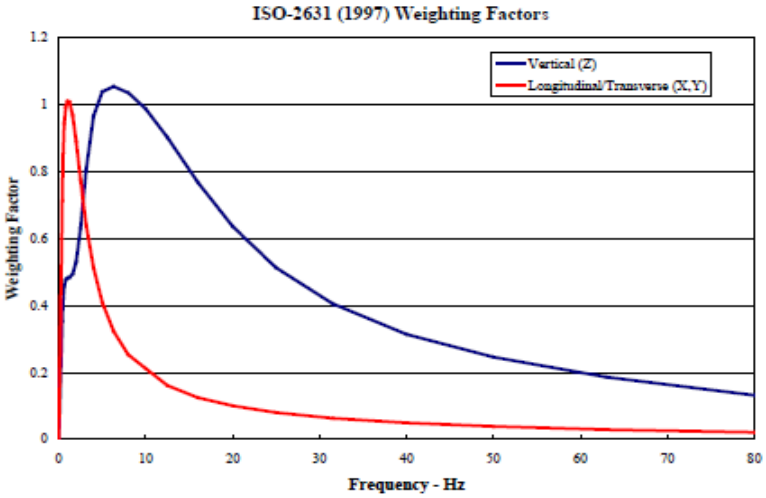

Figure 2.24 ISO-2631-1 weighting curves [37]

Table 2.7 ISO 2631-1 weighting factors [13]

1/3rd Octave Center Frequency (Hz)	Longitudinal/ Transverse Weighting Factor	Vertical Weighting Factor	1/3rd Octave Center Frequency (Hz)	Longitudinal/ Transverse Weighting Factor	Vertical Weighting Factor
0.2	0.243	0.121	5.0	0.409	1.039
0.25	0.365	0.182	6.3	0.323	1.054
0.315	0.530	0.263	8.0	0.253	1.036
0.4	0.713	0.352	10.0	0.212	0.988
0.5	0.853	0.418	12.5	0.161	0.902
0.63	0.944	0.459	16.0	0.125	0.768
0.8	0.992	0.477	20.0	0.100	0.636
1.0	1.011	0.482	25.0	0.080	0.513
1.25	1.008	0.484	31.5	0.0632	0.405
1.6	0.968	0.494	40.0	0.0494	0.314
2.0	0.890	0.531	50.0	0.0388	0.246
2.5	0.776	0.631	63.0	0.0295	0.186
3.15	0.642	0.804	80.0	0.0211	0.132
4.0	0.512	0.967			

2.6.2.2 Procedure for use of Calculated ISO 2631-1 Acceleration

With values for weighted acceleration calculated, vibration exposure limits are determined for the weighted acceleration of each axis independently. Daily exposure limits are determined from weighted accelerations with scaling factors depending on the axis. The ISO standard originally stated that the worst axis is used for computing the limits. However, other sources have begun using the vector sum of the axis if the weighted accelerations from two or more axis are comparable, and the standard has been revised to include this change. For comparing the different axis, a weighting factor is used to compare the longitudinal, transverse, and vertical accelerations. The weighting factors for comparing different axes are listed in Table 2.8.

Table 2.8 Weighting factors for axis comparison [13]

Axis	Weighting Factor
X, Y	1.4
Z	1.0

With the weighting factors applied, a basic comfort condition can be defined based on Table 2.9 below. There is some overlap between the defined comfort regions; it is up to the person analyzing the data or the person experiencing the vibration to determine which is the proper region, as there is some leeway for interpretation.

Table 2.9 ISO 2631-1 comfort reaction guidelines [13]

Vibration Value (m/s^2)	Comfort reaction
< 0.315	Not uncomfortable
0.315 - 0.63	A little uncomfortable
0.5 – 1.0	fairly uncomfortable
0.8 – 1.6	uncomfortable
1.25 – 2.5	Very uncomfortable
>2.5	Extremely uncomfortable

Two health guidance caution zones are listed as part of ISO 2631-1 to assist with interpreting the weighted RMS acceleration. For exposures below the zone, health effects have not been clearly documented and/or objectively observed; in the zone, caution with respect to potential health risks is indicated and above the zone health risks are likely [36].

It is well documented that dissatisfaction with ride increases with time. The health guidelines are based on the chart shown in Figure 2.25 [37], which compares weighted acceleration values and exposure time. There are two distinct regions of the figure. The first region is a horizontal line indicating the limits for short term exposure. The line in the second region is sloped, indicating a region where the exposure limits change due to fatigue. The scientific basis for the time dependency is undocumented, although it has been supported by the studies of Simic 1974 and Miwa et al 1973 [26].

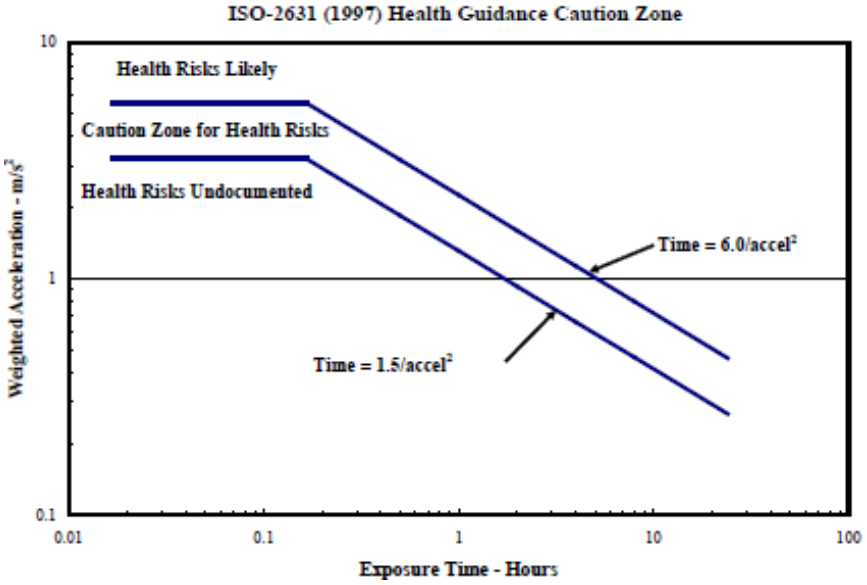

Figure 2.25 ISO 2631-1 exposure limit guidelines [37]

2.6.3 Comparison of ISO-2631-1 and Absorbed Power Methods

When it comes to choosing between Absorbed Power and ISO 2631-1 for Whole-Body Vibration analysis, different entities have different preferences for which standard should be used. Within the United States, the Army uses the Absorbed Power method, while the Navy prefers ISO weighted acceleration [39]. In general, Absorbed Power is a standard more specific to the United States while ISO 2631-1 is used both worldwide and in the Unites States. Both standards agree that unweighted root-mean square should not be considered as a measure of human vibration intensity in all but the most expedient circumstances [39].

2.6.3.1 Relative Merits of the Standards

The methods for quantifying acceleration come from very different schools of thought, however, they both produce similar results. Both standards have also been the subject of considerable research over the years. Revalidation of ISO 2631-1 by independent parties has shown good agreement with the results, except for an underestimation of the frequency weighted vibrations in the lateral direction above 1.6 Hz [38]. This is in the frequency range most critical to humans.

2.6.3.2 Similarities:

- Both models are based on filtering accelerations into weighted frequency bins
- Very similar spectral characteristics
- Use frequency weighted accelerations coupled with human sensitivity to arrive at a single number describing the vibration intensity.

2.6.3.3 Differences:

- Three orthogonal directions are summed to get total Absorbed Power.
- For ISO, each axis measured separately and then vectorially summed or worst-axis limited
- ISO 2631-1 doesn't differentiate between longitudinal and transverse weighting factors

2.6.3.4 Level of ISO Acceleration Corresponding to Six Watts of Absorbed Power

A study comparing the numeric generated by the two standards has come up with the following equation as a best fit equation relating absorbed power to ISO 2631-1 [39]. The equation was derived based on coefficients for the vertical direction.

$$ABS\_PWR = 1.19(ISO)^{2.205} \text{ [39]}$$

For there to be 6 watts of Absorbed Power, the level of the ISO acceleration would have to be:

$$6 = 1.19(ISO)^{2.205} \rightarrow \left(\frac{6}{1.19}\right)^{\frac{1}{2.205}} = ISO = 5.042^{0.4535} \rightarrow ISO = 2.1\frac{m}{\sec^2} \text{ [39]}$$

Thus, ~$2.1\, m/\sec^2$ weighted acceleration is equal to 6 watts of Absorbed Power, depending on the frequency content of the signal. Based on the limit guidelines, a 6 watt limit could be maintained by the ISO standard for up to two hours, depending on the frequency content. 12 watts was shown to be tolerable for less than 25 minutes [39].

2.6.4 Transient Methods for Whole-Body Vibration

In some cases, the basic method for evaluation defined by ISO 2631-1 may underestimate the effects of vibration, due to: high crest factors, occasional shocks, and transient vibration. In these cases, an alternate technique should be used, such as the Running RMS method or the fourth power vibration dose method, which accounts for shocks and transient vibrations.

2.6.4.1 Running RMS method

The running RMS method of evaluation takes into account occasional shocks as well as transient vibrations via the use of a short integration time constant (a 1 second window is common). The running RMS method, otherwise known as the Maximum Transient Vibration Value (MTVV), is defined by the following equation where aw(t) is the instantaneous frequency weighted acceleration as per ISO 2631-1 and tau is the window length. [37]

$$MTVV = a_w(t_0) = \left[\frac{1}{\tau}\int_{t_0-\tau}^{t_0}[a_w(t)]^2\,dt\right]^{\frac{1}{2}} \text{ [37]}$$

2.6.4.2 Vibration Dose Value

The fourth power vibration dose method, also known as the Vibration Dose Value, is more sensitive because it uses the fourth power instead of the second power for averaging the acceleration time history. The units for the Vibration Dose Value (VDV) are meters per second to the power of 1.75. The equation for calculating the Vibration Dose Value is shown below, where aw(t) is the instantaneous frequency weighted and T is the duration of the test [24]. The prescribed limit for the vibration dose value is 15 $m/s^{1.75}$.

$$VDV = \left[\int_0^T [a_w(t)]^4\,dt\right]^{\frac{1}{4}} \text{ [24]}$$

An example comparing a raw acceleration value to the computed RMS and Vibration Dose Value versus time is shown in Figure 2.26. The figure shows how Vibration Dose Value accumulates over time, and is more sensitive to the spikes in the acceleration data than is the RMS value.

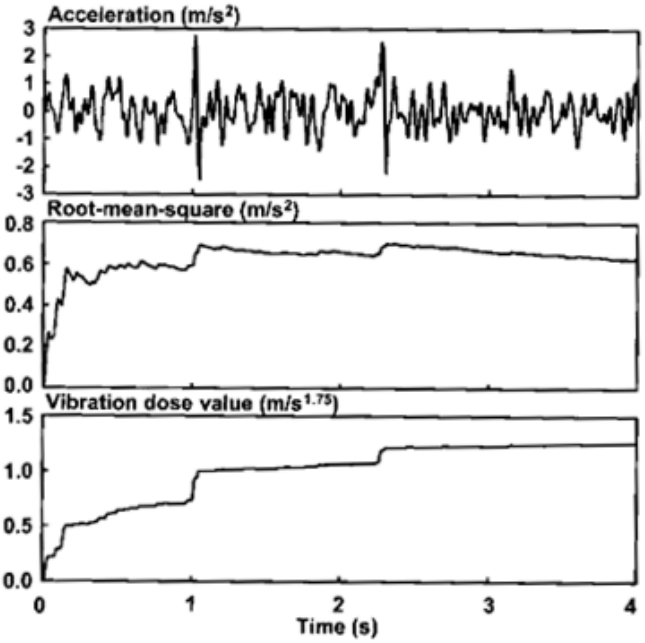

Figure 2.26 Comparison of raw acceleration data, RMS, and Vibration Dose Value [36]

2.6.5 Other Standards for Whole-Body Vibration Analysis

The previous sections contain most of the current relevant standards for Whole-Body Vibration analysis. However, there are other variations of the standards that are relevant to the discussion of Whole-Body Vibration. A few of the other standards are overviewed in this section.

2.6.5.1 ISO 2631-5 Analysis for Multiple Shocks

The ISO 2631-5 standard is to be used where crest factors exceed 9, or where vibration is most stochastic and transient rather than sinusoidal and repeatable. The ISO 2631-5 standard focuses on the lumbar spine response to Whole-Body Vibration. The standard is pertinent to the marine environment because it handles multiple shocks; however, the standard isn't as established within the Human Factors community, and the related models have not been epidemiologically validated [37]. Also, studies correlating the validity of ISO 2631-5 are far fewer than for ISO 2631-1.

2.6.5.2 Marine-Modified Weighted RMS Acceleration

The Boeing Marine Systems Division has published a modification made to the IS0 2631-1 method for correlating quantitative measurements with subjective ride quality assessments in the marine environment. However, the paper is not widely used or considered a standard for the marine environment. According to the paper, marine vehicles have ride properties dominated by low frequency random motions with most of the energy occurring below 1 Hz. Motion and acceleration can be characterized in statistical terms, that change with operating conditions such as sea state, speed, and heading. The paper cites a similar equation to ISO 2631-1 with the following equation for frequency weighted accelerations. Figure 2.27 shows the proposed modified weighted curves of the ISO 2631-1 standard [40].

$$FWRMS = \left[\sum_{n=1}^{N} \left(rms_{1/3}\right)^2 \left(F\omega_n\right)^2\right]^{\frac{1}{2}} \quad [40]$$

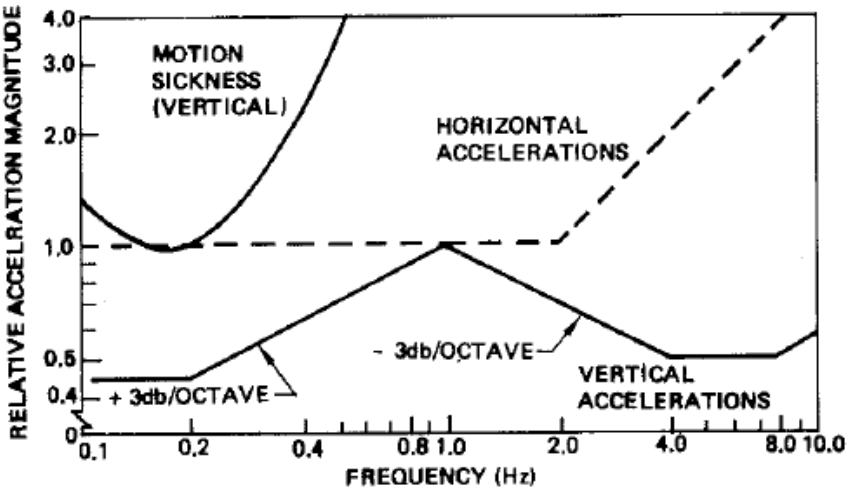

Figure 2.27 Marine-modified ride quality characterization [40]

The group also notes that ride quality of marine vehicles is dominated by vertical and horizontal accelerations. Test subjects have been found to find random vibration more uncomfortable than sinusoidal vibration. Angular motions are secondary, and accelerations are random in nature often from 0-5 Hz, mostly below 1 Hz. For frequencies above 1 Hz, ISO 2631-1 should be used. Below 1 Hz, the ISO standard should be modified based on Shoenberger (1975), Miwa (1972), and Shoenberger (1978) [40].

2.6.5.3 British Standards Institute BS 6841

The British Standards Institute BS 6841 describes multiple approaches for evaluating a human's exposure to a vibration environment. The portion of the standard related to Whole-Body Vibration is only slightly different from ISO 2631-1. The two standards are similar in that they both used weighted RMS acceleration to account for differences in discomfort at different frequencies and in different axes, although the exact weightings vary. BS 6841 is a more all-encompassing set of standards that also explicitly considers health, hand controls, vision, discomfort, motion perception and motion sickness as separate problems, suggesting quantitative limits for each type of problem [21]. Different procedures are described for estimating these parameters. A comparison of the weighting factors for BS 6841 and ISO 2631-1 is shown in Figure 2.28.

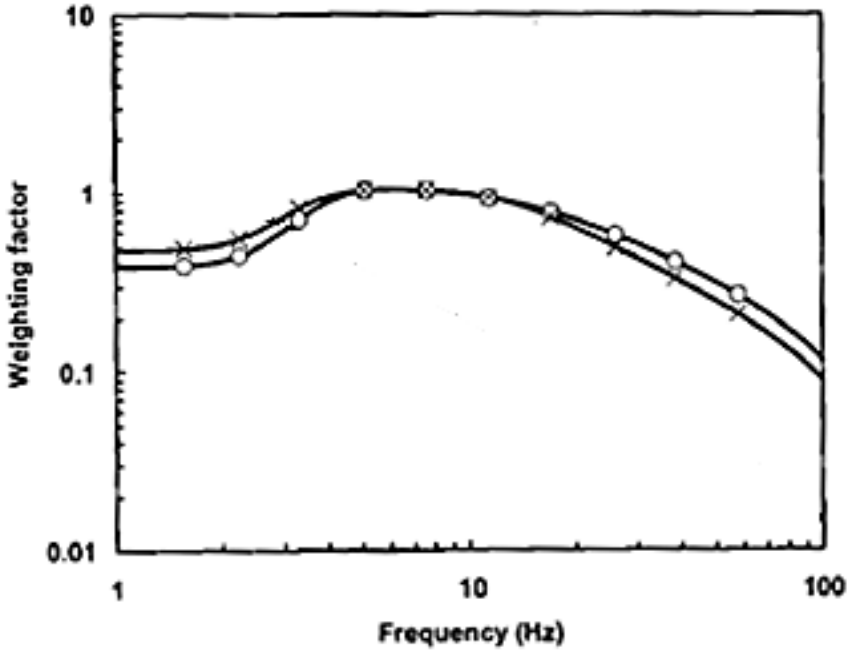

Figure 2.28 Weighting factor comparison (ISO = x, BS 6841 = o) [24]

Chapter 3 Parametric Modeling of the 100-ft WAM-V Proteus

The following chapter provides a discussion of the research towards the modeling of marine vessels equipped with suspension systems made through modeling of the 100-ft WAM-V technology demonstrator 'Proteus.' A chronology of WAM-V development is presented, along with a sample suspension study with the Proteus using a custom multi-body dynamics simulation environment. Finally, the results are used to make recommendations for improvements toward improving the modeling efforts detailed in later chapters.

3.1 Chapter Overview

- Section 3.1 provides an overview of the chapter.
- Section 3.2 gives an introduction to Wave-Adaptive Modular Vessels.
- Section 3.3 discusses the history of WAM-V development.
- Section 3.4 overviews the history of WAM-V testing and evaluation programs.
- Section 3.5 provides a comparison of the properties of WAM-Vs against other catamarans.
- Section 3.6 overviews methods of creating a multi-body dynamics simulation environment.
- Section 3.7 provides the details of an initial parametric model based on the 100-ft WAM-V.
- Section 3.8 details an initial parametric study using the parametric model.
- Section 3.9 discusses the conclusions from the initial parametric analysis.

3.1.1 Significant Contributions

This chapter provides the first study into catamarans dynamics using a virtual 4-post rig for evaluation. The chapter also serves as an initial mapping of WAM-V characteristics compared against more conventional catamarans, giving insight into the unique properties of WAM-Vs and the challenges for WAM-V design.

3.2 Introduction to Wave-Adaptive Modular Vessels

Wave-Adaptive Modular Vessels (WAM-V) are a unique class of marine vehicles, far removed from conventional marine designs. Their design represents a fundamentally new approach to catamaran construction. Catamarans themselves are a common design alteration offering increased stability. Compared to mono-hull designs, catamarans often have a higher vertical center of gravity due to the need to have the superstructure raised above the waterline. However, the multi-hull design offers improved roll moment resisting geometry that often more than makes

up for center of gravity disadvantage. Unlike more conventional catamaran designs, the ultra-lightweight WAM-V designs feature low draft, inflatable hulls with no keel to provide a compliant interface between the vessel and the water surface. Each pontoon is connected to the superstructure via suspension linkages that allow for vertical motion of the pontoons. WAM-Vs have springs and a central spherical joint allowing the vessel to articulate to mitigate some of the wave-induced motion from being transmitted to the main cabin and crew. Figure 3.1 shows the 100-ft WAM-V prototype Proteus that will be the focus of this chapter. Table 3.1 outlines some of the key design information for the Proteus.

Figure 3.1 100-ft WAM-V 'Proteus' [41]

Table 3.1 Proteus design information [42]

Length:	100 ft
Beam:	50 ft
Hull Diameter:	4 ft
Tunnel Width:	42 ft
Displacement:	12 tonnes
Draft Fore:	8 in
Draft Aft:	16 in
Speed:	Up to 30 knots
Range:	5000 nautical miles

3.2.1 Proteus Architecture

The nomenclature used for the major components of the Proteus vessel is shown in Figure 3.2. The payload component of the Proteus is modular in design. Different payload modules can be loaded onto the superstructure for different applications. Figure 3.3 shows the payload module being lowered as part of the module changing process.

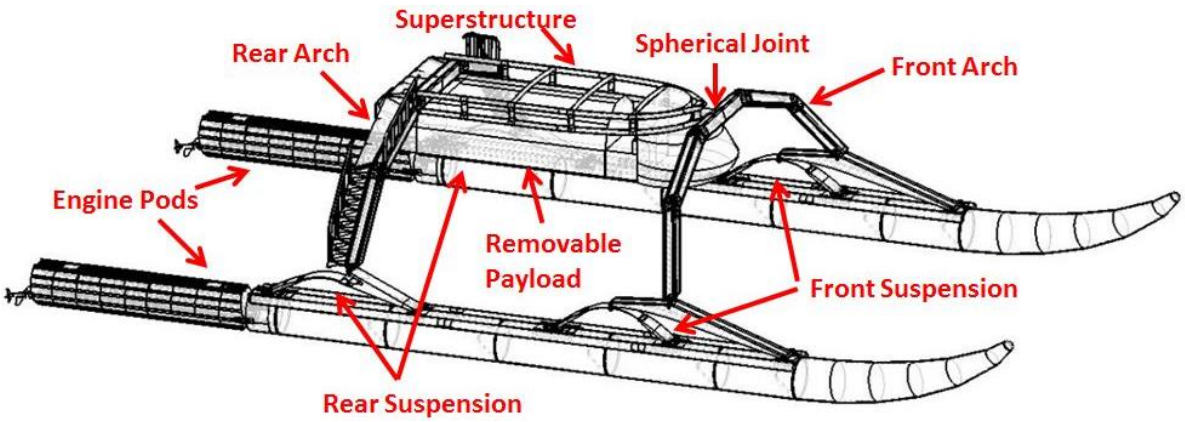

Figure 3.2 Proteus component diagram

Figure 3.3 Modular payload on Proteus [42]

3.2.2 Proteus Suspension System

The suspension linkages on the Proteus are composed of titanium leaf springs mounted on slider assemblies at the ends of each pontoon, connected together through rocker arm assemblies to the front and rear arches. For most of the testing no dedicated dampers were present on the Proteus, although provisions were made for a large off-road vehicle damper to be mounted on the outside of each rocker assembly. The front suspension system on the Proteus is shown in Figure 3.4 and the rear suspension system is shown in Figure 3.5. The rear suspension shown in Figure 3.5 was locked out for testing in an attempt to reduce unwanted resonance between the front and rear suspension systems.

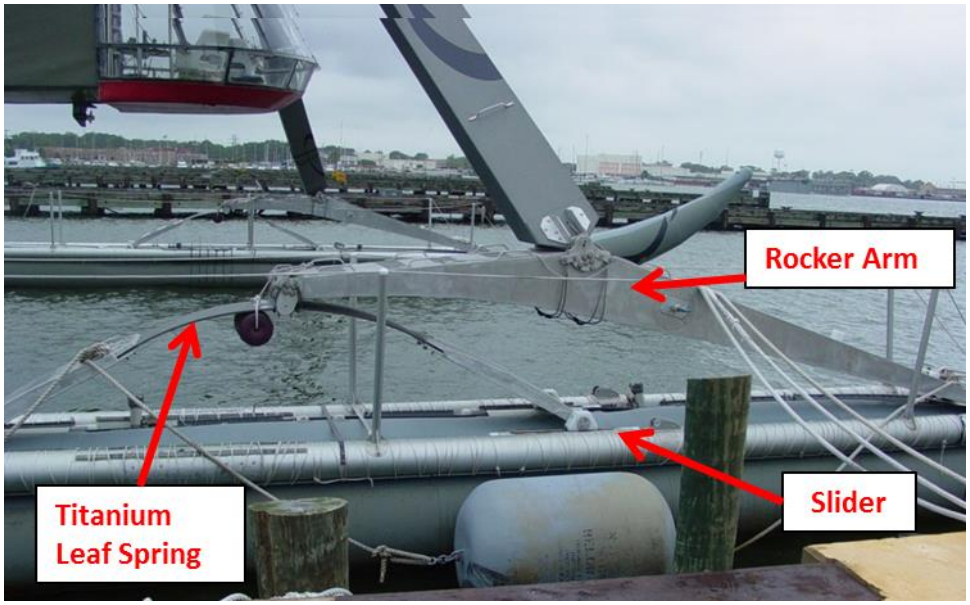

Figure 3.4 Front suspension system assembly

Figure 3.5 Rear suspension system assembly (shown locked out)

Between the front arch and the superstructure, a spherical joint is present to allow for an additional degree of freedom between the front arch and the superstructure. Shown in Figure 3.6, the entire front arch is able to rotate in relation to the superstructure to isolate the payload from the accelerations at the pontoons.

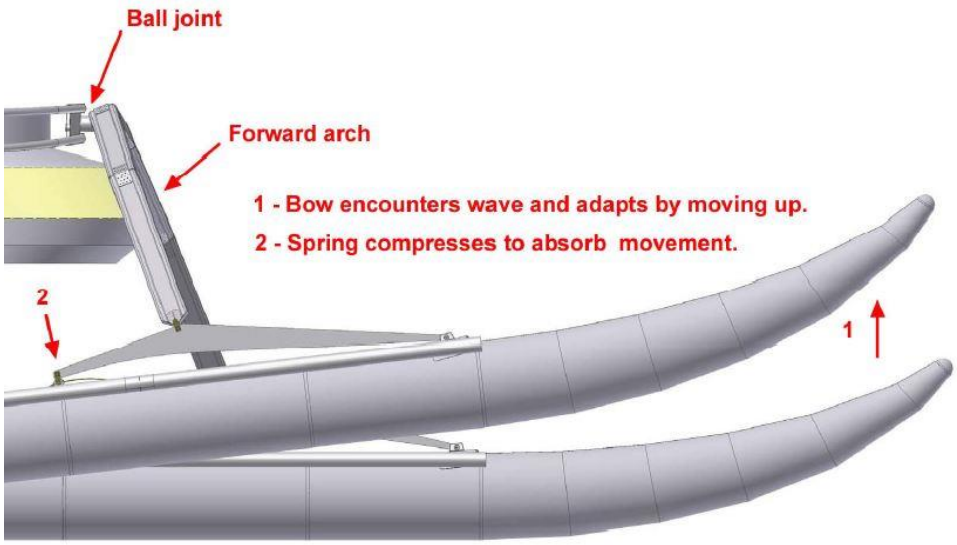

Figure 3.6 Front ball joint diagram [43]

3.2.3 Pontoons and Propulsion Systems

Each pontoon is an inflatable structure that also is able to hold fuel, giving the Proteus a theoretical operating range of 5000 nautical miles. The pontoons also act as an additional shock-absorbing medium, similar to the tires on an automobile. The Proteus maneuvers using differential steering with two engine pods located at the rear of the pontoons. The two engines are each located in separate pod assemblies connected to the rear of the pontoons. Due to its low draft and the high level of movement of the pontoons with respect to the chassis, the engine pods need to articulate to keep the propellers in the water. Each pod is on a hinge and is able to rotate with respect to the pontoon, keeping the propellers submerged when the pontoons are in motion. The engine pod and its hinge are shown in Figure 3.7.

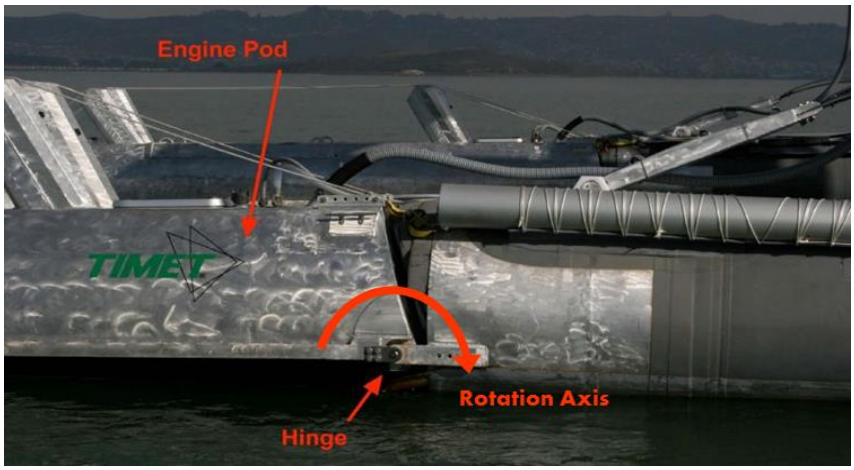

Figure 3.7 Engine pod and engine pod hinge [41]

3.3 History of WAM-V Development

The Wave-Adaptive Modular Vessels presented in this chapter are part of a development program carried out with Marine Advanced Research Inc. in San Francisco, CA. The developmental program has been an iterative process stemming from the idea that better seakeeping could be accomplished by 'moving and dancing' with the waves rather than fighting them [41]. Using this concept, a lightweight vessel with reduced stress loads could theoretically be designed that could outperform conventional ships of far greater displacement.

3.3.1 Early Concepts and Prototypes

The Proteus is not the first WAM-V to be designed by Marine Advanced Research. In order to establish the design principles that would be implemented on the Proteus, two initial prototypes were designed and built to refine the design concept. A 50-ft manned prototype was designed and tested as a first WAM-V iteration. This iteration proved unsuccessful as too many available degrees of freedom made it unstable. Figure 3.8 shows the 50-ft prototype underway.

Figure 3.8 50-ft WAM-V prototype [41]

The second design iteration came in the form of a simple 8-ft remote control prototype that was built to refine design layout and architecture for the Proteus. Figure 3.9 shows the 8-ft prototype, which shares a nearly identical architecture with the 100-ft Proteus.

Figure 3.9 8-ft WAM-V prototype [41]

3.3.2 Proteus Research and Development Platform/ Technology Demonstrator

The 100-ft Proteus was designed as a technology demonstrator to show the future capabilities of WAM-V architecture. The focus of the Proteus design was not to achieve a design optimized for a particular purpose, but rather to provide a platform to showcase the new technology. The Proteus is the focus of this chapter and the parametric study in Section 3.8.

Figure 3.10 100-ft WAM-V prototype [42]

3.3.3 12-ft Unmanned Surface Vessel

After the Proteus, a second remote control WAM-V was designed and tested. The 12-ft unmanned surface vessel (USV) shown in Figure 3.11 has been instrumented, tested, and evaluated by the Center for Vehicle Systems and Safety at Virginia Tech. The instrumentation, testing, data analysis and modeling performed on the 12-ft USV are detailed in Chapter 4.

Figure 3.11 12-ft USV prototype

3.3.4 33-ft Foldable WAM-V Prototype

The final WAM-V design documented as part of this dissertation is a 33-ft WAM-V prototype shown in Figure 3.3.4, capable of manned or unmanned operation. This WAM-V is unique in that employs a foldable arch design, allowing it to achieve a much smaller storage footprint. The 33-ft WAM-V is the subject of Chapters 6-11 of this dissertation.

Figure 3.12 33-ft folding WAM-V prototype

The five WAM-V iterations are compared and contrasted in Table 3.2. The table provides an overview of the purpose of each of the prototypes as well as their ownership, suspension configuration, operation, and unique design features. Figure 3.13 and Figure 3.14 show top and side view size comparisons of the 3 WAM-V prototypes evaluated as part of this dissertation.

Table 3.2 Characteristics of different WAM-V designs

Craft:	Purpose:	Ownership:	Suspension configuration:	Operation:	Unique features:
50-ft prototype	Internal Research and Development Prototype	Marine Advanced Research Inc.	Multi-leg design	Operator onboard	Multi-legs
8-ft prototype	Internal Research and Development Prototype	Marine Advanced Research Inc.	4 corner, independent	Remote control	4 corner leaf springs
100-ft Proteus	Technology Demonstrator	Marine Advanced Research Inc.	4 corner, independent	Operator onboard	Changeable payload design
12-ft USV	Future Autonomous Platform	Office of Naval Research/ Florida Atlantic University	2 corner, front independent	Remote control	Rigid Skis over inflatable pontoons
33-ft WAM-V	Manned/ Unmanned Operation	Office of Naval Research /Virginia Tech	2 corner, front independent	Operator onboard via remote control	Folding arches

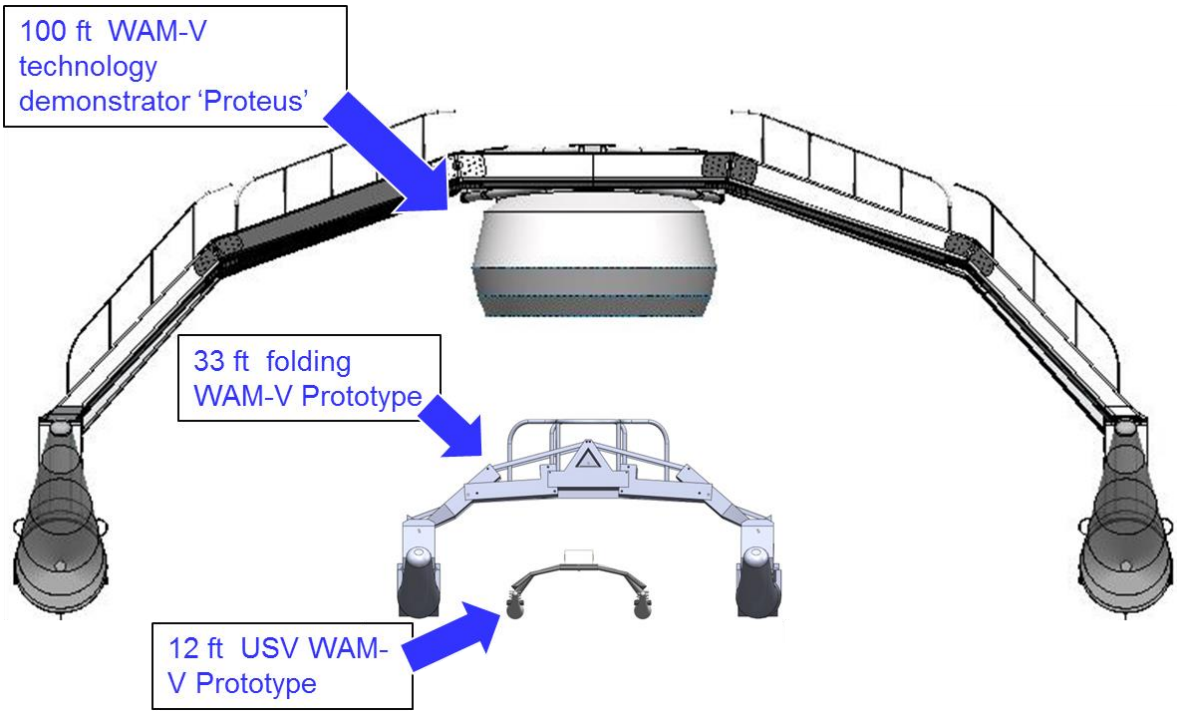

Figure 3.13 Front-view size comparison of three WAM-V prototypes

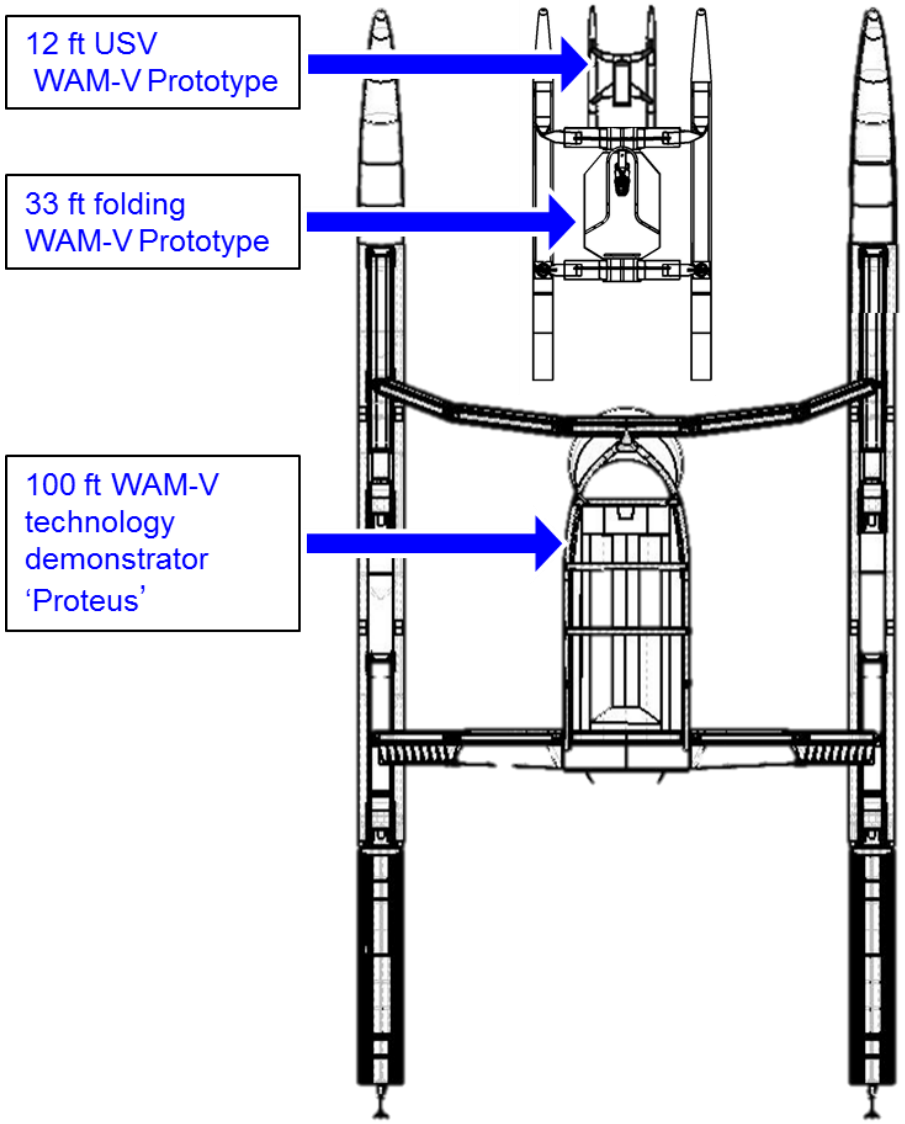

Figure 3.14 Top-view size comparison of three WAM-V prototypes

3.4 History of WAM-V Testing and Evaluation

The concept behind the creation of Wave-Adaptive Modular Vessel (WAM-V) technology began with an effort to extract the many advantages inherent to catamarans coupled with lightweight inflatables and shock mitigating suspension designs. Due to the relative youth of WAM-V technology, only one known study has been conducted outside of the CVeSS laboratory that is relevant to the suspension performance of WAM-Vs.

A technical memorandum was produced by NAVSEA at the Naval Amphibious Base, Little Creek in Virginia Beach, VA on the propulsion and seakeeping characteristics of the 100-ft Proteus vessel. The calm water propulsion tests conducted showed that the Proteus was capable

of a top speed of 23 knots and a range of 1340 nautical miles at top speed. The top speed was consistent for both empty and fully-ballasted loading scenarios.

The seakeeping trials, conducted following the calm water tests, produced the most relevant results for quantifying the WAM-V's performance. During the tests, the front suspension system was found to be highly prone to reaching its full compression and bottoming out during multiple wave impact events. The suspension bottoming out caused large vertical acceleration spikes to be transmitted to the superstructure. The reason such large suspension displacements were able to occur was due to the suspension's leaf spring design having a softening spring rate characteristic throughout its stroke. As the spring was compressed during an impact, the restoring force actually decreased throughout the stroke.

Acceleration spikes were highest when both front suspensions bottomed out simultaneously. The vertical accelerations recorded near the operator's position generally were maintained below 0.5g unless both front suspensions corners had bottomed out, in which case the recorded acceleration reached at maximum value of 1.28g. The acceleration data is consistent with the operator's subjective observations which indicated that strong acceleration variations were experienced throughout the trials. The entire study was conducted with the rear suspension locked out, due to excessive motion caused by a coupling between the frequencies of the front and rear suspension systems. Locking out the suspension was done prior to the study; to the author's knowledge no data is available for the WAM-V with a 4 corner suspension system.

3.4.1 Operator Observations from 100-ft WAM-V Testing

The Proteus vessel was initially instrumented and tested by NAVSEA; however, the data is not available for public release. Despite this limitation, prior to the modeling efforts many unusual observations were conveyed by the operators of the Proteus to help direct the focus of the study toward the unique issues of WAM-V designs they had experienced. The operators had many positive comments about the WAM-V's design. The three behaviors they identified as the most limiting to its performance were:

- A unique surging/swaying motion in the cabin
- Sharp changes in suspension performances in a sea state
- Low design life

Each observation is discussed further to improve the understanding of the WAM-V's design.

3.4.2 Surging/Swaying Motion Observation

The Proteus exhibits a unique surging motion in the superstructure when underway. The motion occurs in calm water; however, it is more dominant in an elevated sea state. During seakeeping trials surging and swaying motions were found to be the WAM-V's most apparent and undesirable ride characteristic. The motions are low in frequency but high in displacement amplitude. This is far different from the impact characteristics that dominate the perception of ride quality in more conventional crafts, as discussed in Chapter 2.

The primary reason for this motion is the rotation of the engine pods with respect to the pontoons. The rotation of the engine pods creates a change in the thrust vector of the WAM-V's propulsion systems which propagates throughout the entire structure. Stretching and contorting of the pontoons along the longitudinal axis further compounds this issue. The stretching of the pontoons has been solved in more recent WAM-Vs through a rigid ski on top of the inflatable pontoon, which constrains the front and rear suspension systems relative to each other longitudinally.

3.4.3 Suspension Performance in a Sea State

The Proteus is characterized as having the greatest area for improvement in the sea conditions where the largest vertical accelerations were recorded, in a head sea condition. This is also the heading where suspension improvements have the greatest influence. The original suspension design of the Proteus has a digressive spring rate, meaning that as the suspension moves through its travel from rebound to compression, the spring rate of the suspension actually decreases. This leads to excessive bottoming out when the springs are heavily loaded.

3.4.4 Low Design Life

The Proteus was designed primarily as a technology demonstrator to showcase the technology and lead the way for future WAM-V designs. As such its design was not heavily optimized and it developed numerous cracks and small structural failures that limited its ability to be tested in an elevated sea state. Most of these issues were improved upon/corrected in subsequent WAM-V iterations.

3.5 Comparison of WAM-V and Other Catamaran Designs

WAM-Vs clearly represent a large departure from traditional catamaran designs. Quantifying the WAM-V's potential place in a future naval shipyard requires comparison of their properties and the characteristics with other vessels. In this section, the design characteristics of 100-ft WAM-V Proteus are compared against other current catamarans may help to highlight the properties that differentiate WAM-Vs and what applications may benefit from the technology. For dimensional comparisons, the measurements of traditional catamarans will follow marine conventions based on the diagram in shown in Figure 3.15.

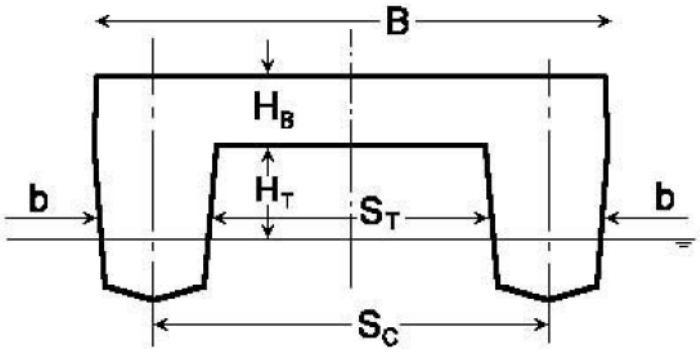

Figure 3.15 Catamaran dimension nomenclature [44]

Two measurements not shown in Figure 3.15 are the length the vessel at waterline L or LWL, and the displacement in metric tons ∇. Displacement is the principle parameter of importance in the design of high speed craft. Hydrodynamic resistance is directly related to displacement. Thus to improve resistance we must minimize Lightship weight, defined as the weight of the craft without any ancillary cargo, crew or fuel. The two dimensionless coefficients of greatest significance for quantifying the performance of multi-hulled vessels are the length to beam ratio of each hull: L/b and the length to displacement ratio $L/\nabla^{1/3}$. Maximizing these two values usually leads to reduced resistance; L is maximized and b is minimized leading to long, slender demi-hulls. The length to beam ratio of the entire WAM-V, L/B, is close to 2:1. However, the length to beam ratio of each demi-hull, L/b is closer to 20:1. The length to beam ratio for a traditional monohull might be in the range of 6:1 [44].

3.5.1 Length vs. Displacement Comparison

Figure 3.16 shows a comparison of the length vs. displacement for several current catamaran designs and the Proteus, indicated by the star. Figure 3.16 shows that the WAM-V is very light for its length compared to other catamaran designs, out of the normal distribution range.

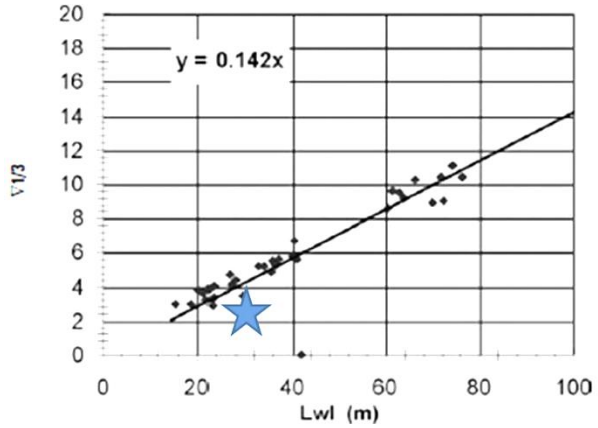

Figure 3.16 Length vs. displacement comparison for current catamaran designs [44] ★= 100-ft WAM-V

3.5.2 Length vs. Hull Spacing Comparison

Figure 3.17 provides a comparison of the length (LWL) of several catamarans vs. their tunnel width S_T, defined as the minimum distance separating the demi-hulls. The chart had to be extended from its original source for the WAM-V. The WAM-V has a S_T/LWL ratio of 0.42:1.

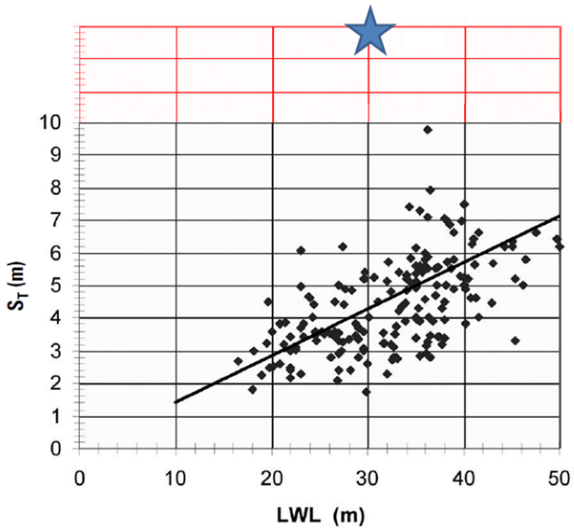

Figure 3.17 Tunnel length vs. width comparison for current catamaran designs [44] ★=100-ft WAM-V

The ratio of tunnel width and overall length of the WAM-V plays an important role in the added resistance of the two hulls that occurs due to the interaction between the flow structures of the hulls, a common phenomenon of catamarans. The difference in interference due to hull spacing for a typical catamaran is shown in Figure 3.18, the interference changes both at different hull spacings and at different Froude numbers. For some value of S_T, there will be a greater or lesser total resistance. Generally resistance decreases as hull separation increases, above a certain value this effect is small. Figure 3.18 is for a catamaran with L/b = 10.37, the WAM-V is 20:1.

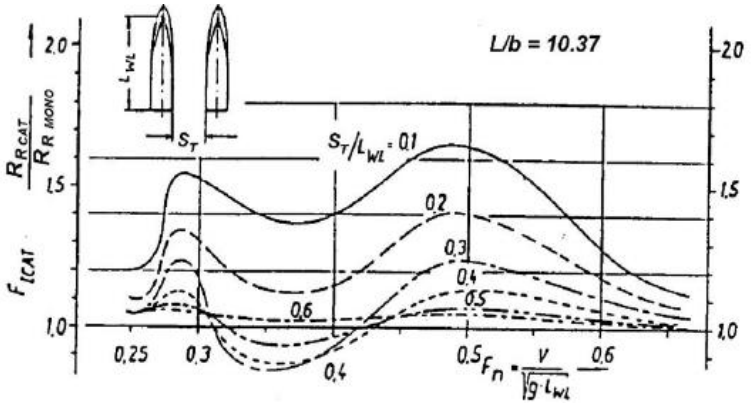

Figure 3.18 Change in added resistance vs. Froude number for different hull separations [44]

3.5.3 Beam vs. Depth Comparison

All of the WAM-V designs feature a very low draft. The 100-ft Proteus has only 8 inches of draft near the bow and 16 inches draft near the stern. Figure 3.19 gives a comparison of the depth of several designs vs. their total Beam B. Like most of the other comparisons, the WAM-V is an outlier to the rest of the data, with a far less depth for a given beam than more conventional craft.

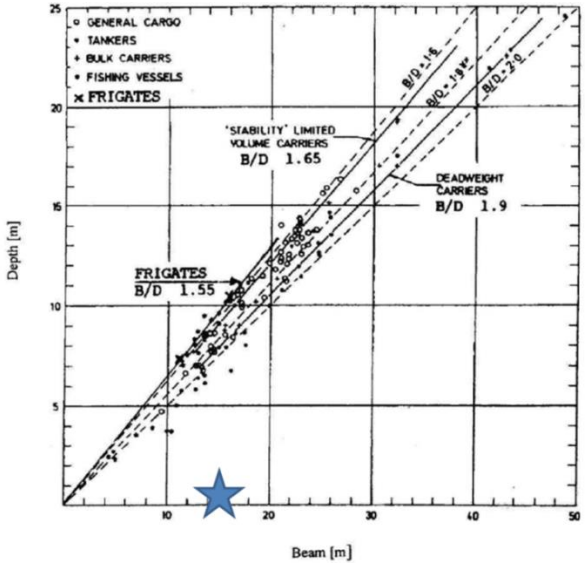

Figure 3.19 Depth vs. beam comparison [44] ★= 100-ft WAM-V

3.5.4 Other Possible Comparisons

The lightweight design of WAM-Vs is not without cost in terms of payload capacity or deadweight tonnage (DWT), defined as a measure of how much ancillary weight a ship can safely carry. The main advantage of the WAM-V designs does not come from a large payload capacity, particularly when compared to monohull vessels. The payload capacity also varies greatly between WAM-V prototypes, and hasn't yet been directly tested in a sea state.

3.6 Multi-Body Dynamics Modeling Environment

The multi-body dynamics model of the 100-ft WAM-V Proteus was constructed within the Matlab environment using a subsystem of its Simulink package known as SimMechanics. In order to better demonstrate the advantages and disadvantages of object-oriented programming, a single degree of freedom mass spring damper system, shown in Figure 3.20, has been modeled using a variety of different methods to highlight the advantages and disadvantages of each method.

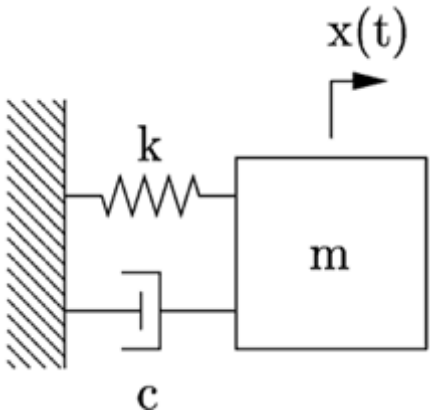

Figure 3.20 Mass spring damper system

The mass spring damper system shown in Figure 3.20 can be easily solved either by analytical or numerical simulation methods. For the analytical solution, the equation of motion is a linear second order differential equation, shown below:

$$\ddot{x} + \frac{c}{m}\dot{x} + \frac{k}{m}x = 0 \text{ [45]}$$

The numerical solution to the differential equation will produce an identical response to the analytical solution. Three methods are discussed for solving for the numerical solution using, Matlab, Simulink, and SimMechanics, an example program is shown for each solution. Figure 3.21 shows an example code written using the Matlab code to solve the differential equations of motion numerically. The code is included to illustrate the difficulty of interpreting line by line coding even for a fairly simplistic code.

```
m = 1;                  %  mass of the system in meter
k = 50;                 %  stiffness of the spring (N/m)
c = 20;                 %  damping coefficient
wn = sqrt(k/m);           %  natural frequency (rad/sec)
zeta = c/(2*wn*m)          %  viscous damping factor
 x_0 = 1;                %  initial displacement
x_dot_0 = 0;              %  initial velocity
X_0 = [x_0,x_dot_0];       %  form a vector(array) of initial conditions
tol = 1e-6;             %  tolerance of error for ODE45 solver

%function
[t,y] = ode45('pmsd_sol',0,t_final,X_0,tol);
 x = y(:,1);             %  displacement x(t)
x_dot  = y(:,2);          %  velocity x  dot(t)
yd1 = y(2);
yd2 = -(k*y(1)+c*y(2))/m;
ydot = [yd1;yd2];
```

Figure 3.21 Example Matlab coding of a mass spring damper system

The example Matlab code for the mass spring damper system is a short code of less than 20 lines, and the purpose of the lines of code are documented on the right. However, as the complexity of the model grows, so does the complexity of the code, and it becomes more difficult to decipher by a second or third party. Pictorial based modeling and block diagram algebra are advantageous in this situation because they are more easily understood than interpreting line by line coding. Figure 3.22 shows the same differential equation modeled in Simulink.

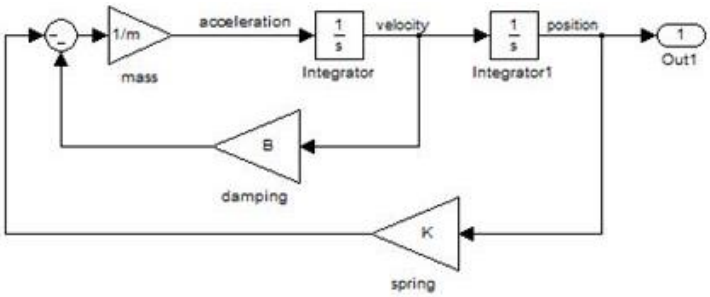

Figure 3.22 Simulink block diagram solution to mass spring damper system

Using Simulink, components of the equation of motion are more easily arranged out and visualized. In order to generate a readable model Simulink requires care in where blocks and lines are positioned and constructing a model is not always intuitive.

A fourth method for solving for the response of the mass spring damper system involves the use of a multi-body dynamics software package such as SimMechanics. Figure 3.23 shows the representation of the mass spring damper system and its single degree of freedom modeled using SimMechanics.

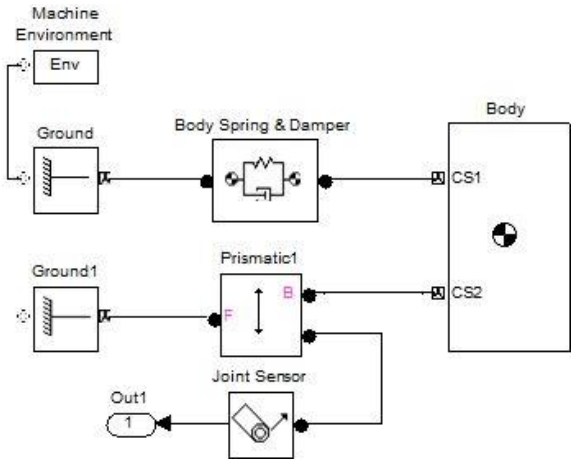

Figure 3.23 Pictorial representation of mass spring damper system using SimMechanics

A total of eight blocks make up the model in Figure 3.23. The body block represents the sprung mass, and is connected to ground through two blocks. One of the blocks is a body spring and damper that contains the numerical properties of the spring damper system. The second is a joint block, for this model the block has 1 translational and no rotational degrees of freedom. A joint sensor attached to the prismatic block converts the motion along the axis into data usable in Simulink and Matlab. The two ground blocks are identical and represent a globally fixed reference. The machine environment block specifies the coordinate system used for the simulation and the direction of gravity. Compared to the other three methods, this method is the most easily understood. However, some loss of information occurs since the equations of motion that govern the simulation are not visible in the diagram.

3.7 100-ft Proteus Parametric Model

In order to generate a knowledge base that will be applicable to future WAM-V designs, a versatile model is needed that can be built upon to suit many future vessel designs. The need for a parametric model stems from the drawbacks inherent to a kinematically-defined model due to the time required to model the kinematic complexities of the suspension. By minimizing the number of component definitions needed to run the model, quick adjustments can be made between iterations. In order to facilitate rapid developments to suspension parameters, it was desirable to bypass the guess and check process that would have occurred in defining the kinematics of motion for each model iteration.

3.7.1 Model Generation

The procedure for creating an initial model can be broken down into the following steps:

1. Creating a complete assembly file using CAD software composed of a series of parts representing the components of the vessel to be simulated. Each part should include a representative mass and inertia. Mating constraints should reflect the vessel being modeled.
2. Import the model into the SimMechanics environment using SimMechanics link.
3. Refine the joint constraints to be consistent with the desired degrees of freedom.
4. Add a method of applying inputs to the model.
5. Add sensors to measure the vessel's response for outputting into Matlab for analysis.

A simplified CAD assembly was developed using Solidworks to represent the WAM-V. The assembly contains all of the degrees of freedom of the Proteus vessel, while minimizing the complexity by modeling the kinematics of the each corner of the suspension as simplified translational joints. Since the focus of the current modeling is to improve the dynamic properties of the vessel above the levels of the pontoons, the pontoons are not included in the CAD model, the interaction of the pontoons can be included mathematically in the phases and magnitudes of the inputs. A rendering of the parametric model is shown in Figure 3.24.

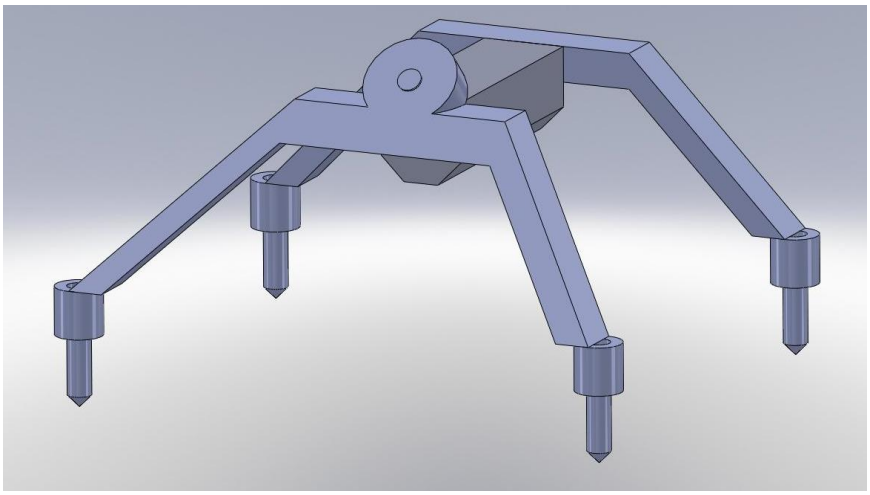

Figure 3.24 Parametric model render

SimMechanics is a subprogram of the Simulink programming environment. Each part modeled in CAD can be inputted as a rigid body with a series of user defined ports/connection points corresponding to points of attachment for the structure, or points of interest for sensors. The bodies are attached by connecting the ports on different rigid bodies with joints and defining the

relative degrees of freedom of each joint; with as many as three rotational and three translational degrees of freedom giving fully uncoupled motion, or as few as zero degrees of freedom representing a rigid/welded connection.

For the parametric model, the sprung mass is constrained by a three degree of freedom joint located at the center of gravity of the sprung mass components. The joint allows for linear translation in the vertical direction, as well as rotation along the pitch and roll axes. The model is constrained from movement in the lateral and longitudinal planes, as well as from rotation about the yaw axis. The front arch has a revolute joint allowing a rotational degree of freedom relative to the main body; differing from the Proteus which uses a spherical joint. The spherical joint relies on the pontoons to limit the yaw and pitch motion of the front arch, otherwise the model would collapse. Each of the four corners also has a prismatic joint which represents the suspension degree of freedom acting between the arches and the unsprung mass. In the model, each prismatic joint is connected to a spring and damper element, allowing not only spring rate and the damping constant to be varied, but additional nonlinear characteristics to be added as well. A brief summary of these degrees of freedom can be viewed in Figure 3.25. The model has four input degrees of freedom under the suspension, and a total of four output degrees of freedom, three for the chassis and one for the revolute joint on the front arch. The full SimMechanics model diagram is shown in Figure 3.26.

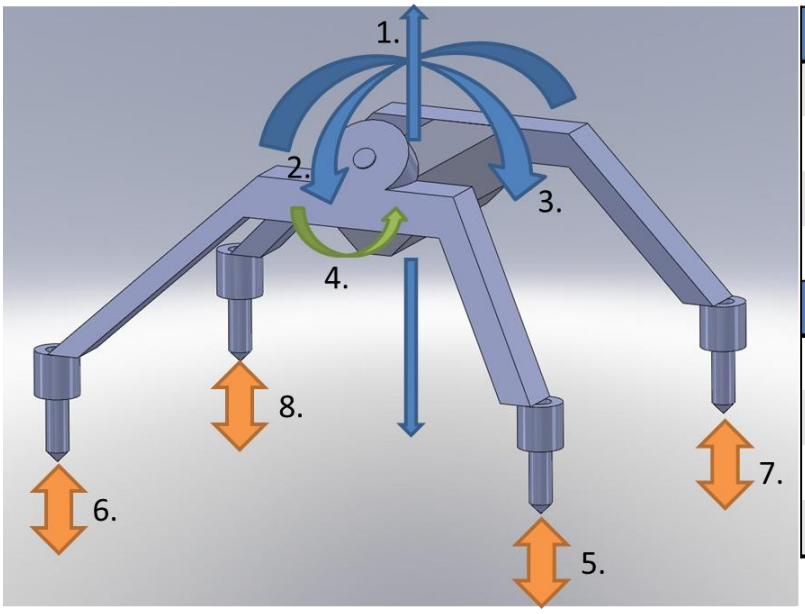

Degrees of Freedom:
1. Chassis Vertical Translation
2. Chassis Rotation Pitch
3. Chassis Rotation Roll
4. Front Arch Rotation Roll
Inputs:
5. Front Left Suspension
6. Front Right Suspension
7. Rear Left Suspension
8. Rear Right Suspension

Figure 3.25 Parametric model degrees of freedom

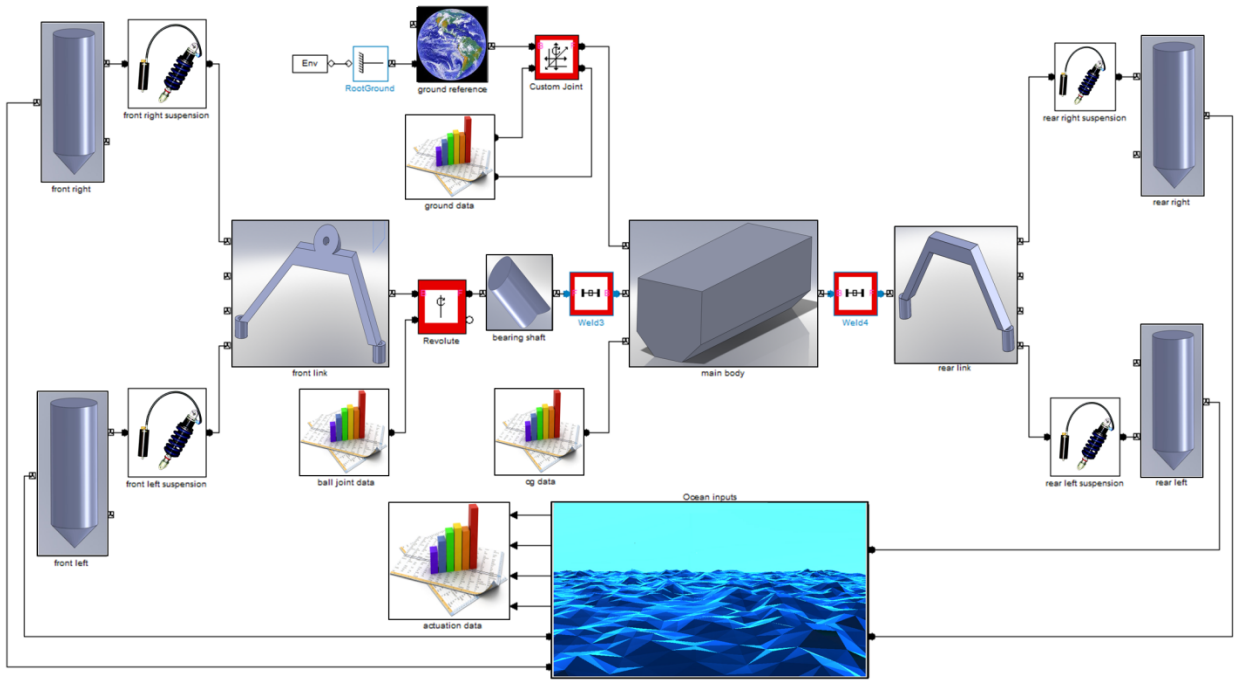

Figure 3.26 Full parametric model diagram

3.7.2 Model Parameterization

Once a functional SimMechanics model was constructed, the internal dimensions, masses, and inertias contained within the model were replaced by variables, and all of the scalar values that correspond to the new variables were stored in a master Matlab m-file. By removing the variables from the individual SimMechanics blocks, it is easier to make changes to dimensions, masses, and inertia values; it is also possible to make changes automatically by developing a code. Automatic adjustment to parameters is extremely valuable in a parametric study, in that multiple iterations can be run without constant management by the operator. Parameterization also allows a user to develop a vessel of different physical dimensions to the current Proteus without having to be familiar with the model architecture, or even the Simulink and SimMechanics environments. When the m-file is run, the parameters are automatically updated in the SimMechanics model and an output plot is produced to show dimensional changes to the vessel. An example of this plot is shown for a vessel 2 meters shorter and 75% of the width of the original in Figure 3.27. The lines represent component dimensions and the circles represent the centers of gravity of the various bodies; the changed vessel is shown in red, the original is shown in blue.

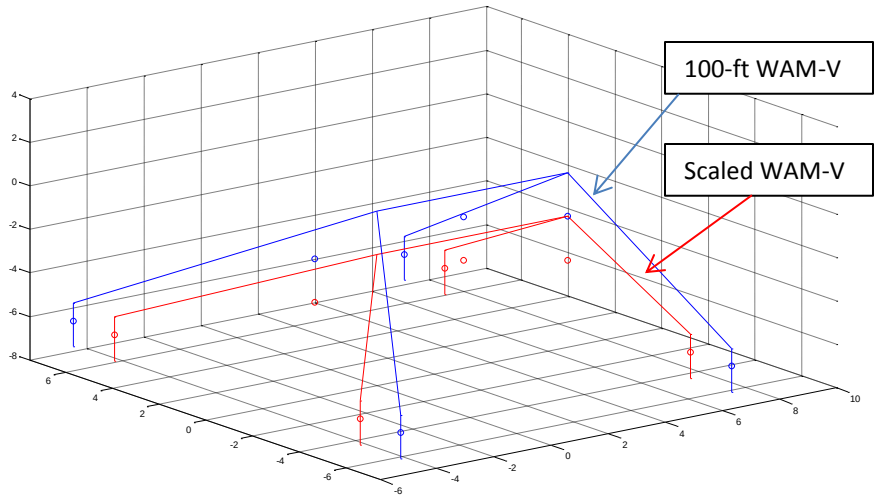

Figure 3.27 Matlab parameter model output showing model changes

Suspension and input parameters were also parameterized and incorporated into the Matlab m-file. These parameters will be updated several times during each iteration of the parametric study, so they need to be easily accessible. For the initial model, the suspension elements were modeled as body springs and dampers acting on prismatic axes; having spring forces based linearly on position and damper forces based linearly on velocity. Later models have been updated with user defined forcing elements acting along the same axes with a force based on any measurable system parameter. This gives the advantage of being able to specify nonlinear functions corresponding to kinematics such as in a rising rate suspension, as well as the ability to change damping characteristics based on the reactions between the 4 corners or the center of gravity, creating a semi-active suspension.

3.7.3 Model Inputs

Suspension iterations will be evaluated by applying displacement inputs to each corner of the model. The inputs are applied as individual displacements occurring at the base of the each suspension, directly above the relative pontoon. Simulink was used to generate input signals and a method of interfacing with SimMechanics to translate a set of desired displacement into individual desired motions at the joints. Currently the displacements are in the form of sine waves with discrete magnitudes and frequencies. The sine waves are specific to each of the four corners, and can be set to move in or out of phase with the other corners. There are currently two formats for specifying the relative phases of the input displacements. The first method requires the user to specify the degree to which the inputs are in phase with the other inputs. The second

method is designed to input parameters as though the model were operating in a sea state. Each method requires similar input information, the required variables for both input types are listed in Table 3.3, and the method of achieving inputs is summarized in Table 3.4.

Table 3.3 Inputs required for parametric analysis

Phase based inputs:	Oceanic based inputs:
Magnitude of input	Magnitude of input
Frequency	Vehicle Speed
Pitch Phase	Wave Speed
Roll phase	Angle of waves relative to vehicle direction
	Distance between wave peaks

Table 3.4 Differences between input methods

Desired motion:	Phases inputs:	Oceanic inputs:
Heave Input	0 degrees pitch, 0 degrees roll	(wave length*cos(wave angle))/ (Vehicle length)=n*360 (wave length*sin(wave angle))/ (Vehicle width)=n*360
Pitch Input	180 degrees pitch, 0 degrees roll	(wave length*cos(wave angle))/ (Vehicle length)=n*360 (wave length*sin(wave angle))/ (Vehicle width)=n*180
Roll Input	0 degrees pitch, 180 degrees roll	(wave length*cos(wave angle))/ (Vehicle length)=n*180 (wave length*sin(wave angle))/ (Vehicle width)=n*360
Warp Input	180 degrees pitch, 180 degrees roll	(wave length*cos(wave angle))/ (Vehicle length)=n*180 (wave length*sin(wave angle))/ (Vehicle width)=n*180

The two methods are different ways to achieve the same inputs; the difference is a matter of modeling preference. Specifying the inputs as phases as shown in Figure 3.28 will be more useful to identify critical frequencies and phases for suspension iterations in the preliminary design stages. While having oceanic based inputs as shown in Figure 3.29 will be more useful for validating the parametric model against on-water testing data, or to simulate a particular sea state prior to testing.

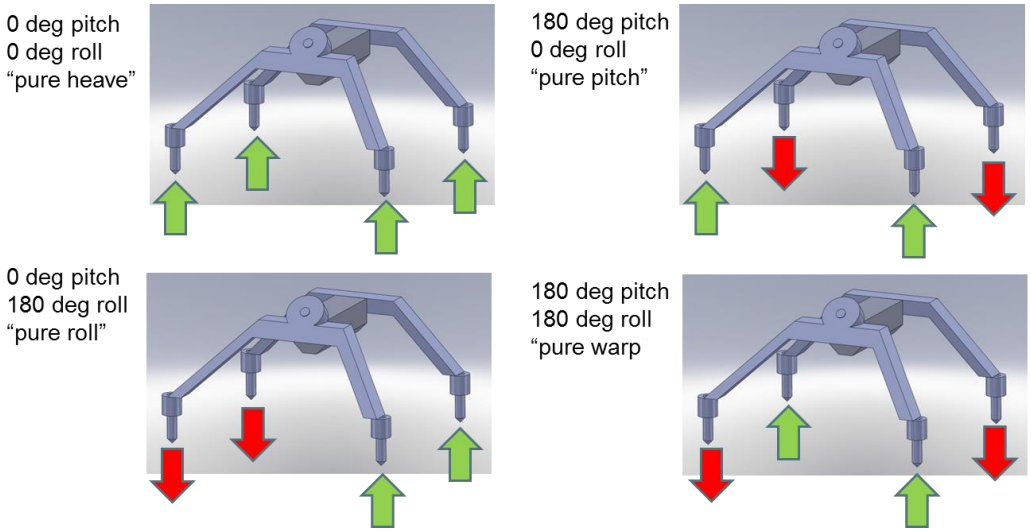

Figure 3.28 Input modes to parametric model

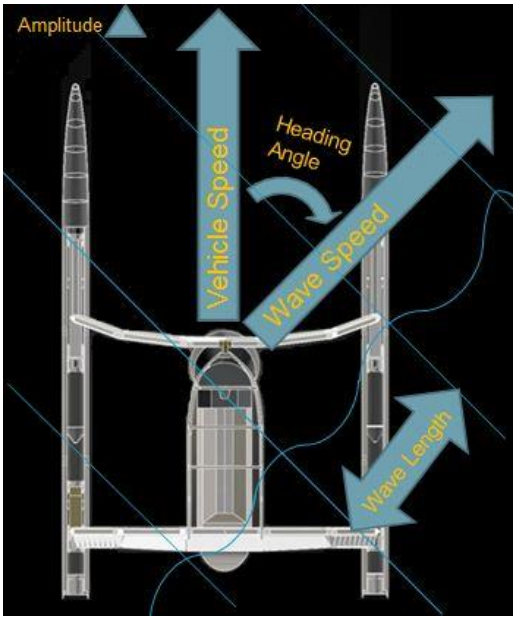

Figure 3.29 Ocean heading input method parameters

3.7.4 Model Outputs

In order to quantify the performance of the parametric model, a series of output plots needed to be generated based on the data gathered from the model. The use of joint sensors in the SimMechanics environment allows for Simulink signals to be generated. The use of Simulink allows for outputting into the Matlab environment for further manipulation of the data. Sensors were incorporated at various points of interest in the parametric model; each provides an array of output data under a specific variable name into the Matlab environment. Currently the parameters that are being viewed are summarized in Table 3.5.

Table 3.5 Parametric model outputs measurements

Displacements:	Accelerations:	Forces:	Velocities:
Unsprung mass	Center of gravity	Normal Force (4x)	Center of gravity
Corners (4x)		Springs (4x)	Dampers (4x)
Center of gravity		Dampers (4x)	
Center of gravity (pitch)			
Center of gravity (roll)			
Front Arch(rotation)			

A Matlab m-file was then created that generates a page of output plots displaying all of the channels of data. An example output piece of simulation data displayed for the various sensor channels is plotted in Figure 3.30.

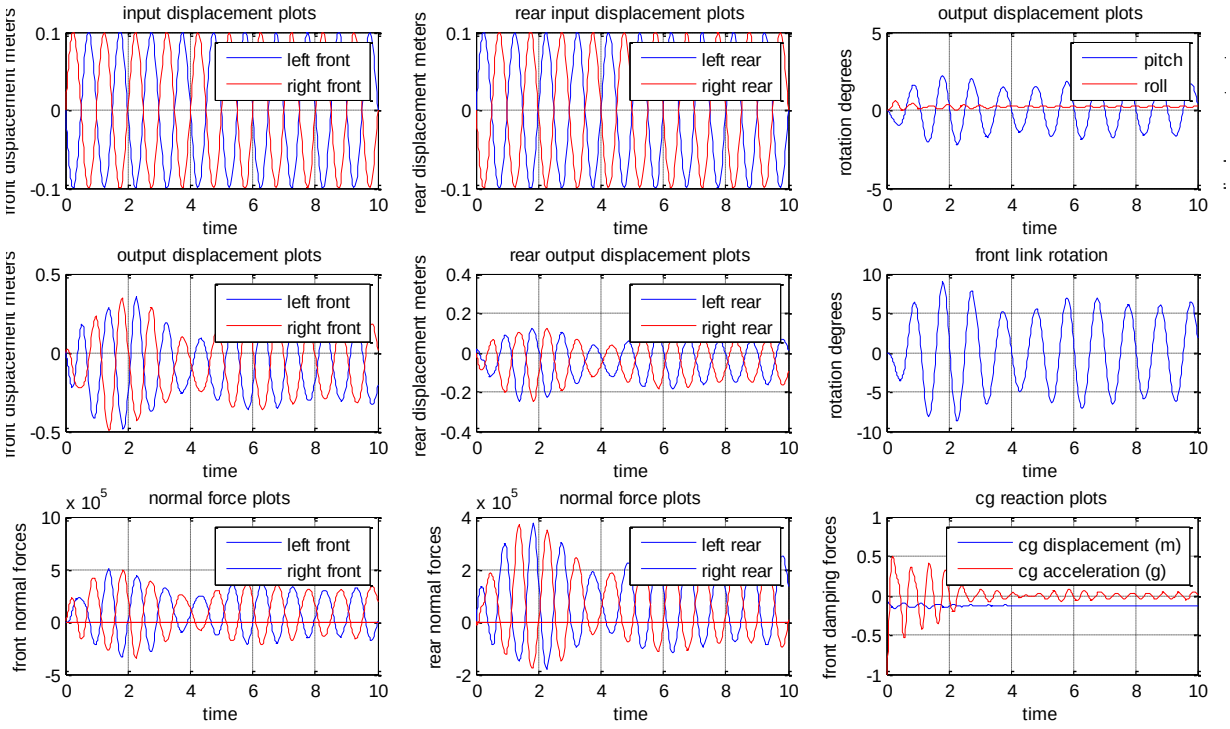

Figure 3.30 Matlab simulation output plots

More parameters are available for analysis than currently displayed, including the dynamic forces and torques acting on joints, constraints and between components. This will prove useful when designing the actual components for future WAM-Vs, especially if integrated with Finite Element Analysis software. Conceptual visualization of the simulation is also possible by

viewing the model as an animation. Each of the components designed in CAD can be saved as a .STL file and linked to the corresponding SimMechanics body. The .STL files do not update when changes are made in Matlab, so their use is primarily in visualizing and debugging the model. A screenshot of the visualization is shown in Figure 3.31.

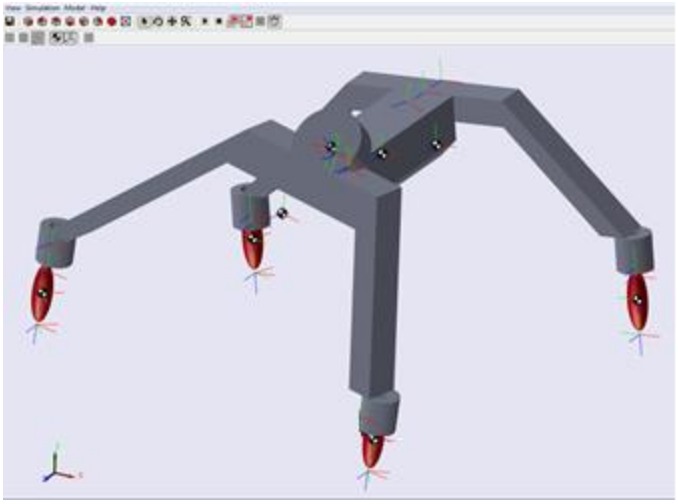

Figure 3.31 STL file based model visualization

3.8 Initial Parametric Study

In order to test the functionality of the parametric model, a preliminary parametric study was conducted by varying a few key parameters and comparing their effects. Although it is possible to study the effects of varying almost all of the model's parameters individually, the overall dimensions of the vessel, as well as the component's masses and inertias were held constant throughout the initial parametric study. The purpose of the initial parametric study was to test the functionality of the modeling environment to aid in determining areas for future development, rather than to determine an optimized set of suspension properties for the Proteus vessel or for the other WAM-Vs detailed in further chapters.

3.8.1 Initial Baseline Configuration

The values of the masses, dimensions, and inertias used for this study were specified based on available information about the Proteus vessel. However, the suspension settings that were evaluated were all far different than the actual Proteus suspension configuration. No significant attempt was made to replicate the actual installed suspension setup on the Proteus within the model. The installed suspension is prone to binding kinematically, and it is also highly nonlinear

with minimal damping; the spring rate decreases as the suspension moves in compression causing the suspension to bottom out excessively in rough seas. Instead of modeling an outdated design that wouldn't be carried over to future WAM-Vs and using that as the baseline for future comparisons, a baseline configuration with linear vertical spring rates was modeled instead with an initial stiffness that would yield 0.25m of static deflection. For a vessel with a sprung weight of approximately 10,600 kg as tested, this corresponds to 400,000 N/m total heave stiffness.

Nominally, the rear suspension was set to provide 60% of the total heave stiffness, giving 160,000 N/m stiffness in the front and 240,000 N/m stiffness in the rear, corresponding to 80,000 N/m vertical stiffness in each front corner and 120,000 N/m vertical stiffness in each rear corner. Damping constants for the baseline configuration were chosen for the front and rear such that the model had approximately 60-70% critical damping front and rear, the ratios were confirmed via initial condition (drop) tests of the model and calculating the logarithmic decrement of the motion as it decayed. Figure 3.32 shows the logarithmic decrement of the system initially set to 10% critical damping.

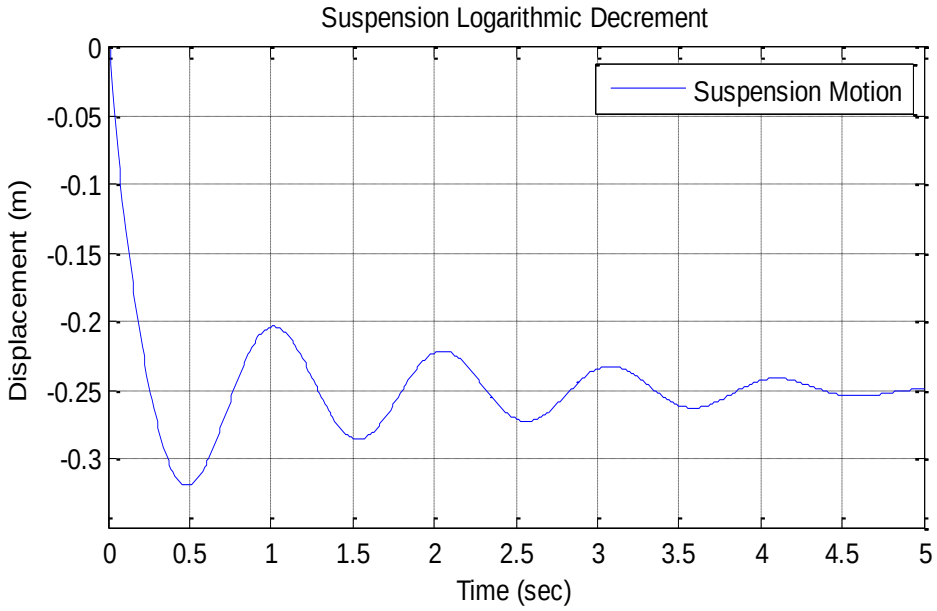

Figure 3.32 Suspension amplitude decay at 10% critical damping

The logarithmic decrement of the system was calculated from the following formulas, where T is the period of oscillation and δ is the logarithmic decrement:

$$\delta = \ln \frac{x(t)}{x(t+T)} \quad \zeta = \frac{\delta}{\sqrt{4\pi^2 + \delta^2}} \quad [45]$$

For the initial study, only linear changes to the stiffness and damping coefficients were evaluated. The suspension systems contained no travel limitations or bump stops, meaning the model effectively had infinite rattle space. Table 3.6 gives an overview of the key parameters for the baseline configuration.

Table 3.6 Initial parametric model settings

Parameter:	Value:
Overall Mass	10,600 kg
Front spring stiffness	80,000 N/m
Rear spring stiffness	120,000 N/m
Front damper rate	20,000 N*s/m
Rear damper rate	30,000 N*s/m

3.8.2 Model Testing Parameters

The first parametric study was conducted using the frequency and phase input method to the 4-post model described in Section 3.7.3. Ten frequencies, three amplitudes, three pitch phases and three roll phases were run for each suspension configuration, giving a total of 270 simulations per suspension configuration tested. Table 3.7 lists the testing input configurations used for the initial parametric study. Changes in pitch phase indicate that the sinusoidal signals applied to front and rear corners are moving out of phase, changes in roll phase indicate that the sinusoidal signals applied to the left and right corners are moving out of phase.

Table 3.7 Testing parameters

Frequency (Hz):	Phase (deg):	Amplitude (m):
0.5	0 pitch, 0 roll	0.1
1.0	0 pitch, 90 roll	0.3
1.5	0 pitch, 180 roll	0.5
2.0	90 pitch, 0 roll	
2.5	90 pitch, 90 roll	
3.0	90 pitch, 180 roll	
3.5	180 pitch, 0 roll	
4.0	180 pitch, 90 roll	
4.5	180 pitch, 180 roll	
5.0		

3.8.3 Output Measurements

Given the immense amount of data the model generates for each simulation and the large number of model iterations intended to be tested, a sensible and concise method of evaluating the data was required for the initial study. Though a large number of channels are being logged from within the model, the vertical acceleration at the center of gravity of the superstructure was chosen as the channel that would be used to differentiate relative suspension performance between different suspension configurations for the first study. Furthermore, since the input frequency and amplitude was held constant throughout the individual simulation, discrete acceleration values can be used as a representation of the time series data. A side view diagram showing the sensor location and its relation to the centers of gravity of the different components and the model's constraining joint is shown in Figure 3.33.

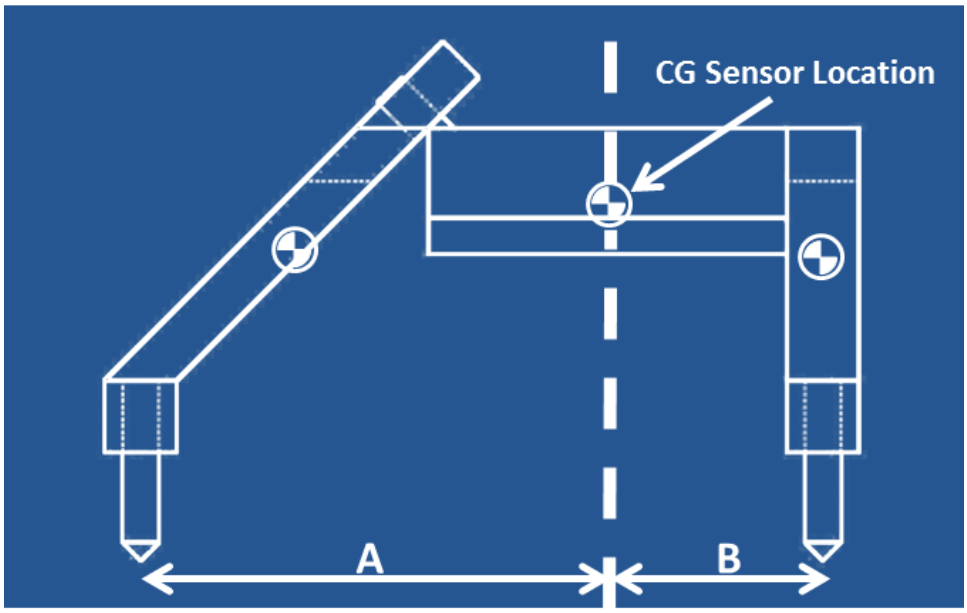

Figure 3.33 Side view diagram showing location of sensor in model

Seven discrete values of acceleration were calculated as a representation of the data; three were values for positive acceleration, representing the average of the 80th percentile, 90th percentile, and the maximum acceleration; three values for negative acceleration representing the average of the 20th percentile, 10th percentile and the minimum acceleration; as well as the standard deviation of the acceleration for the data.

3.8.4 Comparing Sets of Data

In order to compare the acceleration metrics from each configuration against the results from the baseline configuration, each of the seven metrics was divided by the corresponding metric from the baseline acceleration data. Using this method a unity value on the graph corresponds to identical performance between the baseline and the new configuration. Outputs greater than one indicate improved performance from the baseline configuration, outputs less than one indicate improved performance from the new configuration. The data from a single set of simulations is shown in Figure 3.35, a comparison between two runs is shown in Figure 3.36. The legend for both figures can be found in Figure 3.34. For the purposes of this study, it is more important to look at general trends in the different metrics than to look at absolute values, in order to better understand the effects of changing different parameters on suspension performance.

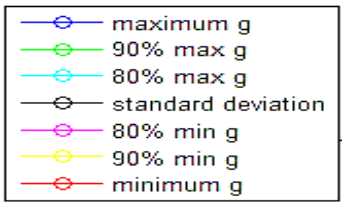

Figure 3.34 Legend for parametric study data runs

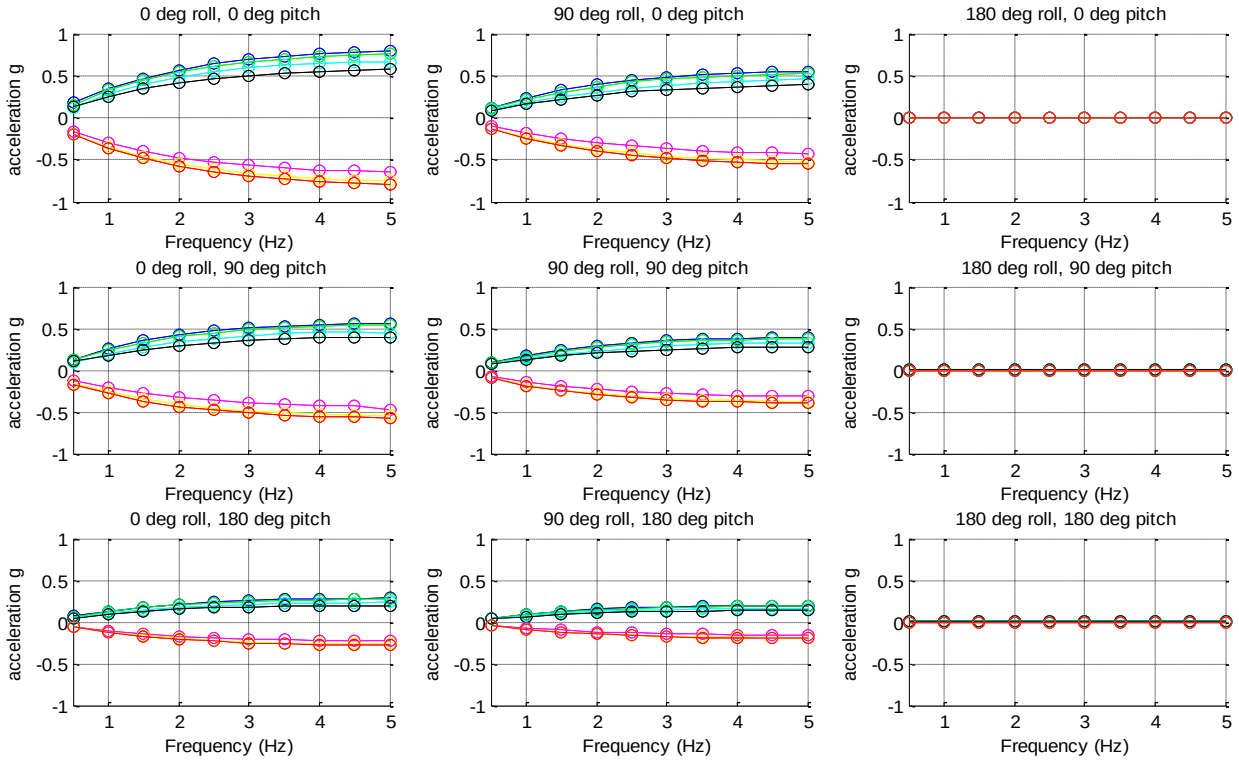

Figure 3.35 Example data for a simulation run

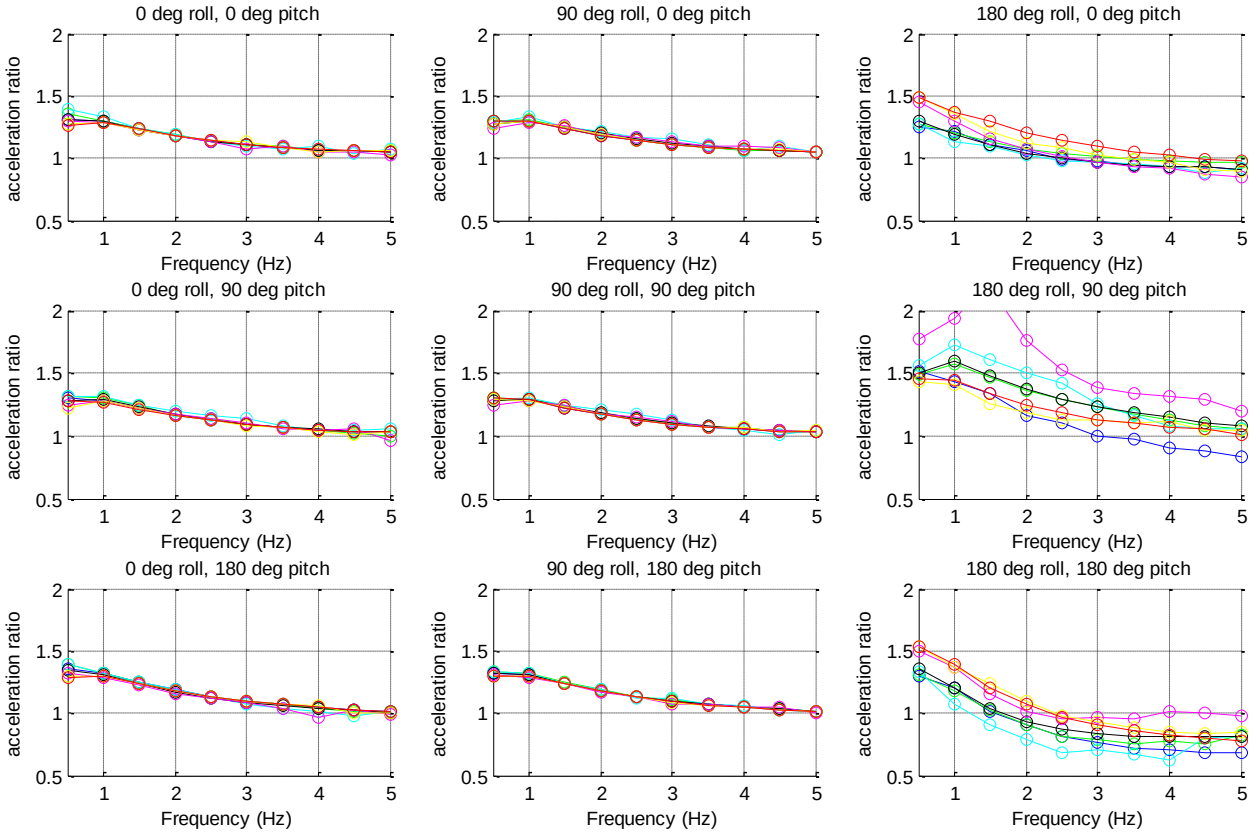

Figure 3.36 Sample comparison of metrics between two datasets

3.8.4.1 Correlation of 180 Degree Roll Simulations:

For the nine combinations of pitch and roll phases tested, all of the suspension configurations showed good correlation between the different data metrics with the exception of the iterations tested with a 180 degree phase offset in roll. The three graphs in the rightmost column of Figure 3.35 show that the data for these simulations produces far lower levels of acceleration than simulations with different phases. This causes the comparison plots in the rightmost column of Figure 3.36 to show less correlation than the other 6 plots. As shown in Figure 3.37, the difference can most likely be attributed to the roll motion exciting the cabin perpendicularly to the axis of measurement used for quantifying the simulation data. Future, more in depth studies will include longitudinal and lateral acceleration as metrics for suspension performance.

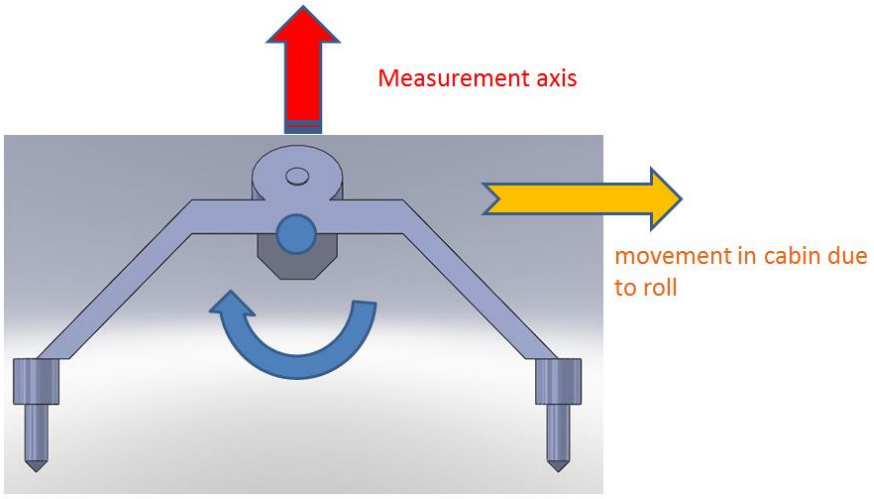

Figure 3.37 Clarification of 180 degree roll phase data

The simulations run with 90 degrees of roll offset did not experience the same correlation issues because the 90 degree phase shift produced a beating motion between the left and right posts, which provided significant vertical excitation. It is also noteworthy that the same issue was not experienced for the simulations with 180 degrees of pitch offset. This can most likely be attributed to a combination of the chassis being pinned at the WAM-V's center of gravity, the WAM-V having a rear weight bias as simulated, and the motion of the front arch attenuating acceleration levels for roll inputs and not acting in pitch. Also, the suspension stiffnesses were not equal front and rear for a majority of the simulation runs, so the pitch center most likely did not lie on the pinned axis in the side view; whereas the roll center was likely on the centerline in the front view. The same displacement in roll induced rotational and lateral accelerations, which were outside the focus of this study.

3.8.5 First Study: Overall Damping

The first segment of the initial parametric study involved testing changes to the overall damping ratio of the suspension systems. Four incremental changes in damping of 25% each were evaluated, corresponding to increases and reductions of 25% and 50% in the damping of the system. The corresponding damping values for the simulations are listed in Table 3.8.

Four new simulations were conducted and plotted against the baseline configuration described in the previous section. Based on the plots shown, a 25% reduction in the overall damping was chosen as the best solution, the results are shown in Figure 3.38.

Table 3.8 Damping percent changes and rates for overall damping study

Iteration:	Front Stiffness: (N/m)	Front Natural Frequency: (Hz)	Front Damper Value: (N*s/m)	Front Damping Ratio:	Rear Stiffness: (N/m)	Rear Damper Value: (N*s/m)	Rear Damping Ratio:	Rear Natural Frequency: (Hz)
-50% damping	80,000	0.98	10,000	0.38	120,000	15,000	0.31	0.98
-25% damping	80,000	0.98	15,000	0.58	120,000	22,500	0.47	0.98
Baseline	80,000	0.98	20,000	0.77	120,000	30,000	0.63	0.98
+25% damping	80,000	0.98	25,000	0.96	120,000	37,500	0.78	0.98
+50% damping	80,000	0.98	30,000	1.15	120,000	45,000	0.94	0.98

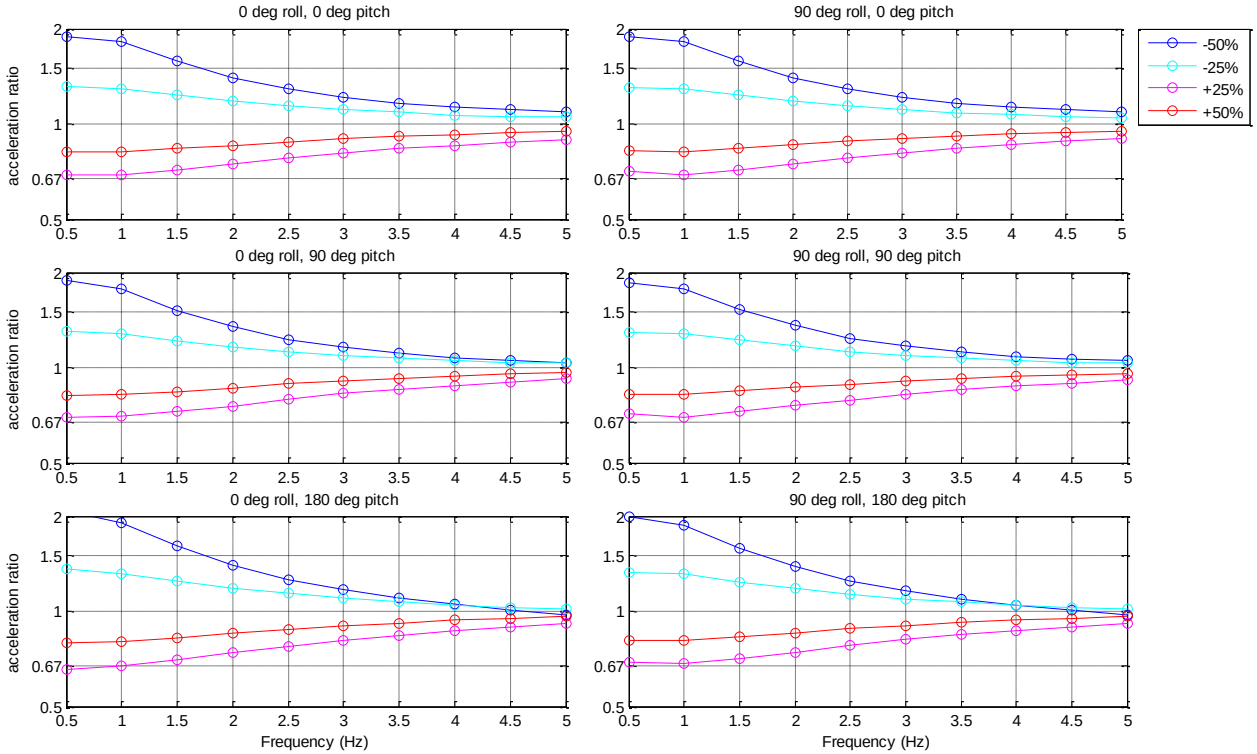

Figure 3.38 Damping change result comparison

It is interesting to note how similar the data is from the 6 damping simulations shown in Figure 3.38. This shows that changing the overall damping level did not produce a compromise between the performances of different input phases. The data plots appear to be so similar because the phasing proportionally effects the acceleration experienced for each damping setting. The 25% reduction in damping showed the lowest acceleration between the 5 different damping settings (four new iterations and the baseline). In the end, the damping performance was not a compromise between performance at different frequencies.

3.8.6 Second Study: Overall Stiffness

The next component of the initial parametric study involved incremental changes to the overall stiffness of the four suspension systems as a whole. For the study, four incremental stiffness changes were evaluated, corresponding to 25% and 50% increases and reductions in the overall heave stiffness of the system. Table 3.9 shows the stiffness values as simulated, as well as the corresponding damping values. For this study, the damping values were adjusted for each simulation to keep the damping ratios constant using the following formula for damping ratio:

$$\zeta = \frac{c}{2\sqrt{km}} \text{ [45]}$$

Therefore, in order to keep the damping ratio constant with a constant mass, for a given change in spring rate, the damping constant needed to be changed according to the following ratio:

$$\frac{c_1}{2\sqrt{k_1 m_1}} = \frac{c_2}{2\sqrt{k_2 m_1}} \rightarrow \frac{c_1}{c_2} = \sqrt{\frac{k_1}{k_2}}$$

Also shown in Table 3.9 are the changes in the natural frequencies of each of the suspension systems, calculated using the following formula:

$$\omega_n = \sqrt{\frac{k}{m}} \text{ [45]}$$

Table 3.9 Overall stiffness coefficients

Iteration:	Front Stiffness: (N/m)	Front Natural Frequency: (Hz)	Front Damper Value: (N*s/m)	Front Damping Ratio:	Rear Stiffness: (N/m)	Rear Damper Value: (N*s/m)	Rear Damping Ratio:	Rear Natural Frequency: (Hz)
-50% stiffness	40,000	0.69	57,000	0.58	60,000	85,000	0.47	0.69
-25% stiffness	60,000	0.85	69,000	0.58	90,000	104,000	0.47	0.85
Baseline	80,000	0.98	15,000	0.58	120,000	120,000	0.47	0.98
+25% stiffness	100,000	1.09	89,000	0.58	150,000	134,000	0.47	1.09
+50% stiffness	120,000	1.20	98,000	0.58	180,000	147,000	0.47	1.20

Four new simulations were conducted and compared with the new baseline set to the -25% overall damping ratio iteration chosen from the previous segment of the study. The four new simulation results plotted against the baseline configuration are shown in Figure 3.39.

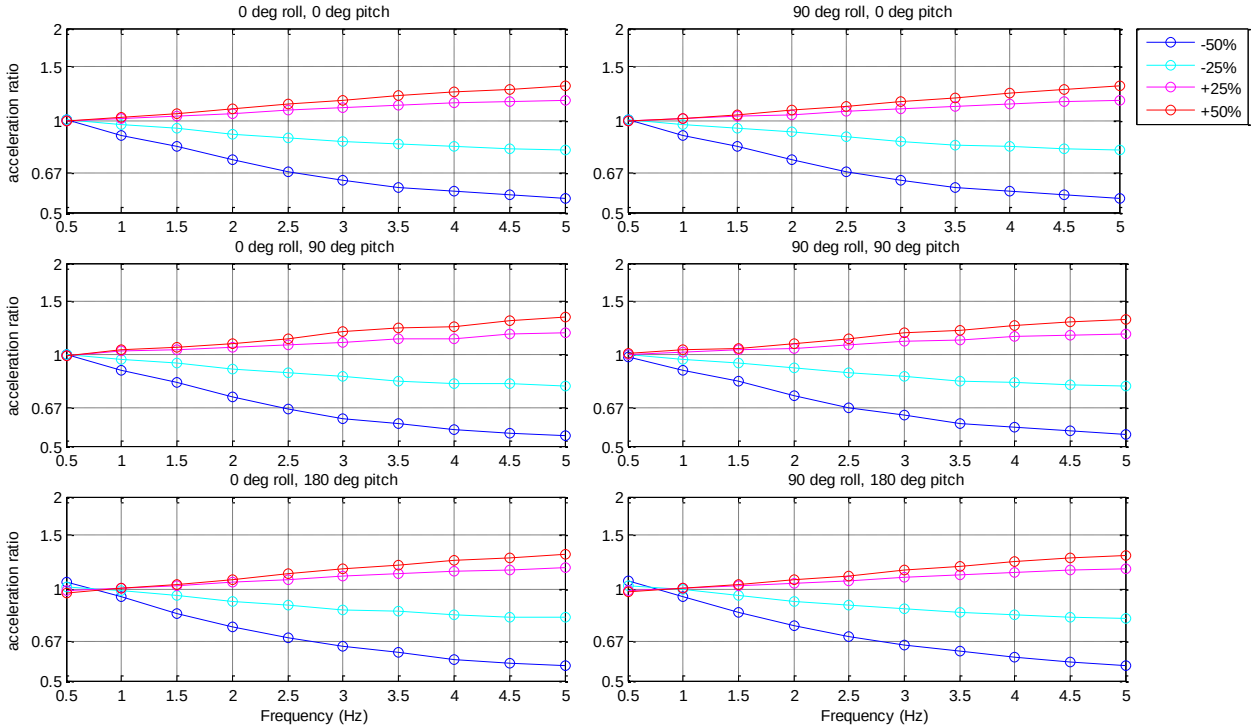

Figure 3.39 Suspension stiffness simulation comparisons

Based on the 4 plots shown, a 50% reduction in the overall stiffness of the suspension system was chosen as the best solution. Because the solution chosen was the lowest stiffness in the range of stiffnesses tested, an additional three lower stiffnesses were also tested, corresponding to 75%, 87.5%, and 93.75% reductions in the overall stiffness compared to the baseline chosen at the end of the first study. Since the -50% configuration proved the best of the original 4 iterations, the results from the subsequent three simulations were compared using it as the new baseline.

Table 3.10 Overall stiffness coefficients – trial 2

Iteration:	Front Stiffness: (N/m)	Front Natural Frequency: (Hz)	Front Damper Value: (N*s/m)	Front Damping Ratio:	Rear Stiffness: (N/m)	Rear Damper Value: (N*s/m)	Rear Damping Ratio:	Rear Natural Frequency: (Hz)
-93.75% stiffness	5,000	0.24	20,000	0.58	7,500	30,000	0.47	0.24
-87.5% stiffness	10,000	0.35	28,000	0.58	15,000	35,000	0.47	0.35
-75% stiffness	20,000	0.49	40,000	0.58	30,000	60,000	0.47	0.49
Baseline	40,000	0.69	57,000	0.58	60,000	85,000	0.47	0.69

None of the additional stiffnesses were shown to be improvements over the new baseline, and the model became unstable for the lowest stiffness tested, so a 50% reduction in the overall stiffness was chosen as the best result from this study. It is noteworthy that although reductions in suspension stiffness showed a correlation with reduced vertical accelerations, they also tended to produce larger displacements at the center of gravity. This indicates lower frequency excitations at the cabin, which may or may not improve human or vessel performance. These effects are outside the focus of this study.

3.8.7 Third Study: Stiffness Distribution

With the studies on overall stiffness and overall damping ratio complete, the front to rear distribution of the suspension stiffness was the next parameter to be evaluated. Four new simulations were run corresponding to 10% and 20% forward and rearward shifts in the suspension stiffness distribution, the stiffness values used are listed in Table 3.11. As with the overall stiffness study, the damping values were adjusted to match the changes in stiffness to maintain constant damping ratios between the iterations. The four new simulation results were plotted against the baseline established from the second study, the results are shown in Figure 3.40

Table 3.11 Stiffness distribution parameters

Iteration:	Front Stiffness: (N/m)	Front Natural Frequency: (Hz)	Front Damper Value: (N*s/m)	Front Damping Ratio:	Rear Stiffness: (N/m)	Rear Damper Value: (N*s/m)	Rear Damping Ratio:	Rear Natural Frequency: (Hz)
-20% front stiffness distribution	20,000	0.49	57,000	0.58	80,000	85,000	0.58	0.80
-10% front stiffness distribution	30,000	0.60	69,000	0.58	70,000	104,000	0.58	0.75
Baseline	40,000	0.69	15,000	0.58	60,000	120,000	0.58	0.69
+10% front stiffness distribution	50,000	0.77	89,000	0.58	50,000	134,000	0.58	0.63
+20% front stiffness distribution	60,000	0.85	98,000	0.58	40,000	147,000	0.58	0.56

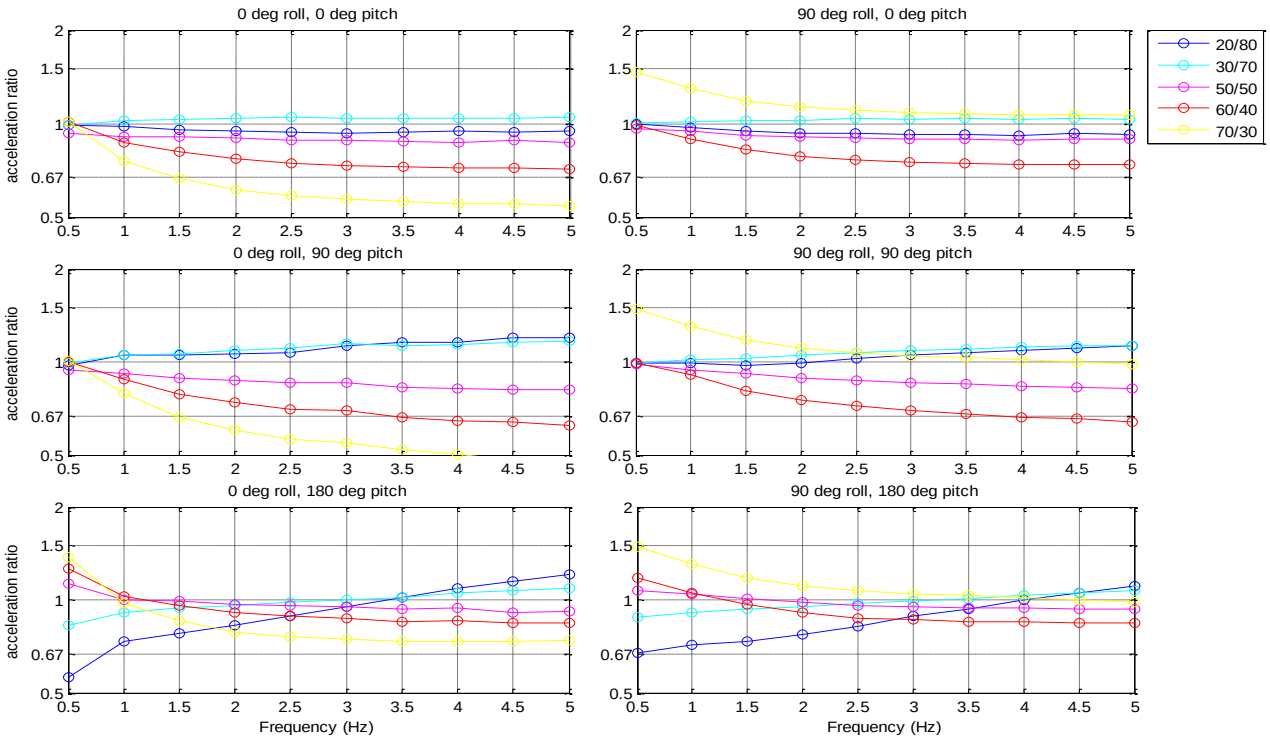

Figure 3.40 Stiffness distribution simulation comparisons

Based on the plots shown in Figure 3.40, a 60%-40% front stiffness bias was chosen as the best solution. This is interesting because it implies that a stiffer front end equates to better suspension performance. This is counterintuitive to what was expected to be found. Revisiting the sensor location diagram shown in Figure 3.33, we can see that the sensor is closer to the rear arch than the front. This implies that making the end further away from the sensor carry more of the stiffness will improve performance at the other end. This is useful information for the WAM-Vs detailed in future chapters which have a more even weight distribution and the passengers and payload are further forward in the superstructure.

3.8.8 Fourth Study: Damping Distribution

The final segment of the initial parametric study involved changes in the front to rear damping distribution of the system. For this segment just two additional iterations were tested, corresponding to 10% shifts between the front and rear balance in both directions, shown in Table 3.12.

Table 3.12 Stiffness distribution parameters

Iteration:	Front Stiffness: (N/m)	Front Natural Frequency: (Hz)	Front Damper Value: (N*s/m)	Front Damping Ratio:	Rear Stiffness: (N/m)	Rear Damper Value: (N*s/m)	Rear Damping Ratio:	Rear Natural Frequency: (Hz)
-10% front damping distribution	30,000	0.85	69,000	0.58	70,000	104,000	0.58	0.56
Baseline	40,000	0.85	15,000	0.58	60,000	120,000	0.58	0.56
+10% front damping distribution	50,000	0.85	89,000	0.58	50,000	134,000	0.58	0.56

The results from the two iterations were plotted against the new baseline established from the third study on stiffness distribution are shown in Figure 3.41. Neither change in the stiffness distribution showed a definitive improvement in the acceleration performance, the improvements and detriments of each incremental change were small and highly frequency dependent. With no definitive improvements found, the baseline damping distribution was chosen as the best configuration.

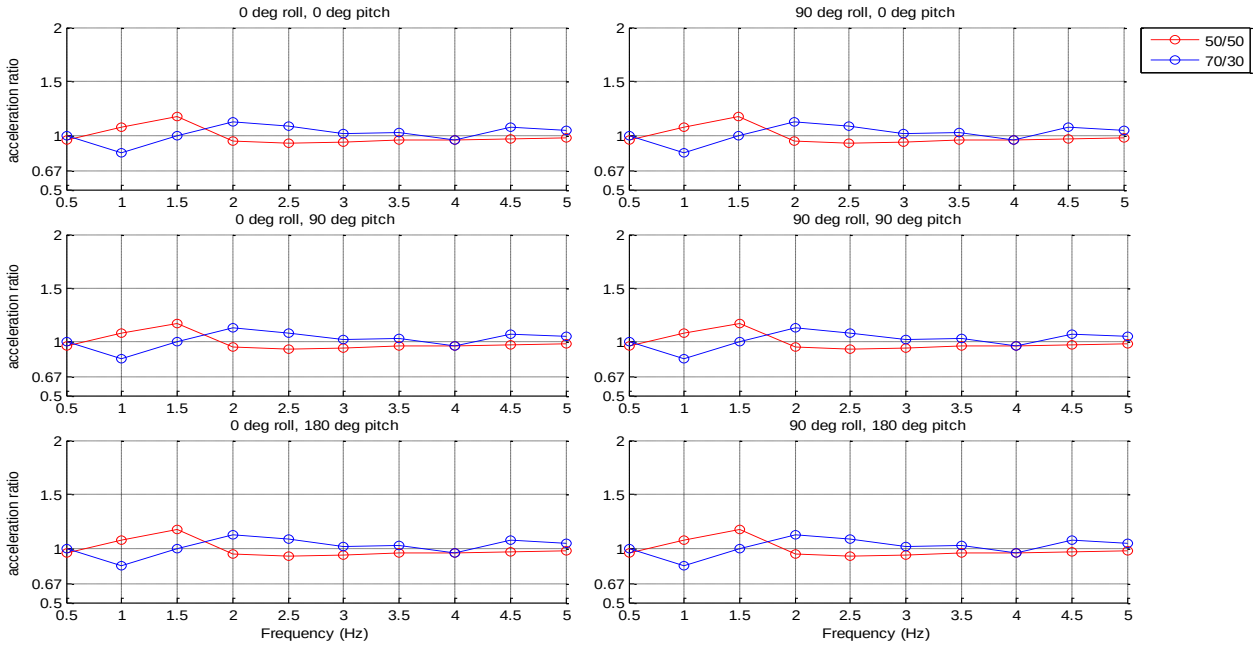

Figure 3.41 Damping distribution simulation comparisons

With the fourth study complete, the final results for the study are shown in Figure 3.42 plotted against the original baseline with the results from the 180 degree roll data omitted. Figure 3.42 shows the results from the largest of the three amplitudes simulated (0.5 meters) during the

study. The suspension system shows between a 20% and a 67% reduction in accelerations, with greater performance improvements coming at higher input frequencies. The results show consistent improvement for all the phases shown, as well as for the different input amplitudes. Though the simulations shown consistent improvement, the methodology presented is not validated as a sequence of steps for optimizing a suspension system, this was not the focus of the initial parametric study. It is possible that the final solution presented is a local minimum, and the final solution chosen would be different if the sequence of the studies were reconfigured.

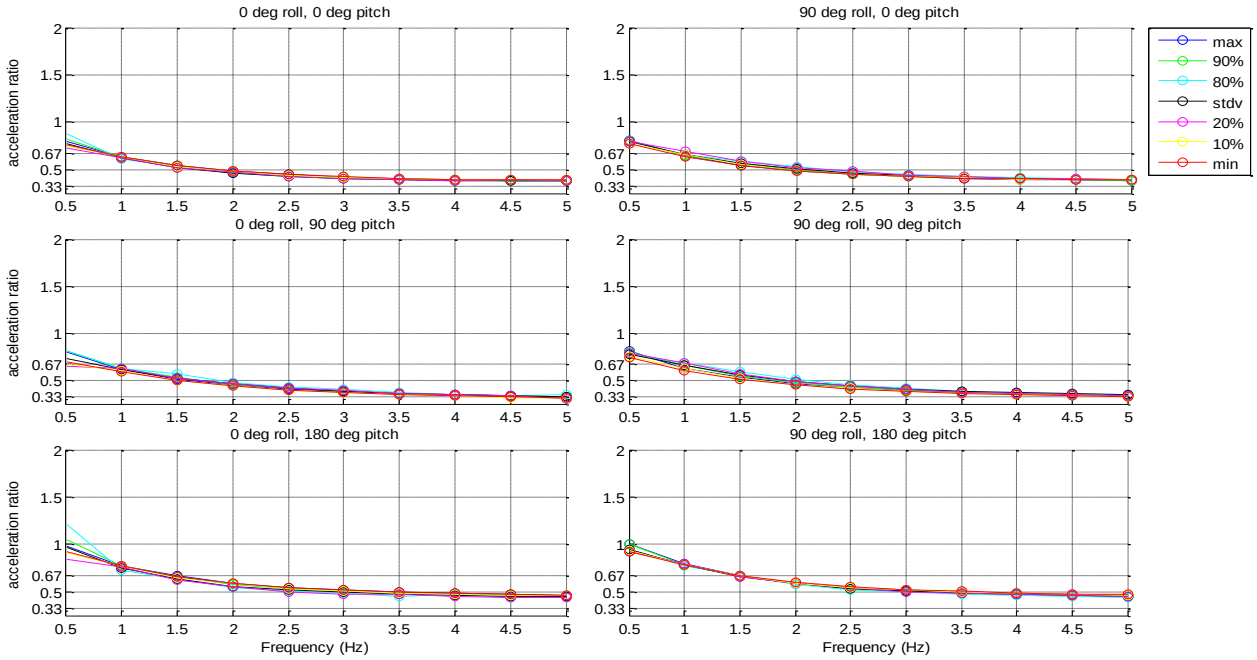

Figure 3.42 Final study simulation comparisons

3.8.9 Fifth Study: Locked vs. Free Ball Joint Rotation

With the all of iterations for the initial parametric study complete, one additional simulation configuration was evaluated with the rotational degree of freedom between the front arch and the superstructure locked out. This makes the WAM-V and the front arch affectively one rigid body with the body having three degrees of freedom in the simulation, with the body still attached to a suspension system at each of the four corners of the WAM-V. The results plotted against the baseline with a freely rotating arch are shown in Figure 3.43.

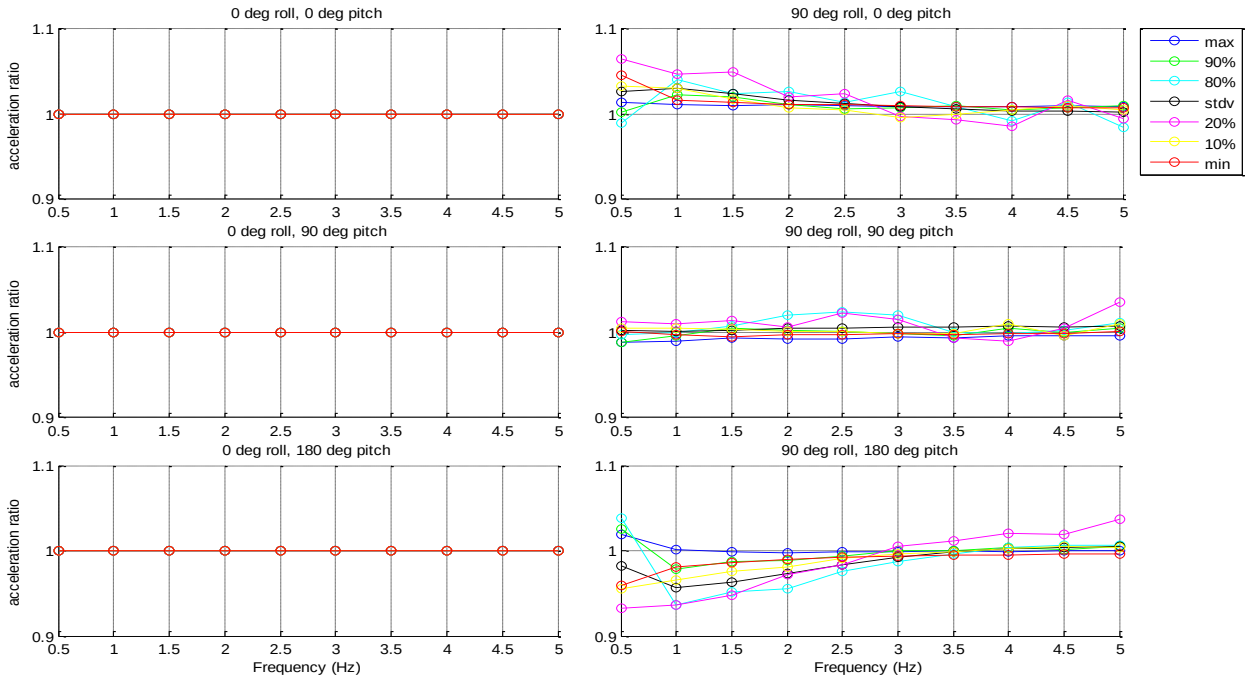

Figure 3.43 Locked out testing simulation comparisons

It can be seen that for the given suspension configuration used in both simulations, removing the degree of freedom between the front arch and the superstructure did not correlate to an increase in the acceleration levels experienced. Predictably, the front spherical joint has no effect on the simulations in the leftmost column without any difference in roll phasing. The simulations with 90 degree of roll phasing indicate marginal detriments with 0 degrees of pitch phasing, and marginal improvements with 180 degrees out of phase in pitch simulations. However, the changes are highly frequency dependent, with the accelerations levels improving at some frequencies and getting worse at others, making a decisive conclusion difficult.

For the Proteus, removing this degree of freedom is possible only in the simulation environment. Because the pontoon constraints are not part of the parametric model there is an extra degree of freedom in the suspension design which is removed by simulating the front spherical joint as a revolute joint. If the Proteus were fitted without a spherical joint it would bind kinematically; however, the simulation data may be useful in determining the direction for future suspension designs.

3.9 Conclusions from Parametric Analysis

From this study, the capabilities and limitations of the modeling environment were evaluated in a concise manner. The method of reducing the required number of iterations that needed to be evaluated in the solution set by testing suspension properties in a sequential order (overall damping, overall stiffness, stiffness distribution, damping distribution) produced between 20% and 67% reductions in the vertical accelerations experienced at the payload, with greater improvements occurring at higher frequencies. Other methods could have been used to converge on a similar result, such as using a Taguchi array or an iterative method of optimization, while still limiting the number of simulations needed to run. It is also possible that using the same method in a different order may have produced a different optimum solution. The problem of local minimums misdirecting the final solution is plausible.

The frequency range chosen provided a range of data which could have corresponded to high frequency vibrations to low frequency wave inputs. Since all frequencies were run at a constant amplitude, the higher frequency simulations experienced larger acceleration levels. The linearity of the suspension systems should not have made this much of a concern; however, for future iterations it is possible that high frequencies should be run at reduced amplitudes to match energy levels with the lower frequencies.

The method of dividing the acceleration data the new iterations by the baseline provided a concise method of interpreting the effect suspension changes on performance; however, it did not show the magnitude of the changes. Small improvements in parameters that were already producing low accelerations could show the same level of improvement percentage-wise as areas where large improvements in the acceleration levels were found; however, because the overall acceleration levels were greater in the areas of larger improvement, the improvements were smaller percentages-wise. Subtracting the baseline from the new iteration would have better highlighted these changes, and should be incorporated as a method in future studies.

Chapter 4 12-ft USV Instrumentation, Testing, and Modeling

The following chapter provides a discussion of the research into the modeling of marine vessels equipped with suspension systems made through the testing of a 12-ft Unmanned Surface Vessel (USV) developed by Marine Advanced Research, Inc. The 12-ft USV's design is compared and contrasted with the 100-ft Proteus vessel detailed in Chapter 3, and the details of the instrumentation setup and test procedure are discussed. The methodology behind the modeling and the simulation packages used is detailed, and the applications of the modeling and analysis to the work documented in further chapters are also discussed.

4.1 Chapter Overview

- Section 4.1 provides an overview of the chapter.
- Section 4.2 introduces the 12-ft USV WAM-V compared with the 100-ft WAM-V 'Proteus.'
- Section 4.3 provides an overview of the data collection for the 12-ft USV.
- Section 4.4 discusses the static testing and calibration for the 12-ft USV.
- Section 4.5 introduces the testing methodology.
- Section 4.6 provides the details of creating a simulation environment based on the 12-ft USV.
- Section 4.7 discusses different input methods for the model.
- Section 4.8 discusses a method for generating displacement inputs from accelerometer data.
- Section 4.9 shows the model validation results for the 12-ft USV model.
- Section 4.10 details model visualization using Virtual Reality Modeling Language (VRML).
- Section 4.11 provides the conclusions and recommendations for further research.

4.1.1 Significant Contributions

This chapter provides the first study on WAM-V performance specifically with the focus of evaluating the suspension system and the first academic study into remotely operated WAM-V technology. The method and the validation method for integrating acceleration data to create displacement inputs for a virtual 4-post model is novel and new for the marine domain; it is also applicable to the automotive domain. The methodology of using testing data to validate a marine 4-post model is also novel, and to the author's knowledge the first attempt at such research.

4.2 Overview of the 12-ft USV

The 12-ft USV is a second generation WAM-V design, which shares many properties with the 100-ft Proteus technology demonstrator detailed in Chapter 3. Like the Proteus vessel, the 12-ft USV was initially designed independently from the CVeSS laboratory. The USV is the next design evolution of WAM-V technology, based on the experienced gained with the testing and development from the first generation Proteus. The USV was instrumented and tested by CVeSS to gain a better understanding of the application of suspension systems for improving the dynamics of marine vessels. The 12-ft USV operating during rough water trials is shown in Figure 4.1.

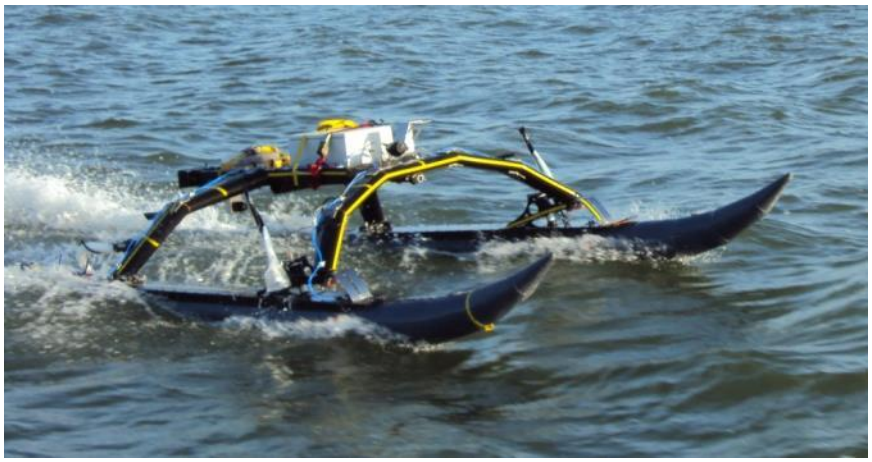

Figure 4.1 12-ft USV WAM-V

4.2.1 USV Design Architecture

The 12-ft USV shares many design features with the 100-ft WAM-V Proteus. Both the Proteus and 12-ft USV are catamarans with inflatable hulls which provide multiple degrees of freedom between the vessel and the water surface. Each pontoon is connected to the superstructure/payload tray via a series of joints and suspension linkages that move in relation to one another. Along with its lightweight structural design, the 12-ft USV has front-mounted springs and a central spherical joint that allows the vessel to articulate to mitigate some of the sea inputs from being transmitted from the pontoons to the payload tray. The component diagram for the 12-ft USV is shown in Figure 4.2.

Figure 4.2 12-ft USV component diagram

The front suspension systems on the 12-ft USV consist of an air spring and a titanium leaf spring mounted on the front corner of each pontoon. The two components are connected together via a rocker arm to a spherical joint which connects to the front arch. Like the Proteus, no dedicated damper is present on the USV. Likely due to resonances on the rear suspension on the Proteus, no rear suspension is present on the USV. Instead, the rear arches connect to the pontoons via custom two degree of freedom joints which allow for rotation along the pitch and yaw axes only. A picture of the front suspension system and aft connection joint can be found in Figure 4.3 and Figure 4.4 respectively.

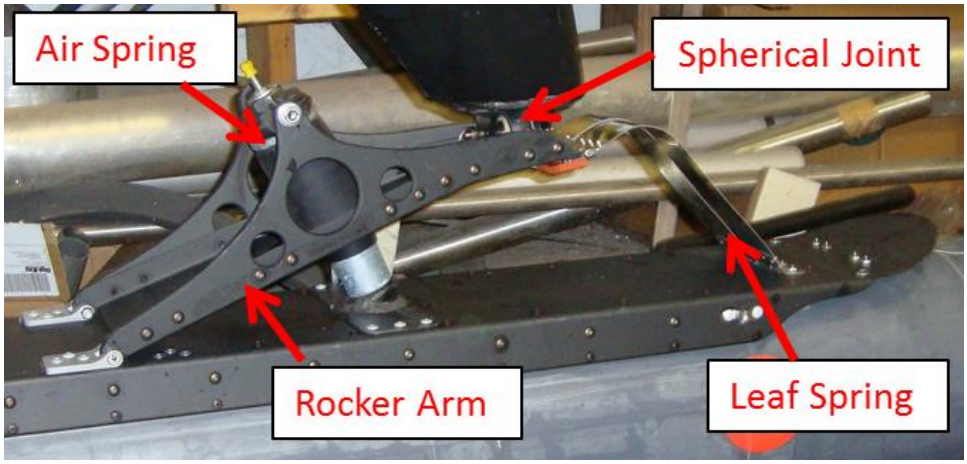

Figure 4.3 12-ft USV front suspension design

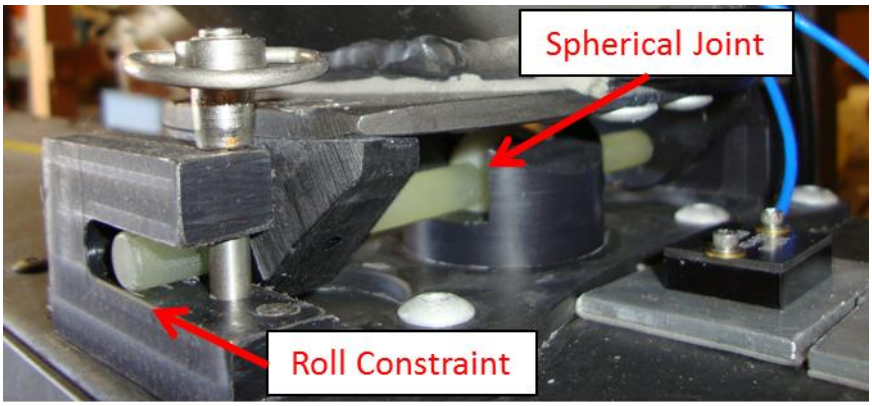

Figure 4.4 12-ft USV aft two degree of freedom joint

Each pontoon is an inflatable structure comprised of a 1mm thick Hypalon rubber shell inflated to 3 psi. The pontoons are relatively stiff in the vertical direction, compressing only minimally under heavy loading during testing. The bending stiffness of the pontoons is supplemented through the addition of aluminum skis on top of the pontoons. Each pontoon is braced by an aluminum ski that runs the across the top of the pontoon lengthwise. The skis also serve as attachment points for the suspension components and the engine pods.

The front arch which connects the two suspension systems to the superstructure uses a spherical joint for each of the three connections. A view from under the USV showing how the spherical joint connects the front arch to the superstructure is shown in Figure 4.5.

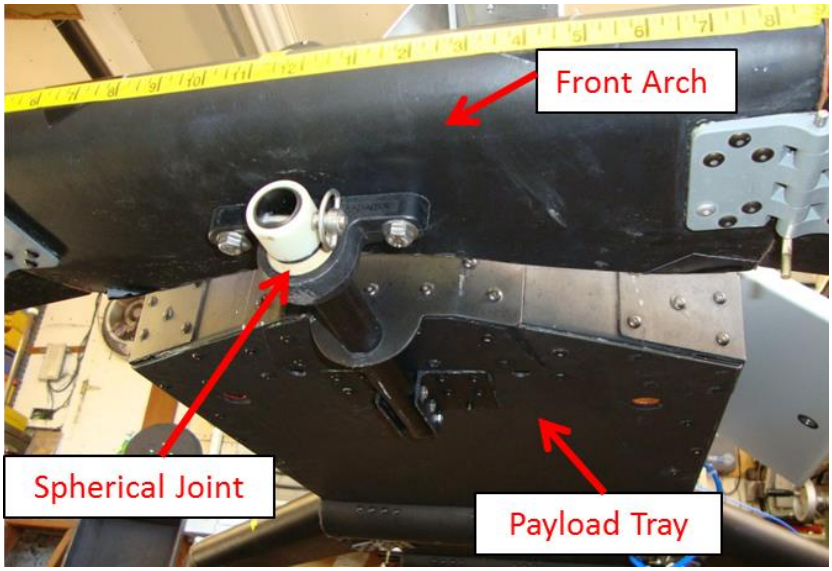

Figure 4.5 12-ft USV front spherical joint

Due to the operation of the central spherical joint, the USV has no effective stiffness as the 4 corners of the suspension move in warp. A suspension with effectively zero warp stiffness is desirable for attenuating irregular and out of phase vibrations between the four corners of the USV as is most often seen during bow-quartering maneuvers.

Like the Proteus Vessel, the 12-ft USV maneuvers primarily by using differential steering, with two engine pods located at the rear of the pontoons. The engine pods have a hinge located perpendicular to the USV's centerline, in plane with the thrust vector from the jet propulsion units, giving the engine pods an available degree of freedom to rotate with respect to the pontoons. The engine pod hinges have no spring or damper units; they rely on the buoyancy of the pods in the water to maintain proper operation. The engine pod design is shown in Figure 4.6. The engine pods are very close to being neutrally buoyant, with a mass of 31-33lbs each depending on the fuel load, and a volume of 290 cubic inches each, giving then roughly 88% the density of water. This makes for some dynamic properties as the engine pods move and the thrust vectors from the jets change with respect to the rest of the USV.

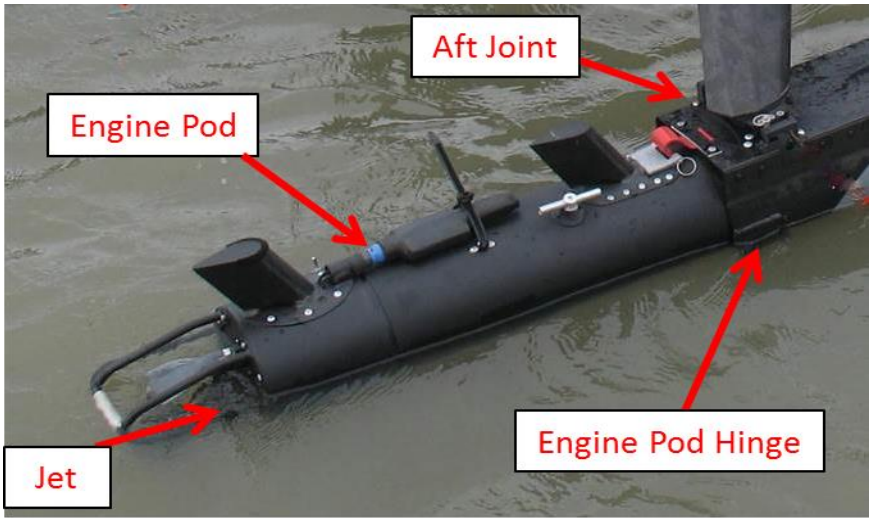

Figure 4.6 12-ft USV engine pod assembly

4.3 Overview of Data Collection

In order to quantify the dynamic properties of the 12-ft USV, a digital data acquisition system was designed and implemented to capture the USV's dynamics for analysis. A CompactRio data logger was used in combination with Labview software from National Instruments to log the data. Data was recorded at 250 Hz and 13 channels of data were recorded. Figure 4.7 shows a diagram on the USV with the locations of each of the sensors.

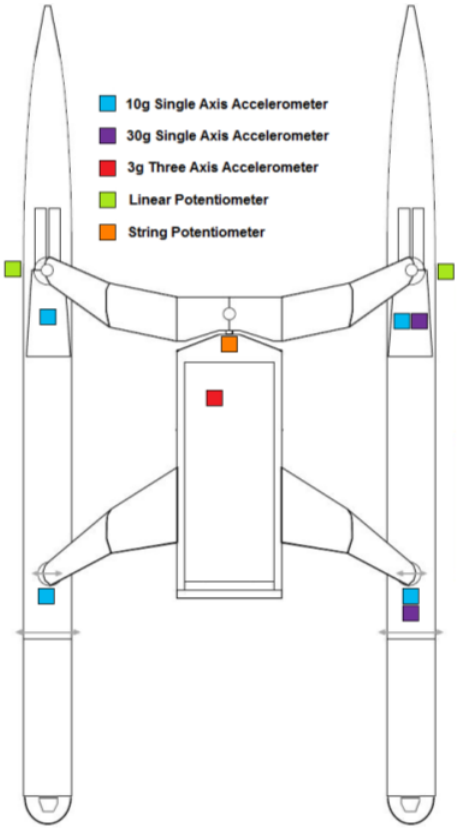

Figure 4.7 12-ft USV sensor location diagram

The CompactRio, its circuit boards, battery, and a 3g tri-axial accelerometer were mounted inside a waterproof container attached to the front of the payload tray. Holes were drilled into the side of the container to mount waterproof connectors to send power and receive signals from the other sensors. Figure 4.8 shows the data acquisition box with the top open and the waterproof connectors. The data acquisition system and some of the sensors were also implemented on the Quarter-Boat test rig detailed in Chapter 5, and on the 33-ft WAM-V for both the on-water testing detailed in Chapter 6, and for testing with the 2-post rig detailed in Chapter 10.

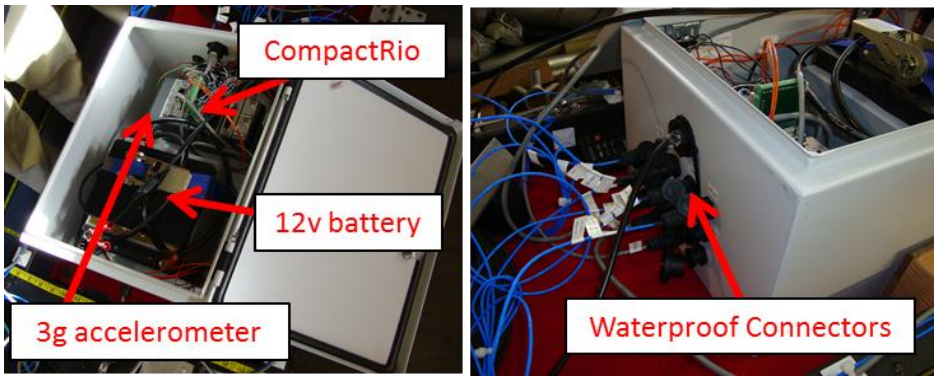

Figure 4.8 Internal data acquisition unit and waterproof connectors

4.3.1 Sensors

Four, 10g accelerometers were bolted onto 1/8th inch thick aluminum plates and the plates were mounted onto the top of the skis on the pontoons as close as possible to the suspension systems using double sided weatherproof servo tape. At the rear where no suspension is present, the accelerometers were mounted directly behind the aft joints. Two additional 30g single-axis accelerometers were mounted adjacent to the accelerometers on the starboard pontoon in case any larger events were recorded which may have exceeded the capacity of the 10g accelerometers. The 30g accelerometers also offered a possible comparison point against the 10g accelerometers to quantify any irregularities that might be seen in the data. The front accelerometers on the starboard pontoon are shown in Figure 4.9, the rear accelerometers on the starboard pontoon are shown in Figure 4.10.

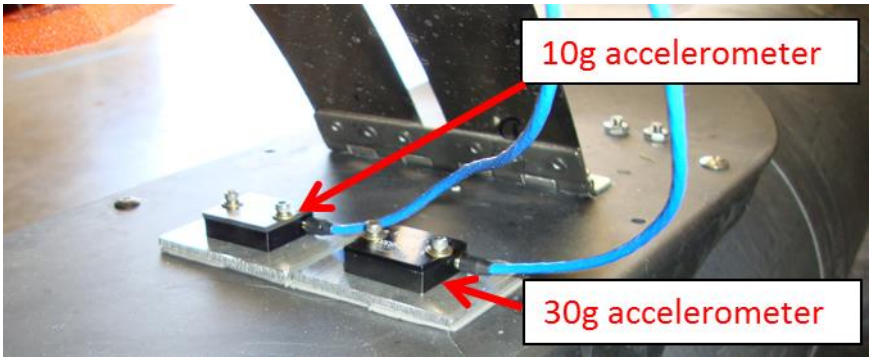

Figure 4.9 Front single-axis accelerometers

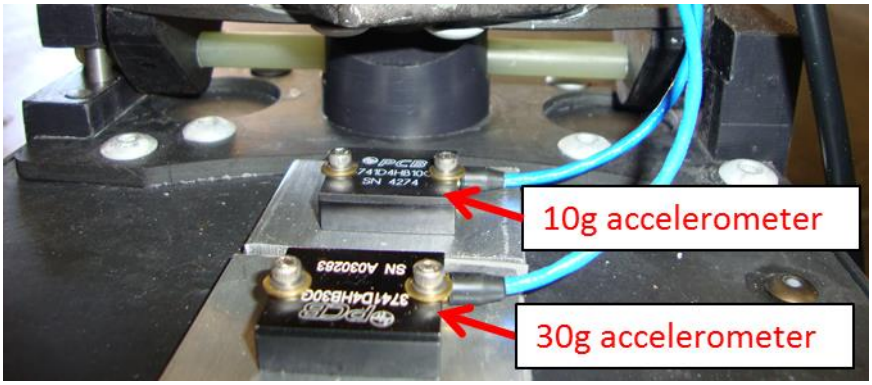

Figure 4.10 Rear single-axis accelerometers

A string potentiometer was mounted tangent to the roll axis of the USV, between the superstructure and the front arch, to measure rotation of the front arch. Since the front arch connects to the superstructure via a spherical joint, some out of axis rotation also occurs to allow

the system to avoid binding kinematically. This motion is also inadvertently recorded in the potentiometer data. However, since the primary rotation was about the axis being measured, the differences should be negligible. Figure 4.11 shows the mounting of the string potentiometer, the potentiometer is mounted to the superstructure, the end of the string is mounted on top of the front arch.

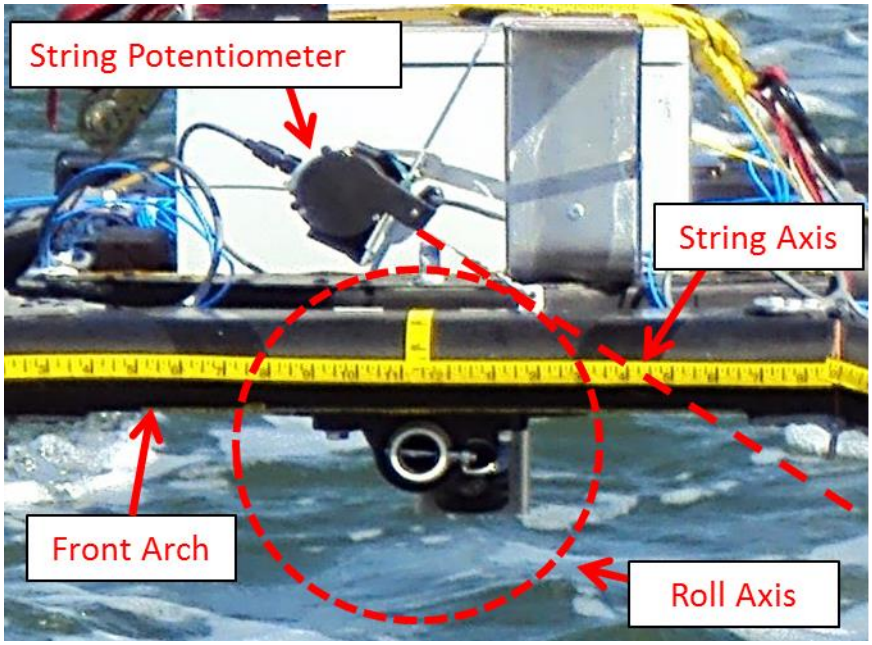

Figure 4.11 String potentiometer mounted between superstructure and front arch

Two linear potentiometers were mounted in line with the air springs in order to measure suspension displacement. The potentiometers were mounted between the rocker arms and the skis and were free to rotate as the rocker moved through its travel. Figure 4.12 shows the mounting of one of the linear potentiometers on the starboard suspension system.

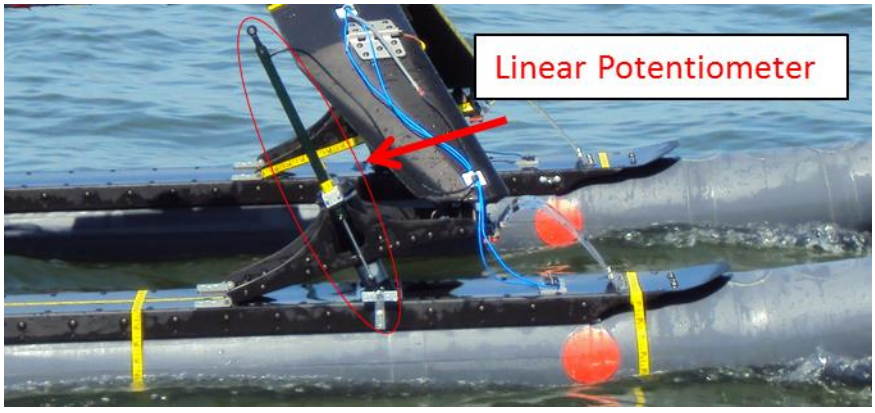

Figure 4.12 Starboard linear potentiometer mounted between rocker and ski

4.3.2 Video Acquisition

In addition to the data acquisition system, a standalone video logging system with GPS was mounted below the payload tray along the centerline of the USV. Figure 4.13 contains a screenshot taken from the onboard camera while idling in calm water. A second camera was operated from the chase boat during the testing to record additional video data of the USV. Figure 4.14 shows a screenshot taken of the USV from the chase boat camera during one leg of a bow-quartering testing run.

Figure 4.13 Screenshot taken from onboard camera

Figure 4.14 Screenshot taken from camera on chase boat

4.4 Static Testing and Calibration

Prior to conducting instrumented on-water testing with the 12-ft USV, a number of static tests and calibrations were performed to aid with future modeling efforts and data analysis of the USV. This section details the tests on the USV that were conducted prior to the on-water testing.

4.4.1 Spring Rate Testing

Due to the difficulty of performing an analytical analysis on the titanium leaf spring/air spring combination, a static physical test was conducted to determine the effective vertical spring rate of the entire suspension system. The air spring used on the USV is a Goodyear Sleeve-Lobe type air spring, model #1S3-011. The manufacturer provided air spring data is shown in Figure 4.15.

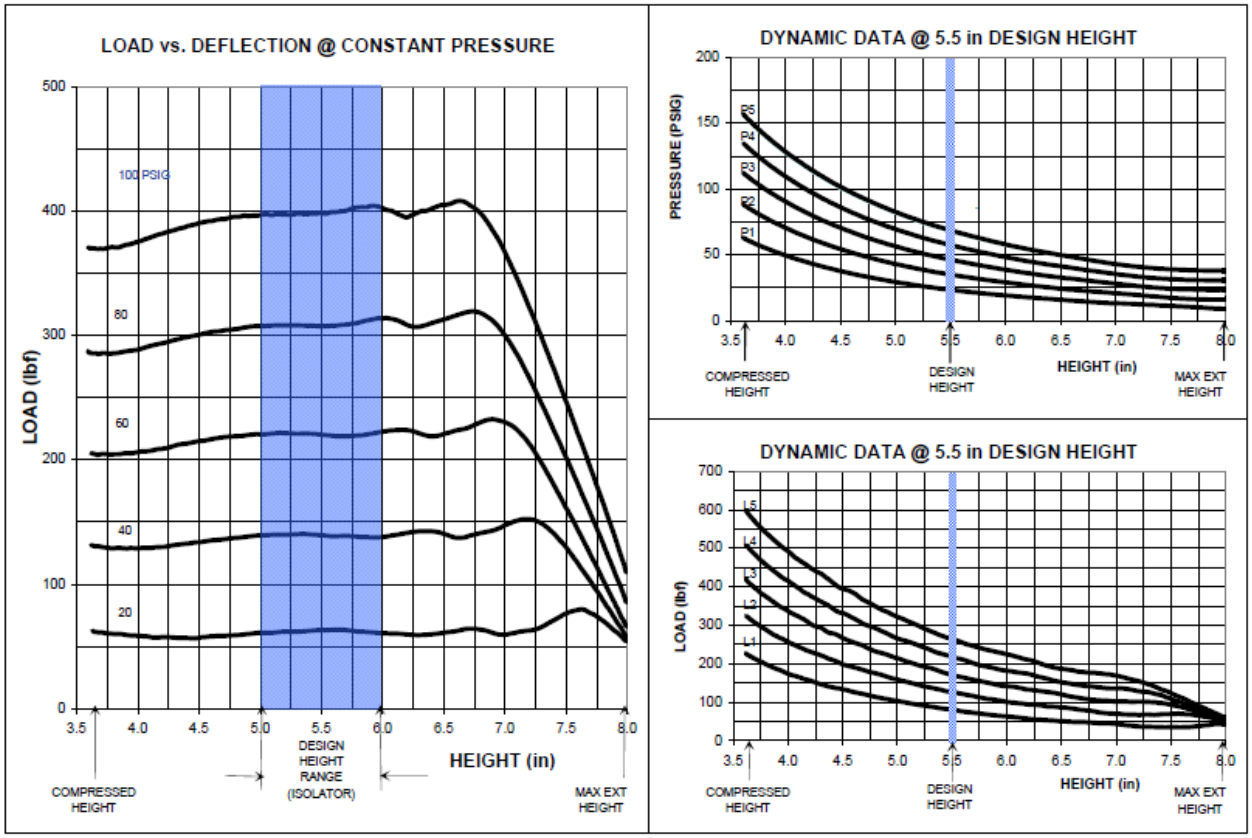

Figure 4.15 Manufacturer provided air spring data [46]

Due to the lightweight nature of the USV, the air spring had to be operated below its intended pressure range to achieve the desired ride height, operating at only 14.5 PSI. The data from the manufacturer is listed from 20-100 psi. This likely introduces further nonlinearities into the system, making a physical test all the more pragmatic. The air springs were already installed on

the USV and no load testing equipment was available at the shop where the USV was instrumented prior to testing, so the installed stiffness of the air springs was evaluated by applying various weights to the payload tray of the USV and measuring the suspension deflection where the spherical joint connects to the rocker arm. The resulting force vs. displacement curve produced for the suspension assembly from the test is shown in Figure 4.16, the points on the graph represent the actual measurements from the test.

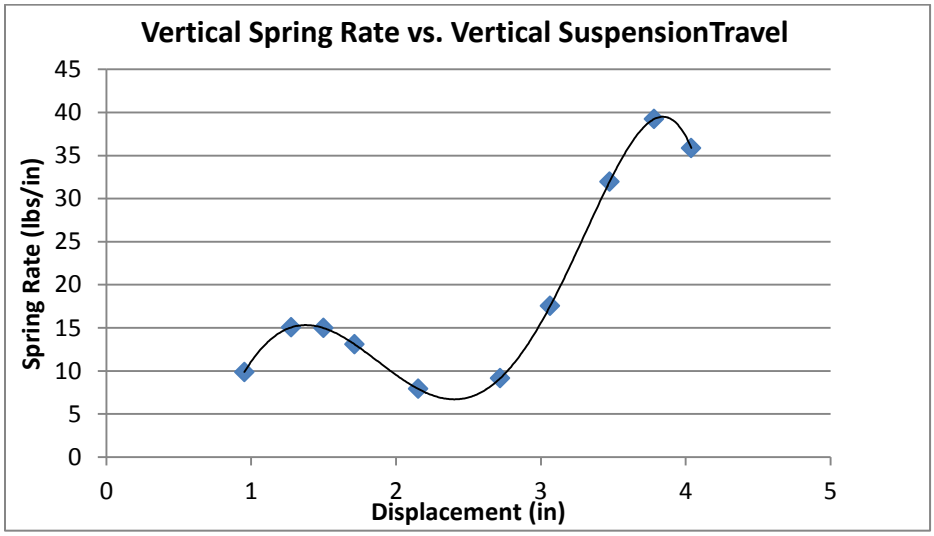

Figure 4.16 12-ft USV spring rate vs. spring displacement

Due to the nature of the test, no force information could be gathered above the static deflection of the suspension (< 1 inch) with no additional load applied. From the testing, the suspension was found to be both very stiff and highly nonlinear in its suspension stiffness. During compression, the suspension is initially stiff, then it softens in the middle of its stroke, then it becomes very stiff near the end of the stroke as the suspension nears full compression. The result is a suspension system that does not show much movement for small inputs, and then shows similar levels of deflection for medium and large inputs. However, the suspension system is not prone to excessive bottoming out in compression.

4.4.2 Center of Gravity Testing

The longitudinal center of gravity of the 12-ft USV was determined by conducting a knife test on the USV. The center of gravity was determined by finding the point at which the USV would balance on a 2 inch diameter piece of tubing placed perpendicular to the USV's centerline under the pontoons. A piece of tubing was used in place of a knife edge to reduce the local deflection

of the pontoons. Measurements were made with the hinged engine pods disconnected, and then the center of gravity of each engine pod was measured separately using the same method. The fuel load of the engine pods was also recorded. Figure 4.17 shows the USV dimensions in the side plane needed to interpret the longitudinal center of gravity tests results. Table 4.1 shows the center of gravity measurements made with and without the engine pods. The vertical center of gravity was not tested for directly. The USV has a slight forward weight distribution (53.2%) with no engine pods and a large rearward weight distribution (76.8%) with the pods installed.

Table 4.1 12-ft USV center of gravity measurements

Center of Gravity Measurements		
Distances:	**A (in)**	**B (in)**
No engine pods	25.8	29.2
With engine pods	42.2	12.8
Weight Distributions:	**Front %**	**Rear %**
Without Engine Pods	53.2	46.8
With Engine Pods	23.2	76.8

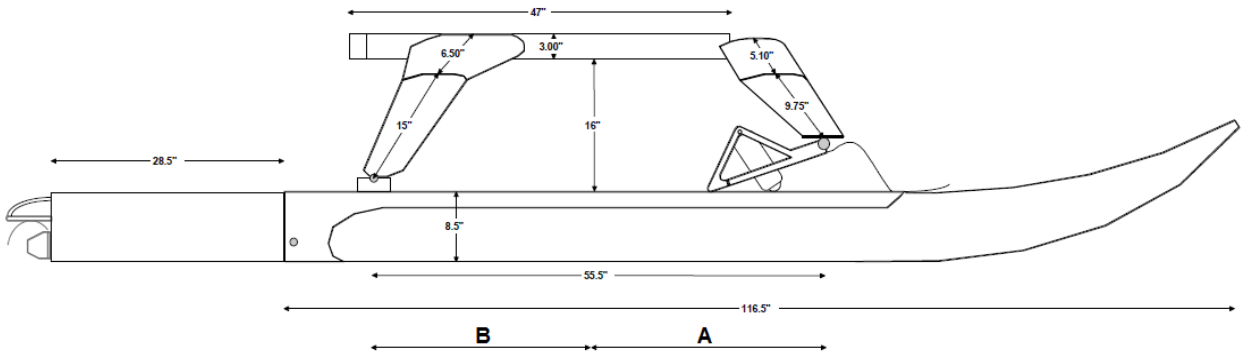

Figure 4.17 Side view measurements

4.4.3 String Potentiometer Calibration

The relationship between the linear movement of the string potentiometer and the rotation of the front arch relative to the superstructure was established through a static a physical test conducted in the lab prior to testing on the water. Since the potentiometer was mounted asymmetrically, the calibration had to be performed in both directions of front arch's rotation. It is noteworthy that the potentiometers used are designed in such a way that they displayed a step change in resistance once every rotation as the string wraps around the pulley inside the potentiometer. Because of this feature, the potentiometer can go from full to near zero resistance if operated out

of range. This is important in case large spikes are recorded in the data at rotations corresponding to the limits of the potentiometer's designed travel. The relationship between the angle of the front arch relative to the superstructure and the ratio of the measured voltage from the string potentiometer divided by the input voltage is shown in Figure 4.18.

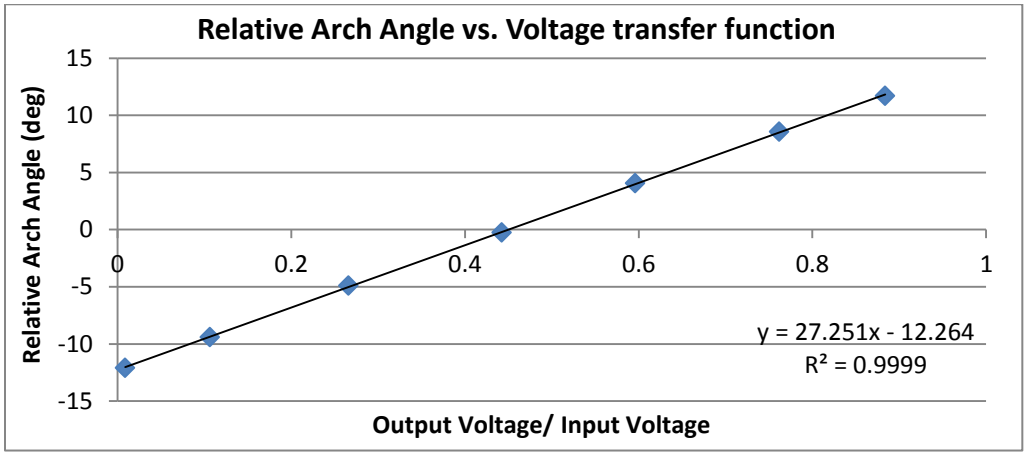

Figure 4.18 Angle between front arch and superstructure vs. output/input voltage

4.4.4 Linear Potentiometer Calibration

The relationship between the displacement of the linear potentiometers and the displacement of the spherical joint connecting the rocker arm to the front arch was also measured. A graph showing the movement of the linear potentiometers and the ratio of the input battery voltage to the measured voltage from the linear potentiometer is shown in Figure 4.19. The graph shown is an average between the left and right potentiometers, which showed nearly identical force versus displacement responses.

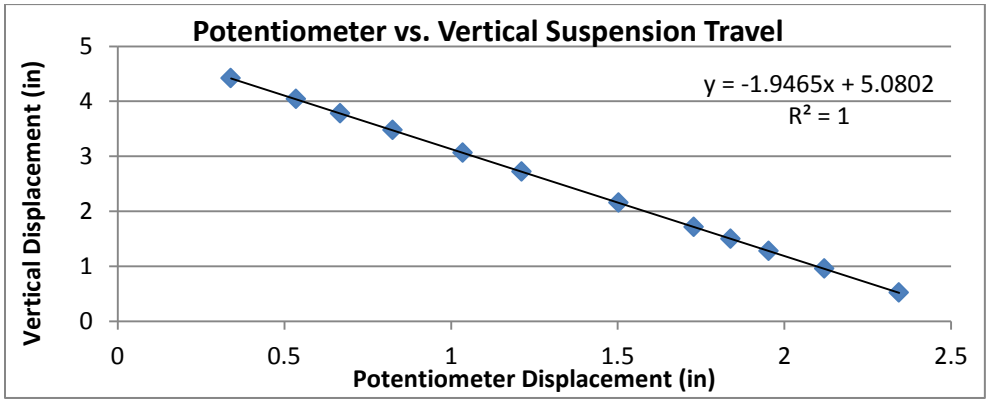

Figure 4.19 Linear potentiometer displacement vs. output/input voltage

4.4.5 Component Weights

In order to create an accurate model of the 12-ft USV, the weights of the individual components also needed to be measured. After instrumenting the 12-ft USV with the data acquisition system, the USV needed to be disassembled for transportation from the shop to the marina for testing. At this time, all of the components were weighed individually. Table 4.2 contains the weight of each of the major components as measured.

Table 4.2 Individual component weights

Component:	Quantity:	Weight Each: (lbs)
Arches:		
Front arch	1	13.1
Right rear arch	1	6.3
Left rear arch	1	6.45
Pontoons:		
Right pontoon assembly	1	22.65
Left pontoon assembly	1	22.87
Superstructure:		
Chassis/ Payload Tray	1	35
Battery	1	21.7
Data acquisition box	1	21.5
Engine Pods:		
Right engine pod	1	30.9
Left engine pod	1	31.1
Radio Receivers	2	2.65
Fuel load	2	4.03
Total Weight (lbs):		**224.93**

4.4.6 Moment of Inertia Estimation

In order to complete the model for the USV, not only are the component's masses needed, but the moments of inertia of the components as well. Since the component models were being imported from the CAD model, the inertias were estimated by specifying a constant density for each component that would correspond to the correct component mass, and recording the moments of inertia at the center of mass aligned with the output coordinate system from CAD for input to the model.

4.5 Testing Methodology:

The goal of the testing methodology was to evaluate the boat's performance at 45 degree angle increments relative to the wave headings found within the San Francisco Bay where testing was conducted. By assuming the boat's response is symmetrical about its centerline, the eight possible orientations can be reduced to five: Head, Quartering, Beam, Bow Quartering, and Stern were the tested directions. As recommended by NAVSEA, the two patterns shown in Figure 4.20 used for testing. The patterns are the same except that Pattern A ends in the same place it begins and Pattern B has equal testing lengths and requires a smaller area for testing. For most of the testing Pattern B was used. The pattern was carried out twice for each speed, with times of approximately 2-3 minutes per leg. The testing directions and speeds are listed in Table 4.3.

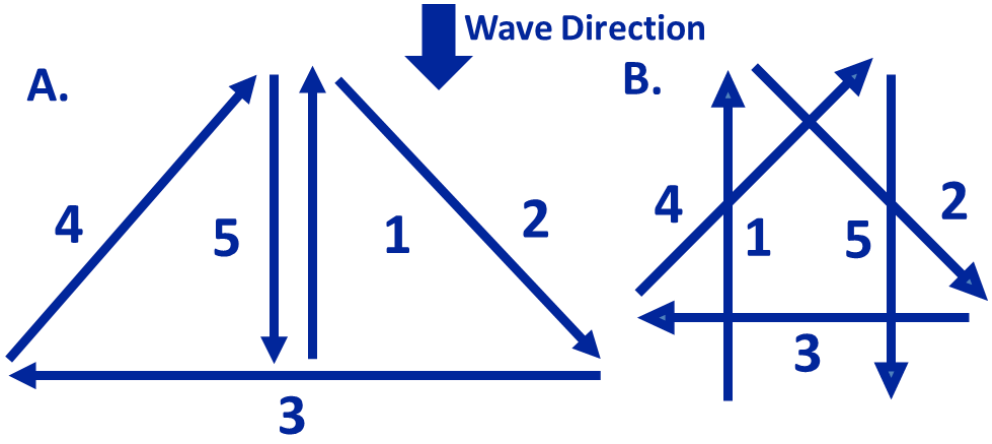

Figure 4.20 Diagram of testing directions

Table 4.3 Test directions and speeds

Test Leg #	Heading angles: (deg)	Heading Type:	testing speeds: (knots)
1	180	Head	4, 7, 12
2	315	Stern Quartering	4, 7, 12
3	90	Beam	4, 7, 12
4	225	Bow Quartering	4, 7, 12
5	0	Following	4, 7, 12

The USV's speed and orientation were synchronized with the chase boat. The USV was positioned to the side of the chase boat facing the direction of the wave heading to minimize disturbances from the chase boat. Speed was measured by GPS, wave direction was estimated at the beginning of a test and not updated between pattern legs. Actual wave directions varied; waves in the bay are highly affected by ships operating in the vicinity of the testing area.

4.6 12-ft USV Modeling

Expanding upon the parametric model constructed for the previous dynamics simulations in Chapter 3, a three-dimensional, multi-body dynamics model was desired for the 12-ft USV to help to quantify its dynamic properties. As with the parametric model, Simulink and SimMechanics were chosen as the modeling environments due to their ability to interface with Matlab for analysis. However, compared to the parametric model, significant changes were made due to the different architecture of the 12-ft USV. The following section details the process of constructing a model for the 12-ft USV, the model is validated with testing data in Section 4.9.

4.6.1 Model Complexity

For the purposes of simulating the dynamics of a 4-post shaker rig, two possible models of different complexity are normally used to evaluate a vehicle's performance. The first model type, shown in Figure 4.21, has three degrees of freedom of the chassis in heave, pitch, and roll, as well as the vertical motion of each of the four suspension systems.

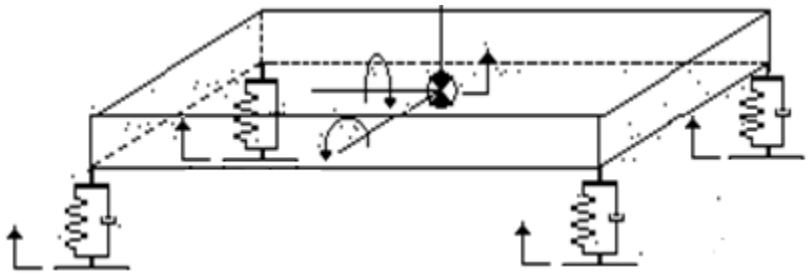

Figure 4.21 4-post model conceptual schematic (adapted from [47])

The simulation developed for the 12-ft USV is built similarly to a three degree of freedom 4-post model. The data used to create the model's inputs is taken at the top of the pontoons, and the overall response is measured at the payload. The 4-post model is modified for the USV since the 12-ft USV does not have rear suspension systems, which effectively removes the roll degree of freedom of the chassis relative to the rear inputs from the model. However, the spherical joint located on the front arch provides an additional degree of freedom, so in fact the chassis on the 12-ft USV model can still be considered to have three degrees of freedom.

A common drawback to conducting a 4-post simulation with the degrees of freedom shown in Figure 4.21for an automobile is that the dynamics of the unsprung mass and tires are not considered in the model. This is also particularly relevant to the 12-ft USV, where the

accelerometers were mounted on top of the pontoons, so any displacementss calculated from testing data represent the motion of the pontoons only, not necessarily correlating to the height of the waves experienced during the tests. Therefore, changes to the USV's properties in the model, such as shifting the center of gravity or altering the suspension stiffness and damper rates could cause the inputs that were recorded for the original configuration to become unrepresentative of the new vessel's configuration as simulated. As an example, it is likely that for a given wave event a more softly-sprung suspension would experience greater pontoon motion due to the suspension compressing more over the wave; whereas a more stiffly sprung suspension would tend to crash through the wave with less vertical pontoon motion. This would not be accurately reflected in the simulations if the same inputs were used for both simulations.

A more complex 4-post model for an automobile that incorporates tire dynamics and unsprung masses is shown in Figure 4.22. For the WAM-V, the tire spring rate and damping would be replaced by the water's hydrodynamic stiffness and damping. The unsprung mass at a given corner would be equal to the portion of the pontoon's mass under that corner plus an added mass coefficient representing the water that is moved during vertical oscillation of the pontoons. It is also noteworthy that the inflatable pontoons have their own degrees of freedom. However, since the pontoons are far less compliant than the water surface, the non-rigid pontoon dynamics have limited impact on the USV's overall performance.

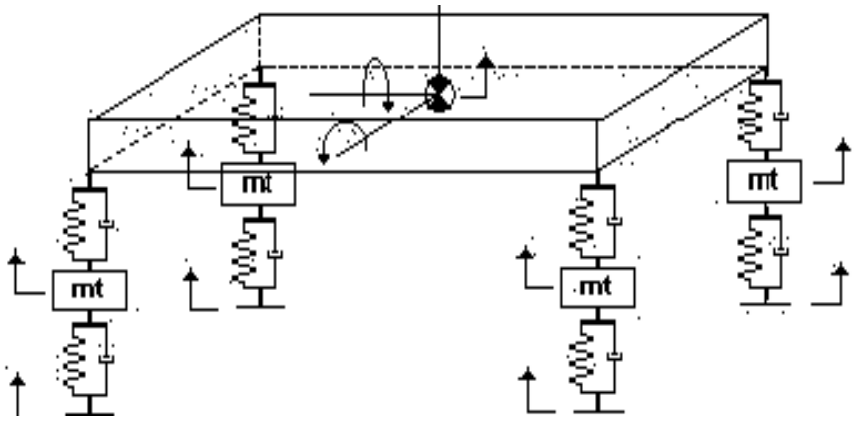

Figure 4.22 4-post model incorporating tire dynamics [47]

For the purposes of modeling the 12-ft USV, a model incorporating tire dynamics was not deemed necessary. Chapter 5 covers a possible method for investigating and incorporating such dynamics into a model. Models incorporating these dynamics are covered in Chapters 8 and 11.

4.6.2 Exported CAD Model for Model Generation

The process of creating a simulation environment for the 12-ft USV begins using CAD to generate a representative, but simplified model of the USV. An initial model can be generated using CAD to develop blocks with the proper dimensions, masses and inertias; modeling individual subcomponents that are rigidly attached to one another is not necessary and will further complicate the modeling process later on. Properties from the CAD model can be imported into SimMechanics using the SimMechanics Link plugin. It is possible to have the model display the proper joint constraints as well, although this is only effective for basic models. Figure 4.23 shows a simplified Solidworks representation of the USV.

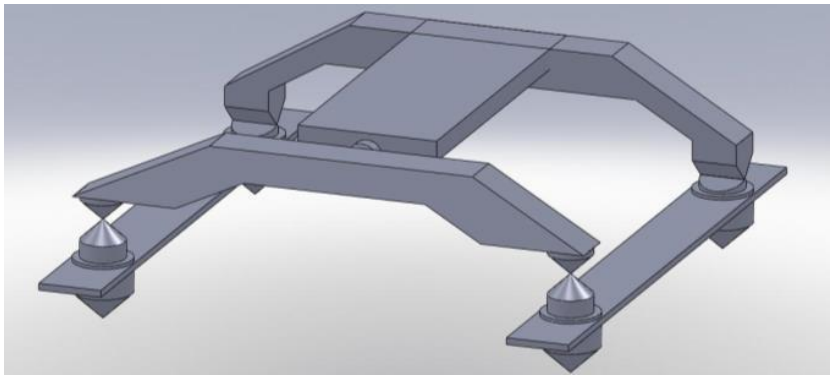

Figure 4.23 Simplified CAD representation of the 12-ft USV

After importing the CAD model, the joints need to be reconfigured to match the degrees of freedom of the model. Figure 4.24 shows the available degrees of freedom of all of the joints of the 12-ft USV model individually, Figure 4.25 shows the available degrees of freedom on the USV with all of the joints connected.

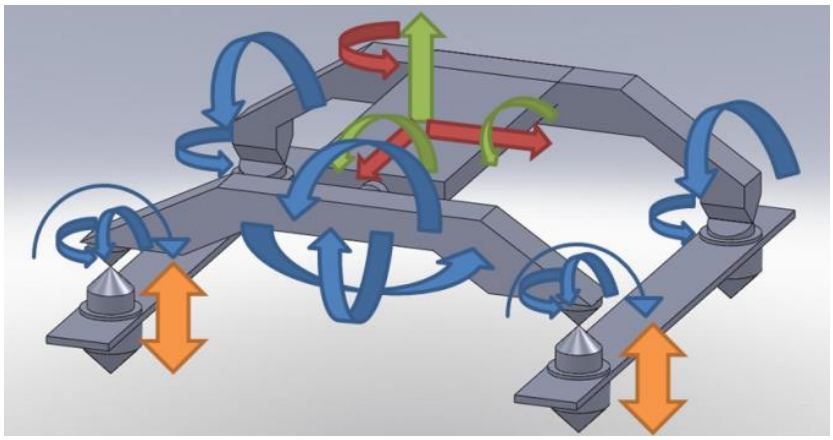

Figure 4.24 12-ft USV model individual joint degrees of freedom

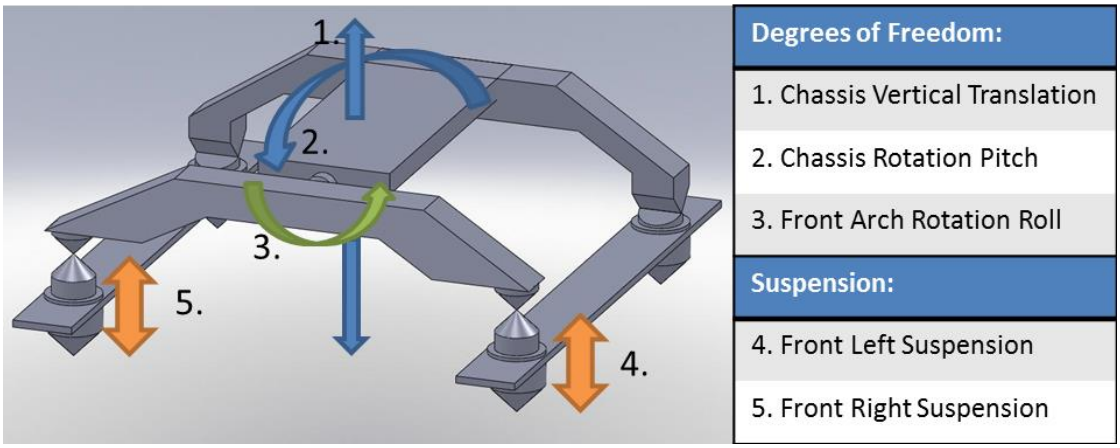

Figure 4.25 12-ft USV model assembled degrees of freedom

The roll degree of freedom of the center of gravity joint is not included in Figure 4.25. Due to the USV's architecture, the roll angle of the chassis is constrained by the aft inputs; it is not available as an independent degree of freedom.

4.6.3 Model Damping

Since no dedicated damper is present on the USV, the damper settings in the model were approximated using an initial condition response to generate an appropriate damping ratio for the model. The response of the model to the initial condition is shown in Figure 4.26. Note the damping is approximated using a viscous damping response, rather than the coulomb friction damping present in the joints. The model has a ~15% critical damping ratio.

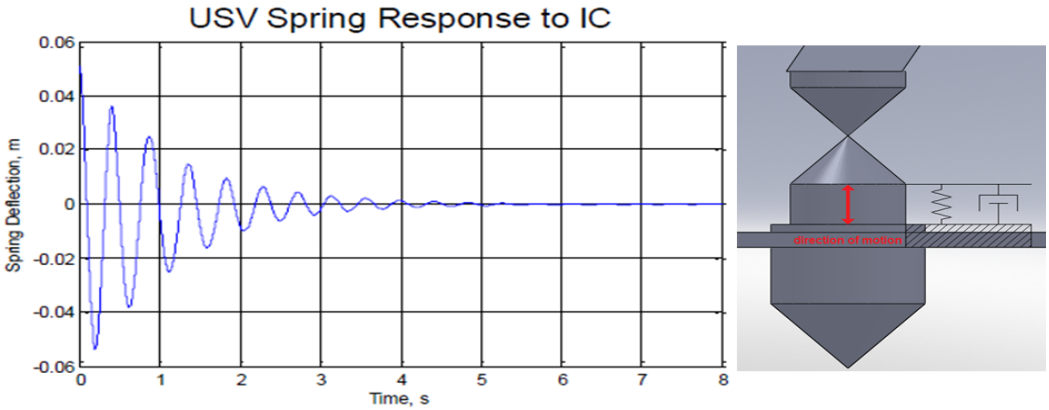

Figure 4.26 Suspension degree of freedom and damping decay response

The suspension configuration for the model was simplified from the rocker arm configuration with the leaf spring and the air spring found on the USV. Instead, the suspension is represented by a prismatic joint with the same vertical suspension properties as the USV.

4.6.4 Block Diagram Model of the 12-ft USV

Figure 4.27 shows the complete block diagram model for the 12-ft USV constructed using SimMechanics. Each of the red blocks represents a joint constraint between two component bodies. The superstructure, labeled 'main body' on the block diagram, has a further connection to the ground via a three degree of freedom joint which allows for vertical translation, and pitch and roll rotation, but prohibits longitudinal and transverse displacement, as well as rotation in yaw. It is also noteworthy that the connection between the pontoons and the engine pods is represented as a zero degree of freedom weld joint for this model. This is not an accurate representation of the hinge present on the pods of the USV; however, since the actuators for the model are connected to the pontoons directly, the motion of the engine pods does not contribute to the dynamics of the rest of the model. Models for other WAM-Vs may be reconfigured to include input actuators under the engine pods and rotational joints on the pods. A 6-post model incorporating actuators for the engine pods is detailed in Chapter 11 for the 33-ft WAM-V.

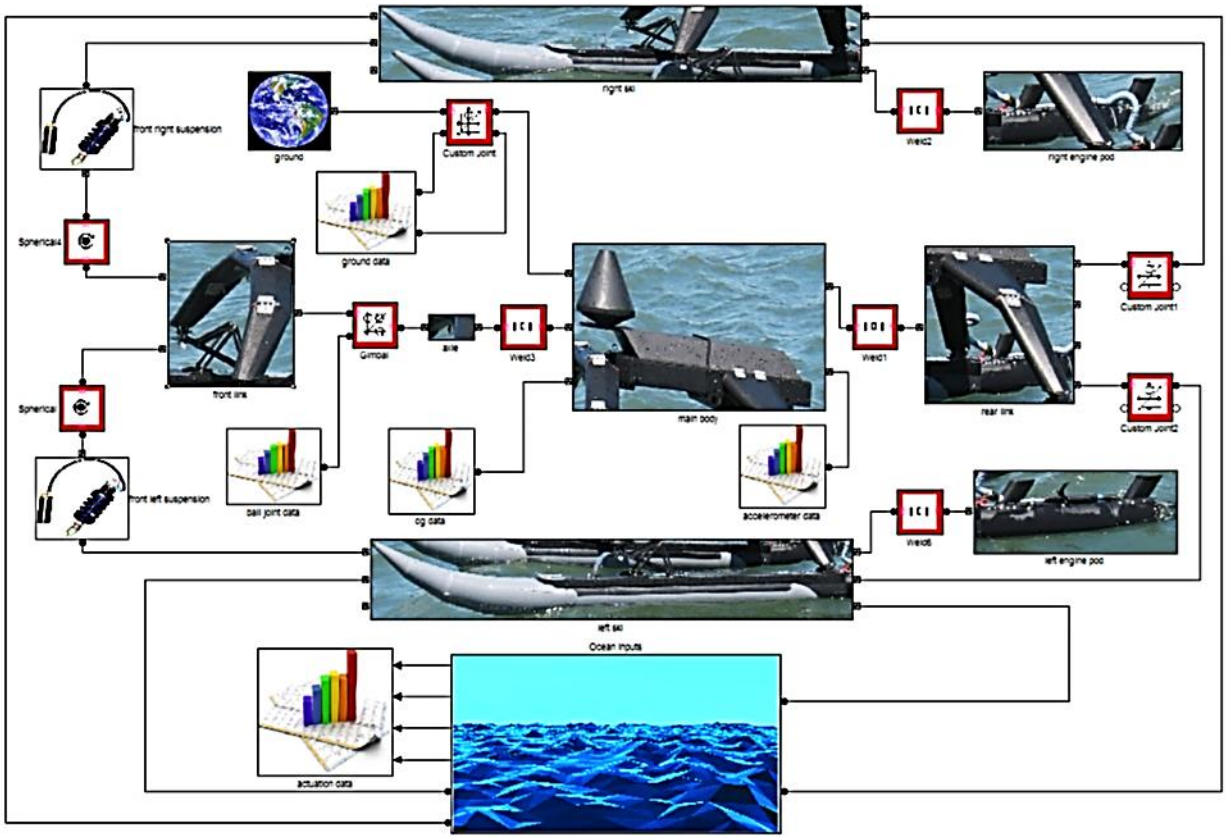

Figure 4.27 Block diagram model of the 12-ft USV

4.7 Base Excitation Model Inputs

In a time domain simulation, the states of each rigid body can be classified by their respective positions and velocities. With two known states of the model and a time between the two states also established, the required acceleration to reach the second state from the first can also be determined. This process becomes slightly more complicated in a completely discrete-time environment when each state is solved for independently of the other states. Designing a method of base excitation within the SimMechanics environment requires the use of discrete time steps. Furthermore, within Simulink, the signals themselves are indeterminate, meaning that the current state of the model is independent of all the previous states. Because of this, the states required for a simulation using SimMechanics model include the position, velocity, and acceleration at each time interval. This leads to additional stability requirements in order for the model to run properly within a certain error tolerance. The position, velocity, and acceleration terms need to be transmitted into the joint actuators at each individual time step, as shown in Figure 4.28. A few possible methods for determining these three signals are presented in the following sections.

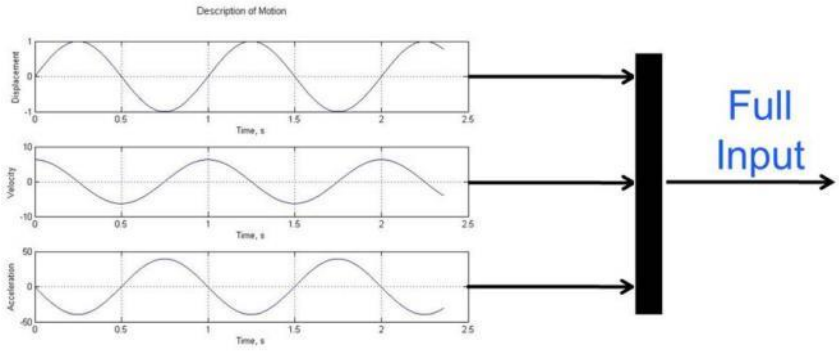

Figure 4.28 Three component signals required for data input

4.7.1 Derivative Method

The derivative method is the simplest method of producing a three component signal of position, velocity, and acceleration. Simulink provides a commonly used derivative block for numerical differentiation of a signal. Figure 4.29 shows an example of using a derivative block for generating a three component signal from a sine wave. The derivative method is fine for sending sine wave signals generated in code. However, due to the possibilities of discontinuities, derivative blocks are not recommended for differentiating motion signals from stochastic data.

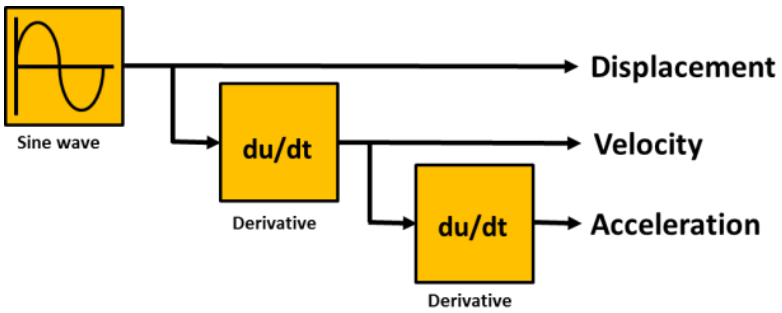

Figure 4.29 Derivative method of sending vertical displacement signals

4.7.2 Transfer Function Method

The use of a transfer function block can also be used to differentiate a displacement input into a three component signal. Using a Laplace block as in Figure 4.30 actually performs a Laplace transform convolution to smooth the output of a signal, which is not an exact representation of the derivative. Thus, performing two Laplace transforms will not exactly produce an acceleration that is representative of the changes to the input displacement as a function of time.

This drawback can be eliminated by filtering the original signal, then defining exact derivatives of the filtered signal by adding higher orders to the transfer function numerator. The order of the denominator should be equal to or greater than the number of output signals. For the displacement the filtered signal should be used, as well as the two filtered derivatives.

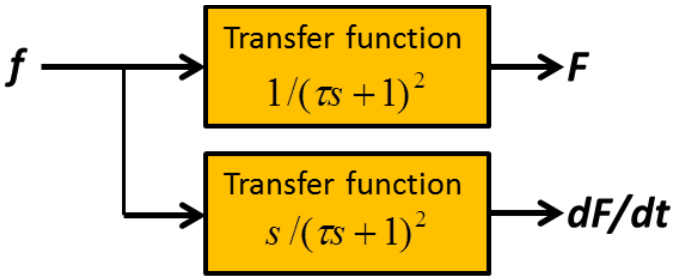

Figure 4.30 Transfer function differentiation of position signals

In the example shown in Figure 4.30, the constant τ represents a smoothing time. The transfer functions define a filtered signal and its first derivative. Therefore, the denominator of the transfer function should be second order or higher transfer function. Increasing the smoothing time τ will increase the filtering of the signal; τ should be made as small a possible though to avoid discontinuities. The transfer function method for differentiating a single is recommended by The Mathworks to create a three component signal for use in SimMechanics [48].

4.7.3 Numerical Differentiation

The most accurate method of producing a three component signal is to individually filter and take derivatives of the three signals and adjust them manually while checking for discontinuities that might lead to errors in the simulation. This method is very similar to the derivative block method, but differs in that it is far less likely to produce discontinuities in stochastic data. Figure 4.31 shows an example of using lookup tables to form a three component signal and then applying the full input signal to the machine blocks in SimMechanics.

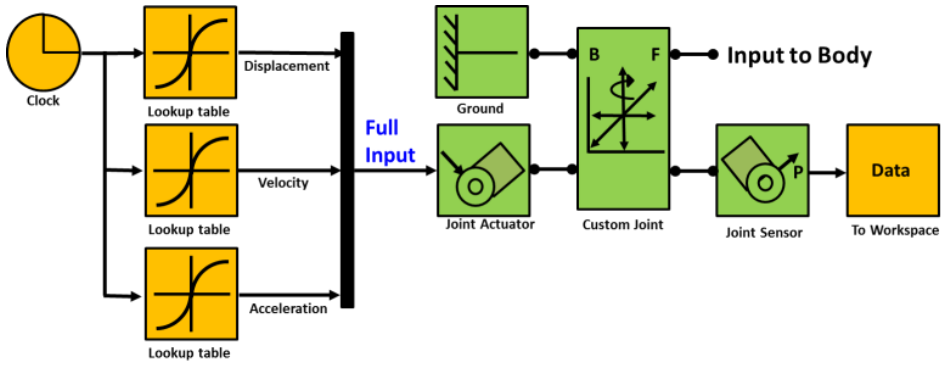

Figure 4.31 Direct input method for specifying displacement inputs

4.7.4 Integration of Acceleration Signals

Specifying the highest derivative of a three component signal and then integrating the signal to obtain lower derivatives can be accomplished using two integrations. For continuous data this is an inherently stable method. However, it is possible that integrating the signal will cause a diverging dc offset to occur in the integrals, producing unwanted rigid body motion. This is particularly prevalent when integrating accelerations from a digital data acquisition system. Figure 4.32 shows an example of specifying an acceleration signal and integrating using a 1/s transfer function. A method used for integrating accelerometer data into displacement inputs is presented in the next section.

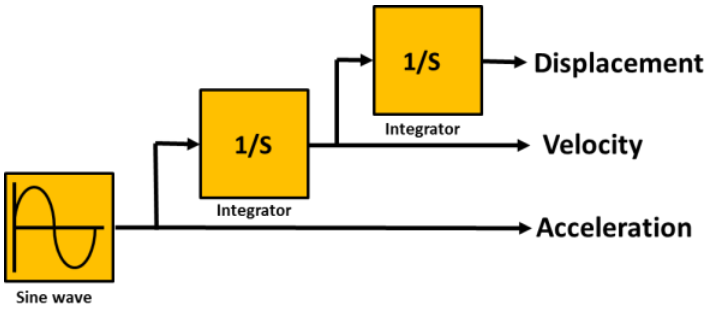

Figure 4.32 Integration of acceleration signal with transfer functions

4.8 Generating Model Inputs from Accelerometer Data

A significant part of the motivation for performing on-water testing with the 12-ft USV was to obtain better inputs for the 4-post model. On the water, global displacements cannot be measured directly; however, accelerations can. The following section details the process for creating a method to convert raw acceleration testing data into displacement data for the 4-post model.

Integration of discrete data can be performed either in the time domain or the frequency domain. Each domain has relative advantages and disadvantages depending on the application. Frequency domain integration is performed by first using an FFT to sort the raw data as a function of frequency. Integration in the frequency domain is then performed by dividing the data by its respective frequency and then the data is returned to the time domain by performing an inverse FFT. Compared to time domain integration, frequency domain integration is often more simplistic since the mathematical procedures for integration are reduced to simple algebraic operations [49]. Frequency domain integration is most accurate at high frequencies. Problems arise at lower frequencies; as the frequency approaches zero, errors asymptote towards infinity.

Due to the limitations of using frequency domain integration for low frequency data, integrations were performed in the time domain. Integration in the time domain is more accurate for the frequencies of interest for analyzing the dynamics of WAM-Vs. In order to obtain usable outputs, first the data needs to be preprocessed to minimize potential errors prior to integration.

4.8.1.1 Removing Mean from Dataset

The accelerometers employed on the USV generate a DC signal at rest from the acceleration due to gravity. A DC offset in the data will become an unwanted 1st order function in the integral output once the first integration is performed. To remove the offset from the raw data, the mean acceleration of data set needs to be calculated and subtracted from the data prior to integration.

4.8.1.2 Low-Pass Data Filter

The two engines on the 12-ft USV generate significant high frequency vibration at ~35 Hz at idle. This vibration is picked up by the accelerometers on the pontoons, as shown in Figure 4.33. The high frequency vibration is removed from the data through the use of a low-pass filter, set at 30 Hz to avoid disturbing the oceanic inputs in the data which occur at lower frequencies. The filter used is a 5^{th} order Butterworth filter, chosen for its maximally flat pass and stop bands [50]. An FFT comparison of the accelerometers with the engines on and off is shown in Figure 4.34.

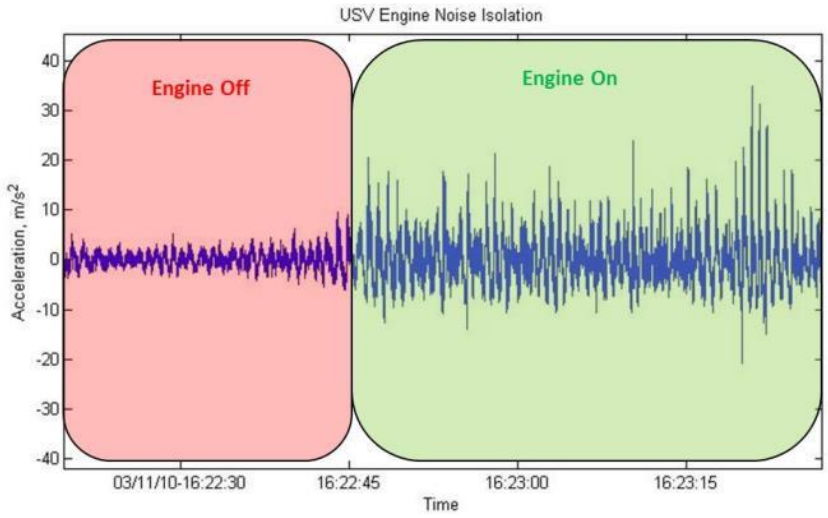

Figure 4.33 Time-series accelerometer data comparison with engine on and off

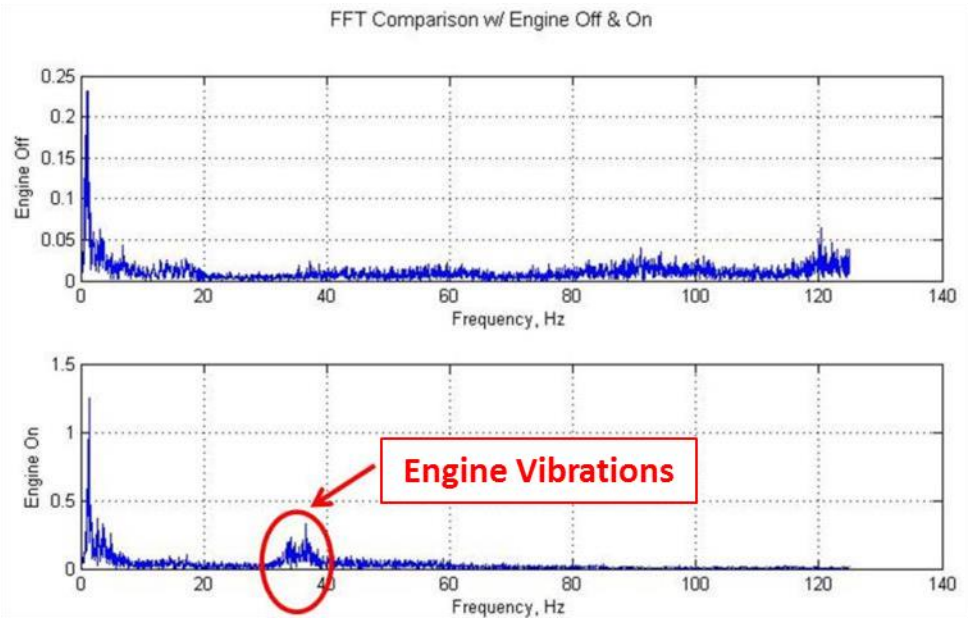

Figure 4.34 FFT analysis of USV with engines on and off

4.8.1.3 High-Pass Data Filter

As the last step prior to integration, a high-pass, 5th order Butterworth filter with a low cutoff frequency of 0.35 Hz is used to eliminate small artifacts in the data that can lead to moving means once integrated. With the introduction of any filter into time series data, the effect of the filter on the phase offset of the data needs to be considered. Since the ultimate goal of the 4-post simulation is to compare time-series simulations against testing data, offsets in time due to filtering will skew the correlation by causing the simulations to be compared to different points

in the dataset. With this in mind, a method for zero-phase filtering needs to be implemented to eliminate any time offsets due to the filtering scheme.

Zero-phase filtering helps preserve features in the filtered waveform exactly where those features occur in the unfiltered waveform. The particular filtering technique used requires processing the input data in both the forward and reverse directions as a function of time. After the data is initially filtered in the forward direction, the filtered sequence is reversed and the data is rerun back through the filter [51]. The resulting twice-filtered data has the following characteristics:

- Zero-phase distortion
- Filter transfer function equal to the squared magnitude of the original filter transfer function
- A filter order that is double the order of the filter run in each direction

4.8.1.4 Trapezoidal Integration

The filtered accelerometer data is now ready to be integrated. A cumulative trapezoid integration scheme is used to generate velocity data. Cumulative trapezoid integration is a basic numerical integration method sufficient for high sampling rates. After running the filter and integration scheme once, the raw acceleration data is transformed into useable velocity data. The velocity data is processed again using the same zero-phase filter and trapezoidal integration scheme to obtain global displacement data as a function of time. Table 4.4 lists the entire procedure for converting raw acceleration data into usable displacement inputs for the 4-post model.

Table 4.4 Acceleration data to displacement integration procedure

#	Step:	Data Type Output:
1	collect data	raw acceleration data
2	low-pass, zero-phase filter	filtered acceleration data
3	detrend data	filtered, zero mean, acceleration data
4	high-pass, zero-phase filter	twice filtered, zero mean, acceleration data
5	1^{st} trapezoidal integration	velocity data
6	detrend data	zero mean, velocity data
7	high-pass, zero-phase filter	filtered, zero mean velocity data
8	2^{nd} trapezoidal integration	displacement data

4.8.2 Model Input Validation

To validate the ability of the filter-integration scheme described in the previous section to convert raw accelerometer data into global displacement data, an experiment was designed to test the filter-integration scheme's performance by collecting acceleration data for known displacement inputs. A damper dynamometer was instrumented with a string potentiometer and a single-axis, 10g accelerometer also used for on-water testing with the 12-ft USV. Figure 4.35 shows the testing setup used; the same data acquisition system used for testing the 12-ft USV was also reconfigured to log data from the tests. The accelerometer was mounted on the dynamometer piston and a string potentiometer was connected between the piston and the machine's stationary head. Testing of different sine wave signals of the frequencies and amplitudes listed in Table 4.5 was performed, and the accelerometer and position data were recorded during the tests. Validation of the filter-integration scheme involves comparing the known displacement inputs recorded by the string potentiometer with the accelerometer data after it is run through the filter-integration scheme to see how the two signals compare.

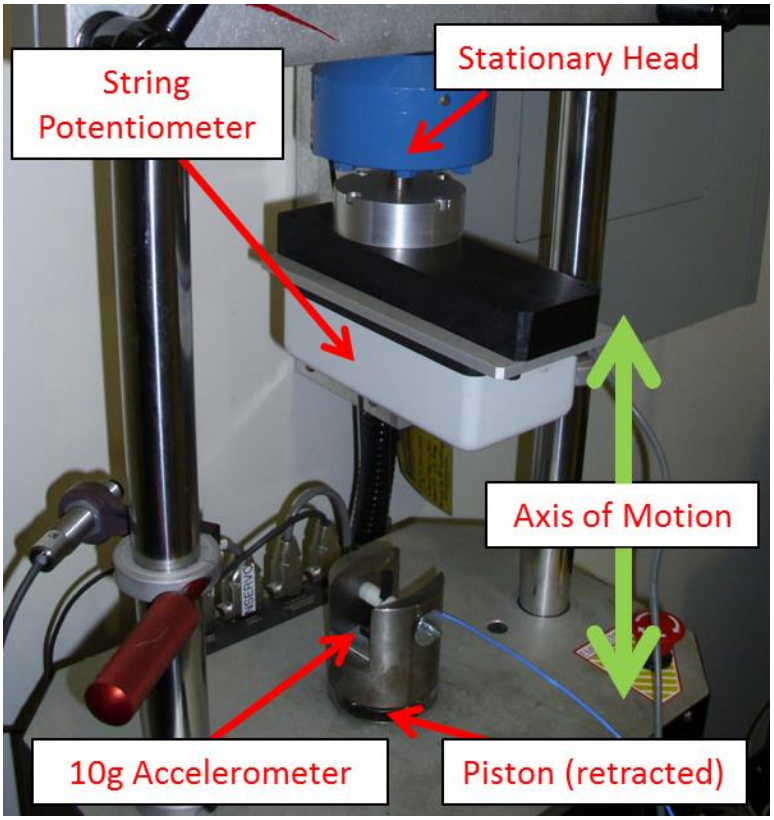

Figure 4.35 Accelerometer integration testing setup

Table 4.5 Accelerometer integration testing matrix

Amplitudes/ Frequencies	7 inches	2 inches	1 inch	0.5 inch
0.1 Hz	X	X		
0.2 Hz	X	X		
0.5 Hz	X	X		
1 Hz	X	X		
2 Hz	X	X		
5 Hz		X		
10 Hz			X	
20 Hz				X

The measured data from the string potentiometer was compared against the filtered and integrated data from the accelerometer. The results from a test of a 7 inch magnitude sine wave of five different frequencies are shown in Figure 4.36.

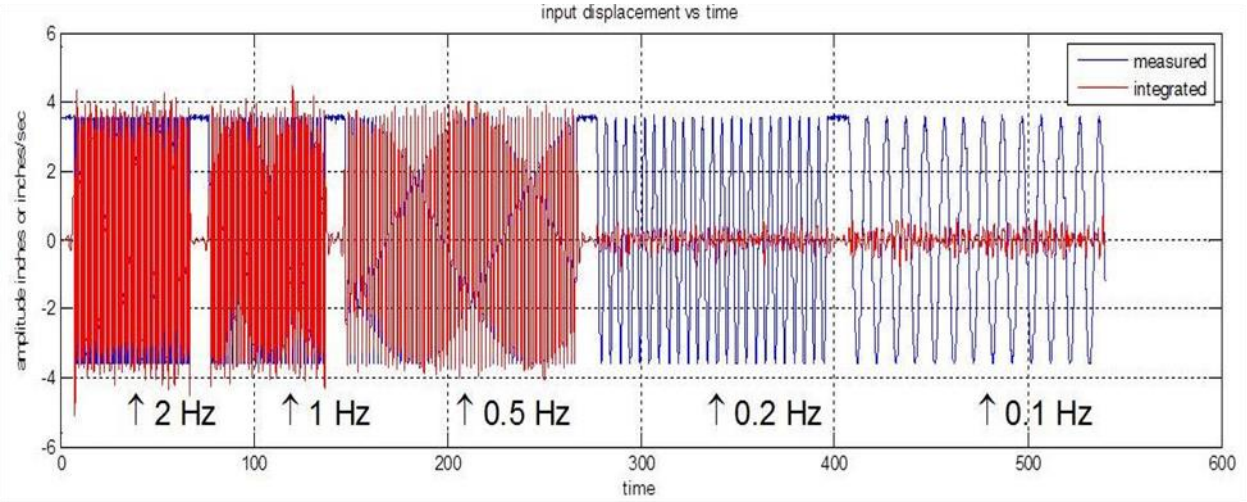

Figure 4.36 Accelerometer integration results from maximum displacement tests

The data from the 0.2 Hz and the 0.1 Hz tests is nearly completely attenuated, since they are both below the cutoff frequency of the Butterworth filter. This is acceptable since the primary frequencies of interest from testing as they relate to the suspension performance occur at 0.5 Hz and above. Figure 4.37 shows a small segment of data for three primary frequencies of interest, 0.5, 1 and 2 Hz. The data show that the data filtering and integration produces no noticeable phase lag between the two signals. Errors between the potentiometer and the accelerometer are limited to ±0.25 inch, errors do not compound with time.

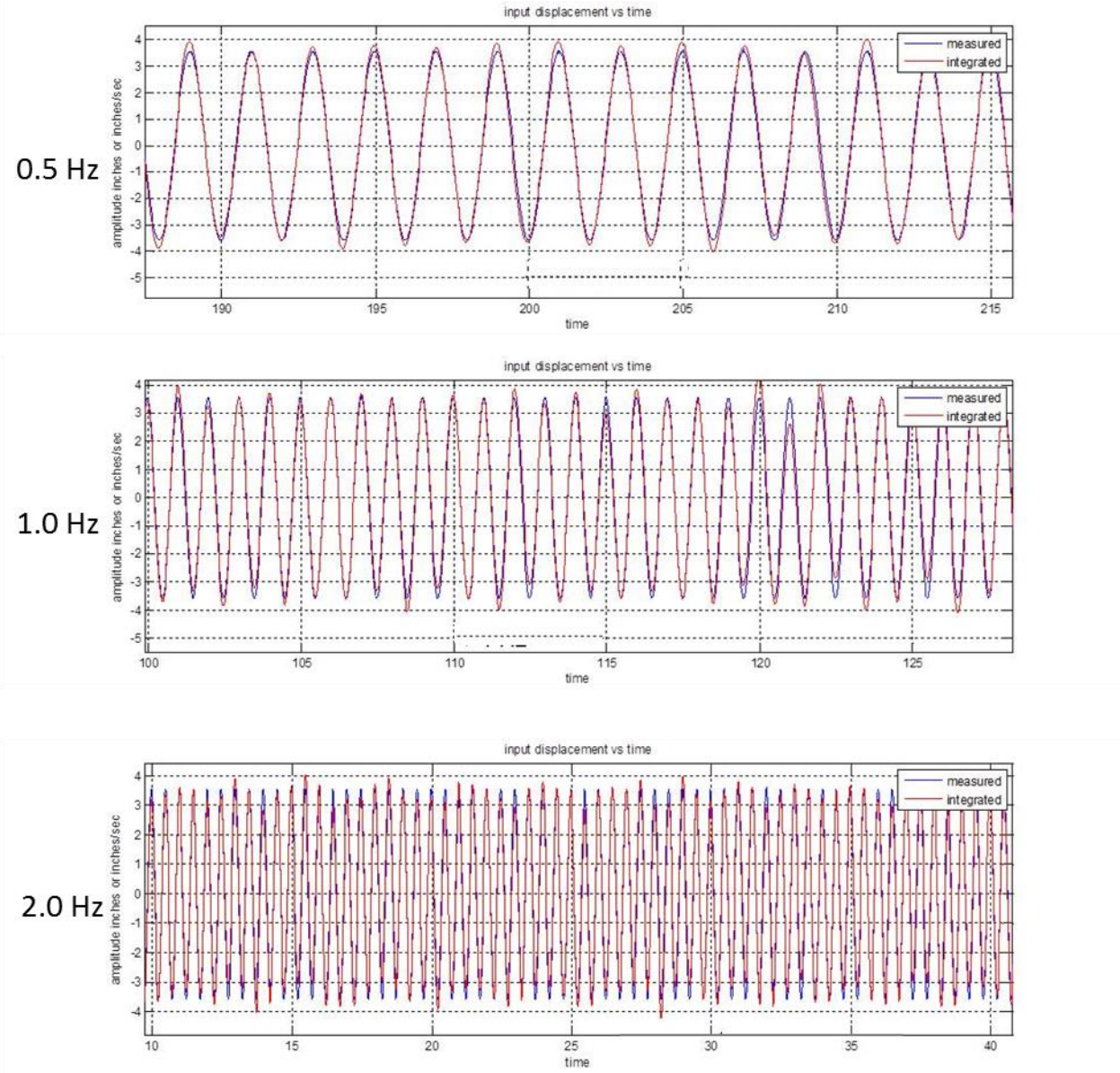

Figure 4.37 Accelerometer data for frequencies of interest

After the first test was run, a second test was run at lower displacements, using the same five frequencies, plus two additional frequencies of 5 and 10 Hz, the results are shown in Figure 4.38. A problem occurred during the 10 Hz test when the maximum acceleration capability of the string potentiometer was exceeded, causing erratic undamped motion of the pulley inside the potentiometer to be recorded in the data. The data resulting from the string potentiometer malfunction is circled in green in Figure 4.38. Because of this problem, an additional 10 Hz test was run at a lower amplitude to reduce the peak acceleration of the potentiometer.

Figure 4.38 2 inch displacement multi-frequency test displacements

The top plot in shows a 10 Hz run at a lower 1 inch displacement amplitude. By reducing the amplitude the string potentiometer's acceleration capabilities were not exceeded and the data no longer shows erratic behavior. The bottom plot Figure 4.39 shows an attempt to use the filter to record very low displacement/high frequency movement by running a test at 20 Hz at 0.5 in magnitude travel.

The 10 Hz and 20 Hz frequencies are not expected to be within the dynamic frequencies of interest in either the wave encounter frequencies during testing or in the range of suspension natural frequencies under evaluation. However, it is possible the engine frequencies may be near the frequencies conducted in these tests. The magnitude of the error is still roughly 0.25 inches, even though the percent error has increased significantly due to the lower levels of displacement.

If so desired, the high frequency performance of the filter-integration scheme can be improved by increasing the cutoff frequency of the high-pass filter. Figure 4.40 shows the same 10 Hz and 20 Hz tests compared with data run through the filter-integration scheme with a 2 Hz filtering frequency of the same filter design. The accuracy is greatly improved and the hunting in the data is also removed. This improvement in high frequency performs comes at the expense of the lower frequencies in the dynamic range of interest, so a filter of this cutoff frequency was not implemented for analyzing any testing data.

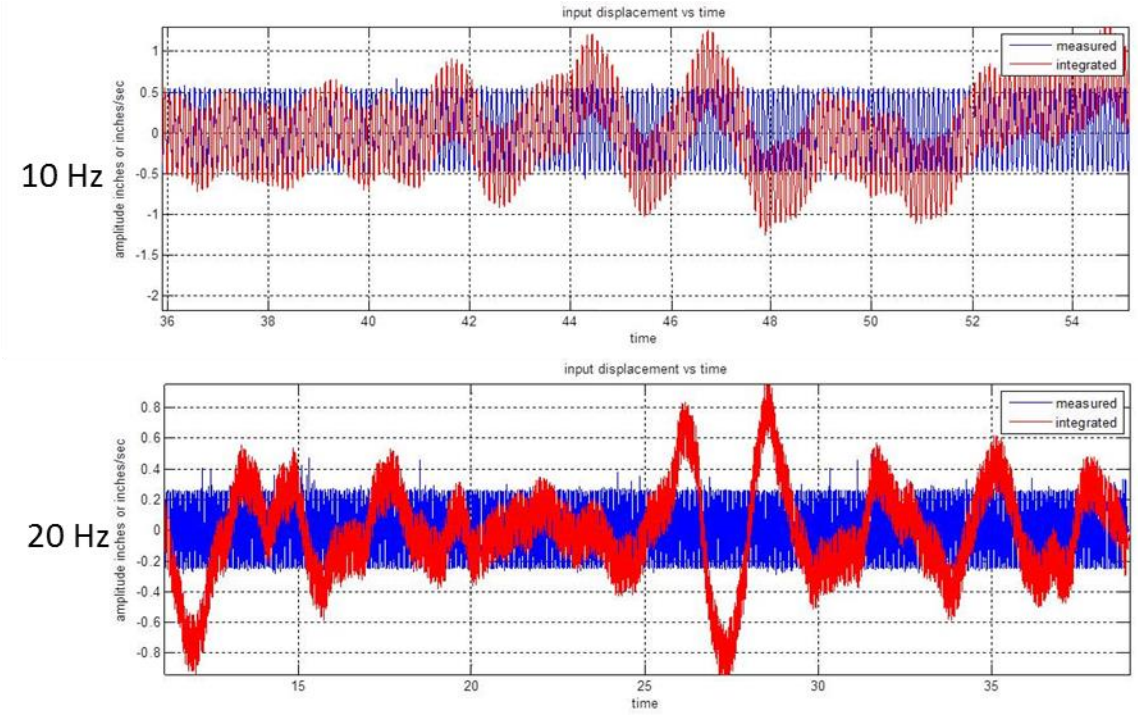

Figure 4.39 10 Hz and 20 Hz accelerometer integration: low cutoff frequency

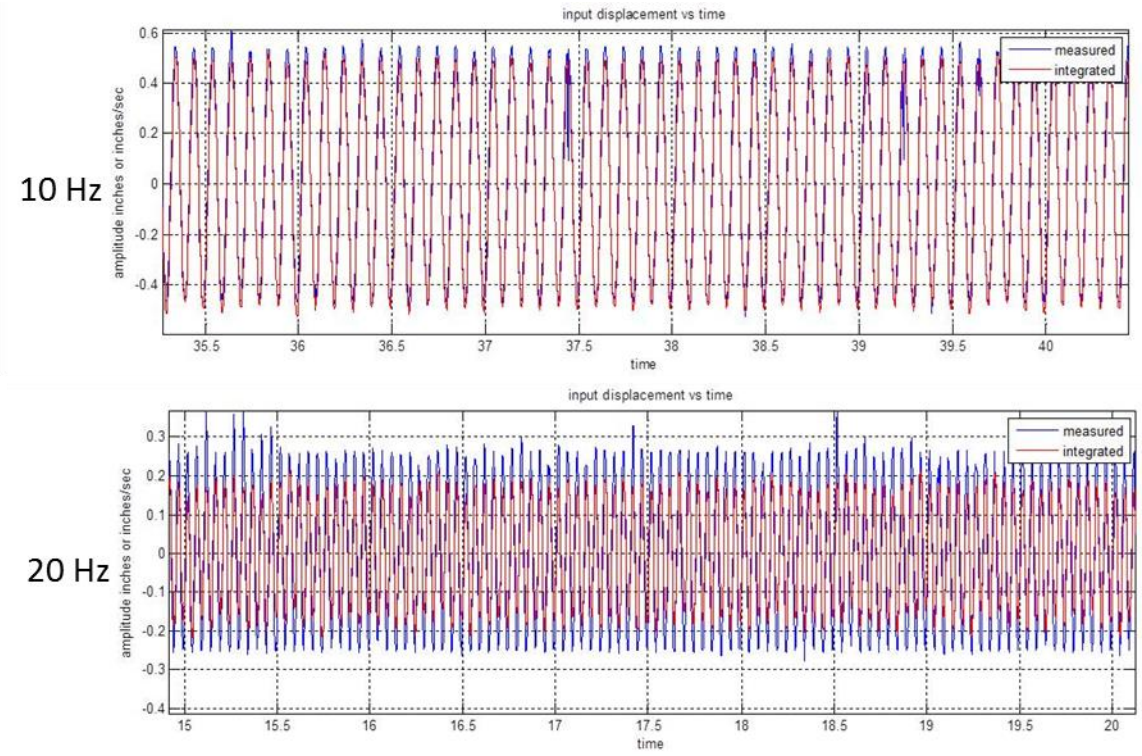

Figure 4.40 10 Hz and 20 Hz accelerometer integration: high cutoff frequency

4.9 Model Validation with Accelerometer Data

With the method of generating model inputs complete, the next step into researching the dynamics of the 12-ft USV is to validate the 4-post model. The validation occurs in two parts, discussed in the following section. Section 4.9.2 details the validation of the model using the pontoon motion as inputs and the acceleration at the payload as the output. Section 4.9.3 details the validation of the model based on comparing the motion of suspension systems and the front arch. The data used for validating the model is also discussed.

4.9.1 Data Chosen for Validation

A large amount of data (3-4 hours) was collected for the 12-ft USV during the day of testing. The data chosen for validation came from a 6 minute segment of data. This data was chosen for multiple reasons. The lower speed data at 4 and 7 knots was not considered for validation due to the relatively calm conditions during those tests failing to excite the suspension. Also, only limited portions of the tests have data from two functioning suspension potentiometers. The segment chosen contains a bow quartering maneuver and a head seas maneuver, which produced the best levels of motion of the suspension and the front arch.

4.9.2 Acceleration Data Validation

To validate the model using the acceleration data, the accelerometer data taken at the pontoons during testing must be first be converted into displacement data using the filter-integration scheme detailed in Section 4.7. The displacements inputs can then be applied within the 4-post model, and the acceleration at the payload within the model can be recorded. The payload acceleration from testing and the payload acceleration in the model are then compared, to determine if the simulation accurately recreates the levels of acceleration seen during testing. The steps for validating the model using the available acceleration data are listed in Table 4.6.

Table 4.6 Steps for model validation using acceleration data

#	Step:
1	Collect accelerometer testing data at pontoons and payload of the 12-ft USV
2	Convert pontoon accelerometer data to displacement inputs
3	Apply inputs to 4-post model and measure acceleration at payload of the model
4	Compare accelerometer test data with model acceleration, model is valid if the same inputs at pontoons produce the similar outputs at the payload

Figure 4.41 shows a comparison of the payload acceleration recorded during testing and the payload acceleration output from the 4-post model using the displacement inputs calculated through the filter-integration scheme. The payload accelerometer tracks a very accurate fitment of the test data. This is very encouraging because the acceleration at the payload is the most important parameter for the simulation to model accurately. Expectedly, there is significantly more high frequency content in the test data than there is in the model, most likely due to local structural vibrations and engine vibrations propagating from the engine pods to the payload.

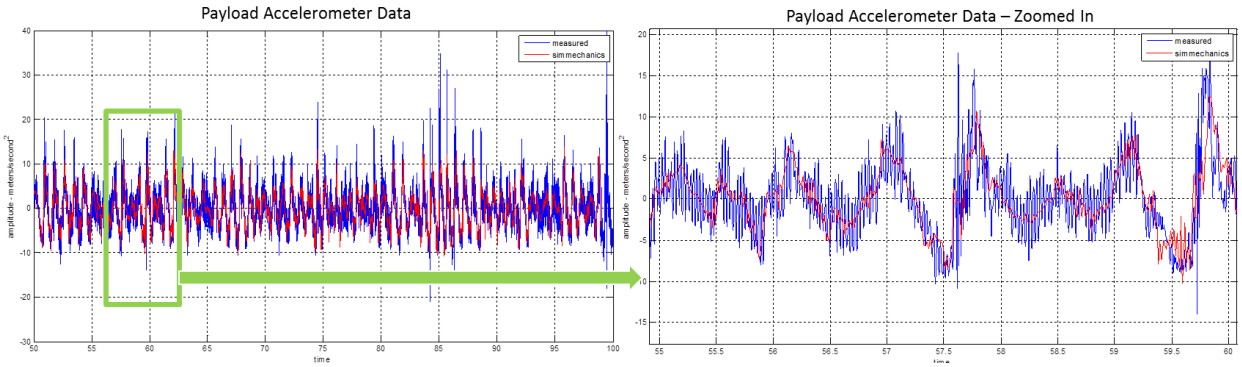

Figure 4.41 Payload accelerometer data comparison between testing and model data

4.9.3 Displacement and Rotation Data Validation

To validate the model using displacement sensor data, the first step is the same as validating the model using accelerometer data. The displacements of both suspension systems as well as the rotation of the front arch should also be recorded in the testing data. Like the acceleration validation, the displacements inputs must then be applied within the 4-post model. However, the suspension system displacement and the front arch rotation are the outputs which should be compared between the test data and the model to determine the validity of the model. The steps for validating the model using displacement sensor data are listed in Table 4.7.

Table 4.7 Steps for model validation using displacement data

#	Step:
1	Collect accelerometer data at pontoons, and displacement data at suspension and front arch
2	Convert pontoon accelerometer data to displacement inputs
3	Apply inputs to 4-post model and record suspension and front arch displacement
4	Compare displacements from testing data with model displacements, model is valid if the same inputs at pontoons produce the similar outputs at the suspensions and front arch

Figure 4.42 shows a comparison of the suspension motion and front arch rotation from the 4-post model compared against testing data. All of the data channels follow the testing data reasonably well. The data from the suspension systems show excellent correlation. This is promising because some of the suspension properties such as the damping ratio had to be estimated for the model rather than measured or calculated directly.

The data collected from the potentiometer on the front arch showed good trends compared to the simulation program. However, the correlation was not as good as the correlation between other data channels. There are many possibilities for why this may be the case. The problem is the method of measurement of the rotation of the spherical joint about the roll axis being affected by the rotation about the pitch axis. This could be added as an additional component to model for future model iterations.

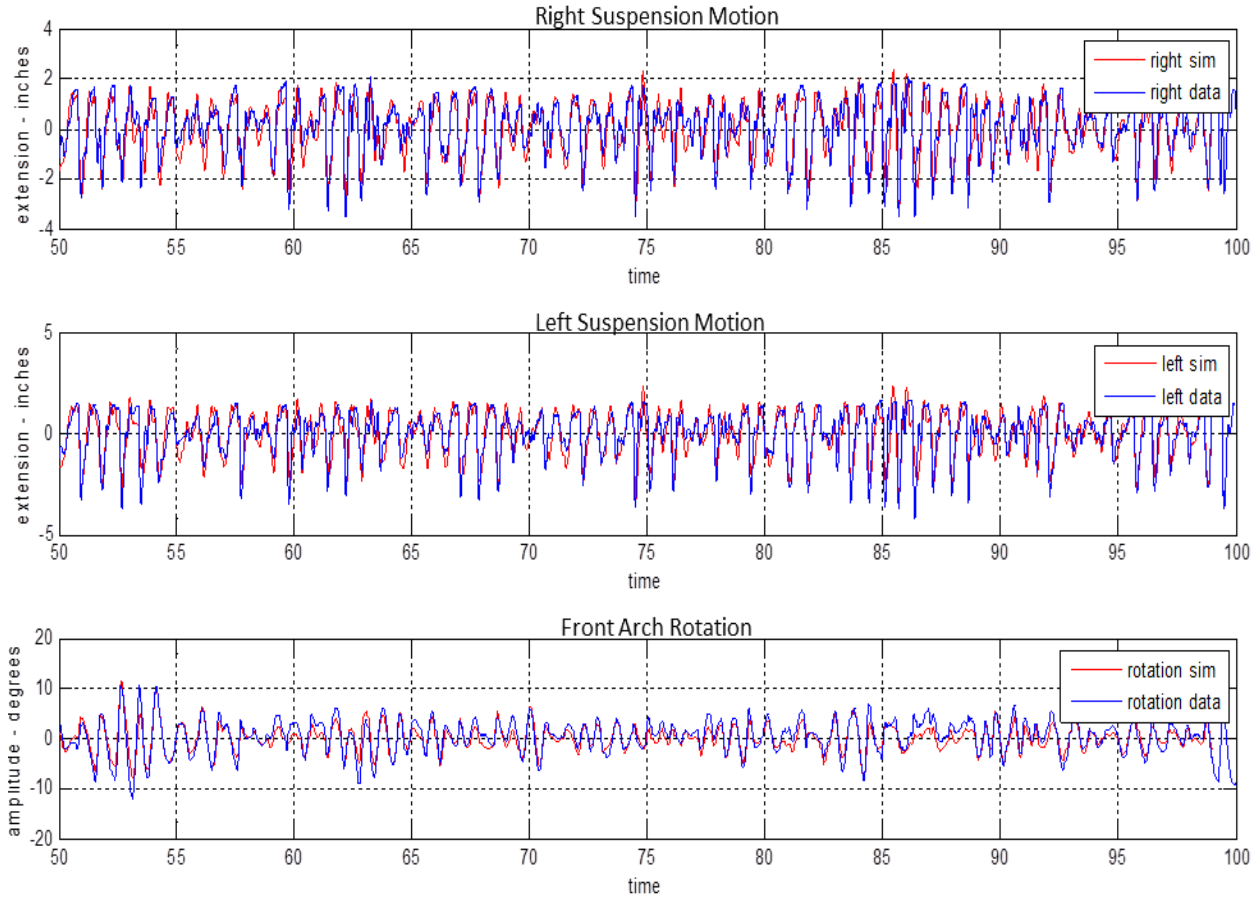

Figure 4.42 Suspension motion and spherical joint data validation

4.10 Model Visualization and Qualitative Analysis with VRML

After a successful correlation was established between the 4-post model and the on-water testing data, a qualitative method was designed using Virtual Reality Modeling Language (VRML) for evaluating the simulations against both the onboard videos and the videos from the chase boat. The ability to use video data serves as another method to validate the model, and also provides a qualitative method to help with understanding the 12-ft USV's dynamics.

4.10.1 VRML Background

VRML is a standard three-dimensional graphics file format for representing 3-D worlds. The Simulink 3-D animation toolbox provides a functional link between the 4-post model and the VRML modeling environment. 3-D images can be imported from CAD using the .wrl extension, and then added to groups and transforms in VRML. In addition to the ability to import parts from CAD, 2-D and 3-D polygons can be designed within the VRML environment directly.

Despite having similar visualization capabilities, VRML uses a fundamentally different architecture compared to most CAD software programs. Most computer aided design programs classify their components in terms of extrusions, parts, sub-assemblies, and assemblies; based on the way the objects mate with one another. VRML classifies objects in classes of groups, transforms, anchors, and billboards, and then the subsequent children of each class. The classes are based on how each class changes from a given viewpoint within the world. CAD can be considered a model-centered program, while VRML can be considered a viewpoint centered program; which is why VRML is more common for animation applications [52]. V-Realm Builder 2.0 is an open-source editor being used to design the world which will be manipulated using Simulink. This section serves as a guide for developing 4-post visualizations using VRML.

4.10.1.1 CAD Model Generation

Figure 4.43 shows a model of the USV rendered using Solidworks to be imported into VRML. The assembly shown consists of a total of seven components: the superstructure, front and rear arches, left and right pontoon assemblies, and left and right springs. The component count could be further reduced by modeling the superstructure and rear arch as a single component, since no relative motion occurs between the two. For the VRML visualization of the 12-ft USV, the USV's components were the modeled in CAD, while the rest of the virtual world was modeled using VRML.

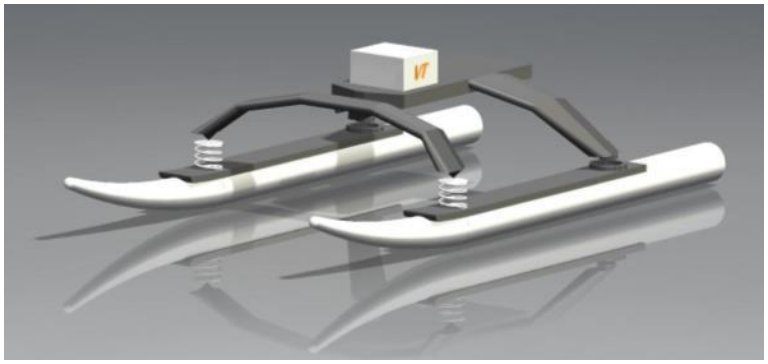

Figure 4.43 High-resolution CAD model created for import into VRML environment

4.10.1.2 VRML Model Generation

Within VRML, a world needs to be created to place the components converted from CAD and to import signals from Simulink. It is advantageous to run the animation after pre-processing the data and running the simulation, rather than running the simulation and visualization programs at the same time. A new VRML model can be started by inserting the VR Sink block into a Simulink model. Within VRML, using the insert transform function will add a transform, corresponding to the first part added to the assembly. Parts can then be added to the transform by adding them to the transform's children. In order for parts to mesh, each transform needs to be shifted by the part's distance from the origin in the CAD assembly.

4.10.1.3 Suspension and Spring Modeling

For the suspension springs, it was desirable to have a representative coil spring that could deflect to represent the motion of the suspension system. Due to the nonlinear nature of the suspension and the difficulty of viewing its operation in a simulation, a functional representation of the model has been created by a deformable coil spring with the nonlinear properties of the combination leaf spring/air spring system described in Section 4.4.1.

4.10.1.4 VRML Coordinate System

When creating an assembly from individual components in CAD, it is necessary to keep the coordinate systems of each component oriented in the same direction they will be oriented in VRML. When the components are converted, they are saved individually as .WRL files, and they will be saved with their original coordinate systems. A non-standard coordinate system is used by VRML; it is a right-handed coordinate system with the Z axis as the longitudinal axis, the Y axis as the vertical axis, and X axis as the transverse axis. The VRML coordinate system for the 12-ft USV visualization is shown in Figure 4.44.

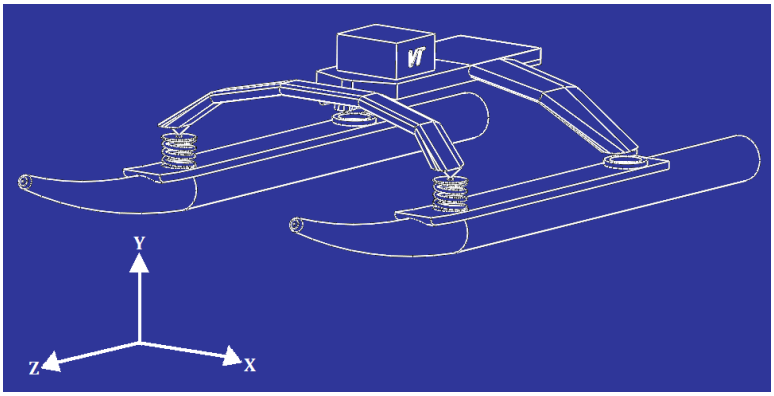

Figure 4.44 VRML coordinate system axes

4.10.2 Modifying the VRML Environment

In order to render waves based on the displacements of the two pontoons, an elevation grid transform was generated. Anytime a high resolution simulation is presented with data analysis, a careful line needs to be drawn between articles of simulation and animation. In this instance, that line is a horizontal line at the level of the waves. Unlike a ground vehicle, the exact waveform experienced during a test cannot be easily measured. The general shape of the wave can be very roughly estimated from the acceleration data taken directly at pontoons for animation purposes only. In the case of this simulation, ¾ of the height of the displacement of the front two pontoons was used to show the wave height, and the relative wave speed was set to12 knots.

In order to speed up processing time, the extended wave environment was drawn with a separate elevation grid from the local grid. For the extended grid, no wave data was entered; however, a texture transform was used to simulate the current; set to move at the same speed as the relative wave speed in the local wave grid. Figure 4.45 shows a wireframe model of the USV and the two grids, the local wave grid has 0.5m spacing; the extended grid has 10m spacing.

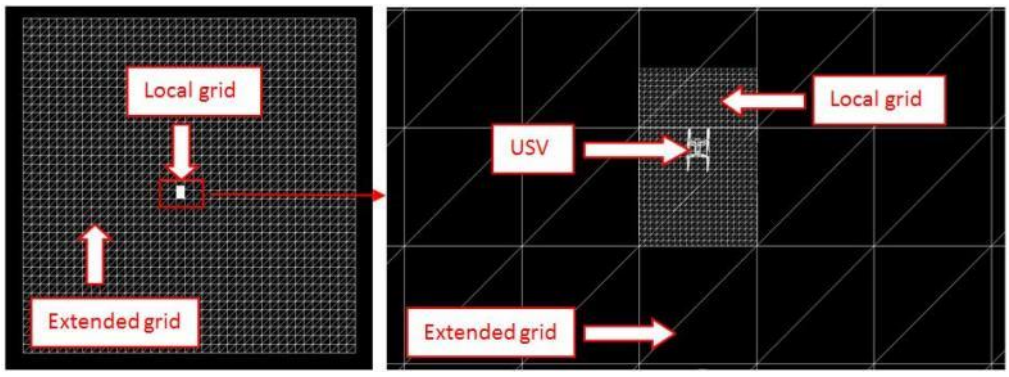

Figure 4.45 Top-view wireframe showing of local and global elevation grids

Within the VRML environment, the USV is fixed like it would be on a 4-post rig. To give movement to the waves with respect to the fixed USV, the local wave surfaces are given a moving texture transform. The texture is then translated across the extended grid, with the speed the texture moves corresponding to the USV's speed relative to the waves. As the texture translates, it will loop and repeat itself, similar to an 8-track tape. To avoid abrupt change in the texture, the image used must be a properly cropped tessellation. If starting from an existing image, a second option is to create an image from two images with one of the images inverted. An example of this is shown in Figure 4.45.

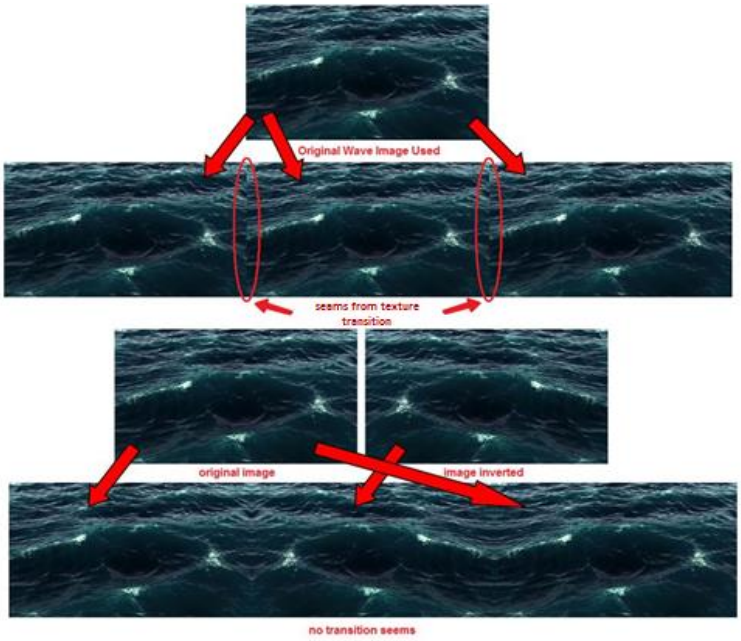

Figure 4.46 Texture transform method

At its limits, the VRML world is contained within a large cube, so a background image can be placed for each side of the cube. For adding background images, there is a problem of corners creating seams. This can be dealt with in a similar manner to the problem of texture. By making the left and right walls the inverse of the image of the front and back walls, no seams are visible.

4.10.2.1 Importing Signals into VRML

Once all of the parts are placed in VRML as children of the transforms and the transforms are named, the VR Sink block can be updated to include the inputs from SimMechanics. Each component needs a rotation and a translation signal sent to it. The springs will need a scaling signal input; the scale signal will need to be converted to a three component signal with a constant scaling on the x and z axis, and a variable scaling on the y axis.

4.10.3 Comparison of VRML Modeling and Video Data

Once the VRML visualization program was complete, the simulations and visualization were run to key pieces of data and compared side by side with video data from the onboard and chase boat cameras. Figure 4.47 shows two screenshots from the onboard camera and VRML onboard camera with the WAM-V idling in calm water. Figure 4.48 shows a screenshot from the chase boat and isometric view from VRML during the bow-quartering leg of a test run.

Figure 4.47 Onboard video vs. VRML comparison

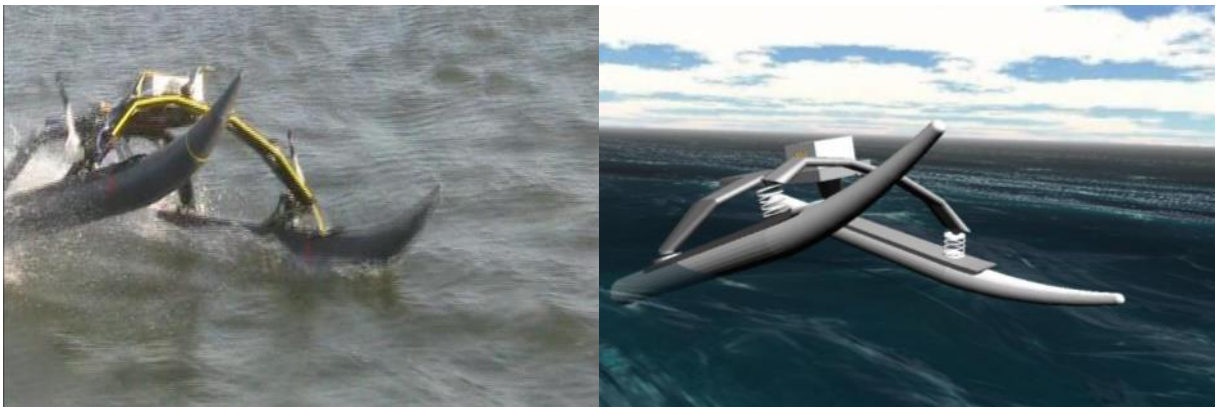

Figure 4.48 Chase boat vs. VRML visualization

4.10.4 Accelerometer Input Validation from VRML

The VRML visualization can be used for qualitative validation of the 4-post model by comparing it side-by-side with the video data. As an example of the usefulness of performing a qualitative analysis on the 12-ft USV, while the filter-integration scheme detailed in Table 4.4 was still being validated, the high-pass filters in steps 4 and 7 of the table were at one point set a 0.2 Hz cutoff frequency. Figure 4.49 shows the four-corner inputs calculated from a 20 second piece of testing data taken during a bow-quartering leg; calculated with the high-pass filters set to 0.2 Hz.

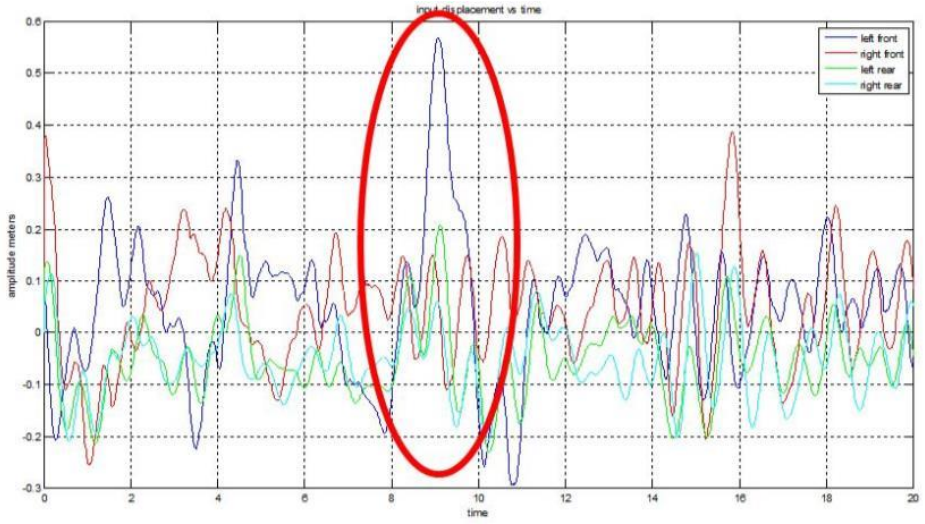

Figure 4.49 Four corner inputs for head seas maneuver

Looking at the four inputs to the 4-post model, at approximately 9 seconds into the data there is a large positive (upward) input to the front left corner (blue) and a negative downward input to the front right corner (red). The difference in the two inputs indicates a large rotation of the front arch, possibly the largest seen during the entire day of testing. When the data from the simulation is compared against the video as shown in Figure 4.50, the two do not seem to match very well. The video data shows a relatively small angle difference between the front two corners. This likely indicates that there is a local mean shift in the data caused by the filtering.

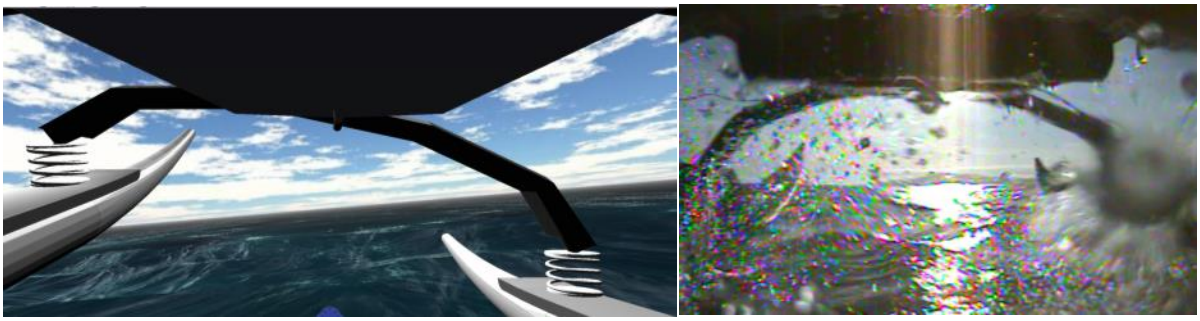

Figure 4.50 Initial VRML simulation vs. onboard camera

Two changes in the filtering frequency used were evaluated to see their effects on the model. The simulations were rerun using a 0.5 Hz filter and a 0.35 Hz filter and the results between the 0.2, 0.35, and 0.5 Hz filters were compared against the video for the same segment of data, as well as the damper dynamometer data detailed in Section 4.8. The 0.5 Hz filter was found to flatten out most of the data, and its results were not included. The 0.35 Hz filter, however, changed the input shown in Figure 4.49 to the different input shown in Figure 4.51.

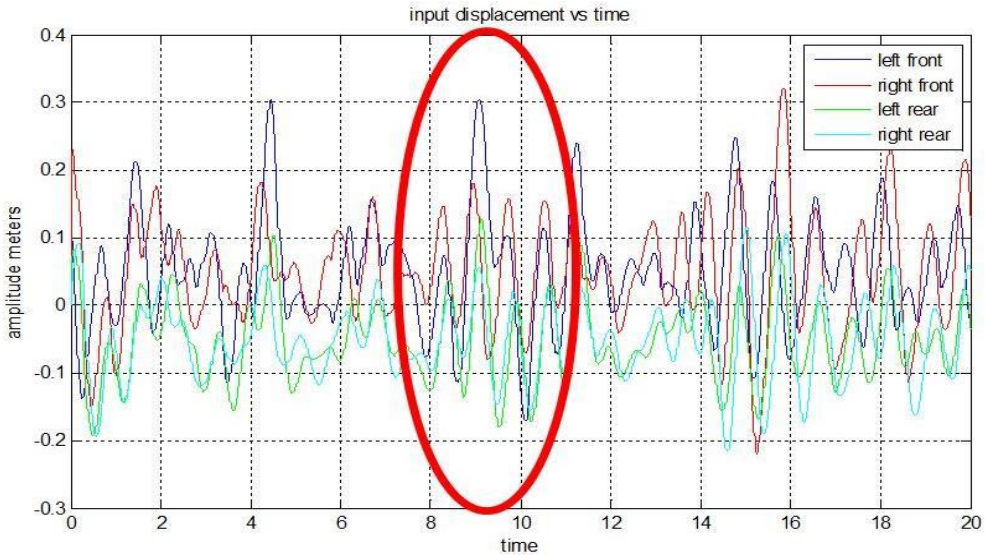

Figure 4.51 Four corner inputs with 0.35 Hz filter

Looking at the four inputs in Figure 4.51, it can be seen that the input at nine seconds into the simulation has changed from a large roll input to a still significant pitch input. The left corner has reduced slightly in magnitude; however, the right input has changed from a negative to a positive displacement, much more closely matching the left input. Figure 4.52 shows the results of the VRML simulation for these inputs compared against the video screenshot. It is clear from Figure 4.52 that the two match more closely than with the lower filter frequency. Other pieces of data were tested with this filter frequency, also correlating well between the video and the simulation. Care should be taken when changing filter frequencies to manipulate testing results. Theoretically, with the right filter any desired input can be generated. It is likely that the filter-integration scheme as designed is sensitive to the frequency the data is sampled at. Future WAM-V testing should be run at a higher sampling frequency to reduce possible errors from the cumulative trapezoidal integration scheme.

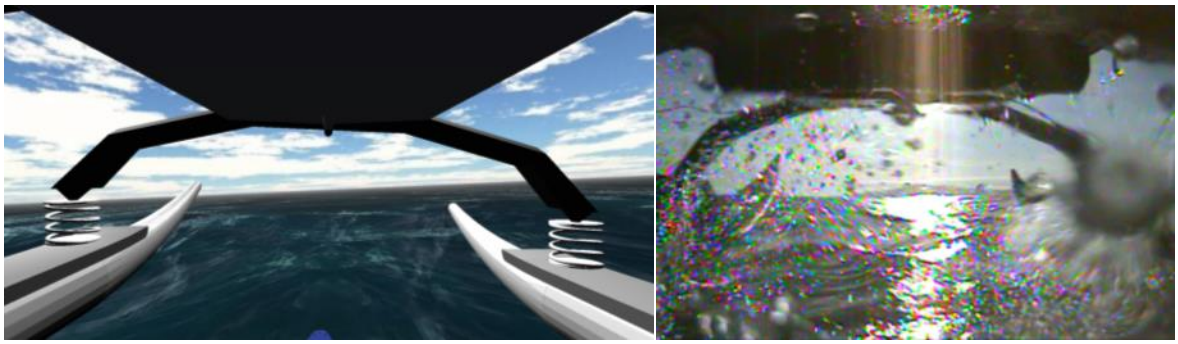

Figure 4.52 Revised VRML simulation vs. onboard camera

4.11 Conclusions and Recommendations

The instrumentation and testing plan implemented for the 12-ft USV was highly successful in generating useful data for analysis. This section details some possible improvements based on the results of the testing and modeling of the 12-ft USV.

4.11.1 Recommendations for Future Testing

Increasing the sampling rate from 250 Hz to 500 Hz may improve the quality of the data. On future WAM-V tests additional sensors may improve the overall data as well. Incorporation of angular rate gyros in addition to accelerometers would make the process of arriving at global displacements easier and would be more accurate than relying solely on accelerometer data. The addition of accelerometers to the engine pods may make their interaction with the waves clearer in terms of their effect on vehicle performance. The engine pods create a net thrust rotating the entire craft under operation; the thrust vector created changes dynamically as the pontoon moves. The effects of the engine pods should be studies more closely in future tests.

4.11.2 Recommendations for Modeling Improvements

The 4-post model and the validation of the 4-post model showed excellent correlation to the test data. Future WAM-V models can build upon these results. Improvements can also be made to the models to make them more useful for quantifying the dynamics of future WAM-V designs. The model indicated that changes to the suspension were ineffective at changing the acceleration at the payload. Like the 100-ft Proteus, the 12-ft USV does not have a dedicated damper as part of the suspension system. Because of this, the damping comes from other sources, such as damping from the air spring, material damping from the leaf springs, coulomb friction, and energy dissipation through the waves. Because of the many types of damping involved, it seemed as though getting accurate correlations would be very sensitive to how the damping was modeled. However, this did not turn out to be the case. The payload acceleration data showed good correlation for a wide range of damping rates. This indicates that the suspension has a limited impact on the overall ride quality. More suspension travel and softer spring rates may improve the suspension's performance.

Chapter 5 Quarter-Boat Testing and Simulation

The following chapter provides a detailed description of the experimental setup used for the testing of the Quarter-Boat vertical hydrodynamics test rig designed and constructed specifically for this study. The experimental setup section includes descriptions of the testing equipment, data acquisition hardware and software, and testing procedures. The modeling section details the efforts to develop and correlate a multi-body dynamic simulation program to the testing data.

5.1 Chapter Overview

- Section 5.1 provides an overview of the chapter.
- Section 5.2 provides an overview of Quarter-Car modeling and Quarter-Car testing rigs.
- Section 5.3 discusses conversion of the parameters of a Quarter-Car to the marine domain.
- Section 5.4 presents a design overview of the Quarter-Boat testing rig.
- Section 5.5 introduces the Quarter-Boat testing rig and details its design and construction.
- Section 5.6 discusses the modifications to the data acquisition setup for the Quarter-Boat rig.
- Section 5.7 discusses the initial testing procedure for the Quarter-Boat rig.
- Section 5.8 presents the Quarter-Boat model based on the single degree of freedom tests.
- Section 5.9 details the two degree of freedom suspension modeling of the Quarter-Boat rig.
- Section 5.10 compares the Quarter-Boat model against experimental hydrodynamics data.
- Section 5.11 provides a review of computational methods for time domain hydrodynamics.
- Section 5.12 presents a linearized version of the Quarter-Boat model
- Section 5.13 provides the conclusions and recommendations from the chapter.

5.1.1 Significant Contributions

The concept of a Quarter-Boat itself is novel, this chapter presents the first design and application of a Quarter-Boat model and a Quarter-Boat rig. The results from testing add to the literature on marine drop test rigs; while single degree of freedom drop tests of wedge and cylindrical shapes are common in marine research laboratories, the two degree of freedom tests with a suspension system are unique. The Quarter-Boat model, particularly the representation of the vertical hydrodynamics of the pontoons in the model is novel as well. Finally, the test results and modeling can be applied to the 4-post and 6-post models detailed in Chapters 3, 4, and 11, as well as the Quarter-Boat analysis of the 33-ft WAM-V detailed in Chapter 8.

5.2 Quarter-Car Modeling and Testing

A Quarter-Car model is a classic representation of an automotive suspension system used for representing the vertical dynamics of one corner of a vehicle. Quarter-Cars are often modeled as systems having two degrees of freedom, both in the vertical direction. The two degrees of freedom correspond to the two sets of mass-spring-damper systems used to model the Quarter-Car's dynamics. Figure 5.1 shows a graphic representation of a Quarter-Car model and each of its components.

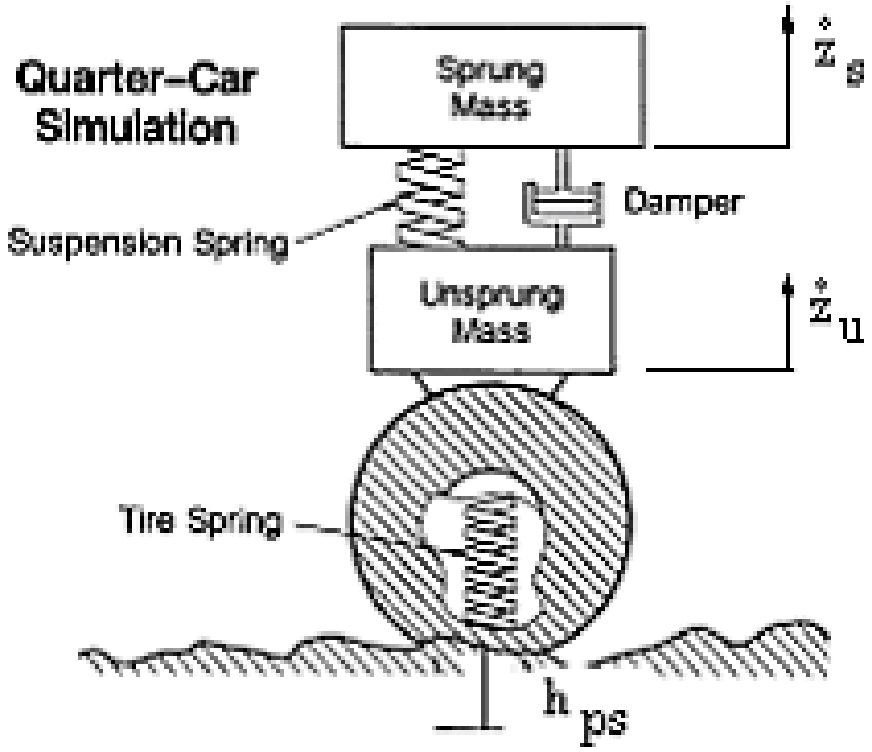

Figure 5.1 Quarter-Car Model [55]

5.2.1 Quarter-Car Modeling Parameters

For modeling a Quarter-Car, the sprung mass is representative of the vehicle weight supported by the suspension at the corner of the vehicle being analyzed. The upper spring and damper combination shown in Figure 5.1 represents the vehicle's suspension system as installed for that particular corner of the vehicle. The lower spring and damper combination for a Quarter-Car model represents the tire's vertical spring rate and the internal damping of the tire (Figure 5.1 shows a Quarter-Car model where damping of the tire is not considered). The unsprung mass represents the combined mass of the tire, wheel, and upright assembly, as well as a portion of the mass of the vehicle's suspension system.

5.2.2 Quarter-Car Test Rig Designs

Figure 5.2 shows two different schematics for Quarter-Car testing rigs. Figure 5.2(a) shows a Quarter-Car schematic for a rig designed for testing a MacPherson strut type suspension. Figure 5.2(b) shows a schematic for a rig designed for testing a trailing arm suspension. The two schematics are very similar in design, it is possible both suspension types could be tested using the same setup. Compared to the rocker arm suspension designs found on the 100-ft Proteus, 12-ft USV, and 33-ft WAM-V detailed in Chapters 3, 4, and 6 respectively, the trailing arm suspension in Figure 5.2(b) is a closer representation of the suspension systems installed on the current generations of WAM-V technology.

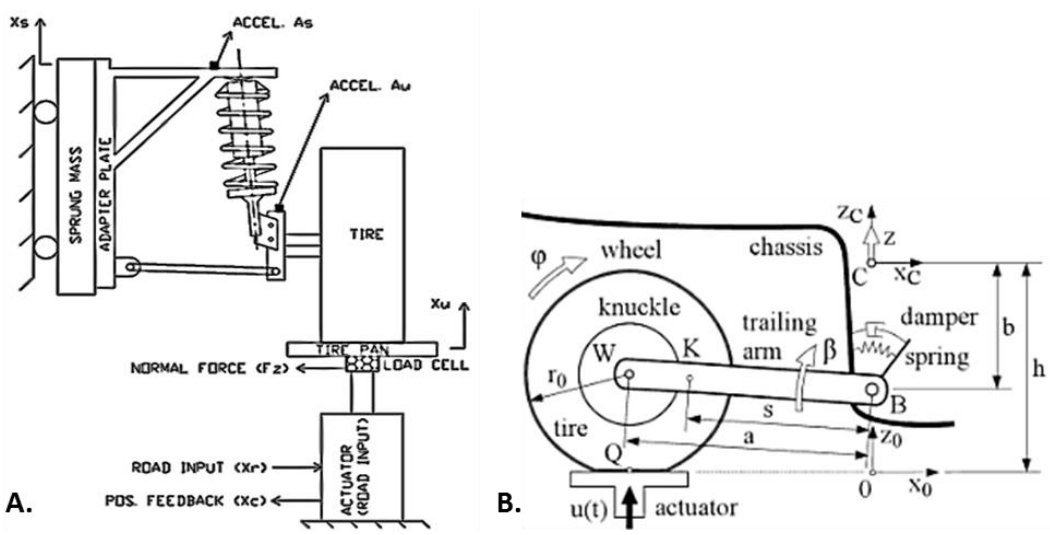

Figure 5.2 Two possible Quarter-Car test rig schematics ([56] and [57])

Compared to the more complicated multi-post shaker rigs detailed in Chapter 10, Quarter-Car rigs have a number of advantages, including the following:

- Simplified construction requiring a fraction of the components of a full vehicle test rig.
- Lower cost of testing, both in the cost of the rig itself and the cost of suspension and vehicle components tested for different design iterations.
- A greater number of design configurations can be tested for a given time frame and within a given cost limitation.
- Quarter-Car rigs generally take up less space in the laboratory and are easier to work on.

However, compared to full-vehicle test rigs, Quarter-Car rigs have a number of disadvantages that need to be considered as well:

- Inability to include some dynamics such as later forces and weigh transfer.
- Quarter-Car rigs often do not incorporate actual suspension geometry as installed on the vehicle; this alters the kinematics and dynamics of the suspension being evaluated.
- Quarter-Car rigs cannot incorporate the effects of pitch and roll inputs on the sprung mass.
- Special fixtures often need to be fabricated to replace the components of the vehicle not used as part of the Quarter-Car rig. Full vehicles cannot be tested without disassembly.
- Estimates are often required for properties of the vehicle that are removed for testing, such as the equivalent sprung mass of one corner of the vehicle.

Figure 5.3 shows a Quarter-Car test rig in the laboratory with some of its major components annotated. Not shown in the figure is the control system required for the hydraulic actuator for and the hydraulic pump unit. The hydraulic actuator, control system and pumps are the most expensive components required for constructing a Quarter-Car rig. A discussion of these components can be found in Chapter 10 for the hydraulic test setup for the 2-post rig constructed for the 33-ft WAM-V.

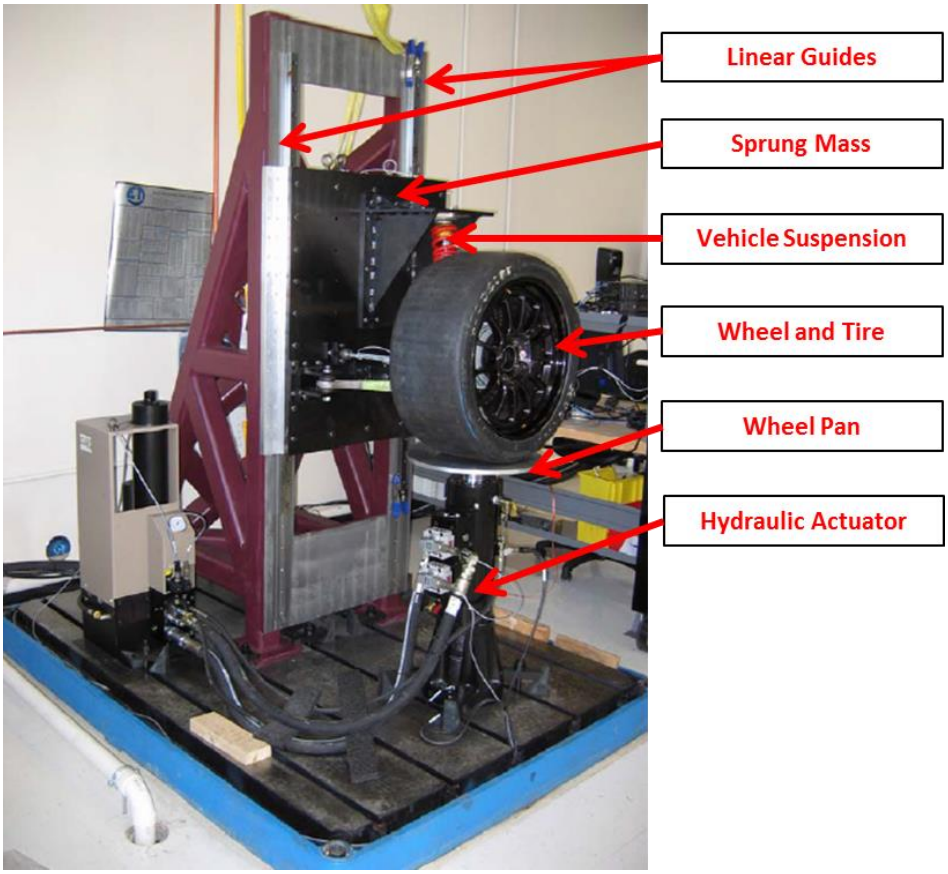

Figure 5.3 Quarter-Car testing rig (annotated from [56])

A Quarter-Car testing and modeling approach was initially chosen for evaluating the dynamics of WAM-Vs over incorporating tire/pontoon dynamics on a complete 4-post rig to avoid overcomplicating the testing and simulations to give a better focus on understanding the pontoon's vertical dynamics. The model developed, known as the Quarter-Boat model, has some properties that are not easily defined or solved for mathematically, such as the damping and added mass of the pontoons in the water, which change as a function of frequency. A Quarter-Boat testing rig was constructed to gain a better understanding of these properties. The following section provides a conceptual overview of the confounding factors in converting the parameters of a Quarter-Car model into the marine domain.

5.3 A Marine Representation of a Quarter-Car Model

The dynamics simulated by a Quarter-Car model can be translated from the automotive domain to the marine domain to be applied to future WAM-Vs fitted with advanced shock-mitigating suspension systems. In converting the parameters of a Quarter-Car for marine applications, the modeling properties of the upper mass-spring-damper system representing the sprung mass and the suspension system remain unchanged. The translation of the properties of the lower mass-spring-damper system that in the automotive domain represents the unsprung mass and the tire spring rate and damping is not an entirely straightforward conversion to the marine domain, making it a novel and interesting area of research. The principles of Quarter-Car modeling can be transferred from the automotive domain to the marine domain in the representation of a Quarter-Boat model, which is the primary focus of this chapter.

5.3.1 Equivalent Spring Rate for a Quarter-Boat Model

In transferring the model parameters between the automotive and marine domains, the tire spring rate can be replaced by the hydroelasticity of the water due to the buoyancy of the vessel. The balance between the hydrostatic forces and the gravitational and inertial forces acting on a submerged or partially submerged object can be explained by using Archimedes' Principle.

Archimedes' Principle states that the upward force experienced by an object submerged in a fluid is equal to the weight fluid displaced by the object [58]. For an object that is partially submerged, such as a floating object with a density less than the density of water, forcing the object to a displacement of greater depth than its static water line will result in a net upward force on the object and ultimately an acceleration of the object once the object is released. Up to a certain

limit, a larger displacement will cause a greater upward force on the object, analogous to the increase in force required to further compress a mechanical spring.

For cylindrical objects such as the hulls on the current WAM-V prototypes, the change in volume for a given vertical displacement of the cylinder varies depending on the displacement of the cylinder; therefore, the effective hydrodynamic spring rate of the water will also be a nonlinear function of displacement. Submerging a cylindrical shape will provide a rising spring rate until the pontoon reaches 50% submersion, followed by a falling spring rate until the hull is fully submerged. Once fully submerged, the spring rate is effectively zero; a constant upward force acts on the hull independently of the hull's vertical position relative to the waterline.

A theoretical hull designed to have a linear spring rate would thus have vertical walls in the anticipated region of vertical deflection, as shown in the diagram of Figure 5.4. It is possible that cylindrical hulls may be approximated as linear over small displacements near 50% submersion.

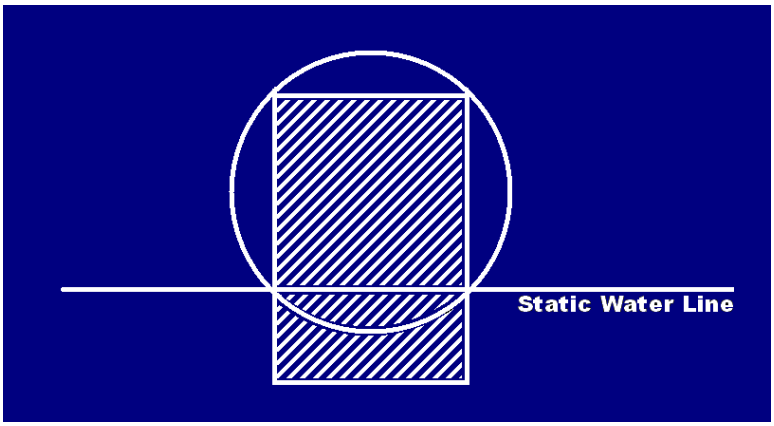

Figure 5.4 Hull shape designed for linear hydrodynamic spring rate

For the purposes of the Quarter-Boat modeling, a linear spring rate is desirable to simplify the modeling, since only linear changes in the suspension system's spring rate and damping are being evaluated. The model for a more advanced, nonlinear spring based on Archimedes' Principle can be derived from the following formula for the volume of a partial cylinder:

Formula for a partial cylinder area for a given radius r and waterline wl:

$$a_{partial} = \left(r^2 + a\cos\left(\frac{r - wl}{r} \right) \right) - (r - wl) * \sqrt{r^2 + (r - wl)^2}$$

Submerged volume:

$$v_{partial} = a_{partial} * l$$

Buoyant force:

$$F_{partial} = v_{partial} * g * \rho$$

For use in the Quarter-Boat model, the spring rate must also fitted with a saturation block so that the resultant force cannot be negative so that the spring has no capacity to pull the pontoon downward when the pontoon lifts out of the water. In the automotive domain, this concept is equivalent to an advanced tire spring rate model incorporating tire lift dynamics, so that the tire cannot itself provide resistance being lifted from the road surface.

For modeling purposes, the unsprung mass of the Quarter-Boat is considered rigid. For applying the Quarter-Boat models to WAM-Vs with inflatable hulls, the hulls are therefore assumed to be far less compliant than the water surface. This assumption was verified qualitatively based on observing the pontoons during the 12-ft USV testing in Chapter 4. The primary deflection of the WAM-V's hulls has been shown to an upward bending of the bows (shown in Chapter 7, Figure 7.5). Figure 5.5 shows a possible three degree of freedom schematic for considering the effects of vertical stiffness of the hulls on the overall system dynamics. A model such as the three degree of freedom model in Figure 5.5 would next have to be expanded to consider the effects on the flexible pontoons of the hydrodynamic spring rates compared to a rigid body.

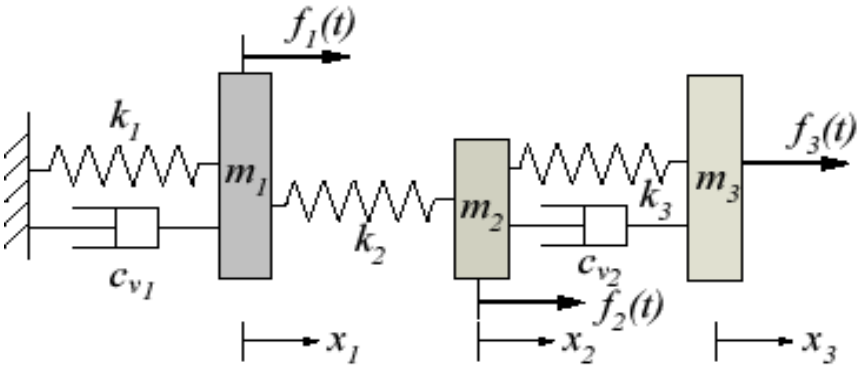

Figure 5.5 Possible three degree of freedom model including vertical pontoon compliance [45]

5.3.2 Equivalent Damping Coefficient for a Quarter-Boat Model

The damping coefficient of a submerged or partially submerged body in water quantitatively depends on many factors, though fundamentally the damping of a given body is a function of frequency. Damping represents an energy absorption term in the fluid. For a partially submerged body in a sufficiently large body of water, the primary mechanism for this absorption of energy comes from the radiation of waves from the body. The waves radiate outward due to the oscillating mass. The waves have both potential and kinetic energy, and it is assumed that the energy expended in creating these waves does not reenter the system, though this is not necessarily the case for catamaran designs such as the WAM-V.

5.3.3 Added Mass Coefficient for a Quarter-Boat Model

For a body to move within a fluid, a certain mass of fluid must also move. This additional mass changes the dynamic properties of an oscillating system, and thus must be considered for modeling purposes. Though every particle of fluid surrounding the system will be accelerated to a different degree depending on its location relative the oscillating body, the added mass coefficient represents a weighted integration of this entire movement. For the Quarter-Boat model, the added mass coefficient can be considered to be the additional mass of fluid that oscillates with the pontoon. When applied to Newton's second law, the added mass coefficient transforms the relationship between applied force and resultant acceleration as follows:

$$F = m_{body}a \rightarrow F = (m_{body} + m_{added})a$$

5.3.4 Vugt's Experimental Curves for Damping and Added Mass

Many methods have been used by hydrodynamicists in the past to quantify the added mass coefficient and damping coefficient of submerged and partially submerged bodies. An experimental approach was taken by J. H. Vugt's in 1968 [59], who defined nondimensional curves for different shapes moving in the shapes in each of the six degrees of freedom available to a ship (heave, surge, sway, yaw, pitch, and roll). For the purposes of the Quarter-Boat modeling, only the data from the heave mode is necessary; possible incorporation of a pitch mode could be incorporated into a half-boat model for future WAM-V research. Figure 5.6 shows the experimental Vugt's Curves for a partially submerged cylinder in the heave mode.

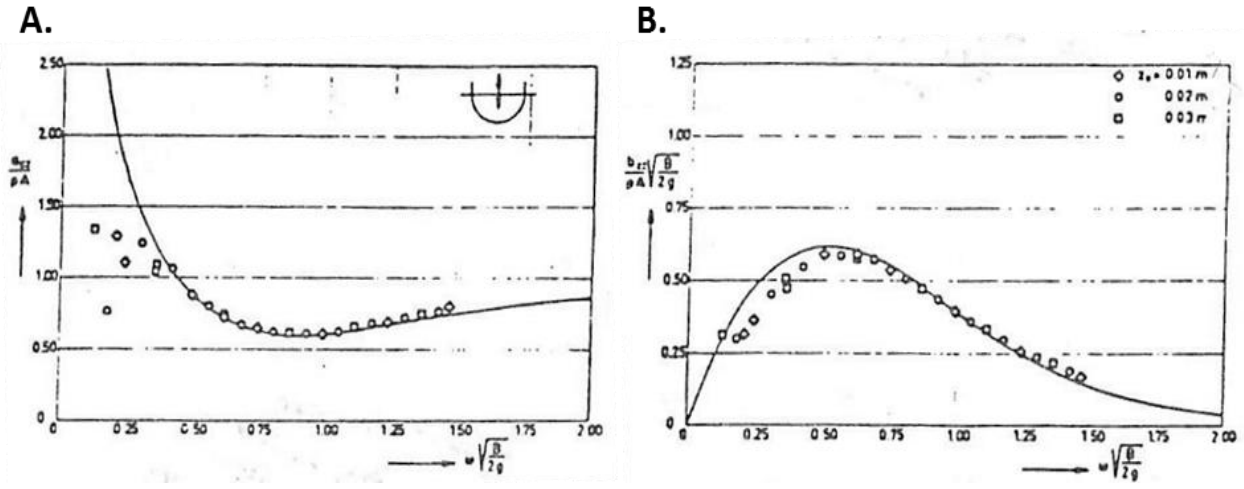

Figure 5.6 Vugt's Curves for a partially submerged cylinder operating in heave mode [59]

In the Vugt's curve shown in the Figure 5.6, the added mass coefficient and the damping are both nondimensionalized, as is the frequency term plotted along the horizontal axis in each of the graphs. This frequency term represents the frequency of encounter. The frequency of encounter for a vessel depends on the velocity of the waves, the velocity of the vessel, and the heading. For the Quarter-Boat model, this can be assumed to be the frequency of excitation.

Nondimensional Variables:

$\frac{a}{\rho A} \rightarrow$ nondimensional added mass term

$\frac{b}{\rho A}\sqrt{\frac{B}{2g}} \rightarrow$ nondimensional damping term

$\omega\sqrt{\frac{B}{2g}} \rightarrow$ nondimensional frequency term

Table 5.1 lists the required variables for inputting to the Vugt's curves to derive the added mass term (a) and the damping term (b). Figure 5.7 provides a graphic representation of how the parameters A and B are defined for the curves for a cylindrical hull. Note: both the added mass and damping terms are given as terms per cylinder length.

Table 5.1 Coefficients and dimension inputs for Vugt's curves

Symbol:	Parameter:	Value:	Units:
a	Added Mass Coefficient	?	kg/m
b	Damping Term	?	kg*s/m^2
omega	Frequency of Encounter	1.5708- 18.8496	rad/sec
A	Cross Sectional Area Submerged	0.0402	m^2
B	Width at Water Line	0.5279	m
rho	Density of Liquid	1000	kg/m^3
g	Acceleration Due to Gravity	9.81	m/sec^2

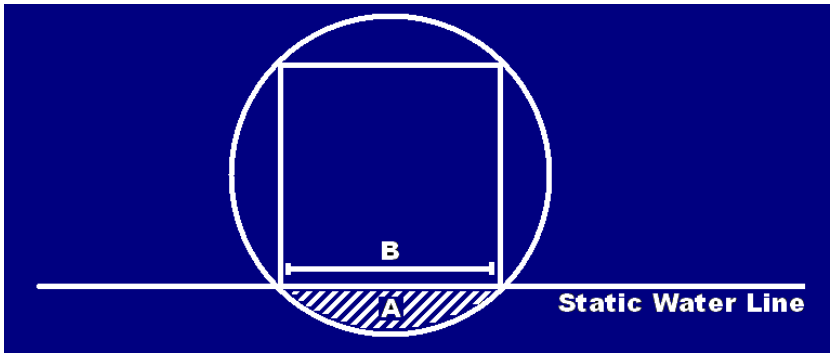

Figure 5.7 Parameters and dimensions used to fit Vugt's coefficients

5.4 Quarter-Boat Rig Design

In designing a Quarter-Boat test rig for evaluating the dynamic properties of WAM-Vs, a few major design considerations have to be considered because the differences in the dynamics a Quarter-Boat rig would be evaluating would dramatically impact whether or not the rig would be successful. In beginning the design process for the Quarter-Boat testing rig, the first deviation from a Quarter-Car design comes in the method of applying inputs to the rig.

5.4.1 Initial Design Considerations

For an ideal version of a Quarter-Boat rig, a base-excitation input system is desirable, as with a conventional Quarter-Car rig. A general schematic for what a base-excitation Quarter-Boat rig might look like is shown in Figure 5.8 (the components in the figure, particularly the relative size of the tank, are not drawn to scale).

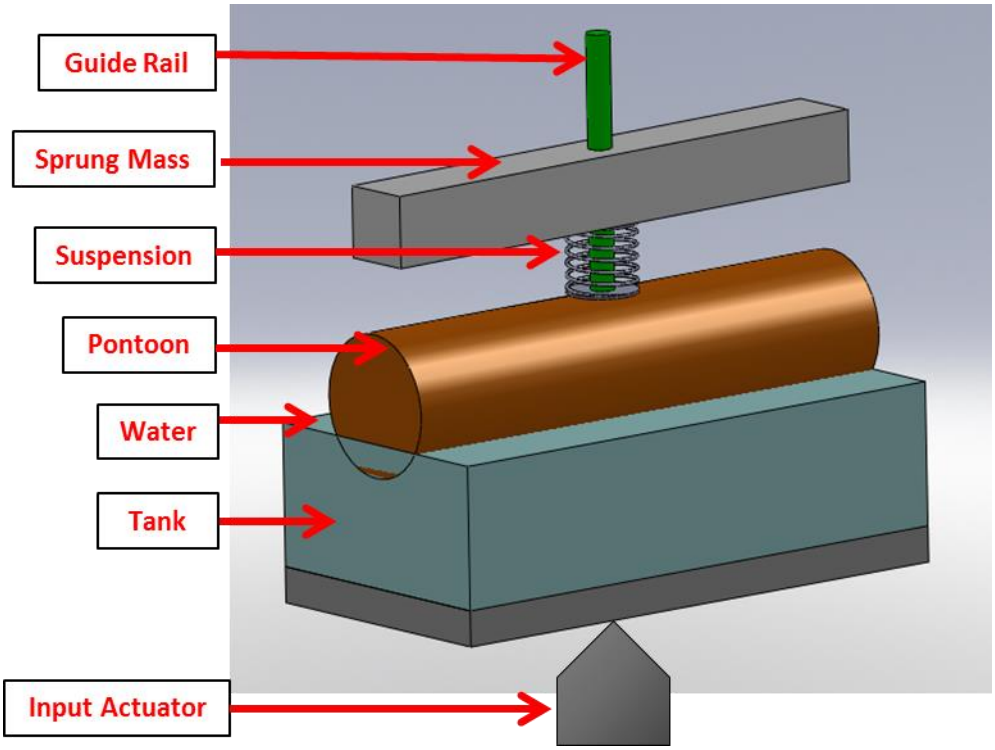

Figure 5.8 Base-excitation Quarter-Boat rig conceptual schematic

The design concept shown in Figure 5.8 has a fatal flaw in that the size of the water tank required for the rig would have to be excessively large, on the order of thousands of gallons. Otherwise the forces acting on the pontoon in the tank would be dominated by the reflection of the waves bouncing off the walls of the tank, rather than by the vertical interactions between the pontoon

and the water surface. For this reason, the base-excitation rig concept was abandoned early on in the Quarter-Boat design cycle. For the Quarter-Boat rig design, an alternate method of excitation would be developed. Two methods were considered, using a rotating unbalanced mass or an initial position input (drop test). A comparison of the two input types for single degree systems is shown in Figure 5.9.

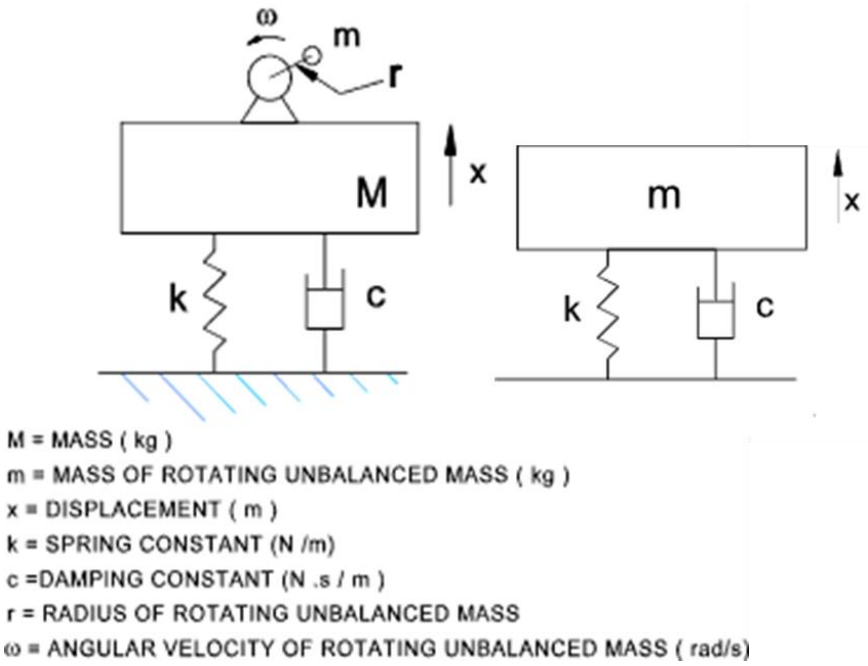

Figure 5.9 Rotating unbalance and initial position diagrams for Quarter-Boat rig

Both of the vibration types shown in Figure 5.9 have advantages and disadvantages for the modeling of marine suspension systems. A Quarter-Boat rig using a rotating unbalance input might be more simple to create simulations for, but would be more difficult to construct, while a Quarter-Boat rig using initial position inputs would be easier to build, but more difficult to correlate simulations for. Also, the rotating unbalance method would be preferable for creating small displacements, while the initial position method would be better for creating large inputs.

Ultimately, it was decided that the Quarter-Boat rig could be designed to accommodate both input types for separate tests. Initially, the rig would be built to test initial position inputs, and then a rotating unbalance component could be added to the rig at a later date with minimal modifications. For both input types, the rigs would be placed in a calm body of water for testing.

5.4.2 Quarter-Boat Rig Design Concept

A schematic of the design of the Quarter-Boat test rig and its major components are shown in Figure 5.10. The rig is designed to have the base plate submerged at the bottom of a calm-body of water. The height of the rig limits the water depths that it can be tested in. The rig is designed to be placed in depths of water ranging from 50-70 inches. Ballast is added to the baseplate to keep the frame submerged; while the pontoon and sprung mass are free to float using the degrees of freedom provided by the linear bearings in the sprung mass and pontoons. The linear bearings ride on the two linear guide rails that run between the base plate and the top plate.

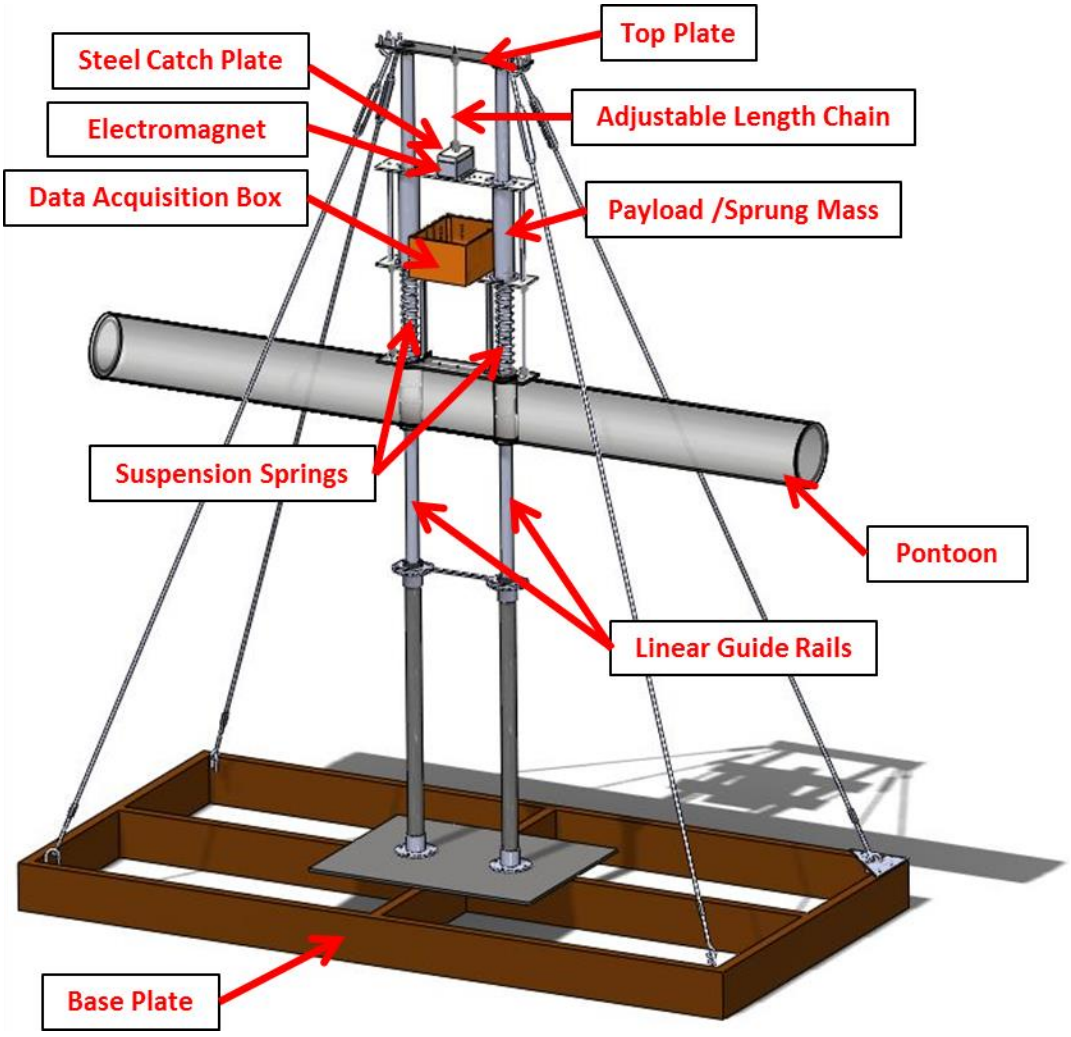

Figure 5.10 Quarter-Boat testing rig during the design phase

The sprung mass and pontoon on the Quarter-Boat rig will be raised from the water surface manually. To hold the pontoon in position, an electromagnet located on top of the sprung mass is activated and latched to a steel catch plate that hangs from the top plate by a chain that is

adjustable in length. Releasing the electromagnet will cause the pontoon and the payload to fall; the response will be recorded by a number of different sensors on the rig.

The dimensions of the Quarter-Boat rig are designed to closely approximate the size of the 12-ft USV. The purpose of the rig, however, is to generate useful information for WAM-Vs of any size, rather than to tests suspension system concepts specifically for the 12-ft USV. With this in mind, the suspension system design for the Quarter-Boat rig is a simple linear coil spring design, with two coil springs located coaxially with the linear guide rails. The overall mass, as well as the ratio of sprung to unsprung mass, is adjustable to test a number of different configurations to help generate more robust models applicable to a variety of WAM-V configurations.

For the Quarter-Boat rig, the inflatable pontoons on the 12-ft USV are replaced with rigid pontoons. Future iterations could incorporate inflatable pontoons into the design; however, the design of the linear guide rails would have to be reconsidered.

5.4.3 Obstacles in Converting from a Quarter-Car Model to a Quarter-Boat Model

With an initial design for the Quarter-Boat established, it is important to note some of the other obstacles outside of the design of the Quarter-Boat rig that will impact the overall modeling results. Some of these obstacles include the following:

- For WAM-Vs with two hulls, the front and the rear unsprung masses are coupled. This is a major departure from automobiles where the four corners are largely independent, which some exceptions such as live axle vehicles and sway bar linkages.
- The pitch properties of a hull affect the hydrodynamic performance of the hull. This is a drawback of Quarter-Car modeling as well, which doesn't consider pitch and roll inputs.
- Forces on a hull are distributed over a significantly greater area than on automobile. A typical automobile tire may only have a contact patch area of a few square inches, making changes in the center of pressure of the tire are far less significant.
- The tests with the Quarter-Boat rig are conducted in relatively calm water. Effects of forward speed are not considered. This no different than Quarter-Car rigs, which do not consider the differences in a rotating versus a stationary tire in the results.
- Interactions between the two hulls are not considered. For WAM-Vs, the hulls are spaced considerably further apart that for a conventional catamaran, reducing their interaction.

5.5 Quarter-Boat Testing Rig Overview

The Quarter-Boat test rig shown in Figure 5.11 was designed to provide a controlled environment for evaluating the vertical hydrodynamic interactions between a pontoon and the water surface, with the degree of freedom for the suspension system to isolate the payload.

Figure 5.11 Quarter-Boat test rig

The Quarter-Boat Rig consists of two linear shafts that connect to a steel baseplate and wooden support structure. The rails are braced by four threaded rods that run from an aluminum support at the top of the rails to the corners of the wooden base. The shafts are 6 foot long, 1.5 inch diameter ceramic coated aluminum, with additional 3 foot aluminum pipe extensions on the bottom. The total structure height is approximately 10 feet high. The purpose of the two shafts is to support and guide the linear vertical motion of a clear polycarbonate pontoon that is 8 inches

in diameter and 8 feet in length, as well as the motion of payload tray isolated from the pontoon by two springs. The motion is facilitated via four Polytetrafluoroethylene (PFTE) self-lubricating bushings on both the pontoon and the payload tray; the bushings are shown in Figure 5.12. Figure 5.13 shows a close-up view of the central portion of the pontoon and payload assemblies.

Figure 5.12 1.5 inch PTFE bearings used for rig (8 total bearings used on Quarter-Boat rig)

Figure 5.13 Close-up of pontoon and payload assemblies

5.5.1 Quarter-Boat Suspension System

The Quarter-Boat rig is designed to accommodate between two and five coil springs for testing, as well as a single degree of freedom configuration that locks the connection between the payload and the pontoon to mimic the response of a traditional hullform. The lockout is shown installed in Figure 5.13. No dedicated damper has been fitted to the Quarter-Boat Rig, although it

would be possible to mount one where the lockout mechanism is currently located. The properties of each individual spring are listed in Table 5.2. Figure 5.14 shows the Quarter-Boat Rig configured to use all five springs. Three and four spring configurations are also possible.

Table 5.2 Quarter-Boat individual spring properties

Parameter:	Value:
Outside Diameter	2.062 in
Inside Diameter	1.75 in
Free Length	9.75 in
Spring Rate	7.4 lbs/in
Wire Diameter	0.156 in
Total # of Coils	16.5

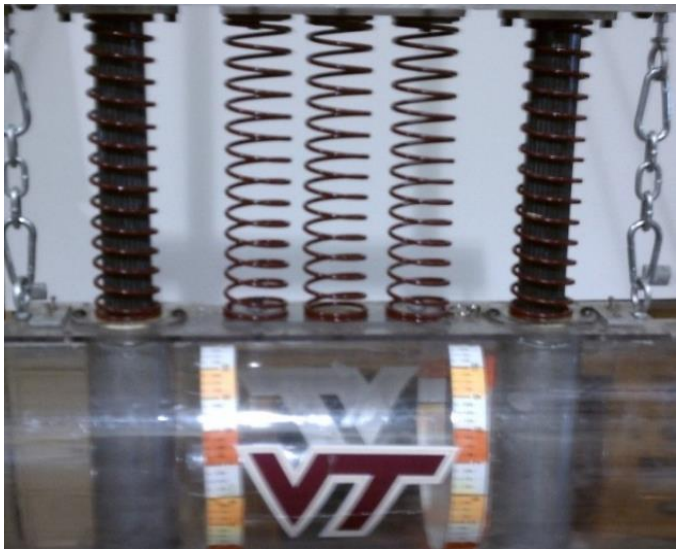

Figure 5.14 Quarter-Boat rig with all five coil springs installed

5.5.2 Quarter-Boat Drop Height Configuration

Prior to each drop, the Quarter-Boat Rig is suspended by the magnetic connection made between the electromagnet and the steel catch plate as illustrated in the Quarter-Boat diagram of Figure 5.10. The steel catch plate hangs from a chain attached to the top plate; changing the length of the chain allows for different drop heights to be tested. In order to set the rig to different drop heights, the length of the chain can be adjusted in two ways. Course height adjustment is accomplished by moving a carabineer connected to a threaded eye bolt on the top plate between the different links of the chain, changing the carabineer by one link raises the drop height by 1 inch. Fine adjustments are made by threading or unthreading the eyebolt on the top plate.

5.5.3 Quarter-Boat Ballast Configuration

The mass of both the sprung and unsprung components can be varied through the addition of up to eight steel ballast plates shown in red in Figure 5.15. The ballast plates are 1/8 in x 1 in x 18 in steel plates that bolt to the structure adding 1.25 lbs per plate. The plates can be shifted between the pontoon and payload structures to test different ratios of sprung to unsprung mass.

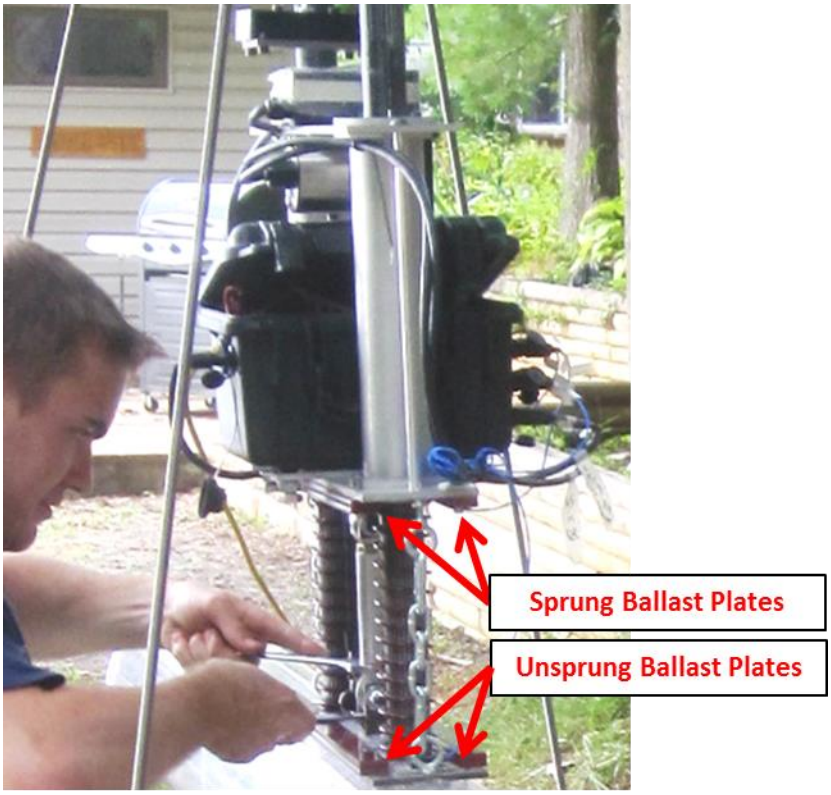

Figure 5.15 Steel ballast plate locations

5.5.4 Damper Dynamometer Compatibility

The pontoon and payload structures of the Quarter-Boat rig are designed to be interchangeable with components from the Roehrig damper dynamometer located in the CVeSS lab. The damper dynamometer also has two 1.5 inch diameter rails (a), spaced 12.875 inches apart (b). This will allow for the possibility of components of the Quarter-Boat rig to be tested out of the water in the laboratory in the future, if so desired. A picture of the damper dynamometer in the laboratory is shown in comparison with the Quarter-Boat rig in Figure 5.16 to show the linear guide rails on the two testing rigs.

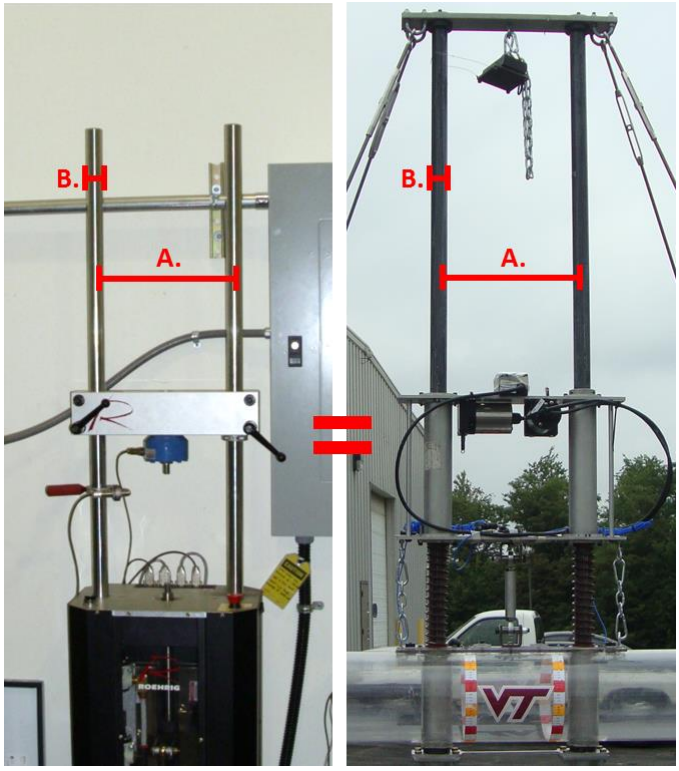

Figure 5.16 Roehrig damper dynamometer and Quarter-Boat rail comparison

5.6 Quarter-Boat Data Acquisition Setup

The same data acquisition setup used on the 12-ft USV detailed in Chapter 4 was reconfigured for use on the Quarter-Boat test rig to measure and record signals from the various sensors on the pontoon and the payload structures. Accelerations are measured using four accelerometers; displacements are measured using two string potentiometers. The CompactRio data acquisition is used for logging the data from testing with Labview software from National Instruments. The sensor diagram for the Quarter-Boat testing rig is shown in Figure 5.17.

Despite using the same data acquisition unit as from testing the 12-ft USV on the Quarter-Boat testing rig, the sensor diagram has changed significantly. For the Quarter-Boat rig, 10 channels of data were recorded: two channels for the vertical 10g and 30g accelerometers on the unsprung mass, four channels for the vertical 10g accelerometer and the triaxial 3g accelerometer on the sprung mass (the lateral and transverse axes measurements were not analyzed), two channels for the string potentiometers, and two channels for recording the voltage across the electromagnet and the battery voltage.

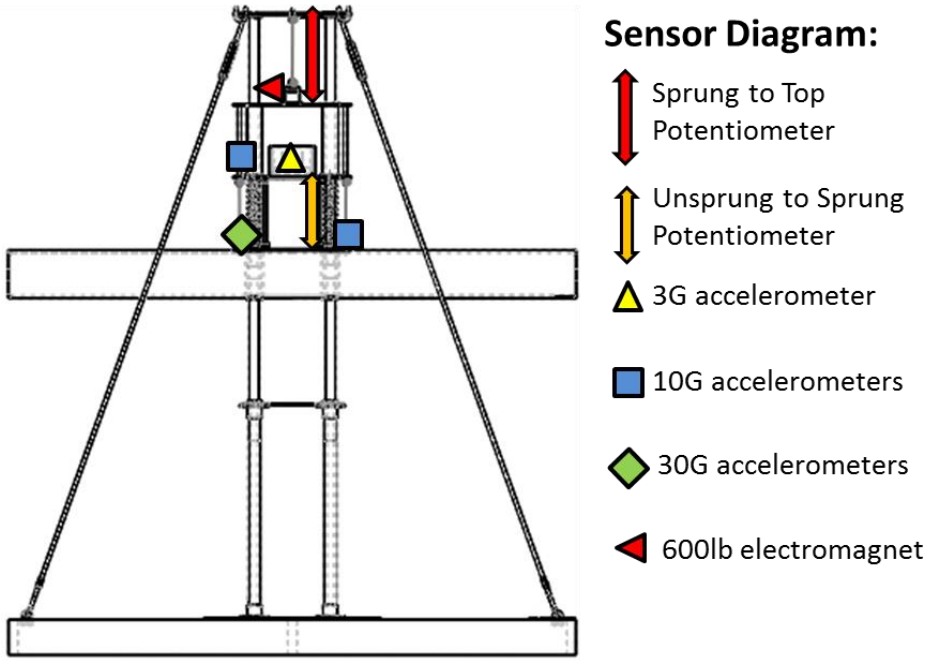

Figure 5.17 Sensor location diagram for Quarter-Boat testing rig

5.6.1 Data Acquisition Hardware

The data acquisition unit is housed in a waterproof container that is bolted to the sprung mass for testing; the data acquisition box makes up a significant portion of the overall sprung mass. Twelve waterproof connectors are located on the right side of the data acquisition box. A waterproof Ethernet connector, a connection for the electromagnet, and an LED light are located on the left side of the box. The data acquisition box is shown in Figure 5.18.

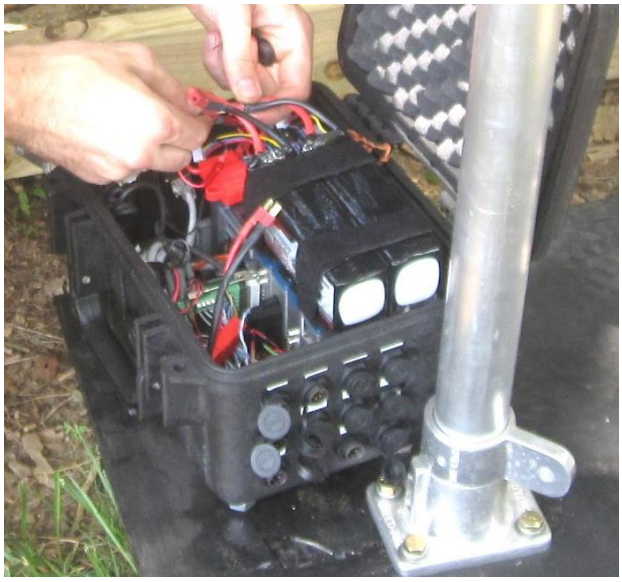

Figure 5.18 Data acquisition box setup (shown removed from payload structure)

5.6.2 Electromagnet System Design

The electromagnet used for initiating the drops is a 12 volt, 600 lb holding force magnet that consumes 29 watts when activated at 12 volts. The electromagnet is run off of a separate 9.9 v Lithium Ion battery identical to the battery powering the CompactRio. The magnet is activated via radio control from a 2.4 GHz transmitter that controls two redundant 10 amp relay switches thought the circuit shown in Figure 5.19.

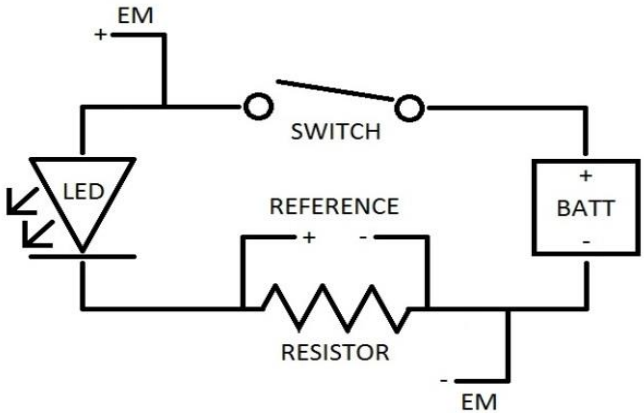

Figure 5.19 Electromagnet, led light and data acquisition system wiring

The blue LED light connected to the outside of the data acquisition box was used to indicate when the electromagnet was activated. The electromagnet's voltage was measured by the data acquisition unit as shown in Figure 5.20, to determine when in the data each drop was initiated.

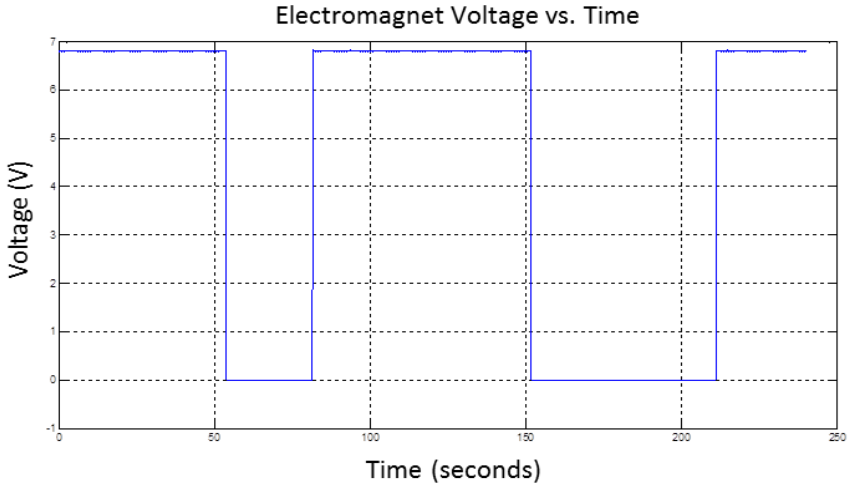

Figure 5.20 Electromagnet voltage versus time sample data

Using the electromagnet voltage as the reference point for the drops introduced a problem, in that the inductance of the electromagnet produced a residual force after the electromagnet had been deactivated. This delay, shown in Figure 5.21, was found to be of the order of roughly 100

milliseconds. The actual drop point time was determined by averaging the position data over the five seconds prior to deactivating the magnet, and determining activation to occur at the last value of data greater than this average.

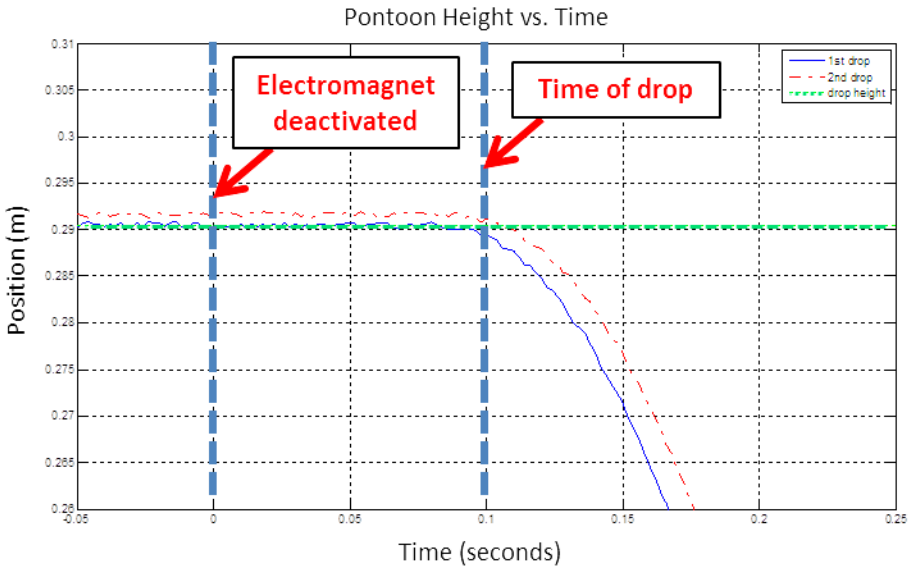

Figure 5.21 Electromechanical delay in magnet due to inductance

5.6.3 Quarter-Boat Potentiometers

Two string potentiometers are used to record the displacements of the sprung and unsprung masses during the drop tests. The locations of the string potentiometers on the payload structure are shown in Figure 5.22(a). Both of the string potentiometers are mounted on the top aluminum support plate on the sprung mass. The string for the string potentiometer used for measuring the global motion of the sprung mass extends up and connects to the top plate. The string for the string potentiometer used for measuring the suspension displacement extends down and connects to the top of the pontoon. From these two displacements, the global motion of the pontoon relative to the base of the water can be calculated using the following formula:

$$Pontoon\_height = -1 * Top\_string\_pot - bottom\_string\_pot$$

5.6.4 Quarter-Boat Accelerometers

Multiple accelerometers are used to measure the response of the Quarter-Boat rig during testing. Four accelerometers are used to measure the acceleration of the pontoon and the payload structure. The two accelerometers mounted on the pontoon are a 10g and a 30g single axis accelerometer, shown in Figure 5.22(b). The two accelerometers mounted on the payload are a 10g single axis accelerometer and a 3g tri axial accelerometer inside the data acquisition box.

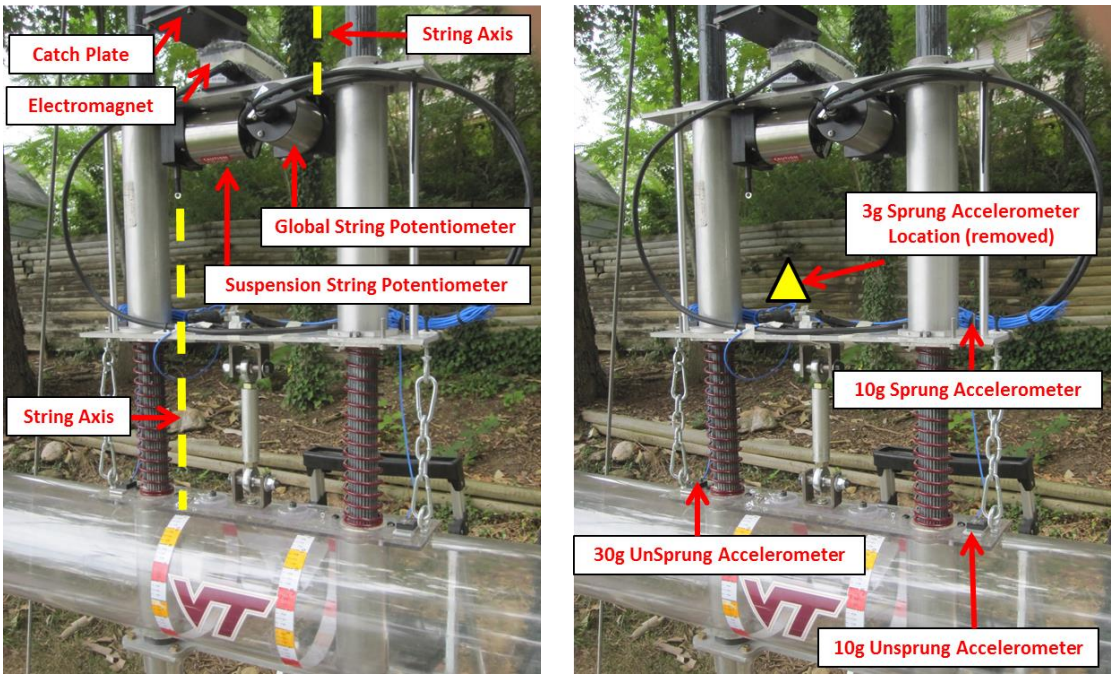

Figure 5.22 Location of the string potentiometers (a) and accelerometers (b) (data acquisition box removed)

5.7 Quarter-Boat Testing Procedure

The first test of the Quarter-Boat rig occurred at Claytor Lake in Radford, VA. The system was deployed at a water depth of approximately 62 inches. The non-floating structure was leveled by placing bricks under the support structure and the structure was ballasted with approximately 200 lbs of concrete blocks to anchor the structure in position. Testing was done at times when the water was most calm to avoid the ripples in the water surface impacting the results; however, deviations from true calm water conditions were unavoidable. Figure 5.23 shows the system at the testing location. Figure 5.24 shows the sequence of events for a drop test.

Figure 5.23 Quarter-Boat rig in initial testing location

The Quarter-Boat drops were executed by manually lifting the pontoon and sprung mass out of the water and holding the sprung mass with the electromagnet. The drop height can be raised in increments of one inch by moving a carabineer along the chain, finer adjustments can be made by turning a threaded eyebolt. Two chains are located between the payload and the pontoon so that when the payload is lifted out of the water, the pontoon will also be lifted. The preload of the springs is also adjustable via a carabineer and an eyebolt. For the initial testing the chains were set to be slightly shorter than the unloaded length of the springs to minimally preload the springs.

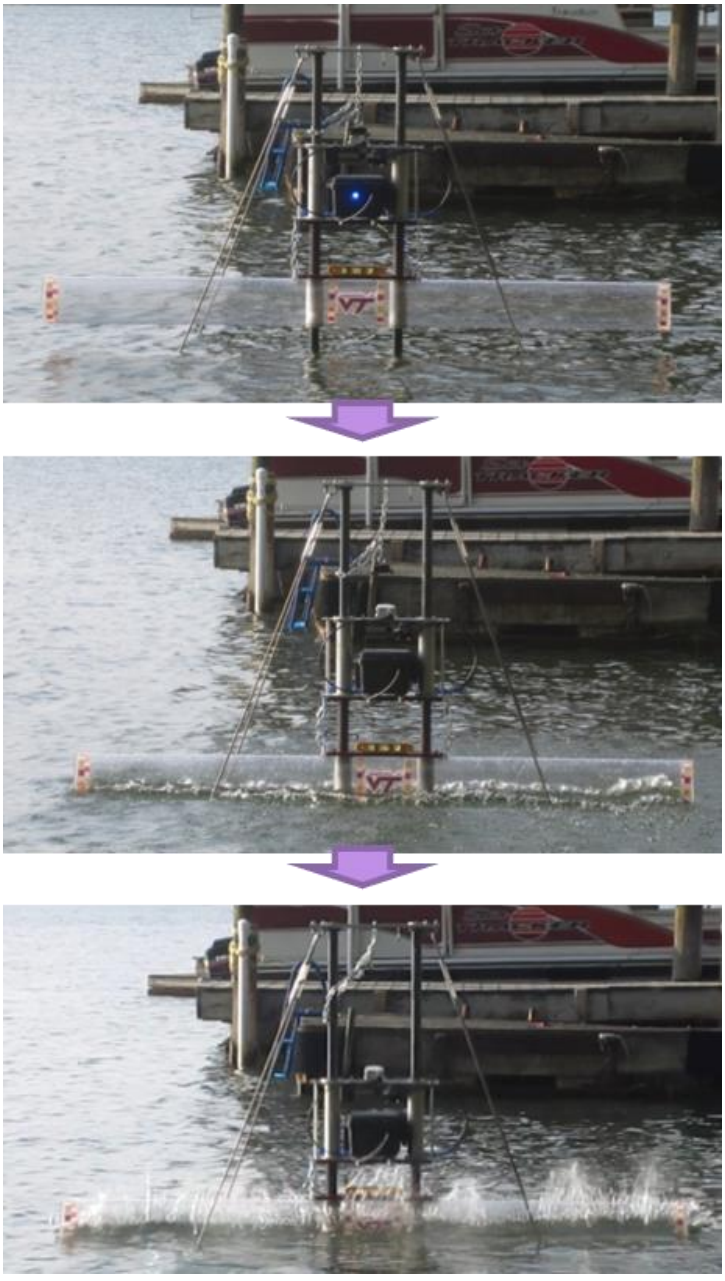

Figure 5.24 Sequence of events during Quarter-Boat drop test

In total, 48 drops were performed during the first round of testing. Table 5.3 shows the drop height, spring configuration, and ballast configuration for each test; two drops were performed for each different configuration. Figure 5.25 shows a comparison of two drop tests from identical heights that will be the subject of the first round of correlating the Quarter-Boat models.

Table 5.3 Drop test configuration information

Test #:	Height above water (m):	Spring Configuration:	Ballast Configuration Sprung / Unsprung (lbs):
1, 2	0.00	locked	5, 5
3, 4	0.07	locked	5, 5
5, 6	0.15	locked	5, 5
7, 8	0.22	locked	5, 5
9, 10	0.30	locked	5, 5
11, 12	0.37	locked	5, 5
13, 14	0.00	2 springs	5, 5
15, 16	0.07	2 springs	5, 5
17, 18	0.15	2 springs	5, 5
19, 20	0.22	2 springs	5, 5
21, 22	0.30	2 springs	5, 5
23, 24	0.37	2 springs	5, 5
25, 26	0.00	2 springs	0, 0
27, 28	0.07	2 springs	0, 0
29, 30	0.15	2 springs	0, 0
31, 32	0.22	2 springs	0, 0
33, 34	0.30	2 springs	0, 0
35, 36	0.37	2 springs	0, 0
37, 38	0.00	locked	0, 0
39, 40	0.07	locked	0, 0
41, 42	0.15	locked	0, 0
43, 44	0.22	locked	0, 0
45, 46	0.30	locked	0, 0
47, 48	0.37	locked	0, 0

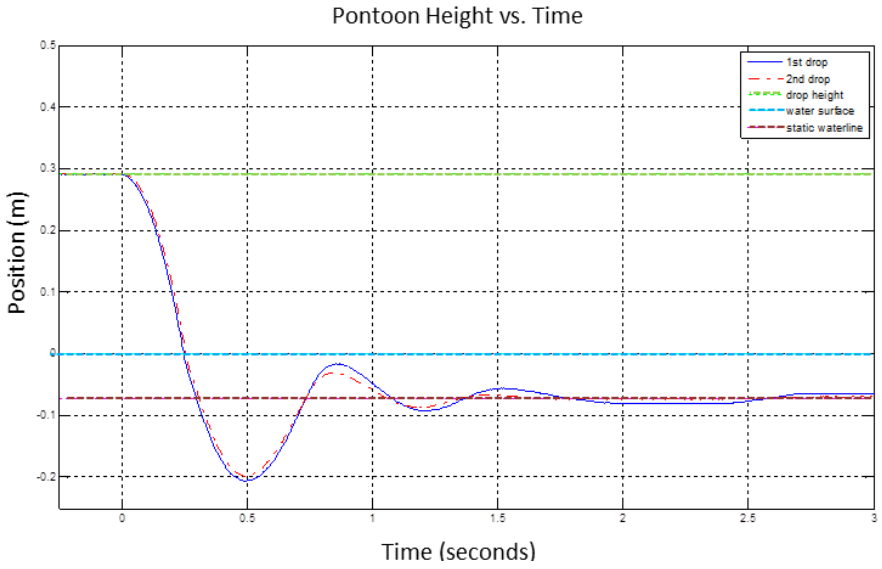

Figure 5.25 Pontoon displacement vs. time from 11th and 12th drop tests

Figure 5.26 and Figure 5.27 show the displacement results of the 24 tests conducted with the lockout mechanism in place. Figure 5.26 shows the fully ballasted configuration used in drops 1-12, Figure 5.27 shows the non-ballasted configuration used in drops 37-48.

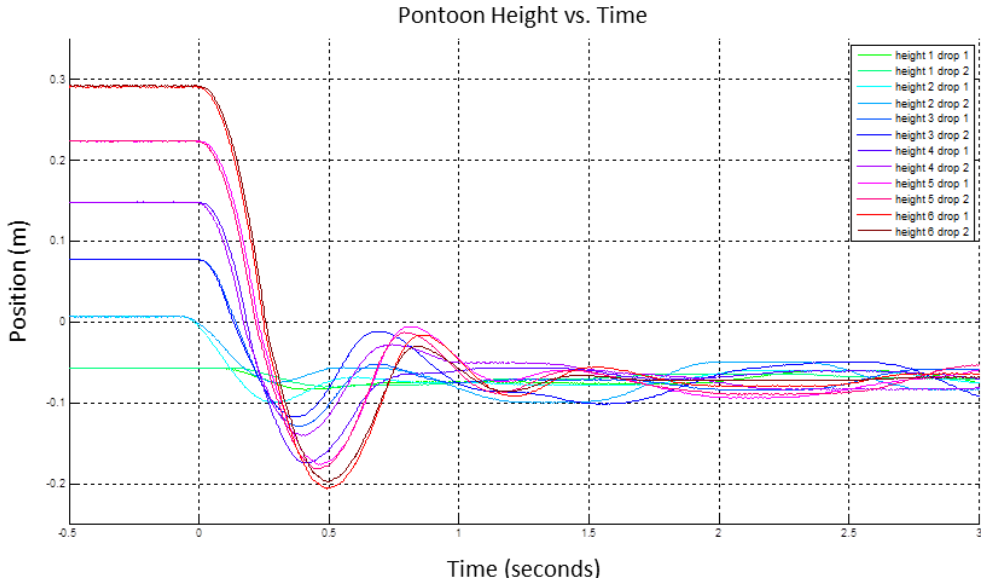

Figure 5.26 Displacement vs. time for ballasted 24.84kg drops

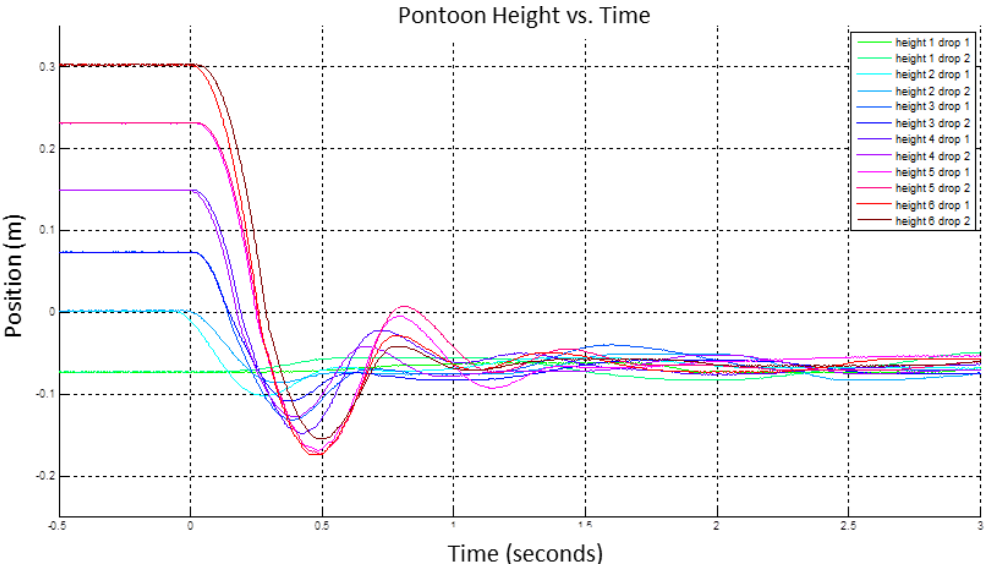

Figure 5.27 Displacement vs. time for ballasted 20.30kg drops

5.7.1 Displacement Data Nonlinearity:

An intricacy in the data was found in the results from the second highest drops. The highest return maximum heights occur in the second highest drop heights both with the ballast and without the ballast. Examining the video data from the tests, this effect is believed to be due to the spray directing outward at lower drop heights, and inward at the highest drop height.

5.8 Quarter-Boat Single Degree of Freedom Modeling

The remainder of this chapter focuses on the research into creating a simulation environment based on the data from the Quarter-Boat test rig. The simulations incorporate a hydro-mechanical modeling solution for the vertical pontoon/water surface interactions. This section documents the modeling of the single degree of freedom simulations of the Quarter-Boat tests conducted with the lockout mechanism installed between the pontoon and the suspension system. The schematics and block diagrams in this section show representations of two degree of freedom systems. For the single degree of freedom simulations, the degree of freedom of the suspension system is modeled as rigid. The modeling efforts for creating two degree of freedom simulations for the Quarter-Boat rig tests with an operational suspension system are presented in Section 5.9.

A mechanical model of the pontoon/water surface interaction is desired for use in future WAM-V simulations. Some of the reasons a mechanically-based modeling solution is desirable include the following contributing factors:

- Mechanical solutions are easier to simulate in the time domain. Using classical hydrodynamics methods, the added mass and damping coefficients are calculated as frequency-dependent variables, requiring computations in the frequency domain.
- A mechanical model is more simplistic and easily understood. The simulation results can be compared with the existing knowledge base on tuning two degree of freedom mass-spring-damper systems to improve suspension performance.
- A simple mechanical model has the potential to be faster running and more computationally efficient than a solution using computational fluid dynamics software.
- A mechanically-based model could be used as a plant model for future controls applications involving WAM-Vs. Future controls applications might include active or semi-active suspension control and/or controls applied to the actuators on multi-post shaker rigs for simulating hydrodynamic forces.
- Mechanical modeling solutions are easily integrated with Matlab, Simulink, and SimMechanics to couple the models with current and future 4-post simulations.

Using more traditional methods of modeling the vertical hydrodynamics of the Quarter-Boat rig is also a possible area of future research. A few other possible methods of modeling based on the Quarter-Boat rig data are listed in Table 5.4 along with the section each method is discussed.

Table 5.4 Other possible methods of integrating hydrodynamics into Quarter-Boat model

Method:	Section Discussed:
Impulse Response Function	5.11.1
Slamming Model	5.11.2
Strip Theory	5.11.3
CFD Coupling with Multi-Body Dynamics Code	11.5

More information on the application of the Quarter-Boat models to the 33-ft WAM-V can be found in Chapter 8. Future applications of the Quarter-Boat models are discussed in Chapter 12.

5.8.1 Quarter-Boat Data Analysis

During the iterative process of creating the Quarter-Boat model, a detailed analysis of the data from the two drops previously shown in Figure 5.25 was performed. The analysis gives valuable insight into the required modeling parameters for the spring rate, added mass, and damping variables in order for the Quarter-Boat model to best correlate with the test data.

5.8.1.1 Initial Impact Data Analysis

The initial impact of the pontoon with the water surface contains a great deal of information that can be applied to the modeling of the Quarter-Boat rig. A close-up view of the position traces of the pontoon during the impact with the water surface is shown in Figure 5.28.

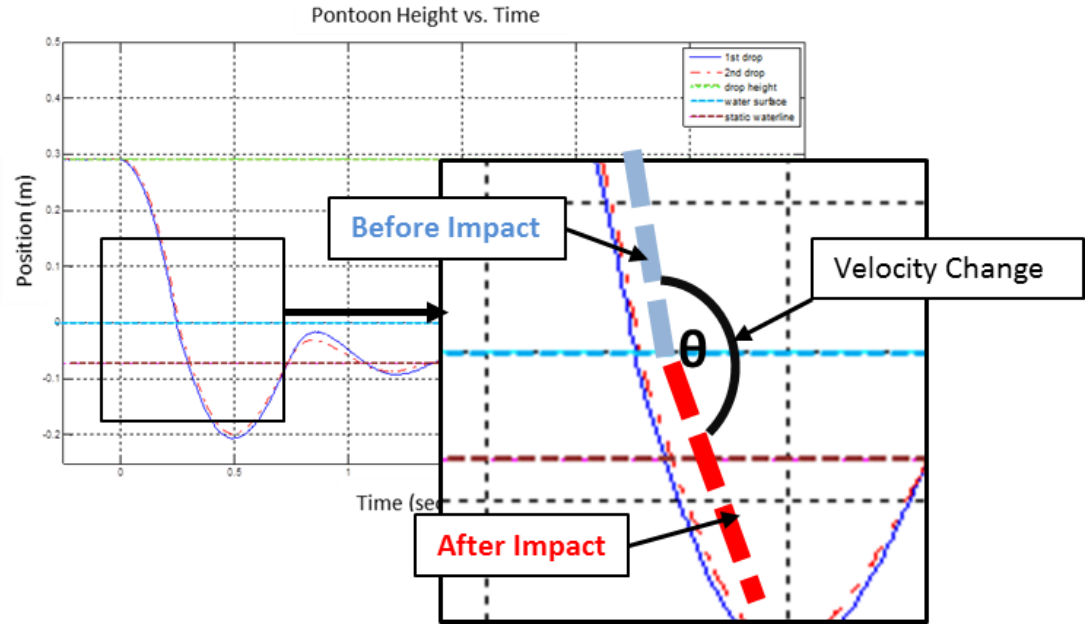

Figure 5.28 Pontoon position data showing change in velocity at impact

As shown in Figure 5.28, the pontoon's response to the impact with the water surface can be interpreted as a step change in velocity immediately following impact. Based on this segment of the drop data, a few insights have been gained that can be applied to the Quarter-Boat model parameters to better simulate the pontoon's response at impact.

- At impact, the damping level should be at its highest to simulate the step change in velocity. A linear damping model with a large enough damping constant to correctly model the impact will likely have too much damping to properly simulate the remainder of the test, even though the velocity is lower in magnitude after the impact phase.
- At impact, the added mass should be minimal. Adding inertia to the system at impact above the inertia from the pontoon's mass would cause the pontoon to have a greater resistance to a change in velocity impact like the change in velocity shown in Figure 5.28. Added mass should not be a constant value when submerged, a constant added mass would have added mass at impact, which is undesirable. Added mass should also not be change proportionally with velocity, since the pontoon's velocity is highest at impact.

5.8.1.2 First Oscillation Data Analysis

By analyzing the data from impact to the first local maximum value, a great deal can be learned about the properties of the Quarter-Boat system. Figure 5.29 shows a close-up view of the pontoon position data from the time of impact through the first oscillation.

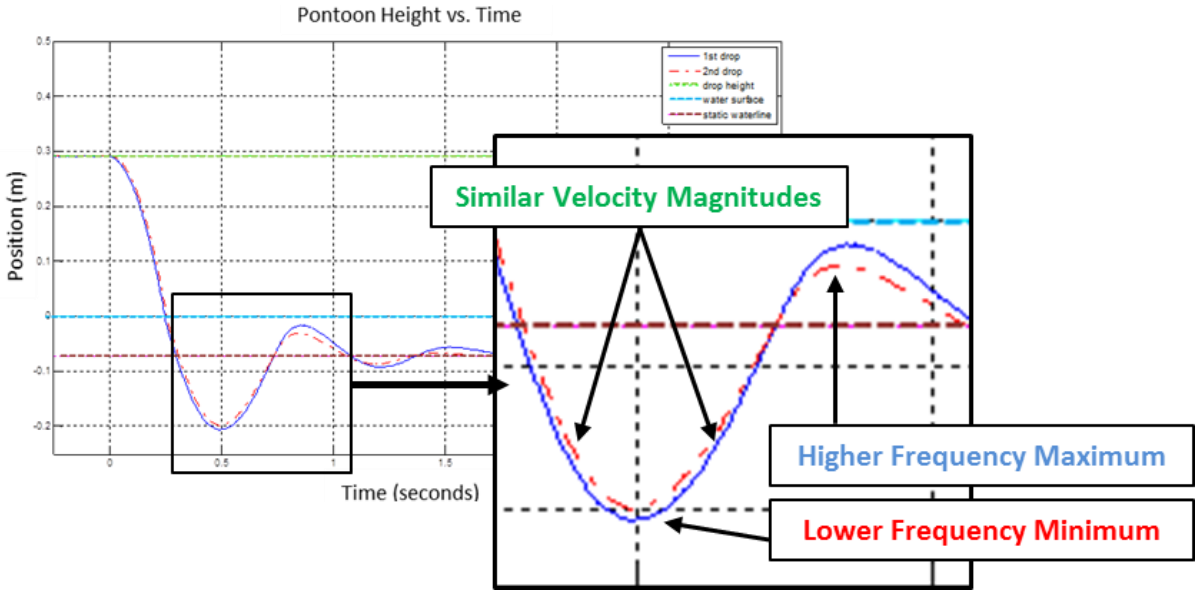

Figure 5.29 Pontoon position data showing first oscillation

The pontoon's response over the first oscillation contains some valuable information about the properties of the system that can be translated to the Quarter-Boat models:

- The time for the pontoon to complete the first half of the oscillation (submersion greater than the static waterline) is significantly greater than the time to complete the second half of the oscillation (submersion less than the static waterline). The change in frequency more than counteracts the frequency change due to the nonlinear hydrostatic spring rate.
- For the frequency of the system to change so dramatically, the added mass of the system must also be changing. This indicates that the added mass should be greatest when the levels of displacement are highest.

Also visible in Figure 5.29 is the velocity of the pontoon before and after the first minimum, inferred based on the slopes of the position data. The velocity magnitudes are roughly similar between the two directions of travel, indicating that the damping of the system is not significantly different in either direction.

5.8.1.3 Velocity Trace Analysis

Figure 5.30 shows a differentiated velocity trace created from the position data from one of the drops, compared with the undifferentiated position data from the same drop test.

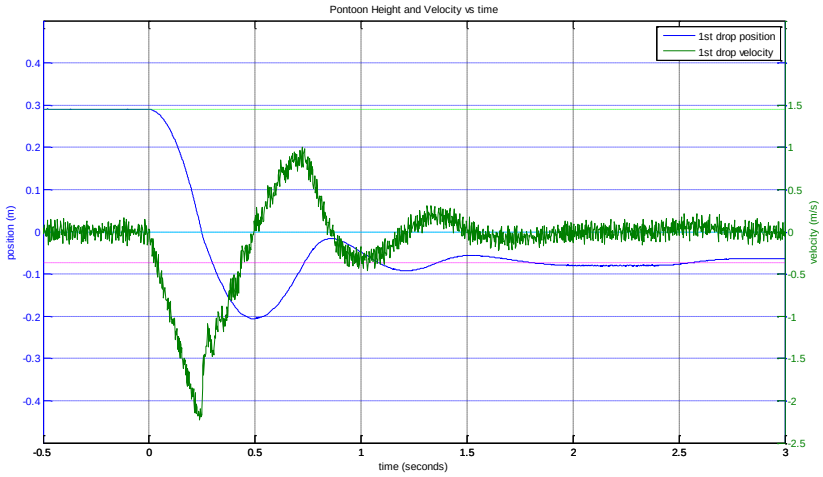

Figure 5.30 Position and velocity traces (drop 11/48 shown)

At the time of impact, the pontoon is traveling at its maximum velocity of ~2.2 m/s. The near step change in the velocity of the pontoon can be seen just after impact by the near vertical slope of the pontoon velocity trace. The velocity of the pontoon is reduced by half in less than 100 milliseconds. After the step velocity change occurs, the change in velocity of the pontoon is relatively linear up to the first velocity peak.

5.8.2 Quarter-Boat Model

A dynamic model of the Quarter-Boat test rig was formulated based on the conceptual schematic shown in Figure 5.31. This section overviews the finalized model parameters, the model is implemented again in Chapter 8, applying the modeling results to the 33-ft WAM-V.

The schematic shown has two degrees of freedom, for the tests modeled with the Quarter-Boat rig in the locked out configuration, two orders of magnitude were added to the spring rate and damping coefficients to make the suspension effectively rigid. Alternatively, the prismatic joint could be replaced with a weld joint in the model, or the system could be modeled as a single lumped mass.

For the Quarter-Boat Model, the added mass of the system due to the pontoon/water surface interaction is modeled as a variable mass mounted on a cart attached to the pontoon via a pulley. The added mass on the cart varies throughout the drops, based on the volume of the pontoon in the water at a given time. When the pontoon is out of the water, the cart has no mass and the system behaves the same as it would if the cart were not present. The since the added mass is based on the volume of water displaced by the pontoon, the added mass units are given in kg/m^3.

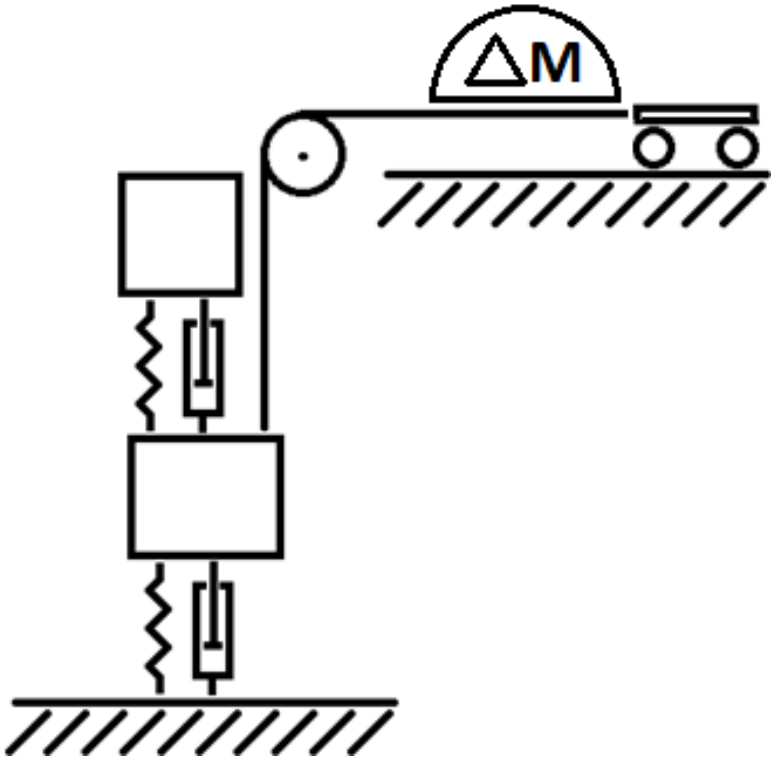

Figure 5.31 Quarter-Boat model conceptual schematic

5.8.2.1 Unsprung Spring Rate: Quarter-Boat Model

For the Quarter-Boat model, the spring rate of the spring acting on the unsprung mass is modeled based on solely on the hydrostatic stiffness of the water surface. The hydrostatic spring rate used for the initial modeling is derived from Archimedes' principle, which states that any object wholly or partially submerged in a fluid is buoyed by a force equal to the weight of the fluid displaced by the object [58].

Determining the gradient of this upward buoyant force will be the focal point for establishing the spring rate calculations. For a cylinder, the Archimedes' spring rate is a nonlinear function of displacement, with the greatest spring rate occurring at a submersion of half the pontoon's diameter and the greatest force acting on the pontoon at full submersion, after which the upward force becomes constant with respect to displacement. The spring force and spring rate data for the 8 inch diameter, 8 foot long cylinder used on the Quarter-Boat rig are shown in Figure 5.32.

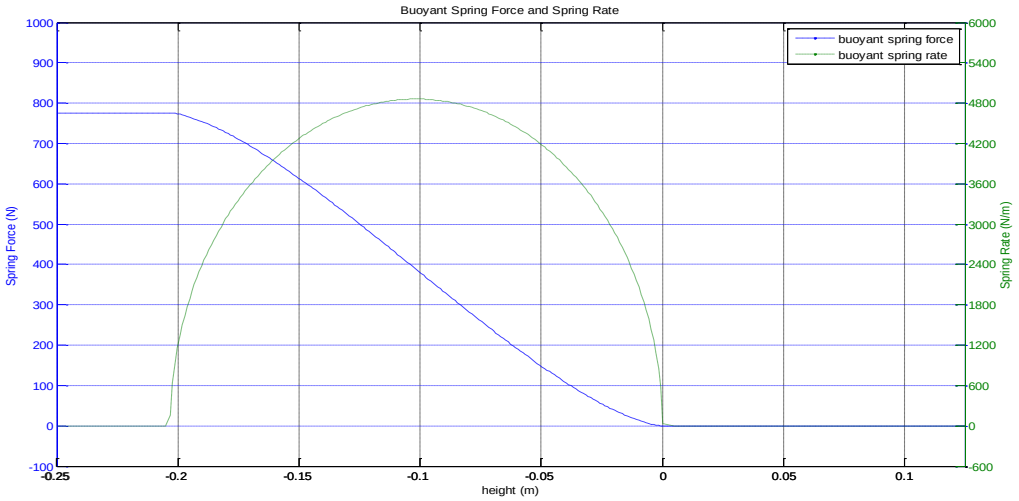

Figure 5.32 Cylindrical spring force and spring rate derived from Archimedes' Principle

5.8.2.2 Unsprung Added Mass: Quarter-Boat Model

For the Quarter-Boat model, a solution for modeling the added mass is desired where the frequency of the system could be adjusted/lowered without changing the static equilibrium of the system. Preliminary Quarter-Boat simulations were conducted without modeling the added mass to investigate its effect on the simulations. Figure 5.33 shows the Quarter-Boat simulations compared with the test data for ten different damping ratios with no added mass coefficient included in the model to simulate the frequency effects of the water/surface interaction.

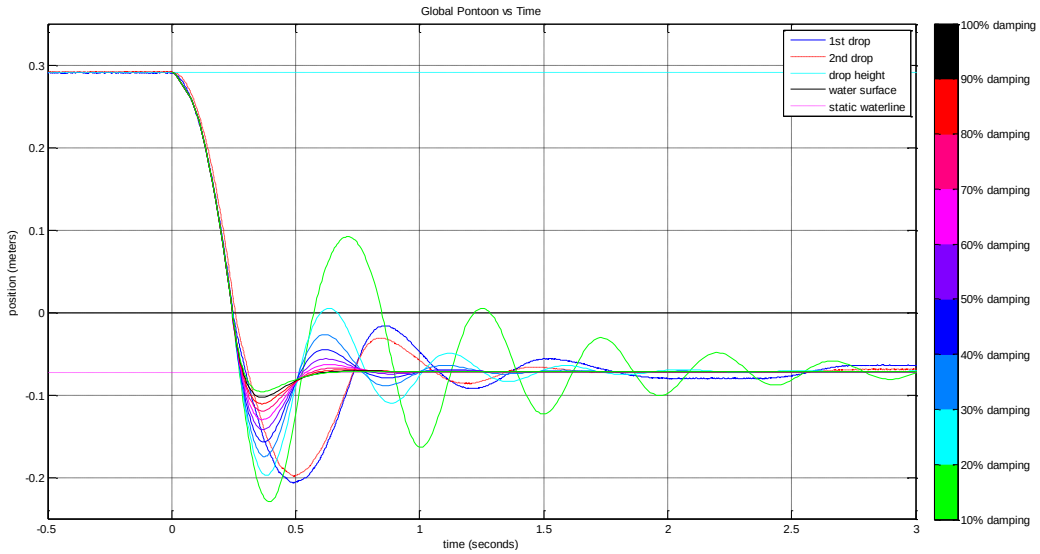

Figure 5.33 Quarter-Boat simulations with no added mass coefficient modeled

The simulation results shown in Figure 5.33 indicate that while the amplitudes of the peaks in the data can be simulated (the 20% and 30% critical damping simulations best approximated the height of the first two peaks from the test data), the frequencies in the data cannot be adequately matched. In order to lower the natural frequencies of the system, the unsprung spring rate of the model must be decreased, or the unsprung mass of the model must be increased. A solution for lowering the system's natural frequency by reducing the hydrostatic stiffness was also simulated, and ultimately not incorporated in the model because the static waterline of the system was also altered. A number of solutions for raising the mass of the system were tested with varying results. A model where the added mass was varied based on the velocity of the system, so at static equilibrium (zero velocity), the static waterline would be maintained, was evaluated. The model correlated poorly with the test data, as predicted in the data analysis in Section 5.8.1.

For some of the parametric studies, both positive and negative values were investigated for the added mass coefficient in the simulations. It is noteworthy that negative added mass values are actually possible in free-surface oscillations problems [68]; damping however, is necessarily a non-negative quantity [68]. Adding mass for the same spring stiffness will lower the system's natural frequency by the following ratio for a linear mass-spring-damper system:

$$\text{Change in Natural Frequency} = \Delta\omega_n = \sqrt{\frac{k}{\Delta m}} \Rightarrow {}^{1}\!/\!_{\Delta m} \propto \Delta\omega_n{}^{2} \quad \text{(for a given k)}$$

The ultimate solution for lowering the systems natural frequency must add inertia to the pontoon without affecting the mass of the pontoon that is acting on the spring. In advanced automotive suspension systems, a system that is used to achieve similar results is an inertial damper, also known as an inerter or J-damper. An inerter is essentially a flywheel connected through a gearbox between the sprung and unsprung masses of a vehicle, mounted in parallel to the viscous dampers. Relative motion between the sprung and unsprung masses causes the rack to move, the gears to turn, and the flywheel to spin up. The inertia the flywheel adds to the system is disproportionate to the weight of the flywheel itself because of the gearing between the flywheel and the inerter's mounting points.

An inerter is not a replacement for conventional viscous dampers as there is no mechanism to dissipate energy, only a method to store energy in the flywheel. The inerter is able to lower the natural frequency of the system significantly with only a small change in the overall mass of the system. Figure 5.34 shows a diagram of an inerter which uses a rack and pinion to convert the linear motion of the damper into rotational motion of the gears and flywheel [60].

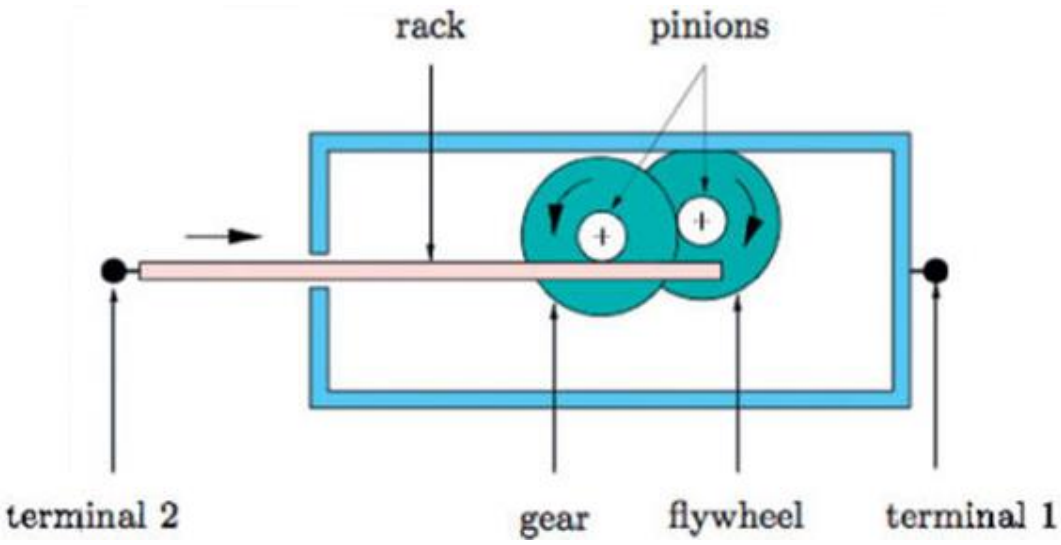

Figure 5.34 Inerter/J-damper schematic [60]

For the Quarter-Boat model, the inerter would not be located between the sprung and unsprung masses as it would be on a vehicle; the inerter would be located between the unsprung mass and the water surface. A conceptual schematic of an added inertia Quarter-Boat model is shown in Figure 5.35. Modeling the added mass coefficient as an inerter would add inertia to the system without an increase in mass, so the static waterline would be unchanged.

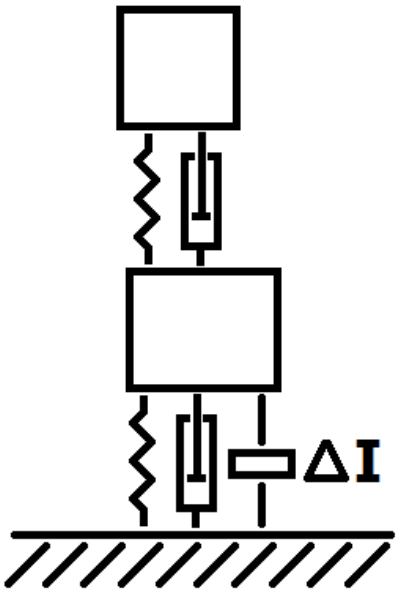

Figure 5.35 Added inertia model conceptual schematic

A simpler and more intuitive method of modeling the added inertia of the system (compared to the model shown in Figure 5.35) was implemented as shown in Figure 5.31, using a pulley and a mass translating along the horizontal axis. The translating mass would act in the same manner as the added inertia; changes to the mass acting on the pulley would not affect the static waterline. The pulley mechanism is conceptually simpler to quantify since the units of the added mass are still in units of mass (kg), rather than inertia (kg*m^2). For the simulations, the pulley is modeled as two directional; the cable can be pushed and pulled. For the Quarter-Boat model, the added mass is proportional to the volume of the pontoon submerged, the units are in kg/m^3.

5.8.2.3 Unsprung Damping: Quarter-Boat Model

For the Quarter-Boat model, a nonlinear damping model with respect to velocity was implemented. Initially a linear damping model was used, which was found to correlate well with the test data, except during the initial impact of the pontoon; it is not surprising that a linear damping model was not sufficient for modeling the transient response of an impact [8]. In order for a linear damping model to have sufficient damping to create the velocity change shown in the data analysis in Figure 5.28, the damping level would be too great for the rest of the simulation, despite the velocities being less than at impact.

Ultimately, two different damping models were found to demonstrate the best performance for both simulating the impact and the secondary oscillations that occur post-impact. The first model is a second order damping function as a function of velocity, as shown in Figure 5.36.

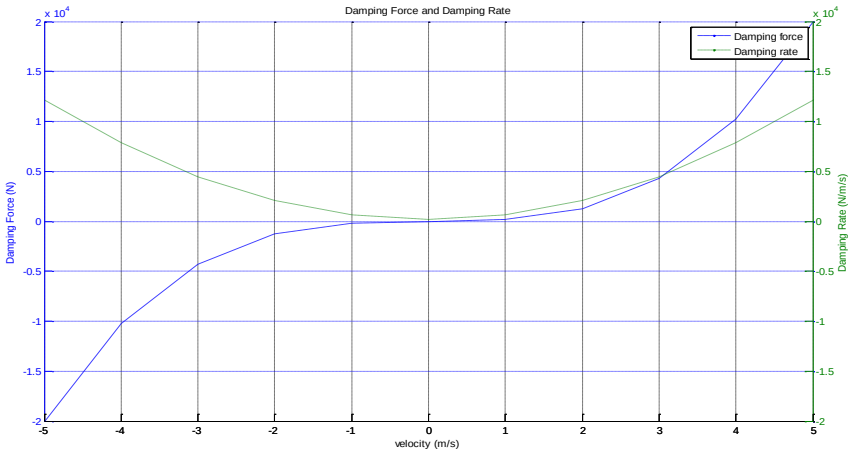

Figure 5.36 Second order damping rate for Quarter-Boat models

The second order damping model shown in Figure 5.36 has significantly increased damping at high velocities to model the impact, without overdamping the system during small oscillations. The other damping model found to correlate well with the test data is a bi-linear damping model, which also has greater levels of damping for high velocities. The damping rates of the bi-linear damping model are shown in Figure 5.37. For the bi-linear damping model, the knees in the damping curves occur at +/-1 meter/second, approximately half of the maximum velocity recorded during the Quarter-Boat rig tests.

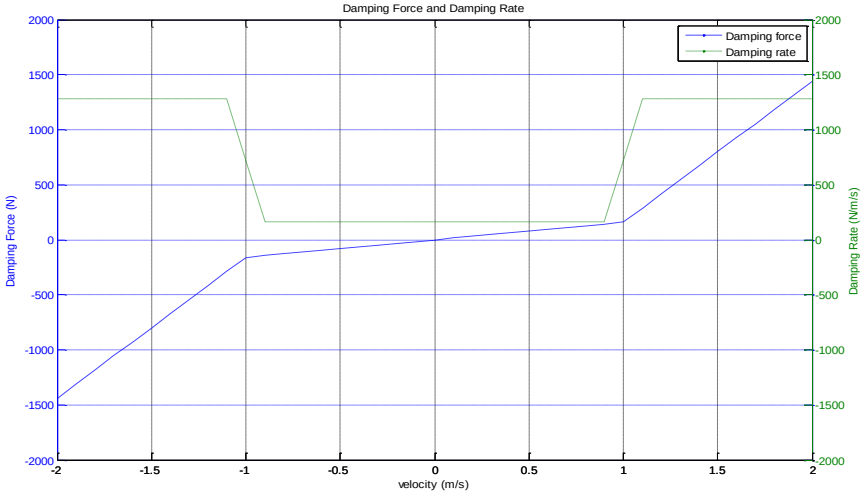

Figure 5.37 Bi-linear damping rate for Quarter-Boat models

The spring rate after the transition is 8 times greater than the spring rate before the transition. The ramp transitions in the damping rate plot shown by the dotted green line are due to the step size used for the numerical simulation. The two damping models showed nearly identical correlation results, the choice between the models will depend on the application. For some

linearized numerical solutions, the bi-linear model could be more easily implemented. The bi-linear model is also easier to fit to a new dataset, as the damping at impact and during the secondary oscillations can be tuned independently. If a continuous damping curve is desired, the second order damping model should be implemented. The simulation results in this section are shown for the bi-linear damping rate solution.

5.8.2.4 Block Diagram Model: Quarter-Boat Model

The Quarter-Boat model was created using SimMechanics; a block diagram of the model is shown in Figure 5.38. The model has three linear prismatic joints representing the degrees of freedom between the pontoon and the base plate, the pontoon and the sprung mass, and the sprung mass and the top plate. The two bodies represent the sprung and unsprung masses. The two initial condition blocks represent the drop height and the initial displacement of the springs. The water interface subsystem contains the mathematical properties for calculating the spring rate, added mass, and damping of the pontoon/water interface. The two sensor blocks measure the acceleration, velocity, and position of the bodies. The added mass of the cart, which is very light compared to the variable added mass, moves on a prismatic joint along the horizontal axis.

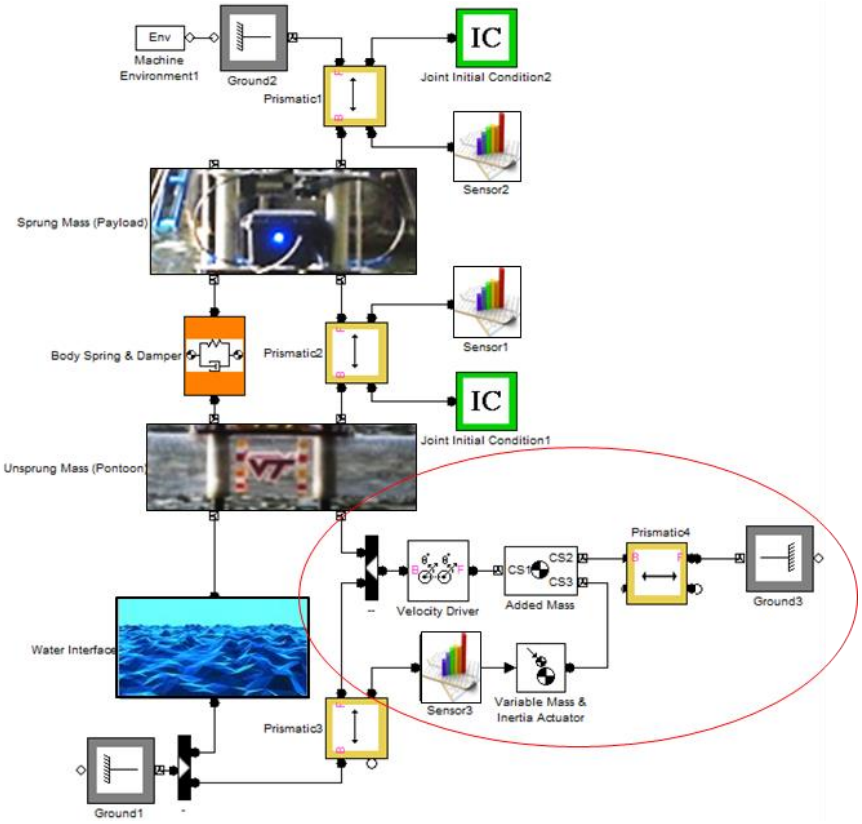

Figure 5.38 Quarter-Boat model block diagram

The displacement of the unsprung mass is measured by a sensor on the bottom of the pontoon. A variable mass and inertia actuator is used to vary the added mass based on the displacement sensor output. The variable added mass system components are circled in red in Figure 5.38. Table 5.5 contains the key properties of the water interface for the Quarter-Boat model.

Table 5.5 Coefficients of spring force, added mass, and damping for Quarter-Boat model

Parameter:	Coefficients:	Units:
Spring Force	9810	N/m^3
Added Mass	735.7	Kg/ m^3
Damping Force	160 (v < 1), 1280 (v>1)	N/m/s

For the spring force and added mass, the denominator units could be replaced by a coefficient of submersion (cs) varying from 0-1 based on the percentage of the pontoon volume submerged. The coefficients of the spring force and added mass are 775.7 N/(cs) and 58.19 kg/(cs).

5.8.2.5 Simulation Results: Quarter-Boat Model

Figure 5.39 shows the results of the simulation for the Quarter-Boat model compared with the data from the 11th and 12th drop configurations listed in Table 5.3. The results show excellent correlation, providing an initial validation of the modeling approach.

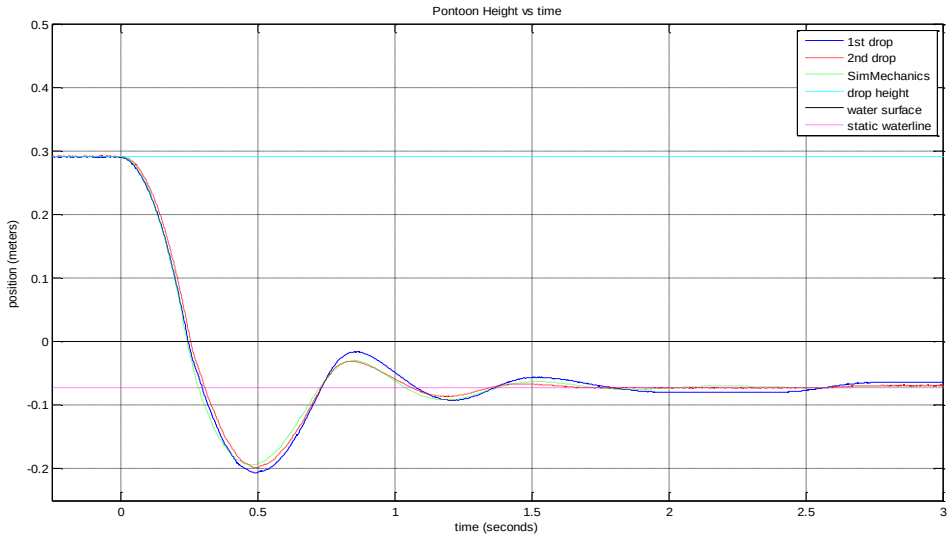

Figure 5.39 Quarter-Boat model simulation results

Additional simulations were run for other drop heights and ballast configurations to compare with the data from other tests. Figure 5.40 shows the simulations results compared with the data from the four highest drop heights for both ballast configurations. The simulations show good correlation for each of the comparisons.

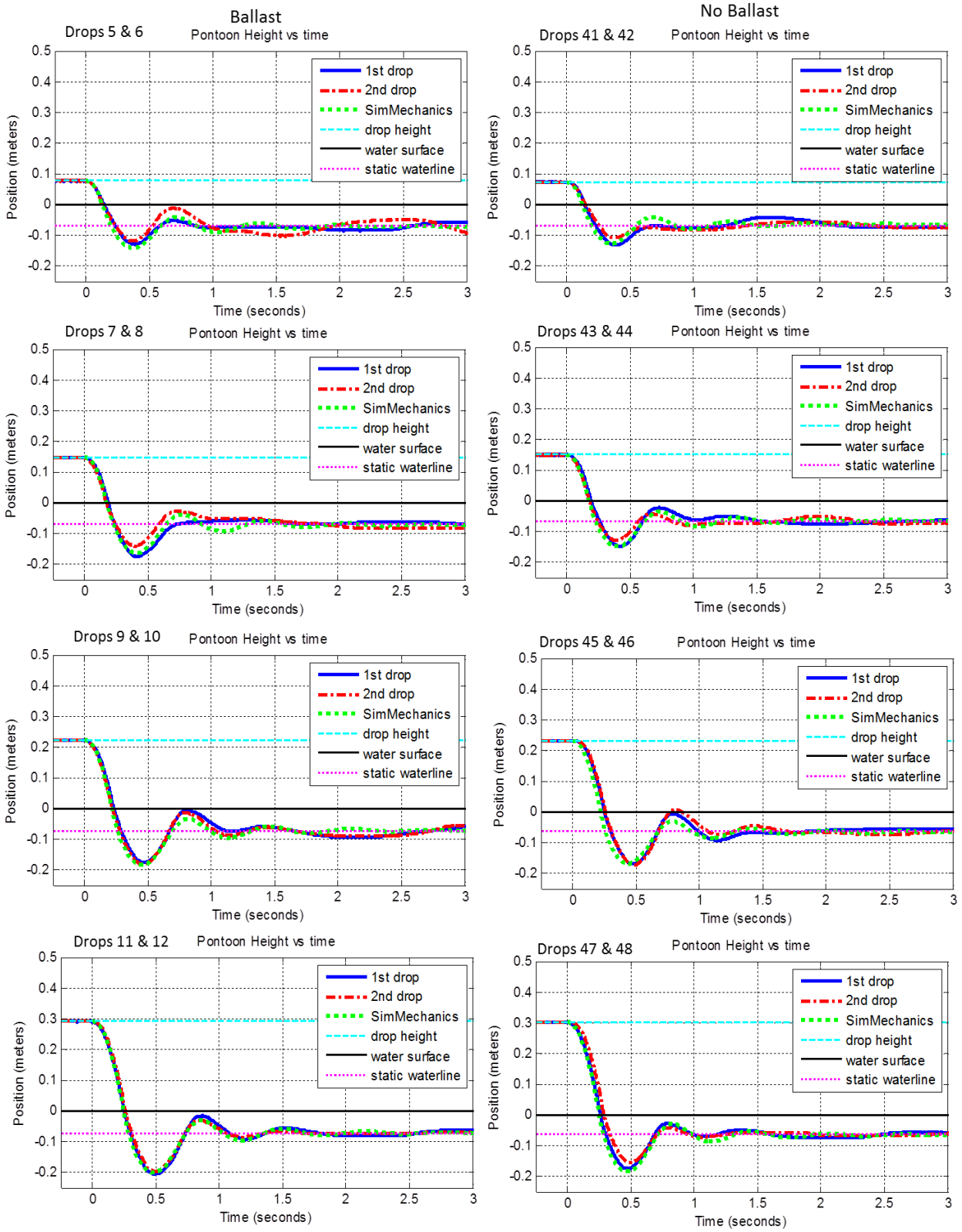

Figure 5.40 Single degree of freedom simulation results for eight drop tests

5.9 Two Degree of Freedom Quarter-Boat Model

Once satisfactory correlations were achieved between the single degree of freedom model and the Quarter-Boat test data with the locked out mechanism installed, the Quarter-Boat model was expanded to incorporate the dynamics of both the sprung and unsprung masses, so the model could be applied to the Quarter-Boat tests with a suspension system. For comparing the models the data, the 23rd and 24th drops are shown. These drops were conducted with the same height and ballast configuration as the drops shown for the single degree of freedom modeling.

5.9.1 Suspension Spring Rate: Two Degree of Freedom Model

In order to model the dynamics of the suspension system, a mathematical representation of the two coil springs needs to be established. The spring rate model of the system is derived directly from the spring properties listed in Table 5.2. A graph of the spring force versus displacement is shown in Figure 5.41. The spring force model is analogous to a three part linear system. The upper limit nonlinearity is modeled as an order of magnitude increase in the stiffness when the chains are pulled into tension. The lower limit nonlinearity is modeled as an order of magnitude increase in stiffness when the spring coils go into coil bind.

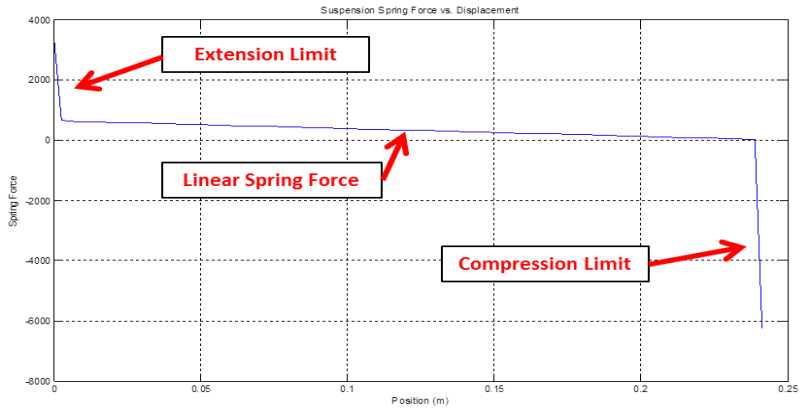

Figure 5.41 Spring rate model for the two degree of freedom system with nonlinearities at end stops

5.9.2 Suspension Damping: Two Degree of Freedom Model

When the Quarter-Boat rig was being designed and constructed, a great deal of care was taken to minimize the friction in the guide rails so the friction wouldn't skew the results of the test. Still, there is a small amount of friction in the system, and for the suspension model to correlate well some damping needs to be modeled in the suspension. While the majority of the damping on the actual Quarter-Boat rig comes from Coulomb friction, for the model, the damping is modeled as viscous with the damping value set to provide 5% critical damping of the sprung mass.

5.9.3 Block Diagram Model: Two Degree of Freedom Model

The block diagram of the two degree of freedom model is shown in Figure 5.42. The model is nearly identical to the single degree of freedom Quarter-Boat model detailed in the previous section, with a slight alteration to the suspension system block, circled in red.

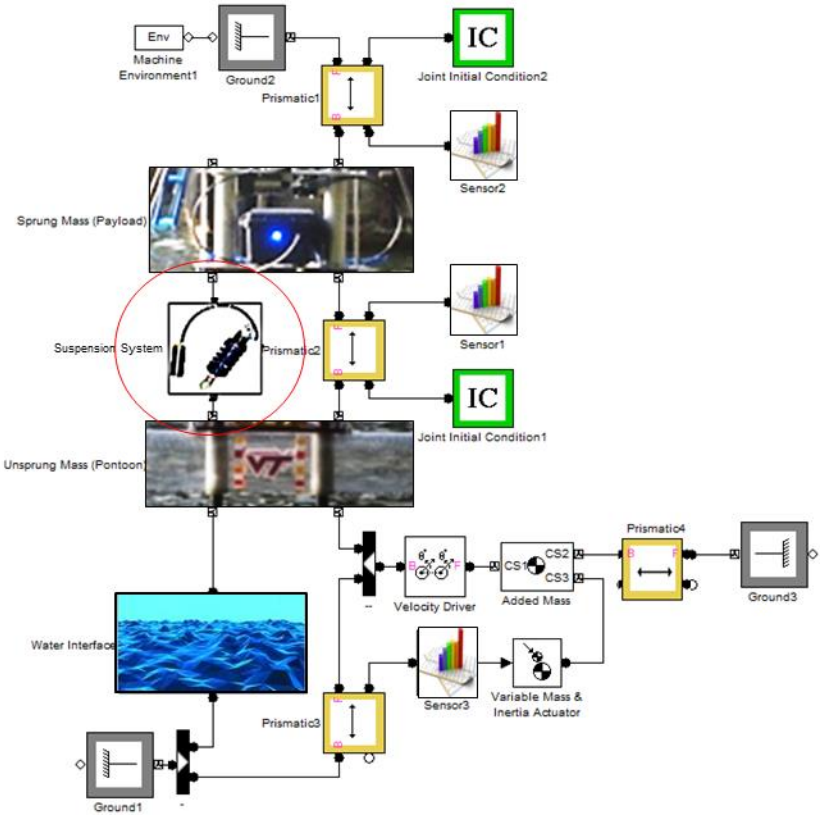

Figure 5.42 Two degree of freedom model block diagram

The suspension block was altered for the two degree of freedom model even though the single degree of freedom model already incorporated a body spring and damper block (the spring stiffness and damping were increased by two orders of magnitude to simulate a rigid connection). The body spring and damper block could have been reused for the two degree of freedom model, except that the block does not have a mechanism to incorporate the nonlinear end stop behavior of the springs shown in Figure 5.41. Instead, a nonlinear suspension subsystem has been modeled using an identical subsystem to the suspension subsystems created for the model of the 12-ft USV detailed in Chapter 4; except the subsystem contains the spring rate and damping properties of the Quarter-Boat suspension system instead of the 12-ft USV.

5.9.4 Simulation Results: Two Degree of Freedom Model

Figure 5.43 shows a comparison between the Quarter-Boat model with two degrees of freedom and the test data from the 23rd and 24th drop tests. Figure 5.43 displays two plots showing the suspension motion (a), and the pontoon motion (b) versus time.

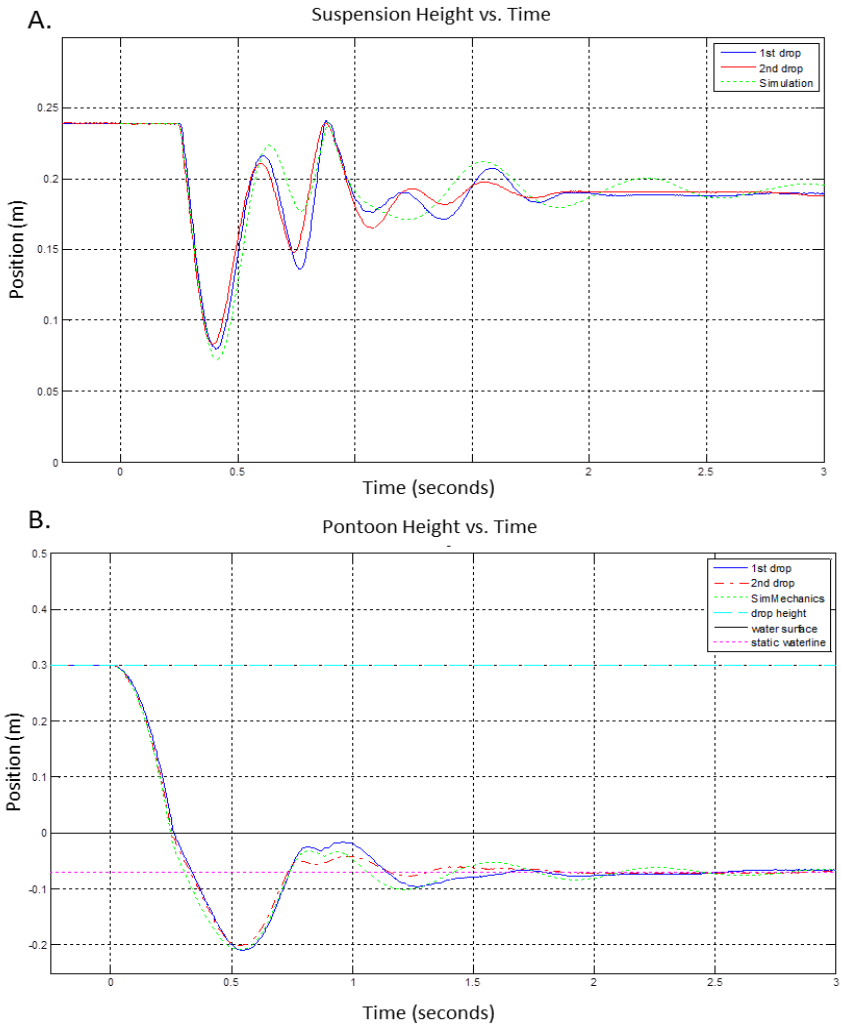

Figure 5.43 Suspension (a) and pontoon (b) displacement simulation results for the 23rd and 24th drops

The results from the simulation correlate to the data from the drop tests extremely well. To further validate the two degree of freedom model, Figure 5.44 shows the simulation's ability to track suspension displacement (a) and pontoon displacement (b) versus time for six different drops at the three highest drop heights, with and without ballast. The simulations show excellent correlation for the suspension and pontoon data for all six drop tests.

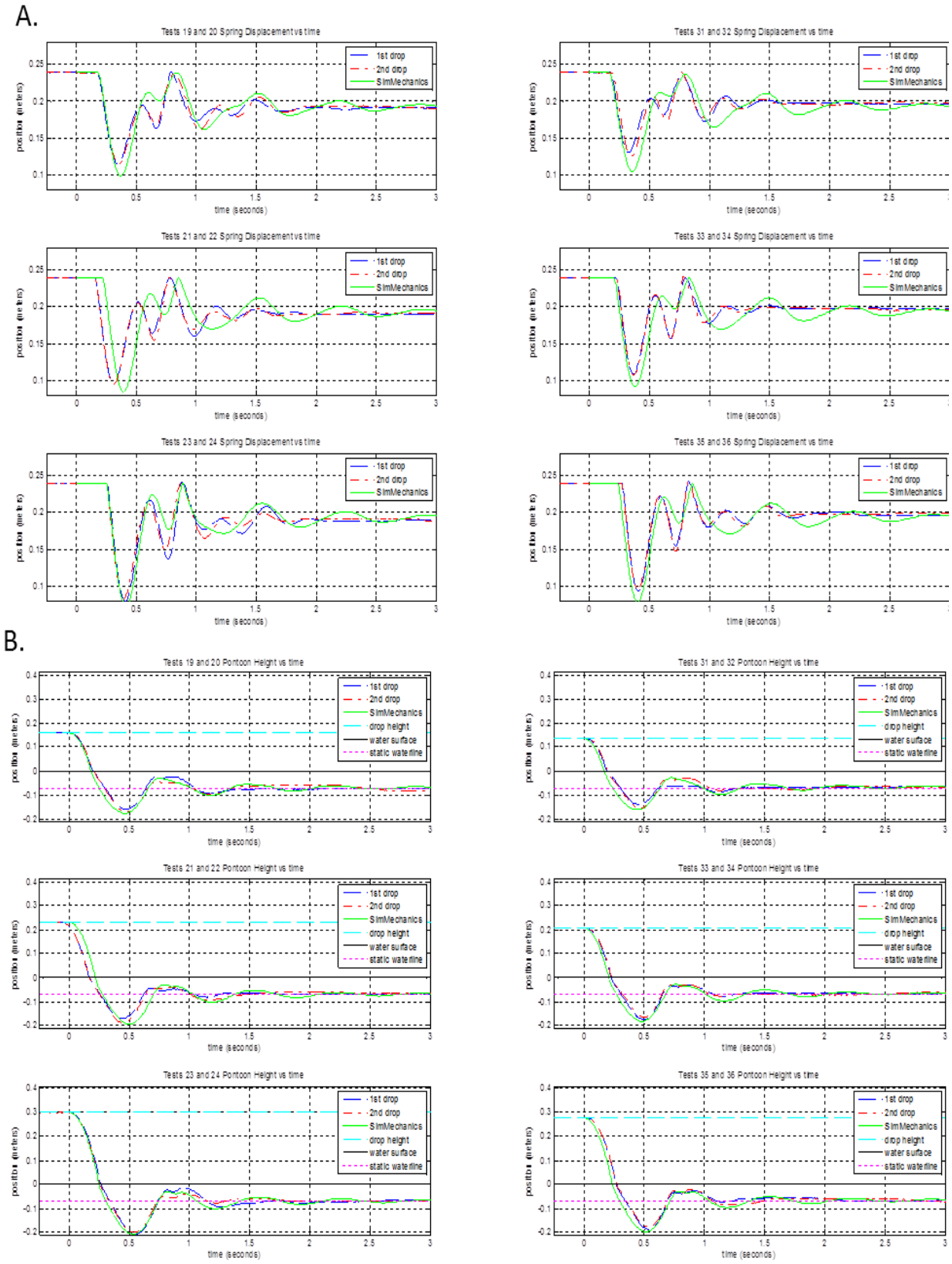

Figure 5.44 Two degree of freedom suspension (a) and pontoon (b) displacement results for 6 drops

5.10 Quarter-Boat Model Comparison with Experimental Hydrodynamics Data

With the initial model based on the Quarter-Boat test rig complete, the model is to be compared against more conventional hydrodynamic theories. In Section 5.3.4, experimental curves for computing the added mass of cylinders in the heave mode were presented. The nondimensional curves shown in Figure 5.6 can be dimensionalized with the properties of the Quarter-Boat model and compared to the added mass and damping values of the Quarter-Boat model. Figure 5.45, shows the dimensionalized added mass and damping plots; the plots were dimensionalized with the parameters listed in Table 5.6.

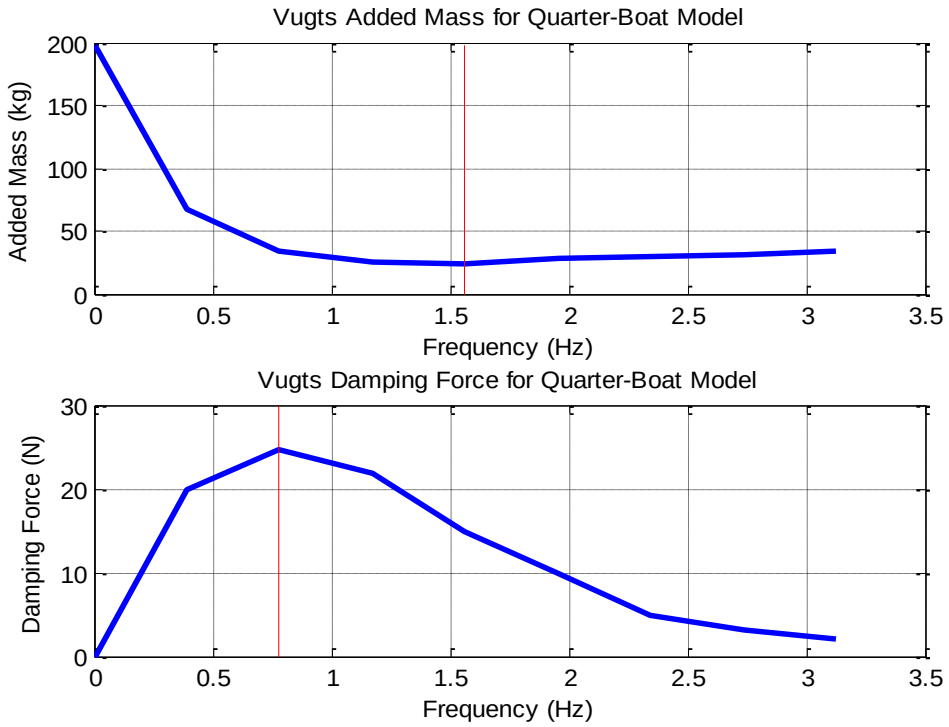

Figure 5.45 Dimensionalized Vugt's curves for added mass and damping

Table 5.6 Properties for dimensionalization of Vugt's curves

Symbol:	Parameter:	Value:	Units:
a	Added Mass Coefficient	See Figure	kg/m
b	Damping Term	See Figure	kg*s/m^2
omega	Frequency of Encounter	0 - 3.13	Hz
A	Cross Sectional Area Submerged	0.0162	m^2
B	Width at Water Line	0.2032	m
rho	Fluid Density	1000	kg/m^3
g	Acceleration Due to Gravity	9.81	m/sec^2
L	Cylinder Length	2.44	m

The curves shown in Figure 5.45, were plotted with A and B values calculated at 50% submersion. The actual A and B values change as a function of time during the drop. Figure 5.46 shows how the computed A and B values change during the drop tests; A and B are both functions of displacement, so the position of the pontoon is also shown for comparison purposes.

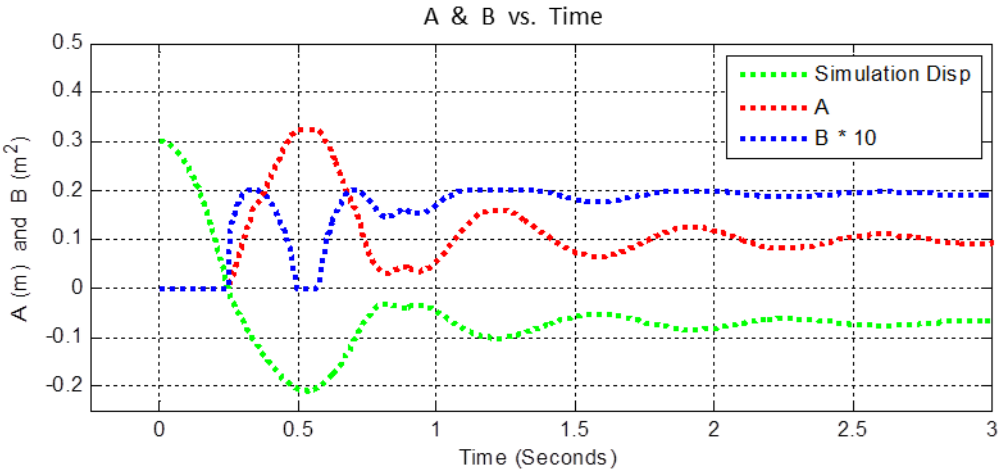

Figure 5.46 A and B values for Vugt's curves as a function time during drop tests

In Figure 5.46, when A reaches its maximum value, B is equal to zero. This is because A reaches its maximum value at displacements equal or greater than full submersion, so the width at the waterline B is nonexistent. By revisiting the nondimensional variables that were shown in Section 5.3.4, a prediction can be made as to what affect this will have on the system.

Nondimensional Variables:

$\frac{a}{\rho A} \rightarrow$ nondimensional added mass term

$\frac{b}{\rho A}\sqrt{\frac{B}{2g}} \rightarrow$ nondimensional damping term

$\omega\sqrt{\frac{B}{2g}} \rightarrow$ nondimensional frequency term

Examining the nondimensional variables, damping will be greatest when A/B is largest, which occurs at maximum submersion. The nondimensional added mass term is not a function of B, so the variable is greatest for a given frequency when the width at the waterline is at its largest value, which for a cylinder occurs at 50% submersion. This information does not line up exactly with the Quarter-Boat model as designed. To gain a better understanding of the variables within the Quarter-Boat model, the spring forces, damping force, and added mass were plotted as a function of time. The results are shown in Figure 5.47 (drop 23/48 shown).

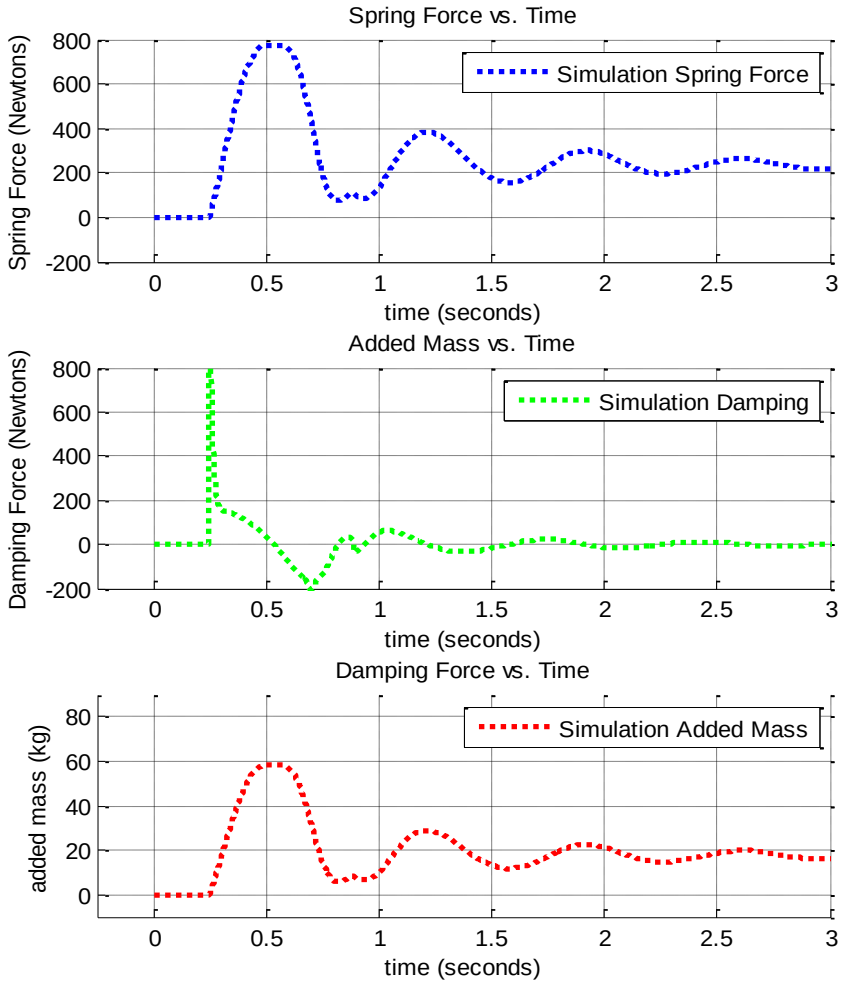

Figure 5.47 Simulation spring force, damping force, and added mass as a function of time

The plots of the added mass and damping can also be compared with the dimensionalized Vugt's curves shown in Figure 5.45. For the added mass term, the magnitudes of the two plots are similar. The added mass in the simulation peaks at ~60 kg, according to the Vugt's curves 60 kg occurs at a frequency of 0.4 Hz. It is entirely possible that the pontoon is oscillating at this frequency. The maximum added mass term also occurs at full submersion, while Figure 5.45 is shown for 50% submersion. At full submersion, 60 kg of added mass might occur at 0.75 Hz, which is also in appropriate range of the frequencies for the pontoon given the displacement plot shown in Figure 5.46.

The damping curve in Figure 5.45 does not show the same range of damping values as the damping force plot shown in Figure 5.49. In Figure 5.49, the damping plot shows an 800 N peak at impact, while the damping curve in Figure 5.49 shows a peak damping force of 25 N, occurring at 0.75 Hz. This difference can possibly be attributed to the damping levels required to

simulate an impact event; however, the damping plot also shows a minimum of -200 N (a negative value for the plot indicate a force in the opposite direction, not negative damping adding energy to the system), followed by peaks at 30 N, -40 N, and 60 N, all of which exceed the peak damping value of the Vugt's curve. Further investigation is need to determine what other factors may be effecting the poor correlation between the damping values.

5.11 Review of Other Methods of Time Domain Hydrodynamics

For the application to WAM-Vs, the Quarter-Boat modeling method is advantageous compared to more conventional hydrodynamics theories for a number of reasons:

- The codes easily integrates with multi-body dynamics software packages.
- The codes could be used as plant models for controls applications.
- The components can be visualized as a physical system, capable of being built.

The fundamental issue with applying conventional hydrodynamic theory to the Quarter-Boat model comes in the integrations of frequency-dependent added mass and damping values into the time domain. The generalized equation of motion with six degrees of freedom is shown below:

$$\sum_{k=1}^{6}\left[\left(M_{jk}+A_{jk}\right)\ddot{n}_k+B_{jk}\dot{n}_k+C_{jk}n_k\right]=F_j e^{i\omega_e t}) \quad (j=1,\ldots,6) \quad [61]$$

Where M_{jk}, A_{jk}, B_{jk}, and C_{jk} are the components of the generalized mass, added mass, damping, and restoring matrices of the ship in six axes.

The solution deals with wave-induced ship response in the frequency domain by analyzing the steady-state solution in regular waves. This involves a number of assumptions. In an irregular sea there are a number of different excitation frequencies. Because added mass and damping are frequency dependent, we cannot directly use the equation system above in the time domain; there would be a conflict in which frequency should be used in calculating the equations of motion.

A multitude of hydrodynamicists and mathematicians have presented analytical and numerical solutions to the issue of applying classical hydrodynamic theories in the time domain. The number of relevant works is too great to be covered as part of this dissertation; the following section highlights a few key works regarding time domain hydrodynamic computations. The section presents three theories covering: the linearized time domain response, the transient response for slamming events, and computations in the frequency domain. It is by no means a complete representation of the available literature.

5.11.1 The Impulse Response Function and Ship Motions

The principle theory on time domain ship hydrodynamics was presented by W.E. Cummins in 1962, in the paper: "The Impulse Response Function and Ship Motions" [62]. According to Cummins, there are two distinct time periods regarding research on seakeeping: the classical period, and the modern or statistical period. Cummins uses the analogy of shoe that doesn't fit right to describe the mathematical model of a ship's response as a system of second order differential equations. The poor fit is due to the frequency-dependent coefficients used to make the mathematical models fit the physical models. When a well-defined frequency is not present, the mathematical model becomes almost meaningless [62]. Cummins presents a method for determining the equations of motion for an oscillating ship with coefficients in the equations that are independent of frequency; the parameters required for the model are also separately determinable. Cummins proposes the use of an impulse response function for determining the response to irregular waves, stating that the reason for the limited application of impulses to studying to ship motions is that "waves look sinusoidal."

5.11.1.1 Impulse Response Function

Irregular excitations have magnitudes and frequencies that vary with time. A common nonperiodic vibration source is the sudden application of a large-magnitude, short-duration force known as an impulse. An impulse excitation represents one example of a shock loading; it is a force that is applied for a very short, or infinitesimal, length of time. The response of a system to an impulse is identical to the free response of the system to certain initial conditions [45]. Figure 5.48 shows an example response of a single degree of freedom system subject to an impulse.

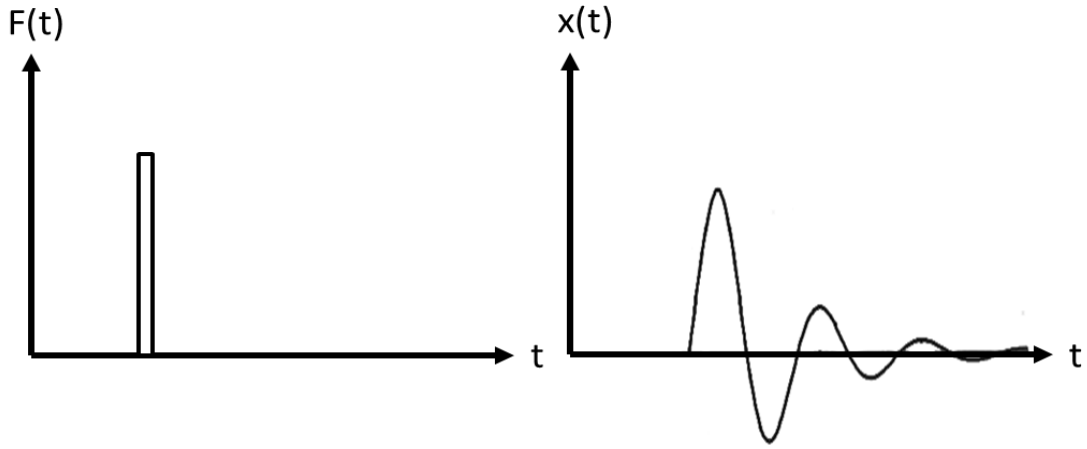

Figure 5.48 Impulse response forcing function and damped system response

5.11.1.2 Computing the Impulse Response of a Ship

A system's response to an impulse function can be represented as the response to an initial condition [45]. The Cummins equation is used to relate the equations of motion of the marine structure within the linear-time-invariant framework. A fundamental assumption is that the ship is modeled as a linear system and linear superposition applies. Linear theory assumes the motion amplitudes are small relative to the ship's cross section.

5.11.2 Parametric Model Identification

The convolution term representing the fluid memory effects associated with the dynamics of the radiation forces in the Cummins equation is inconvenient for simulation and also for analysis and design of motion control systems. Methods of approximating the model can result in a linear-time-invariant model more appropriate for controls applications. The time domain identification of radiation force models of marine structures consists of obtaining a parametric model from data of the impulse response. Finding the state-space model approximation involves the use of system identification for the convolution term, three steps are generally required [63]:

1. Determine the structure and order of the model
2. Estimate the parameters
3. Validate the model

Two specific methods have been proposed for parametric model identification [63]:

- Impulse response Least Squares (LS) fitting
- Realization Theory

5.11.3 Slamming Models

The tests run with the Quarter-Boat test rig contribute to the available hydrodynamics literature on slamming impacts. Slamming is a subsection of ship hydrodynamics involving rapidly changing loads in time and space. In terms of ship design, slamming should be analysed as a combination of hydrodynamics and structural mechanics [61]. Even for a rigid cylinder, the water impact problem is not easy to solve exactly. While during slamming events the effects of viscosity and surface tension can be considered negligible, the free surface changes very rapidly, and the impact may involve many complicated effects, such as air cavities, flow separation, and breaking waves. Most studies assume 2D vertical water entry. An example flow sketch for a cylindrical impact is shown in Figure 5.49.

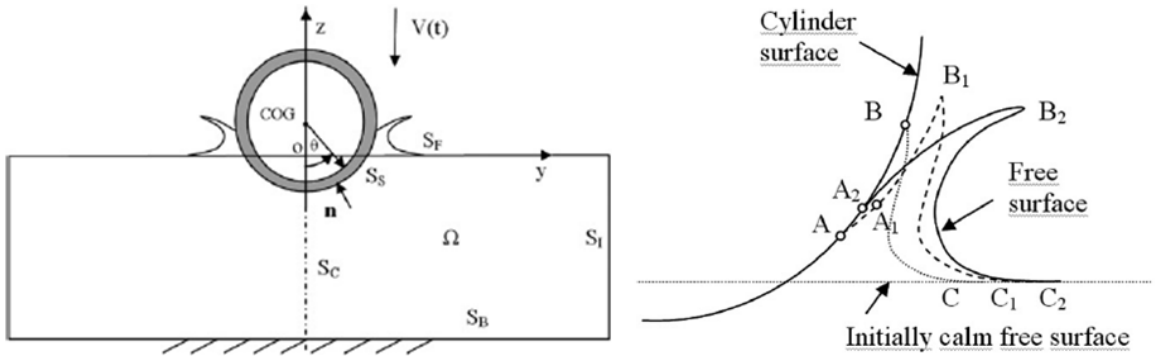

Figure 5.49 Coordinates and free surface for a slamming water impact problem [64]

Two methods used for computing the reactions of slamming on rigid bodies are [64]:

- Von Karman method
- Wagner method

Von Karman's impact model is based on momentum conservation; it neglects the water surface elevation and the added mass and impact load are underestimated, particularly for small deadrise angles (β), defined as the angle of entry of the surface at impact.

The Wagner method accounts for the local uprise of the water. Wagner's impact theory assumes small deadrise angles, but not so small that air trapping and compressibility of water play an important role (β < 3 deg) [61]. When the local angle between the water surface and the body surface is small at impact position, an air cushion may be formed between the body and the water. In this case, the air flow interacts with the water flow. Wagner's theory can be applied to arbitrarily shaped bodies as a long as the deadrise angle is sufficient not to trap air. According to Wagner's theory, the initial rate of the water's velocity change is infinite for a cylinder at impact.

For thick cylinders and low the impact velocities, the cylinders can be regarded as rigid, otherwise hydroelasticity must be considered. The cylinder on the Quarter-Boat rig could potentially be considered rigid, although the inflatable hulls on the WAM-Vs certainly could not.

5.11.4 Strip Theory

Strip Theory is not a method for computing time domain hydrodynamic coefficients. Strip Theory methods are the standard and most widely used tools for ship seakeeping computations; their widespread use merits further discussion. Strip Theory methods reduce a three dimensional problem to a set of two dimensional boundary value problems, which can be solved analytically or by panel methods [65].

Frequency domain analysis is based on the Strip Theory developed for predicting the response of ships to sea loads. Strip Theory assumes that the flow at one cross section does not affect the flow any other section, so the flow over the ship's hull can be approximated by a number of 2D sections, as shown in Figure 5.50. Strip Theory methods work under the assumption that the body is slender, the motions are relatively small in amplitude compared the ship beam or draft, and the frequency oscillation must be high [66]. Also, the fluid is considered incompressible and inviscid, and the flow is irrotational [65]. Using Strip Theory, formulas can be derived for the hydrodynamic heave force and pitch moment, from which added-mass and damping coefficients can be easily obtained [66].

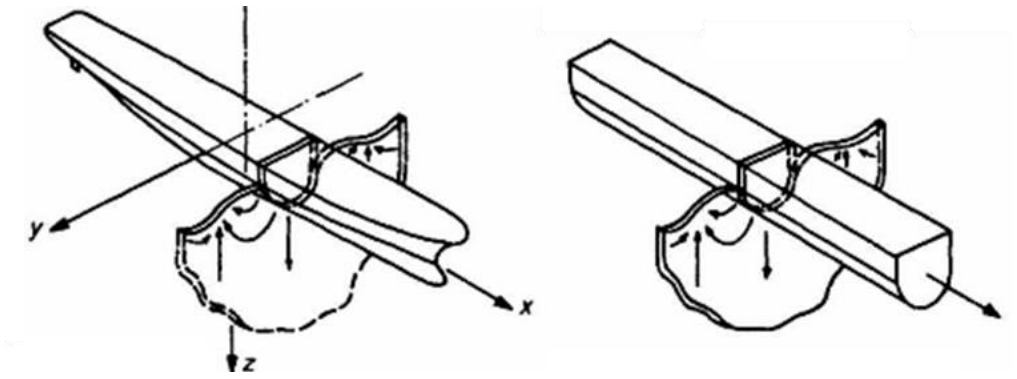

Figure 5.50 Two-dimension approximation using Strip Theory [65]

Strip Theory methods sufficiently accurate are for most problems despite their theoretical shortcomings. Strip theory can be introduced in the time domain using a lookup table for the frequency at each interval; however an assumption must be made that the frequency is known. By using Strip Theory, the problem of the water surface/ pontoon interaction can be solved by applying the equations of motion and solving within the frequency domain. Using a Fourier transform the equation of motion can be expressed as a function of the frequency:

$$\left\{-\omega^2[M+A]+i\omega[C_1+C_2]+[K+k]\right\}=\{F(\omega)\} \quad [67]$$

Where:

M =mass of the system

A = added mass (frequency dependent)

C_1 =Damping coefficient of the structure

C_2 = hydrodynamic damping coefficient (frequency dependent)

K = stiffness of the structure

f = hydrostatic stiffness (restoring force)

F(t) = forces acting on the structure

The set of algebraic solutions can be solved as a set of algebraic equations at each different frequency, so the responses can be determined. This compares favorably with the same second order different equation in the time domain, shown below, particularly when the equations for motion are being computed for six degrees of freedom:

$$\left\{\left[M+A\right]\ddot{X}+i\omega[C_1+C_2]\dot{X}+\left[K+k\right]X\right\}=\left\{F(t)\right\} \quad [67]$$

A substantial amount of experimental data exists for the hydrodynamic coefficients (A and C_2) for ships, particularly for commonly used cross sections such as the cylindrical hulls on the WAM-V and the Quarter-Boat rig. An example set of steps for frequency-domain calculations of the Quarter-Boat rig is presented below (adapted from [67]):

1. Compute the physical properties of the Quarter-Boat.
2. Compute the hydrodynamics coefficients – frequency dependent added mass and frequency dependent damping, of the pontoon.
3. Compute the hydrostatic stiffness of the pontoon.
4. Calculate suspension and other loading terms.
5. Build a finite element model of the pontoon and the suspension, as a collection of nodes, and beam elements.
6. Solve the equation of motion in the frequency domain to obtain the frequency responses, the magnitudes of which are referred to as Response Amplitude Operators (RAOs).
7. Perform a spectral analysis to obtain the maximum values of the responses with the desired probability of being exceeded.
8. Combine the responses with other loadings such as the suspension and structural loading to calculate the final response.

Some of the other most important linear methods of computing frequency-domain hydrodynamics include the following [65]:

- Unified Theory
- High-Speed Strip theory (HSST)
- Green Function Method (GFM)
- Rankine Singularity Method (RSM)
- Combined RSM – GFM approach

5.12 Linearized Quarter-Boat Model

In some instances, the nonlinear parameters of the Quarter-Boat model detailed in Sections 5.8 and 5.9 may be overly complicated for the given application. In these cases, a linearized Quarter-Boat model may be a more advantageous solution. The following section describes the linearization of the Quarter-Boat model parameters, and comparisons of the linearized model with the single degree of freedom drop tests. Figure 5.51 shows two conceptual schematics of linearized Quarter-Boat models, one with the added mass directly acting on the unsprung mass, and the other with the added mass connected to the unsprung mass through a pulley system.

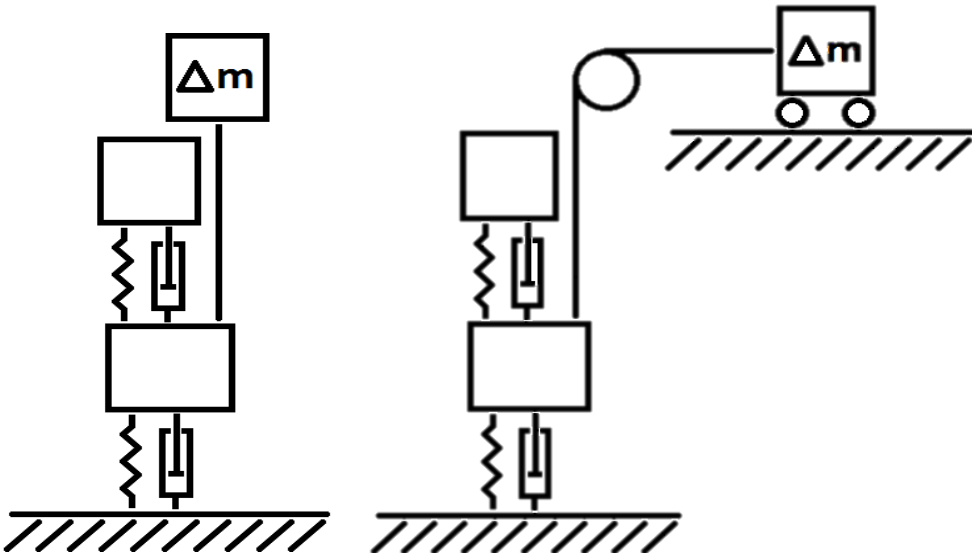

Figure 5.51 Two possible lumped parameter Quarter-Boat conceptual schematics

5.12.1.1 Unsprung Spring Rate: Linearized Quarter-Boat Model

The nonlinear hydrostatic spring force of the cylindrical pontoon with respect to displacement requires a nominal operating point to be chosen for linearization. Possible nominal operating points about which the hydrostatic spring rate could be linearized include: the static equilibrium point, 50% submersion of the pontoon, and about the average spring rate from zero to full submersion. Table 5.7 lists the spring for each of the three linearization methods.

Table 5.7 Linearized spring rate parameters

Linearization Method:	Spring Rate (N/m):
Static Equilibrium	4.54 kN/m (no ballast)
	4.73 kN/m (full ballast)
50% Submersion	4.86 kN/m
Average Spring Rate	3.82 kN/m

Linearizing about the static equilibrium will provide a spring rate closest to the spring rate of the nonlinear Quarter-Boat model (for small displacements); however, the model will require updating for different loading scenarios. Linearizing about 50% submersion will provide the highest possible spring rate, which will be greater than the nonlinear spring rate for all other displacements. Linearizing about the average spring rate may under or over predict the spring rate, depending on the loading scenario and displacement. In this section, the spring will be linearized about the average spring rate, as the best approximation of the changing spring rate at a number of different displacements. Figure 5.52 shows the linearized Quarter-Boat spring force and spring rates curves.

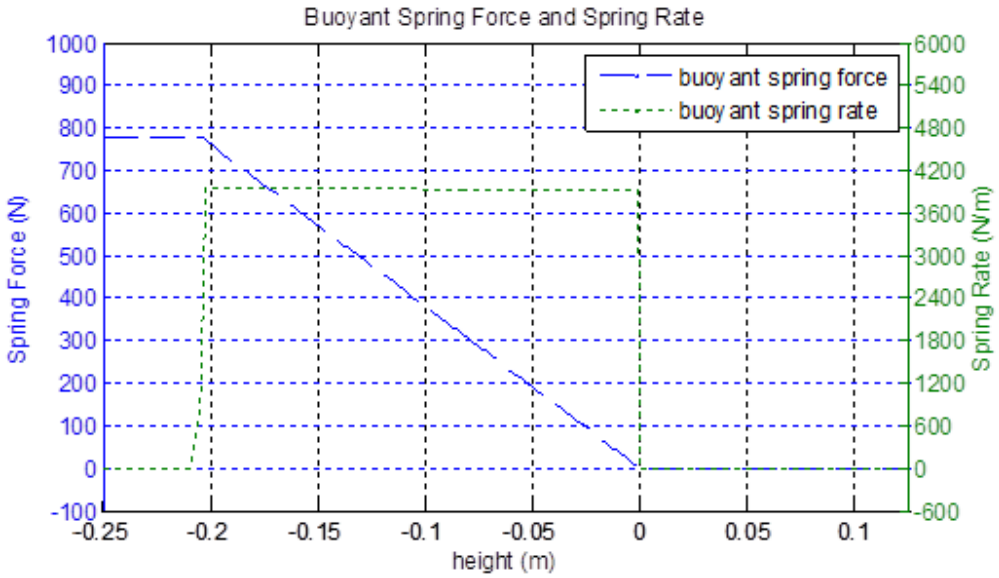

Figure 5.52 Linearized hydrostatic spring parameters

5.12.1.2 Unsprung Added Mass: Linearized Quarter-Boat Model

The two conceptual schematics shown in Figure 5.51 represent different linearized methods of modeling the added mass due to the pontoon/water surface interaction. The model shown on the left of Figure 5.51 will correctly model the pontoon coming out of the water, but will also have an impact on the static equilibrium of the system; while the model on the right of Figure 5.51 will accelerate during free fall at a rate of less than 1g, but will maintain the correct static waterline. The schematic on the right of Figure 5.51 will be applied in this section; with the model altered to contain added mass only once the pontoon has contacted the water. This makes the black diagram of the linearized model the same as the nonlinear Quarter-Boat model shown

in Figure 5.38, since the mass is still variable, in this case there are only two possible added mass values (zero and the maximum added mass value) for the linearized version of the model.

With the mass and spring rate information known, initial estimates for the natural frequency and period of oscillation of the linearized Quarter-Boat system can be calculated using the following formulas [45]:

$$\text{Natural frequency} = \omega_n = \sqrt{\frac{k}{m}} = \sqrt{\frac{3793}{24.84}} = 12.36\frac{rad}{\sec} = 1.967Hz$$

$$\text{Period} = \frac{1}{1.967\sec} = 0.508\sec$$

The calculations above are performed for a system with no added mass coefficient. Adding mass to the system with the same spring stiffness will lower the system's natural frequency by the following ratio based on a linear mass-spring-damper system:

$$\text{Change in Natural Frequency} = \Delta\omega_n = \sqrt{\frac{k}{\Delta m}} \Rightarrow 1/\Delta m \propto \Delta\omega_n^{\,2} \quad \text{(for a given k)}$$

For the linear simulations, the added mass of the model will be varied in percentage changes to the overall mass. Ten increments have been chosen that will vary the total mass of the system between 25% and 250% in 25% increments.

5.12.1.3 Unsprung Damping: Linearized Quarter-Boat Model

For the initial simulations with the linearized Quarter-Boat model, models with different damping ratios were simulated and compared with data from the Quarter-Boat test rig. The damping ratios used for the initial simulations were tested in 10% increments, calculated using the following formula for damping ratio with the mass as the combined mass of the sprung and unsprung mass and the spring constant based on linearized mass-spring-damper system parameters:

$$\text{Damping Ratio: } \xi = \frac{C}{2\sqrt{km}} \text{ [45]}$$

The results of the incremental damping sweeps were previously shown in Figure 5.33. Based on the simulations, a 25% critical damping value was chosen as the best solution. For determining the linearized added mass parameters, the damping ratio will be varied to maintain 25% critical damping across the different simulations.

5.12.1.4 Simulation Results: Linearized Quarter-Boat Model

Figure 5.53 shows a parametric sweep for different added masses at a constant damping ratio of 25% critical damping. Based on the simulations, the 40 kg and 60 kg added mass simulations showed the best correlation with the test data.

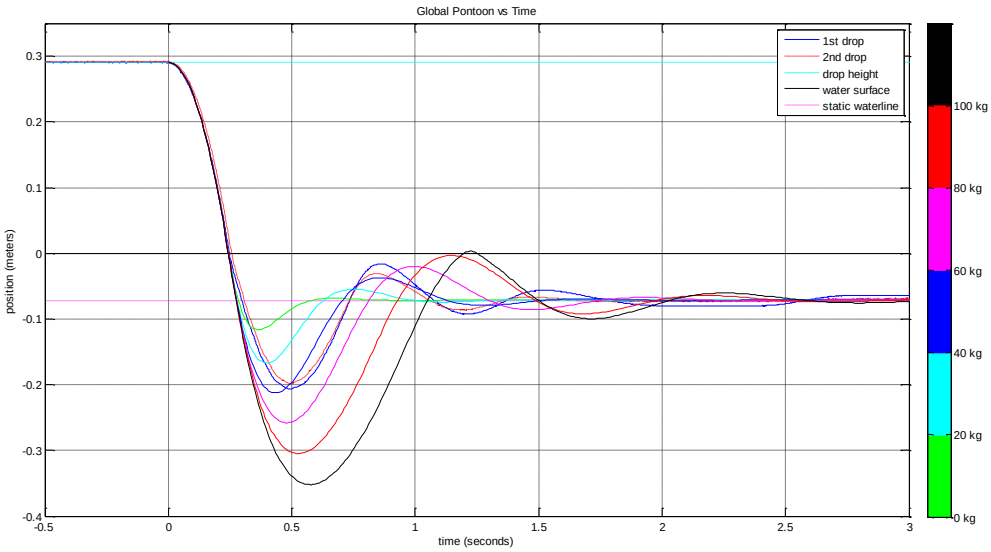

Figure 5.53 Linearized Quarter-Boat simulation results for different added mass coefficients

Figure 5.54 shows the linearized Quarter-Boat model compared with the test data. While the correlation is quite good, it is not as strong as with the nonlinear model, which was also found to correlate more consistently with the data from multiple drop tests. The model could be improved by better optimizing the chosen damping and added mass coefficients; however, for many applications the correlation results are sufficiently accurate.

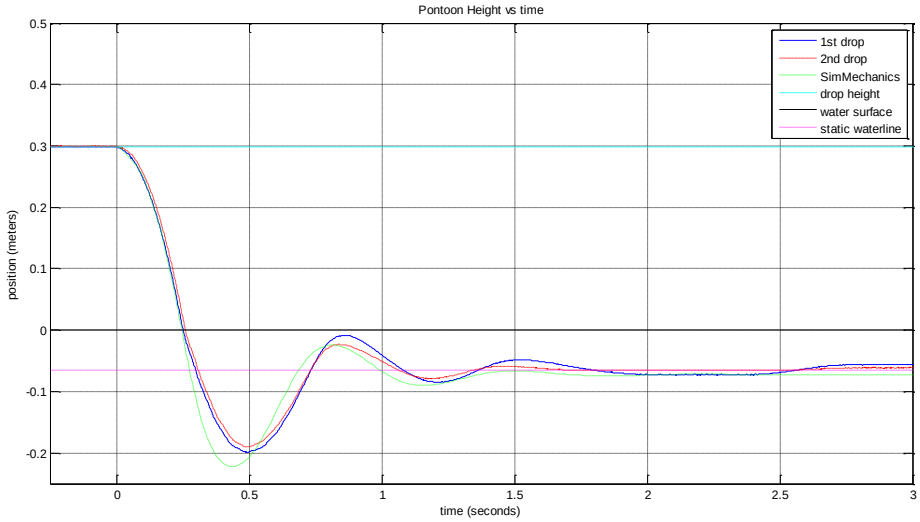

Figure 5.54 Linearized Quarter-Boat model correlation results

5.13 Conclusions and Recommendations

The results of the Quarter-Boat research will be used to improve future models of WAM-Vs by bridging the gap between the fields of multi-body dynamics, suspension design, and free surface hydrodynamics. The findings from the research and possible directions for further research are presented in this section.

5.13.1 Future Work

The data collected during the Quarter-Boat testing and the Quarter-Boat modeling results are implemented to study the suspension of the 33-ft WAM-V in Chapter 8, with the following additional required steps:

- Scaling of the data to make the Quarter-Boat model useful across a range of pontoon sizes.
- Validation of the model against other drop test data.
- Applying the scaled models to the 33-ft WAM-V.
- Developing a base-excitation model using the coefficients of the Quarter-Boat model.
- Using the Quarter-Boat models to aid in the design of an improved second generation suspension system for the 33-ft WAM-V.

Other possible areas of future research might include:

- Applying the Quarter-Boat models the 2-post rig detailed in Chapter 10.
- Using the Quarter-Boat data to as a possible validation method of the multi-body dynamics and computation fluid dynamics codes in Chapter 11.
- Incorporating the Quarter-Boat models into the controller design for advanced WAM-V suspension systems.

5.13.2 Recommendations

For future testing with the Quarter-Boat rig, a frame design with adjustable leg lengths would dramatically lower the setup time for leveling the rig on an uneven surface. If a new Quarter-Boat rig is to be designed, testing with a larger pontoon diameter is recommended. The larger diameter would be less affected by ripples in the water surface; however, the rig might also have to be tested in deeper waters, and the rig might become too heavy to lift manually. Testing of other hull shapes on the Quarter-Boat rig is also possible; the cylindrical hull could be replaced with a wedge shape to compare with the existing literature on wedge drop tests.

Chapter 6 33-ft WAM-V Instrumentation and Testing

The following chapter details the efforts made in testing the 33-ft WAM-V prototype produced by Marine Advanced Research Inc., under ownership of Virginia Tech and the Office of Naval Research. The 33-ft WAM-V was tested in collaboration with NAVSEA at the Norfolk Naval Base in Norfolk, VA. Calm water testing was also performed at Claytor Lake in Radford, Virginia. Research related to the 33-ft WAM-V is the focal point of the remainder of this dissertation, and thus a significant effort is made to document the relevant aspects of the 33-ft WAM-V's design that are relevant to its dynamic performance.

6.1 Chapter Overview

- Section 6.1 provides an overview of the chapter.
- Section 6.2 provides a design overview of the 33-ft WAM-V.
- Section 6.3 details the original suspension design on the 33-ft WAM-V.
- Section 6.4 details the instrumentation and data acquisition setup for the 33-ft WAM-V.
- Section 6.5 discusses the testing of individual components of the WAM-V in the lab.
- Section 6.6 discusses the determination of model parameters for future WAM-V simulations.
- Section 6.7 details a second generation suspension design for the 33-ft WAM-V.
- Section 6.8 provides the conclusions and recommendations from the chapter.

6.1.1 Significant Contributions

The main purpose of this chapter is to provide the information necessary to understand the research documented in the remaining chapters of this dissertation, such as the methodology for generating model parameters that are used in Chapters 8 and 11. The background information is also necessary for the documentation of the project, which will continue beyond the time frame of this dissertation. A number of the topics discussed in this chapter are extensions of items discussed in previous chapters, such as the specific testing methodology for on-water evaluation of Wave-Adaptive Modular Vessels and the marine data acquisition system detailed in Chapter 4. Other documented items, such as the water inclining of the WAM-V, required a novel approach for applying existing standardized techniques to a new technology platform.

6.2 33-ft WAM-V Design

The 33-ft WAM-V is the third generation in the line of WAM-V prototypes to be tested and evaluated by Virginia Tech. With an unfolded overall length of 33 feet and a width of 16 feet, the new WAM-V fits in nicely between the 100-ft Proteus detailed in Chapter 3, and the 12-ft USV detailed in Chapter 4. Figure 6.1 shows the 33-ft WAM-V in operation during calm water testing at Claytor Lake in Radford, VA.

Figure 6.1 33-ft WAM-V prototype

6.2.1 33-ft WAM-V Design Concept

The design concept that led to the design and construction of the 33-ft WAM-V was that a highly stable marine platform could be created with similar architecture to the 100-ft Proteus and 12-ft USV, which would also be able to fit into a standard 8 ft x 20 ft x 8 ft ISO shipping container. In order to fit inside the container, the 33-ft WAM-V would need to be capable of folding up to reduce the size of its platform during transportation and storage. Given that its extended footprint is 33 feet by 16 feet, the 33-ft WAM-V must be able to significantly reduce both its width by folding the arches upward and inward to bring the hulls closer to the payload tray in the folded position, and its length by rotating the engine pods inward and the bows upward. The 33-ft folding design concept is shown in Figure 6.2.

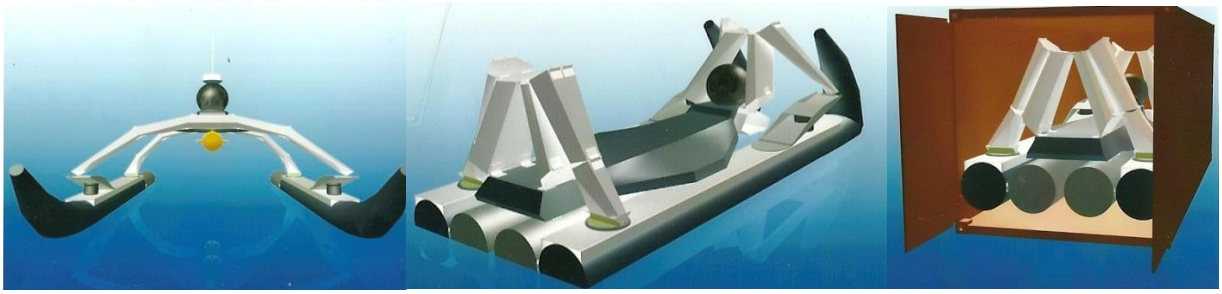

Figure 6.2 33-ft WAM-V folding design concept [43]

The folding concept was first incorporated in a passive manner on the 12-ft USV; where a series of removable cotter pins were installed between segments of the arches to allow the arches to be folded up manually. With the arches folded and the engine pods removed, the 12-ft USV could then fit inside a cargo van without being completely disassembled. The 12-ft USV in the folded position for transportation is shown in Figure 6.3.

Figure 6.3 12-ft USV in the folded position [41]

The 33-ft WAM-V takes the concept of folding arches and extends it further by incorporating hydraulic folding mechanisms into the design. The foldable arches allow the WAM-V to reduce in width from 16 feet wide to just less than 8 feet wide. The WAM-V reduces its footprint further by rotating the engines pods about a vertical hinge so that they fit between the pontoons. Deflating the front chambers of the inflatable hulls also allows the front of the hulls to be folded upwards to further reduce the overall length of the WAM-V. Figure 6.4 shows the 33-ft WAM-V at the dock in the folded and unfolded position. The inflatable bows have not been deflated for the picture in the folded position. The ability to fold up allows the WAM-V to be trailered and towed on the road, since the WAM-V fits on a standard width trailer when folded.

Figure 6.4 33-ft WAM-V in the folded and unfolded positions

6.2.2 Folding Mechanism

The WAM-V unfolds using a scissor-type mechanism composed of two 4-bar linkages with unequal arm lengths. The mechanism allows the pontoons to move both downward and outward in relation to the payload tray without the pontoons rotating throughout their travel. The front and rear arches use different variations of the same linkage design to accomplish the desired motion. The front linkage uses two struts to constrain the different components of the arches. The rear arch uses a similar mechanism to the front arch with an extra connection in place of the suspension and rocker arms. Each arch is composed of a number of individual linkages. For the purposes of standardization, each linkage component has been given a name analogous to a corresponding part on the human leg. The nomenclature used for the arch components is shown in Figure 6.5.

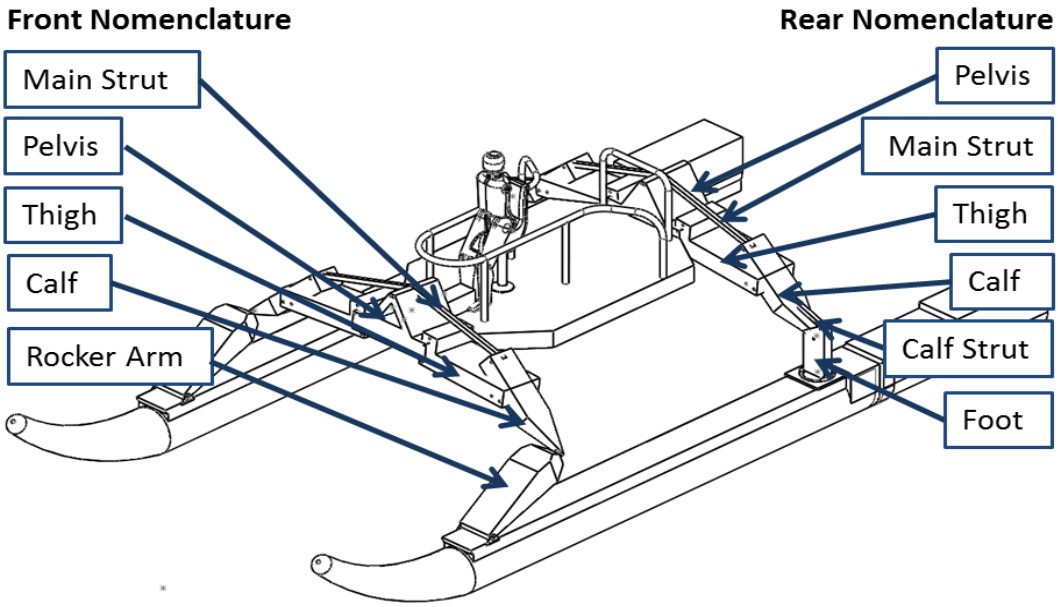

Figure 6.5 33-ft WAM-V folding mechanism nomenclature

6.2.2.1 Hydraulics System Operation

The hydraulic system for folding and unfolding the arches is composed of two hydraulic rams on each arch that move together in parallel. A Z-bar linkage between the left and right arches ensures that the two sides unfold at the same rate. Once the WAM-V reaches full width, two clamping actuators are activated to secure the arches in their final positions. With the WAM-V at full width, the engine pods are rotated backwards one at a time using the thrust from the engines by steering the jet nozzles. The engine pods are locked in position horizontally by a pin that is lowered by an electric actuator. The WAM-V unfolding on the water is shown in Figure 6.6.

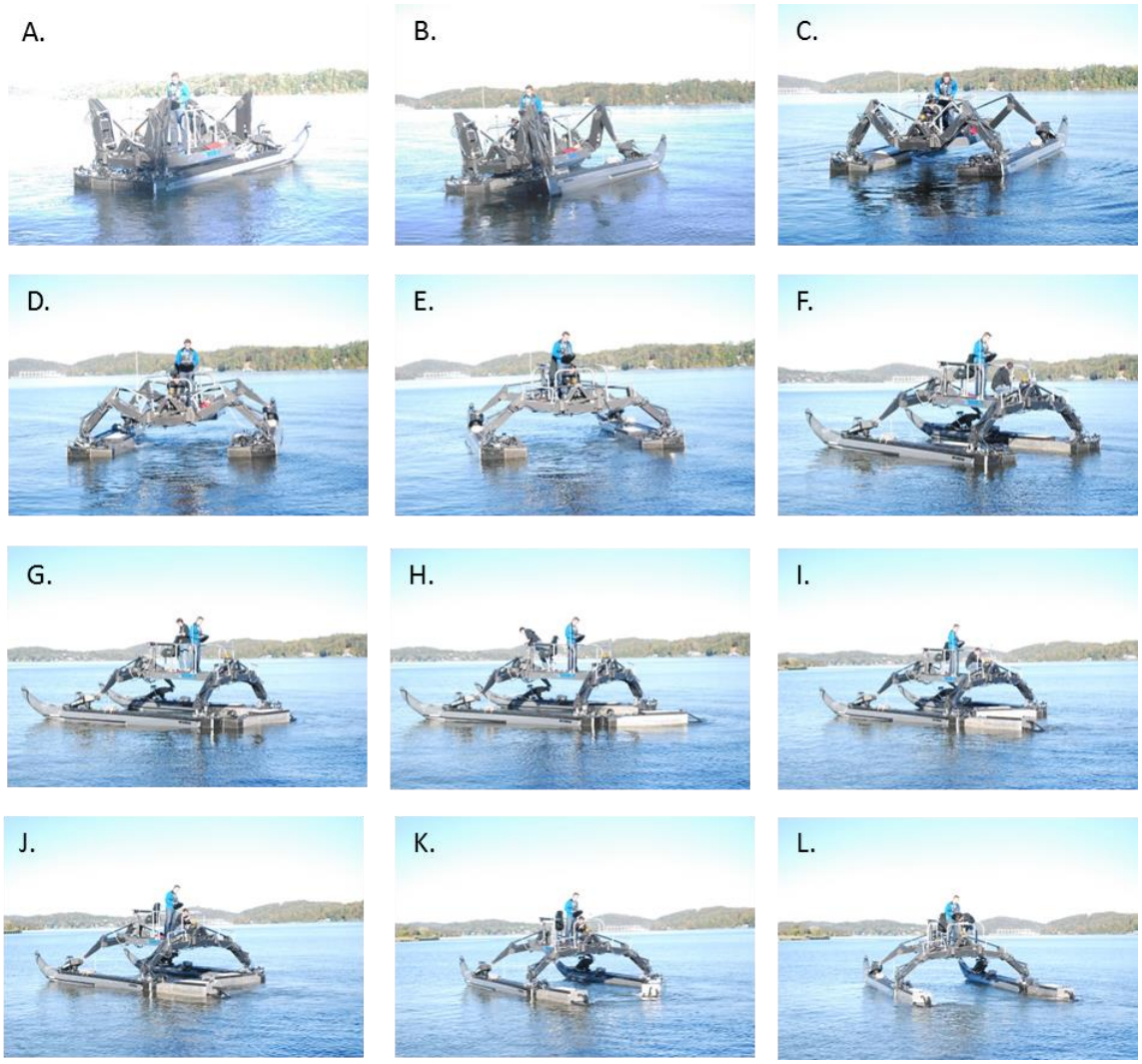

Figure 6.6 33-ft WAM-V transitioning from the folded to unfolded position

6.2.3 Pontoon Design

The maximum possible diameter of the WAM-V's pontoons was limited based on the requirement of the WAM-V to fold up to less than 8 feet in width, and the necessity to have the engine pods fold between the pontoons to meet the overall length requirement. Because of these limitations, the pontoons and engine pods have a diameter of 21 inches. Like the 12-ft USV, the 33-ft WAM-V uses a rigid ski design on top of the pontoons to connect the front suspension to the rear arch. For the 33-ft WAM-V, each ski is composed of two 8 inch x 3 inch aluminum rectangular extrusions, welded together. The skis also double as additional fuel tanks capable of holding 40 gallons of fuel each to extend the WAM-V's operating range. The pontoons on the 33-ft WAM-V also have an electronic air pump that allows for a pressure of 4 psi to be maintained in the pontoons during operation.

The limitation on the maximum pontoon diameter means that the WAM-V doesn't have as large a payload capacity as would otherwise have been possible. Nonetheless, ballast is able to be added to the WAM-V at several locations on the payload tray and to the skis for the purposes of testing the WAM-V under different loading conditions. Ballast can also be shifted from front to rear on the payload tray to change the WAM-V's weight distribution.

6.2.4 Engines and Engine Pods

The WAM-V uses two 110 hp Yamaha R1 engines removed from a Yamaha VX1100 jetski for propulsion. The two engines give the WAM-V a top speed of approximately 20 mph. The engines were chosen from a limited set of available engine types that met the 21 inch width requirement necessary to fit inside the WAM-V's engine pods.

Each engine is housed in an engine pod assembly at the rear of the WAM-V. The engine pod assemblies on the 33-ft WAM-V are different from the other WAM-V prototypes, in that there are two hinge joints between the engine pods and the skis. Like the other WAM-Vs, the first hinge is a horizontal hinge that allows the hulls to freely rotate as the WAM-V goes over waves. The hulls are free to move from approximately 5 degrees up and 15 degrees down relative to the skis. The horizontal hinge on the 33-ft WAM-V is on a connector plate that also houses a vertical hinge and locking actuator assembly. The vertical hinge is used for folding the engine pods inward for trailering purposes; it is locked out by the locking actuator when the WAM-V is on the water. The port-side engine pod and its hinge assembly are shown in Figure 6.7.

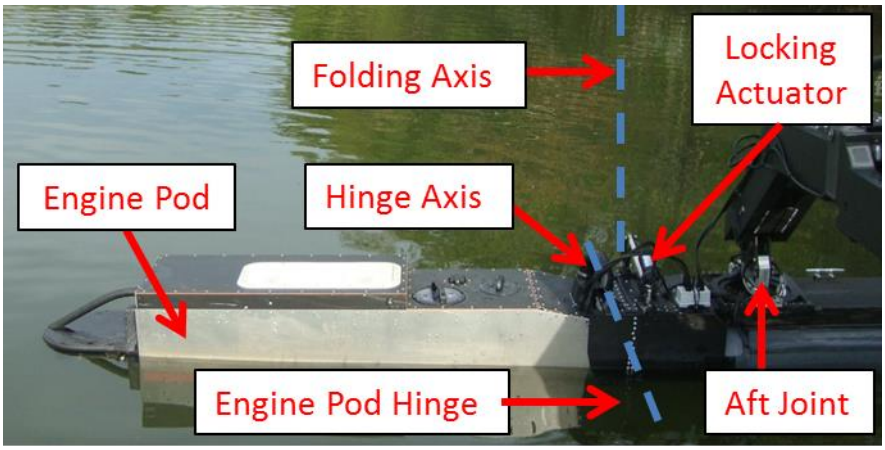

Figure 6.7 Hinged engine pod assembly

6.2.5 33-ft WAM-V Control System

The 33-ft WAM-V was originally designed for unmanned operation like the 12-ft USV. Naval and Coast Guard regulations, as well as practical considerations for visibility in rough seas made unmanned operation impractical; so the radio control system was used with the operator onboard the WAM-V. The WAM-V's control system and the functions of its different controls are shown in Figure 6.8. The operator has a total of nine channels to control with the transmitter. The channel numbers and their functions are listed in Table 6.1.

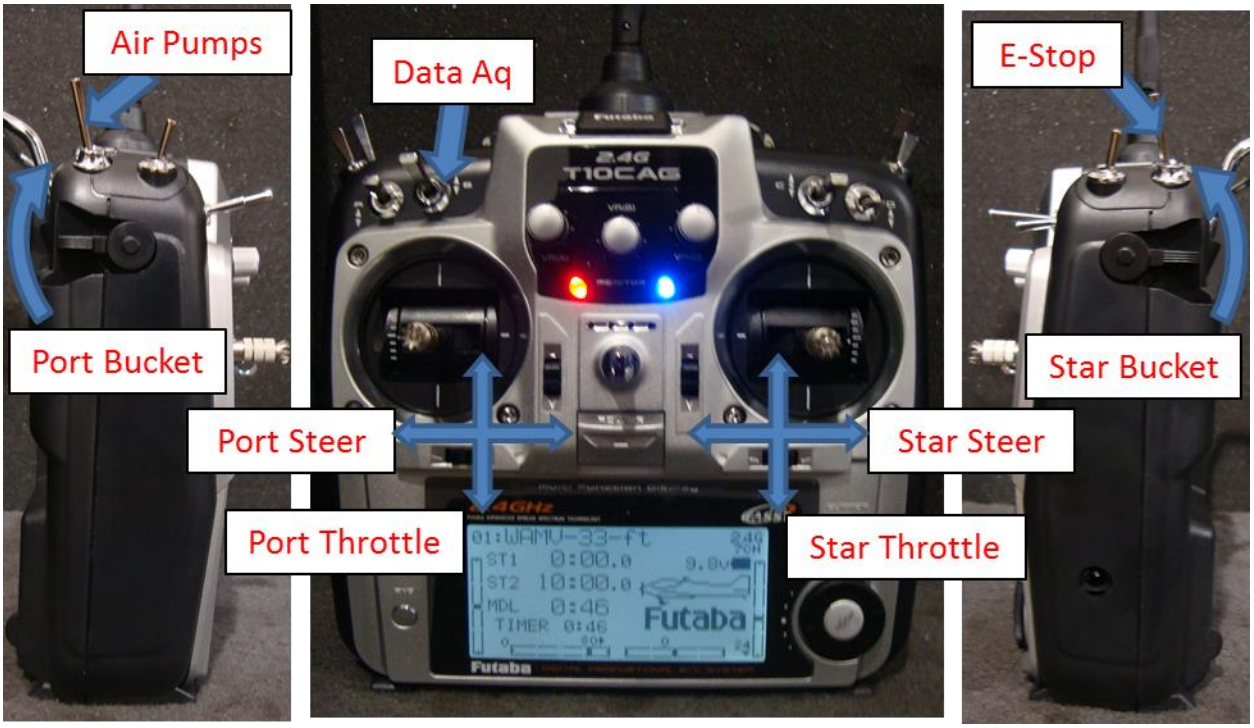

Figure 6.8 WAM-V control transmitter

Table 6.1 WAM-V operator control channel functions

Channel #	Control Function
1	Starboard Steering
2	Starboard Throttle
3	Port Throttle
4	Port Steering
5	Port Bucket
6	Starboard Bucket
7	Emergency Stop
8	Air Pumps
9	Data Acquisition Relay

Prior to rough water testing, the radio control unit was mounted in a splash-resistant enclosure that was then mounted to the operator's life vest so the operator could remove his hands from the controls without the transmitter moving. The operator and the control unit enclosure are shown in Figure 6.9.

Figure 6.9 Operator with control enclosure

In addition to the radio transmitter controls, the operator has access to an FHS radio and an emergency stop switch capable of disabling the engines. The controls for the WAM-V's folding mechanism could originally be activated remotely; however, the controls for folding and unfolding were moved to the rear of the payload tray prior to testing to prevent accidental activation. It is also noteworthy that during rough water testing the radio control units showed deficiencies that lead to motion induced interruptions. Proposed upgrades based on the author's experience as the primary operator of the 33-ft WAM-V are detailed in Chapter 12.

6.2.5.1 Safety Radio

In addition to the primary transmitter for controlling the WAM-V, a secondary radio unit was incorporated into the WAM-V's design that could be used to remotely shut off the WAM-V's engines. The transmitter for the safety radio was kept on the support craft, and a beacon was added to the rear of the WAM-V to show when the WAM-V was in range of the safety radio signal. The safety radio is not capable of piloting the WAM-V, only shutting down the engines in the event of an emergency.

6.3 33-ft WAM-V Original Suspension Design

The suspension and the folding mechanism on the 33-ft WAM-V are the two most unique features that set the WAM-V apart from conventional marine vessels. The suspension system and how its performance impacts the WAM-V's overall dynamics is the primary focus of this dissertation. The following section details the original suspension design on the 33-ft WAM-V. A second generation, improved suspension system design for the 33-ft WAM-V is detailed in Section 6.8.

6.3.1.1 Front Rocker Arm Design

The front suspension design of the 33-ft WAM-V is a rocker arm design similar to the design used on the 12-ft USV. However, for the 33-ft WAM-V the orientation of the rocker arms is flipped so the hinges of the rocker arms are now forward of the spherical joints that connect to the front arch. The rocker arms on the 33-ft WAM-V are each connected to an air spring and two viscous dampers. Figure 6.10 shows the front rocker arm assembly and its components. The original rocker arm suspension design allows for 16 inches of vertical travel of the front arch relative to the skis.

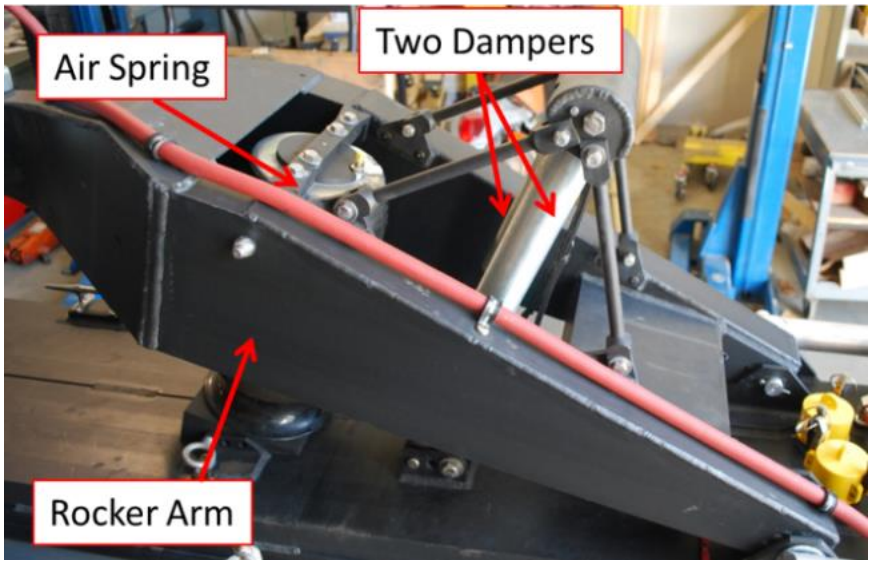

Figure 6.10 33-ft WAM-V front rocker arm assembly

Properties on the design of the 33-ft WAMV's suspension system and their effect on the WAM-V's overall dynamics are presented in many different sections of the remainder of this dissertation. Table 6.2 provides a listing on the major analysis types performed on the 33-ft WAM-V's suspension and their locations within the dissertation.

Table 6.2 Listing of 33-ft WAM-V suspension design analysis locations

Suspension Property Discussed:	Section Discussed:
Original suspension component testing	6.5
Second generation suspension design and component testing	6.7
Original suspension performance during single-wave input test	7.3
Original suspension performance during rough water testing	7.4
Second generation performance during rough water testing	7.4
Quarter-Boat simulations of the original suspension design	8.6
Quarter-Boat simulations to design the second generation suspension	8.7
Second generation performance during Sea State 1 testing	9.4
Second generation analysis for Whole-Body Vibration standards	9.5
Second generation suspension performance on 2-post rig	10.6
Original and second generation suspension comparison on 2-post rig	10.8
2-post analysis of suspension for Whole-Body Vibration standards	10.9
6-post simulations of the second generation suspension	11.3
Recommendations for a third generation suspension design	12.2

6.3.1.2 Aft Joint Design

Like the 12-ft USV, the 33-ft WAM-V has no rear suspension system. The aft joints on the 33-ft WAM-V are identical in function to the joints on the 12-ft USV; they are two degree of freedom joints that allow for rotation along the pitch and yaw axes. However, the 33-ft WAM-V's aft joints are different in their construction and the way they allow for the two degrees of freedom. Each aft joint is essentially a hinge joint located on top of a turntable. Figure 6.11 shows the design of one of the aft joints and its two rotational degrees of freedom.

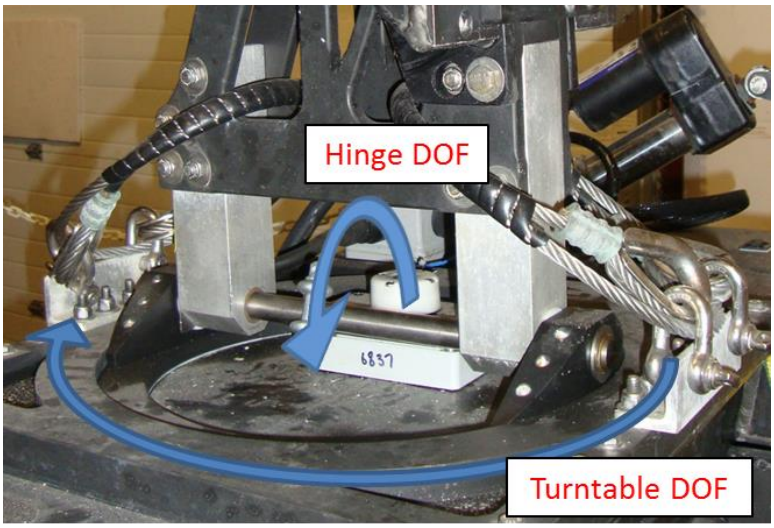

Figure 6.11 Two degree of freedom aft joint design

6.4 33-ft WAM-V Instrumentation Setup

To quantify the dynamics of the 33-ft WAM-V, a digital data acquisition system was implemented based on the data acquisition unit used for testing the 12-ft USV detailed in Chapter 4. Like the 12-ft USV, A CompactRio Data Logger was used in combination with Labview software from National Instruments to log the data. The CompactRio, data acquisition circuit boards, and a 13.2 V, 10,000 mah lithium ion battery were mounted inside a waterproof container shown in Figure 6.12, along with a 3g tri-axial accelerometer. The container was mounted to the front of the superstructure near the footrests and the emergency stop switch (E-stop). Data was recorded at 500 Hz.

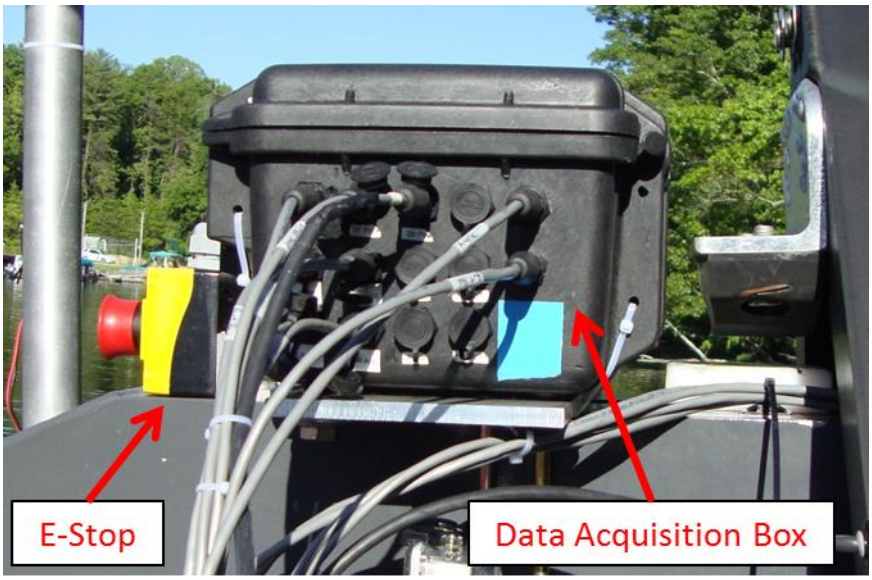

Figure 6.12 Data acquisition box mounting location

Compared to the 12-ft USV, a number of additional sensors were added for capturing different types of data on the 33-ft WAM-V for analysis. Figure 6.13 shows a diagram of the WAM-V with the locations of the sensors. Eighteen channels of data were recorded: eight channels for the single-axis accelerometers, three for the tri-axial accelerometer, four for the rotary potentiometers, one for the string potentiometer, one for the radio data trigger switch, and one for the battery voltage. The following section details the relevant information for each of the different sensor types used on the 33-ft WAM-V.

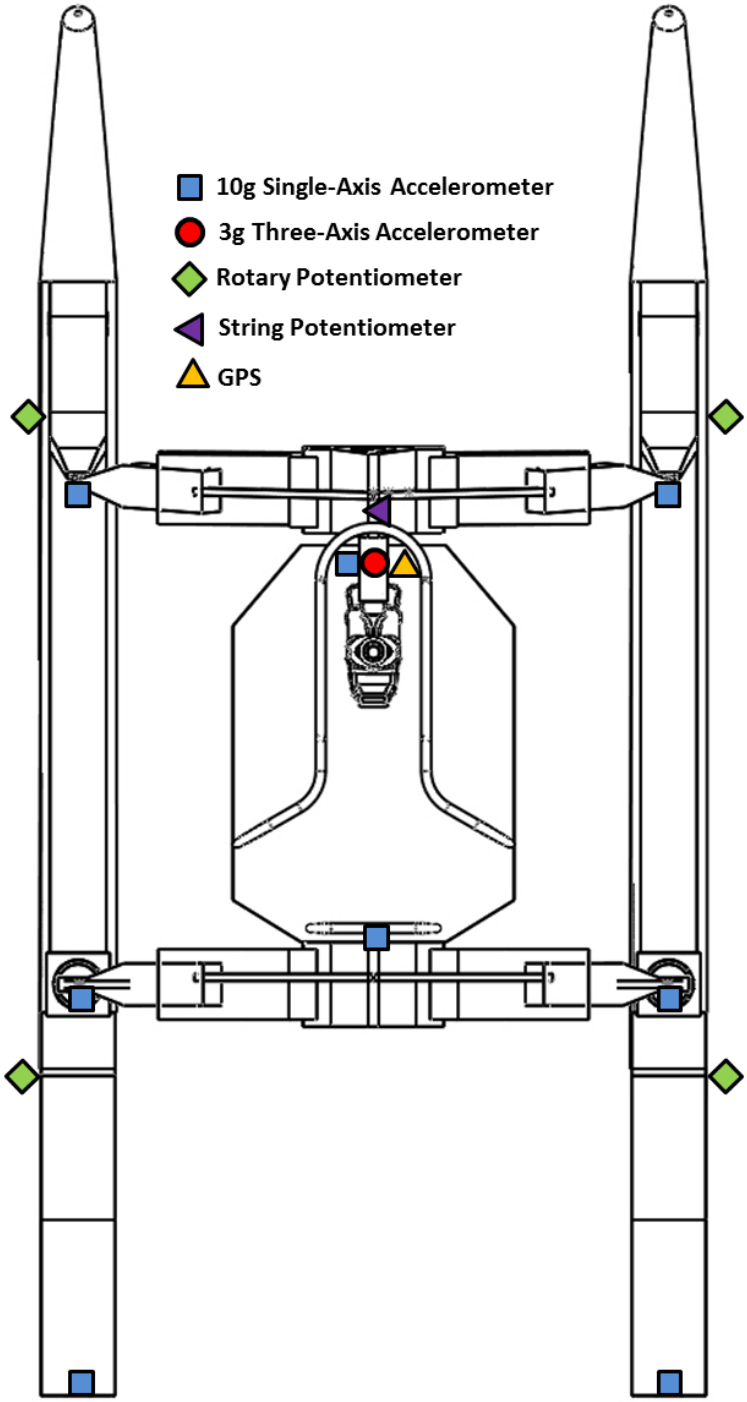

Figure 6.13 Sensor location diagram for the 33-ft WAM-V

To track the 33ft WAM-V on the water, a GPS unit was also mounted on top of the data acquisition box. The GPS unit, a Garmin 18x-5Hz, transmits data at a rate of 5 Hz. The Garmin GPS takes information such as time in Universal Coordinated Time (UTC), longitude and latitude readings in degrees and minutes, speed in knots, and heading in degrees.

6.4.1 Accelerometer Setup

A total of eight 10g vertical accelerometers were mounted at various locations on the 33-ft WAM-V. The accelerometers were originally bolted onto 1/8 inch aluminum plates; for the WAM-V's winter testing program, the accelerometers were relocated into waterproof containers to reduce their exposure to the elements. At the front of the skis, the accelerometers were mounted on top of the skis as close to the location of the spherical joints of the suspension as possible. At the rear of the skis, the accelerometers were mounted behind the aft two degree of freedom joints. The locations of the front and rear ski accelerometers are shown in Figure 6.14.

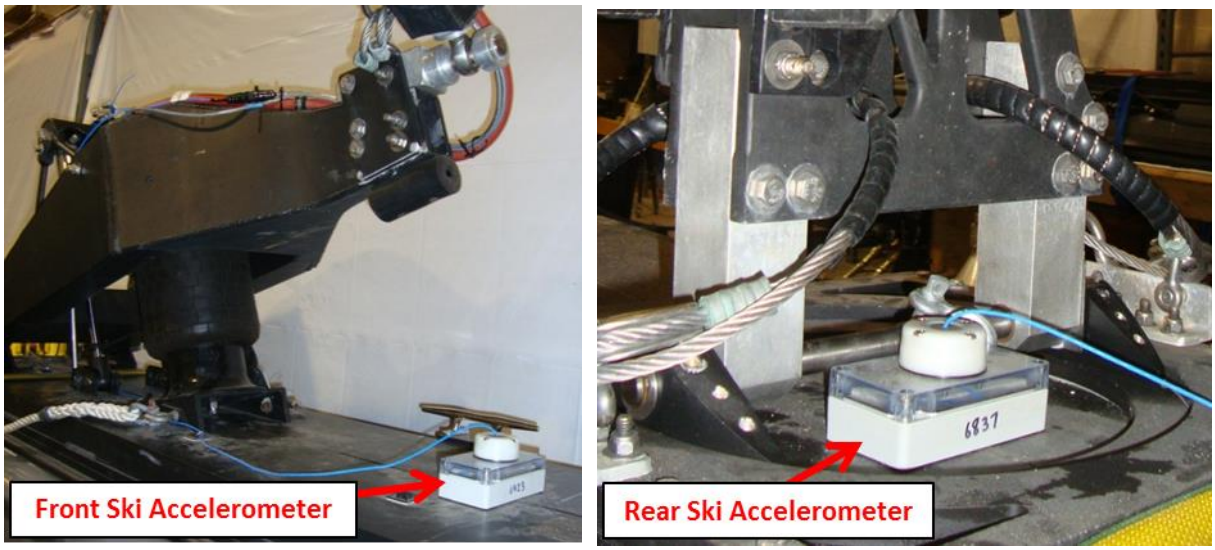

Figure 6.14 Front and rear 10g accelerometer mounting locations

Two 10g accelerometers were mounted at the rear of the engine pods to record the acceleration levels seen at the pods during testing, as well as to detect cavitation in the waterjet propulsion units. The mounting of the engine pod accelerometers is shown in Figure 6.15.

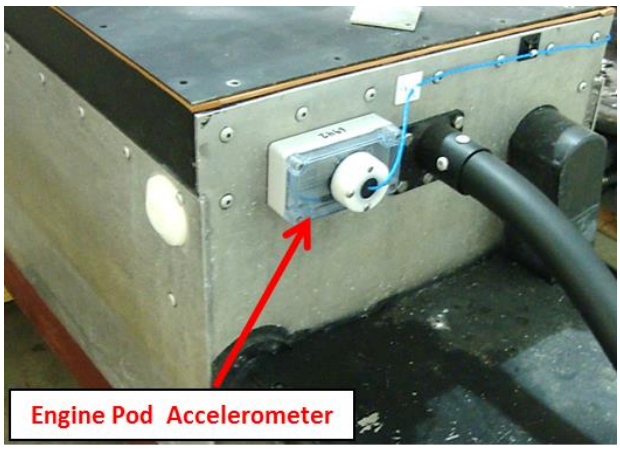

Figure 6.15 Engine pod accelerometer mounting location

Two additional 10g accelerometers were mounted onto the front and rear of the payload tray as well. The front payload accelerometer was mounted near the data acquisition box to record large events that might exceed the capacity of the 3g triaxial accelerometer located inside the box. The accelerometer at the rear of the payload tray was added to record and study how vertical accelerations are transmitted through the rear arch. The locations of the front and rear payload accelerometers are shown in Figure 6.16.

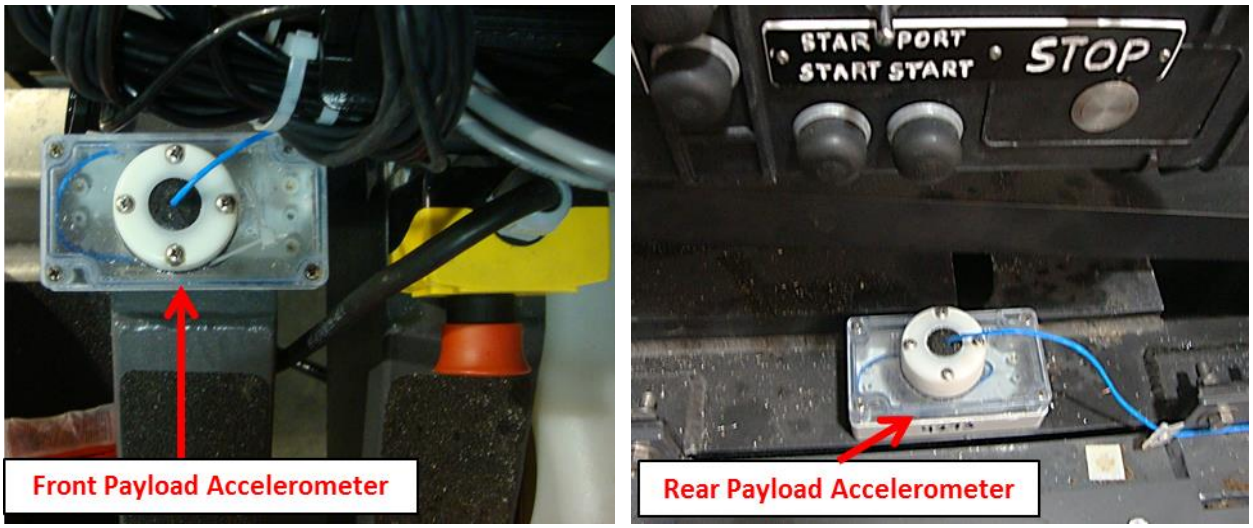

Figure 6.16 Front and rear 10g payload accelerometers

6.4.2 Potentiometer Setup

Two rotary potentiometers were mounted on 4-bar linkages to measure vertical suspension displacement. The potentiometers were mounted on top of the rocker arms; the lever arms mounted to the potentiometer shafts were free to rotate as the rocker arms moved throughout their travel. Figure 6.17 shows the mounting of one of the rotary potentiometers on the starboard rocker arm, as well as a close-up view of the 4-bar linkage.

In order to measure the rotation of the engine pods, a design similar to the 4-bar rotary potentiometer linkages for measuring the suspension's travel was used for the engine pods. Rotary potentiometers were mounted to the top of the engine pod connector assemblies. Lever arms were connected to the rotary potentiometers shafts and to the 4-bar linkages. The mounting of one of the engine pod potentiometers is shown in Figure 6.18.

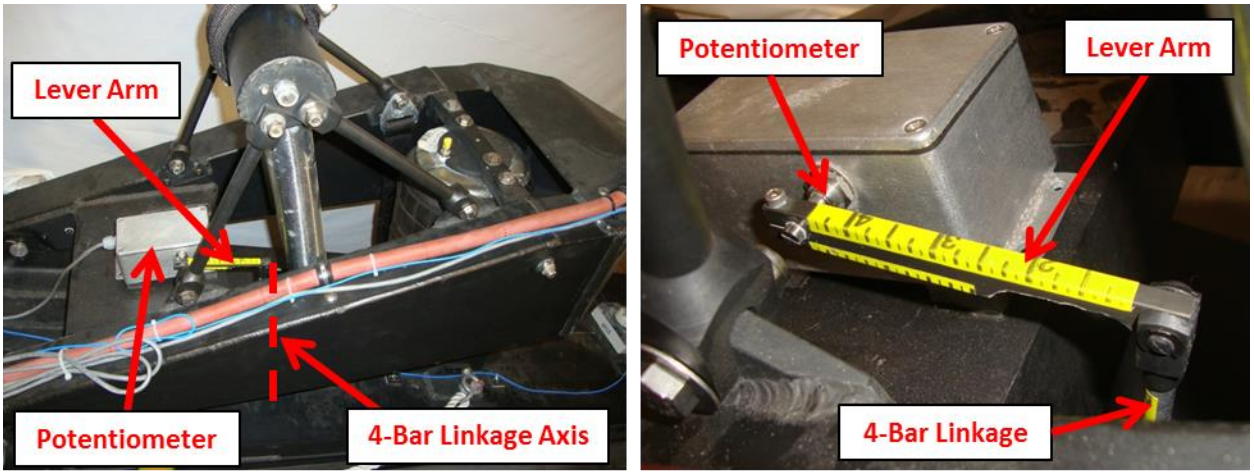

Figure 6.17 Suspension potentiometer linkage

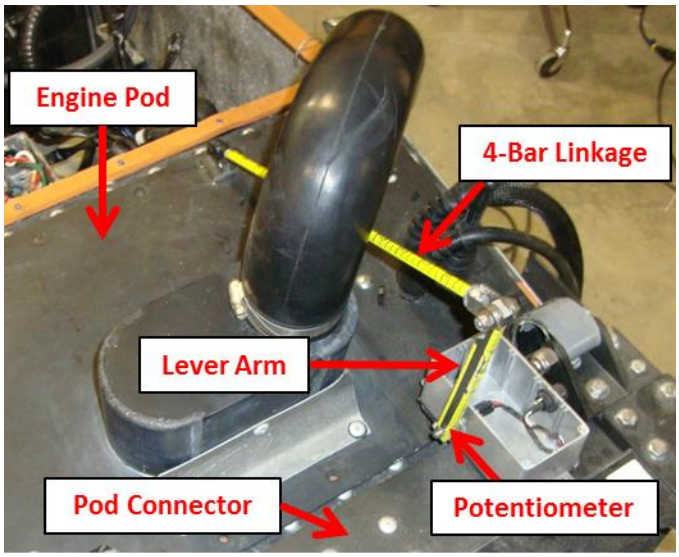

Figure 6.18 Engine pod potentiometer linkage

For measuring the rotation of the front arch, a string potentiometer was mounted between the superstructure and the front arch, similar to the instrumentation design on the 12-ft USV. As with the 12-ft USV, since the front arch connects to the superstructure via a spherical joint, some out of axis rotation will occur to allow the joints to avoid binding kinematically. This motion will also be recorded in the string potentiometer data. By mounting the string tangent to the primary axis of rotation and mounting the string potentiometer in plane with the spherical joint, unwanted measurement of the out of axis motion can be minimized in the data. Figure 6.19 shows the mounting location of the string potentiometer.

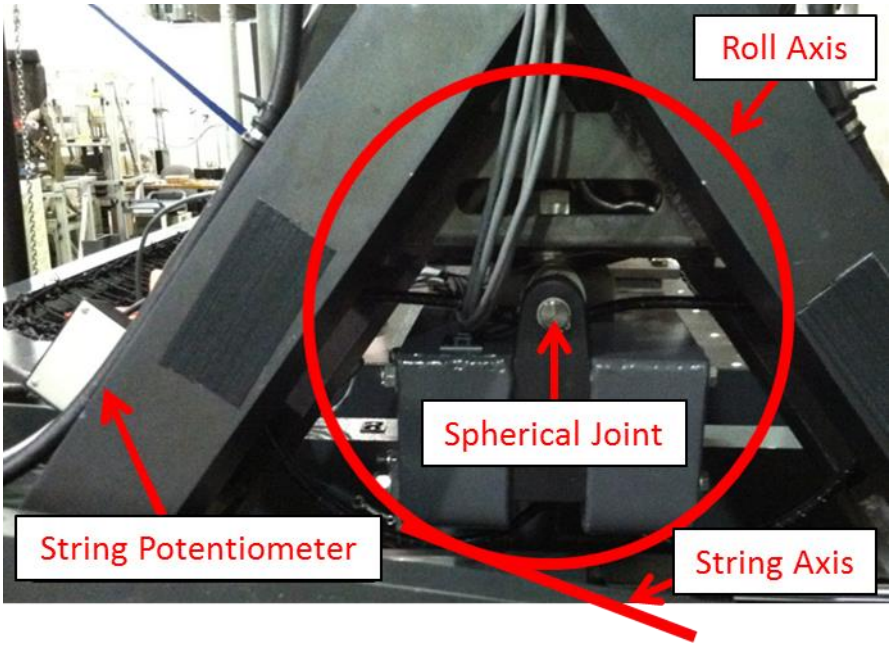

Figure 6.19 Front arch string potentiometer mounting location

6.4.3 Data Acquisition Relay Switch

A switch was added to the data acquisition unit that could be triggered from the radio control transmitter for the purpose of marking specific locations in the data on a dedicated channel. When the switch is activated, a relay in the data acquisition box is turned on and the data acquisition unit reads a change in voltage measured across a resistor. This creates a binary on/off signal that can be used to easily mark specific points in the data. An example piece of data recorded on the data acquisition switch channel is shown in Figure 6.20.

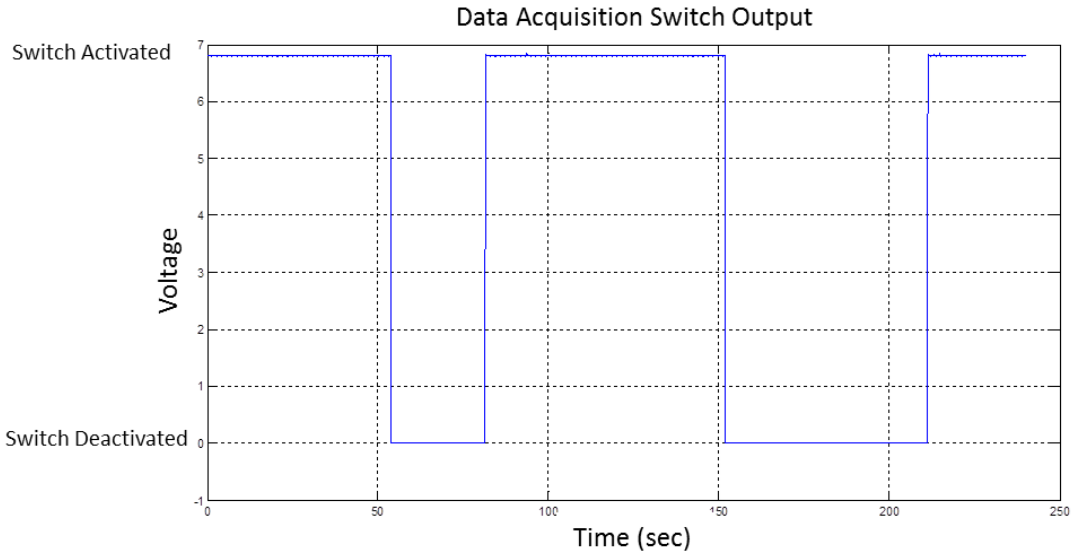

Figure 6.20 Data acquisition switch channel measured output voltage

6.4.4 Video Acquisition System

In addition to the data acquisition system, a video acquisition system with four synchronized cameras was used to capture qualitative data on the WAM-V. The positions of the four main cameras used are shown in the diagram in Figure 6.21; one camera was mounted under the payload tray facing forward, two cameras were mounted in the rear corners of the payload tray facing the port and starboard suspension systems, and one camera was mounted on a pole above the payload to view the operator and the bow of the WAM-V. The under-payload camera, pole-mounted camera, and of the one suspension cameras are shown in Figure 6.22. The cameras were synchronized and the videos were stamped with time, speed and heading recorded by GPS. A synchronized screenshot of the four cameras from testing is shown in Figure 6.23.

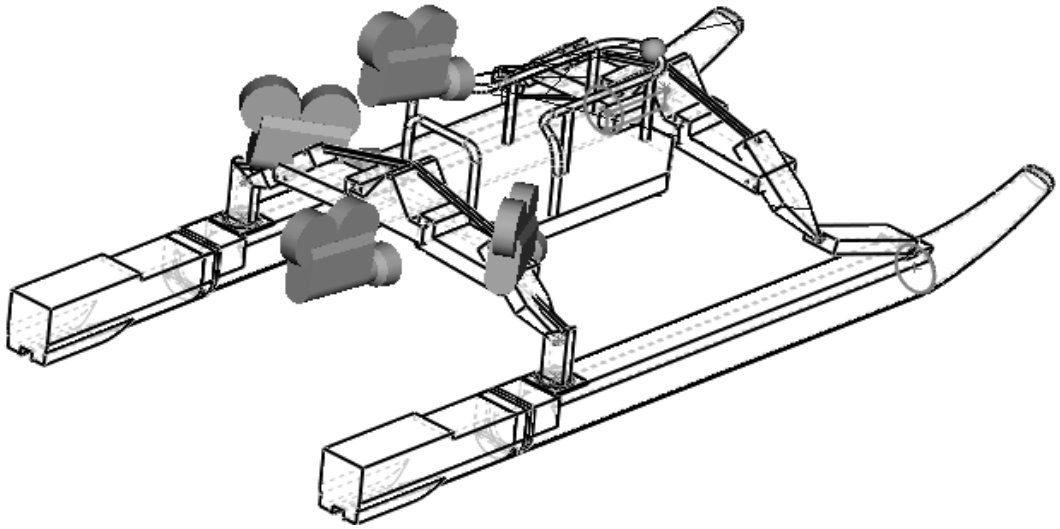

Figure 6.21 WAM-V camera locations for testing

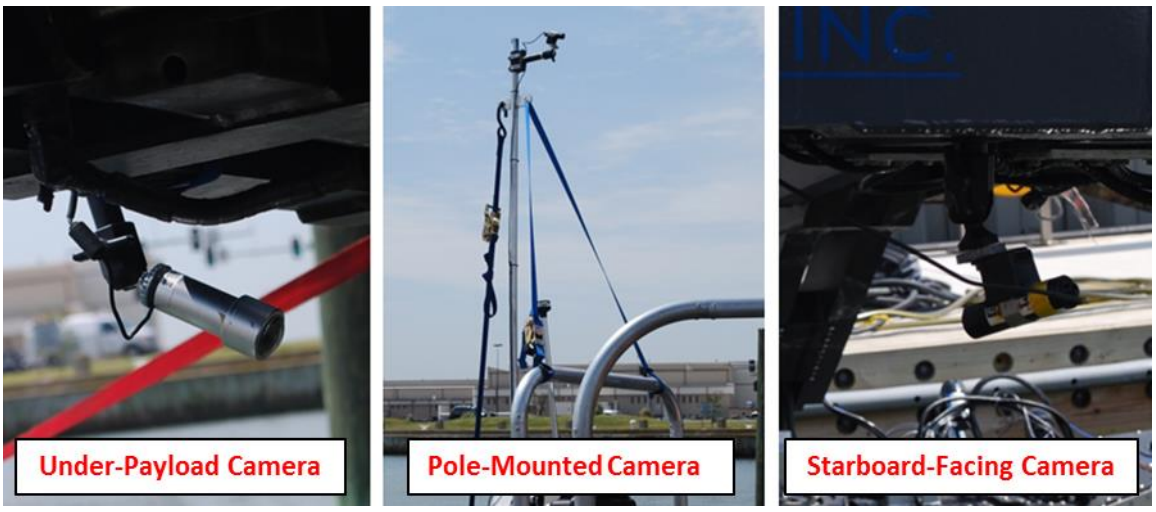

Figure 6.22 WAM-V video acquisition system cameras

Pole-Mounted Camera

Port-Facing Suspension Camera

Starboard-Facing Suspension Camera

Under-Payload Camera

Figure 6.23 Synchronized screenshots from testing

6.4.4.1 Modular Cameras

In addition to the fixed synchronized video acquisition system, two modular GoPro cameras were mounted at a variety of different locations on the WAM-V during different tests. One of the GoPro cameras being used to record the motion of the string potentiometer and front arch is shown in Figure 6.24.

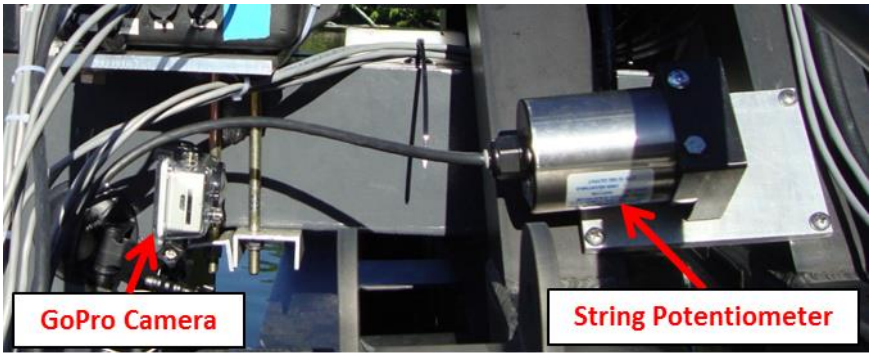

Figure 6.24 GoPro camera recorded string potentiometer and front arch motion

Some of the other views recorded on the WAM-V using the GoPro cameras include:

- Side view of suspension system
- Rearward view facing the engine pods
- Side view of engine pod potentiometer
- Forward view of bows

Additionally, for two of the tests a GoPro head camera mount was used by the operator to record the visual and audio information the operator receives during a test. The camera mounted to the operator during a day from the winter testing program is shown in Figure 6.25.

Figure 6.25 Head-mounted GoPro camera on WAM-V operator

6.4.4.2 Chase Boat Cameras

A second handheld camera was used from the chase boat during testing to capture the WAM-V's movements from a distance. Figure 6.26 shows a screenshot taken from the chase boat camera during a calm water test. Also visible in Figure 6.26 is the pole-mounted camera on the rear of the WAM-V.

Figure 6.26 Screenshot of WAM-V from chase boat camera during calm water testing

A pole-mounted camera was also mounted at the rear of the support craft to record video of the support craft during testing. The pole-mounted support craft camera is shown in Figure 6.27.

Figure 6.27 Support craft onboard pole-mounted camera

6.5 Component Testing

The second portion of this chapter provides the necessary information for understanding the testing programs for the 33-ft WAM-V. A more in depth testing and evaluation was conducted for the 33-ft WAM-V; greatly expanding upon the testing performed with the 12-ft USV. The 33-ft WAM-V could be tested in greater depth because it is under ownership of Virginia Tech and The Office of Naval Research. The following section deals with the in-lab testing of components of the 33-ft WAM-V and its data acquisition system. On-water testing and 2-post rig testing of the WAM-V are detailed in Chapters 7 and 10 respectively.

6.5.1 Damper Dynamometer Testing

The original dampers on the 33-ft WAM-V were removed from the WAM-V and tested on the Roehrig damper dynamometer to determine the properties of the dampers. The original dampers are off-road dampers manufactured by Fox Racing Shox, the model used is the 2.0 Emulsion Smooth Body Shock. Emulsion type shocks do not separate the oil from the air inside the damper. The dampers are also not adjustable, except by rebuilding and revalving the damper's shims. One of the original dampers on the dynamometer is shown in Figure 6.28.

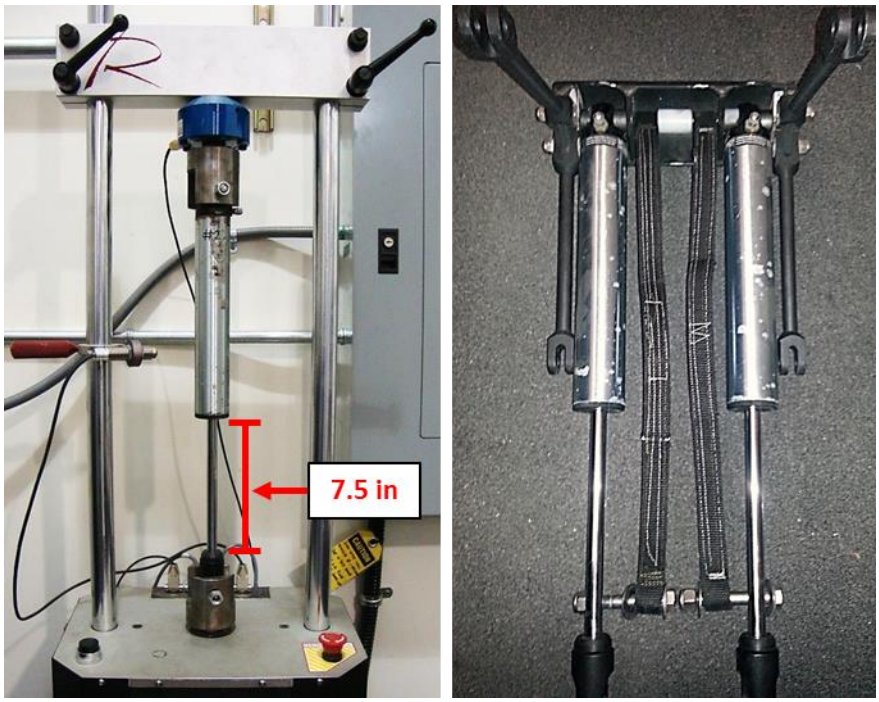

Figure 6.28 Roehrig damper dynamometer and original damper assembly

All four dampers were tested on the dynamometer to ensure that all of the dampers were built with similar levels of damping and friction to one another. A graph showing the damping curves from the tests is shown in Figure 6.29. The dampers have a maximum stroke of 7.5 inches.

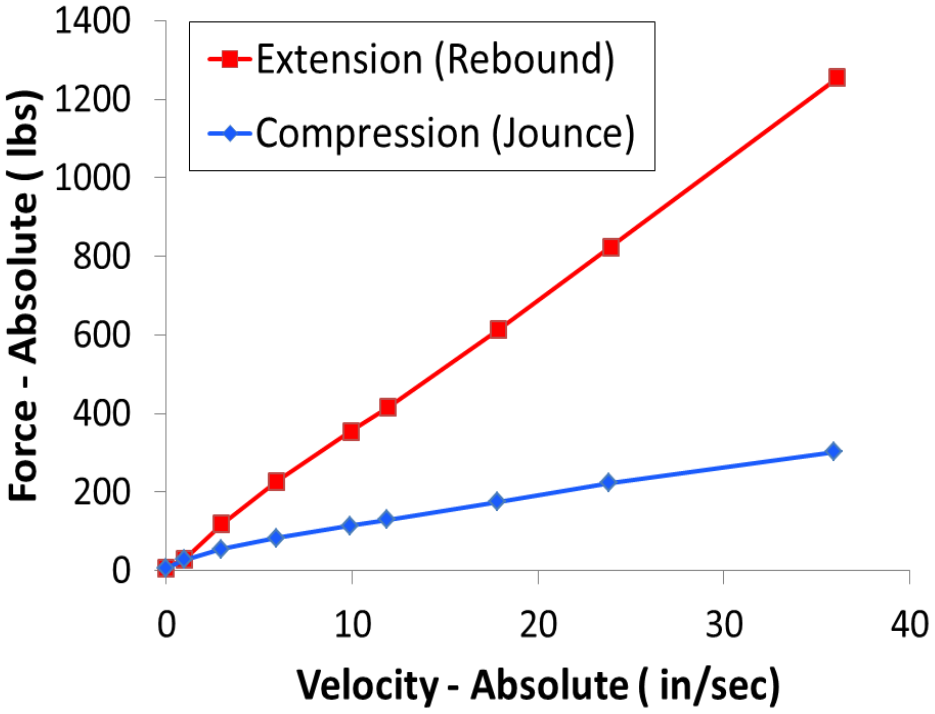

Figure 6.29 Damping force vs. velocity of the original dampers (curve for a single damper shown)

As shown in Figure 6.29, the original dampers have significantly more damping in rebound than in compression. The ratio of compression to rebound damping is approximately 3.5-4:1, depending on the velocity of the test. This is a common characteristic of most dampers used in automotive applications. Automotive dampers typical have little compression damping to allow the suspension to compress more quickly and transmit less force to the chassis when traveling over bumps. The majority of the stored energy in the suspension springs is then dissipated during the rebound phase. On rough roads, this can sometimes lead to a 'jacking down' effect, where the ride height of the suspension decreases over time as the suspension goes over a series of undulations. This only happens if the suspension cannot rebound fully after each compression before the next compression input occurs.

The plots in Figure 6.29 are shown with the static force due to the gas pressure inside the dampers removed. For these particular dampers, the gas force acting on the damper rod is not insignificant. The gas charge was measured to be approximately 45lbs for each damper. For a

vehicle with a relatively light sprung mass compared to the overall mass of the vehicle, such as the WAM-V, this can have an impact on the ride height of the vehicle. The result is detrimental to the WAM-V's dynamics since due to the characteristics of the air springs, the WAM-V already sits near the top of its travel at its static ride height. The WAM-V's air springs are analyzed in detail in the next section.

6.5.2 Air Spring Testing

The air springs on the 33-ft WAM-V are manufactured by Firestone: model number 1T14C-3. The air spring manufacture provides force versus displacement curves for their air springs; however, the curves do not consider changes in air pressure throughout the stroke. Instead the curves are generated as though the ports on the air spring are connected to a large air supply at constant pressure, as is often the case for the buses, semi-trucks, and other heavy vehicle applications for which the air springs are designed.

The air valve on the air springs is shown in Figure 6.30. On the WAM-V, the air ports are connected to Schrader valves that are only used for filling up the air springs before testing. As supplied by the manufacturer, the air springs have a ¼-NPT female threaded port designed for connecting to an external air supply. When using the air springs with the valve on the top of the spring completely closed, the manufacturer's curves underrate the spring force considerably.

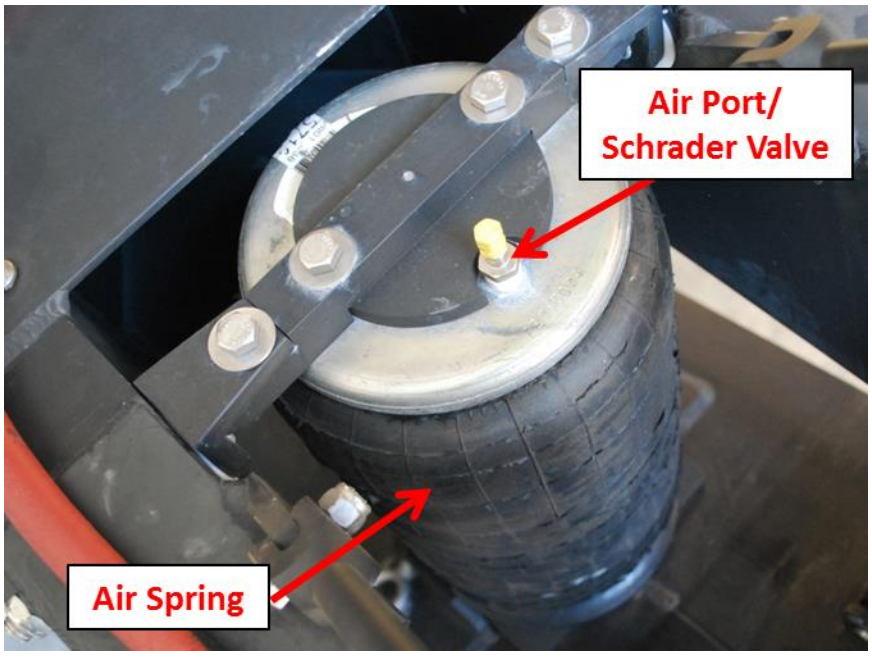

Figure 6.30 Air spring air valve location

The original manufacturer's spring curves are shown in Figure 6.31 . In order to improve the usefulness of the force versus displacement graphs provided by the air spring manufacture, a test was setup to measure the forces generated by the air spring.

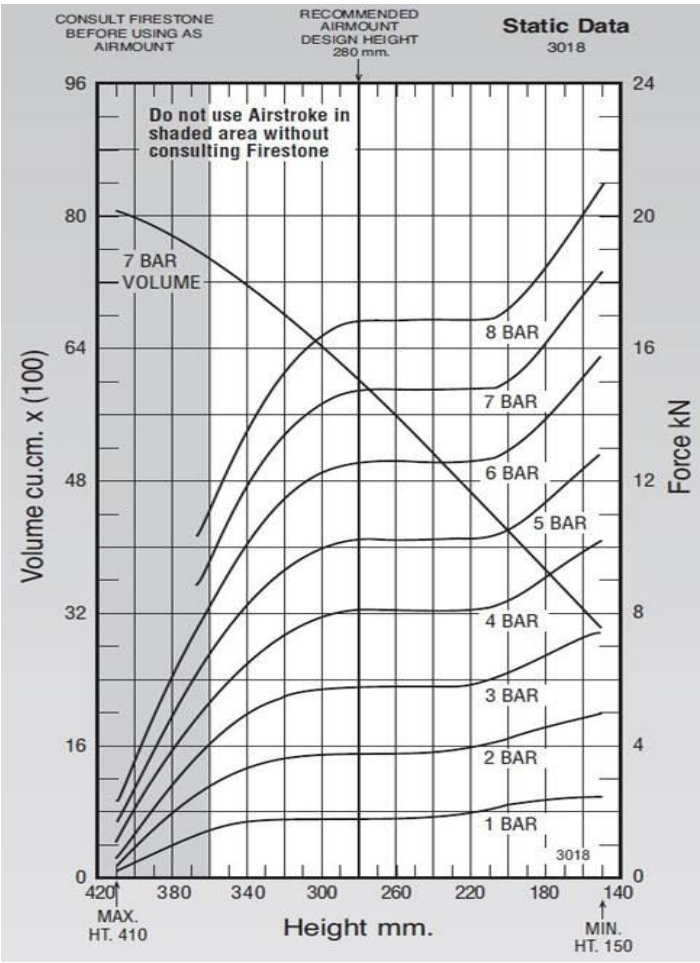

Figure 6.31 Manufacturer provided table for 33-ft WAM-V air springs [69]

6.5.2.1 Air Spring Testing Setup:

Tests were conducted using a Material Test System (MTS) load frame: MTS 810, using a 5500lb load cell to measure the air spring's force output. To control the MTS, a 458.20 Micro-Console Programmable Controller is used. The data is taken separately from the MTS via a virtual instrument in the dSPACE environment. The air spring setup on the MTS load frame and the load cell are shown in Figure 6.32.

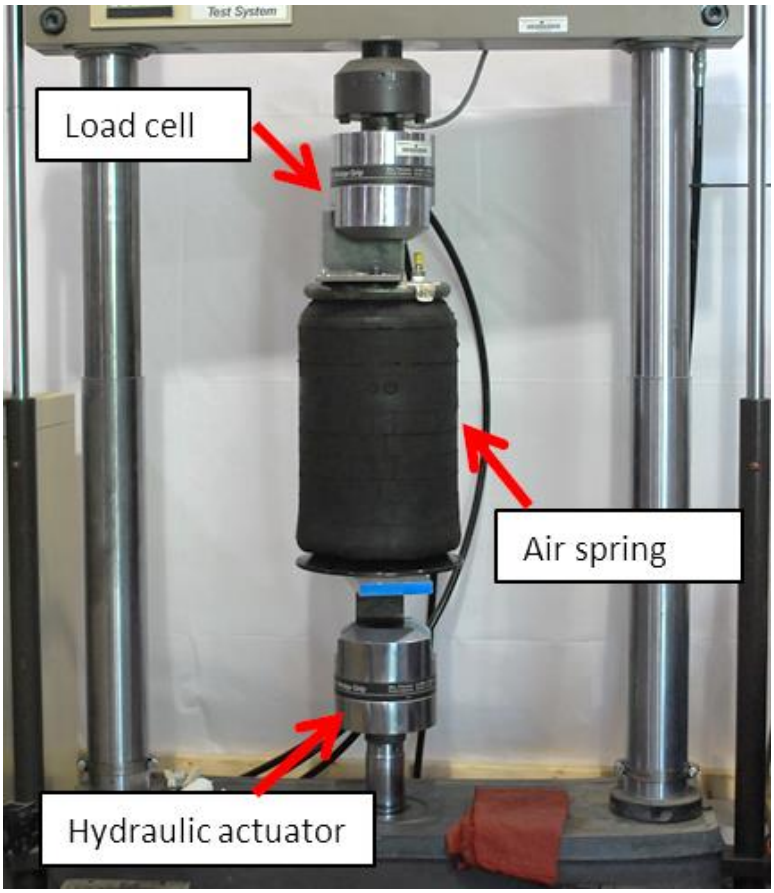

Figure 6.32 Air spring set up on MTS load testing rig

The MTS machine is capable of performing tests for up to 6 inches of travel. The air spring has approximately 10 inches of available displacement, so two tests were required to cover the air spring's entire dynamic stroke range. The MTS machine was reset when the air spring height was changed between the two tests. The tests were run with two inches of overlap between the testing heights to help correlate the data between the two tests.

6.5.2.2 Air Spring Testing Results

The first test was run at the upper limit of the air spring's travel range, moving from heights of 10 to 16 inches. Prior to running the test, the air spring was set to 25 psi at an air spring length of 15 inches. The test began at a height of 14 inches and then extended up to 16 inches before contracting down to 10 inches. The rig was then extended back up to 16 inches, and then contracted down to the original 14 inch height, ending the test. Figure 6.33 shows the force versus displacement plot for the first test shown in red, and the second test shown in blue.

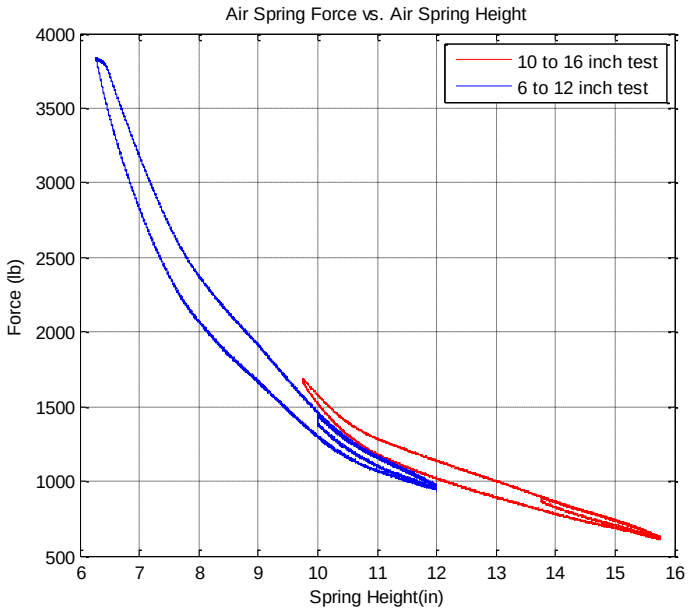

Figure 6.33 Air spring test 1 and 2 force vs. displacement curves

The curves from the first and second tests do not line up exactly. Between the two tests, the air spring had to be depressurized to change the height of the rig for the second test. When the height of the air spring was lowered for the second test, the air pressure in the spring also needed to be set to a higher pressure to maintain the same volume of air in the spring, and thus the same spring properties. To find out what that pressure should be reset to for the second test, between the two tests the air spring height was changed on the MTS in one inch increments, and the air pressure inside the spring was measured at each interval. The force was also recorded at each interval. Table 6.3 shows the changes in force and pressure at each of the spring heights. Furthermore, the force the air spring produces depends not only on the displacement but on the direction of motion of the test. This is due to hysteresis in the air springs.

Table 6.3 Pressure changes at different air spring heights

Spring Height (inches)	Pressure (psi)	Force (lbs)
10	40	1436
11	36	1167
12	31	1020
13	29	902
14	26	786
15	23.5	700
16	21.5	600

The second test was run down to the lower limit of the spring's travel, moving from heights of 6 to 12 inches. Prior to running the test, the air spring was set to 40psi with the spring length set to 10 inches. The test begins at a height of 10 inches and then extends up to 12 inches before contracting down to 6 inches. The rig was then extended back up to 12 inches, and then contracted down to the original 10 inch height, ending the test.

6.5.2.3 Suspension Modeling of Air Spring Data

For the purposes of modeling the 33-ft WAM-V's suspension, a single force versus displacement curve for the suspension is desired. Figure 6.34 shows the trend line and equation for the suspension deflection that will be used for the air spring for simulation purposes. The equation for the trendline that was generated from the two curves does not consider the hysteresis in the air springs which is dependent on the direction of motion.

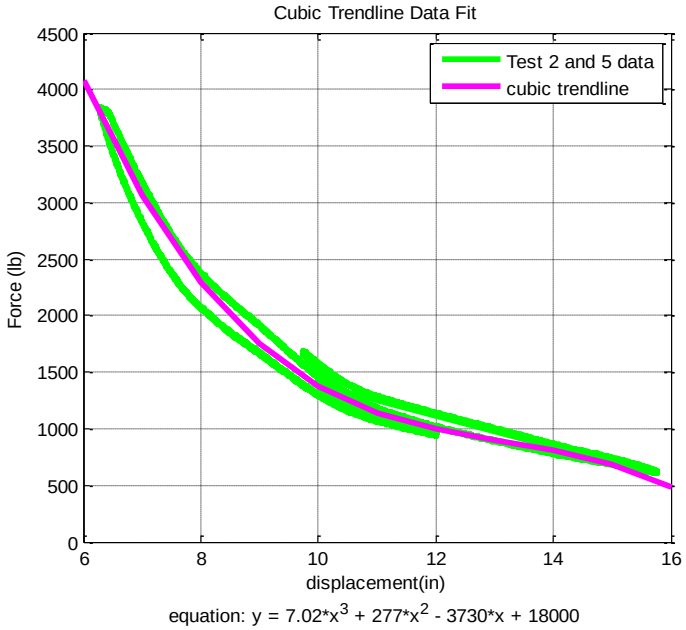

Figure 6.34 Air spring test 1 and 2 force vs. displacement with trend line and equation

With a force versus displacement curve for the air spring generated, the curve can be compared with the manufacturer's data for the air springs originally shown in Figure 6.31. Figure 6.35 shows the calculated force versus displacement curve overlaid with the manufacturer's air spring data. The spring pressure measurements taken from Table 6.3 are also included on Figure 6.35. The air spring pressures, shown with red dots, are based on the pressure curves for each bar of pressure labeled on the right side of the figure.

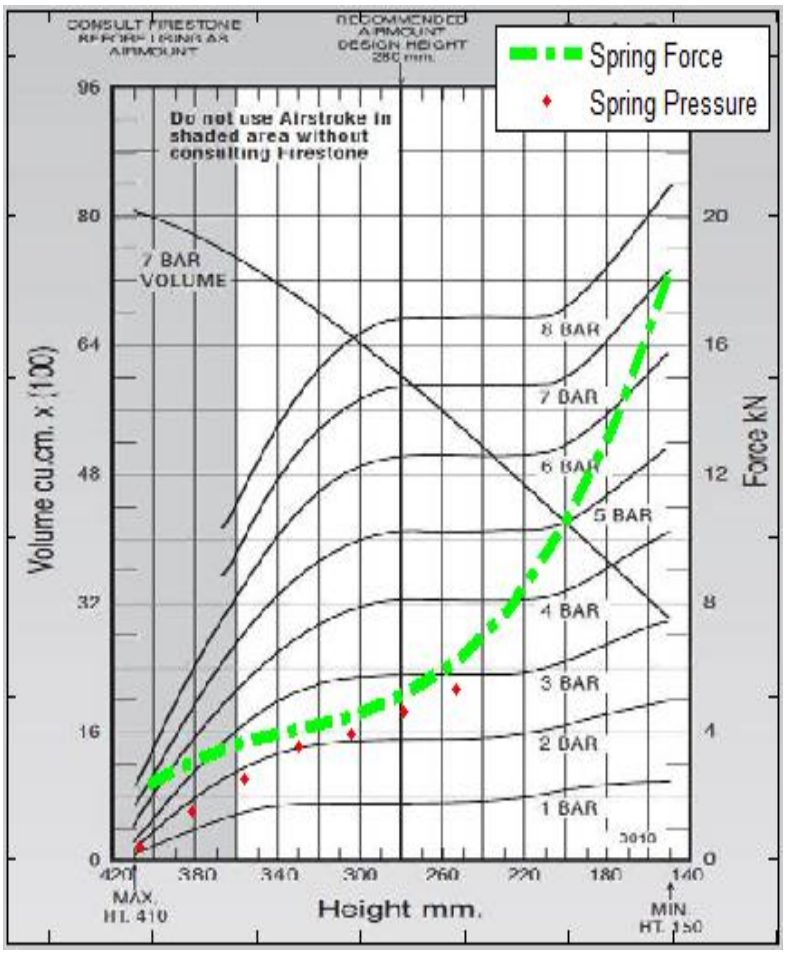

Figure 6.35 Air spring force vs. displacement plotted against manufacturer's data (modified from [69])

By taking the derivative of the equation from the force vs. displacement curve, the equivalent spring rate of the air springs can be determined. The spring rate is highly nonlinear; Figure 6.36 shows the spring rate in pounds per inch of the spring displacement throughout its stroke plotted with the spring force versus displacement curve as well. It can be seen that moving from a height of 16 to 13 inches the spring rate actually decreases, before increasing dramatically from 13 to 6 inches.

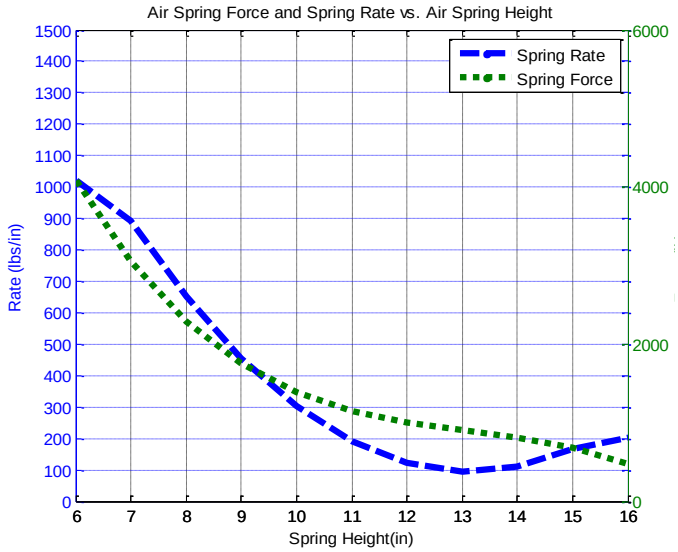

Figure 6.36 Spring force vs. spring rate

The air springs operate with an equivalent motion ratio of 1.82:1 to the spherical joint on the rocker arm that connects to the front arch. The air springs were replaced on the second generation suspension with an equivalent coilover spring acting at the location of the original dampers. The dampers operate with a motion ratio of 2.81:1 to the spherical joint, so the equivalent spring rate at the dampers is different than at the air spring. This is important for comparing the air springs with possible coilover spring rates. Figure 6.37 shows a graph of the equivalent spring force vs. spring rate to be used for choosing a coilover spring for the suspension. Figure 6.38 shows the spring rate translated to the spherical joint, with the area of the suspension bump stops shown in red.

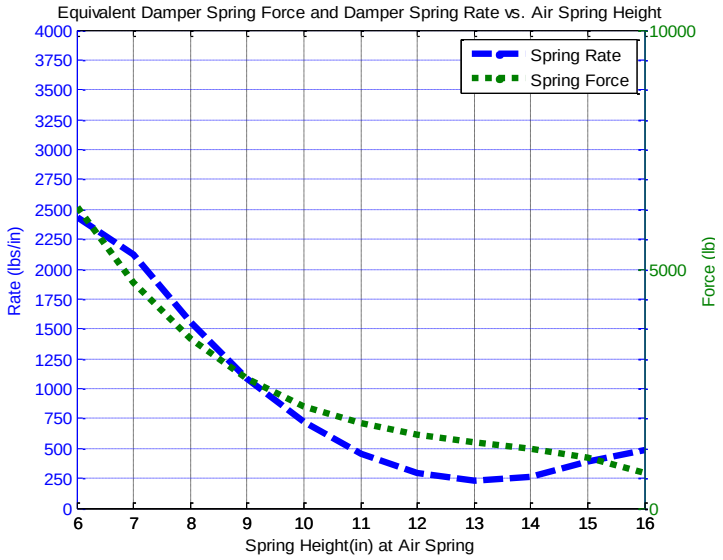

Figure 6.37 Equivalent spring force vs. spring rate at the damper location

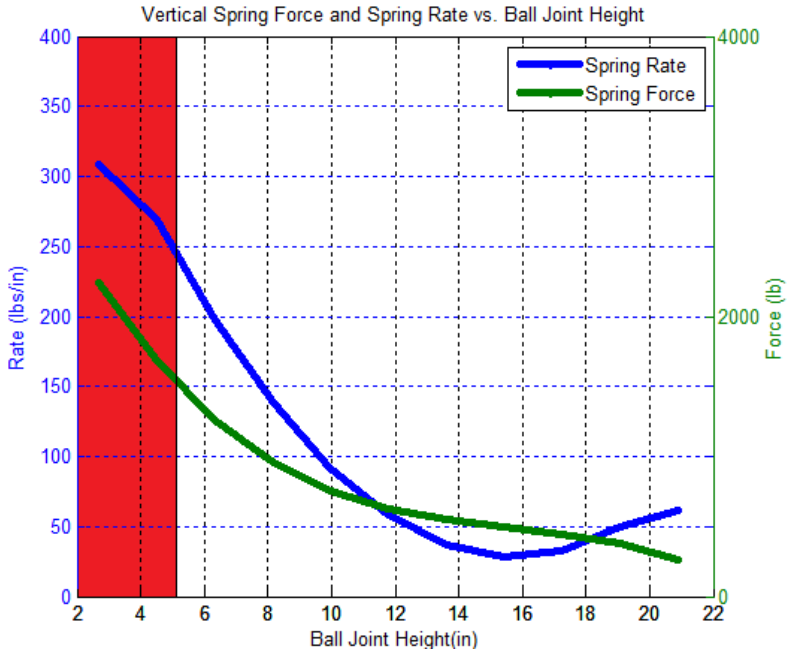

Figure 6.38 Equivalent spring force vs. spring rate at the spherical joint

6.5.3 Sensor Calibration

Each of the sensors detailed in Section 6.4 needs to be calibrated for use of the WAM-V. For the accelerometers, the calibration can be done separately, without the sensors installed on the WAM-V. However, for the potentiometers there is a nonlinear correlation between potentiometer motion and the desired parameter being measured. Figure 6.39 shows the calibration for the port and starboard suspension potentiometers, along with a fitted third order equation for data analysis of the dynamics of the suspension system.

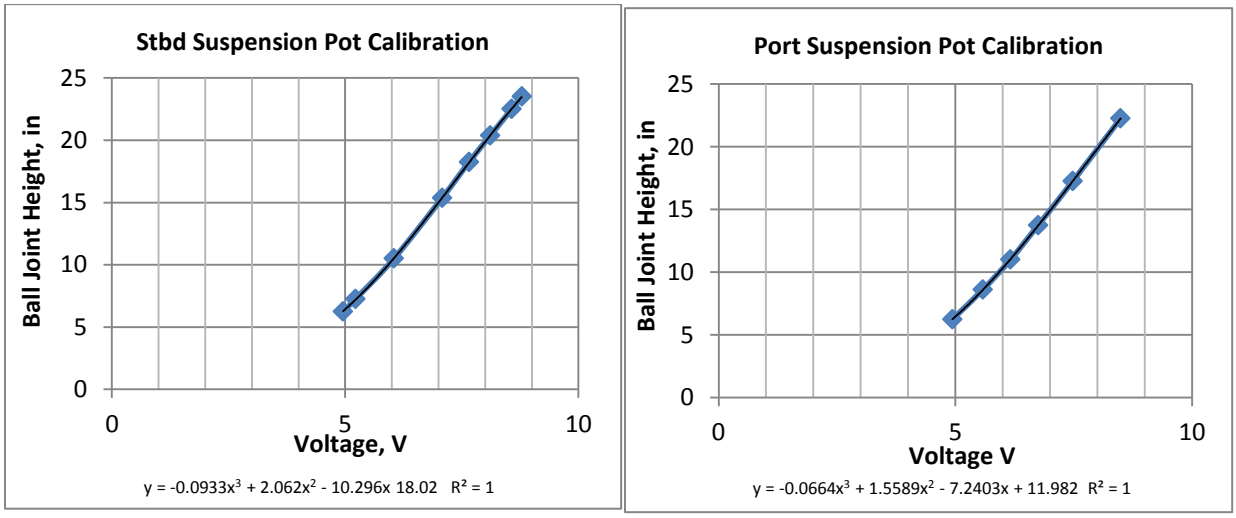

Figure 6.39 Suspension potentiometer calibration curves

For both the suspension and the engine pod potentiometers, a third order equation was used to approximate the nonlinear relationship between the motion of the suspension/engine pods and the rotary potentiometers. The nonlinearity comes from the 4-bar linkage used to connect the potentiometers to the suspension/engine pods. The nonlinearity can be noticed by the slight s-curve in all of the plots. Figure 6.40 shows the calibration of the port and starboard engine pod potentiometers, along with a fitted third order equation for analysis of the engine pod dynamics.

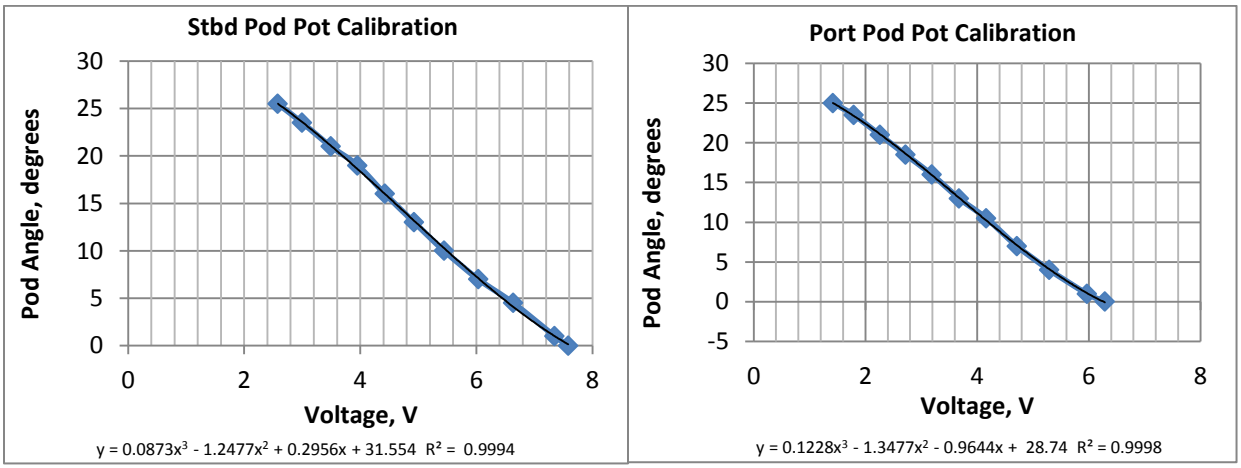

Figure 6.40 Engine pod potentiometer calibration curves

The correlation between the linear movement of the string potentiometer and the rotation of the front arch relative to the superstructure was established through a static physical test conducted on the water by raising and lowering the suspension. Since the potentiometer was mounted asymmetrically the calibration had to be performed in each direction of the front arch rotation. A table listing the angle measurements recorded between the front arch and the superstructure, and the output voltage measured from the string potentiometer are shown in Table 6.4.

Table 6.4 String potentiometer calibration data for front arch rotation

Starboard Suspension Height (in):	Port Suspension Height (in):	Relative Angle (Deg):	String Potentiometer Voltage (V):
+4	-4	2.73	5.60
+2	-2	1.36	5.42
0	0	0	5.25
-2	+2	1.36	5.09
-4	+4	2.73	4.92

6.6 Determination of 33-ft WAM-V Model Parameters

The water inclining results for the 33-ft WAM-V documented in Appendix A did not prove to be of sufficient resolution to determine an accurate center of gravity location for the WAM-V. To improve the results, the boat was lifted and weighed without the engine pods installed using four corner scales, allowing the longitudinal center of gravity of the WAM-V minus the engine pods to be determined. The engine pods were then weighed separately, with a full fuel load, using two scales to determine their longitudinal centers of gravity. The scales used were four 2000lb capacity, 0.5lb resolution corner scales, designed for weighing and adjusting the individual corner weights on race cars. The locations of the scales are shown in Figure 6.41. The positioning of the scales in a separate test to measure the weight and longitudinal center of gravity of the engine pods is shown in Figure 6.42.

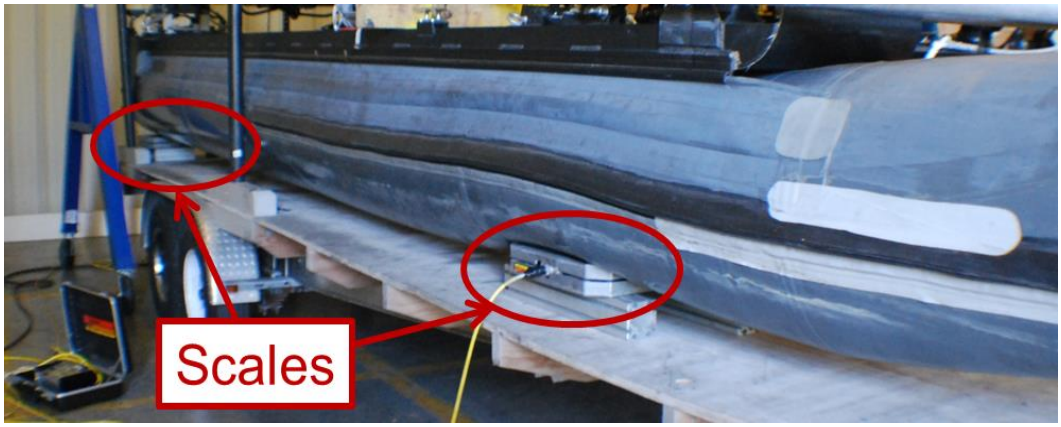

Figure 6.41 Scale positions for weight and longitudinal center of gravity determination

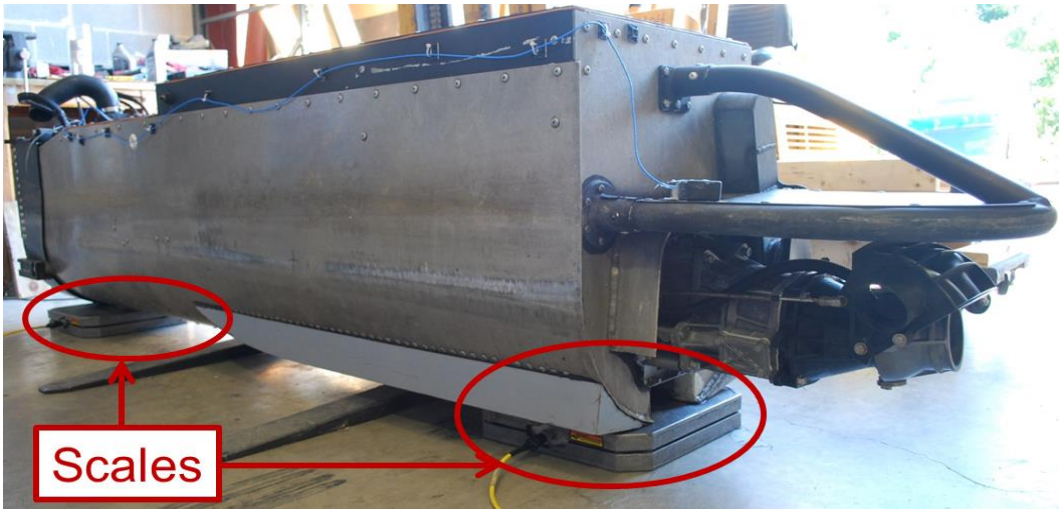

Figure 6.42 Scale positions for engine pod weighing (starboard engine pod shown)

Due to the complexity of unfolding the WAM-V out of the water, all measurements were taken with the WAM-V in the folded position. The front arch was secured in a vertical position to match its unfolded position. Four corner scales were placed under the corners of the WAM-V and individual measurements were taken. Multiple weighings were conducted with and without an additional 50lb weight placed on the operator's seat, to determine what percentage of the operator's weight is positioned over the front suspension systems.

After the initial weight measurements were taken, the air springs were disconnected from the rocker arms and two of the scales were repositioned on top of the skis between the front spherical joints and the skis, to measure the effective sprung mass acting on each of the front suspension systems. The placement of the scales for the sprung mass measurement is shown in Figure 6.43.

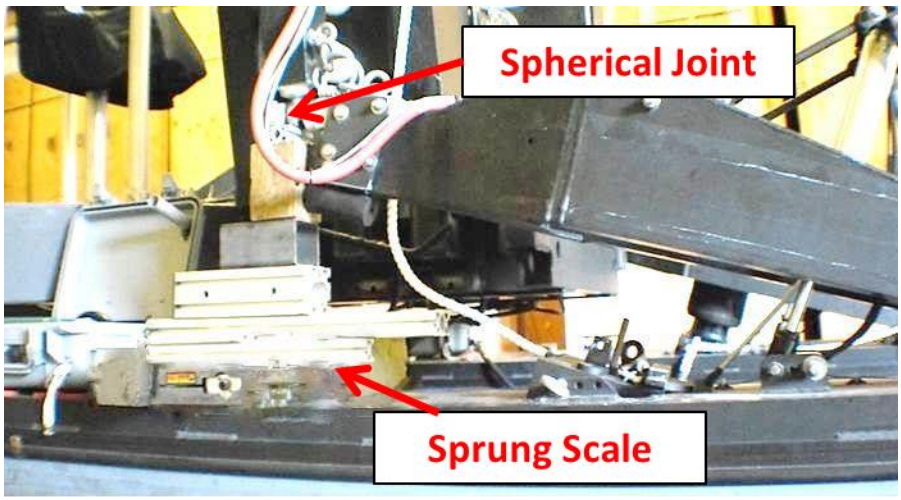

Figure 6.43 Replacement of corner scales for sprung weight measurement

Using the different weight measurements and the inclining test, mass and center of gravity estimates were able to be made for the WAM-V's major components. The CAD models were used to estimate what the required mass of the each of the major components must be to achieve the correct fore-aft weight distribution and the correct sprung weight over the front suspension systems. The total operational weight of the 33-ft WAM-V with a driver and a full fuel load on the day tanks and no fuel in the extended range tanks was found to be 4300 lbs. Table 6.5 lists the weight measurement results and calculations used to determine the component masses for the models.

Table 6.5 33-ft WAM-V component weights

Parameter:	Value:
Four corner test without pod or driver	
Front Corner weight (each)	620 lbs
Rear corner weight (each)	660 lbs
Percent weight front	48.5 %
Percent weight rear	51.5 %
Operator Weight Distribution:	
Weigh added (per corner)	17.5 lbs
Operator weight distribution (front)	70 %
Sprung Weight Distribution (200lb operator)	
Sprung Weight	1050 lbs
Unsprung weight	1510 lbs
Sprung weight per corner	525 lbs
Engine pod weighing	
Engine pod weight (fully fueled)	740 lbs
Fuel weight	100 lbs

With all the component weights determined, the CAD model could then be used to determine the overall center of gravity location. A side view of the CAD model is shown in Figure 6.44; the centers of gravity of all the major components are shown in black, the center of gravity of the entire vessel in the static operating condition is shown in red. The total center of gravity for the model is listed below, defined from the origin at the centerline of the rear joint.

X: 24.57 inches

Y: 0.00 inches

Z: 15.03 inches

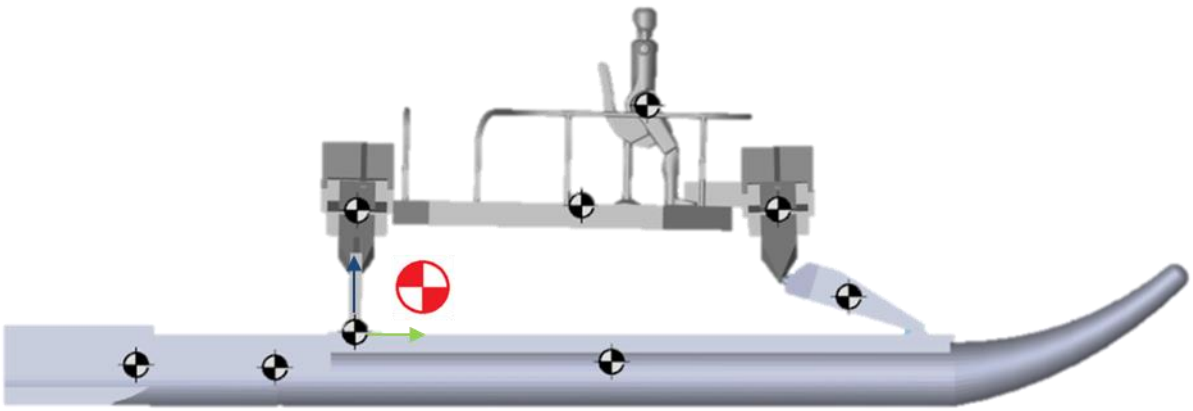

Figure 6.44 Side view of 33-ft WAM-V with component and vessel center of gravity estimates

6.7 Second Generation Suspension Design

Following the summer testing in Norfolk, VA, the 33-ft WAM-V received significant upgrades both for reliability and for improved performance. Much of the work was focused on servicing the WAM-V and repairing some of the powertrain failures that occurred during the summer testing; however, significant suspension upgrades were also made including a completely new second generation suspension configuration. The new suspension design is the focus of this section.

6.7.1 Summary of Findings – Original Suspension System

The original suspension system on the 33-ft WAM-V consisted of an air spring and two viscous dampers. The system was shown to have a few areas of deficiency, such as, a highly nonlinear spring rate and insufficient travel in rebound to keep the suspension from topping out on the extension limiting straps. Furthermore, the air springs were difficult to set up repeatedly, and their spring rates and ride heights were sensitive to small changes in the volume of air in the springs. The main improvements desired for the new second generation suspension system are:

- Increased travel, particularly in rebound to prevent topping out.
- Sufficient spring stiffness and ride height to avoid bottoming out without being so stiff that overall ride quality is compromised.
- Linear or slightly progressive spring stiffness. Previous design was far too progressive compromising ride quality at low displacements, and making the suspension excessively harsh for medium to high displacements.
- Greater levels of overall damping, particularly in compression to manage the WAM-V's high level of unsprung mass.

For the second round of on-water testing, the air spring and two dampers were to be replaced with a single coilover spring and damper unit. There were a number of advantages to this design path that led to it being chosen over a different setup that still utilized an air spring as part of the design. The main reasons a coilover spring and damper unit were chosen are:

- The linear spring rate will allow for increased energy to be transferred through the spring.
- A larger range of commercially available springs and dampers exists.
- Improved repeatability of testing; testing will be less affected by ambient temperature.

- Independent adjustment of ride height possible without affecting spring stiffness.
- Lack of off the shelf air springs that meet the design requirements of the WAM-V.

It is noteworthy, that even though air springs were not utilized as part of the second generation suspension design, this was more of a reflection of the characteristics of the available air springs in the size range for the 33-ft WAM-V, rather than the application of air spring technology to future WAM-Vs. Air springs were not deemed to be inadequate for future WAM-V designs; only the current air spring setup was determined to be suboptimal. In fact, air springs have several advantages over coilover springs that if carefully exploited could prove to be highly beneficial for WAM-Vs. Some of these inherent advantages are:

- Adjustable spring rate and ride height for different loading conditions.
- Possibility of load leveling designs for high payload capacities.
- Possibility of adding remote or actively controlled pressure adjustments to design.

For the coilover spring setup, a new damper had to be chosen as well. As with the coilover spring, the main criteria for choosing a new damper setup for the 33-ft WAM-V was not necessarily a comprehensive reflection on other alternative damper types that were not chosen. The main purpose of the suspension testing program is to generate accurate and repeatable data for the WAM-V program. Future WAM-V setups will likely find improved damper configurations beyond what has been added to the 33-ft WAM-V. The second generation damper has been chosen with adjustability in mind and the following key parameters:

- External adjustments of the damping rates are easily accomplished.
- Suitable long stroke to accommodate a desired increase in suspension travel.
- Appropriate range of forces corresponding to the range of desired damping ratios.
- Revalving of the dampers is possible by the manufacturer to suit the WAM-V's unique damping requirements.

Sections 6.7.3 and 6.7.4 describe the damper configuration that was chosen and the in-lab testing and analysis performed on the dampers prior to the WAM-V's winter testing program in Norfolk, VA. The calculations for determining suitable spring rates for the coilover springs are detailed in the next section.

6.7.2 Spring Rate Determination

To determine a suitable spring stiffness of the coilover spring for the second generation suspension system, two different methods were employed. The first method, based on analysis of quasi-static formulas, is documented in this section. The second method, based on analysis of the Quarter-Boat model and dynamic simulations of the WAM-V, is detailed in Chapter 8. The baseline capacities of the springs were determined using the following basic formulas:

Maximum Load: $Max\_Load = Spring\_Rate * Damper\_Travel$

Equivalent Spring Rate at Ball Joint: $Spring\_Rate\_at\_Ball\_Joint = Spring\_Rate * (IR^2)$

Percent Compression at Ride Height: $\%\_compression = Sprung\_Mass / Max\_Load * 100$

Maximum G loading (quasi-static): $Max\_G\_Load = Max\_Load / Sprung\_Mass$

Undamped Natural Frequency: $\omega_n = \sqrt{\frac{k}{m}}$

Damper Rate for Critical Damping: $C_{crit} = 2 * \sqrt{m * k}$

Damper Rate for Desired Damping: $C_{ratio} = \zeta_{desired} * C_{crit}$

Table 6.6 applies the formulas to a range of coilover springs varying from 200 lbs/in to 600 lbs/in. From the results, 500 lb/in springs were chosen as the optimal suspension setup, corresponding to a spring rate of 64 lbs/in at the front spherical joints, giving an undamped natural frequency of ~0.8 Hz. Additionally, a set of 400 lb/in springs were also selected, in the event that the 500 lb/in springs proved to be too stiff to provide a good ride quality. Unfortunately, the 400 lb/in springs were not able to be evaluated during the winter testing.

Table 6.6 Coilover spring computations for different spring rates

Spring Properties	Spring Rate (lbs/in)	200	300	400	500	600
	maximum load (lbs)	1600	2400	3200	4000	4800
Properties @ Ball Joint	Ball Joint Spring Rate (lbs/in)	25.35	38.02	50.69	63.37	76.04
	maximum load @ ball joint (lbs)	569.60	854.40	1139.20	1424.00	1708.80
	% comp. @ Ride Height w/o preload	92.17	61.45	46.08	36.87	30.72
	maximum g loading (quasi-static)	1.08	1.63	2.17	2.71	3.25
Damping Properties	undamped natural frequency (Hz)	0.69	0.84	0.97	1.09	1.19
	Damper Rate for Crtical Damping	65.69	80.45	92.90	103.86	113.78
	Damper Rate for 0.2 Damping Ratio	13.14	16.09	18.58	20.77	22.76
	Damper Rate for 0.7 Damping Ratio	45.98	56.32	65.03	72.70	79.64

6.7.3 Damper Rate Design

The damper design for the original WAM-V suspension employed two off the shelf off-road automotive dampers per suspension corner. The original dampers were tested in Section 6.5.1, and the damping curves were shown in Figure 6.29. While in some regards the original dampers performed adequately, there was room for improvement in the following areas:

- The original dampers are not externally adjustable, greatly limiting their tuning ability.
- The damping in the original dampers was heavily biased towards damping in rebound. This is common in dampers designed for automotive application, where the ratio of sprung to unsprung mass is in the range of ~8-10:1. The bias in damping is less desirable for the WAM-V's ~2:1 ratio of sprung to unsprung mass.
- Having two dampers per side represents extra parts and design complications.
- The current dampers do not support the use of coilover springs.

For these reasons, a new set of dampers was chosen to be used as part of the second generation WAM-V suspension. The damper's bodies chosen were manufactured by Ohlins racing with the original intended application for off-road motor racing. The dampers were modified at the factory with a custom valving for use on the WAM-V. The reasoning behind the specifications chosen is discussed in greater detail in Chapter 8. In summary, the dampers were built with considerably more damping in compression than is common in automotive applications. The ratio of rebound to compression damping in approximately 1:1. The second generation damper is shown with a 500 lb/in coilover spring installed in Figure 6.45.

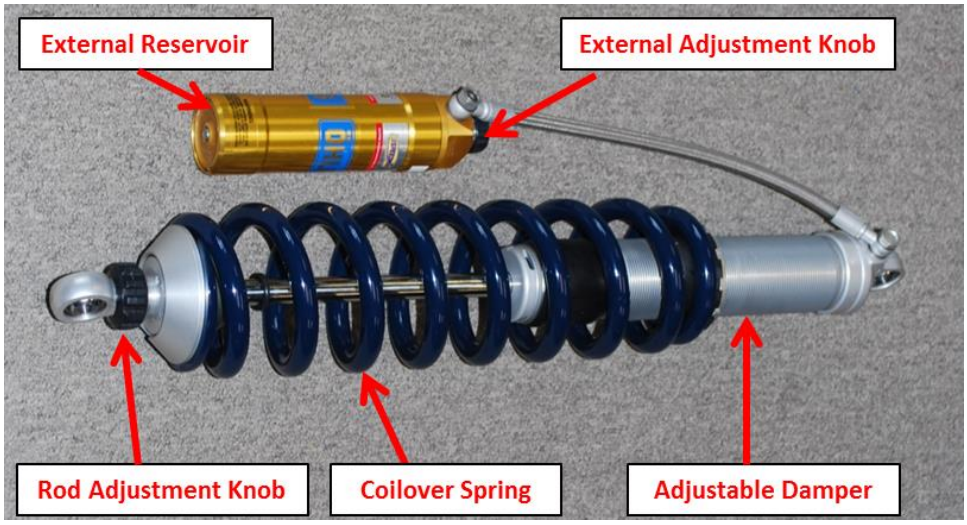

Figure 6.45 Second generation damper with 500 lb/in coilover spring installed

The new dampers are gas-pressure type dampers with an external reservoir and 2-way adjustable damping. The damper bodies are manufactured by Ohlins racing: model LMJ 2390 Series Shocks. The level of damping can be adjusted by turning the black knob at the end of the damper rod, or by turning the black knob on the external reservoir. The dampers were built with roughly equal damping rates in compression and rebound. This change is different from a conventional automotive application because of the ratio of sprung to unsprung weight of the WAM-V. The dampers have a wide range of adjustment that will open up tuning options for testing on the WAM-V. With a 500lb/in spring installed, the dampers give an available adjustment range of 15-85% critical damping in compression and rebound.

6.7.4 Second Generation Damper Testing

Like the original dampers, the second generation adjustable dampers were tested on the Roehrig damper dynamometer to learn how to tune the dampers using the adjustment knobs and to ensure the dampers were valved to the prescribed specifications. The spring rates were also verified using the dynamometer to confirm they matched the manufacturer's specifications. The range of adjustability of the new dampers compared with the original dampers is shown in Figure 6.46

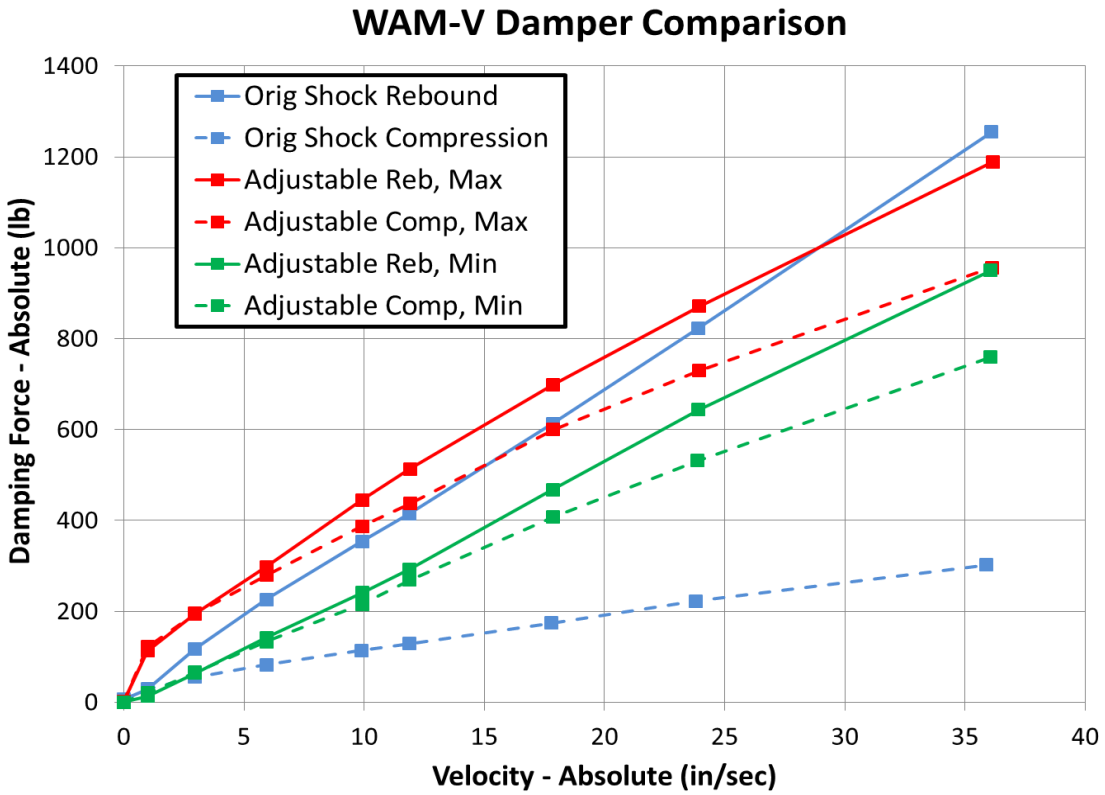

Figure 6.46 Range of damper adjustment curves compared with original dampers

For the purposes of testing on the WAM-V, three specific damping adjustments were often used during the course of the different rounds of testing. The three damper settings were meant to correspond to the minimum, middle, and maximum available settings of the damper. The damping curves for the three settings are shown in Figure 6.47. The damping rate of the damper changes nonlinearly as the damper is adjusted; the adjustments used to achieve each setting are listed in Table 6.7.

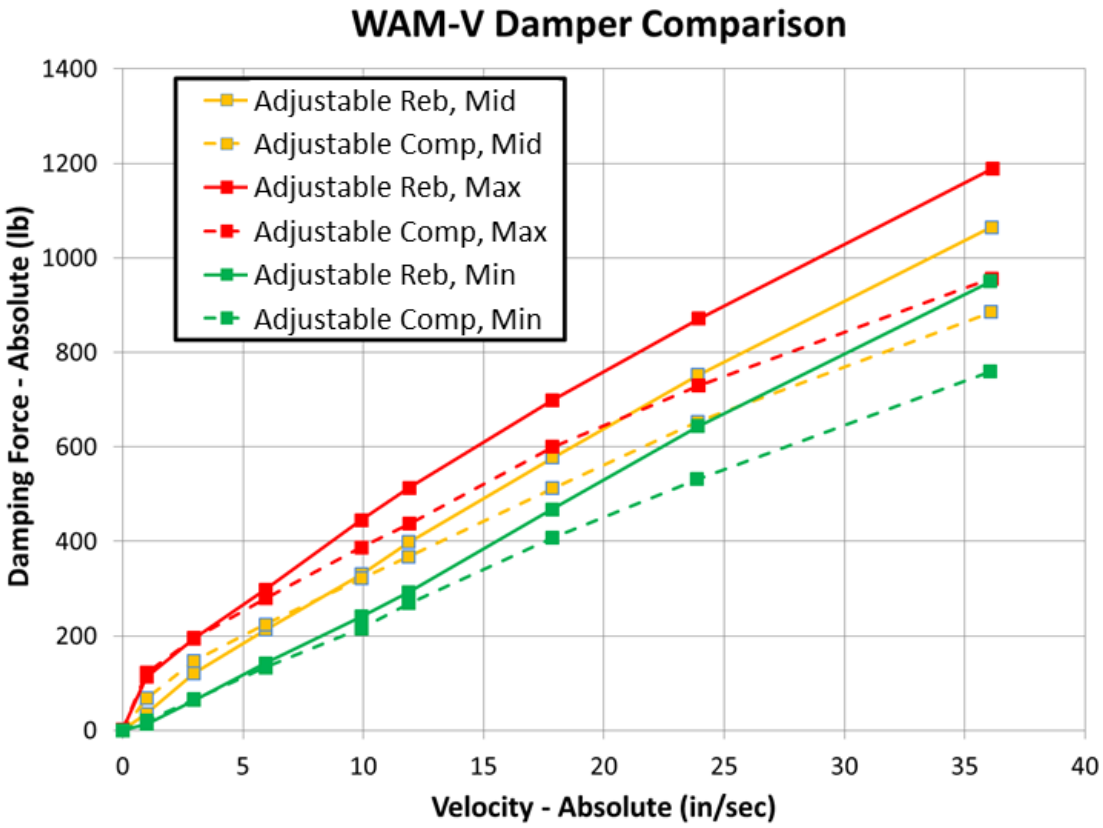

Figure 6.47 Damper curves for the three damper settings used for testing

Table 6.7 Damper information for three damper settings

Parameter:	Minimum Damping:	Middle Damping:	Maximum Damping:
Compression/Rebound Ratio (average)	0.984	1.073	0.915
Damping Ratio Compression (average)	0.151	0.256	0.344
Damping Ratio Rebound (average)	0.160	0.233	0.365
External Adjustment Position	Fully Open	Fully Closed	Fully Closed
Rod Adjustment Position	Fully Open	6 Clicks from Closed (24 Clicks total)	Fully Closed

6.7.5 Suspension Kinematics Changes

For the second generation suspension design, the kinematics of the WAM-V's suspension systems were also adjusted to take advantage of the extra stroke available from the new dampers. The new dampers have a range of stroke of 8.5 inches and can move between 15 and 23.5 inches in length. In order to take advantage of the extra available damper stroke, the kinematics on the suspension were adjusted to increase the available suspension travel in rebound with the new dampers installed.

The new suspension design allows the ball joint to move up to 28 inches in height before the limit straps (which were also upgraded to a higher-strength design and moved to a different location on the rocker arm) engage. The revised suspension geometry with the second generation suspension installed is shown in Figure 6.48. Properties for the second generation suspension design compared with the original suspension are listed in Table 6.8.

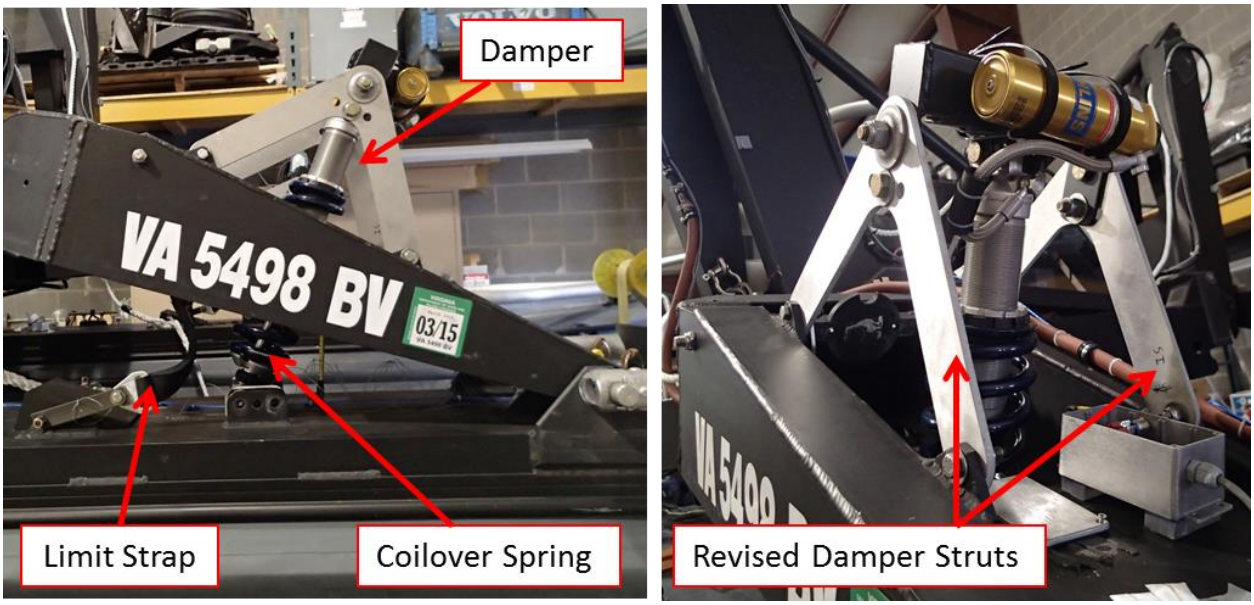

Figure 6.48 Second generation suspension/rocker arm configuration

The rocker arm design of the original suspension was modified to take advantage of the extra available damper length by moving the upper pivot point of the damper. New damper struts were designed to house the damper and the coilover spring and to hold the damper's external reservoir. With the new damper struts, the location of the top mounting point was lowered 0.75 inches to increase the available suspension travel in rebound. Changing the pivot point location

only altered the motion ratio of the rocker arm slightly (0.356 for the original damper vs. 0.346 for the revised damper location), and it opened up the available stroke of the suspension. The change in the pivot point location is shown in Figure 6.49.

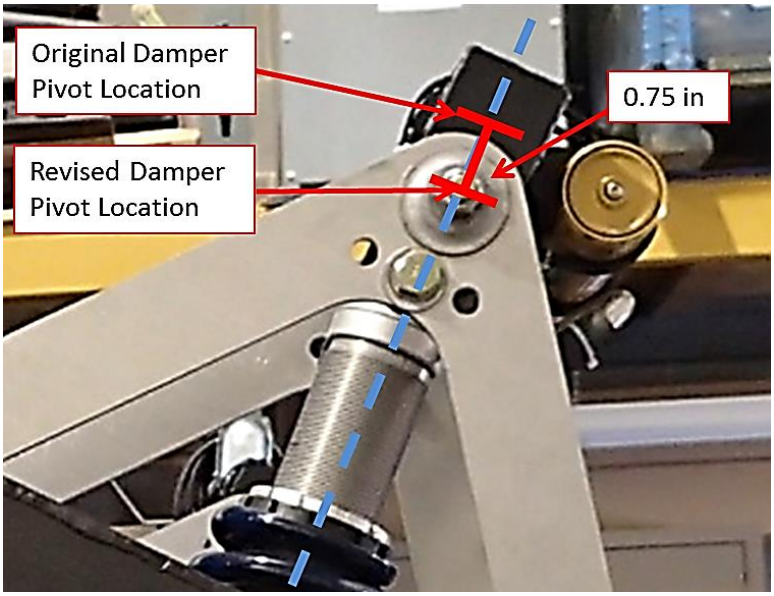

Figure 6.49 Revised damper pivot point location for adjustable dampers

Table 6.8 Second generation suspension design property comparison

Parameter:	Original Suspension:	Revised Suspension:
Spring Damper Motion Ratio	0.356:1	0.346:1
Equivalent Spring Rate at Ball Joint	33.3	63.37
Maximum Suspension Height	23 inches	28 inches
Height of Bump Stops	6 inches	6 inches
Total Suspension Travel	17 inches	22 inches
Inches of Compression Travel	15 inches	15.5 inches
Inches of Rebound Travel	2 inches	7.5 inches
Percentage of Travel in Compression	88%	70%

6.8 Conclusions and Recommendations for Future Work

The design and testing of different components of the 33-ft WAM-V detailed in this chapter will be highly beneficial to the remaining chapters of this dissertation. The conclusions and recommendations in this section are applicable to both the current 33-ft WAM-V, as well as the simulation and testing of future WAM-V designs.

6.8.1 Conclusions from Instrumentation

The data acquisition package detailed in Section 6.4 was highly successful for capturing the relevant dynamics of the 33-ft WAM-V. The additional sensors were beneficial for recording data types that were not logged when the 12-ft USV was tested with a similar data acquisition setup. Increasing the data logging rate from 250 Hz to 500 Hz did produce slightly higher quality data, particularly for the accelerometer data being that was integrated to generate displacement inputs for the models, using a shorter time step reduced integration errors. The increased logging rate comes at the expense of larger file sizes and longer computation times, which were not found to be problematic.

The rotary potentiometers used on the suspension and engine pods were found to be a good upgrade made for reliability purposes over the linear potentiometers used on the 12-ft USV. The single-axis accelerometers that were used on the 33-ft WAM-V developed water ingress issues that were not seen using the same accelerometers during testing of the 12-ft USV. The sensors were initially mounted in exposed locations, and then were moved into IP-68 rated enclosures. Desiccant packs were also required inside the accelerometer boxes to absorb small amounts of moisture that led to the failure of one of the accelerometers.

6.8.2 Conclusions from Component Testing

Individual component testing for parts of the 33-ft WAM-V proved to be highly beneficial, as it revealed areas such as the difference in the manufacturer's air spring data compared to the air springs as tested; that would have otherwise gone unnoticed. Testing showed the air springs to be extremely nonlinear, with poor energy storage during compression for most of their travel; the spring rates of the air springs were found to change by as much as an order of magnitude throughout their travel. A slightly progressive suspension design is often beneficial to keep a suspension from bottoming out in compression; however, the original suspension was found to be too progressive, allowing the sprung mass to accelerate downward and crash into the

nonlinear region of the suspension travel, and also causing the suspension to top out excessively in rebound.

The fact that the measured air spring data was so different than the manufacturer supplied air spring curves makes it difficult to accurately specify an air spring for future use on the WAM-V. This is not a comment on the quality of the manufacturer's data, but rather a reflection on the difference in using the air springs with and without an external reservoir tank to keep the air springs at a constant pressure, which is how the manufacturer's curves are generated.

The original suspension dampers were found to have insufficient damping in compression. If the use of off the shelf automotive dampers on future WAM-V's is desired, the rocker arm design on the WAM-V could be used to reverse the direction of the damper's travel relative to the motion of the spherical joints. This would effectively increase the compression damping, at the expense of rebound damping.

6.8.3 Conclusions from Inclining and Determination of Model Parameters

A water inclining test was found to be unsuitable method for determining the vertical center of gravity of the 33-ft WAM-V. It is also believed that this method would be unsuitable for other lightweight, low-draft designs with wide hull spacing; other methods, such as an air inclining test or a tilt test, should be performed instead.

The model parameters that were generated in this chapter are used with the Quarter-Boat models for the 33-ft WAM-V in Chapter 8 to investigate the dynamics of the second generation suspension system. The parameters are used with the 6-post model of the 33-ft WAM-V in Chapter 11.

6.8.4 Conclusions from Second Generation Suspension Design

Based on initial laboratory testing, the second generation suspension system was found to be a mathematical improvement over the original suspension system. Simulations comparing the original and the second generation suspension system are conducted in Chapters 8 and 11. On-water testing of the second generation suspension system is detailed in Chapters 7 and 9. Testing of the original versus the second generation suspension system using the 2-post shaker rig is detailed in Chapter 10.

Chapter 7 33-ft WAM-V On-Water Data Analysis

The following chapter provides a detailed analysis of the data collected from the 33-ft WAM-V's on-water testing programs. The initial testing methodologies, as well as the modifications made to the testing plans are included, along with documentation from the tests that were analyzed. This chapter details the on-water trials with the 33-ft WAM-V and the first round of rough water testing for the 33-ft WAM-V, both conducted with the original suspension system. The data from the winter testing program with the second generation suspension system is also analyzed and discussed. Additional testing analysis from the on-water tests can be found in Chapters 8 and 9.

7.1 Chapter Overview

- Section 7.1 provides an overview of the chapter.
- Section 7.2 presents the testing methodology along with the test plans and timelines.
- Section 7.3 details the single-wave input analysis.
- Section 7.4 compares the data from the summer and winter testing programs.
- Section 7.5 provides conclusions and recommendations from the chapter.

7.1.1 Significant Contributions

The results of this chapter contribute to the sparely populated field of knowledge regarding suspension systems in a marine environment. The method for breaking down a single-wave impact into short components for suspension analysis is unique to this research.

The data analysis presented in this chapter is used in Chapter 8 to direct the design of the second generation suspension system for the 33-ft WAM-V, and to improve the unique simulation method shown in Chapter 8 for suspension testing using the Quarter-Boat Rig dynamics. The testing results are also applied in Chapter 11 to improve the CFD inputs to the 6-post simulations, and in Chapter 12 to provide possible directions for future WAM-V development.

7.2 Testing Methodology

The following section provides a description of the plans for the on-water testing programs with the 33-ft WAM-V to give context to the data analysis documented in the remainder of the chapter. The 33-ft WAM-V, detailed in Chapter 6, first came to the CVeSS laboratory in the fall of 2011; however, it wasn't until the WAM-V returned to the lab in the spring of 2012 that the on-water testing programs officially began.

The primary reason for conducting the WAM-V testing programs detailed in this chapter, as well as in the rest of this dissertation, is not to optimize a particular WAM-V design for a specific mission or purpose. The motive behind the tests is the more all-encompassing purpose of developing a set of tools for designing the next generation of WAM-Vs. The on-water testing will help to generate data to improve these tools.

The WAM-V on-water testing program can be broken down into three major phases, each phase was motivated by different goals which are reflected in the different testing methodologies. The phases are listed below:

1. Initial calm water testing
2. Summer initial rough water testing program
3. Winter upgraded testing program

7.2.1 Overview of Calm Water Testing Plans

The calm water testing program was designed to build a knowledge base about the testing procedures for the WAM-V while considerable upgrades were made to prepare the WAM-V for rough water testing. Testing with the 33-ft WAM-V requires considerable preparations and maintenance, the initial tests were meant to develop a set of safe testing procedures prior to rough water testing. The data collected was used to generalize the WAM-V's overall dynamics to serve as a baseline for future comparisons of the WAM-V's dynamics in an elevated sea state, as well as to help to determine the most relevant rough water tests to be conducted with the WAM-V. The data analysis from the calm-water testing of the 33-ft WAM-V is documented in Appendix B.

7.2.2 Overview of Summer WAM-V Testing Plans

Following the calm water testing, the goal for the first rough water testing with the 33-ft WAM-V was to rigorously test the WAM-V with as many parametric configuration changes as possible in a number of different sea conditions. Since the WAM-V is a prototype craft, the tests would need to incrementally build in severity in order to test the WAM-V safely. For the summer testing program, the following parameters are available to be parametrically changed on the 33-ft WAM-V; additionally, the sea state, speed, and heading can also be varied for the different configurations:

- Damper configuration (0, 1, or 2 dampers per side)
- Air spring pressure (20, 25, or 30 psi in pontoons)
- Pontoon pressure (1, 2, or 4 psi in pontoons)
- Ballast configuration (none, payload forward, payload rearward, pontoons)
- Degree of freedom lockouts (suspension, spherical joint, engine pods)

The configuration changes were made far more sparingly than what is listed above and fewer tests configuration changes were tested than originally laid out on the grounds of safety. The number of dampers on each suspension system was left unaltered because even the two-damper configuration was found to be under damped in compression, and marginal in rebound. Limited on-water testing was conducted at 20, 25, and 30 psi on the air springs; however, as shown in Section 6.5, the air springs are highly nonlinear, and are being run outside of their normal operating window. Ride quality with the springs 20 psi was deplorable, the tests at 20 psi caused the WAM-V to repeatedly bottom out in compression over even the smallest waves. The tests at 30 psi kept the suspension pressed against the limit straps, producing undesirable negative accelerations. Changing the air pressure is also linked with changing the ride height which compounded the problem. Different pontoon pressures were not evaluated because the bows of the WAM-V's pontoons were found to be quite prone to bending even at 4 psi. Higher pressures were not run because the pontoons have internal pressure relief valves set to 5 psi.

Lockout mechanisms were designed for the 33-ft WAM-V that would inhibit the degrees of freedom of its joints during on-water tests. There was reasonable concern over damage this might cause to the WAM-V, so the lockout mechanisms were designed to be placed in parallel with the degrees of freedom rather than to replace them. The lockouts were also designed with

known and limited strengths that would act as mechanical fuses, so the lockouts would fail before the WAM-V could be damaged, and the tests could build up in severity using mechanical fuses of different strengths. Due to the limitations of the WAM-V's powertrain reliability, the number of tests run during the summer testing program was limited and testing the lockouts never advanced beyond the design stage. For future on-water testing the idea could be revisited, with careful consideration to how the lockout designs would be implemented and safely tested.

7.2.3 Overview of WAM-V Winter Testing Program

The winter on-water testing program for the 33-ft WAM-V was designed to augment the summer testing program, when many of the desired testing configurations could not be evaluated due to reliability issues with the WAM-V powertrain units and a lack of available windows for rough water testing in the summer months in Norfolk, VA. Although the testing conditions are far less hospitable for the persons onboard the WAM-V and the support craft, testing the WAM-V during the winter months provides more testing windows in elevated sea state conditions.

For the winter testing program, the parameters to be evaluated on the WAM-V were narrowed to only include parametric changes to the suspension systems. The winter testing program was meant to include a back to back comparison of the original and second generation suspension designs. The second generation suspension system was also tested at a number of different damping ratios. The back to back comparison was not completed due to reliability issues with the WAM-V's powertrain units. It was also the WAM-V operator's opinion that the conditions were too rough to safely test with the original suspension system.

7.2.4 Overview of the Tests Analyzed for the 33-ft WAM-V

In this dissertation, the data from five on-water tests of the 33-ft WAM-V is analyzed to give a better understanding of the WAM-V's dynamics. Four of the on-water tests are detailed in this chapter, a fifth test is detailed separately in Chapter 9 with a focus on the application of Whole-Body Vibration standards to the WAM-V. The tests are detailed in the order the tests were conducted. Chapter 8 contains additional analysis of the single-wave test documented in Section 7.3, to compare the test data with the Quarter-Boat simulations used to design the second generation suspension system for the 33-ft WAM-V.

7.3 Single-Wave Input Testing Analysis

As part of the summer testing program for the 33-ft WAM-V, a test was conducted by maneuvering the 33-ft WAM-V over the stern wake of a large freighter ship at a speed of 10 knots. The freighter produced an estimated 48 inch tall wave, with an estimated wave length approximately equal to the length of the WAM-V, as estimated by video footage. The wave was significantly large enough to launch the WAM-V airborne during the test. Speed was measured by GPS, heading was set for a head sea condition relative to the freighter's wake. The 33-ft WAM-V and the freighter ship are shown in Figure 7.1

Figure 7.1 33-ft WAM-V and the freighter ship

Sensor data was recorded on the WAM-V and video data was taken from the WAM-V's onboard cameras, as well as from a camera on the support craft. The video data captured from the support craft was analyzed and broken down into seven screenshots representing critical phases of the test. The phases were chosen based on the suspension performance, as well as the operator's response. Video and sensor data collected during the test were compared and broken into seven phases, highlighting the most important information toward determining the WAM-V's performance envelope. Screenshots from each phase of the test are shown at the beginning of each section. The seven phases of the single wave input test are listed in Table 7.1, along with the time at which each screenshot was taken. Figure 7.2 shows a diagram of the onboard sensors that were analyzed during the single-wave test.

Table 7.1 Relevant phases of the single-wave input test

Phase Number:	Phase Name:	Elapsed Time:
1/7	Initial Encounter	0.00 seconds
2/7	Loading Phase	0.79 seconds
3/7	Unloading Phase	1.50 seconds
4/7	Free-Fall Phase	1.74 seconds
5/7	Initial Impact	1.84 seconds
6/7	Maximum Compression	2.17 seconds
7/7	Secondary Oscillations	2.94 seconds

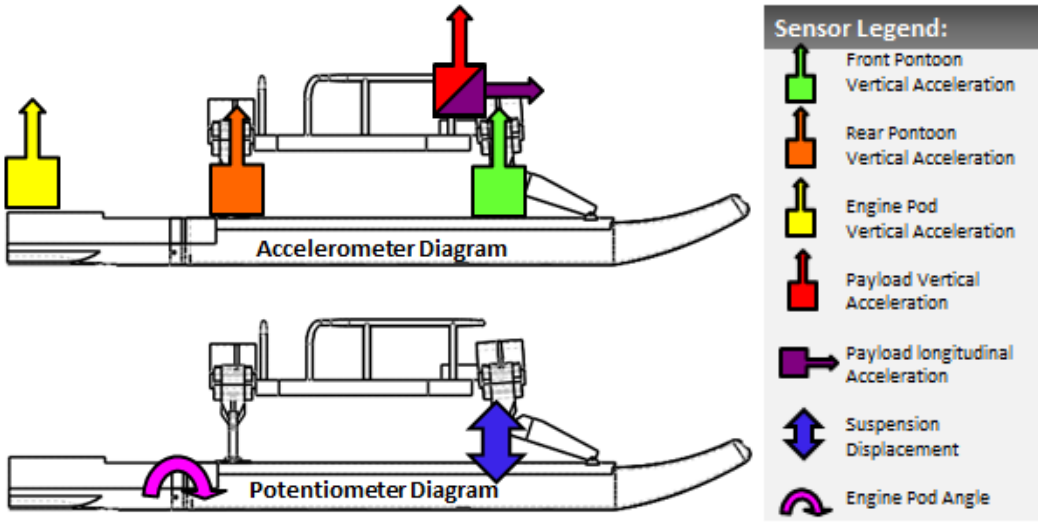

Figure 7.2 Sensors evaluated during the single-wave test

A diagram of the onboard sensors that were analyzed from the test in Figure 7.2 doesn't show that some of the sensors analyzed have a mirrored counterpart on the port and starboard side of the WAM-V. The test conducted is a head sea condition and the craft is assumed to be symmetrical; so the sensors from starboard pontoon and engine pod were chosen for analysis. The port accelerometers showed a near symmetrical response, their results were not included separately except for the port suspension motion, which is shown for both sides of the WAM-V.

7.3.1 Phase 1/7: Initial Encounter

During the test, sensor data was recorded using the WAM-V's data acquisition package, and video data was taken from cameras on the WAM-V and the support craft. Video and sensor data collected during the test were analyzed and broken into seven distinct phases to help determine how the performance of the suspension affects the performance of the WAM-V. A video screenshot from Phase 1/7 of the test is shown in Figure 7.3.

Figure 7.3 Initial WAM-V orientation

The seven phases were chosen based on the suspension's performance as well as the operator's response. For each phase, a figure is displayed with a screenshot of the WAM-V taken from the support craft, along with enlarged views of the operator and the suspension system. Annotated graphs with data from the most relevant sensors are also included, along with the elapsed time.

The first phase of the test represents the steady-state operating condition of the WAM-V at the test speed of 10 knots as the WAM-V begins to approach the wave. As part of the WAM-V's data acquisition package, two rotary potentiometers were mounted to the rocker arms in order to measure the suspension's displacement during the test. Plots of the suspension displacements recorded during testing are shown in Figure 7.4.

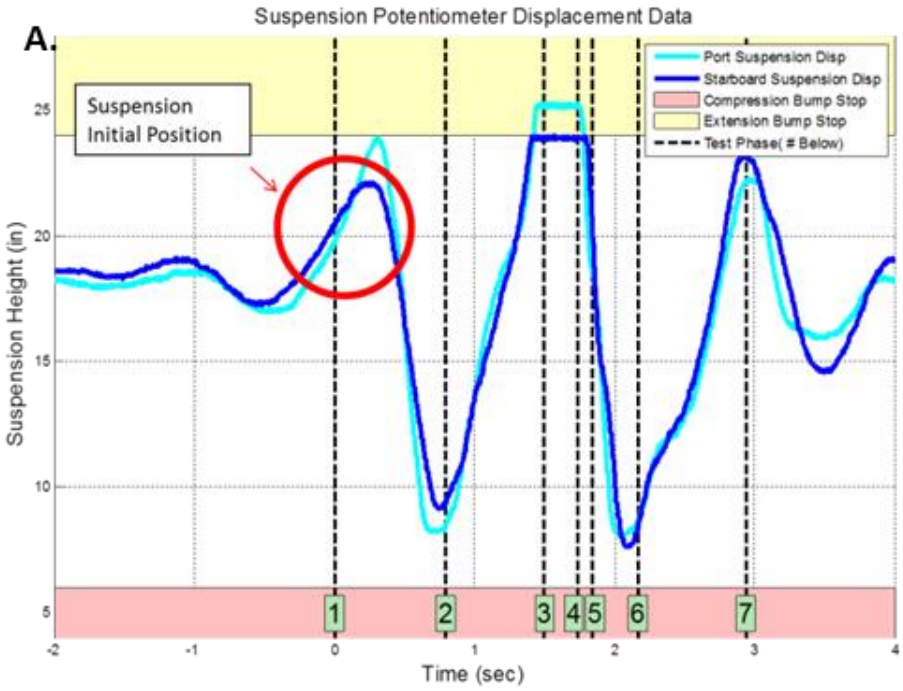

Figure 7.4 Phase 1/7 suspension displacement

Figure 7.4 shows the position of the suspension system versus time for both of the front corner suspension systems. At time t = 0, the suspension position is approximately at its calm water ride height. The positive slope of the plots for both suspension systems at time = 0 indicates upward relative motion; the suspension is extending. The relative upward motion can be attributed to the WAM-V's pontoons moving downward into a small trough of relatively long wavelength that preceded the larger wake created by the freighter ship. A similar trough existed following the wake. Analyzing the suspension motion during each phase is critical to gain a better understanding of its effect on the operator and the vessel's dynamic performance.

7.3.2 Phase 2/7: Loading Phase

During the second phase of the test, the WAM-V's suspension becomes loaded in compression from the initial encounter with the wave. The encounter with the wave causes the inflatable bows to deflect and fold upward, and the suspension to compress heavily, as shown in Figure 7.5.

Figure 7.5: WAM-V orientation during Phase 2/7

The loading of the suspension occurs more quickly than the pontoons are able to move upward to negotiate the wave. The delay in the response is partially due to the high unsprung mass of the pontoon/ski assembly compared to the sprung mass of the WAM-V. The wave is taller and steeper in nature than the waves likely encountered during a typical rough water test, which results in a more severe impact in the longitudinal direction.

The enlarged view of the suspension shown in the top left corner of Figure 7.5 shows a significant difference in the suspension's position compared to Phase 1 of the test. The initial encounter with the wave causes both suspensions to compress through 85% of their respective travel limits, as shown in Figure 7.6(a). The suspension compresses nearly as much during this phase as during the initial impact after jumping the wave (Phase 5/7). Between Phases 1 and 2, the port suspension extends and compresses slightly more than the starboard suspension; possibly indicating that the wave is more severe on the port side, closer to the freighter.

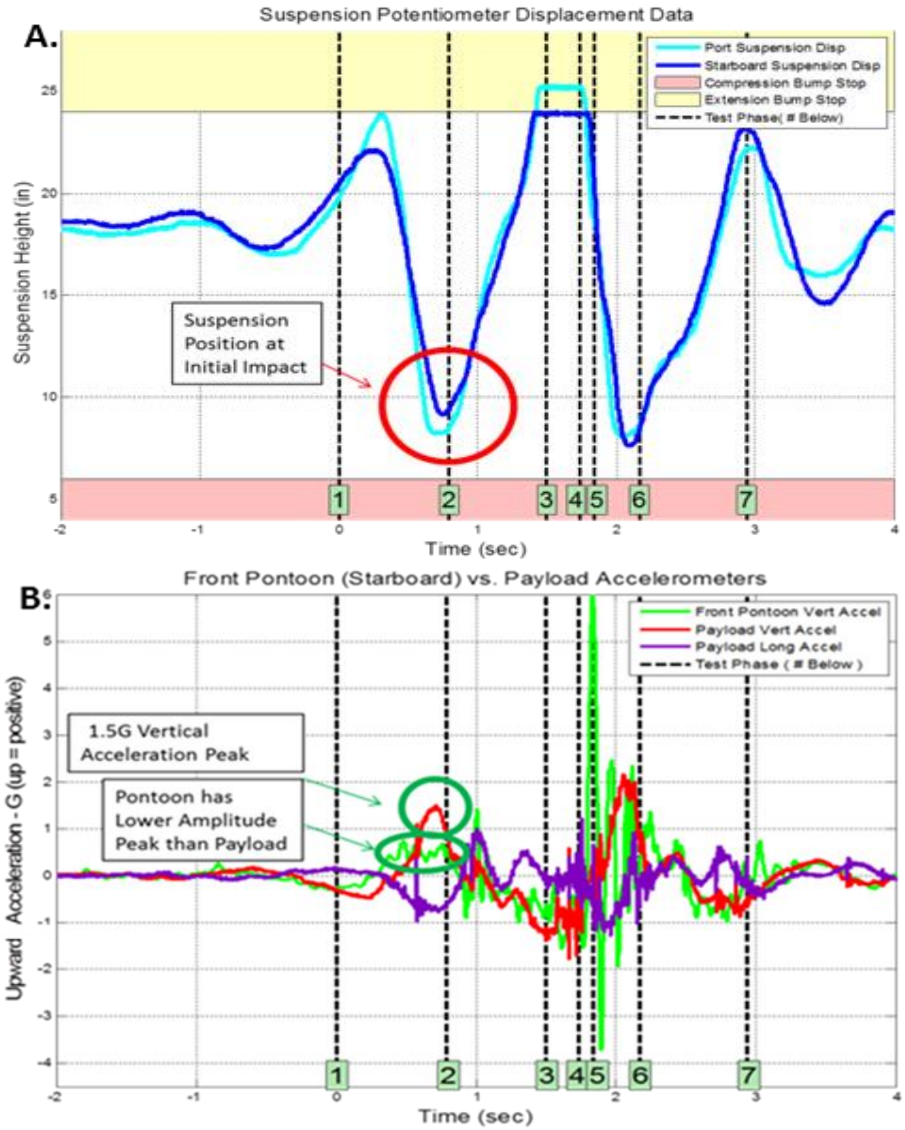

Figure 7.6: Phase 2/7 suspension displacement (a) and vertical acceleration (b) comparisons

Data from seven accelerometers was logged throughout the test. Six single-axis vertical accelerometers were mounted at the front and rear of each pontoon, as well as at the rear of each engine pod. A single tri-axial accelerometer was also mounted on the payload close to the operator's seat. A comparison between the vertical accelerometers at the front of the pontoons and the payload is shown in Figure 7.6(b). The initial compression causes a hard 1.5g vertical acceleration peak at the payload, while only 1g was recorded at the pontoons. Despite the suspension compressing, no acceleration attenuation occurs, as the operator actually experiences slightly greater acceleration levels than are present at the pontoons for this phase of the test.

7.3.3 Phase 3/7: Unloading Phase

During the third phase of the test, the bows launch upward and reach their maximum height off the water, with the stern still partially submerged and the engine pods now fully submerged. The operator is still seated, as shown in the close-up in the top right corner of Figure 7.7. The momentum of the chassis, combined with the preload of the air springs, pulls hard on the suspension's limit extension straps, as can be seen in the suspension close-up in the top left corner of Figure 7.7.

Figure 7.7: WAM-V orientation during Phase 3/7

During normal operation at static ride height, the suspension rides high, with most of its available travel in compression, and little of its available travel in rebound. This causes the extension straps to engage repeatedly during both moderate and severe wave inputs.

Shown in Figure 7.8 are two annotated graphs of the suspension displacement and the vertical acceleration of the front of the pontoon and the payload. During Phase 3, the suspension has maxed out in extension on the limiting straps. The two suspensions reach slightly different heights, possibly due to a combination of differences in stiffness and manufacturing tolerance of the two limiting strap assemblies that are used to keep the suspension systems from exceeding their travel limits.

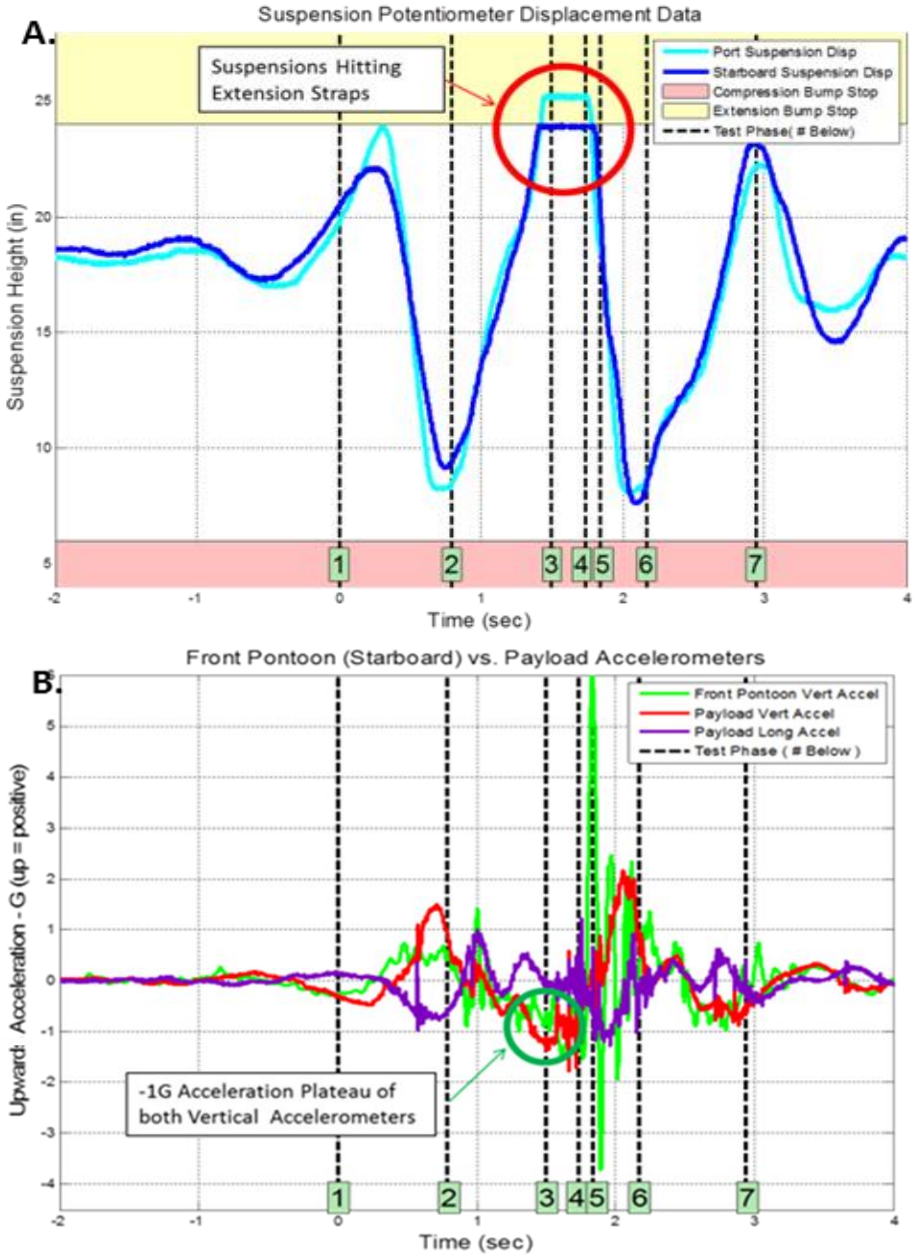

Figure 7.8: Phase 3/7 suspension displacement (a) and vertical acceleration (b) comparisons

As shown in Figure 7.8(b), the accelerometers at the front of the pontoon and the payload both register -1g vertical acceleration plateaus because no relative motion occurs between the two accelerometers while the suspension is on the limiting straps. The lack of relative motion is also shown in Figure 7.8(a) by the flat suspension plot lines. Acceleration values of -1g indicate free fall, thus marking the transition between the unloading phase (3/7) and the free-fall phase (4/7).

7.3.4 Phase 4/7: Free-Fall Phase

During Phase 4 of the test, the bows are in free-fall, traveling downward as the stern portions of the pontoons come out of the water. The angle of the pontoons is close to horizontal, as seen in Figure 7.9. It is at this point that the engine pods reach and pull on their limiting straps in the downward direction.

Figure 7.9: WAM-V orientation during Phase 4/7

Figure 7.10 shows two graphs comparing engine pod acceleration versus engine pod angle, as well as vertical acceleration of the payload versus the pontoons. The engine pods on the WAM-V are mounted to the pontoons via a hinge mechanism, allowing the pods to rotate freely to keep the two jet propulsion units submerged at all times. In order to measure the rotation of the pods during the test, two rotary potentiometers were mounted on the engine pods along the axis of the hinge. A comparison between the engine pod angle and the vertical acceleration of the rear of the engine pods is shown in Figure 7.10(a).

During Phase 4 of the test, the engine pods reach their minimum angle of –13 degrees relative to the pontoons, and their angle plateaus as the pods pull on the limiting straps. The vertical acceleration of the engine pod follows the same trend as the longitudinal acceleration of the payload, indicating a possible coupling effect between the two measurements.

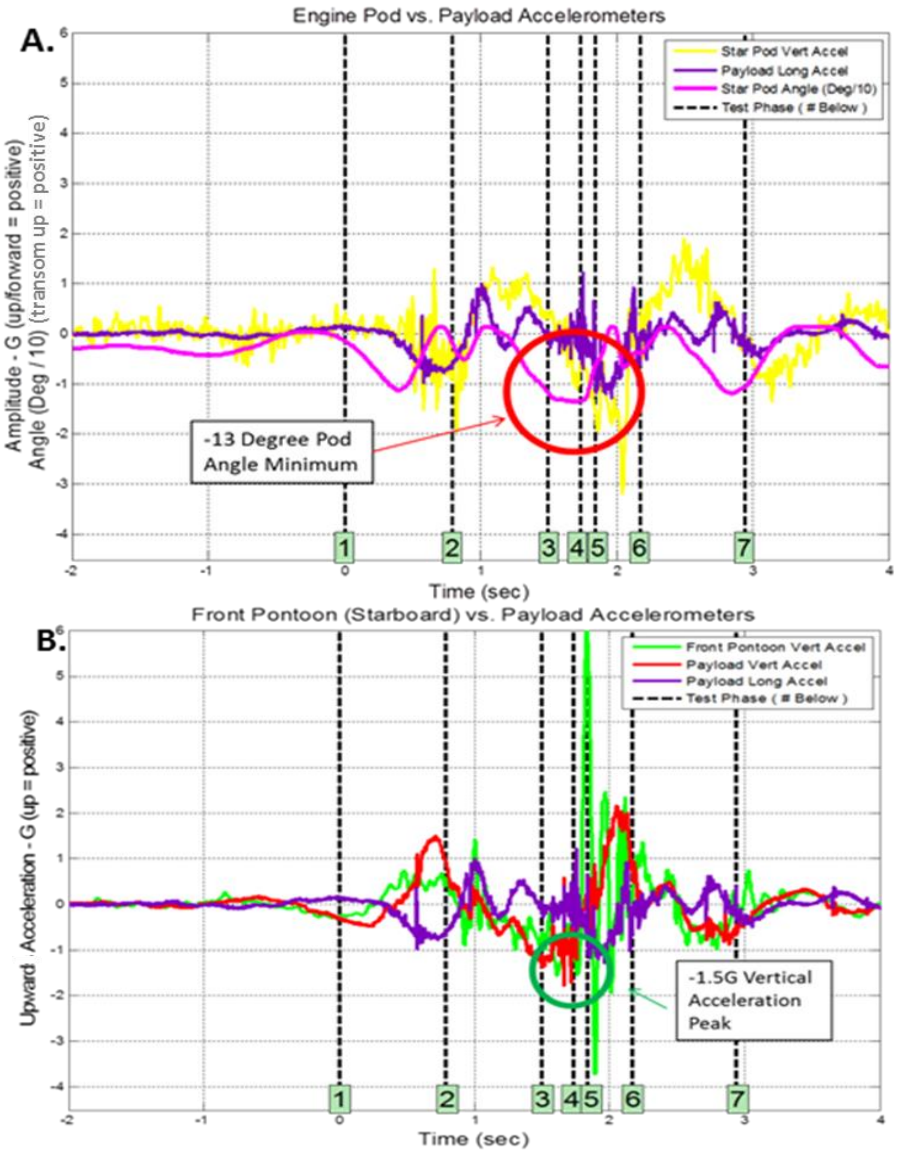

Figure 7.10: Phase 4/7 engine pod angle vs. engine pod acceleration (a) and pontoon acceleration vs. payload acceleration (b) comparisons

As shown in the top right corner of Figure 7.9, during this phase of the test, the operator has come out of the seat as the suspension abruptly contacts the limiting straps, decelerating the payload tray at a rate slightly greater than the acceleration due to gravity, while the operator's momentum continues to carry him upward and out of the seat. Figure 7.10(b) shows the vertical acceleration levels recorded at the payload and the pontoons. Phase 4 is characterized by a -1g plateau and a -1.5g peak at the payload. The -1.5g peak acceleration is of sufficient duration to launch the operator from the seat momentarily.

7.3.5 Phase 5/7: Initial Impact

Phase 5 of the test is characterized by the initial impact of the pontoons with the water. A large impact occurs at the bows of the pontoons first, followed closely by a smaller impact at the sterns. The WAM-V at the time of initial impact of the bows is shown in Figure 7.11.

Figure 7.11: WAM-V orientation during Phase 5/7

At impact, the operator is still partially out of the seat, as shown in the top right corner of Figure 7.11; the operator's position is similar to that of Phase 4/7. The engine pods are still at their maximum downward angle, with their weight pulling on the limiting straps as was previously shown in the plots of Figure 7.10(a). The vertical accelerations of the front pontoon versus the payload are shown in Figure 7.12(a) to highlight the impact attenuation of the suspension, which is far better than the attenuation shown during Phase 2 of the test.

As shown in Figure 7.12(a), the 6g impact vertical acceleration level recorded on the front of the pontoons is attenuated to 2g's at the vertical accelerometer near the operator, indicating a positive attenuation from the suspension system for this phase of the test. Despite being positioned forward toward the bow, the sensor near the operator records the lowest acceleration values of any sensor during the test.

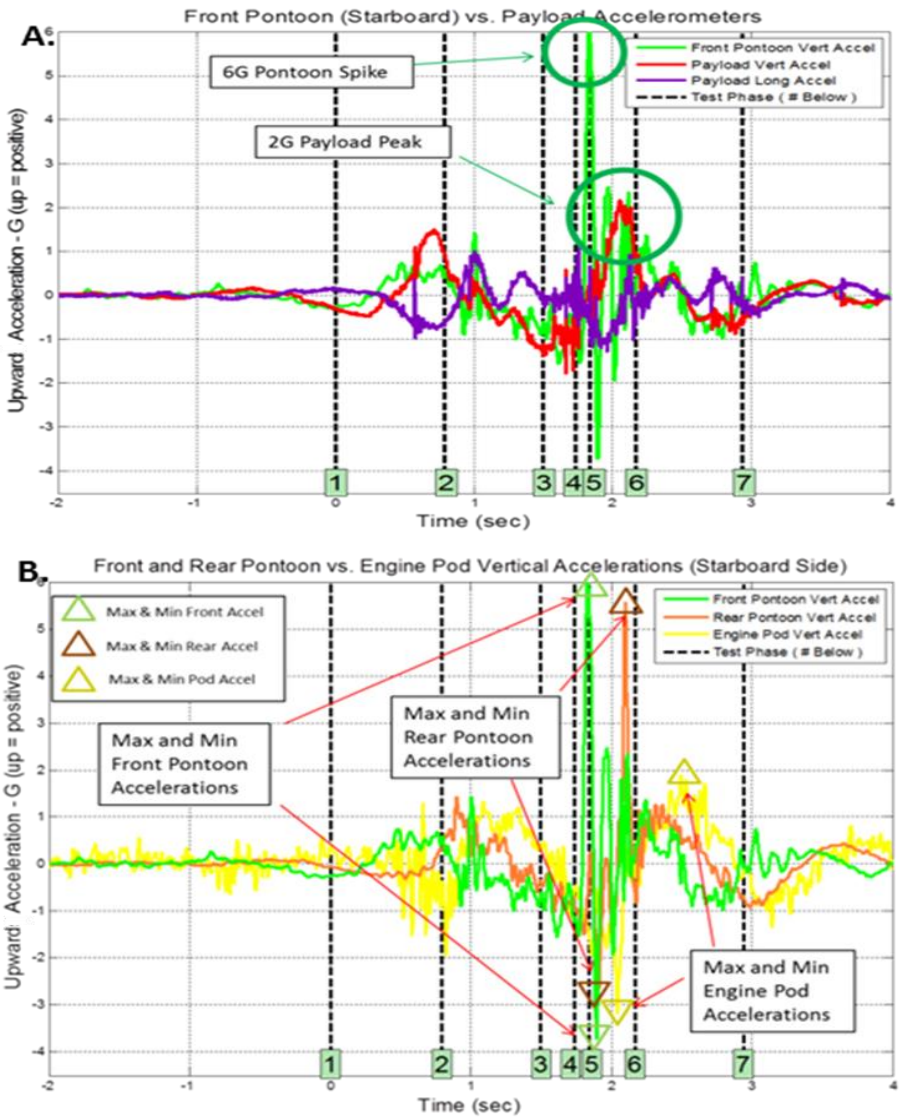

Figure 7.12: Phase 5/7 pontoon vs. payload acceleration (a) and pontoon vertical acceleration (b) comparisons

Figure 7.12(b) compares the acceleration levels at the front and rear of the pontoons, and at the rear of the engine pods during impact. There are large differences in the recorded impact levels at the various sensors. The maximum and minimum accelerations recorded from each sensor are:

- Front Pontoon: - 4g to 6g
- Rear Pontoon: - 2.5g to 5.5g
- Rear Engine Pod: - 3.5g to 2g

The front pontoon sensors register significantly greater vertical acceleration values than are recorded at the rear or pod sensors. This is expected for small craft and short wavelength events.

7.3.6 Phase 6/7: Maximum Compression

Phase 6 of the test follows the initial impact of the WAM-V with the water. During Phase 6 of the test, the suspension compresses heavily such that the operator re-contacts the seat and is launched forward by a sudden longitudinal deceleration of the payload. The operator's posture during Phase 6 is shown in the top right corner of Figure 7.13.

Figure 7.13: WAM-V orientation during Phase 6/7

During Phase 6 of the test, the engine pods rotate rapidly to their maximum upward rotational position, changing the thrust vector from the propulsion jets by a total of 15 degrees; this change in angle occurs in approximately 1/3 of a second. A plot of the rotation of the engine pods is shown as part of the next phase of the test in Figure 7.16(a).

The suspension displacement graph shown in Figure 7.14(a) shows the maximum level of travel used during the maximum compression phase. During Phase 6/7, the suspension uses over 90% of its available travel. The suspension's air springs are highly nonlinear throughout their stroke. Evidence of this nonlinearity is annotated in Figure 7.14(a); the change in the rate at which the suspension rebounds indicates an increase in the suspension's natural frequency when the suspension is close to the limits of its travel. As the suspension rebounds rapidly, the damping ratio also effectively decreases due to the increase in spring rate at high levels of displacement.

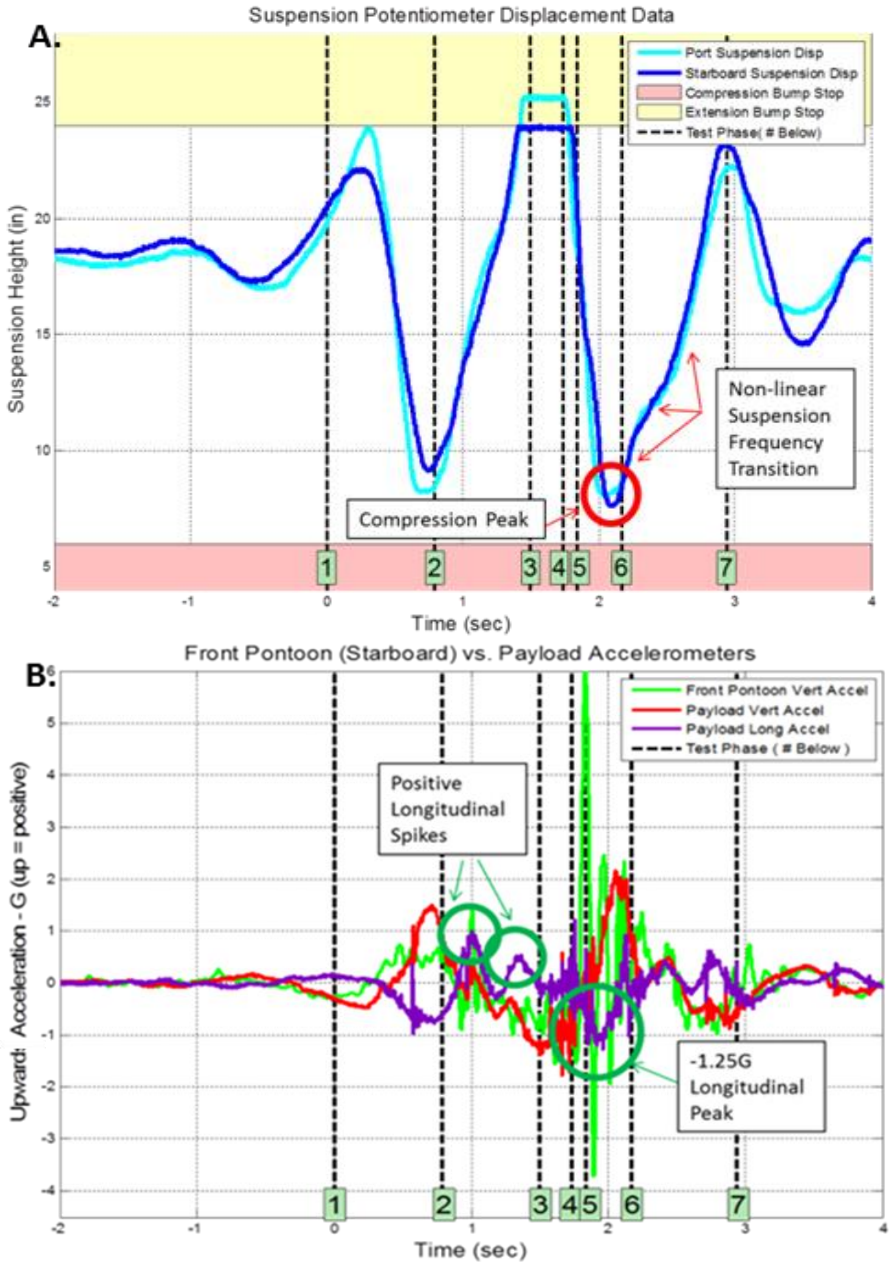

Figure 7.14: Phase 6/7 suspension displacement (a) and pontoon vs. payload acceleration (b) comparisons

The longitudinal acceleration plot in Figure 7.14(b) shows how the WAM-V's longitudinal dynamics impact its overall ride quality, and also possibly explains why the operator was thrown from the seat. The longitudinal acceleration plot shows two small positive acceleration peaks at the payload, followed by a -1.25g peak. The negative peak quantitatively explains how the operator's momentum essentially caused him to be thrown forward after the initial impact.

7.3.7 Phase 7/7: Secondary Oscillations

After the initial impact and maximum compression phases, the suspension unloads and smaller oscillations continue to occur due to the underdamped hydrodynamic stiffness of the pontoons reacting to much smaller wave inputs. The operator is now back in the seat, as shown in the top right corner of Figure 7.15, and is being subjected to far lower levels of vibration.

Figure 7.15: WAM-V orientation during Phase 7/7

Figure 7.16 shows that the engine pod angle changes by a total of 15 degrees during the test, reaching its maximum value five times, and its minimum value three times with little attenuation. The large number of angle changes demonstrates how the engine pod's limited damping properties tend to propagate the inputs throughout the entire test.

During Phase 7 of the test, 1g oscillations occur with relatively little damping on the engine pods, and the suspension oscillates for two to three more cycles before reaching the steady-state condition equivalent to Phase 1 of the test. The engine pod movement, as well as the deadband in the rear arch folding mechanism, allow unwanted longitudinal vibrations to be transmitted to the operator.

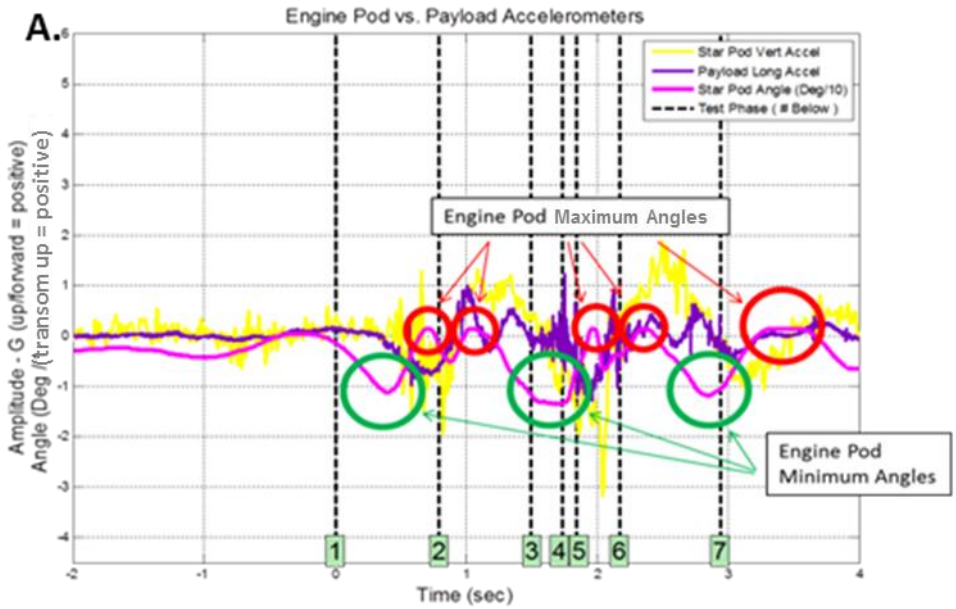

Figure 7.16: Phase 7/7 engine pod angle comparison

7.3.8 Conclusions from Single-Wave Input Testing

The single-wave input test has provided the following key information that can be used to improve the properties of the 33-ft WAM-V, as well as future WAM-V designs:

- The current suspension's performance in compression provides good attenuation of large vertical impacts, but poor attenuation of smaller impacts.
- Suspension improvements are necessary in rebound to reduce negative accelerations being transmitted to the payload and operator.
- A more linear passive suspension design would improve energy absorption and dissipation during heavy impacts.
- Increased damping, particularly in compression, might help to better control the unsprung mass of the pontoons.
- Longitudinal motion dominates the perception of ride quality. Engine pod motion and deadband in the rear arch largely contribute to this undesired behavior.

Based on the findings from this test and the rest of the WAM-V testing program, a new suspension system was designed with improved properties to be tested in a more severe rough water environment.

7.4 Rough Water Testing Analysis

Two separate days of rough water testing were conducted with the 33-ft WAM-V, operating in conditions that could be classified as between a Sea State 2 and a Sea State 3. The first test was conducted as part of the WAM-V summer testing program; the test was run at a speed of 15 knots with the original suspension system installed. The second test was conducted as part of the WAM-V winter testing program; the test was run at a speed of 10 knots with the second generation suspension system installed. Screenshots of the 33-ft WAM-V during the two of the largest wave events from the summer and winter testing programs are shown in Figure 7.17 and Figure 7.18 respectively.

Figure 7.17 33-ft WAM-V during summer rough water testing (original suspension)

Figure 7.18 33-ft WAM-V during winter rough water testing (second generation suspension)

The reason for the difference in speeds between the two tests comes from changes in the conditions in which the tests were run. At the testing location at the Naval Base in Norfolk, VA, the conditions for a typical summer day are considerably calmer than for a typical winter day. The majority of the rough water testing at the naval base is therefore conducted during the winter months. The conditions during the summer months are generally too calm; however, the test data collected during the summer on the particular test day was possible due to the conditions from a tropical storm in the Florida Panhandle (Tropical Storm Debby) trickling up the east coast.

7.4.1 Overview of Data Collected

As described in Section 7.2, the amount of testing data collected during both test days was limited due to component failures within the WAM-V's propulsion systems. During the summer test day, condensation at the bottom of the WAM-Vs fuel tanks caused the engine's spark plugs to foul and an intake valve to drop and contact one of the pistons. During the winter test day, an electrical malfunction of one of the throttle servos caused one of the engines to remain stuck in a partial throttle position. After the test was aborted, the throttle servo in the other engine pod also began to fail intermittently due to a similar electrical problem. Reliability issues are a difficult component of any marine development program; the failures of the WAM-V are more a reflection of the quality of the individual components selected for the prototypes, rather than an indication of the reliability of WAM-V technology as a whole. In fact, the WAM-V's structure greatly outperformed the powertrain units, with no significant failures during any of the testing programs.

Despite the limited testing times, significant data was still able to be collected on the 33-ft WAM-V operating in elevated sea conditions. Approximately 1 hour of data was collected during each test; the data analyzed in this section will consist of two different eight minute sections, one section from the stock suspension testing and the other section from the second generation suspension testing at the middle damper setting.

7.4.2 Sea Conditions during Rough Water Tests

The approximate sea conditions the WAM-V encountered during the rough water tests are available from the National Oceanic and Atmospheric Administration (NOAA) wind stations and wave buoys. NOAA forecasts wind speeds and wave heights that can be used to predict a suitable window for rough water testing. The predictions are available up to four days in advance, and are updated daily. An example of the NOAA wind speed and wave height estimation charts for the test site are shown in Figure 7.19.

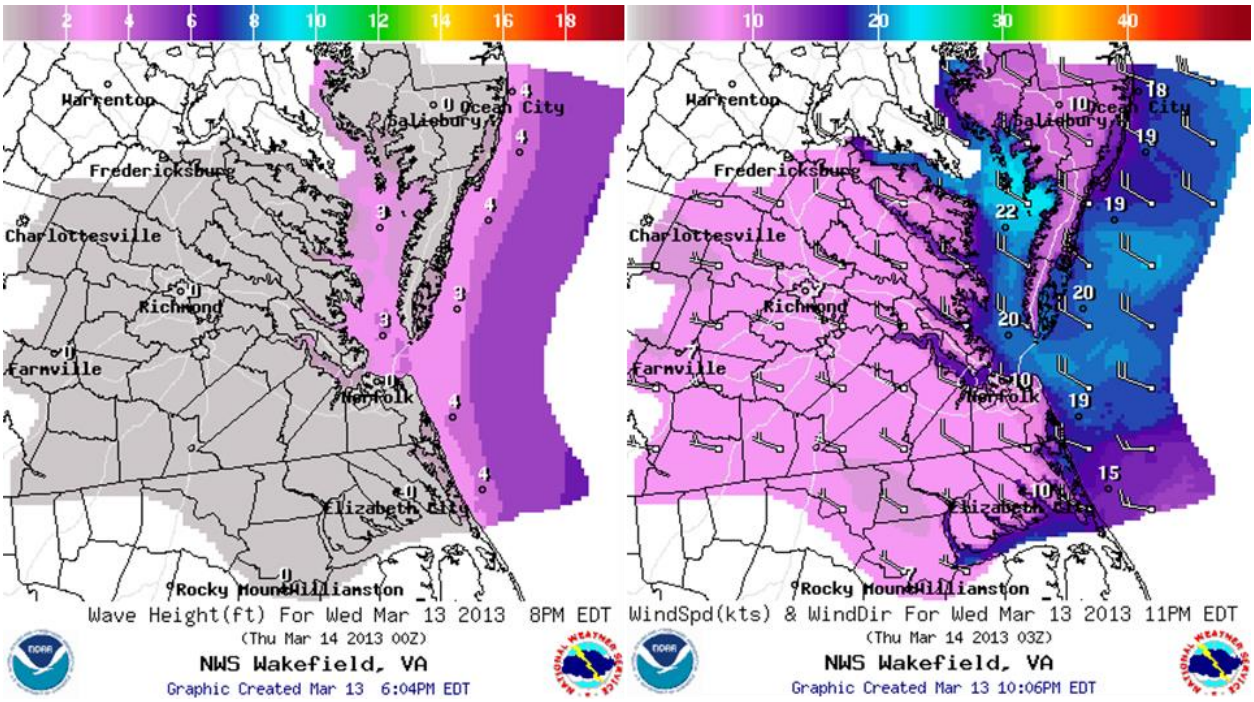

Figure 7.19 Wave height and wind speeds estimations available for test site

Figure 7.20 shows the GPS route map from the winter testing program, along with the location of the closest wave buoys and wind stations to the test site. The GPS unit had not yet been installed on the WAM-V at the time of the June 26th, 2012 rough water test; the route followed a similar path to the December 11th, 2012 (Day 1) GPS trace. Also shown on the map is the route taken during the second day of the winter testing program conducted on December 14th, 2012 (Day 2), which was run in a Sea State 1 condition. The data from this test is analyzed separately in Chapter 9 with a focus of applying Human Factors and Whole-Body Vibration Standards to the 33-ft WAM-V.

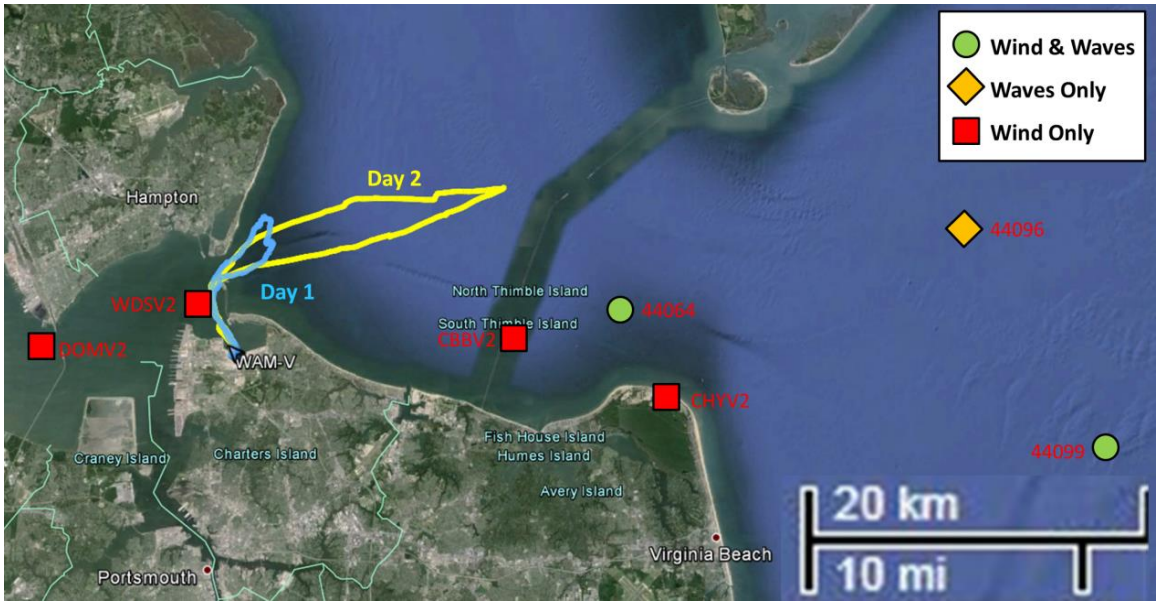

Figure 7.20 Location of wind stations and wave buoys relative to test site

The closest wave buoy is approximately 20 km away from the test site. This isn't close enough to describe the sea conditions at the test site accurately; also, the changes in water depth between the locations of the buoy and the test site will also skew the results. Despite the lack of proximity between the test site and the wave buoys, information can still be drawn about the relative wave heights between the testing days.

Portable wave buoys were not deployed for any of the tests analyzed in this chapter, although they were used during one other WAM-V on-water test. The use of portable buoys requires the WAM-V or the chase boat to loiter for at least 90 minutes while the buoy collects data. The buoys cannot be deployed and left alone during testing, because they are too difficult to find if they are not monitored continuously. Despite their inherent limitations, deploying portable wave buoys was planned to be part of the testing program, to be deployed following some of the tests. The two tests analyzed in this section were cut short due to reliability issues, so the buoys were not deployed following the tests. Future WAM-V testing should include instrumented buoy data as part of the analysis, preferably with some procedure for deploying and leaving the buoy alone, to be retrieved following the test.

Figure 7.21 shows the average wind speed measurement from the six wind stations for the three days of testing. Each of the measurements in this section are shown from the available stations in order from west to east. Correlating wind speed to significant wave height is an area of

considerable research. A mathematical method for estimating wave speed and wave height can be found in "Estimating Wave Height Distributions from Wind Speed Measurements" [71].

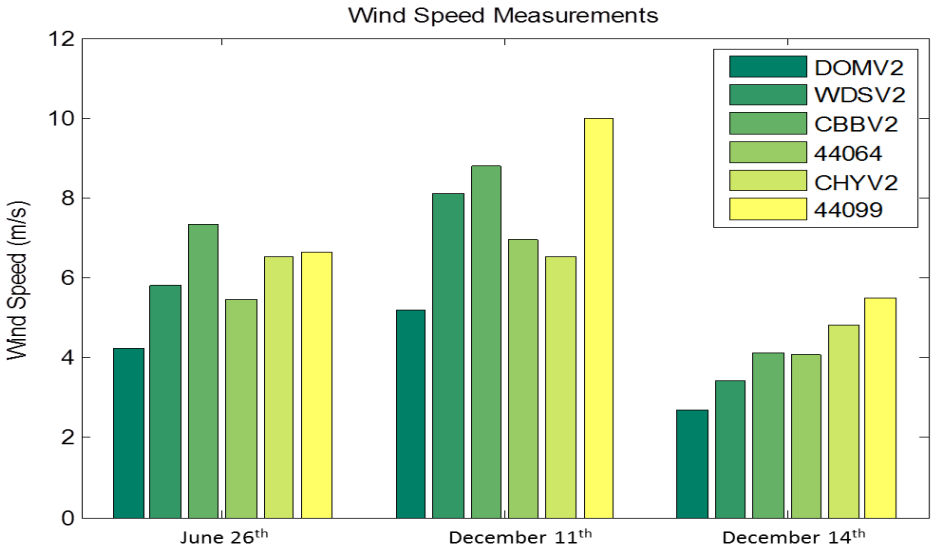

Figure 7.21 Wind speed measurements available for days of testing

Figure 7.22 shows the significant wave heights from the three days of testing, defined as the average of the one-third highest wave heights recorded. The wave heights are highest during the December 11th test, followed by the June 26th test. Wave heights also increase moving from shallow to open water (west to east).

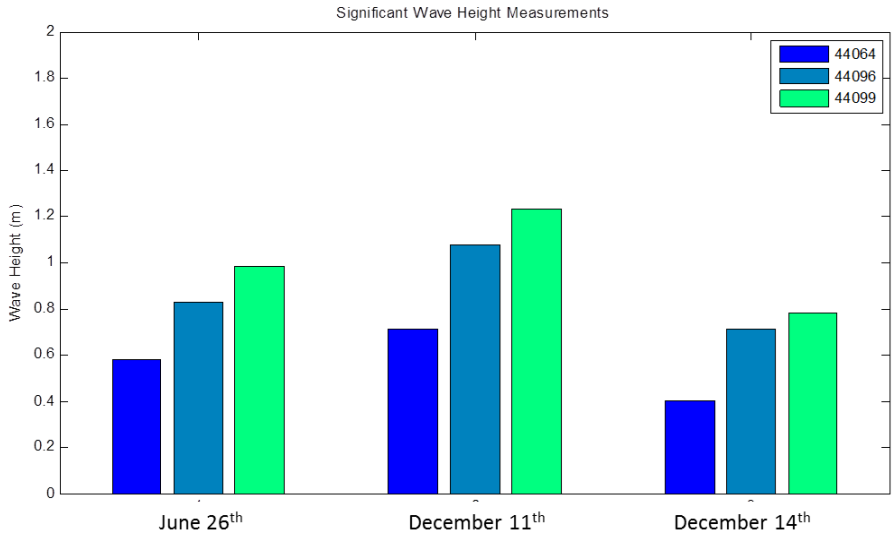

Figure 7.22 Significant wave height measurements available for days of testing

Figure 7.23 shows the dominant wave periods from the three days of testing, defined as the wave period with the maximum energy. The dominant wave periods are similar between the June 26th

and December 11th tests, and the periods are longer during the December 14th test when the wave heights were the lowest of the three tests.

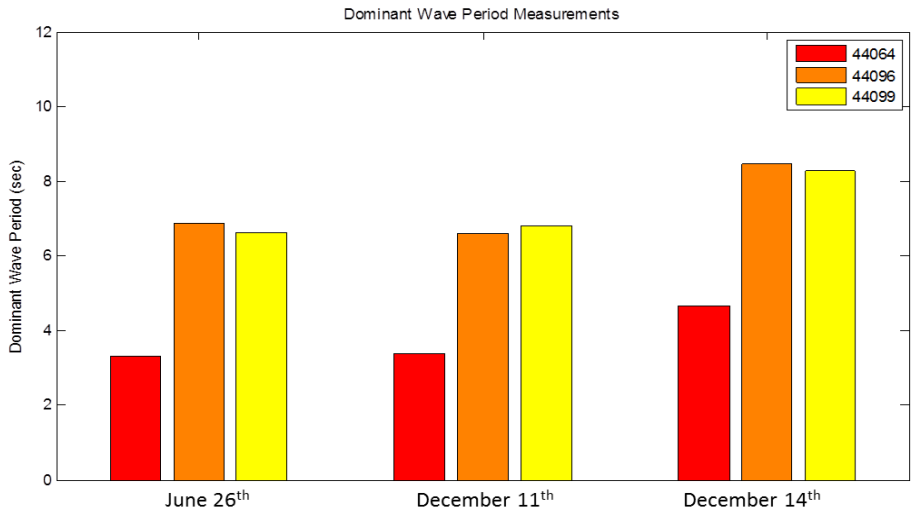

Figure 7.23 Dominant wave period measurements available for days of testing

Figure 7.24 shows the average wave periods from the three days of testing, using the average of all of the wave periods recorded. The average wave period is not available from Station 44064, only Station 44096 and Station 44099 report the average wave period data. Like the dominant wave period data, there appears to be an inverse correlation between wave heights and average wave period for the three testing days.

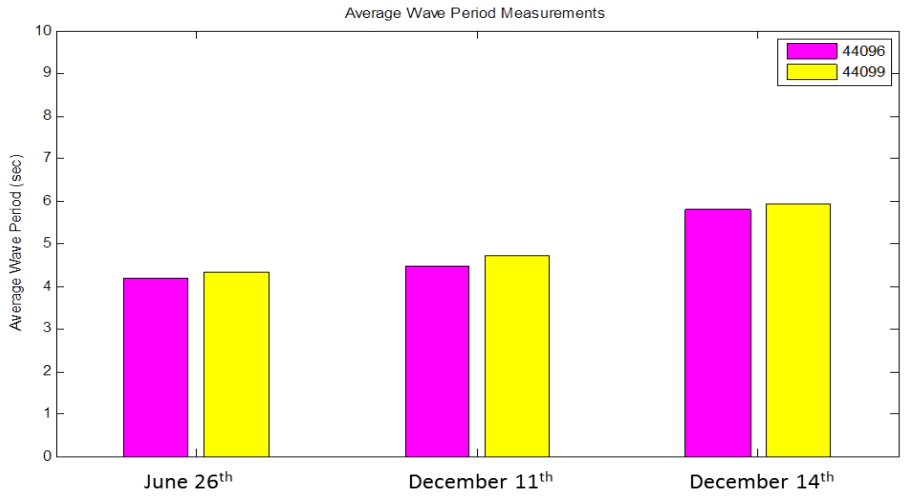

Figure 7.24 Average wave period measurements available for days of testing

7.4.3 Performance Comparison during Rough Water Tests

In this section, a statistical comparison is given between the data collected during the summer and winter testing programs, in an attempt to determine the impact of the changes to the suspension system on the ride quality of the 33-ft WAM-V. The summer tests were conducted with the original suspension system and the winter tests were conducted with the second generation suspension system. Unfortunately, during the winter testing program, a back to back comparison was not able to be run between the two suspension systems as originally planned, so some extrapolation is required to compare the two datasets, and the results may have been different if the two suspension systems were able to be compared in equivalent conditions.

For the comparison, the accelerometer data recorded at the front of the pontoons will serve as the baseline to compare the suspension's relative performance between the accelerations at the pontoons and the accelerations at the payload tray. The original suspension (summer) and second generation (winter) tests were conducted in different sea conditions and at different test speeds, making a direct correlation difficult to quantify. The purpose the comparison is to determine differences between the two suspension systems, not the difference between testing during the summer and winter month as might be suggested by the vernacular of "summer" and "winter" tests. For the comparison, each data set consists of an eight minute section of data; the data is analyzed by computing the acceleration peaks from each data set, using the method outlined in Section 2.5.8. The method of processing the data to analyze the peaks is outlined in Table 7.2.

Table 7.2 Steps for processing rough water acceleration data

#	Step:
1	Acceleration data is passed through a 10 Hz low-pass filter (5^{th} order Butterworth filter type).
2	The RMS of the filtered acceleration data is computed.
3	The number of peaks are calculated from the peaks greater than RMS with a 0.5 second peak separation criteria.
4	The peaks are sorted in order of increasing magnitude.

The results from Steps 1-3 of Table 7.2 are shown in Figure 7.25 with the peaks still in the order they occurred in the dataset, so that the time between peaks can be calculated for each data set.

The average time between peaks is listed for the two datasets for both of the pontoons, along with the standard deviation of the average time between the peaks.

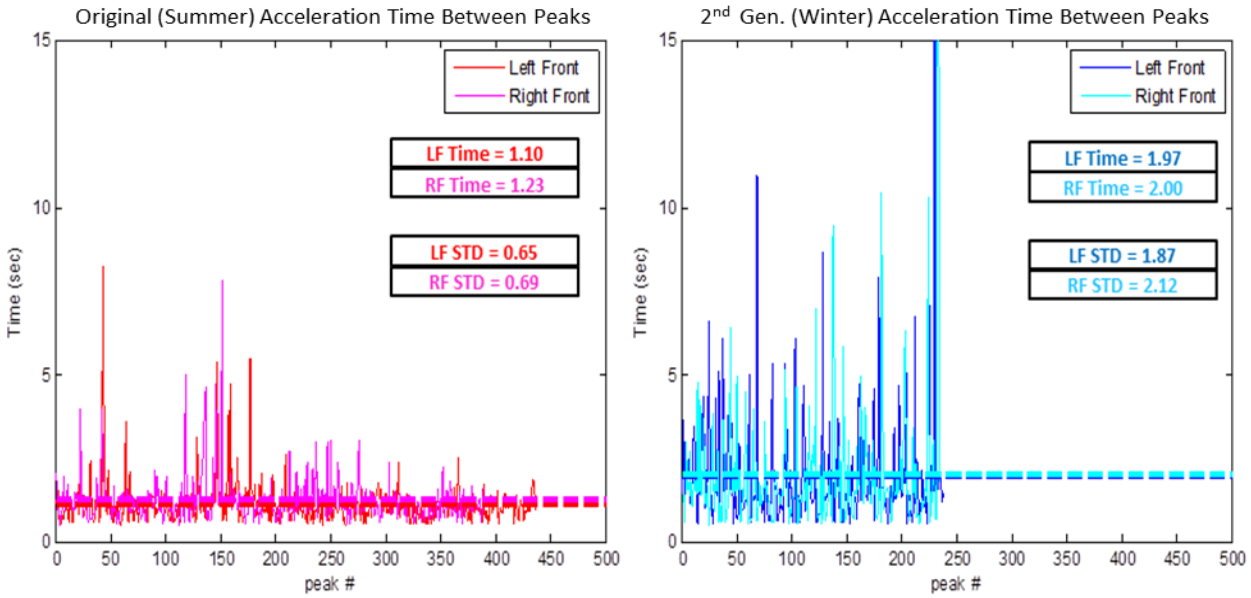

Figure 7.25 Time between vertical acceleration peaks measured at pontoons

The average time between peaks (averaged between the left and right pontoon data) is 1.165 seconds for the original suspension (summer) data and 1.985 seconds for the second generation (winter) data. This corresponds to average input frequencies of 0.86 Hz and 0.50 Hz respectively. The standard deviations between the peak times are also listed in Figure 7.25; the winter data has a larger standard deviation relative to the time peaks than does the summer data, indicating that the winter data is less regular and more stochastic in nature.

The pontoon data from the summer rough water test contains more peaks than the data from the winter test. There are two reasons that this occurred: First and most significantly, the summer test was run at a higher speed than the winter test (15 vs. 10 knots), because the winter test conditions were more severe than the summer test conditions. Second, the criterion for determining the minimum peak amplitude is based on the RMS of the dataset. The RMS of the winter dataset is higher than the summer dataset, as shown in Figure 7.26, so some of the peaks in the winter data that would have met the summer minimum criteria are not counted as part of the dataset. The peaks are shown sorted in order of magnitude in Figure 7.26 and the average of the one-third, one-tenth, and one-hundredth highest peaks for each dataset is shown.

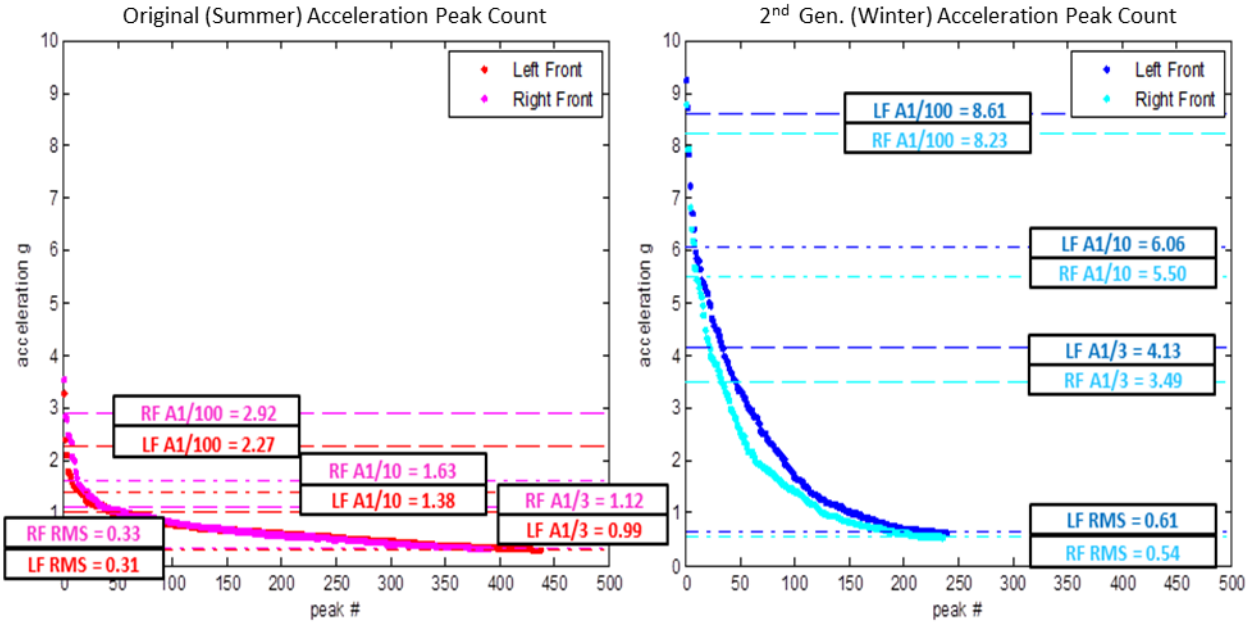

Figure 7.26 Pontoon vertical acceleration peaks analysis

Based on the pontoon acceleration data, the winter test conditions are significantly more severe than the summer test conditions for all the statistical acceleration measures shown in Figure 7.26. Interestingly, the right front data is more severe than the left front data during the summer testing and the left front data is more severe than the right front data during the winter testing. This indicates a difference in the primary wave direction between the two tests, since the tests were run at approximately the same heading in the same testing location, albeit on different dates. Also, since the data is filtered at a relatively low cutoff frequency (10 Hz, as per the standard method [11]), the magnitude of the acceleration peaks is reduced compared to the peaks in the unfiltered data. The difference is on the order of ~20%, depending on the amplitude of the peak. The low-pass filter is included as part of the method in an attempt to filter out local and structural vibrations from impacting the results. This should be considered as part of the analysis.

7.4.4 Payload Vertical Acceleration Analysis

Figure 7.27 shows the filtered and sorted vertical acceleration data peaks recorded from the accelerometer on the payload tray near the operator during both the summer and the winter tests. The positive (impact) peaks are shown, with the acceleration due to gravity removed from the dataset.

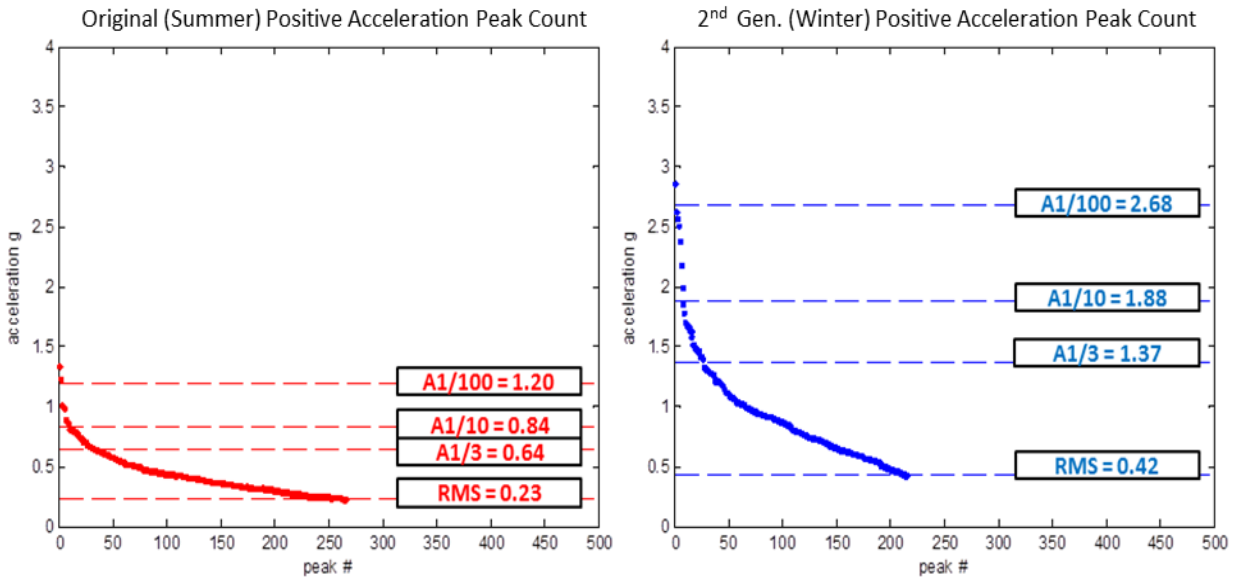

Figure 7.27 Positive acceleration peaks analysis comparison

Compared to the data from the pontoons, the data at the payload accelerometer shows significant reductions in the acceleration peaks for all of the statistical metrics, except for the RMS acceleration, which is of roughly similar magnitude between the payload and the pontoons. The winter testing appears to show more relative improvement than the summer data; further investigation is required, and is performed via a Ride Quality Index analysis in the next section. Figure 7.28 shows the same analysis for the negative acceleration peaks from the vertical accelerometer for the summer and the winter test data.

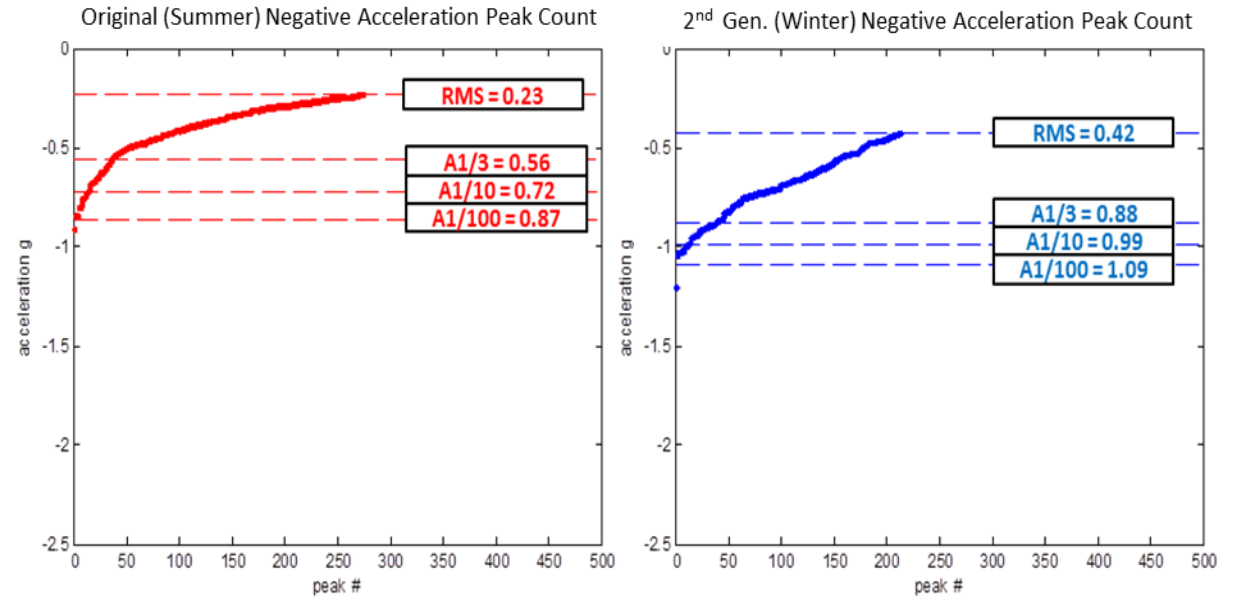

Figure 7.28 Negative acceleration peaks analysis comparison

Comparing the acceleration peaks in Figure 7.27 and Figure 7.28, the positive and negative peaks in the summer data are roughly similar in magnitude, while the winter data has higher positive acceleration peaks compared to the negative acceleration peaks. The negative acceleration peaks in the winter data are reduced to a comparable level to the summer data, even though the winter tests were run in significantly more rough conditions. Since one of the goals of the second generation suspension design was to reduce the negative accelerations experienced by the operator during the single-wave and summer rough water tests, this is a very positive result.

A more detailed analysis between the datasets is required and will be performed using the method of the Ride Quality Index detailed in Section 2.5.8; the Ride Quality Index comparisons are detailed in the next section.

7.4.5 Ride Quality Index Comparison Analysis

Figure 7.29 shows the computed Ride Quality Index for each of the fours metrics shown in Figure 7.27 and Figure 7.28, comparing the vertical accelerations at the pontoons and the accelerations at the payload tray. The Ride Quality Indexes are all greater than 0, indicating improved conditions at the payload tray relative to the pontoons.

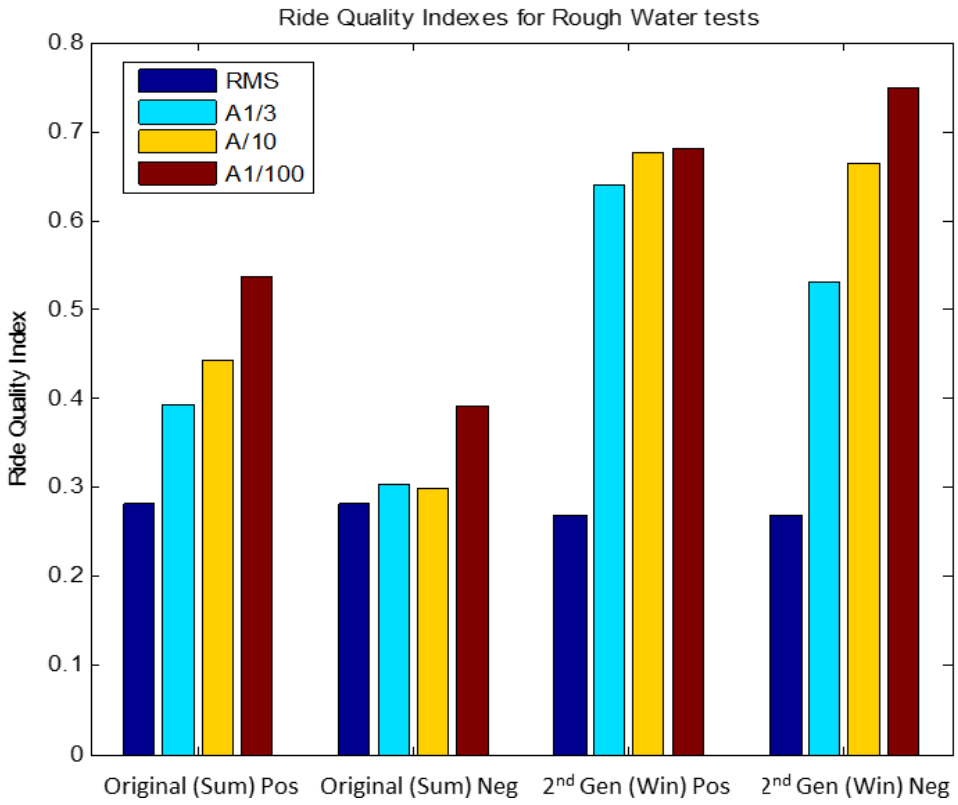

Figure 7.29 Ride Quality Indexes for WAM-V tests

Comparing the summer and the winter acceleration data, the Ride Quality Indexes appear to be similar for the RMS data, and improved for the other three acceleration metrics. The Ride Quality Index is greatest for the most severe acceleration peaks, indicating that both suspension systems are more effective for large acceleration events.

To give a more detailed comparison, the Ride Quality Indexes from the summer testing are shown plotted against the winter Ride Quality Indexes in Figure 7.30. On Figure 7.30, the dotted line where y = x represents the region of the graph where the summer and winter testing showed equal performance as defined by the Ride Quality Indexes. The RMS accelerations happen to fall very close to this line. Upward shifts from the line indicate improved ride quality from the winter test, and lateral shifts to the right indicate improved quality from the summer tests. Shifts along the dotted line indicate equally improved or diminished performance from both tests.

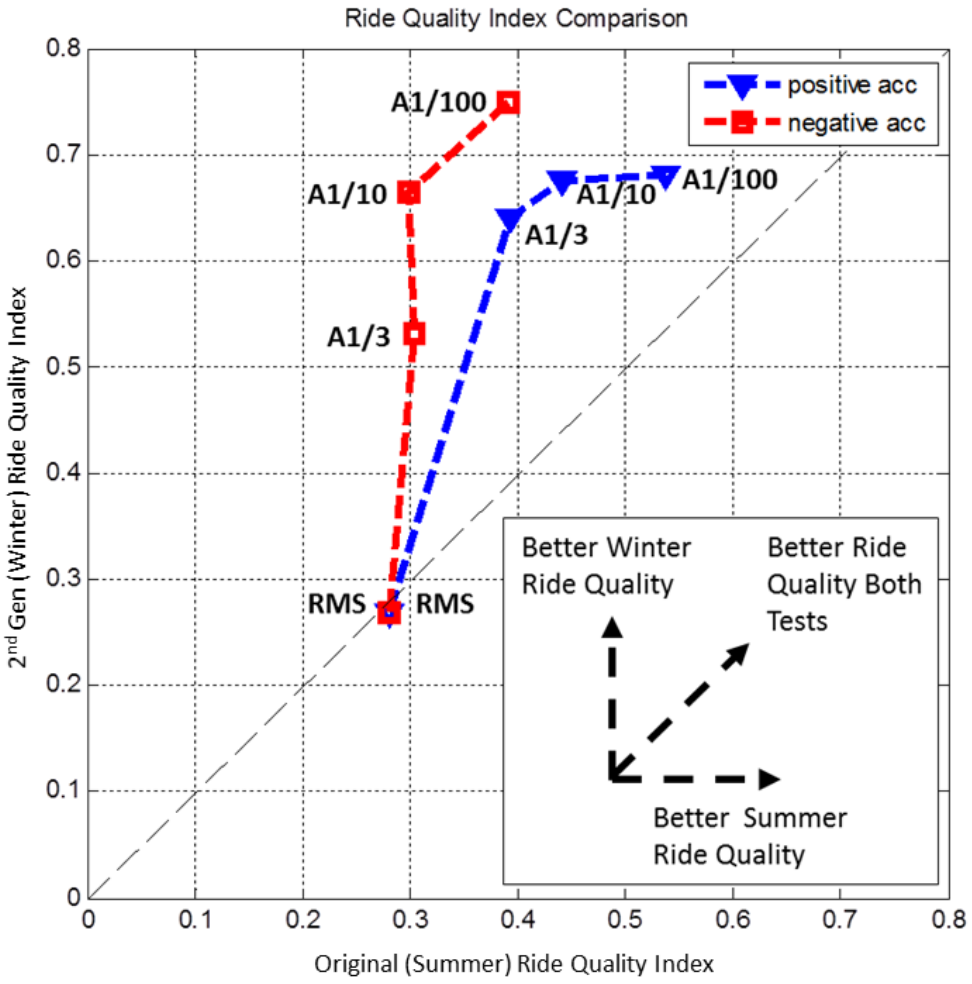

Figure 7.30 Ride Quality Index comparison plot

The datasets shown in Figure 7.30 represent the ratios of the winter and summer Ride Quality Indexes, shown to highlight the performance differences between the two tests. The plots for the negative and positive peaks show improvements from the winter tests, except for the RMS acceleration which shows equal performance.

The positive acceleration shows the best results for the A1/3 accelerations and the A1/10 accelerations, the A1/100 accelerations are still an improvement over the original suspension system; however, the slope of the line between the A1/10 and the A1/100 is less than the slope of the y = x line, indicting the performance is beginning to decline. There was one event during the winter testing where the suspension bottomed out in compression. It is likely that this event is the reason this trend appears in the A1/100 accelerations. This event only occurred because the ride height was set to a lower than optimal height for the test because the conditions at the dock before the test were too rough for the ride height to be adjusted once the WAM-V was unfolded on the water. Had the suspension properly adjusted, it is unlikely it would have bottomed out at all during the test.

The negative acceleration Ride Quality Indexes show great improvements from the second generation suspension used during the winter testing compared to the original suspension system used during the summer testing. The improvements are significant for the A/13, A1/10, and A1/100 acceleration metrics. Between the three metrics, the improvements are greatest between the RMS and the A1/3 accelerations and between the A/13 and the A1/10 accelerations. The interpolated lines between these metrics are both nearly vertical, indicating that the Ride Quality Index is improving for the winter data and not improving for the summer data. Between the A1/3 and the A1/10 accelerations, the slope of the line actually goes past vertical, indicating that the Ride Quality Index of the winter data is improving while the Ride Quality Index of the summer data is actually slightly decreasing. This can possibly be attributed to the suspensions in the summer data contacting the limit straps for accelerations magnitudes greater than the A1/3 accelerations, making the ride quality worse in those cases. The improvement in the summer ride quality between the A1/10 and A1/100 peaks occurs despite the suspension contacting the straps, because the wave inputs are becoming more severe than the rebound effects. The limit straps were not reached during the winter testing. The analysis shows good improvements with the second generation suspension system compared to the original suspension on the 33-ft WAM-V.

7.4.6 Longitudinal Motion Analysis

The longitudinal motion of the payload tray was found to create an undesirable response at the operator's location. The motion was found to be due to compliance in the rear arch folding mechanism. The compliance has not been directly measured by sensors on the WAM-V; however, longitudinal motion due to the compliance was captured on video data during the summer rough water testing. Figure 7.31 shows three screenshots of the rear arch in its middle, forward and rear positions due to the compliance. The screenshots were taken by a GoPro camera mounted under the payload tray, so for a rigid structure there would be no difference between the three images. The effects of the compliance are studied in further detail in Chapter 10 when the 33-ft WAM-V was tested on the 2-post rig. The effects of the compliance are most apparent in mild sea states, such as during the Sea State 1 testing analyzed in Chapter 9.

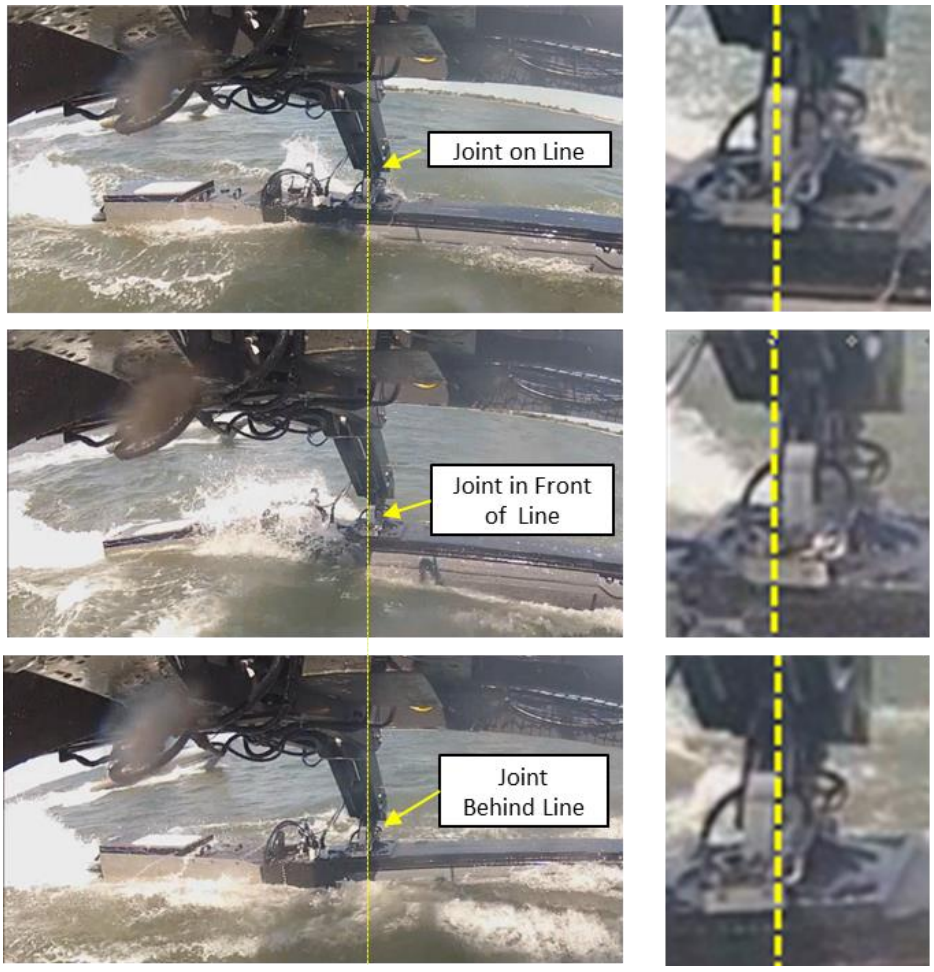

Figure 7.31 Video analysis of WAM-V rear arch compliance

7.5 Conclusions and Recommendations for Further Research

The results and data analysis presented in this chapter were highly successfully in generating a dataset for analysis of the 33-ft WAM-V. The data analysis has provided great insight into the WAM-V's dynamics that occur during on-water testing. The results from this chapter can be compared with the static testing and the laboratory testing of the WAM-V detailed in Chapters 6 and 10 respectively, as well as the simulations detailed in Chapters 8 and 11. This section details the results, conclusions, and recommendations from the various on-water tests.

7.5.1 Conclusions Based on Single-Wave Input Testing

The single-wave input test was highly beneficial for analyzing the WAM-V's dynamics performance in a concise manner. The test results were far easier to quantify and could be analyzed in greater detail than the data from the rough water tests. The biggest drawback to the single-wave test is that is a difficult test to repeat across different testing days because it requires the presence of a large freighter ship with a suitable wake for testing. The advantage of this type of testing is that it doesn't require rough waters. There is also no guarantee that wakes will be similar between different ships. For smaller WAM-Vs, this type of test would be easier to conduct; however, it would be difficult to scale this test for WAM-Vs similar in size to the 100-ft Proteus, since the tests would require a larger wake than required for the 33-ft WAM-V.

7.5.2 Conclusions Based on Rough Water Testing

Comparison of the two rough water tests analyzed in this chapter showed improved performance of the second generation suspension system over the original suspension system. The second generation suspension showed greatest improvement in attenuating negative accelerations from being transmitted to the operator, which was one of the primary goals of the suspension design. The use of the Ride Quality Index was helpful for analyzing the data from different tests and different suspension systems, giving meaningful and concise results from the analysis. Using the attenuation levels between the pontoon and the payload tray continues to be the best measure for quantifying the vertical dynamics of WAM-Vs in an elevated sea state. The longitudinal dynamics of WAM-V require further analysis; the compliance of the rear arch transmits significant longitudinal accelerations to the operator. The elevated operator position and the location of the aft suspension joint also contribute to longitudinal accelerations being transmitted to the operator.

Chapter 8 Quarter-Boat Simulation of the 33-ft WAM-V

The following chapter details the application of the Quarter-Boat model developed in Chapter 5 to simulate the performance of the 33-ft WAM-V's suspension system detailed in Chapter 6. A method for scaling the Quarter-Boat model from the 8 inch pontoon diameter on the Quarter-Boat test rig to a nondimensional Quarter-Boat model, and scaling the model to a 21 inch diameter pontoon (to match the 33-ft WAM-V), is presented. The scaled Quarter-Boat model is configured with the properties of the original suspension system, and a study is conducted on the 33-ft WAM-V's dynamics using the data from the single-wave input test analyzed in Chapter 7.

8.1 Chapter Overview

- Section 8.1 provides an overview of the chapter.
- Section 8.2 discusses theories of scaling between models of different sizes.
- Section 8.3 details the scaling strategy for the Quarter-Boat model.
- Section 8.4 validates the Quarter-Boat parameter scaling against unscaled simulations.
- Section 8.5 validates the scaling approach via comparisons with drop test data from a cylinder model and test data from an external source.
- Section 8.6 compares the Quarter-Boat model with the single-wave input test data.
- Section 8.7 discusses the application of the Quarter-Boat model to aid with the design of the second generation suspension design for the 33-ft WAM-V.
- Section 8.8 discusses the conversion of the Quarter-Boat model to base-excitation inputs.
- Section 8.9 provides a discussion of the results and conclusions from the chapter.

8.1.1 Significant Contributions

This chapter details the first nondimensionalized suspension model for a marine vessel. The model provides a straightforward scaling strategy for applying the novel method of modeling the vertical hydrodynamics of the pontoon/water surface interaction detailed in Chapter 5 with the Quarter-Boat model. The revalidation of the Quarter-Boat model against on-water testing data is unique. Finally, the two part comparison of a single degree of freedom model and a two degree of freedom model is the first of its kind, and provides insight into the dynamics discussed in other chapters, extending the knowledge base on marine suspension dynamics.

8.2 Overview of Scaling Theory

For scaled model testing, the scaled model is usually a physically scaled down version of a full-scale prototype. Model scaling is most useful when it is not practical to test a full-scale prototype for reasons of time, cost, or prototype availability; or when data already exists for another prototype of different dimensions. Instead of testing with the prototype itself, a scaled model can be designed and subjected to similar conditions as the full-scale prototype. Modeling of scaled systems requires that the model and the prototype be similar geometrically, kinematically, and dynamically, as described in this section.

8.2.1 Geometric Similitude

The most common form of scaling criteria is geometric similitude, in which the model and the full-scale version are scaled by a characteristic length. Typically, a model is a scaled down version of the full-scale prototype, although there are exceptions where the model is made to a larger scale than the prototype. The principle of geometric similitude implies that the model and the prototype are related by a characteristic length (λ), where:

$$\lambda = \frac{L_{model}}{L_{prototype}} \quad [72]$$

8.2.2 Kinematic Similitude

Kinematic similitude describes the similitude of motions between the model and the prototype. Similitude of motion requires a time-dependent scale factor (τ), defined as:

$$\tau = \frac{t_{model}}{t_{prototype}} \quad [72]$$

For some model parameters, both kinematic and geometric scaling are required to satisfy the similitude of a particular parameter. The velocity (distance/time) scale factor (φ), fundamentally scales a geometric parameter over a kinematic parameter, therefore:

$$\varphi = \frac{\lambda}{\tau} \quad [72]$$

8.2.3 Dynamic Similitude

Dynamic similitude pertains to the requirement for similitude between the scaling of the external forces and the inertial forces acting on the model and the full-scale prototype. Dynamic

similitude is often expressed in terms of either the pressure scale factor (π), or the energy scale factor (ε), defined as:

$$\pi = \rho\varphi^2 \qquad \text{and} \qquad \varepsilon = \pi\lambda^2 \quad [72]$$

Note: For scaling the Quarter-Boat and the WAM-V, ρ = density scale factor = 1.

8.2.4 Buckingham Pi Theorem

The Buckingham pi theorem is based on dimensional analysis, centering around the idea of substituting a set of dimensionless numbers for the dimensional physical variables that describe the dynamics of a system. The dimensionless numbers are ratios of the physical variables, which reduces the number of variables needed to physically describe a system. The Buckingham pi theorem states that two systems are dynamically similar if both systems, by the selection of the same dimensionless numbers, yield the same nondimensional differential equation [73].

Dimensional analysis procedures, such as the Buckingham-pi theorem, can be used to predict the behavior of important physical parameters in a dynamic system. Table 8.1 lists some dimensionless numbers (pi terms) governing the dynamics of physical systems.

Table 8.1 Important pi-terms and the physical effects they govern [72]

physical effect	reference name:-	π-term	scale factor
compressibility	Mach number:-	$\frac{u}{c}$	$\varphi = \frac{c_m}{c_p}$
gravity	Froude number:-	$\frac{L}{gT^2}$ or $\frac{u^2}{gL}$	$\alpha = \frac{g_m}{g_p}$
pressure	Thomas number:-	$\frac{P}{P_v}$	$\pi = \frac{(P_v)_m}{(P_v)_p}$
surface tension	Weber number:-	$\frac{PL}{\nu}$	$\pi\lambda = \tilde{\nu} = \frac{\nu_m}{\nu_p}$
viscosity	Reynolds number:-	$\frac{uL}{\gamma}$	$\tilde{\gamma} = \frac{\gamma_m}{\gamma_p}$

u: particle velocity — c: acoustic velocity
L: characteristic length — g: acceleration due to gravity
T: response time — P_v: vapour pressure
v: surface tension — γ: kinematic viscosity

8.2.5 Shortcomings of Dimensional Analysis

Dimensional analysis may reveal that multiple dimensionless numbers (pi groups) affect the dynamics of a model, causing a mismatch between pi groups. One such example is the evaluation of a $1/50^{th}$ scale submarine in a water tank [73]. The drag on the submarine depends on both the Reynolds number (viscous friction) and the Froude number (energy lost to wave propagation). The Reynolds number predicts that the submarine would have to travel at 50 times the full-scale speed, while the Froude number predicts 0.014 times the full-scale speed [73]. Both conditions cannot be satisfied simultaneously. To solve this problem, the surface of the scaled model can be artificially roughened, such as by attaching a piece of sandpaper near the bow [73]. For models with large scaling factors compared to the full-scale prototypes, correlation between pi groups for the model and the prototype can be difficult to achieve; therefore, it is wise to test with a model as close to the size of the prototype as is practical.

8.3 Scaling of Quarter-Boat Parameters

In order for the results from the Quarter-Boat testing and modeling to be useful to the design and simulation of future WAM-Vs, the Quarter-Boat model needs to be able to be scaled to a variety of pontoon sizes so simulations can be run for a variety of masses, dimensions, and suspension configurations. Furthermore, scaling of the model must be intuitive enough that the model can be easily validated; retesting with the Quarter-Boat test rig should not be required, nor should a new Quarter-Boat test rig be required for testing pontoons of different sizes.

8.3.1 Scaling Approach

The results from the Quarter-Boat test rig will be scaled in a four-step process. First, the properties of the Quarter-Boat model will be nondimensionalized. Second, the Quarter-Boat model will be scaled to represent a model with a pontoon diameter of 21 inches (diameter of the 33-ft WAM-V's pontoons), and the results will be compared with the unscaled simulations. Third, the Quarter-Boat model will be scaled down in size to simulate cylinder drop test data gathered from an external source. Finally, once the first three steps have been validated, a model with parameters that represent the properties of the 33-ft WAM-V will be simulated and compared with the single-wave input test documented in Chapter 7.

8.3.2 Scaling Parameters

All dimensions will be scaled based on the Froude scaling parameter listed in Table 8.1. Unlike using Froude scaling to compare the properties of ships of different sizes, the characteristic length around which the model will be scaled is the diameter of the pontoons, rather than the ship's (or the pontoon's) overall length. Table 8.2 lists the key scaling coefficients for creating a nondimensional Quarter-Boat model based on Froude scaling. The velocity squared and cubic velocity terms are included in the table for scaling with different nonlinear damping models.

Table 8.2 Froude scaling laws for key model parameters

Parameter:	Scaling Coefficient:
Displacement	D
Velocity	U
Velocity^2	U^2
Velocity^3	U^3
Acceleration	U^2/D
Time	D/U

Where U = Froude number * $\sqrt{g * D}$

8.3.3 Scaling of Dimensions

For applying Froude scaling to the Quarter-Boat models, a number of simplifications are possible. The acceleration due to gravity is not scaled between the model (8 inch pontoon diameter Quarter-Boat model) and the prototype (Quarter-Boat model scaled to a 21 inch diameter pontoon). The majority of the scaling is dependent on the ratio of the pontoon diameters between the model and the prototype.

For comparing the Quarter-Boat model with the 33-ft WAM-V, the pontoons need to be scaled from 8 to 21 inches prior to the first round of simulations. For validating the scaling, the pontoon length will be held constant at 8 feet. The pontoon length is not scaled because the pontoon's interaction with the waves is modeled as a purely two dimensional effect, pontoon length is assumed to have a linear relationship with all the scaled parameters. The drop heights are also scaled linearly based on the change in pontoon diameters to satisfy the geometric similitude between the scaled model and the prototype. Since the model and prototype fall at the same rate,

scaling the drop height will cause the model and the prototype to contact the water surface at different simulation times, which will impact the relative timing of other key events in the simulations as well. This is dealt with by also scaling the time axis of the output data, the scaling is detailed in Section 8.4.

8.3.4 Scaling of Mass Properties

The mass of the system is scaled so that the same percentage of the pontoons are submerged at the static waterlines once the simulations have reached steady state. This implies that dynamic similitude is achieved between the model and the prototype via similitude of the external forces between the two systems. For the scaled static waterlines to match between the model and the prototype, the model mass is scaled by the square of the ratio of the diameters (D) using the following formula:

$$m_2 = m_1\left(\frac{D_2}{D_1}\right)^2$$

8.3.5 Scaling of Hydrostatic Restoring Force

The hydrostatic restoring force (spring rate) of the Quarter-Boat model is established directly from Archimedes' Principle. This means that changes in the restoring force are based solely on the volume of the pontoon submerged in the model or the prototype, making the scaling trivial between different hull forms. For scaling a cylindrical pontoon to a different diameter with the same overall length, the force will scale by the ratio of the pontoon diameters squared, for a given percentage of the pontoons submerged.

8.3.6 Scaling of Water Damper Rates

For scaling the hydrodynamic damping forces, the method of scaling depends on the damping model used. Two different damping models are discussed in Section 5.8.2.3 for modeling the Quarter-Boat test rig data. For a bilinear damping model with different damping rates for the impact (high velocity) and secondary (low velocity) oscillations, the damping forces (d) will each scale by the formula based on the ratio of the pontoon diameters (D) for a given velocity:

$$d_2 = d_1\left(\frac{D_2}{D_1}\right)^{1.5}$$

The location of the transition point between the sets of two linear damping rates using a bilinear damping model will also be scaled using the formula above. For other nonlinear damping models, which may include second order and cubic terms with respect to the velocity of the pontoon, the damping forces will be scaled by the following formulas, based on the ratio of the diameters of the pontoons:

$$d_2 = d_1\left(\frac{D_2}{D_1}\right) \text{ (2^{nd} order)} \qquad \text{and} \qquad d_2 = d_1\left(\sqrt{\frac{D_2}{D_1}}\right) \text{ (cubic)}$$

8.3.7 Scaling of Suspension Parameters

For scaling the two degree of freedom Quarter-Boat models, the change in spring force as a function of displacement is scaled linearly for a given stiffness, based on the ratio of the pontoon diameters. The natural length of the springs is also scaled linearly with respect to the ratio of the diameters. The small amount of damping added to the suspension system of the two degree of freedom Quarter-Boat model was modeled as a linear function of velocity, so scaling the suspension damping forces is a function of the square root of the pontoon diameters, as with the scaling formula shown for a bilinear damping model.

8.3.8 Model Limitations

The Quarter-Boat model can be implemented to analyze the vertical dynamics of the 33-ft WAM-V, incorporating the vertical dynamics of the pontoons into the simulations. The following parameters, however, are not considered within the models and require separate analysis methods not covered in this chapter.

- Pitch inputs
- Effects of the central spherical joint on the front arch
- Longitudinal dynamics

The limitations listed above can have a significant effect of the WAM-V's overall dynamics. Other analysis methods, such using the 6-post model, and testing with the 2-post rig, are used to analyze these effects separately in other chapters of this dissertation. This chapter focuses on the suspension's impact on the WAM-V's vertical acceleration performance.

8.4 Simulation Results Comparison

The scaled Quarter-Boat simulations can be compared with the unscaled Quarter-Boat simulations detailed in Chapter 5, as well as the Quarter-Boat test rig data. Figure 8.1 shows the pontoon and suspension displacement simulation results for the two degree of freedom Quarter-Boat model and the Quarter-Boat model scaled to the diameter of the 33-ft WAM-V's pontoons.

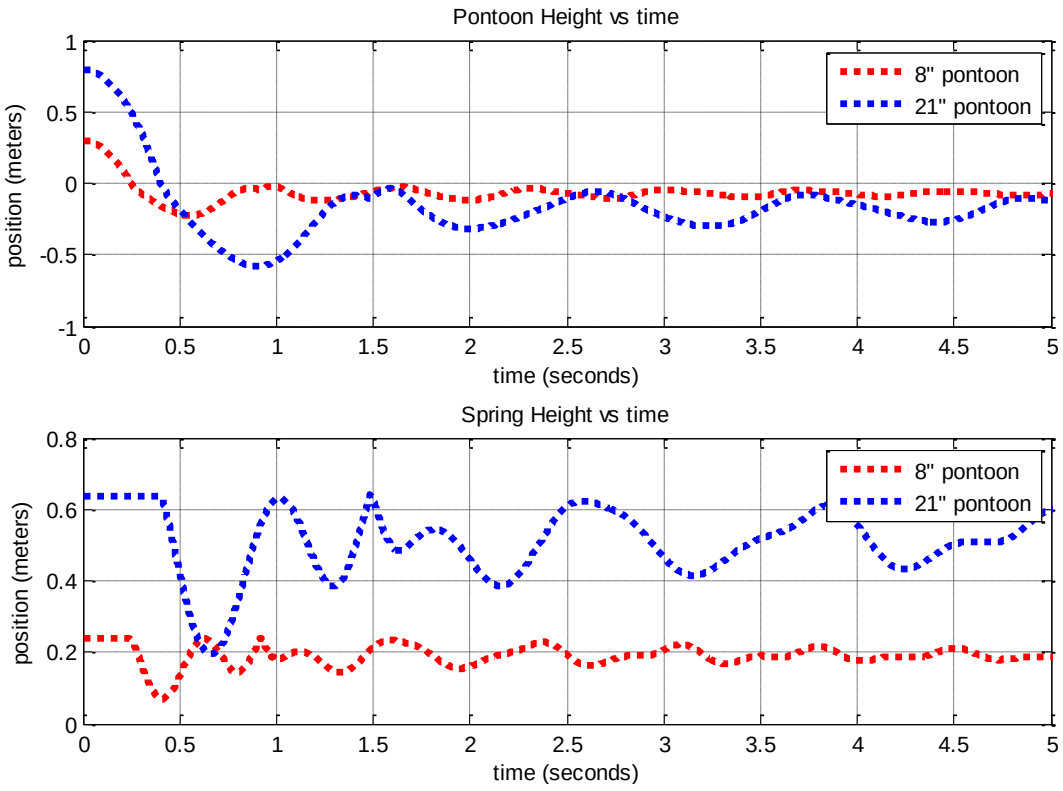

Figure 8.1 Scaled vs. unscaled Quarter-Boat simulations

The scaled and unscaled data appear to show similar trends; however, based on Figure 8.1 alone, a conclusion cannot be drawn as to whether or not the scaling parameters can be considered valid. In order to provide a more accurate comparison of the simulations, the original Quarter-Boat simulation results must be scaled after the simulations are run to match the diameter of the 33-ft WAM-V's pontoons as well. The plots must be scaled along both the displacement and time axes. For a position verses time plot such as Figure 8.1, the required scaling is different for the two axes. Figure 8.2 shows the required scaling for the position and the times axes for comparing the scaled and unscaled Quarter-Boat simulation results.

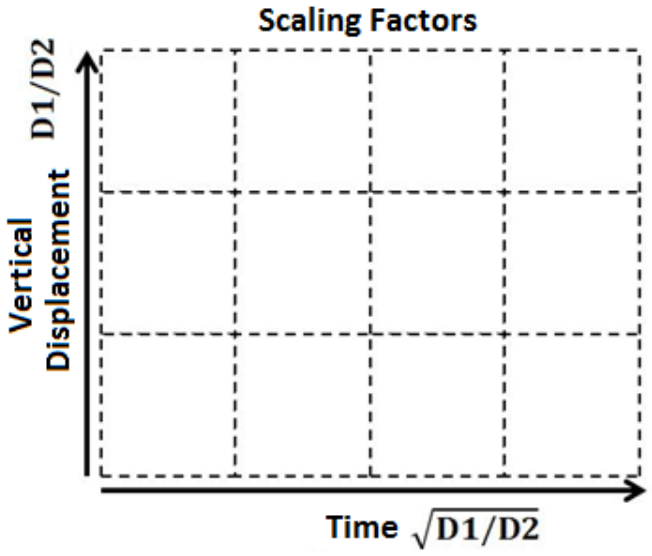

Figure 8.2 Axis scaling properties for comparing scaled and unscaled simulations

Figure 8.3 shows the scaled simulation results compared with the results from the 8 inch diameter Quarter-Boat simulations with the axes scaled according to Figure 8.2. The results match up well for the pontoon and the spring displacement, validating the scaling factors used for the different model parameters.

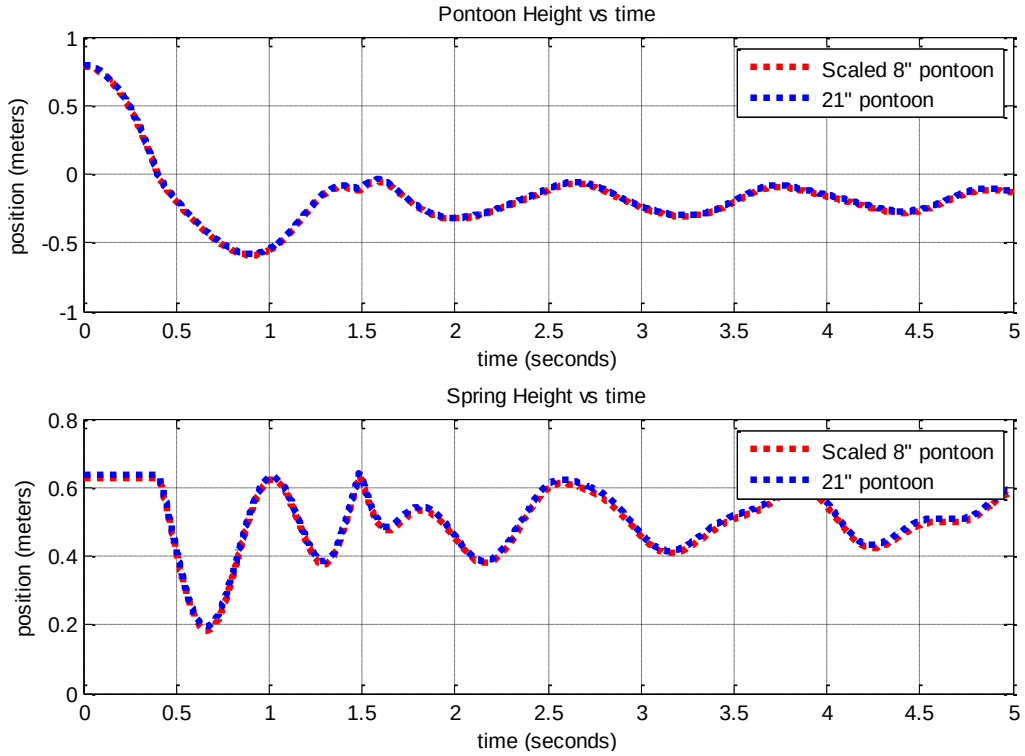

Figure 8.3 Scaled Quarter-Boat simulations comparison

8.5 Scaling Validation against External Drop Test Data

As a secondary validation of the overall scaling approach for the Quarter-Boat models, the single degree of freedom Quarter-Boat model can be applied to drop test data from an external source [64]. Figure 8.4 shows a comparison of the drop data from two 0.11 meter diameter cylinders, each dropped from a height of 0.445 meters. The first cylinder tested was neutrally buoyant, the second cylinder was 50% buoyant.

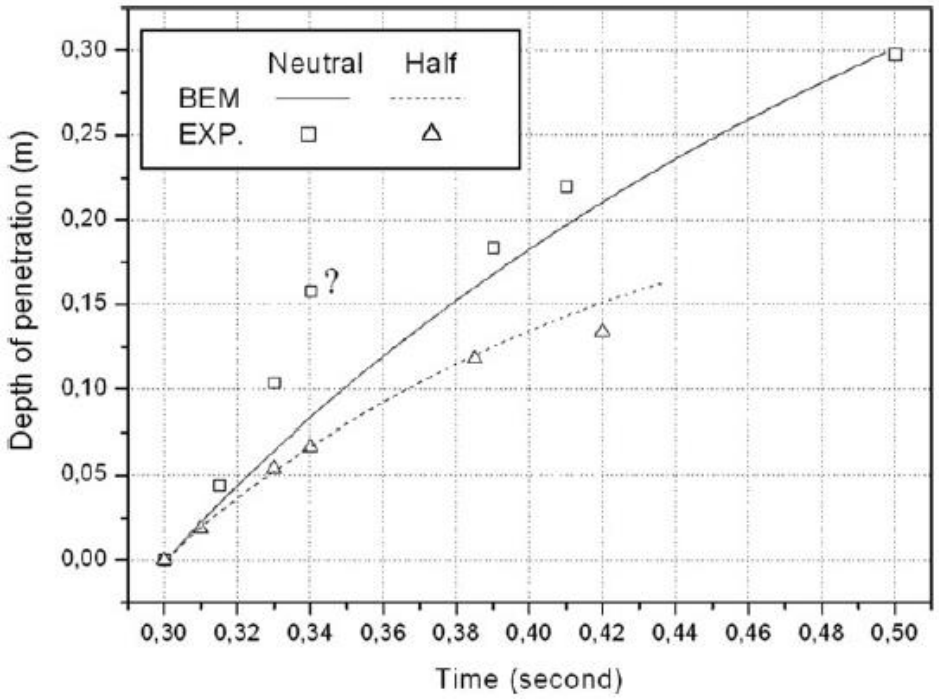

Figure 8.4 Half and neutrally buoyant cylinder drop test data from external source [64]

Figure 8.4 shows a comparison of experimental data from the two drops (shown by the square and triangle data points), and experimental computations simulating the drop test results (represented by the solid and dotted lines). The simulations shown predict the response of the cylinders using Wagner's method for the first 0.0015 seconds following impact, and a two dimensional boundary element method (BEM) for the remainder of the computations [64]. The neutrally buoyant data point with the question mark is documented as not being understood by the authors; it is considered to be a faulty measurement point. The measurements made were by visual estimation from video data, like the screenshots shown in Figure 8.5. Errors in reporting the correct displacements are possible; the data point will not be considered in the analysis.

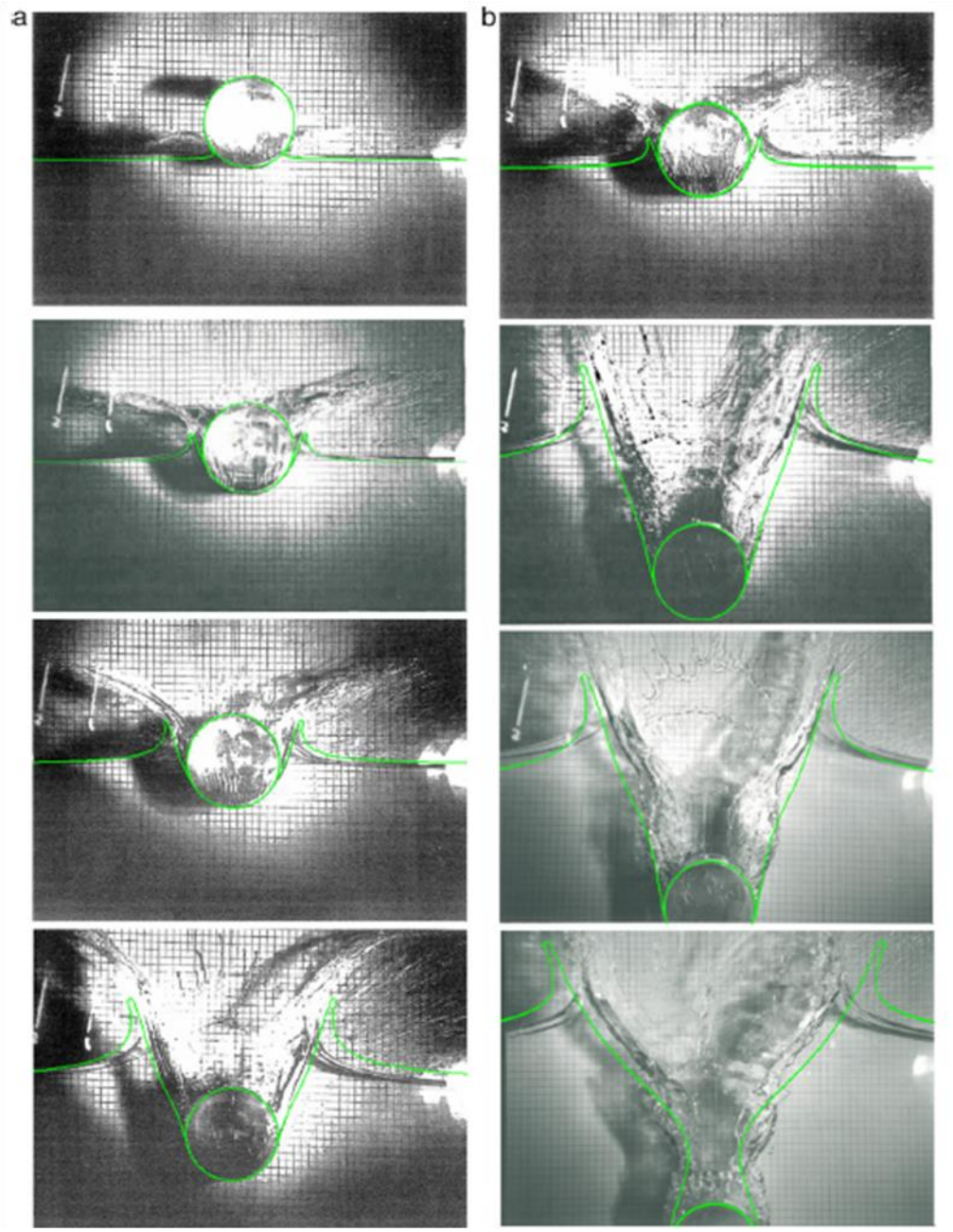

Figure 8.5 Half (a) and neutrally buoyant (b) cylinder drop test visualization [64]

The Quarter-Boat model can be scaled to simulate the same cylinder drop tests. Compared to the data shown in Figure 8.4, the parameters of the Quarter-Boat model were developed using a larger diameter (8 vs. 4.33 inches), and more buoyant cylinder (25.6% and 31.4% vs. 50% and 100%), with lower velocity impacts (2.2 vs. 2.955 m/s). The scaling parameters used to scale the Quarter-Boat model to the cylinder drop test data are shown in Table 8.3.

Table 8.3 4.33 inch cylinder drop test scaling parameters

Parameter:	Scaling Type:	Scaling:
Pontoon Diameter	Linear	D_1/D_2
Pontoon Weight	2nd order	$(D_1/D_2)^2$
Drop Height	linear	D_1/D_2
Spring Rate (Restoring Force)	2nd order	$(D_1/D_2)^2$
Added Mass	2nd order	$(D_1/D_2)^2$
Damping	Square Root	$(D_1/D_2)^{0.5}$

Figure 8.6 shows the simulation results for the Quarter-Boat model scaled to simulate the same drop tests shown in Figure 8.4. The half buoyant simulation show similar trends to the Quarter-Boat simulations shown in Chapter 5, while the vertical position of the neutrally buoyant simulation continues to decrease after the initial impact and does not reach equilibrium. For the neutrally buoyant cylinder drop simulations, the restoring force is equal to the weight of the cylinder, so there is no net upward force acting on the cylinder.

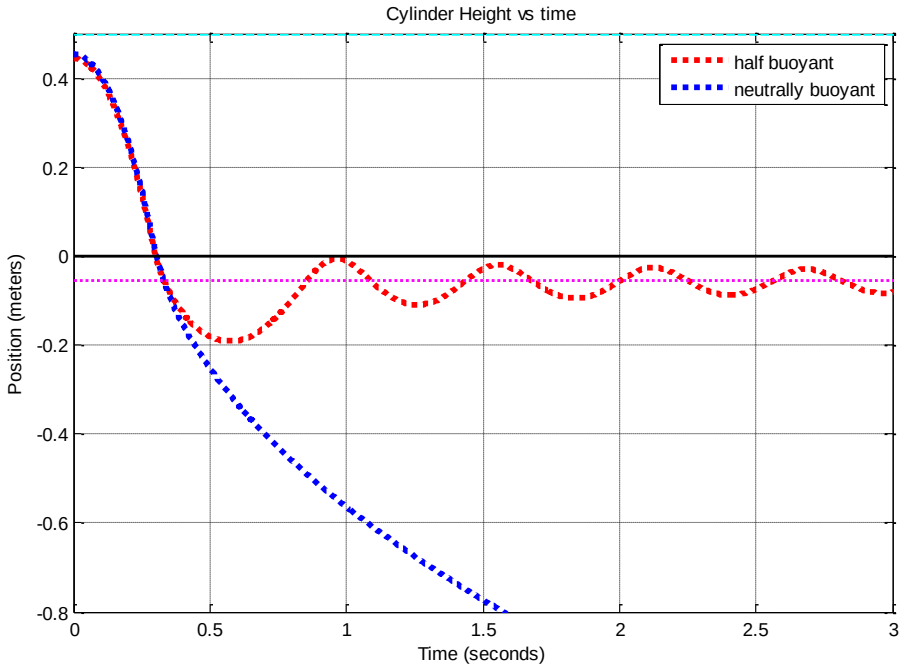

Figure 8.6 Scaled drop test simulations using Quarter-Boat model

Figure 8.7 shows the scaled Quarter-Boat simulation data overlaid with the data and external simulation data shown in Figure 8.4. For the half-buoyant simulation, the Quarter-Boat simulation falls nicely between the experimental measurements and the computational simulations conducted using a combination of Weber's method and the boundary element. The half-buoyant Quarter-Boat simulation matches the data better than does the neutrally buoyant Quarter-Boat simulation, which falls at a slightly lower rate than the experimental measurements and the computational simulation method. This is not unexpected, since the half buoyant simulations are significantly closer to the specifications of the Quarter-Boat test rig from which the Quarter-Boat model was derived.

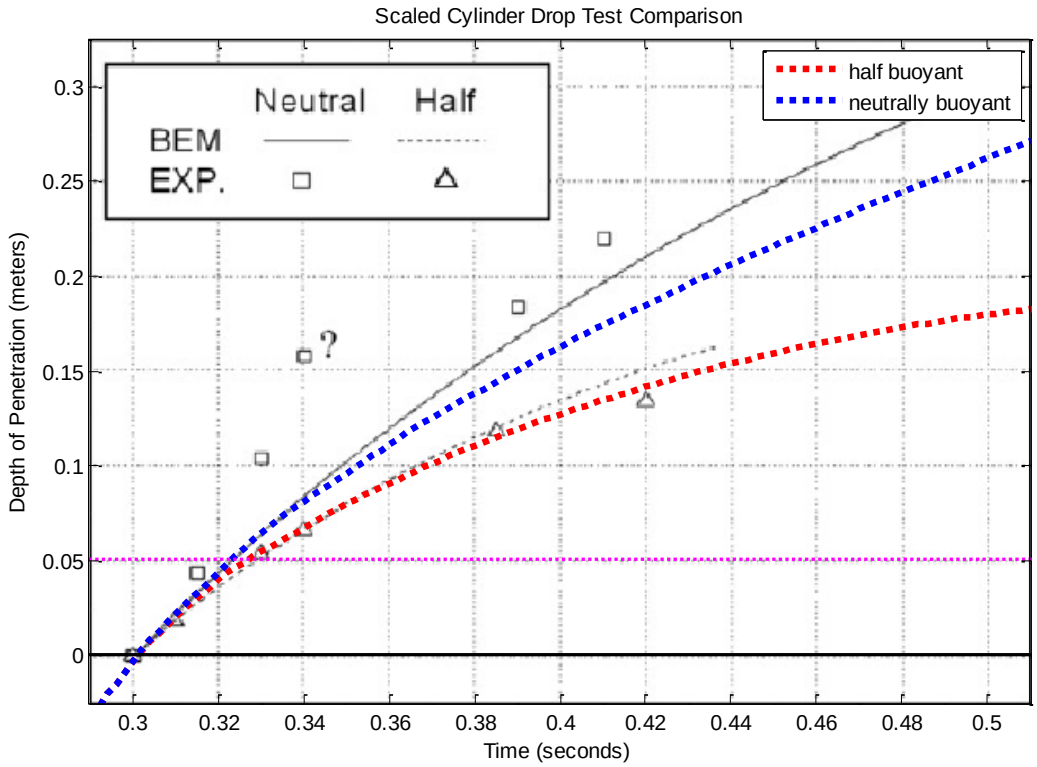

Figure 8.7 Comparison of scaled Quarter-Boat simulations and external drop test data (modified from [63])

If so desired, the neutrally buoyant Quarter-Boat simulations could be improved to show better correlation with the experimental and computation results by making slight adjustments to the Quarter-Boat model parameters, such as slightly increasing the added mass parameters or decreasing the damping parameters. However, the simulation already matches fairly well, and it is unlikely that a WAM-V would be designed with pontoons that are close to neutrally buoyant. Overall, the simulation results serve as further validation of the Quarter-Boat models.

8.6 On-Water Validation testing

With the properties of the Quarter-Boat model scaled to fit the 33-ft WAM-V, the next step in the modeling process is to conduct a simulation of the 33-ft WAM-V using the Quarter-Boat model and compare the results against on-water testing data. The ability of the Quarter-Boat model to be scaled is highly advantageous; the scaling is straightforward for any size and doesn't require reworking the coefficients of the model. The Quarter-Boat model will be compared with the data from the single-wave input test documented in Section 7.4.

8.6.1 Single-Wave Input-Test Review

As part of the 33-ft WAM-V's summer testing program, an on-water test was conducted where the WAM-V was piloted across the wake of a large freighter ship. The wake launched the WAM-V airborne, creating a comparable impact at the bow of the WAM-V to the impacts tested with the Quarter-Boat test rig. The data from the single-wave input test was analyzed and broken down into seven segments, corresponding to key points during the encounter with the wave in terms of the suspension and operator's performance.

The Quarter-Boat model can be compared with the single-wave input test by comparing the simulation with the phases of the test after the pontoons reach their maximum height. This corresponds to Phases 3-7 of the single-wave test, as shown in Figure 8.8.

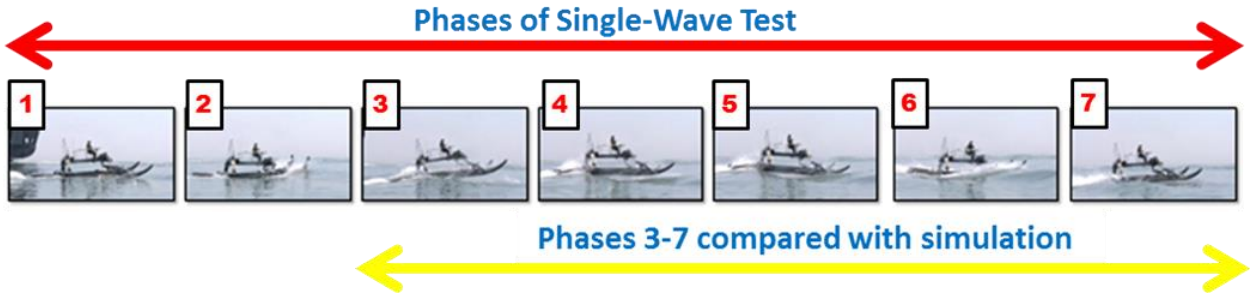

Figure 8.8 Phases from single-wave test that can be simulated via the Quarter-Boat model

8.6.2 Input Parameters

To compare the Quarter-Boat model with the single-wave test, the simulation was set up for an initial displacement input equal to a 24 inch drop height. The drop height was estimated by comparing the height of the pontoon assembly with the air gap below it during Phase 3 of the single-wave input test, as shown in Figure 8.9. For reference, the pontoon and ski assemblies on the 33-ft WAM-V are 24 inches tall.

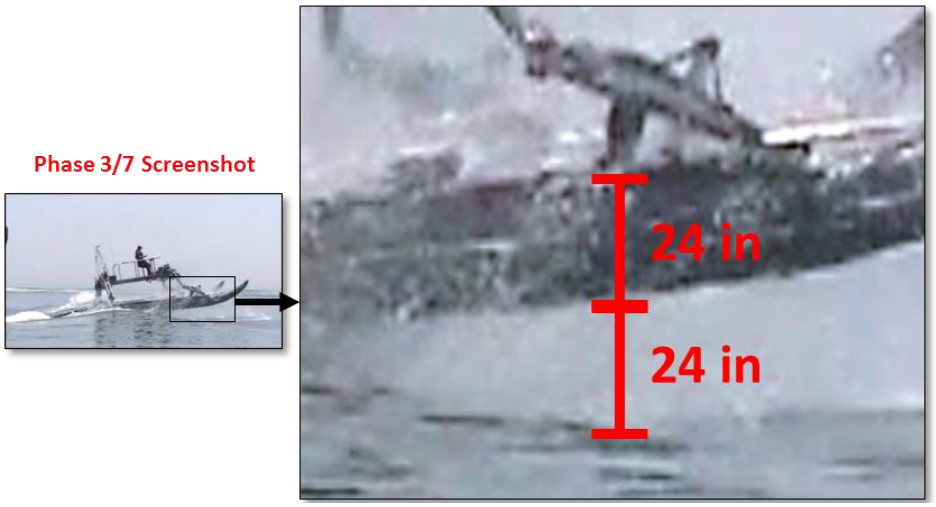

Figure 8.9 Drop height determination based on Phase 3 of single-wave test

To confirm the drop height, a second estimate of the drop height was also made by integrating the acceleration data taken at the pontoon's vertical accelerometers, and using the filter-integration scheme detailed in Chapter 4. The integration results could not be used to determine the height directly due to the filter scheme's effect the data at very low frequencies; however, the position and velocity as a function of time were able to be compared with the simulation once the 33-ft WAM-V's pontoons were in free-fall.

8.6.3 Model Configuration

In Section 6.6, the model parameters of the 33-ft WAM-V were determined. Some of the parameters can also be applied to the Quarter-Boat model. Table 8.4 lists the parameters used for the 33-ft WAM-V in the Quarter-Boat model simulations.

Table 8.4 33-ft WAM-V Quarter-Boat parameters

Parameter:	Value:
Sprung Mass	525 lbs
Unsprung Mass	210 lbs
Pontoon Diameter	21 inches
Pontoon Length	13 feet
Spring	Air Spring
Damper	Emulsion shocks (2)
Drop Height	24 inches

8.6.4 Output Sensors

Of the 33-ft WAM-V's data channels recorded by the data acquisition unit during the single-wave test, only a few sensors are able to be compared with the Quarter-Boat model. The accelerometers from the rear of the pontoons, the engine pods, the rear of the payload tray, and the transverse and longitudinal data from the triaxial accelerometer are not required; nor are the displacements from the string potentiometer on the front arch or the potentiometers on the engine pods. To validate the scaling of the Quarter-Boat model, data from only five sensors is required. Data from the potentiometers on the suspension systems and the accelerometers at the front of the pontoons and the front of the payload tray were compared with the corresponding sensors in the simulation. Since the single-wave test was conducted in a head seas orientation, data from only one side of the WAM-V is required for analysis. During the single-wave analysis, data from both suspension potentiometers were compared; while for the accelerometer data, only the data from the starboard-side sensors was shown. A diagram of the compared sensors is shown in Figure 8.10.

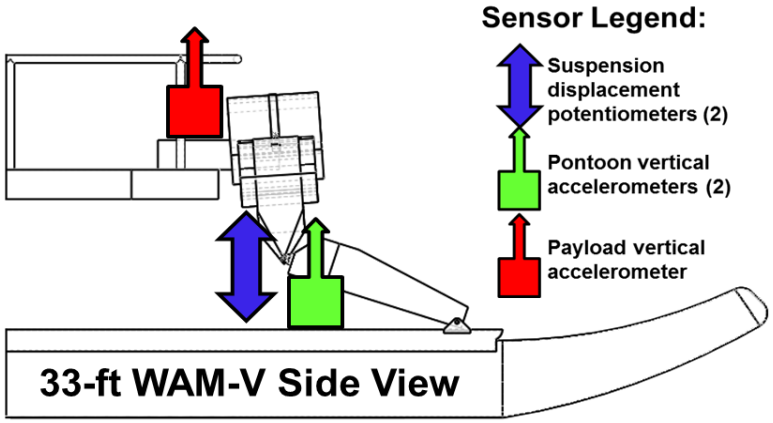

Figure 8.10 Sensors that can be compared with the Quarter-Boat model

8.6.5 Simulation and Single-Wave Data Comparison

The simulation results can be compared with the plots shown in Section 7.3. Figure 8.11 shows the suspension motion data (a) and acceleration data (b) that will be used to compare with the Quarter-Boat model. The longitudinal data, shown in purple in Figure 8.11(b) cannot be compared with the Quarter-Boat model. The purpose of the data comparisons in this section is to evaluate whether the scaled Quarter-Boat model is able to provide an accurate representation of the single-wave input test. If the correlations are successful, the parameters of the WAM-V's

suspension can be altered and simulations can be run to see the different effects on the accelerations recorded by the payload accelerometer. Simulation and test data comparisons are presented for the suspension displacement and the unsprung and sprung vertical accelerations.

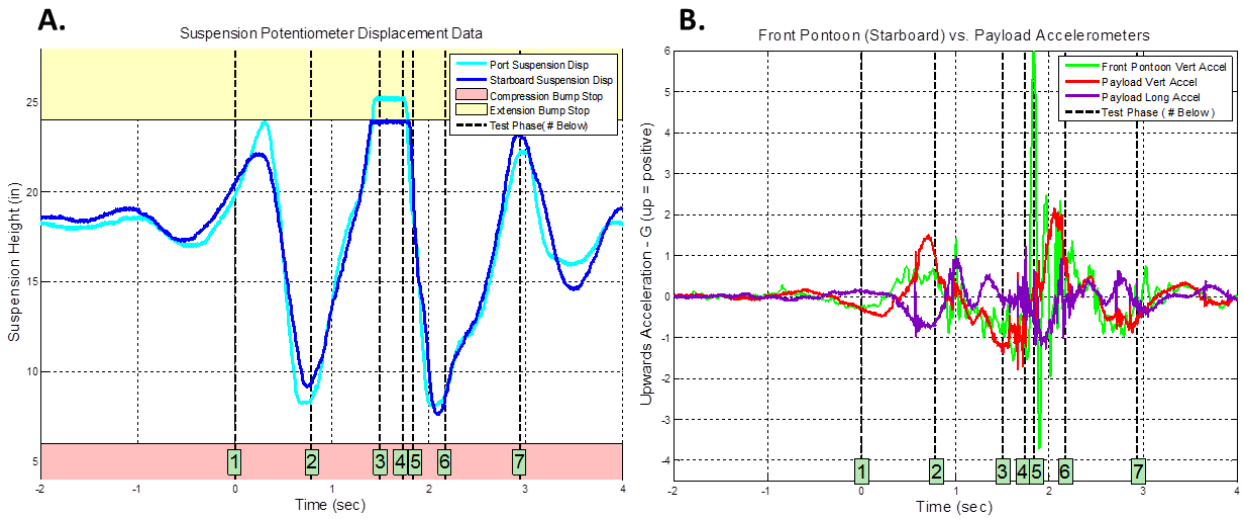

Figure 8.11 Suspension motion (a) and accelerometer (b) data review from single-wave test

8.6.5.1 Suspension Data Comparison

Figure 8.12 shows a comparison between the suspension displacement from the Quarter-Boat simulation and the suspension potentiometer data from the 33-ft WAM-V during Phases 3-7 of the single-wave input test.

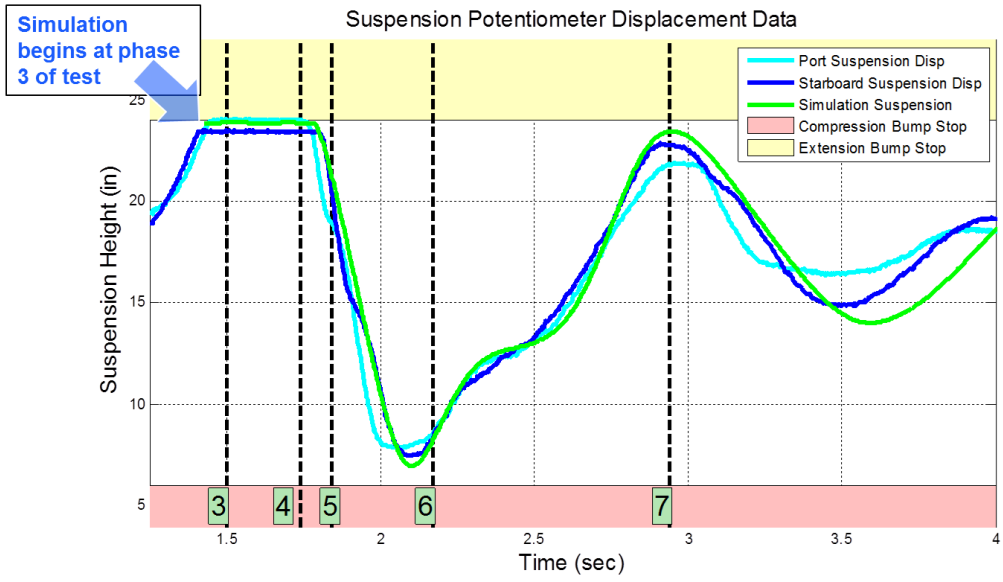

Figure 8.12 Suspension motion comparison between Quarter-Boat model and single-wave test

The suspension data in Figure 8.12 shows that the impact from the test was substantial enough to move the suspension through almost its entire range of travel. Also, the air spring delivers a highly nonlinear response at high displacements. The change of the suspension's frequency at time = 2.25 seconds is a result of this nonlinearity, and is present in both the on-water test and the Quarter-Boat simulation, which show good correlation results.

8.6.5.2 Accelerometer Data Comparison

Figure 8.13 shows the results of the comparison between the vertical accelerations from the Quarter-Boat simulation and the accelerometer data from the vertical pontoon and payload accelerometers on the WAM-V during the single-wave test.

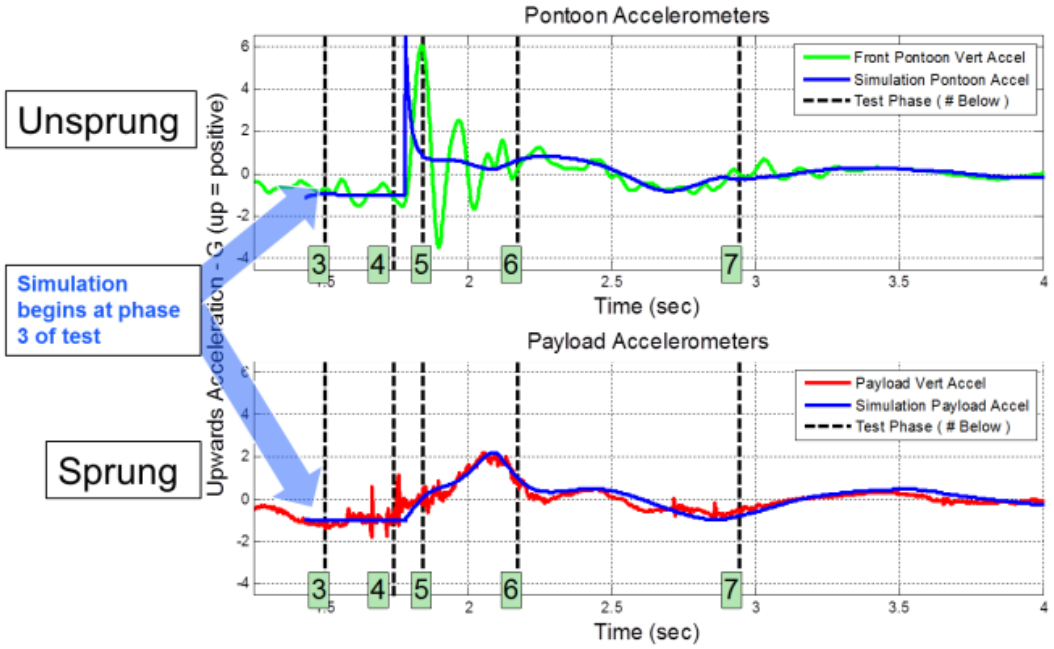

Figure 8.13 Unsprung and sprung comparison between the Quarter-Boat and single-wave test accelerometers

The acceleration profile of the sprung mass plots in Figure 8.13 shows excellent correlation with the data. The unsprung mass simulation peaks faster than in the data; however, the peaks occur at the same level of acceleration. In the unsprung data there is a strong 8 Hz signal present in the testing data that is not replicated in the simulation. This frequency is believed to be the first order bending frequency of the ski assembly that supports the pontoon. In the simulation, the assembly is modeled as one rigid body with the pontoon. For further validating the simulation's usefulness against data from the 33-ft WAM-V, the model could be converted to simulate base-excitation inputs, so that all seven phases of the single-wave input test could be evaluated.

8.7 Quarter-Boat Modeling of Second Generation Suspension Design

With a successful correlation between Phases 3-7 of the single-wave input test and the scaled Quarter-Boat model established, a series of simulations can be run, altering the parameters of the 33-ft WAM-V's suspension. The suspension's effects on the vertical accelerations experienced by the operator can be examined, and a more suitable suspension system for the 33-ft WAM-V can be designed and simulated prior to on-water testing.

8.7.1 Review of Second Generation Suspension Calculations

In Section 6.7.2, quasi-static suspension calculations were performed for different coilover springs, ranging from 200-600 lb/in. A 500 lb/in spring rate was chosen; however, the spring rate was not chosen based on quasi-static calculations alone. In Section 6.7.3, a second generation damper design was also presented for the 33-ft WAM-V. The final specifications for the damper were analyzed, and some qualitative notes were given about how the damping parameters were determined.

8.7.2 Original vs. Second Generation Suspension Comparison

Figure 8.14 shows a comparison of the original and second generation suspension systems during a drop test simulation similar to the single-wave input test documented in Section 7.4.

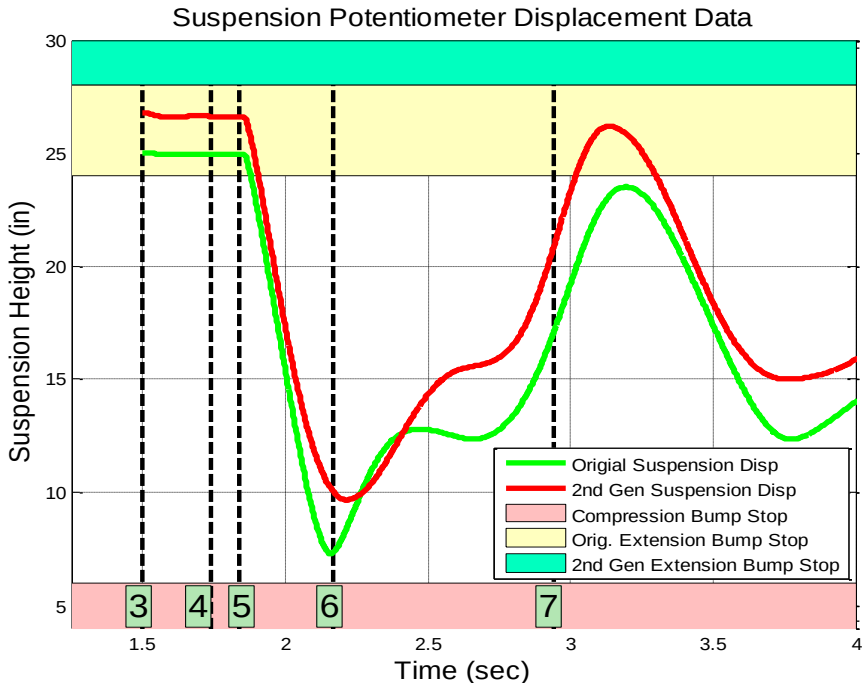

Figure 8.14 Suspension displacement comparison of original and second generation suspension systems

During the free-fall phase of the simulations, the original suspension is pulling against the limit straps; while the second generation suspension system does not contact its limits straps, although the suspension is riding higher, due to its the increased available travel. The second generation suspension system has greater reserve compression travel at impact (Phase 6), using 2.5 inches less compression travel. This does not necessarily mean that the second suspension system has a more harsh ride quality, the suspension actually moves through the same amount of travel from Phases 5 to 6 as the original suspension system; there is simply more travel available. The second generation suspension system rebounds more slowly from maximum compression. This is advantageous for mitigating the acceleration response; the energy is absorbed by the suspension over a longer time period. The slower response is due to the linear coilover spring rate, compared to the highly nonlinear air springs on the original suspension system.

8.7.3 Original vs. Second Generation Acceleration Comparison

Figure 8.15 shows the pontoon and payload vertical acceleration response of the original and second generation suspension systems during the drop test simulations.

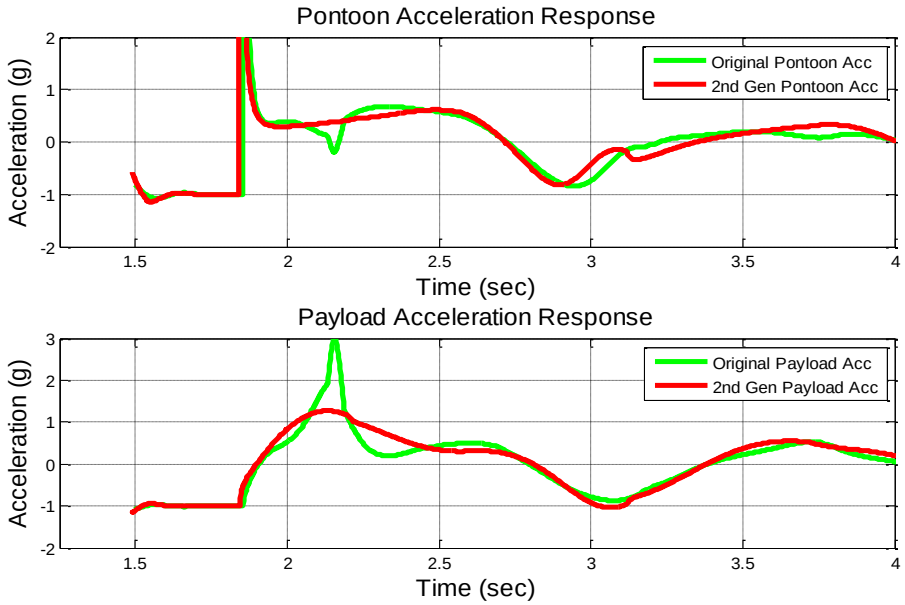

Figure 8.15 Pontoon and payload acceleration comparison for original and second generation suspensions

Based on the acceleration response, the payload shows a more even acceleration profile for the second generation suspension system than the original suspension system. Even though the original suspension system does not bottom out in compression, as shown in Figure 8.14, there is still a harsh spike in the acceleration profile during maximum compression. This is because the

nonlinear suspension becomes so stiff that the system's response is similar to what would be seen if the suspension had bottomed out during the simulation. The harsh response can also be seen in the negative spike in the pontoon acceleration data, which occurs due to the motion of the suspension, rather than the motion of the waves. The pontoon accelerations are more consistent for the second generation suspension, indicating improved control over the unsprung mass.

8.7.4 Original vs. Second Generation Global Displacement Comparison

Figure 8.16 shows the global displacements of the sprung and unsprung masses for the original and second generation suspension systems during the simulated drop tests. Measurement of the global displacement is an interesting data point, available in the simulation but not available during on-water testing.

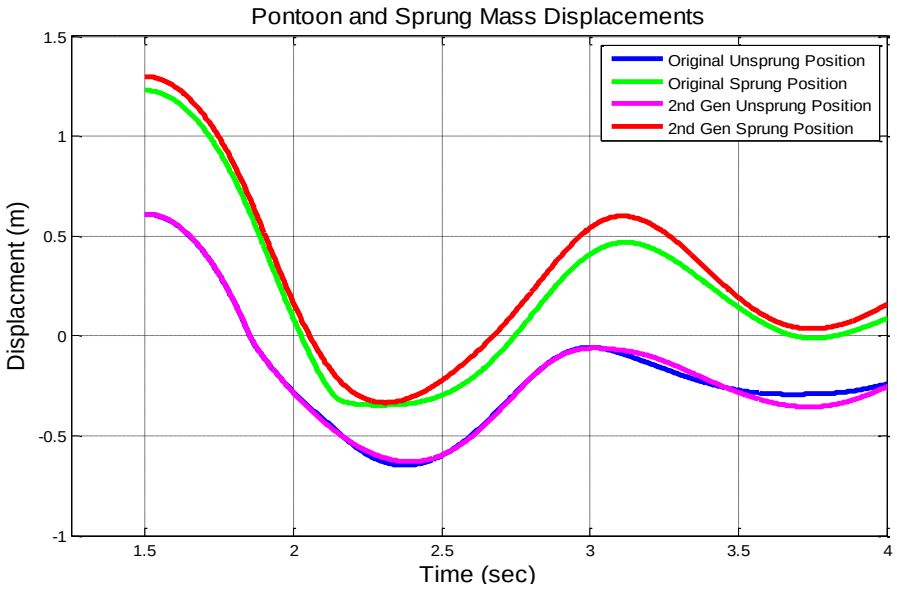

Figure 8.16 Global unsprung and sprung mass displacements

The motion of the sprung masses in Figure 8.16 helps to explain the performance difference of the two suspensions. At approximately 2.25 seconds into the test, the sprung mass of the original suspension system is considerably lower than the second generation suspension system, and the curve is flattening, compared to the second generation's more rounded profile. This shows that even though the original suspension system doesn't bottom out, it effectively responses as though it had, which explains the poor acceleration performance previously shown. The unsprung motions show slightly lower peak heights for the first two peaks from the second generation suspension system. Even though the change is small, the effect is considerable, because the suspension is less susceptible to compound effects from a series of wave inputs.

8.8 Quarter-Boat Rig with Base-Excitation Inputs

When the Quarter-Boat test rig was first being designed, a decision was made that the rig would be used to test initial condition (drop test) inputs rather than base-excitation inputs. The rational for the decision is documented in Section 5.4.1. Once the parameters for the Quarter-Boat model were established, the input type to the model could then be converted to test base-excitations for simulating future WAM-Vs.

The main reason for developing the Quarter-Boat rig was to investigate the differences between single degree of freedom suspension simulations and two degree of freedom simulations. The following section details a comparison of a single degree of freedom simulation and a two degree of freedom simulation using the Quarter-Boat model. Conceptual schematics of the two model types are shown in Figure 8.17.

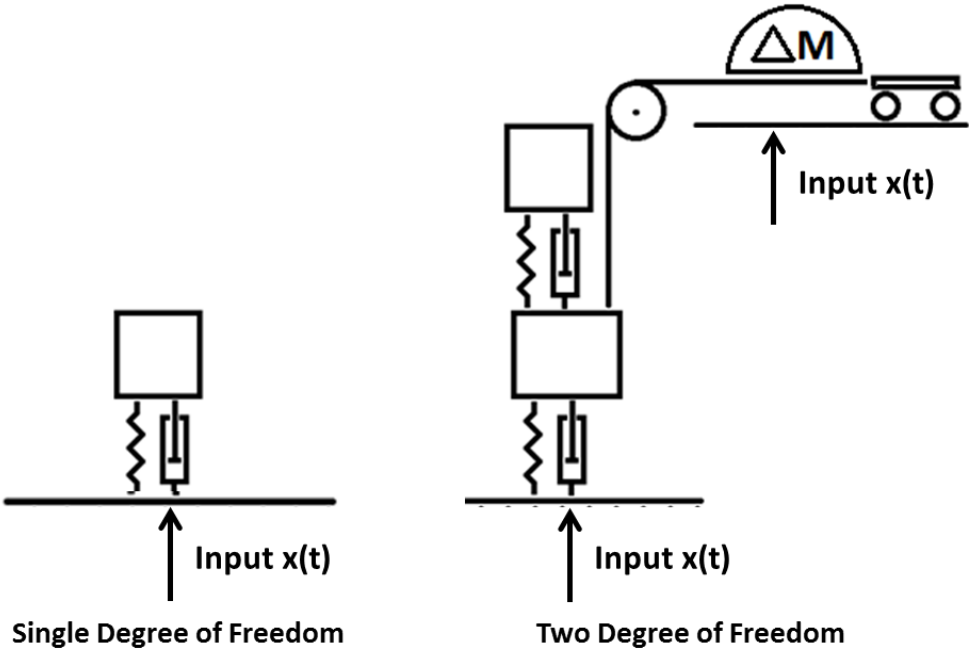

Figure 8.17 Comparison of model conceptual schematics

The 33-ft WAM-V will be configured with the second generation suspension system for the comparison, with the adjustable dampers set to their middle damper settings. Sinusoidal chirp signal inputs will be used to test the models with 6 inch amplitude displacements; the frequency range will increase from 0.5 – 2.5 Hz over the 1 minute test duration. This type of input was chosen to match the input type used for the analysis of the 2-post rig detailed in Chapter 10.

8.8.1 Single vs. Two Degree of Freedom Simulations: Unsprung Response

Figure 8.18 shows a comparison of the input displacements (a), and the displacement (b) and acceleration (c) experienced by the pontoons for the single and two degree of freedom simulations. For the input displacements, the locations of specific frequencies in the chirp signal are also shown.

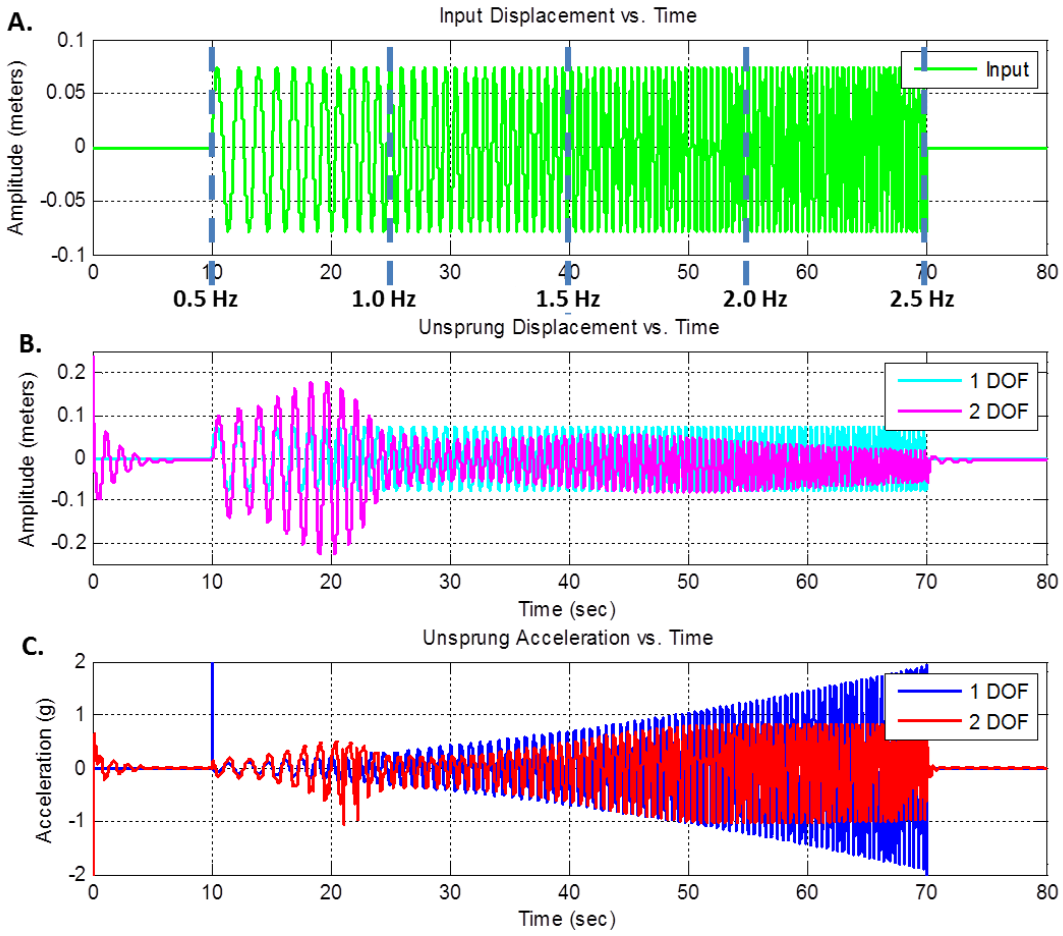

Figure 8.18 Single degree of freedom and two degree of freedom unsprung mass comparison

The pontoon displacement (b) and acceleration (c) plots show a marked difference between the single degree of freedom and the two degree of freedom simulations. The two degree of freedom model resonates strongly at a frequency of 0.8 Hz (t = 19 seconds) and then again less strongly at 1.67 Hz (time = 45 seconds). The second resonant point is more visible in the displacement plot (b), while it is difficult to see in the acceleration plot (c) because the increasing accelerations at higher frequencies from the chirp signal input hides the decreasing displacement amplitudes which occur after the time of resonance.

8.8.2 Single vs. Two Degree of Freedom Simulations: Sprung Response

Figure 8.19 shows a comparison of the suspension displacement (a), the global displacement (b), and the acceleration (c) experienced by the sprung mass for the single and two degree of freedom simulations.

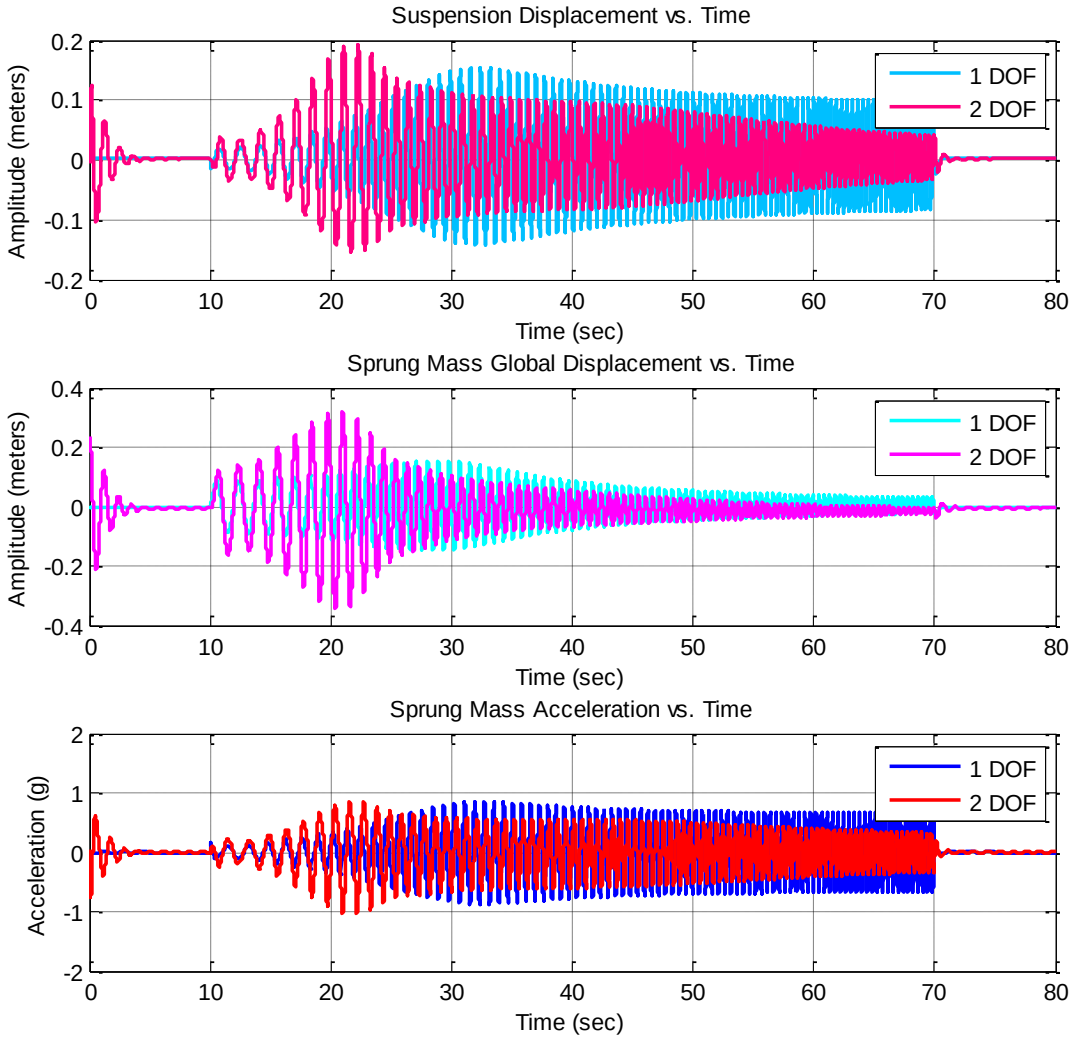

Figure 8.19 Single degree of freedom and two degree of freedom sprung mass comparison

The suspension of the single degree of freedom simulations resonates at a frequency of 1.25 Hz (t = 32.5 seconds), while the two degree of freedom suspension resonates at a frequency of 0.9 Hz (t = 22 seconds). The two degree of freedom simulation shows far greater displacements at lower frequencies, while the single degree of freedom simulation shows greater displacements and accelerations at higher frequencies. Therefore, it is important when evaluating the 33-ft WAM-V's response on the 2-post rig to not overestimate the effects of high frequency inputs.

8.8.3 Analytical Comparison of Single and Two Degree of Freedom Models

The single degree of freedom and the two degree of freedom models compared in the previous section showed very different responses to the same base-excitation input. To determine the effects of the different parameters on the overall response, the two models will be linearized and their natural frequencies will be calculated and compared with the simulations. For the single degree of freedom model, the system can already be considered linear for inputs that do not reach the travel limits of the suspension. For the two degree of freedom model, the hydrostatic spring rate and added mass are linearized about the pontoon's static waterline. Table 8.5 lists the parameters that will be used for calculating the natural frequencies of the two systems.

Table 8.5 Model parameters for linearized natural frequency calculations

Parameter:	Value:
Spring Mass	238.6 kg
Unsprung Mass	95.5 kg
Added Mass (linearized)	295.0 kg
Suspension Spring Rate	10.5 kN/m
Hydrostatic Spring Rate (linearized)	20.0 kN/m

For the single degree of freedom system, the undamped natural frequency of the system can be determined by the following formula:

$$\omega_n = \sqrt{\frac{k}{m}}\ [45] \quad \Rightarrow \quad \sqrt{\frac{11200}{238.6}} = 1.05Hz$$

For the two degree of freedom system, the system has two undamped natural frequencies. The equations of motion of the two degree of freedom system are:

$$238.6\ddot{x}_1 + 10500x_1 - 10500x_2 = 0$$
$$(95.5 + 294.97)\ddot{x}_2 - 10500x_1 + 30500x_2 = 0$$

In matrix form, the equations of motion become:

$$\begin{bmatrix} 238.6 & 0 \\ 0 & (95.5+295.0) \end{bmatrix}\ddot{x} + \begin{bmatrix} 10500 & -10500 \\ -10500 & 30500 \end{bmatrix}x = 0$$

To solve for the natural frequencies, the determinants of the matrix are solved, using the following formula:

$$\det(-\omega^2 M + K) = 0 \quad [45]$$

$$\begin{vmatrix} -238.6\omega^2 + 10500 & -10500 \\ -10500 & -390.5\omega^2 + 30500 \end{vmatrix} = 9.317*10^4\omega^4 - 1.138*10^7\omega^2 + 2.210*10^8$$

$$\omega_2 = 0.76\,\text{Hz} \qquad \text{and} \qquad \omega_1 = 1.59\,\text{Hz}$$

The single freedom of freedom system has a calculated undamped natural frequency of 1.05 Hz, while the two degree of freedom system has calculated undamped natural frequencies of 0.758 Hz and 1.59 Hz. The natural frequencies are considerably different between the two systems. Figure 8.20 shows the calculated undamped natural frequencies compared with the acceleration response of the sprung and unsprung masses from the base-excitation simulations.

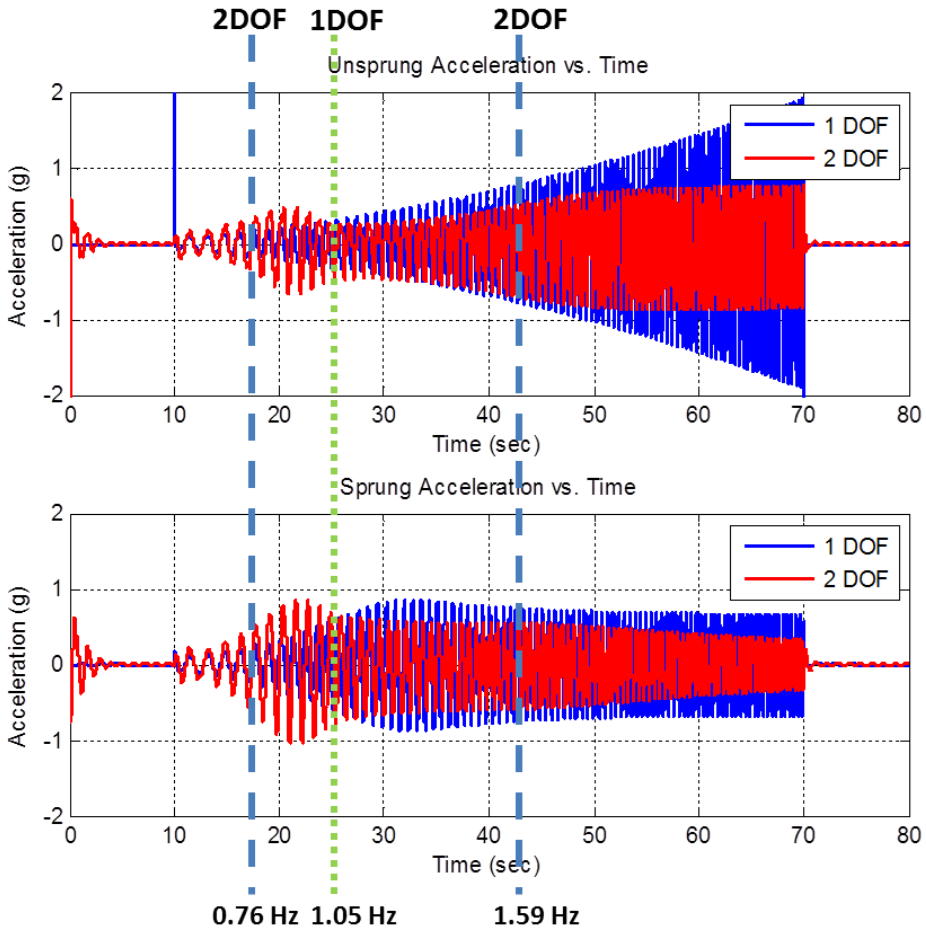

Figure 8.20 Comparison of calculated and simulated acceleration responses

Based on the acceleration response, the calculated natural frequencies do not appear to correlate well with the resonant points found in the simulations. For the single degree of freedom system, the calculated natural frequency of 1.05 Hz does not match the resonant point at 1.25 Hz (t = 32.5 seconds), although the damping in the simulation contributes to the difference.

The lower calculated frequency of 0.76 Hz does not quite match the strong resonant point in the simulation at 0.9 Hz (t = 22 seconds). Although it is difficult to see, the higher natural frequency of the two degree of freedom is close to correlating with a resonant point of the system. The resonant point was shown in the displacement plot of Figure 8.18(b) to occur at 1.67 Hz (time = 45 seconds), which is very close to the calculated value of 1.59 Hz. For further clarification of the differences in the calculated and the simulated responses, it is possible that running the simulations without damping, or with very low damping coefficients, might improve the correlation with the calculated natural frequencies of the systems.

8.8.4 Applications of Hydroelasticity to Quarter-Boat Simulations

Previous modeling efforts have incorporated the dynamics of the Quarter-Boat as a one dimensional system numerically solved in the front view. More in depth analysis methods could be implemented to consider the side-view dynamics of the system and subsequently the hydroelasticity effects on the system as well. In the side view, the WAM-V can be approximated as a free-free beam loaded in bending, with the modes shapes shown in Figure 8.21.

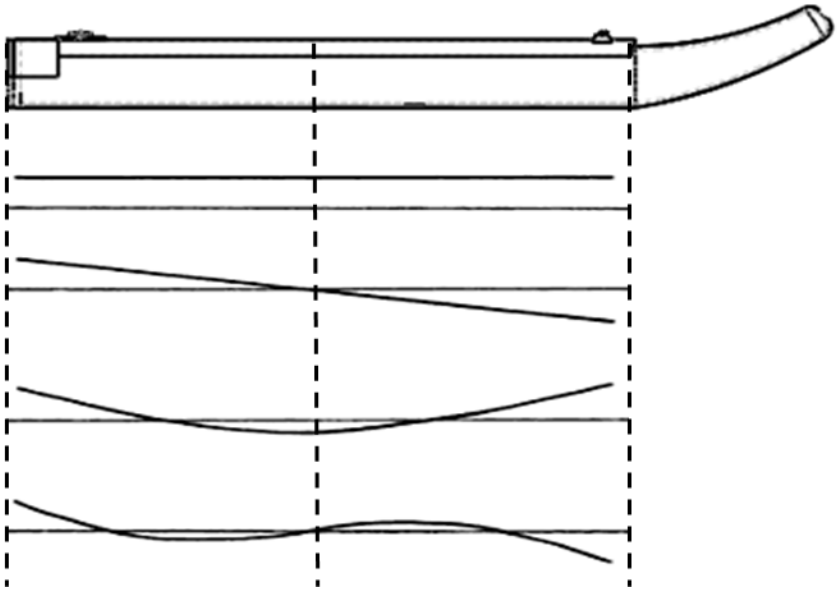

Figure 8.21 Free-free bending mode shapes of WAM-V hulls

In Section 5.11.4, a method for analyzing the added mass and damping effects was outlined using strip theory to approximate the hydrodynamic forces acting on a given structure, which can then be used to calculate the structural loads. This analysis method can be extended to incorporate the effects of the fluid-structure interaction, and the subsequent changes on the fluid flow and the structural vibrations.

For the purpose of the hydroelasticity calculations, a ship is often approximated as a beam of constant cross section with a constant elastic modulus. For the 33-ft WAM-V, assuming the inflatable pontoons contribute little to the overall bending stiffness relative to the aluminum skis, the bending stiffness of each ski is can be solved for explicitly. Each ski is composed of two rectangular tubes welded together, having the cross sectional dimensions shown in Figure 8.22. The skis have an elastic modulus of 70 GPa, and a moment of inertia of $3.34*10^5 m^4$.

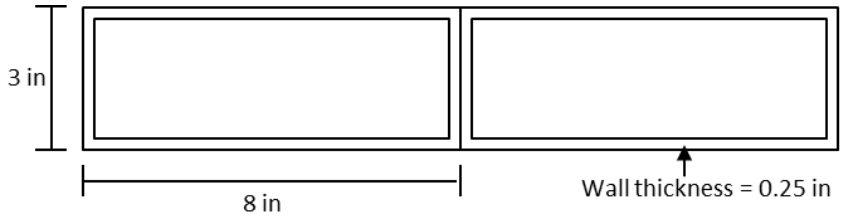

Figure 8.22 33-ft WAM-V aluminum ski beam cross section

To solve for the mode shapes and the natural frequencies of the hulls, beam theories as such as the Euler-Bernoulli or Timoshenko theories can be employed. However, calculations performed on the hulls will not produce the same values on the water as they would for dry hull conditions. The added mass of the accelerating fluid significantly changes the natural frequencies of the different mode shapes. The added mass effects need to be included in the calculations as part of the system. The dynamics of the system could be solved for using energy methods such as the Lagrange equations, where the kinetic and potential energy of the system are defined as follows:

$$KE_{system} = KE_{beam} + KE_{fluid} \text{ and } PE_{system} = PE_{beam} + PE_{fluid}$$

Some of the hydroelasticity effects that could be examined for the WAM-V include:

- Slamming effects such as during impact for the single-wave test
- Springing of the hulls when wave encounter frequencies approach the hull's natural frequency of the hulls
- Whipping of the hulls, and transient vibrations traversing down the hulls after impact

An example of a fluid structure-interaction on the WAM-V was recorded by the vertical accelerometers on top of the front of the skis during the single-wave test documented in Section 7.3. In Section 8.6, data from the accelerometers was compared against the scaled Quarter-Boat simulations as validation of the Quarter-Boat scaling. The results are shown in Figure 8.23.

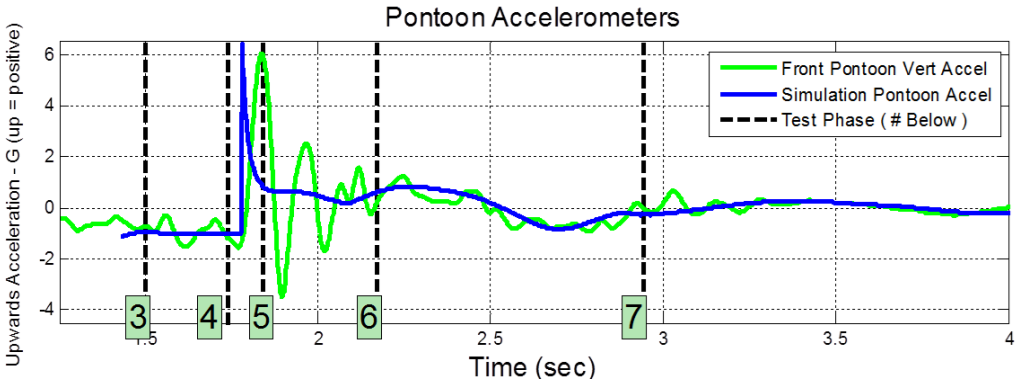

Figure 8.23 Pontoon accelerometer trace showing bending modes

The Quarter-Boat simulation was found to correlate well with the test data for the low frequency response; however, some of the frequency content was not replicated in the simulation. This frequency content is believed to be due to the hydroelasticity of the system, possibly the first bending mode frequency of the skis, which occurs at 8 Hz in the single-wave data.

If the hydroelasticity effects on the WAM-V's structure are to become an area of further research, a more advanced model of the WAM-V compared to the beam with a distributed mass commonly used for ships might be also implemented. A conceptual diagram solution of one possible model is shown in Figure 8.24, which incorporates the response of the WAM-V's suspension at the front of the beam and the mass of the rear arch and engine pod structures at the rear of the beam. Examining the response may help to more accurately determine the loads on the structure which will aid with future WAM-V designs.

Figure 8.24 More advanced WAM-V conceptual diagram for hydroelasticity computations

8.9 Conclusions and Recommendations

The Quarter-Boat model developed in Chapter 5 has been successfully applied to the 33-ft WAM-V for analyzing the performance of the WAM-V's suspension system. The Quarter-Boat model was able to be scaled to different sizes without any of the coefficients being modified. The scaling of the output parameters allowed the scaled model to be easily compared with the unscaled model, validating the scaling parameters.

When scaled to match the cylinder drop data from an external source, the Quarter-Boat model was found to work well for simulating the response of a 50% buoyant cylinder. The response of the neutrally buoyant cylinder showed good correlation; however, slightly greater decelerations were shown than are present in the data. The Quarter-Boat model could be modified to improve the results for a neutrally buoyant cylinder. If so desired, care would have to be taken not to change the properties of the model that led to all the other tests correlating so well. The other correlations are more important to the usefulness of the Quarter-Boat model for simulating the performance of WAM-Vs.

8.9.1 Conclusions from Single-Wave Test Comparison

The scaled Quarter-Boat model of the 33-ft WAM-V was used to compare with the data from the single-wave input, which showed good correlation without modifying the parameters of the Quarter-Boat model. For matching the results between the test and the simulation, the results were very sensitive to the height of the drop used as initial condition.

8.9.2 Conclusions from Second Generation Suspension Modeling

The Quarter-Boat model was successfully implemented to aid in the design of the second generation suspension system. The success of the second generation suspension system itself was discussed for rough water testing in Chapter 7, and found to be an improvement over the original suspension system design.

8.9.3 Conclusions from Quarter-Boat Base-Excitation Modeling

The base-excitation models showed large differences between the simulations for the single degree of freedom and the two degree of freedom models. The differences highlight the main reason the dynamics under the pontoons need to be considered if the WAM-V's suspension performance is to be modeled accurately. The linearized natural frequency calculations did not

line up particularly well with the resonant points found in the simulations; further investigation is required to understand the differences, particularly if a linear two degree of freedom model is used to model the WAM-V's suspension dynamics.

8.9.4 Recommendations for Future Work and Further Research

The next logical step in the modeling process is to apply the Quarter-Boat models to a 4-post or 6-post WAM-V model such as the 4-post model of the 12-ft USV detailed in Chapter 4 or the 6-post model in Chapter 11. Another interesting implementation would be to apply the Quarter-Boat model to the 2-post test rig detailed in Chapter 10. For any of these possible applications, the modeling of the pitch properties of the hulls should also be considered. Future Quarter-Boat models could incorporate Whole-Body Vibration standards into the results to design a suspension that will improve the operator's performance in the same way the current models can be used to improve the vessel's overall dynamics.

Chapter 9 Application of Whole-Body Vibration Standards to WAM-Vs

The following chapter provides a discussion of the dynamics of Wave-Adaptive Modular Vessels, particularly the effects of the dynamics on the response of the human operators and passengers onboard the WAM-V. The most prominent standards for analyzing Human Factors and Whole-Body Vibration were previously discussed as part of the literature review in Chapter 2. The standards have been applied to acceleration data collected from six tests during the winter testing program with the 33-ft WAM-V operating in a Sea State 1 condition, to test different damper settings on the second generation suspension system.

9.1 Chapter Overview

- Section 9.1 provides an overview of the chapter.
- Section 9.2 provides an overview of the testing procedure on the WAM-V.
- Section 9.3 discusses the qualitative notes recorded following testing.
- Section 9.4 analyzes the testing data using standards for acceleration and suspension response.
- Section 9.5 applies Whole-Body Vibration standards to testing data and analyzes the results.
- Section 9.6 provides the conclusions and recommendations from the chapter.

9.1.1 Significant Contributions

The following chapter represents the first application of existing standards for Whole-Body Vibration analysis to a marine vessel designed with a suspension system. This is both interesting and unique because the suspension system has a response that is tunable in frequency; understanding the frequency-dependent effects is highly important to the overall analysis. Existing standards have been applied to High Speed Craft [21]; however, the analysis was conducted after the vessel was designed, so the analysis has little impact on improving the dynamics. Improvements on High Speed Craft after the initial design phase are limited; shock mitigating seats are the most common alteration. This research represents the first known application of the standards to a vessel designed with a significant independent suspension system that is able to be tuned based on the resulting analysis.

9.2 33-ft WAM-V Testing for Whole-Body Vibration

This chapter focuses on the application of marine standards for analyzing vibration and standards for Whole-Body Vibration to the 33-ft WAM-V. The data chosen for the test was taken on December 14th, 2012 as part of the 33-ft WAM-V's winter testing program using the second generation suspension system detailed in Section 6.7. This particular set of data was chosen for evaluation because it is the most complete set of data available and it contains multiple suspension setting changes. This allows the data analysis to highlight the effects of the suspension changes on the WAM-V's performance. The testing was also conducted in conditions that were not extreme enough to cause motion induced interruptions or component failures that otherwise might have affected the tests.

9.2.1 Testing Overview

A day of testing was conducted with the 33-ft WAM-V in a Sea State 1 condition for the purpose of evaluating the WAM-V's ride quality during less extreme wave conditions. The testing location was off the coast of Norfolk, VA, between the Thimble Shoals Lighthouse and the Chesapeake Bay Bridge. A GPS plot of the route taken during the testing is shown in Figure 9.1, the yellow line represents the Day 2 data. The Day 1 route from the December 11th, 2012 testing analyzed as part of Chapter 7 is shown in blue.

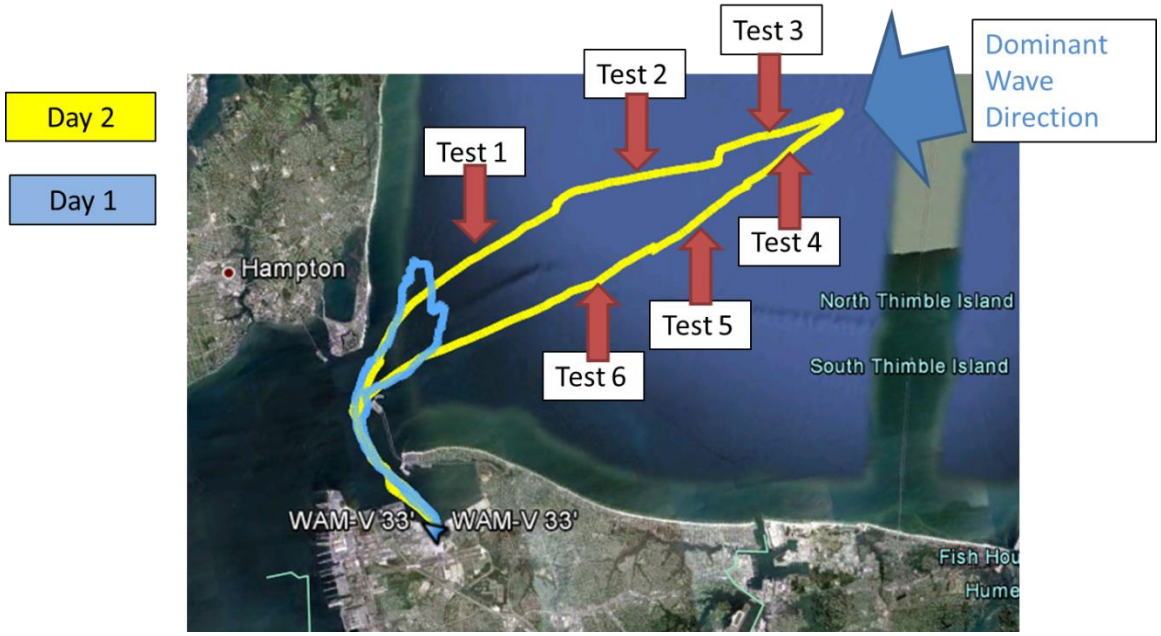

Figure 9.1 GPS trace of WAM-V route during testing showing test legs

For the first half of the testing day, three straight line testing legs were run at lengths of five minutes each with the WAM-V operating as close as possible to a head sea condition. The estimated dominant wave direction changed slightly between the tests; the average dominant wave direction during the time of testing is designated by the arrow in the top right corner of Figure 9.1. All of the tests were run with the WAM-V at a speed of ~20 knots, corresponding to the WAM-V's maximum available speed. Testing speed was increased from the 10 knot speed used on Day 1 to create a more harsh operating environment given the limited wave heights on the day of testing.

Between each leg of the test, different compression and rebound settings were dialed in on the WAM-V's adjustable dampers. For all of the testing legs, 500 lb/in springs were used and the ride height was not altered between the tests; however, the ride height was raised slightly from the ride height on Day 1 based on the findings from Section 7.3.

After the first three testing legs were completed, the WAM-V's heading was reversed and three additional tests were run with the same three different suspension settings in the opposite direction. This time the settings were tested in reverse order compared to Tests 1-3, creating a full set of data for head and following seas in the representative Sea State 1 conditions.

As with the other on-water tests, the WAM-V's heading was established by the support craft based on the dominant wave direction. However, for this series of tests, the speed was set by the WAM-V and matched by the support craft; since the test was conducted at the performance limit of the WAM-V's propulsion systems. Data was collected from the sensors on the WAM-V as detailed in Section 6.3; data was also recorded on the 7 meter RIB that can be used to determine the relative performance baseline for the WAM-V data against a standard hull form. At the time of this writing, the 7 meter RIB data has not been cleared by the Navy for release for a full analysis to be performed. Video data was taken by six cameras on the WAM-V as well as two cameras on the support craft; one camera was recording the support craft during the test and the other camera was recording video of the WAM-V. Suspension changes were made on the water with the WAM-V stopped and the suspension locked out using a custom lockout tool to reduce the chance of injury during suspension adjustments.

9.2.2 Suspension Settings for the Sea State 1 Tests

Between each of the test legs, the suspension damper's settings were adjusted in both compression and rebound. The graph of the available range of damping rates is shown in Figure 9.2. Because the adjustment knobs for changing the damper settings in rebound and compression have coupled effects, the two parameters were not evaluated independently. A full analysis of the damper's performance at different settings can be found in Section 6.7.

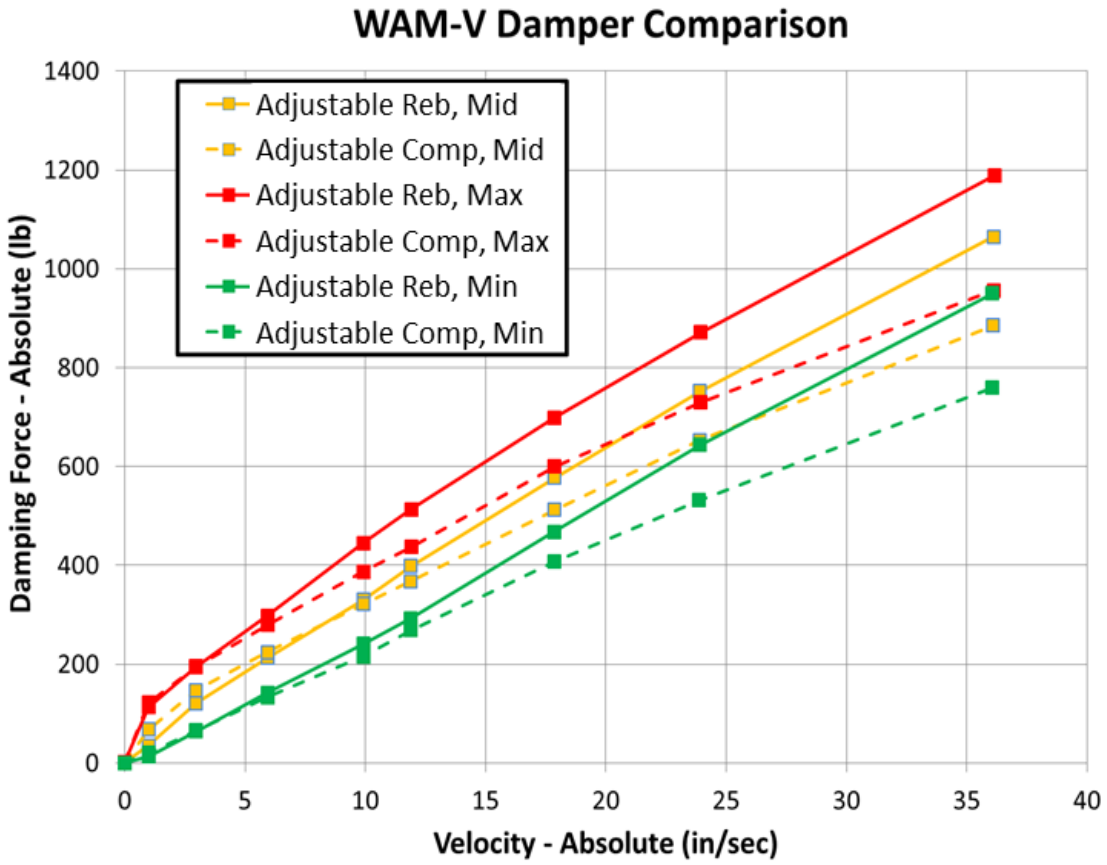

Figure 9.2 Range of damper settings evaluated during Sea State 1 testing

The wide range of damper settings that are available to be selected on the second generation suspension system were able to be tested at the upper and lower limits of the dampers. During more extreme conditions such as the Day 1 testing, the lowest settings in compression and rebound might be unsafe. Care should be used when designing a test plan that involves an adjustable suspension for future WAM-V tests, taking into account the sea conditions on the day of testing, which most likely will not be known ahead of time.

9.2.2.1 Damper Settings for Tests 1 and 6

For the first and sixth legs of the testing day, the dampers were set to their middle setting in compression and rebound. This corresponds to ~50% critical damping in compression, and ~50% critical damping in rebound. The adjustments necessary to the dampers to achieve the correct damping values for each of the three settings is listed in Table 6.7.

9.2.2.2 Damper Settings for Tests 2 and 5

For the second and fifth legs of the testing day, the dampers were set to their maximum setting in both compression and rebound. This corresponds to ~85% critical damping in compression and ~85% critical damping in rebound.

9.2.2.3 Damper Settings for Tests 3 and 4

For the third and fourth legs of the testing day, the dampers were set to their minimum setting in compression and rebound. This corresponds to ~15% critical damping in compression and ~15% critical damping in rebound.

9.3 Qualitative Notes from Testing

Since the focus of the majority of the analysis presented this chapter is on the effect of vibrations on human performance limitations, the WAM-V operator's comments from the Sea State 1 testing are particularly valuable, and thus they are included as part of the data analysis. A qualitative understanding of the WAM-V's performance is important to understand how vibrations are perceived. Only the operator's comments that are relevant to the suspension dynamics and craft motion were included in this section. Comments from the person on the support craft who was responsible for observing the WAM-V at all times are also included in this section. The person on the support craft was in charge of monitoring the WAM-V for safety purposes. Unlike the WAM-V operator, the support craft person was not burdened with the additional task of operating either of the crafts, so he was in an unburdened position to observe the WAM-V and its dynamics.

9.3.1 Operator's Notes from Testing:

WAM-V Operator: Andrew Peterson

- There wasn't a large perceptible difference in the effect of the damping changes on the suspension performance for the six tests conducted.
- Ride quality at low suspension deflections is still poor.
    - Suspension performance doesn't have an effect on longitudinal and lateral vibrations.
    - The effects of the deadband in the rear arch were highly perceptible during testing.
- Longitudinal/lateral vibrations are the dominant undesirable motion in this sea state.
- Seas were not very rough; however, in a few cases the waves were severe enough to produce good suspension motion.
- Since seas weren't very rough, speed was increased to 20 knots (equal to the WAM-V's maximum speed) to increase severity of motion in an attempt to create better data for analysis.
- The head seas conditions of Tests 1-3 were significantly rougher than the following seas conditions of Tests 4-6.
- Tests 1 and 6 were conducted in less rough seas than the other four tests due to the WAM-V being closer to shore during the first and last testing legs.

9.3.2 Support Craft Personnel Notes from Testing:

Person on support craft in charge of observing the WAM-V at all times: Michael Craft

- The boat was run in head and following seas (which were Sea State 1) and quite calm.
- Runs closer to the lighthouse were calmer (damper setup 1 & 6) than those closer to the bridge.
- From the chase boat, the stiff damper settings appeared to result in reduced suspension deflections over the minimum and mid-range damping, but the operator could not readily perceive a difference.
    - The minimal and inconsistent sea state would make these perceptions difficult.
- Because the seas were so calm, the test speed was increased to ~20 knots, the max speed of the WAM-V. Unlike recent tests, the WAM-V jets did cavitate on occasion at these speeds.

9.4 Methods of Analyzing Marine Acceleration Testing Data

The following section presents an application of the methods for analyzing marine acceleration data presented in Section 2.5. This section applies the relevant methods for analyzing the data collected during the Sea State 1 testing to provide additional context to the Whole-Body Vibration data analysis presented in Section 9.5, which is the primary focus of the chapter. All of the computations were based on a constant 240 second record length, collected continuously for each test leg; taken out of the 5 minute test lengths to avoid analyzing the transient data from the beginning and end of the tests.

9.4.1 Root Mean Square Analysis

Possibly the most common method of performing a standard analysis for a set of vibration data is to evaluate the Root Mean Square (RMS) values. RMS accelerations are discussed in detail in Section 2.5.2. The RMS values for the vertical accelerometer data collected from the various sensors during Tests 1-6 are shown in the top-view diagram of WAM-V in Figure 9.3.

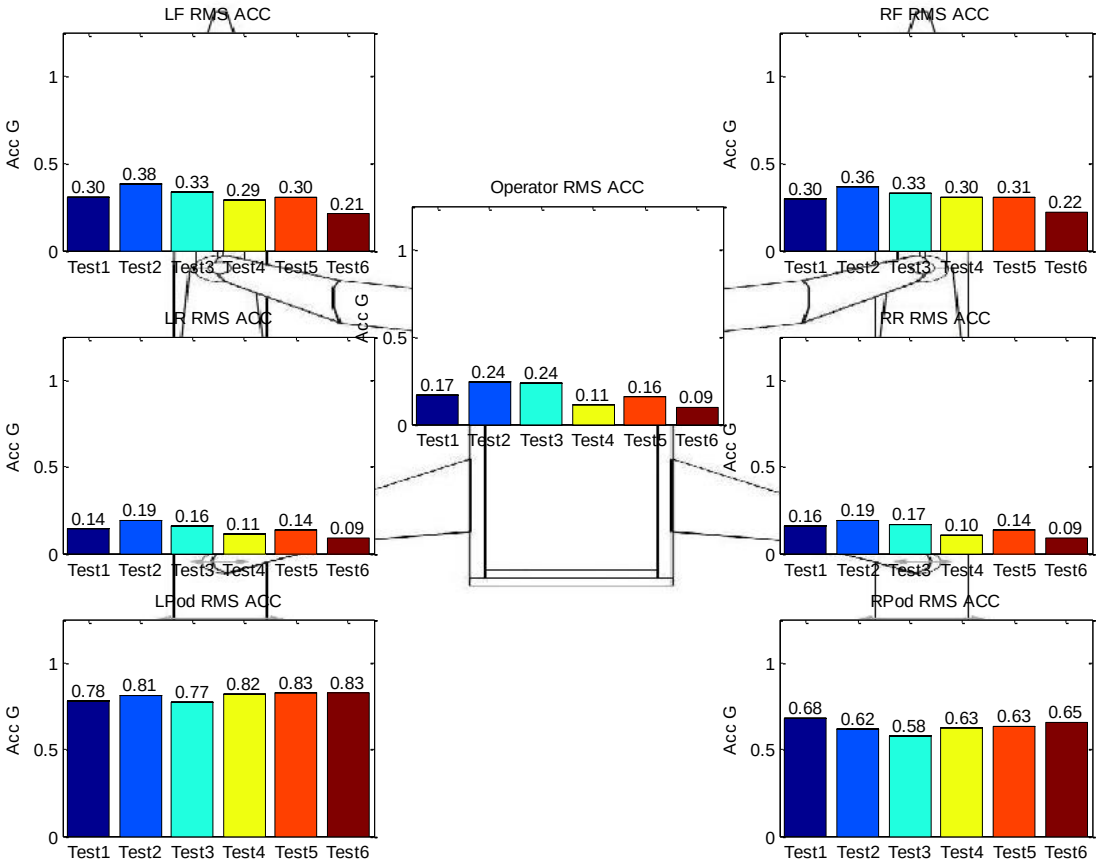

Figure 9.3 Vertical RMS acceleration data for Tests 1-6

By comparing the RMS data from the front pontoon accelerometers with the accelerometer near the operator, it is apparent that based on the RMS acceleration, there is good vibration attenuation between the front of the skis and the front of the payload. This comparison can be used as a metric of the suspension's performance for the different types of analysis presented in this chapter.

The accelerometers at front of the pontoons see significantly higher RMS acceleration levels than do the rear pontoon accelerometers; the engine pods see the highest levels of vibration. It is suspected that the engine pod data contains significant high frequency content from the powertrain units not related to the suspension, sea state, or vessel dynamics. The frequency content of the signals is investigated in Section 9.4.6 by looking at Fast Fourier Transforms of the accelerometer data.

Figure 9.4 shows the longitudinal and vertical RMS values taken at the triaxial accelerometer near the operator. The vertical acceleration RMS values are higher than the longitudinal values consistently across the tests, as much as 70% higher. The transverse data from the triaxial accelerometer is not included due to this axis malfunctioning during testing.

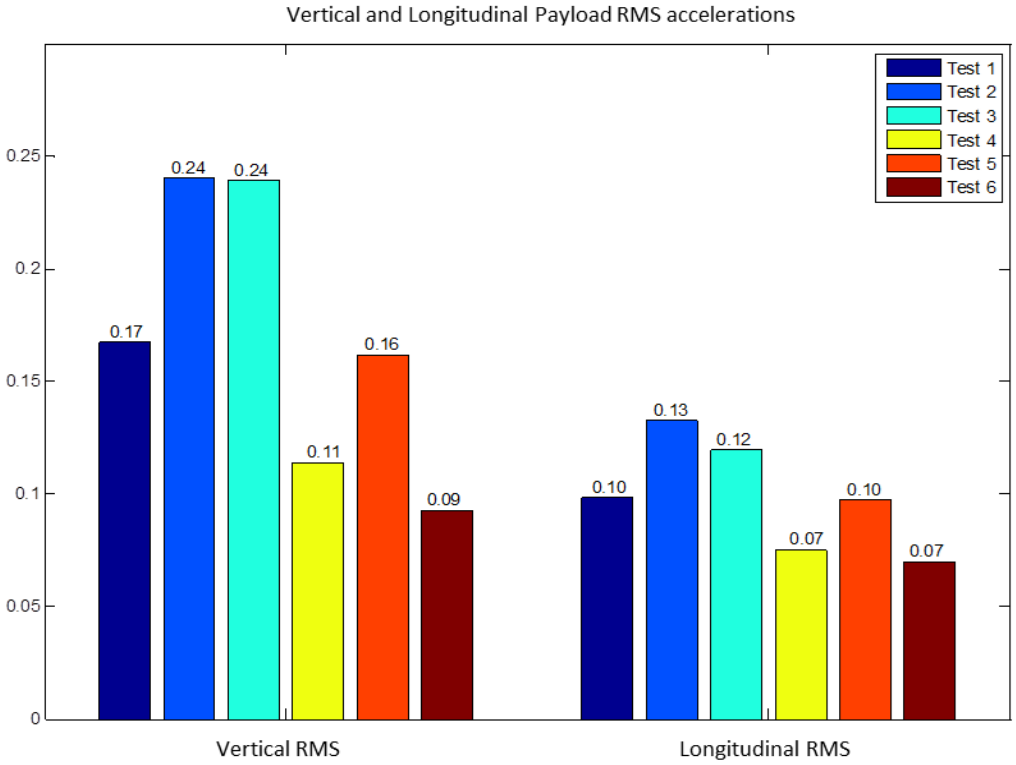

Figure 9.4 Vertical and longitudinal RMS acceleration data for Tests 1-6

9.4.2 Root Mean Quad Analysis

Root Mean Quad (RMQ) analysis is sometimes substituted in place of RMS analysis when transient shocks are present in the dataset; RMS analysis may undervalue the transient effects on output data. Root mean quad analysis is discussed in detail in Section 2.5.1. The RMQ values for Tests 1-6 are shown in the diagram of Figure 9.5 for the vertical direction.

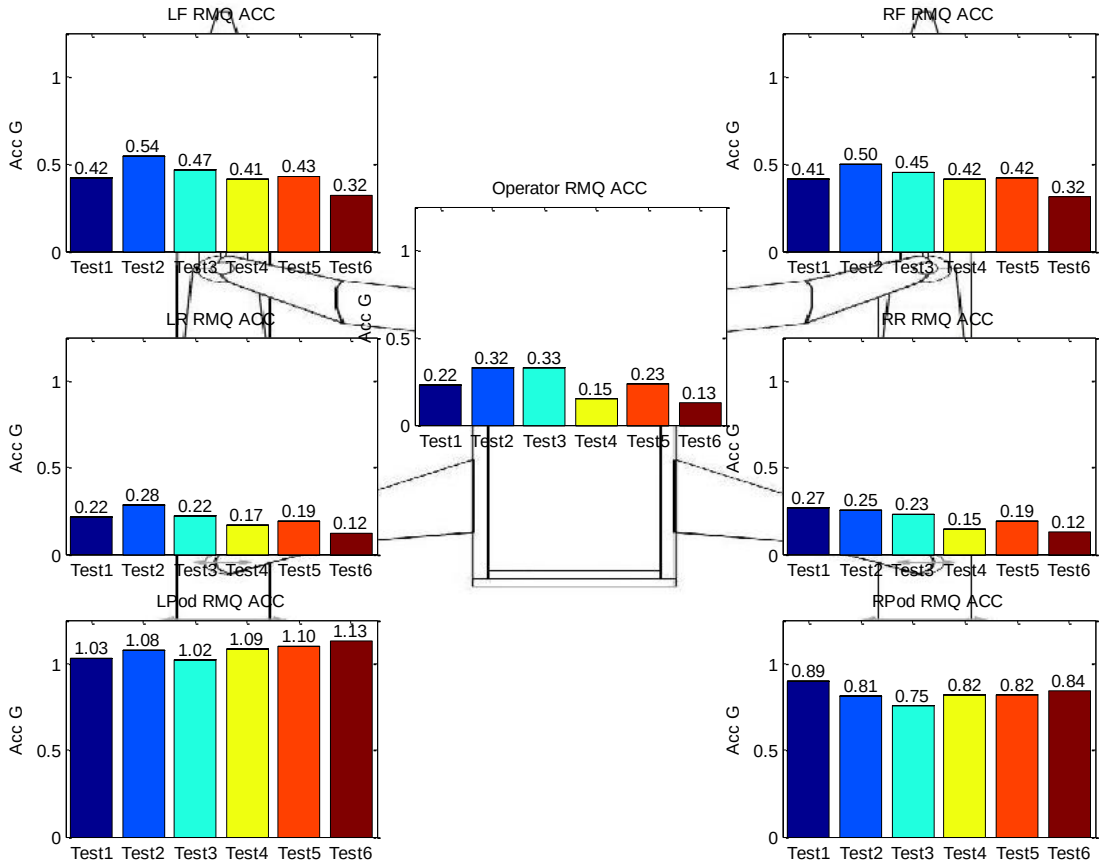

Figure 9.5 Vertical RMQ acceleration data for Tests 1-6

RMQ does a better job of highlighting the effects of impacts in a data set; however, for the Sea State 1 data, both the RMS and RMQ analyses show very similar trends between the different tests. Test 2 and Test 3 are still equal in harshness based on the vertical accelerations near the operator. What is evident from comparing the RMS and RMQ data is that the data from the rear pontoon accelerometers increases in value more than the front pontoon accelerometers. It is possible that this can be attributed to the rear of the pontoons rarely leaving the water, causing more infrequent changes in the acceleration peaks that are better captured with an RMQ analysis.

9.4.3 Maximum and Minimum Peaks Analysis

Figure 9.6 shows the maximum and minimum vertical accelerations recorded during testing. Although looking at only the maximum and minimum values from a particular set of testing data does not give an accurate view of the entire data set, there are some interesting things that can be compared with the data from other sections. A discussion of peak acceleration reporting is given in Section 2.5.2.

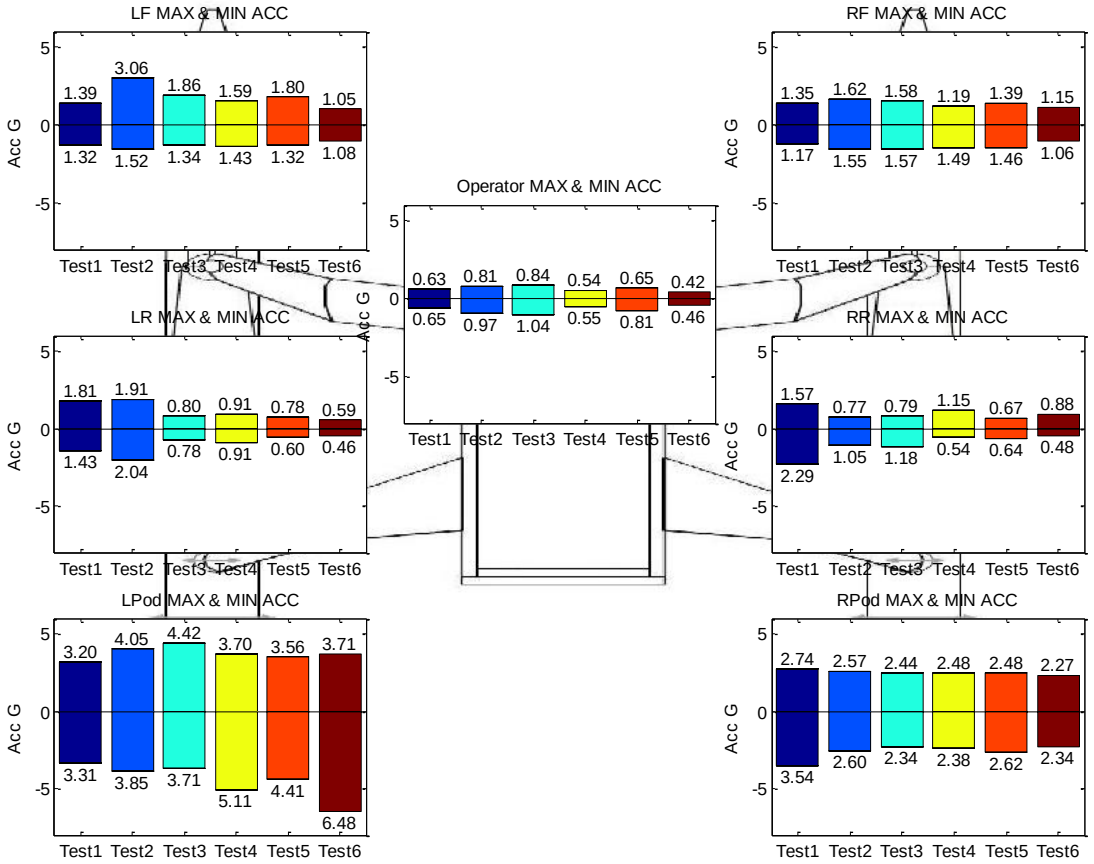

Figure 9.6 Maximum and minimum accelerations for Tests 1-6 (max = positive)

The maximum and minimum acceleration values follow similar trends to the RMS and RMQ analyses; albeit with significantly more deviations in the trends than when comparing the RMS and RMQ analyses against each other. For the majority of the data channels and most of the different tests, the maximum recorded positive acceleration values are greater than the maximum recorded negative acceleration values. However, the results are not consistent enough to form a definitive answer as to why this is this case. It is most likely due to small impacts causing high frequency, short duration, positive acceleration spikes in the dataset.

9.4.4 Average of the 1/3rd, 1/10th, and 1/100th Highest Peaks Analysis

Another method of analysis for marine accelerometer data is to look at the average acceleration over a percentage of the greatest acceleration peaks in the dataset. The method of averaging acceleration peaks is discussed in Section 2.5.3. Analyzing only the maximum and minimum values from a particular set of testing data often does not give an accurate view of the entire data set. For marine analysis, the average of the 1/nth highest peaks is determined by counting the number of peaks (N) greater than the RMS value of the data, then sorting the peaks in order of magnitude and averaging the value of the N/n highest peaks. Figure 9.7 shows the RMS acceleration along with the average of one-third, one-tenth, and one-hundredth highest peaks from two test legs, compared side by side. Tests 2 and 3 were chosen from the Sea State 1 data because the two tests were conducted in comparably rough conditions and the two extreme values of the available damping ratios were run on the adjustable dampers.

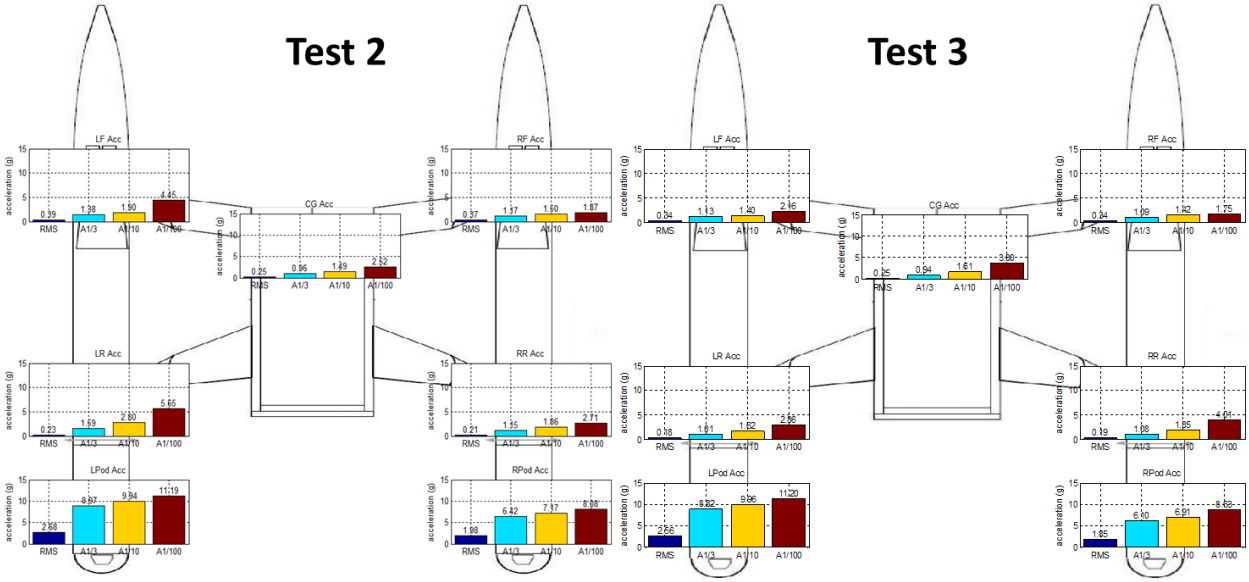

Figure 9.7 Vertical 1/nth average peak acceleration data for Tests 2 and 3

Tests 3 shows similar acceleration values at the operator compared to Test 2 for the RMS and the average of the one-third highest acceleration peaks, and higher values for the average of the one-tenth and one-hundredth highest acceleration peaks What is most evident from Figure 9.7 is how similar the data results are between the two tests. This might indicate that damper's performance is not as critical to the WAM-V's dynamics in a Sea State 1. Further comparison of Tests 2 and 3 will be conducted using the Ride Quality Index method in the next section.

9.4.5 Ride Quality Index Analysis

The Ride Quality Index method detailed in Section 2.5.8 can be used to compute the relative ride quality between a number of different tests and for different sensors on the 33-ft WAM-V. A few possibilities for the application of Ride Quality Index to the WAM-V are:

- Comparison of the front pontoon vs. the front payload accelerometer
- Comparison of relative ride quality for head and following seas for a given suspension setting
- Comparison of the same sensor during tests with different suspension settings

A comparison of the Ride Quality Index between different suspension settings is a useful addition to the average peaks analysis conducted for Tests 2 and 3 in Section 9.4.4. Using the method outlined in Section 2.5.8, first the RMS and peak acceleration levels for Tests 2 and 3 are taken from the analyses in Sections 9.4.1 and 9.4.3 respectively. The two data values are used to compute the crest factors from the tests; a separate analysis of the crest factors from the Sea State 1 testing is detailed in Section 9.4.7. Both of the computed crest factors are greater than 3, above the limit for acceleration analysis based on RMS alone [12]. The RMS, peak values and crest factors from the vertical accelerometer near the operator for Test 2 and Test 3 are listed below:

RMS accelerations:

- Test 2: 0.24 g
- Test 3: 0.24 g

Peak Values:

- Test 2: 0.81 g
- Test 3: 0.86 g

Crest Factors:

- Test 2: 3.35
- Test 3: 3.59

The acceleration data is then passed through a low pass, 10 Hz filter, and the impact peaks are tabulated. The filter used is a 5^{th} order Butterworth filter. The average of the peaks are then computed, the results are plotted against a linear trendline in Figure 9.8.

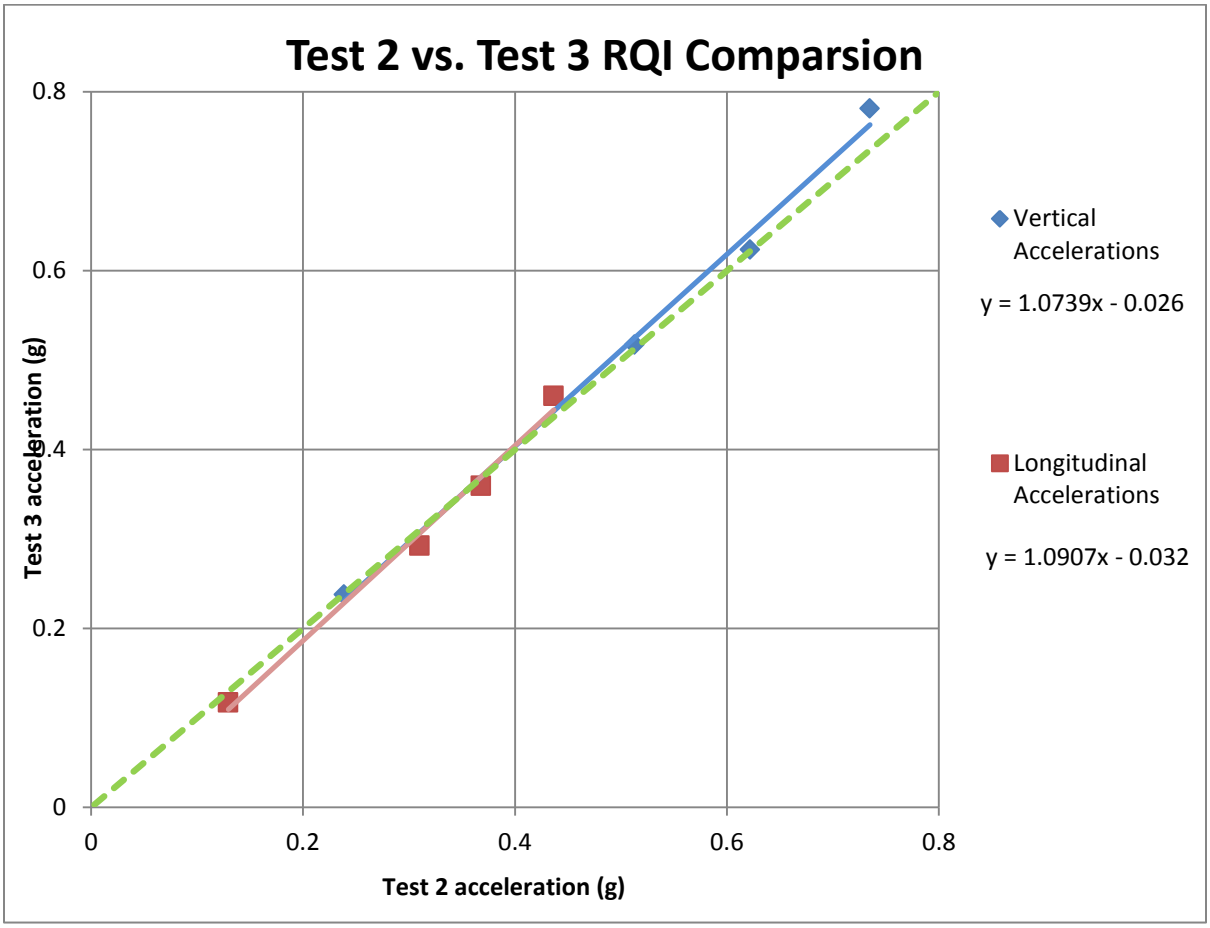

Figure 9.8 Comparison of Ride Quality Index for Tests 2 and 3 at operator

In Figure 9.8, trendlines are created for the vertical and longitudinal accelerations, comparing Tests 2 and 3. From the graph, the Ride Quality Index between the two tests can be computed, the results in the vertical direction are listed in Table 9.1. Table 9.2 lists the results for the longitudinal direction.

Table 9.1 Ride Quality Index values for Tests 2 and 3 in vertical direction

Data Type:	Test 2:	Test 3:	Ride Quality Index:
A 1/100	0.7348	0.7814	-0.0634
A 1/10	0.6218	0.6233	-0.0024
A 1/3	0.5128	0.5173	-0.0088
RMS	0.2386	0.2377	-0.0038
1-Slope	N/A	N/A	0.0688

Table 9.2 Ride Quality Index values for Tests 2 and 3 in longitudinal direction

Data Type:	Test 2:	Test 3:	Ride Quality Index:
A 1/100	0.4366	0.4599	-0.0534
A 1/10	0.3678	0.3593	0.0231
A 1/3	0.31	0.2925	0.0565
RMS	0.1295	0.1171	0.0958
1-Slope	N/A	N/A	0.0832

Computing the Ride Quality Index allows for a finer comparison of two sets of acceleration data than is possible with any of the other methods of analysis previously shown. Because the Ride Quality Index uses multiple data points to quantify a dataset, the results more evidently show trends in the data that aren't noticed with other types of analysis.

Based on the vertical direction data in Table 9.1, there is little difference in the Ride Quality Index between Tests 2 and 3. The results in the longitudinal direction are slightly more significant, slightly favoring the Test 2 condition (minimum damping), over the Test 3 condition (maximum damping). However, the Ride Quality Index for all of the data points is very close to one, so there are not any conclusive improvements to performance that can be inferred based on changes in the damping ratio.

9.4.6 FFT Frequency Content Analysis

Knowing the levels of acceleration in a marine dataset is important for analysis; however, knowing the frequency content within the data signals can often be more valuable in analyzing what the frequency content of the signals means in the results. The range of frequency content in the vertical accelerometers is shown in Figure 9.9 using a Fast Fourier Transform (FFT) method for Test 2 of 6. Fast Fourier Transforms for extracting the frequency content of a signal are discussed in Section 2.5.7. The frequency range in Figure 9.9 is computed from 0 – 250 Hz, the maximum available frequency range that can be accurately computed from the 500 Hz sampling frequency of the data acquisition unit.

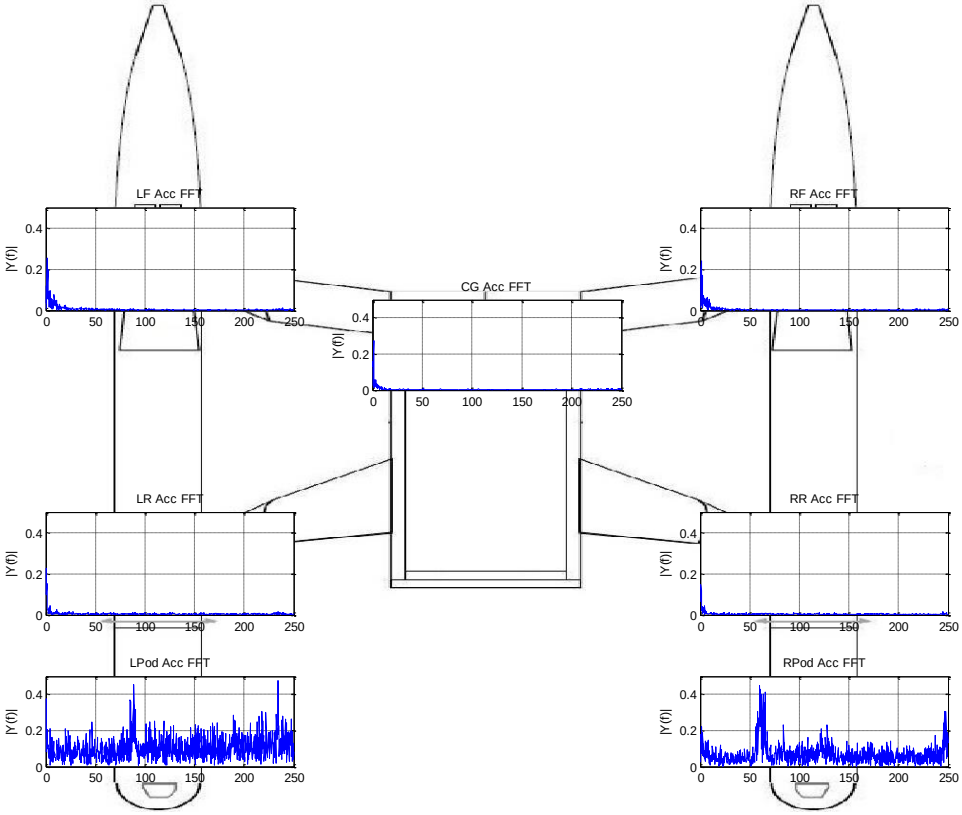

Figure 9.9 FFT's of accelerometer data for Test 2/6 with a 250 Hz cutoff frequency

Looking at the FFT data shown in Figure 9.9, it is fairly evident that for all of the sensors except the engine pods, the majority of the frequency content is found below 10 Hz. Figure 9.10 shows FFTs of the same data for frequencies less than 10 Hz. FFT data from Test 3/6 is also included in Figure 9.10.

In the case of the engine pod FFT data, there is a more broad distribution of the frequency content. Each signal has one specific frequency with greater content than the rest of the frequency range. For the port engine pod, there is a significant peak in the FFT data between 80 and 90 Hz, while on the starboard engine pod, the largest peak occurs at ~60 Hz. The peaks in the data are believed to be directly related to the operating speeds of the two engines. Since the engines were run at maximum throttle during the test, the two engines were likely running at different speeds. The possibility that the port engine was running faster than the starboard even though the WAM-V was moving in a straight line could indicate cavitation of the port-side jet nozzle, which was reported both by the operator and the person on the support craft observing the WAM-V during testing.

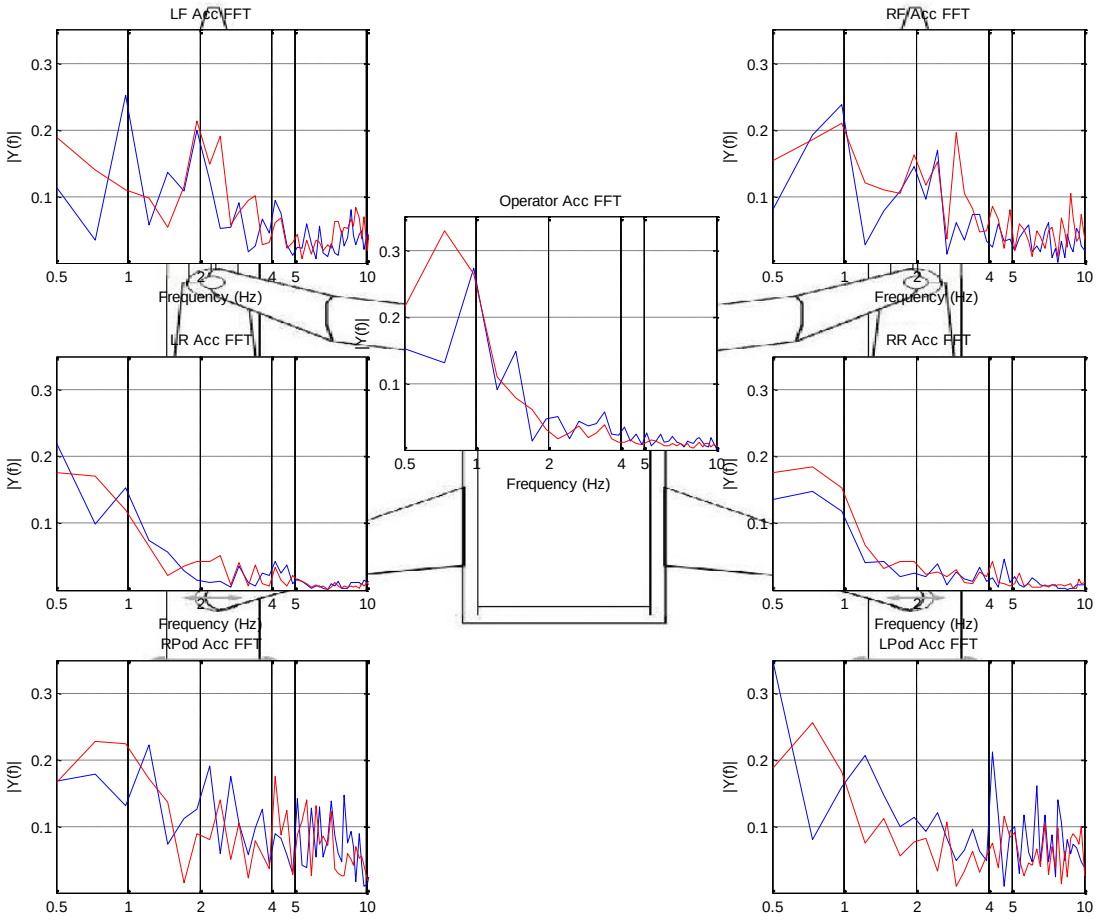

Figure 9.10 FFT's of accelerometer data for Test 2/6 (blue) and Test 3/6 (red) - 10 Hz cutoff frequency

Figure 9.10 shows FFTs from two tests for the vertical accelerometers at each of the different locations. The tests shown are Tests 2 and 3, chosen to highlight the effect of the difference in damping ratio on the frequency content of the signals; Test 2 is shown in blue, Test 3 is shown in red. At the operator, the primary frequency peak in the data occurs at 1 Hz. This is believed to be the primary wave encounter frequency. Even though there is a plateau, rather than a peak at 1 Hz in the Test 3 data, there is still significant frequency content there as well. The same frequency content is present not only in the front accelerometer data, but at the operator, rear pontoon, and even the hinged engine pods accelerometers as well, which is interesting. It is also possible that the low frequency motion can be attributed to the frequency of the engine pod rotation.

The peak at 0.8 Hz is more noticeable in the Test 3 data; it is present, but less noticeable in the Test 2 data. This frequency peak is believed to be due to the suspension's natural frequency, which is more prominent in the Test 3 data due to the lower damping ratio.

9.4.7 Crest Factor Analysis

Figure 9.11 shows the vertical crest factors computed for each of the six tests. What is most interesting about the crest factor data from the different tests is that the crest factors are highest at the rear pontoon accelerometers. The rear accelerometers see reduced low-frequency accelerations compared to the front accelerometers, and reduced high-frequency accelerations compared to the engine pods. This indicates that the rear of the pontoons is subjected to more random shocks and lower levels of sinusoidal vibration than any of the other signals. The rear pontoon accelerometer data was shown in Section 9.4.1 to have very low levels of RMS acceleration compared to the other sensors, which would make shocks more apparent in the data. This was also indicated in the differences in the RMS and RMQ analyses in Section 9.4.2.

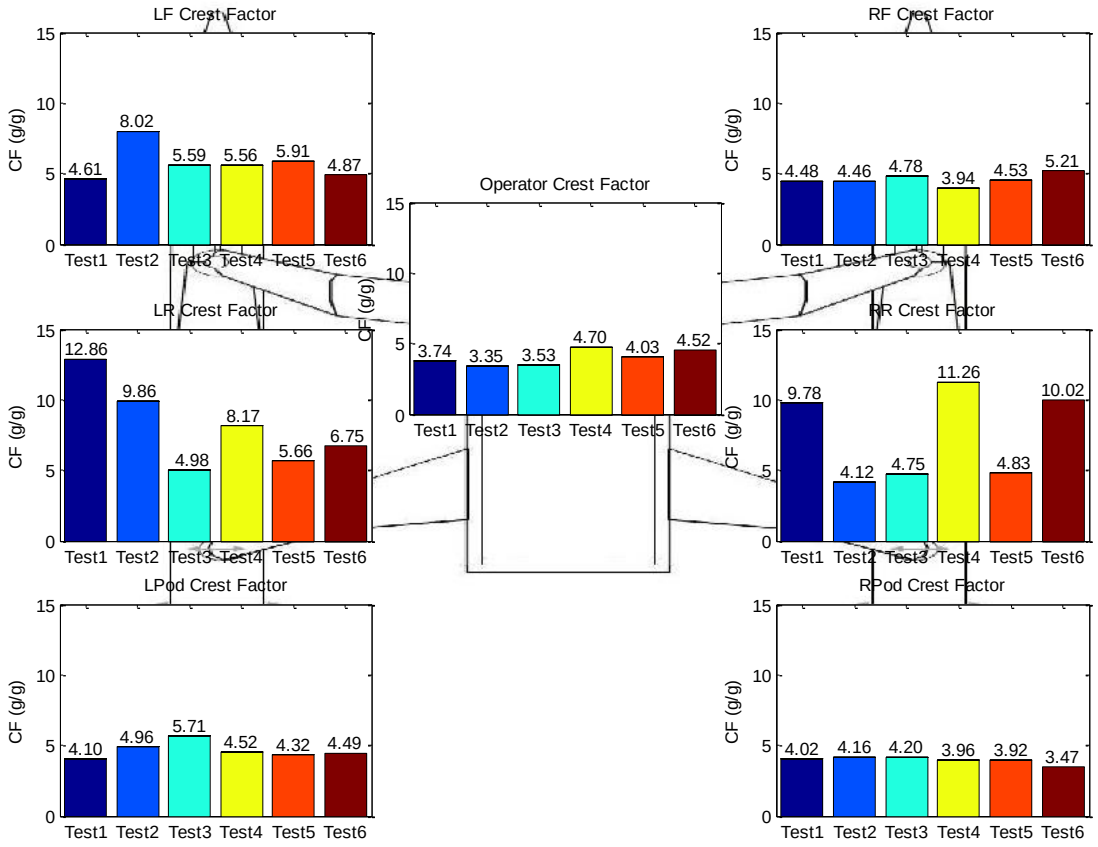

Figure 9.11 Crest factors computed from vertical acceleration data for Tests 1-6

9.4.8 Suspension Displacement Analysis Methods

Some of the methods outlined for analyzing accelerometer data can also be applied to the suspension displacement data recorded during the Sea State 1 testing. Figure 9.12 shows the RMS displacement from the suspension data, as well as the maximum and minimum displacements recorded by the suspension potentiometers for Tests 1-6.

Analysis of the maximum and minimum displacement values from the six tests is more important for quantifying suspension performance than the maximum and minimum acceleration values are for quantifying accelerometer data. For tuning the suspension system, it is important to know how close the suspension is to reaching its limit stops; contacting the stops can have a dramatic effect on ride quality.

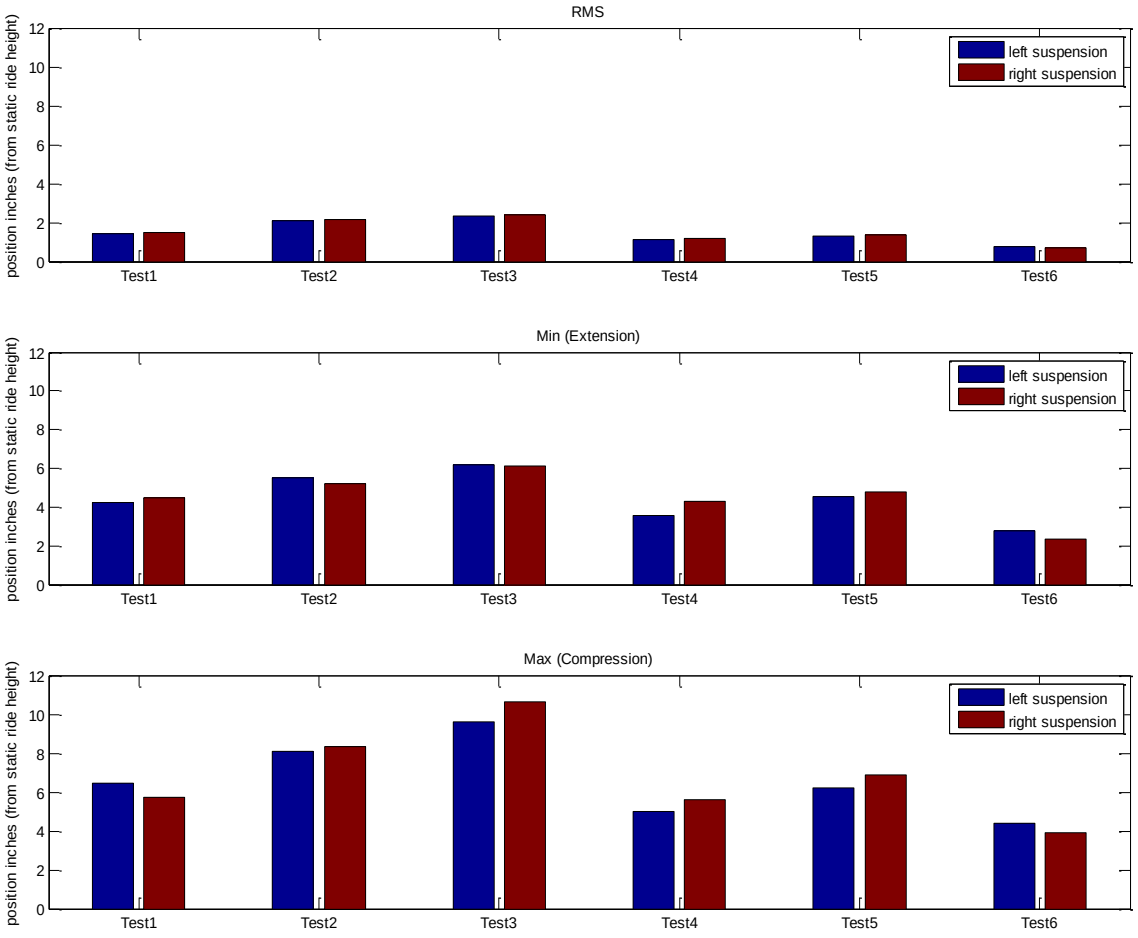

Figure 9.12 RMS, maximum, and minimum suspension travel measurement data from Tests 1-6

For all six tests, the suspension travel is noticeably greater for head seas than it is for following seas. The suspension travel recorded during Test 3 at the minimum damper setting shows greater levels of travel than the suspension travel for Test 2 at the maximum damper setting. It is not surprising that the decreasing the damping ratio increased the suspension travel; however, for Test 1 at the middle damper setting, less suspension travel was recorded than for Test 3 at the maximum damper setting. This is a surprising result; however, since Test 1 was run closer to the shore, the waves were slightly calmer, which explains their being less suspension motion.

For the followings seas data, Test 5 produced greater suspension travel than Test 4. This is the most surprising result from analyzing the suspension data from the six tests. Since Test 4 was run at the minimum damper setting and Test 5 was run at the maximum damper setting, the results are not easily explained. Reexamining the RMS and RMQ acceleration analysis plots shown in Figure 9.3 and Figure 9.4, Test 5 shows greater RMS and RMQ values for the majority of sensors; it is possible that the wave conditions happened to be slightly more intense at the time and location Test 5 was conducted compared to Test 4.

9.4.9 Suspension FFT Analysis

Figure 9.13 shows the frequency content of the suspension potentiometer data for Tests 1-3 of the Sea State 1 dataset. The frequencies were calculated using Fast Fourier Transforms; the data is shown from 0-10 Hz. Analysis of the frequency content of the suspension data can be used to determine the suspension's natural frequency, as well as to investigate the frequencies of excitation of the wave inputs.

Analyzing the frequency data provides additional insight into the suspension motion. The data from all three tests shows elevated frequency content at 1 Hz. A dominant frequency occurring at 1 Hz was also seen on the FFT's of the vertical accelerometers. By analyzing the video data from the tests, it was determined that 1 Hz is most likely the dominant wave input frequency for the test speed and wave conditions.

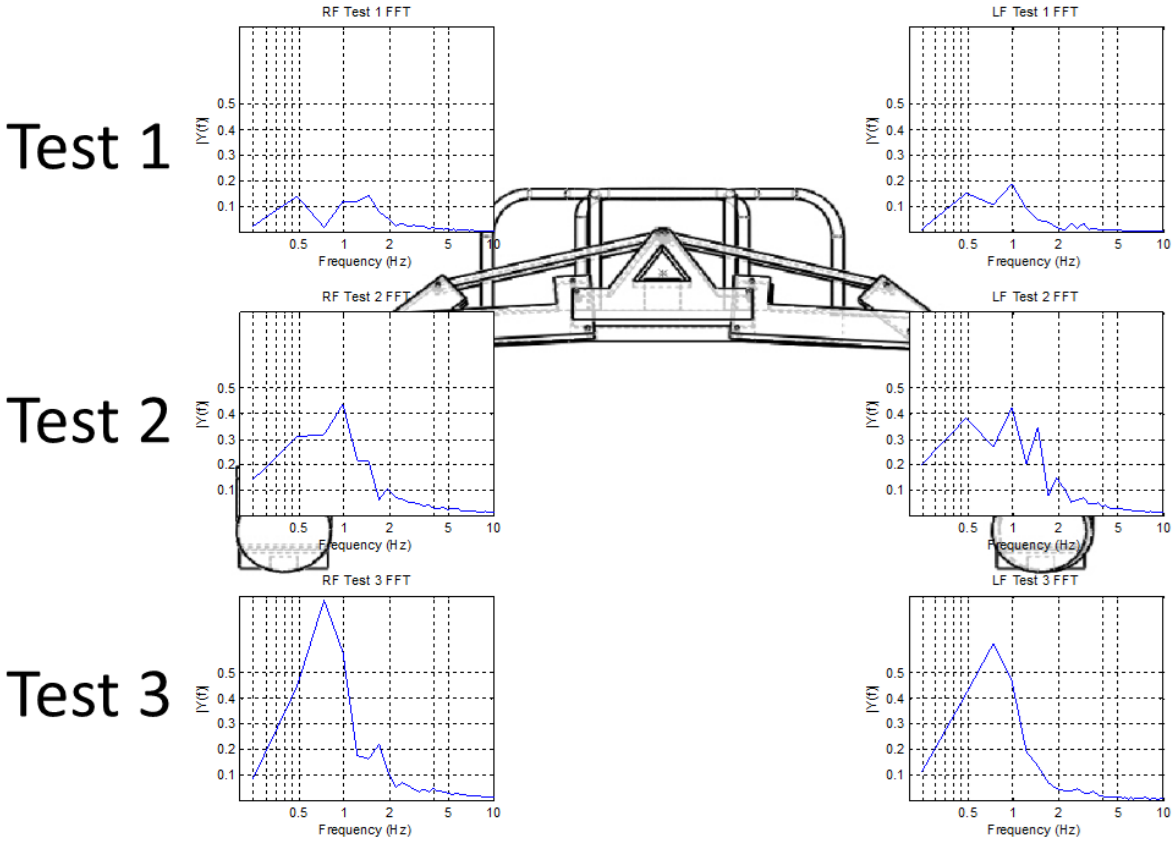

Figure 9.13 Test 1-3 suspension frequency FFT analysis

Another strong peak in the suspension potentiometer data occurs at 0.75-0.8 Hz. This is most likely the suspension's natural frequency, which was calculated to be approximately 0.8 Hz in Chapter 6. The strength of the frequency content at this frequency is greatest during Test 3, which is also the test where the dampers were set to their minimum setting, and it is the test with the greatest amplitude of suspension motion recorded in the data.

The strength of the signal is also strong for this frequency range during Test 2; however, for Test 1 the signal is weaker, most likely due to smaller amplitude waves not sufficiently exciting the suspension system. The smaller amplitude suspension motion was also shown in Figure 9.12, where Test 2 showed greater levels of suspension travel than Test 1, despite Test 2 being run with increased levels of damping.

9.4.10 Engine Pod FFT Analysis

Like the suspension system, an FFT analysis can be performed for the potentiometers on the engine pods as well. Figure 9.14 shows the frequency content of the engine pods potentiometers (shown in red), overlaid with the frequency content of the vertical accelerometers on the engine pods (shown in blue).

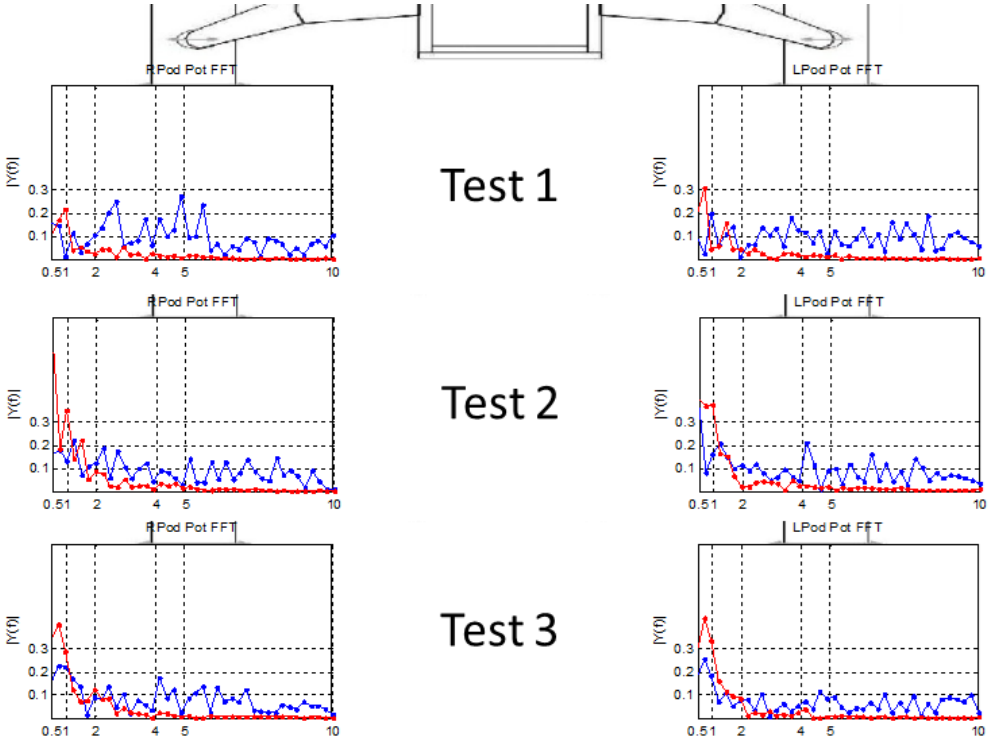

Figure 9.14 FFT of engine pod potentiometer for tests 1-3

The engine pods move at very low frequencies. The FFTs of the engine pod potentiometers show little frequency content above 1.5 Hz, while the accelerometers continue to have significant frequency content up to and above 10 Hz, as was shown in Figure 9.9. The frequency content of the engine pods accelerometers above 10 Hz was previously shown in Figure 9.9. This shows that the frequency content recorded by the engine pods accelerometers is due to high-frequency, low-amplitude vibrations from the propulsion units; not due to the rotation of the engine pods from the wave inputs.

9.5 Whole-Body Vibration Analysis

The following section presents an application of the standards for Whole-Body Vibration (WBV) analysis to the 33-ft WAM-V, based on the methods for applying the standards to accelerometer data presented in Section 2.6. The Whole-Body Vibration standards are also applied to the 33-ft WAM-V for the test data collected using the 2-post shaker rig; the results of which are shown in Section 10.9.

9.5.1 Overview of Applying Whole-Body Vibration Standards to the WAM-V

The primary sensor on the 33-ft WAM-V used for Whole-Body Vibration analysis is the triaxial accelerometer located close to the operator, but not mounted directly to the operator's chair. Figure 9.15 shows the proximity of the sensor to the operator. Some of the standards for Whole-Body Vibration specify that an accelerometer on a seat pad between the operator and the seat is the preferred method for measuring accelerations for Whole-Body Vibration analysis [23]. The location of the WAM-V's accelerometer will not capture the chair's dynamics, which are outside the focus of this study.

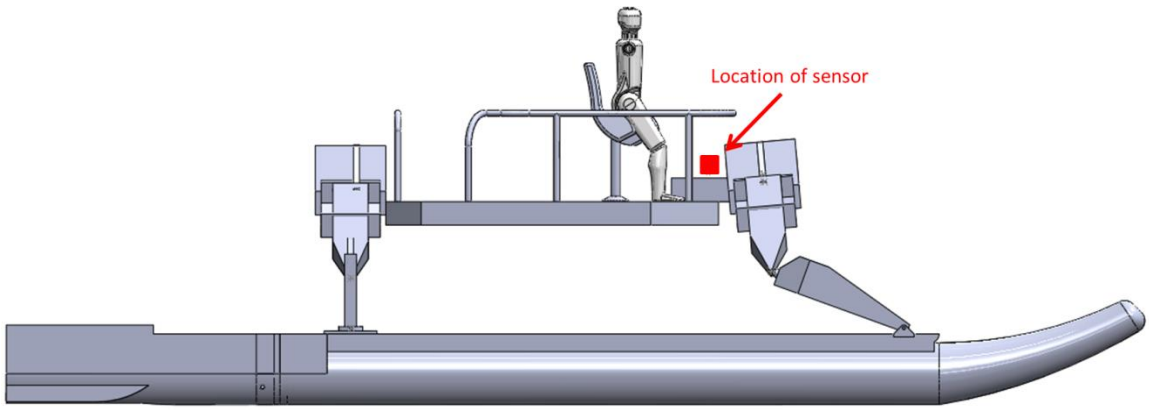

Figure 9.15 Location of sensor on WAM-V analyzed for Whole-Body Vibration analysis

9.5.1.1 Note on the Available Sensor Data from Testing

The data from the triaxial accelerometer data was compromised during testing in the transverse direction. The sensor malfunctioned along this axis only; thus, results are not included for the transverse direction. The longitudinal and vertical axes were not compromised, and the sensors were recalibrated following the test to ensure the validity of the data. The tests were unable to be repeated once the sensor was found to have been damaged, because the malfunction was discovered long after the WAM-V's winter testing program was completed.

9.5.2 One-Third Octave Filter Design

Many of the standards for Whole-Body Vibration analysis require filtering the data into frequency bins to weight portions of the data based on frequency. Frequency bins in one-third octave increments have been found to have sufficiently fine resolution, while producing a manageable number of frequency bins (23 bins for a 0.5-80 Hz spectrum) [37].

In order to apply the weights to the different frequencies based on the standards, a one-third octave filter bank was designed using Matlab that is able to be employed for analysis of the standards of Absorbed Power, ISO 2631-1, Vibration Dose Value, and Motion Sickness Dose Value; all of which are detailed in Section 2.6. The range of frequencies for each analysis type is listed in Table 9.3.

Table 9.3 Center frequency ranges for different Whole-Body Vibration standards

WBV Standard:	1/3rd Octave Center Frequency Range (Hz):
Absorbed Power	0.5 - 80
ISO 2631-1	0.2 - 100
Vibration Dose Value	0.2 - 100
Motion Sickness Dose Value	0.1 0.5

In order to break the acceleration data into its components for each frequency bin, a band-pass filter must be designed using a low-pass and a high-pass filter of the correct cut-off frequencies. The relationship between the center frequency and the minimum band frequency of the high-pass filter and the maximum band frequency of the low-pass filter is different for each of the different standards.

For Absorbed Power, each frequency band has a minimum band frequency of 0.89 times the center frequency and a maximum band frequency of 1.12 times the center frequency. For ISO-2631-1, the cutoff frequencies are located one-third octave away from the center frequency in either direction. The maximum and minimum cutoff frequency band for each center frequency is listed for frequencies from 0.1-100 Hz in Table 9.4 for Absorbed Power and ISO 2631-1.

Table 9.4 1/3rd octave filter frequency bands

1/3rd Octave Center Frequency (Hz):	Minimum Band Frequency (Hz) Absorbed Power:	Maximum Band Frequency (Hz) Absorbed Power:	Minimum Band Frequency (Hz) ISO 2631-1:	Maximum Band Frequency (Hz) ISO 2631-1:
0.1	0.089	0.112	0.08	0.16
0.16	0.1424	0.1792	0.1	0.2
0.2	0.178	0.224	0.16	0.25
0.25	0.2225	0.28	0.2	0.315
0.315	0.28035	0.3528	0.25	0.4
0.4	0.356	0.448	0.315	0.5
0.5	0.445	0.56	0.4	0.63
0.63	0.5607	0.7056	0.5	0.8
0.8	0.712	0.896	0.63	1
1	0.89	1.12	0.8	1.25
1.25	1.1125	1.4	1	1.6
1.6	1.424	1.792	1.25	2
2	1.78	2.24	1.6	2.5
2.5	2.225	2.8	2	3.15
3.15	2.8035	3.528	2.5	4
4	3.56	4.48	3.15	5
5	4.45	5.6	4	6.3
6.3	5.607	7.056	5	8
8	7.12	8.96	6.3	10
10	8.9	11.2	8	12.5
12.5	11.125	14	10	16
16	14.24	17.92	12.5	20
20	17.8	22.4	16	25
25	22.25	28	20	31.5
31.5	28.035	35.28	25	40
40	35.6	44.8	31.5	50
50	44.5	56	40	63
63	56.07	70.56	50	80
80	71.2	89.6	63	100
100	89	112	80	125

9.5.3 Frequency Bin Filter Designs

For analysis using ISO 2631-1, the type of filter that should be used to break the data into the different frequency bins for weighting and analysis is specified in the standard to be a Butterworth filter with an asymptotic slope of -12 dB per octave [13]. This is equivalent to specifying a 2^{nd} order Butterworth filter for analysis purposes.

For the Absorbed Power method, no particular filter type is specified. Furthermore, Absorbed Power is a nonlinear quantity with respect to RMS, changing RMS by a factor of three for a given frequency equates to an approximate ten times the Absorbed Power [39]. If Absorbed

Power is calculated using band-pass filters, the choice of filters is critical. Alternatively, Absorbed Power can also be calculated by computing the Power Spectral Density of the acceleration signal.

For quantifying Absorbed Power, four classic filter types: Butterworth, Chebyshev (types 1 and 2), Bessel, and Elliptic were initially evaluated. At first, a Butterworth filter was chosen as the ideal filter type due to its maximally flat pass and stop bands. However, Butterworth filters have a slower roll off period than the other filter types. The slow roll off period causes acceleration data at a single frequency to spill over into other frequency bins, and the data to be partially attenuated in the correct frequency bin. This is also the reason a Bessel Filter was not considered. Chebyshev filters with ripple in the pass-band (type 1) and ripple in the stop-band (type 2) were also evaluated, and found to be sufficient at all but the lowest center frequencies analyzed as part of the Absorbed Power method. A comparison of the response of four different classic filter types is shown in Figure 9.16. It is also noteworthy that each of the filters also have different phase responses as well, which are not covered in this section.

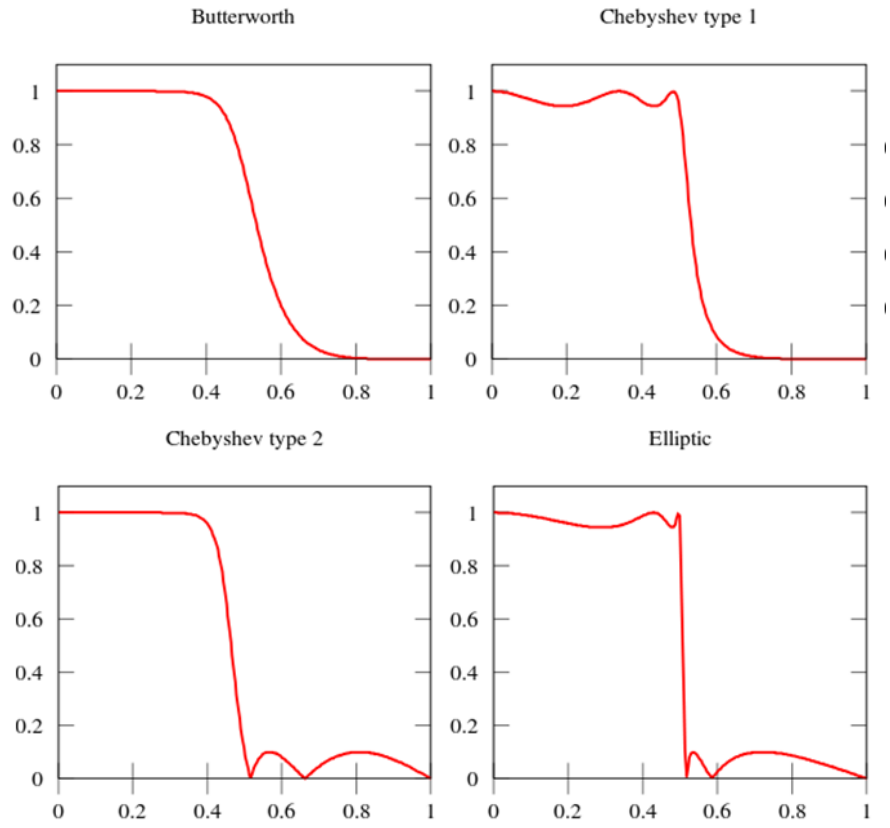

Figure 9.16 Comparison of four classic filter types [74]

Ultimately, an Elliptic filter was chosen as the best filter type for the Absorbed Power analysis. An Elliptic filter has the fastest roll-off rate of any of the filters evaluated, at the expense of some ripple in both the pass-band and stop-band. The Elliptic filter also showed the best performance at very low frequencies (< 0.5 Hz) where distortion of the signal can be problematic, even for high sampling rates. A filter that operates well at low frequencies is also particularly useful for calculating Motion Sickness Dose Values, which are most prevalent for input frequencies ranging from 0.08-0.5 Hz.

The ripple generated by an Elliptic filter is mitigated by the use of a high order digital filter in Matlab, the effect of the ripple was found not to impact the results if a significant time (>10 seconds) of data is used for a sample. A digital filter was designed for splitting the time-domain vibration signal into the relevant frequency bins. If an extremely short sample is being analyzed, such as the single-wave impact detailed in Section 7.3, an alternative filter type should be chosen. Raw acceleration data can be broken into the respective one-third octave bins using the following three steps:

1. A high-pass elliptic filter is applied to the raw acceleration data with the cutoff frequency of the filter set to the maximum band frequency of the first frequency bin listed in Table 9.4.
2. A low-pass elliptic filter is applied to the filtered data with a cutoff frequency set to the minimum band frequency of the first frequency bin listed in Table 9.4. This data is set aside as the filtered acceleration for that frequency bank.
3. Steps 1 and 2 are repeated for each frequency bank until filtered acceleration data has been generated for each frequency band listed in Table 9.4.

With the acceleration data broken into its respective frequency components, the weighting factors in Section 2.6.1 can be applied to each frequency and the weighted RMS acceleration can be calculated for each frequency. The weighted RMS frequencies are then summed to get the Absorbed Power along one axis for a particular sensor.

9.5.4 Absorbed Power Analysis

Figure 9.17 shows the Absorbed Power calculated for each of the vertical accelerometers for Tests 1-6 of the Sea State 1 data. The Absorbed Power levels shown on the pontoons and engines pods are not meant to be used to evaluate the vehicle's ride quality. The Absorbed Power levels from theses sensors are included to show the effectiveness of the suspension system at attenuating inputs at frequencies most relevant to human body dynamics. This is also the case for the ISO 2631-1 analysis presented in Section 9.5.5.

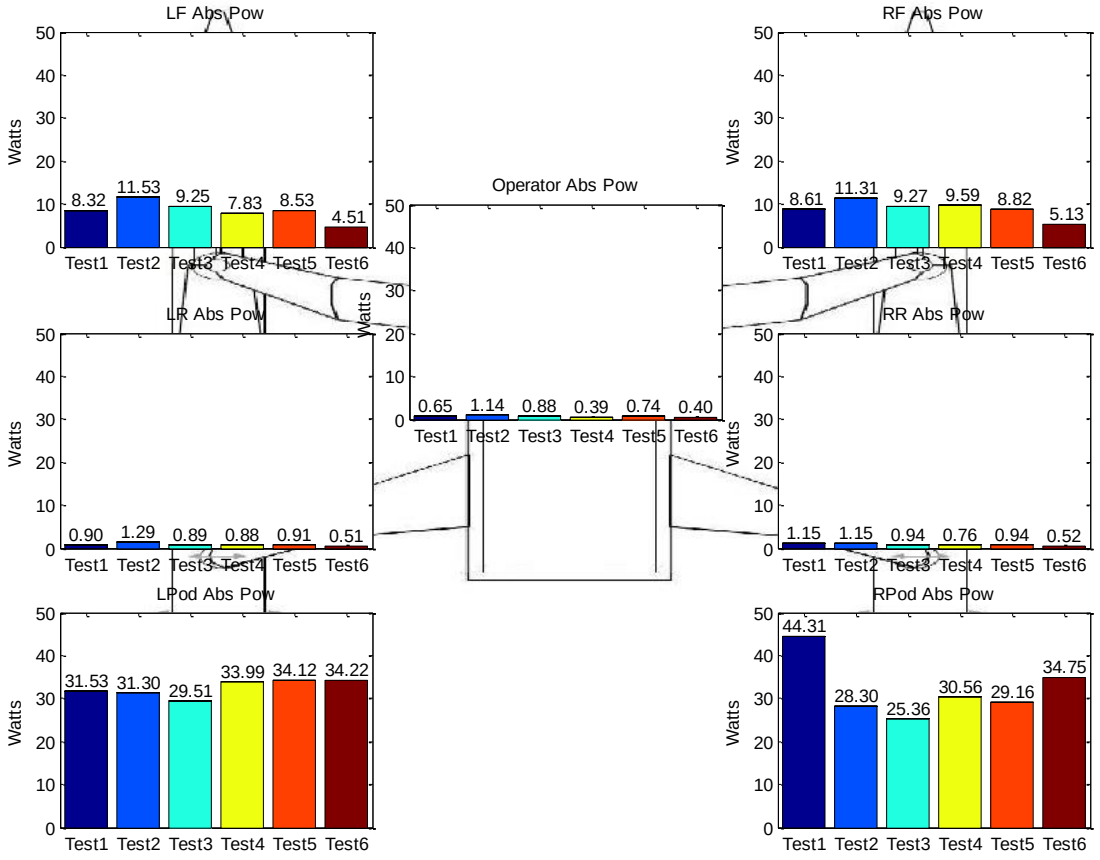

Figure 9.17 Absorbed Power levels in the vertical direction for Tests 1-6

Based on the vertical direction data, the WAM-V's suspension does an excellent job of attenuating the Absorbed Power. If the operator were riding on the front of the pontoons, the ride quality would be quite poor, with Absorbed Power levels as high as 11.53 watts calculated for Test 2. The maximum vertical Absorbed Power level is 1.14 watts at the payload tray (also for Test 2); so based on the Absorbed Power analysis in the vertical direction, the suspension attenuation is excellent.

However, as shown in Figure 9.18, the Absorbed Power levels calculated from the longitudinal accelerometer data recorded near the operator are almost an order magnitude higher than the Absorbed Power levels in the vertical direction for the same sensor. The Absorbed Power levels have been found to exceed the 6 watt limit for Test 2 and Test 3. Since the tests were only run for five minutes each, any effects on the operator from exceeding the limit are minimized.

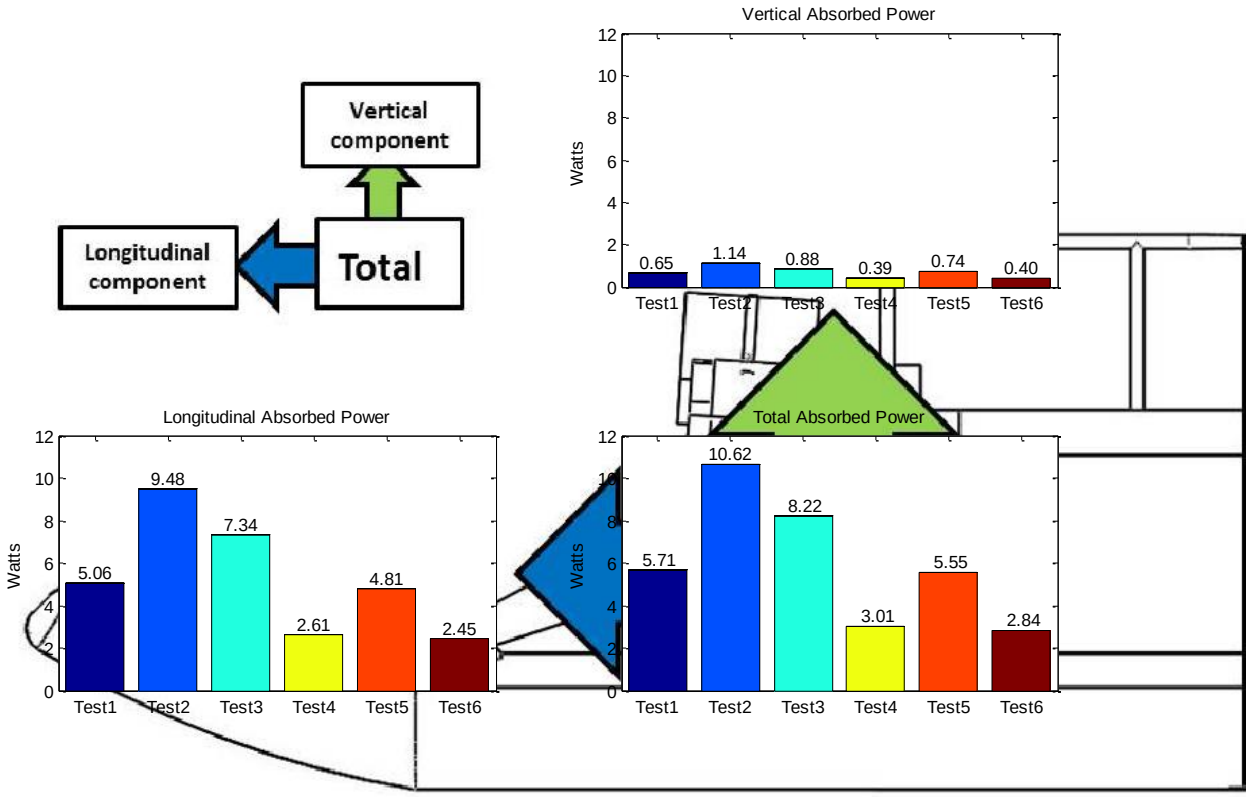

Figure 9.18 Absorbed Powers at triaxial sensor near operator for Tests 1-6

By comparing the differences in the Absorbed Power levels in the longitudinal and vertical directions, it can be seen that the longitudinal Absorbed Power levels are 6-9 times greater in magnitude than the vertical Absorbed Power levels, depending on the test. It is curious why the Absorbed Power levels are so much greater in the longitudinal direction than the vertical direction. Revisiting the results from Section 9.4.1, the RMS acceleration levels reported were marginally greater in the vertical direction. Figure 9.19 shows the reason for the severe longitudinal Absorbed Power levels. The RMS accelerations used to calculate the Absorbed Power levels for Test 2 of 6 are shown in Figure 9.19 for each individual frequency bin. Each point on the graphs represents the RMS level for one frequency bin.

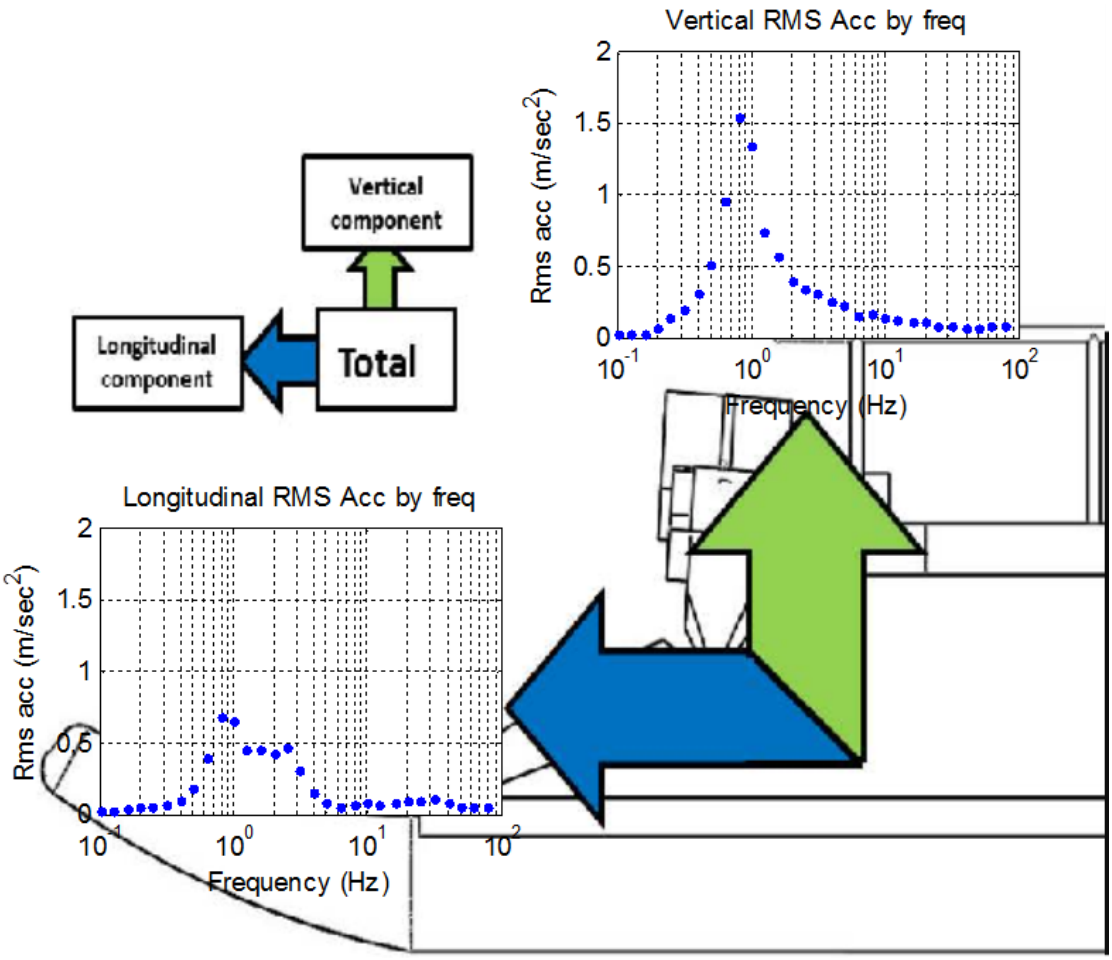

Figure 9.19 RMS frequency components for computing Absorbed Power (Test 2 shown)

Examining the two plots shown in Figure 9.19, the vertical graph shows a two point peak in the data at frequencies of 0.8 and 1.0 Hz. In the longitudinal direction there is also the same two point peak; however, in the longitudinal direction the peaks are half the magnitude of the vertical direction. The longitudinal plot also has a 4 point plateau from 1.25 to 2.5 Hz of roughly 0.5 m/sec^2. The six points in the longitudinal direction from 0.8 to 2.5 Hz correspond to the frequencies of greatest sensitivity for Absorbed Power as was discussed in Section 2.6.1.

The plot of the of the RMS accelerations corresponding to 6 watts of Absorbed Power is shown again in Figure 9.20, to quantify why the Absorbed Power levels recorded during the Sea State 1 testing were so high in the longitudinal direction compared to the vertical direction.

The vertical data points in Figure 9.19 at frequencies of greatest sensitivity in the vertical direction (shown in Figure 9.20 corresponding to the 4-8 Hz range), are significantly lower in magnitudes in Figure 9.19 than the data peaks that contribute to the RMS acceleration total being so high. This explains why the RMS accelerations are relatively high in the vertical direction and the Absorbed Power levels are relatively low.

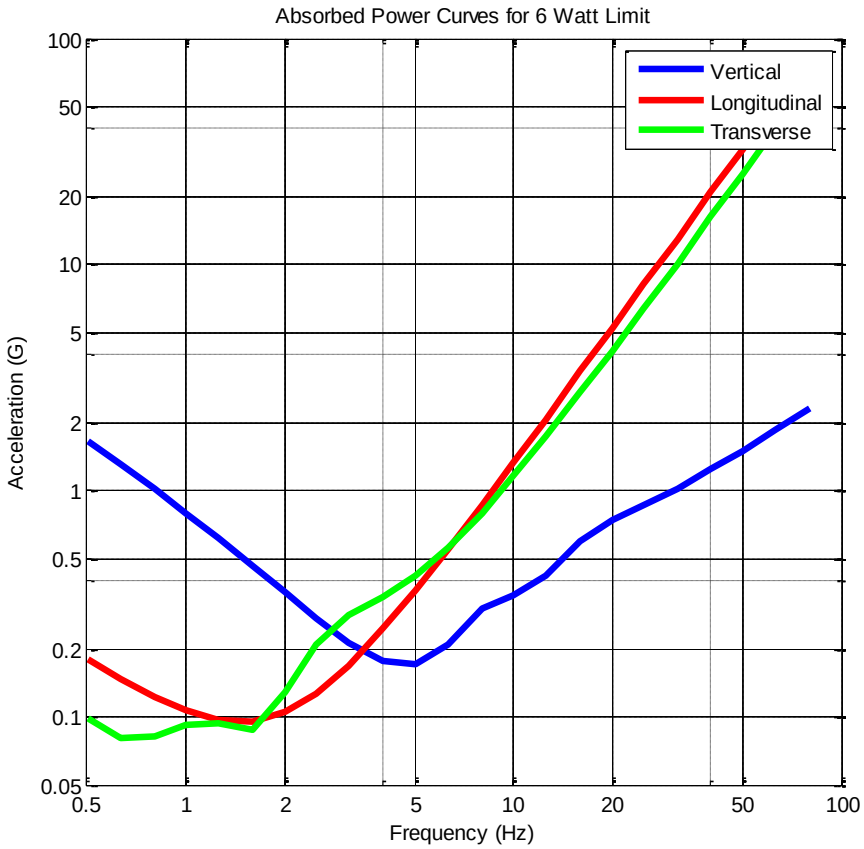

Figure 9.20 RMS acceleration curves for a constant 6 watts of Absorbed Power in each axis

Also, for the frequencies range of greatest sensitivity for each axis, the required RMS acceleration to reach 6 watts of Absorbed Power is significantly lower in the longitudinal and transverse directions than it is in the vertical direction. At their most sensitive frequencies, the longitudinal and transverse directions reach the 6 watt limit at slightly less than 0.1g's RMS, while the vertical direction requires 0.18g's RMS to reach the same 6 watt limit. This offset in the required RMS frequency is by design, based on the differing sensitivities of the human body to vibration along different axes.

9.5.5 ISO 2631-1 Analysis

Figure 9.21 shows the ISO 2631-1 weighted acceleration levels in the vertical direction for Tests 1-6. As with the results from the Absorbed Power analysis, the WAM-V's suspension does a good job of attenuating weighted accelerations, based on the vertical accelerometer data. The weighted acceleration levels are reduced by a factor of 2 from the front pontoon sensors to the vertical sensor near the operator on the superstructure. The level of attenuation is less than for the Absorbed Power analysis; however, changes in weighted acceleration using ISO 2631-1 are linear with respect to RMS acceleration for a given frequency, while they are nonlinear using Absorbed Power; so it is difficult to draw accurate comparisons between changes in the two metrics. A comparison of the two metrics is detailed in Section 2.6.3.

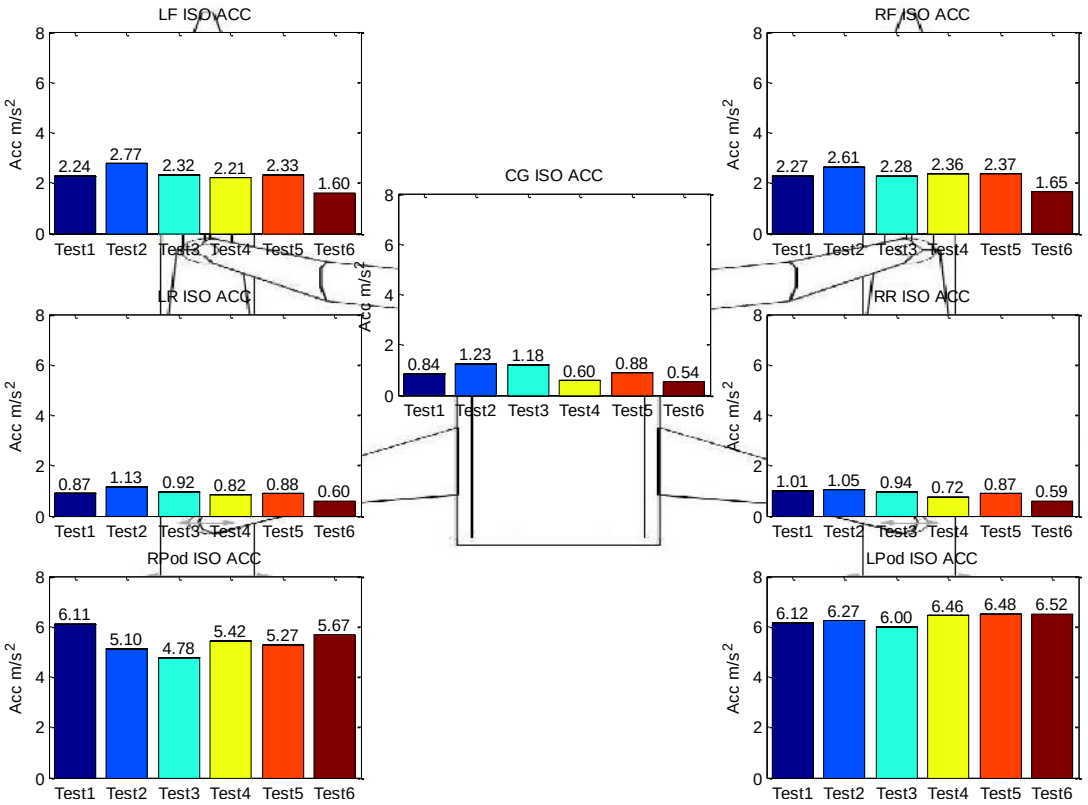

Figure 9.21 ISO 2631-1 accelerations in the vertical direction for Tests 1-6

Based on the vertical sensor data, the weighted acceleration levels are highest at the engine pods, followed by the front of the pontoons, and the weighted accelerations are the lowest at the rear of the pontoons and near the operator. Figure 9.22 shows the weighted accelerations calculated from the acceleration data recorded at the triaxial accelerometer located near the operator.

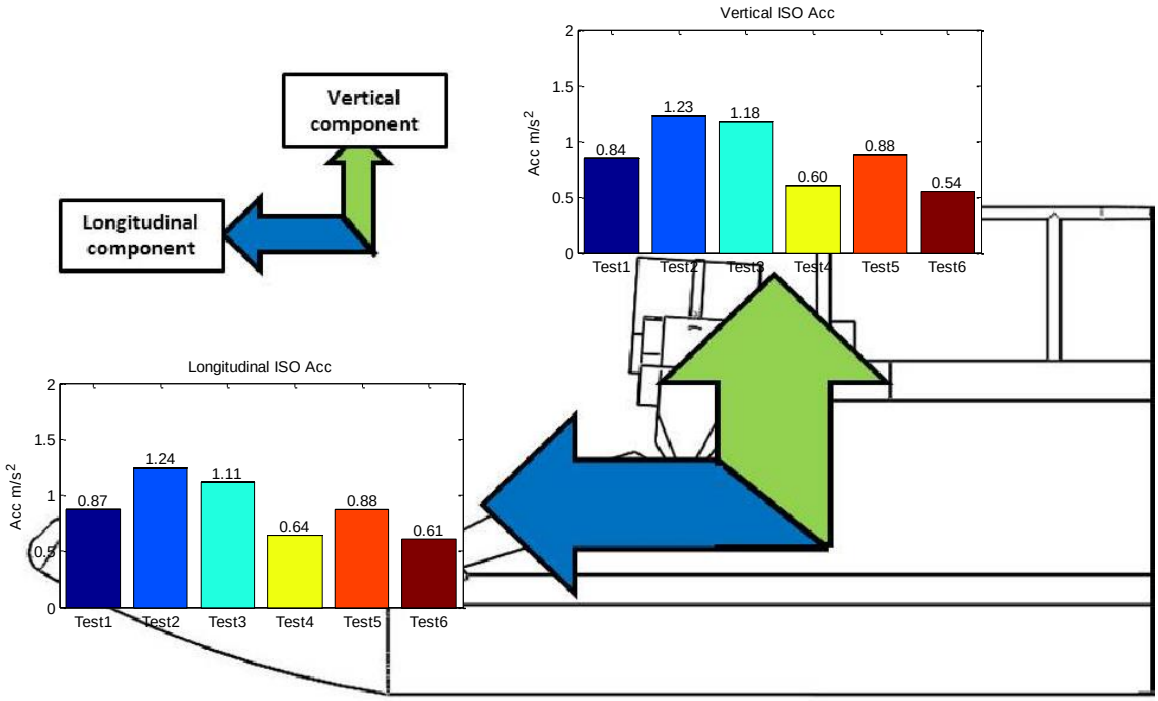

Figure 9.22 IS0 2631-1 acceleration levels at triaxial sensor near operator for Tests 1-6

The weighted acceleration values for the six tests shown in Figure 9.22 are almost identical for the longitudinal and vertical axes. However, for comparing the longitudinal and vertical axes, a multiplication factor of 1.4 needs to be applied to the data in the longitudinal direction based on Table 2.8. Since the values are roughly similar, the multiplication factor makes the longitudinal data effectively 1.4 times more severe than the vertical data for each of the six tests.

The frequency content that makes up the ISO 2631-1 weighting factor at different frequencies is the same data that was shown in Figure 9.19 for the Absorbed Power analysis. However, unlike the Absorbed Power method, there are additional criteria for ISO 2631-1 that can be used to define the level of comfort for given weighted acceleration values, and to define the same exposure time limits as well.

The following two subsections use the calculated weighted acceleration values to define the comfort guidelines and performance limits of the 33-ft WAM-V for the different Sea State 1 tests in the longitudinal and vertical directions. For these subsections, calculations are performed only for the data from the triaxial accelerometer located near the operator; comfort and fatigue analyses are not performed for the vertical accelerometers on the pontoons.

9.5.5.1 Comfort Guidelines Analysis

The weighted acceleration levels for Test 2 as per ISO 2631-1 were calculated as:

- 1.23 m/sec^2 - Vertical
- 1.24 m/sec^2 - Longitudinal

The longitudinal value needs to be multiplied by a factor of 1.4 as per Table 2.8, making its value 1.736 m/sec^2 for comparing with the vertical axis. Thus, the longitudinal acceleration value represents the worst axis from the test. Applying the data to Table 2.9, the vertical acceleration level is best described as 'uncomfortable', while the longitudinal direction is 'very uncomfortable.'

9.5.5.2 Exposure Limit Analysis

The application of the Health Guidance Caution Zone chart previously discussed in Section 2.6.2 to the data from Test 2/6 is shown in Figure 9.23. Both the vertical and longitudinal axes are plotted; the data is extrapolated out to greater exposure times than the 5 minute test length.

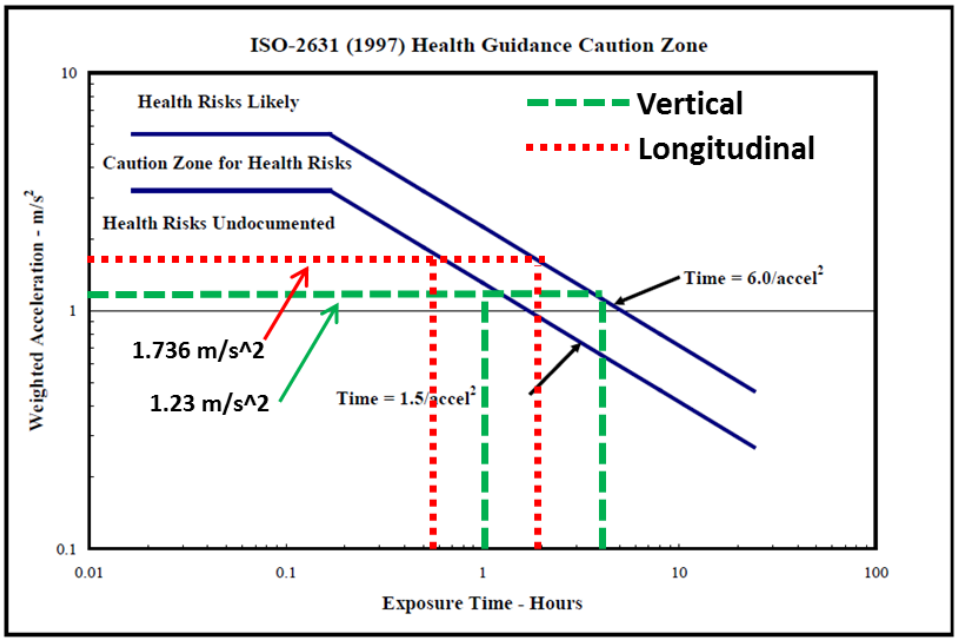

Figure 9.23 Health Guidance Caution Zone for Test 2/6 (modified from [37])

Based on Figure 9.23, it is apparent that both axes are below the threshold for the caution for health risks for short exposure durations. If the testing legs were run for a longer time, it is expected that that the 'Caution Zone for Health Risks' would be reached in ~1 hour on the

vertical axis, and in ~30 minutes on the longitudinal axis. The 'Health Risks Likely' zone would be reached in ~4 hours on the vertical axis, and ~2 hours in the longitudinal axis. The trends in data show that the longitudinal limits are reached in roughly half the time of the vertical limits.

The comfort reaction and exposure limit results for all six tests are listed in Table 9.5 and Table 9.6 respectively. The results are consistent with the other methods of analysis showing the similarities between Tests 2 and 3, as well as the head seas data (Tests 1-3) being significantly more rough than the following seas data (Tests 4-6).

Table 9.5 ISO 2631-1 comfort reactions for Tests 1-6

Test #	Weighted Vertical Acceleration	Weighted Longitudinal Acceleration	Vertical Comfort Reaction	Longitudinal Comfort Reaction
1	0.84	1.218	Fairly uncomfortable	Uncomfortable
2	1.23	1.736	Uncomfortable	Very Uncomfortable
3	1.18	1.554	Uncomfortable	Very Uncomfortable
4	0.60	0.896	Fairly uncomfortable	Fairly uncomfortable
5	0.88	1.232	Fairly uncomfortable	Uncomfortable
6	0.54	0.854	A little uncomfortable	Fairly uncomfortable

Table 9.6 ISO 2631-1 health guidance limits for Tests 1-6

Test #	Caution Zone Limit (Vertical):	Caution Zone Limit (Longitudinal):	Health Risks Likely (Vertical):	Health Risks Likely (Longitudinal):
1	2.1 hours	1.0 hours	8.5 hours	4.0 hours
2	1.0 hours	0.5 hours	4.0 hours	2.0 hours
3	1.1 hours	0.6 hours	4.3 hours	2.5 hours
4	4.2 hours	1.9 hours	16.8 hours	7.6 hours
5	1.9 hours	1.0 hours	7.8 hours	4.0 hours
6	5.1 hours	2.0 hours	20.3 hours	8.1 hours

9.6 Conclusions and Recommendations for Further Research

Whole-Body Vibration analysis of the 33-ft WAM-V has provided significant information as to how the dynamics of the WAM-V and the wave environment specifically affect humans onboard the WAM-V. The following section details the major finding and recommendations from the chapter and discusses possible further application of the Whole-Body Vibration standards to other sets of existing data for Wave-Adaptive Modular Vessels. Conclusions from ISO 2631-1 weighted acceleration analysis are also discussed in the conclusions and recommendations section in Chapter 10, following the application of the standard to the data from the 2-post testing rig.

9.6.1 Overview of Major Findings from Chapter

- Previous research on WAM-Vs focused on vertical vibration attenuation. This chapter has shown longitudinal vibration to be the limiting performance factor of the WAM-V, at least for non-elevated sea states in terms of comfort and exposure time limits.
- Further correlation of Absorbed Power and ISO 2631-1 is needed to decide if these or the other mentioned methods of vibration measurement are suitable for the analysis of future WAM-Vs. Based on this chapter ISO 2631-1 is the preferred method for analysis with the WAM-V; the results are linear with respect to RMS for a given frequency, and the results included comfort and exposure limit guidelines.
- Further advancement of fourth power methods such as RMQ, RQI, and VDV would be useful for establishing a standard method for analyzing all future WAM-V data. A single averaging procedure might be possible using one (or a combination) of these methods, which could be applied over the entire range of vibrations in the marine environment.

9.6.2 Recommendation from Sea State 1 Testing

- Suspension adjustments between the Sea State 1 tests were able to be made because the conditions were not particularly rough. The suspension lockout tool worked well to keep the person making the adjustments safe while the dampers were adjusted.
- It would have been difficult if not impossible to make these changes in a Sea State 3 condition. It would not be overly difficult to add servos to the damper knobs to make the changes via remote control. This would greatly simplify future testing procedures.

9.6.3 Recommendations from Whole-Body Vibrations Analysis

- The results from testing and the analysis of the different Whole-Body Vibration standards show that the WAM-V's suspension is effective in a low sea state based on the suspensions ability to attenuate vertical accelerations.
- The WAM-V shows the greatest needs for improvement for vibrations in the longitudinal direction, confirmed by both the ISO-2631-1 and Absorbed Power analysis methods.
- Changing the damper setting did not have a major impact on the WAM-V's performance in a low sea state. Vertical accelerations were not as significant as longitudinal accelerations, which occurred in the most frequency sensitive range for human exposure.
- Qualitative analysis of the other on-water tests shows that the 33-ft WAM-V begins to show improved performance compared to the support craft in a more elevated sea state than the testing analyzed in this chapter. The WAM-V also performs better than the support craft at lower speeds when the support craft hasn't reached planing speed.

9.6.4 Application of Whole-Body Vibration Standards to Other WAM-V Datasets

The data presented in this chapter is for the 33-ft WAM-V operating in a Sea State 1 with the second generation suspension system. The particular dataset used represented the best available dataset for back to back comparisons of different suspension settings. Other viable datasets exist to which the Whole-Body Vibrations standards could be applied. This section recommends a few possible areas of research that could expand upon the analysis performed on existing WAM-V datasets.

9.6.4.1 WAM-V and Rigid Inflatable Boat Comparison during Sea State 1 testing

A portion of the data analysis in this chapter was originally planned to be a comparison the 7-meter RIB used as the support craft and the 33-ft WAM-V during the same test. Accelerometer data was collected on the support craft by NAVSEA using their own data acquisition equipment. Video acquisition data is also available for the support craft during the same tests as the WAM-V. There are significant differences between the two crafts that would have interesting effects on the data. Most notably, the 7-meter RIB is of significantly higher displacement (12000 lbs vs. 4300 lbs) than the WAM-V. Unfortunately, the data on the 7-meter RIB has to go through the appropriate channels in the government and the Navy before being released to CVeSS for

analysis. The amount of time the data has taken to be processed and released has precluded the data being included as part of this dissertation; however, once the data is available, a data analysis between the WAM-V and the support craft would make for a very interesting comparison.

9.6.4.2 Elevated Sea State data

Two datasets exist for the 33-ft WAM-V operating in more extreme conditions than the Sea State 1 data detailed in this chapter. During the WAM-V's summer testing program, a day of testing was conducted in a Sea State 2 at a speed of 15 knots. During the winter testing program, a day of testing was conducted in conditions up to a Sea State 3 at a speed of 10 knots. Both testing days were shortened by mechanical failures of the WAM-V's powertrain units; however, limited datasets exist for both tests. For the Sea State 3 dataset, data also exists on the support craft from the test. The support craft data can be compared with the data from the 33-ft WAM-V once the data becomes available.

9.6.4.3 Comparison of Sea State 1 Data with Calm Water Data

The data from the Sea State 1 testing could also be compared with the calm water data for the WAM-V detailed in Appendix B. Duplicate calm water data exists for the WAM-V running the same type of tests during the summer testing program as well.

There is some question for the Whole-Body Vibration standards, as to what the contributions the waves make to the vibration data, and what part of the data comes from the general operation of the WAM-V that would occur in any sea state. To help to answer this question, the Whole-Body Standards could be applied to the calm water data also analyzed in Appendix B, and compared with the Sea State 1 data. Unfortunately, data from a test is not available in calm water with the new suspension system. The calm water data would have to be compared to a test with the original suspension system to the Sea State 1 data with the second generation suspension system, to determine the effects of operating in a Sea State 1; then a separate correlation would have to be made between operating with the original and second generation suspension systems.

Chapter 10 2-Post Shaker Rig Testing and Analysis

The following chapter provides a discussion of the analysis of the dynamics of Wave-Adaptive Modular Vessels performed via the design, construction, and testing of a 2-post shaker rig for the 33-ft WAM-V. An overview of multi-post shaker rig testing and lab testing standards for marine vessels is given, along with a discussion of the design methodology, component construction, and instrumentation setup of the 2-post rig. Data analysis of the 2-post tests is shown, along with comparisons of the original and second generation suspensions systems. Finally, an analysis of the standards for Whole-Body Vibration on the 33-ft WAM-V using the 2-post rig is discussed.

10.1 Chapter Overview

- Section 10.1 provides an overview of the chapter.
- Section 10.2 provides a review of vehicle testing using multi-post rigs.
- Section 10.3 describes the design methodology of the 2-post rig.
- Section 10.4 details construction of the 2-post testing rig and its various components.
- Section 10.5 details the initial testing and data analysis procedures for the 2-post rig.
- Section 10.6 details the initial data analysis of the 2-post rig for different damper settings.
- Section 10.7 provides analysis of a longitudinal stiffening brace using the 2-post rig.
- Section 10.8 compares the original and second generation suspensions on the 2-post rig.
- Section 10.9 analyzes Whole-Body Vibration standards with the 2-post rig.
- Section 10.10 provides the results, conclusions, and recommendations from the chapter.

10.1.1 Significant Contributions

This chapter brings together in full circle the major aspects of simulation and testing related to Wave-Adaptive Modular Vessels. The 2-post rig constructed for the 33-ft WAM-V is, to the author's knowledge, the first of its kind for testing a marine vessel. The three component comparison of the simulation environment, the testing knowledge of previous chapters, and the 2-post rig testing of this chapter extends the field of knowledge for Wave-Adaptive Modular Vessels. Finally, the cases studies discussed in later sections suggest possible new directions for the development of future WAM-Vs.

10.2 Vehicle Testing Using Multi-Post Shaker Rigs

In an automotive lab, multi-post shaker rigs can be some of the most elaborate pieces of laboratory testing equipment. Typical shaker rigs for evaluating entire vehicles (as opposed to rigs for evaluating an individual suspension system, such as the Quarter-Car test rigs detailed in Chapter 5) are usually intended to excite all four wheels of a vehicle. However, for racing applications, 7-post and 8-post rigs have become more common. Originally, 4-post testing was primarily used for noise, vibration, and harshness (NVH) applications. However, rig designs have evolved to become very sophisticated multi-input, multi-output systems with many uses. Typically, 4-post rigs are used to test the vehicle's suspension systems during heave, pitch, roll, and warp excitations. A typical 4-post rig is built using four hydraulic actuators, one at each corner of the vehicle. The four actuators support the vehicle by one of two methods:

- For tire-coupled rigs, loading pans on the actuators support the vehicle underneath the tires.
- For hub-coupled rigs, the actuators are mounted directly to the vehicle's spindles or uprights.

A diagram of a typical tire-coupled 4-post rig is shown in Figure 10.1.

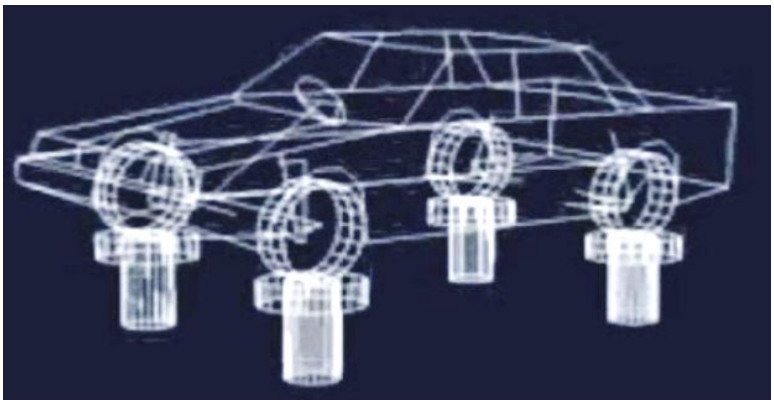

Figure 10.1 4-post model overview

In cases of testing vehicles which use aerodynamic devices to produce high levels of downforce at the tires, traditional 4-post road simulators cannot reproduce the correct suspension loads resulting from the additional aerodynamic forces. 7-post rigs are an extension of 4-post rigs that include 3 additional actuators mounted to the vehicle's chassis that allow for simulating the aerodynamic loading and weight transfer loads acting on a vehicle, in addition to the four corner actuators. Seven-post shaker rigs have become compulsory at the highest levels of motorsports, providing an alternative to on-track testing [75].

Eight-post rigs are similar to 7-post rigs with the addition of a fourth actuator on the chassis. For a theoretical vehicle with an infinitely stiff chassis, there is no difference in the inputs that can be provided by a 7-post and an 8-post rig. During an 8-post test, heave, roll, pitch, and warp inputs are sent to the tires via the four lower actuators; while the four actuators attached to the vehicle's chassis apply heave, roll, pitch, and warp inputs to the chassis to simulate aerodynamic and inertial loadings. The eighth actuator allows for the warp dynamics of a non-rigid chassis to be analyzed during testing. An 8-post rig designed for racing applications is shown in Figure 10.2, with the locations of the 8 posts marked within the figure.

Figure 10.2 8-post shaker rig [76]

Four-post, 7-post, and 8-post rigs have been used to test different components of a vehicle's response with ever increasing complexity. Sensors commonly implemented on the rigs measure actuation force, position, velocity, and acceleration; which can be used to determine the control errors, tire forces, and chassis position. Vehicle handling itself is a complex matrix of variables that includes the characteristics of the chassis itself, as well as the spring rates, damper properties, tire characteristics, weight distribution, and how all the variables interact to affect the overall dynamics of a vehicle. For racing applications, minimizing the variation in normal loading at the tires is a major goal of rig testing to improve road-holding performance. For passenger vehicles, tests with lower RMS accelerations in the cabin are typically more desirable. More advanced models may also consider Whole-Body Vibration standards in the results

Due to the highly competitive nature of the racing and automotive industries, very little of the development work done on multi-post shaker rigs has been published; automotive companies and race teams tend to protect their data to maintain a competitive advantage. A comparison of on-track testing for a vehicle and excitation on an 8-post rig is shown in Table 10.1 [76].

Table 10.1 Comparison of vehicle excitation on track and 8-post rigs [76]

	On Track	On 8-Post
Road Input at time t	A distribution of heights that interacts with the tire contact patch	A single "equivalent" wheelloader displacement
Aerodynamic Forces	A function of the chassis position, which changes with setup	Determined once during drivefile iteration
Driving Line - Road under tires - Acceleration	Driver will seek ideal driving line, which depends on setup	Constant
Tire Dynamics	Rolling, stressed, heated On asphalt or concrete	Stationary on Teflon pad
Anti-Features / Jacking Forces	Braking, acceleration, and cornering interact with vertical motion due to suspension geometry	Lateral/longitudinal acceleration minimal Brakes and driving torque not applied

10.3 2-Post Rig Design

As an extension of the testing program for the 33-ft WAM-V detailed in Chapters 7 and 9, a 2-post shaker rig was designed and constructed to evaluate the dynamics of the 33-ft WAM-V in the laboratory setting. The following section details the design and construction of the rig, as well as the motivation for evaluating the WAM-V in the laboratory environment; as opposed to conducting additional on-water testing and evaluation beyond what was covered in Chapters 7 and 9. The goal of the 2-post rig is to measure the dynamic properties of the WAM-V above the pontoons in the laboratory setting with a high degree of repeatability. The rig is conceptually similar to the 4-post model of the 12-ft USV discussed in Chapter 4. The 2-post rig actually has a total of four posts, with two live actuators at the front corners of the WAM-V, and two stationary posts at the rear corners. A diagram of how the 33-ft WAM-V will be positioned on the 2-post rig is shown in Figure 10.3.

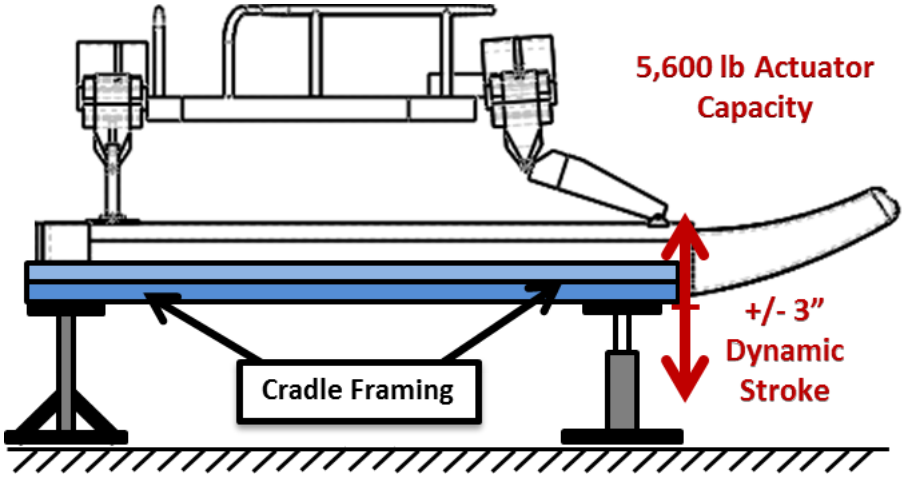

Figure 10.3 2-post rig design overview

Compared to on-water testing, testing with the 2-post rig has a number of distinct advantages:

- **Repeatability of tests:** With on-water testing, it is very difficult to run two identical tests, more repeatable tests will help to evaluate different suspension configurations.
- **Lower cost of testing:** Once the initial rig is constructed, the cost of running a test on the rig is significantly lower than for an on-water test, both in monetary cost and man-hours.
- **No powertrain required for testing:** The initial testing program with the WAM-V showed that the WAM-V's structure outperformed its powertrain units, which required significant upkeep between tests. Powertrain reliability is outside the focus of this study.

However, testing with the 2-post rig also has a number of drawbacks that must be taken into account when making comparisons to the on-water tests. Some of those drawbacks include the following:

- **No longitudinal forces are applied as inputs:** Each wave encounter generates forces in three directions. During on-water testing, the longitudinal dynamics of the WAM-V were found to be its least desirable performance characteristic. Longitudinal motion can be measured during 2-post rig tests, but no forces can be directly applied.
- **Dynamics of the unsprung mass are not considered:** The 2-post rig as designed is effectively a hub-coupled model. The vertical dynamics of the flexible pontoons and the vertical hydrodynamic interactions between the pontoons and the water surface are not considered.
- **Dynamics of the engine pods are not considered:** The engine pods, which have considerable unsprung mass and a changing thrust vector due to the engine pod hinges, have been removed from the WAM-V for testing with the 2-post rig. For any conceivable shaker rig testing, the powertrain units would not be operational.
- **Test data may exceed actuator stroke limits:** During on-water testing, displacement inputs of as much as 4 ft were experienced by the WAM-V. Testing large sea state inputs is not possible with the current actuators.

For the initial 2-post rig design only two active posts were implemented, due to several contributing factors:

- **No suspension is present at the rear of the WAM-V:** Because of the rear arch design on the 33-ft WAM-V, any vertical acceleration at the rear on the pontoons is transmitted to the rear of the payload tray. While this property in itself may not be ideal, it does simplify the optimization of the suspension system, which can only operate in the pitch mode and warp modes.
- **Lower displacements occur at the rear of the WAM-V compared to the front during on-water testing:** For all three WAM-Vs evaluated as part of this program, on-water testing has shown that displacements at the front corners are on the order of 2-4 times greater than the displacements at the rear corners.
- **Reduced cost of building the 2-post rig:** The 2-post rig was built using actuators that already existed in the lab and with an existing control system, lowering the initial cost of building the 2-post rig. Additionally, adding two actuators to the rear corners would cause issues with flow limitations of the current hydraulic pump unit since the limits are already being reached with two actuators. An additional hydraulic pump or smaller volume actuators would be required.
- **Simplified testing matrix:** For studies on vehicle handling and performance, even simplified studies have a multitude of parameters that need to be individually tested and quantified. Testing with four active posts would require a number of additional tests for each suspension configuration. Testing with only two active posts will help to generate valuable information about the WAM-V's dynamics more efficiently.

One of the obvious drawbacks of the lack of two active rear posts is that testing with the 2-post rig becomes further removed from on-water testing, making correlation between on-water and rig testing more difficult. A bridge between the data from the on-water tests and the 2-post testing rig involves using the 6-post virtual model detailed in Chapter 11. Analyzing testing inputs can be done in a three-stage process. First, the inputs are created based using the on-water testing data. Second, the inputs are run at full displacement and with four active posts within the virtual 6-post model. Third, the inputs are modified to run on the 2-post testing rig by removing the rear inputs and scaling the front inputs to fit within the displacement limits of the actuators.

10.4 2-Post Testing Setup

The following section details the design and construction of different aspects of the 2-post rig, as well as modifications made to the data acquisition system for testing on the 2-post rig. Figure 10.4 shows the 33-ft WAM-V on the 2-post rig in the lab after the initial rig construction was completed.

Figure 10.4 33-ft WAM-V on the 2-post testing rig

10.4.1 Actuators

For the front two posts of the rig, vertically-mounted hydraulic actuators are used to excite the WAM-V at different frequencies. The actuators provide motion inputs acting under the pontoons; no actuators are used on the chassis to apply additional aerodynamic or inertial loadings. The two actuators are MTS Model 248.03 hydraulic actuators, which are mounted under the front of skis. Each actuator is controlled independently, allowing the boat to be excited in the pitch and warp modes. During pitch excitation testing, the actuators move in phase. During warp excitation testing, the actuators move 180 degrees out of phase. The majority of the tests were run with the actuators moving in phase. The physical setup for actuation of the suspension during dynamic testing, including actuator and attachments, is shown in Figure 10.5. The actuators have a 6 inch dynamic stroke limit and a 5600lb force capacity, with a cylinder area of 2.25 in^2. It is also noteworthy that the actuators were not placed directly under the spherical joints of the front suspension. For stability purposes, the actuators were mounted as far forward as possible, locating them under the pivot point of the rocker arms, as show in Figure 10.5.

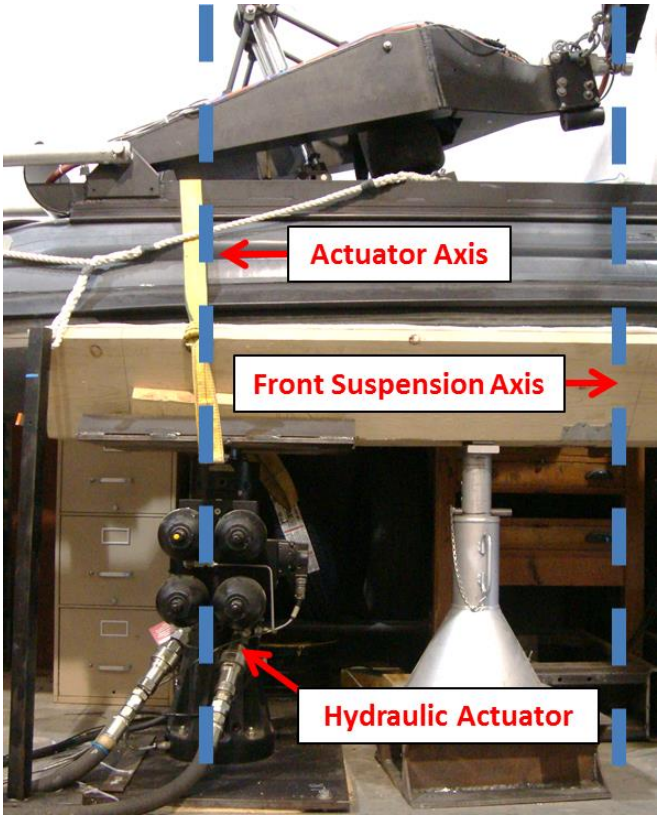

Figure 10.5 2-post shaker rig actuator setup

10.4.2 Control and Hydraulic Power Unit

A computer control unit is used to control the motion of the actuators during testing. For each test, a signal is generated in Simulink and then downloaded into dSPACE Control Desk. dSPACE provides the user interface for controlling the tests and recording data. The dSPACE output is used as an external input to the MTS 458.20 hydraulic controller, shown in Figure 10.6.

Figure 10.6 MTS 458.20 hydraulic control for 2-post rig

The hydraulic pump unit used for powering the actuators is a MTS Silentflo Hydraulic Power Unit, model 505-20. The hydraulic pump has a flow limit of 20 gallons per minute and an operating pressure limit of 3000psi. Four accumulators are located next to each of the actuators to help damp the motion of the hydraulic fluid.

10.4.3 Rear Post and Cradle Assembly

The rear posts of the 2-post rig are stationary posts at the same height as the center position of the front actuators. The WAM-V's pontoons are too flexible for the actuators to be placed directly under the pontoons, as they would be with the tires on an automotive shaker rig. To hold the pontoons, two cradles were constructed of the same length of the skis. The cradles were constructed from three 2 x 12 pieces of wood joined at 45-degree angles. A thin sheet of foam was on top of the wood to prevent the pontoon and the cradle from abrading. The port-side pontoon cradle assembly and rear stationary post are shown in Figure 10.7.

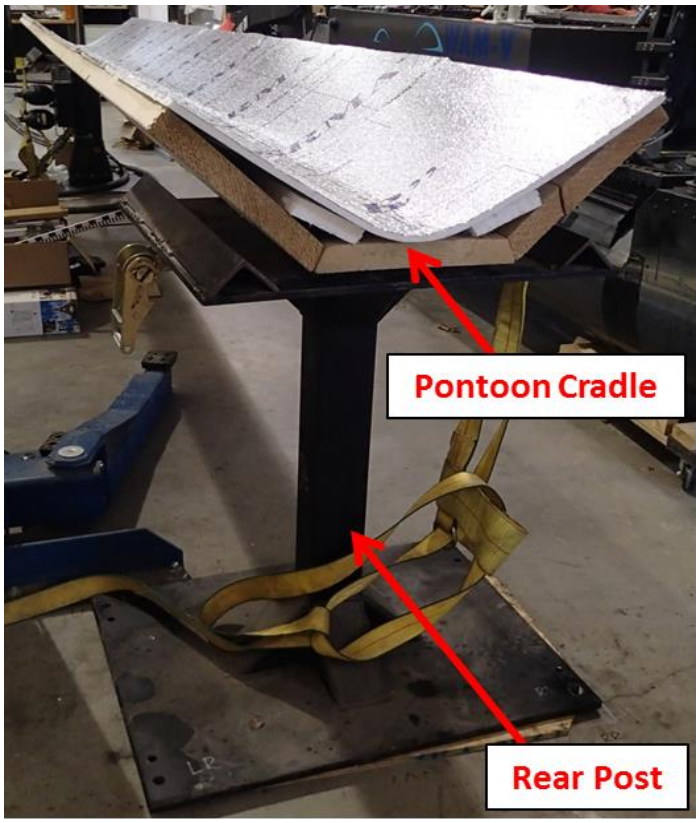

Figure 10.7 Inactive rear post and pontoon cradle

Each pontoon is secured to its cradle assembly using four ratchet straps and the cradles are placed on top of the front and rear posts. One of the four ratchet straps is fastened to the front actuator as well, so that the cradle cannot lift off the actuator during heavy decelerations. The rear posts are not fastened to the cradles; since the rear posts are not actuated and the front actuators are directly fastened to the cradles, this has not been shown to be a problem. Since the rig has no kinematic method of compensating for the change in angle of the pontoons as the actuators move, not strapping down the rear of the cradles has been shown to adequately allow for a small amount of pivot under the pontoons. Given that the actuators are able to move through +/- 3 inches in their stroke and that the front and rear posts are placed 16 feet apart, this change in angle is equal to +/- 0.9 degrees at full stroke.

It is also noteworthy that with the cradles in place, some of the dynamics of the pontoon and ski assemblies observed during on-water testing are lost or altered, such as the bending frequencies of the skis; which are augmented by the additional bending stiffness provided by the cradle assemblies.

10.4.4 Replacement of Operator's Mass

For the 2-post rig, the operator was replaced with a water-filled testing dummy which was used for all of the tests. The testing dummy was filled with water, giving it a weight of 175 lbs. Additional weights were added to weigh the dummy down to 200 lbs, in order to roughly match the weight of the WAM-V's operator with gear. The dummy was fastened to the seat with a lapbelt, and preliminary testing on constraining the dummy showed that an additional chest harness was necessary as well. Multiple attachment methods were evaluated and the conclusion was reached that fastening the dummy to the seat with a lapbelt and chestbelt produced the most consistent test results. Less restrictive methods, such as leaving the dummy free, or only constraining the dummy's hips with the lapbelt, led to the dummy falling off the seat. A bungee cord chest strap was also evaluated; however, issues with the torso resonating led to the cord not being used during testing. The feet were also tied to the footrests. The dummy used for testing is a StarBart (BART) water ballast test dummy and is shown mounted to the operator's seat on the WAM-V in Figure 10.8.

Figure 10.8 Operator dummy (BART) used for 2-post testing

10.4.5 Seat Testing Dummy vs. Human Operator Response

A literature review on the effect of replacing a human operator with a test dummy has provided some interesting insights into how it may affect the data collected on the 2-post rig. When the human body is replaced with a rigid mass having the same weight as the body, similar resonant frequencies may still occur. However, the amplification at resonance may often be grossly overestimated, while the attenuation at high frequencies will also be exaggerated [26]. Figure 10.9 shows an example transfer function plot across the seat for a rigid dummy and a human test subject. For the 2-post rig, the dummy was not installed for the purpose of investigating the seat's dynamics; the dummy was installed to match the sprung mass of the WAM-V during on-water testing with an operator onboard.

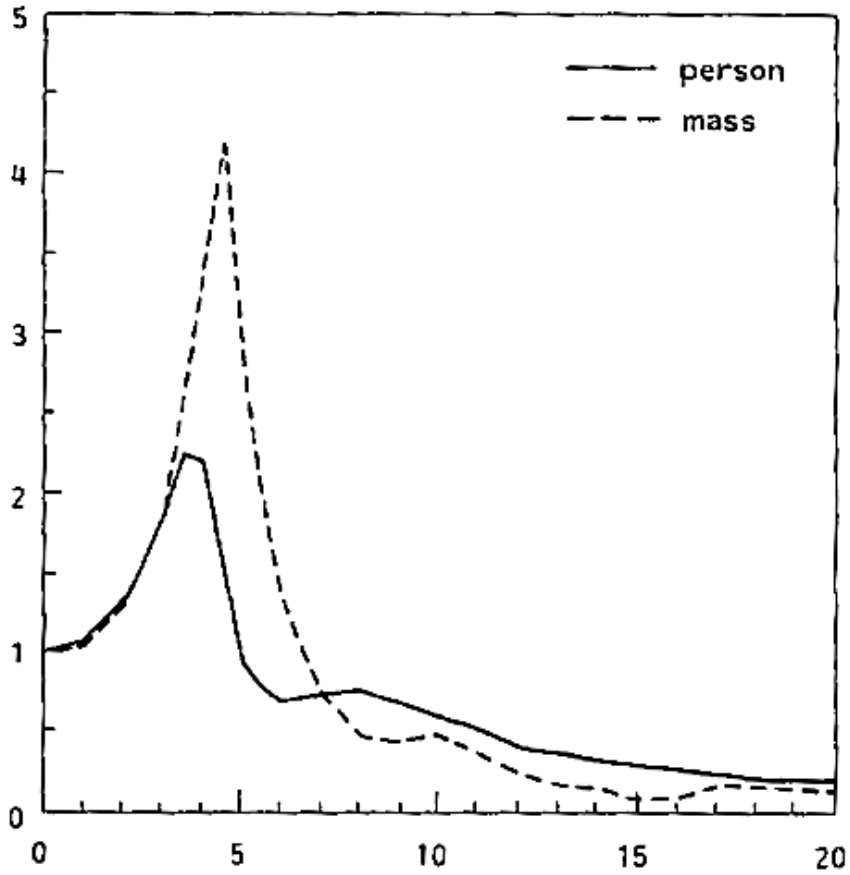

Figure 10.9 Seat vibration vertical transmissibility plot comparison [26]

10.4.6 Data Acquisition Setup

A total of 23 channels of data were recorded on the 2-post rig during testing. As with the on-water testing, the data acquisition unit collects data at 500 Hz. The data acquisition unit first detailed in Chapter 4, and then used on the Quarter-Boat rig in Chapter 5 and on the 33-ft WAM-V testing in Chapter 6, was modified again for use on the 2-post rig. While the majority of the sensors were retained, certain sensors used for on-water testing were not needed for use on the rig, particularly those added to the 33-ft WAM-V to measure the motion of the engine pods, which were not present for the 2-post rig testing. A diagram of the sensors used for testing is shown in Figure 10.10.

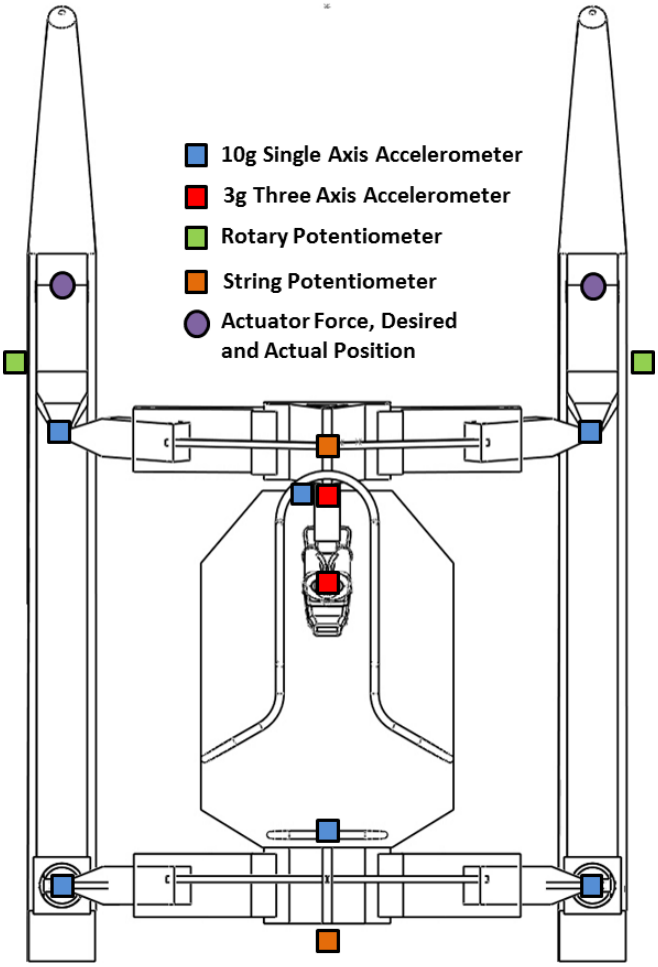

Figure 10.10 Sensor diagram of 2-post rig

Six channels were added to the data acquisition setup to record information from the hydraulic actuators. The desired input position, normal force, and actual achieved position were recorded for both of the posts as a function of time. An additional triaxial accelerometer was mounted on a vertical portion of the dummy's back to measure the difference in acceleration between the front triaxial accelerometer and the acceleration at the seat.

Since the longitudinal dynamics of the WAM-V were shown in Chapter 9 to be an important area of research, a string potentiometer was added to the 2-post rig that measures the longitudinal position of the payload tray compared to a fixed global reference point. The mounting of the longitudinal string potentiometer is shown in Figure 10.11. Like the global vertical string potentiometer on the Quarter-Boat rig, the longitudinal string potentiometer allows for a measurement to be taken that is not possible during on-water testing.

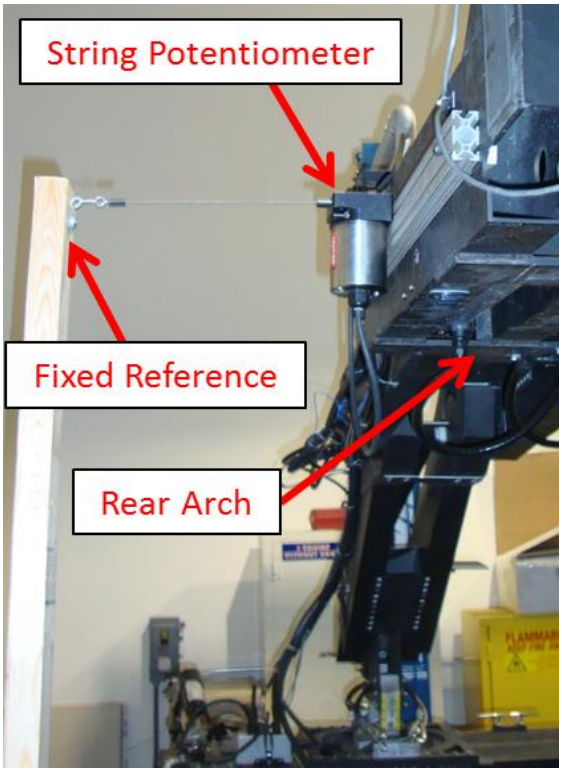

Figure 10.11 Global longitudinal string potentiometer mounted to the rear of the WAM-V

Because of the suspension's kinematics with the pitch center of the chassis located about the rear arch hinge, the longitudinal string potentiometer records both the kinematic motion due to movement of the suspension, and uncoupled motion due to the arch's compliance. Figure 10.12 provides a diagram explaining how the two motion types are both recorded by the same sensor.

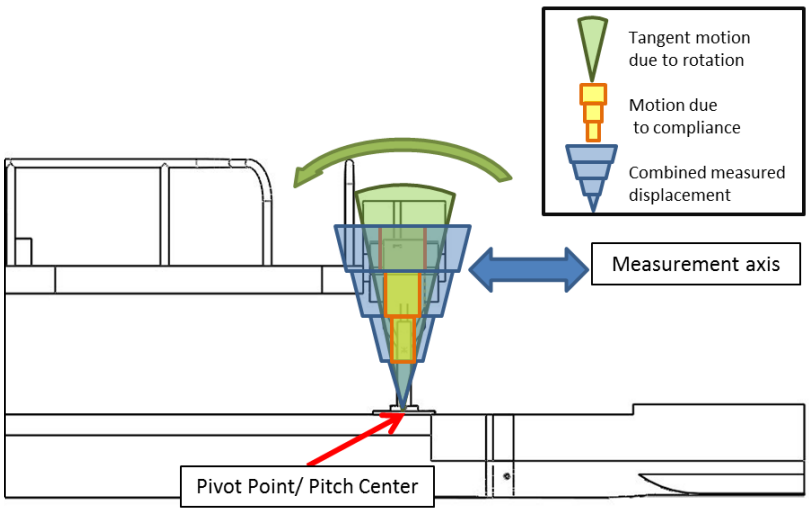

Figure 10.12 Rigid body vs. compliance motion measured by string potentiometer

10.5 Initial 2-Post Rig Testing and Data Analysis

With the design and construction of the 2-post rig complete, initial testing plans were outlined for the 33-ft WAM-V using the rig. This section provides the details of the plans and methodology for testing. Sections 10.6-10.9 detail the data analysis from the different tests. For the initial round of testing, only sine wave input types were tested. Sine waves of discrete frequencies, as well as chirp signals of increasing frequency were tested. A chirp signal varying from 0.5 to 2.5 Hz over one minute in duration was chosen as the primary signal to be presented from all the signals analyzed. This signal represents a concise measure of the lower and upper bounds of the frequency range most relevant to the WAM-V. The frequency range tested is also within the range of frequencies able to be processed by the acceleration to displacement filter-integration scheme discussed in Chapter 4.

The signals were run at different peak excitation amplitudes to look for nonlinearities in the dynamics of the suspension at different levels of displacement. Two levels of displacement were chosen for the initial analysis. For one test, a smaller displacement level was chosen, corresponding to 2 inches of peak to peak displacement. For the other test, a larger level of displacement was chosen, to test the WAM-V under more intense conditions. Initially, it was desired to run both tests with a constant peak displacement throughout the test and only varying the input frequency of the chirp signal. For the larger displacement test, this would have corresponded to a peak displacement equal to the maximum available stroke of the actuators (6 inches). However, the maximum displacement was found to exceed the maximum available flow rate of the hydraulic pump system (20 gallons/minute) when the chirp signals exceeded ~1.5 Hz.

In order to conduct the larger displacement tests at an amplitude that was sufficiently severe to excite the suspension at the low end of the frequency spectrum, without exceeding the capabilities of the hydraulic pumps at the high end of the frequency spectrum, a decreasing amplitude chirp signal was required. A chirp signal was designed which would not exceed the maximum flow rate, while still testing larger amplitudes compared to the 2 inch constant peak displacement test. The tests were run with constant peak amplitudes from 0.5 to 1.0 Hz, equal to the maximum stroke of the actuators; then the peak velocity was held constant from 1.0 to 2.5 Hz, corresponding to a decreasing peak amplitude and a constant peak flow rate from the pumps. The position and velocity versus time for both the constant peak displacement test (0-60 seconds)

and the larger displacement test (70-130 seconds) are shown run back to back on the same timeline in Figure 10.13 with a 10 second break between tests.

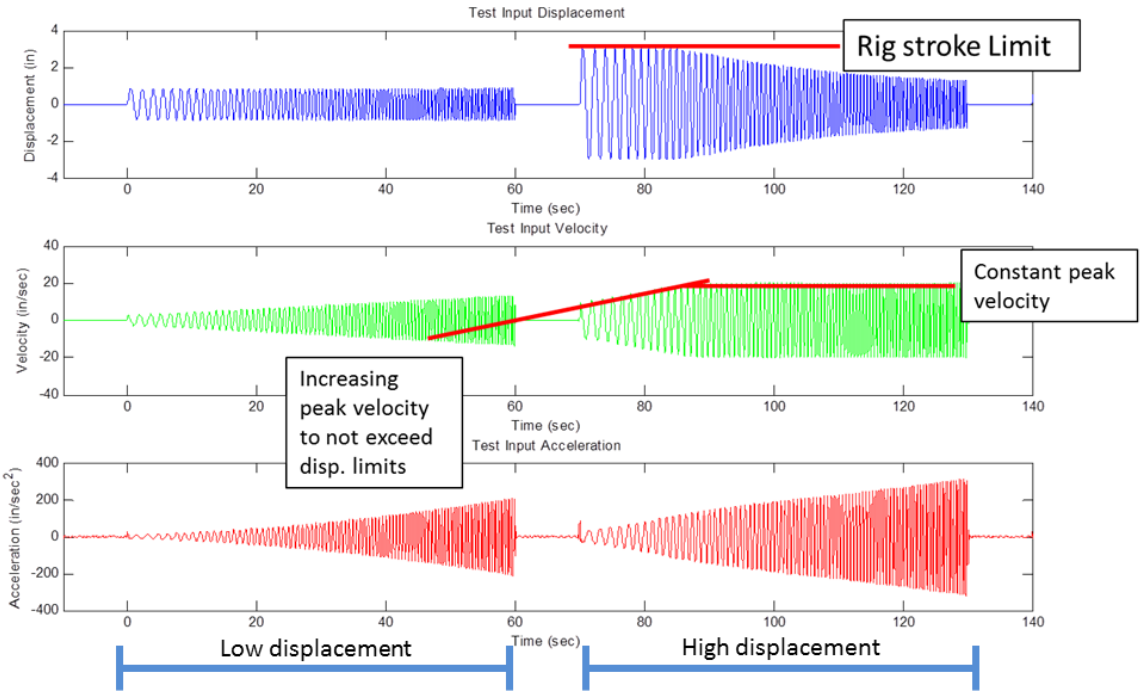

Figure 10.13 Displacement and velocity inputs for the constant peak displacement and velocity tests

The plot of the smaller amplitude, constant peak displacement test is shown overlaid with the plot of the larger, varying amplitude test in Figure 10.14 . Figure 10.14 is also annotated to show the time at which the specific frequencies occur in the chirp signals. The chirp signals increase by 0.5 Hz every 15 seconds.

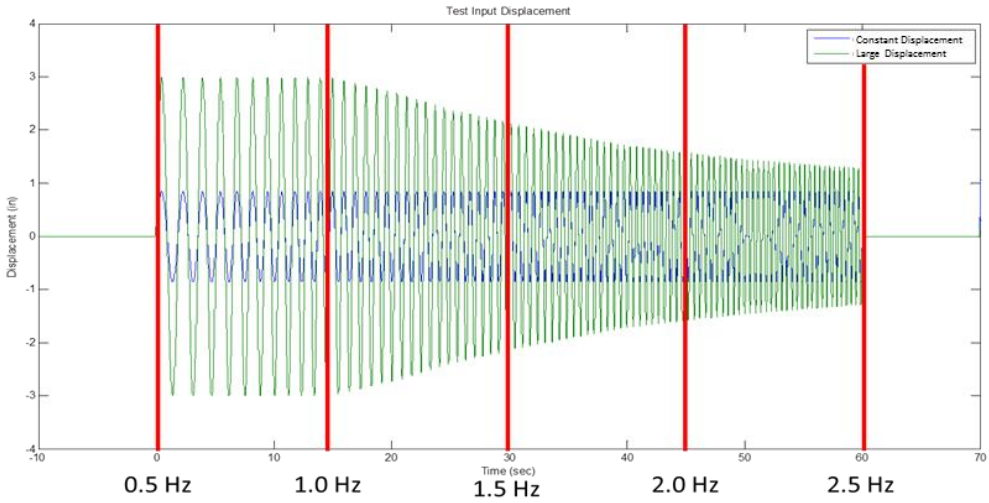

Figure 10.14 Comparison of different displacement inputs showing frequencies tested

A majority of the data was taken with the small and large displacement tests run back to back with 10 seconds between the tests, as shown in Figure 10.13. For many of the data channels from the tests, particularly the acceleration channels, showing all of the data points generated from the chirp signals inputs generates too much data to view on a single plot; particularly when multiple signals are being viewed on the same plot. In such cases, a plot of only the acceleration peaks is shown instead. Figure 10.15 shows a plot of the peaks for the input displacement data.

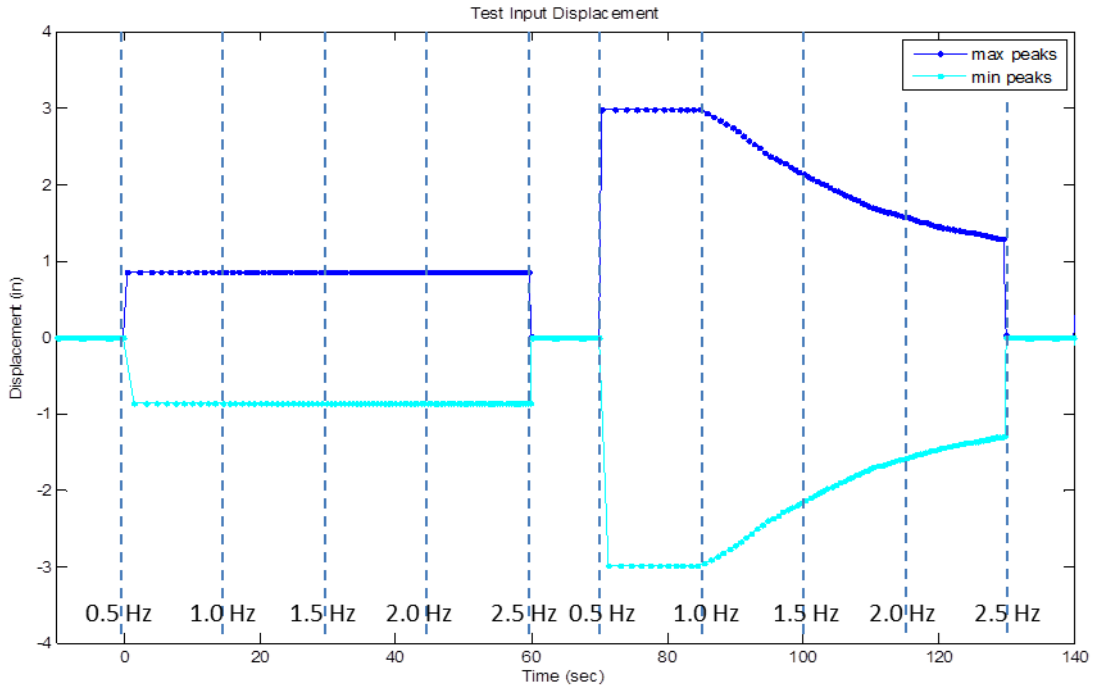

Figure 10.15 Alternative method of displaying data showing only data peaks

10.6 Second Generation Suspension - Damper Configuration Analysis

One of the primary advantages of testing in the laboratory with the 2-post rig is that repeatable back to back comparisons can be easily tested for different setup configurations; this is not the case with on-water testing. In Chapter 9, back to back comparison tests were conducted in head seas for three different suspension configurations. While the testing results and the resulting analysis were highly beneficial to this study, the testing conditions changed slightly between the three tests, making the results more difficult to quantify.

Using the 2-post testing rig, similar tests can be conducted for the three different suspension settings. For each of the 2-post tests that were conducted with the second generation suspension

system fitted on the WAM-V, the tests were run at three different settings on the adjustable dampers. The settings corresponded to the minimum, middle, and maximum available damping rates; the settings also match the damper settings chosen for the on-water testing and data analysis detailed in Chapter 9. The damping range of the dampers is discussed in detail in Section 6.7. A plot of the range of damper adjustment is shown in Figure 10.16.

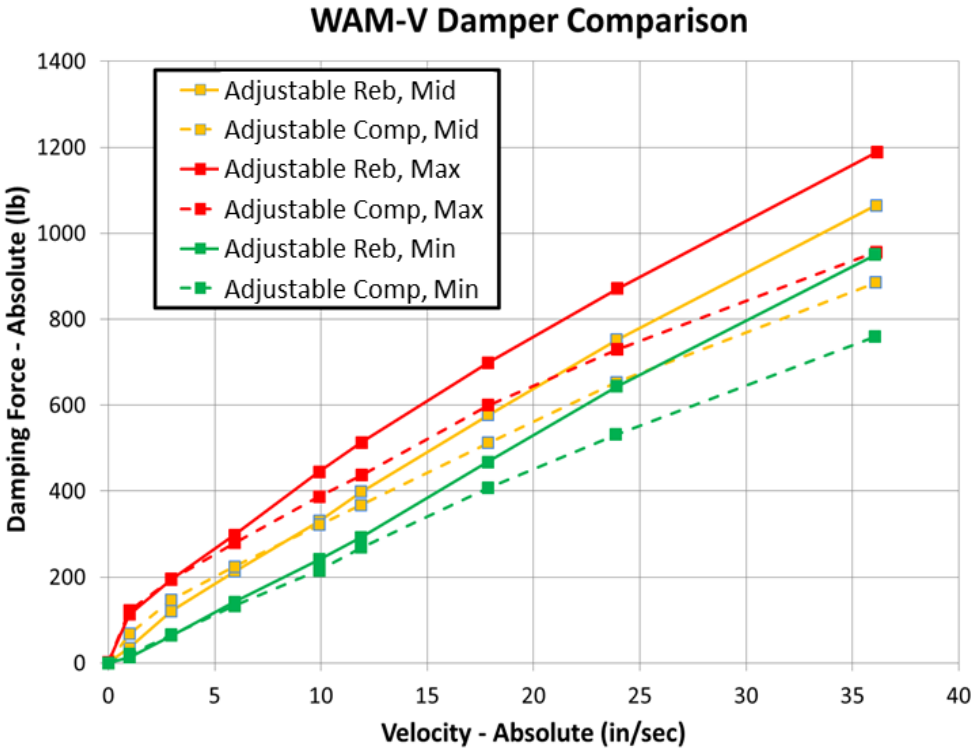

Figure 10.16 Second generation adjustable damper configurations

10.6.1 Pontoon Acceleration Analysis

Figure 10.17 shows the acceleration at the starboard pontoon for the small and large displacement tests, run three times at three different suspension settings. Theoretically, there should be no difference in the acceleration levels at the pontoons between the different damper tests. Since the pontoons are mounted rigidly to the actuators, the only changes in the pontoon accelerations between the different configurations should come from localized vibrations and control errors from the actuators. The highest damping setting seems to have more spikes in the acceleration data; however, this could possibly be attributed either to differences in the damper properties or to slight changes in the controller performance of the hydraulic actuators, making the results difficult to accurately quantify.

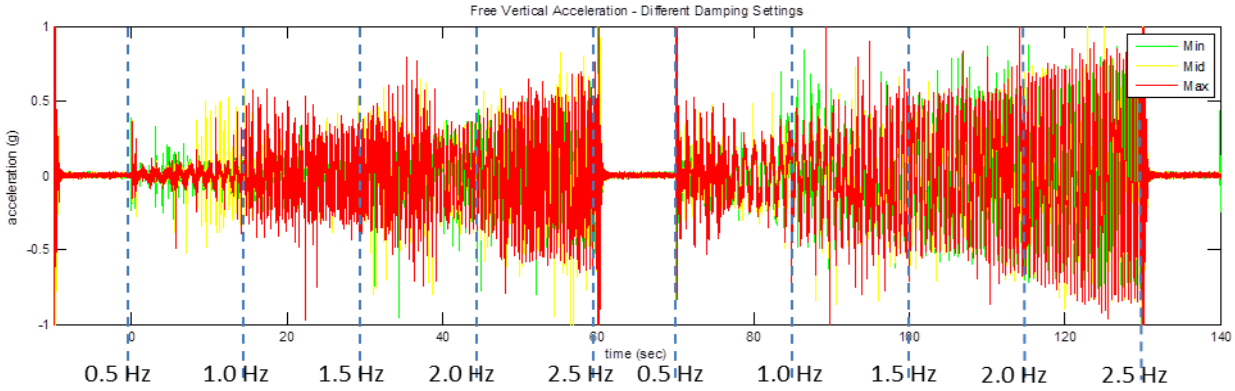

Figure 10.17 Pontoon acceleration levels for three different damper settings

10.6.2 Suspension Motion Analysis

Figure 10.18 shows the vertical position of the starboard suspension system at the spherical joint for both of the testing amplitudes, at three different suspension settings. The upper and lower limits of the vertical axis of Figure 10.18 correspond to the limits of the suspension system in rebound and compression. For the three small amplitude tests shown on the left half of the figure, there is not a great deal of suspension motion for any of the tests compared to the total available travel. For the larger amplitude displacements, the suspension gets very close to engaging the limit straps for the minimum damper setting. For both amplitudes, the lowest damper setting produces the greatest amount of suspension motion, using 5 inches of travel for the smaller amplitude test and 14 inches of travel for the larger amplitude test. The tests at the middle and maximum damper settings saw significantly lower displacement levels; since these settings are more representative of the levels of damping that would be used during future on-water tests, their results are more informative as to the current suspension's performance.

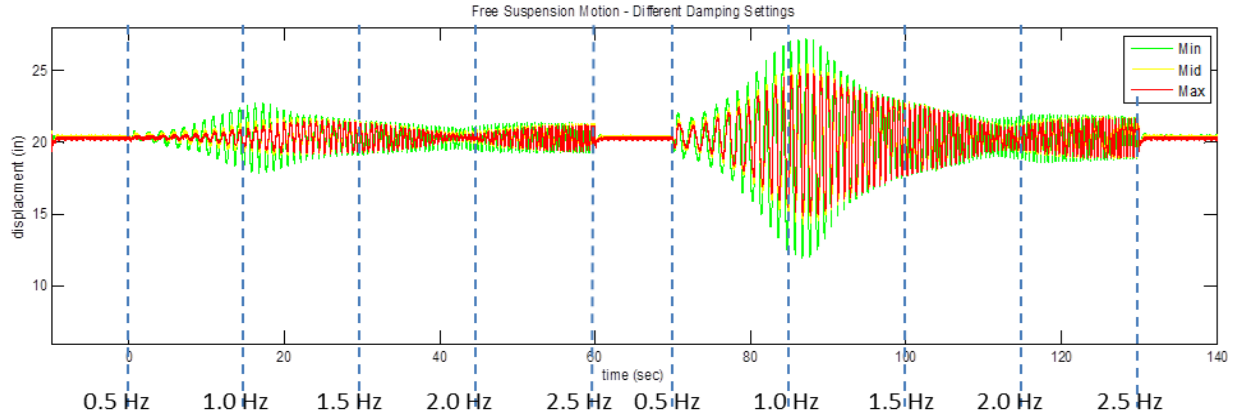

Figure 10.18 Suspension motion measured at spherical joint for three different damper settings

Based on the suspension displacement plots, there does not appear to be a large amount of difference between the middle and maximum suspension settings. The middle setting shows minimally greater motion amplitudes; however, the difference is significantly less pronounced than the difference between the minimum and middle damper settings.

For the small amplitude test data, the resonant frequency of the suspension appears to occur around 15 seconds into the test. This corresponds to a natural frequency of 1.0 Hz. For the middle and maximum settings, the peak displacement occurs at around 25 seconds, indicating a resonant frequency of 1.33 Hz. The change in natural frequency between different damping ratios is more than expected based on changing the damping level of a single degree of freedom mass-spring-damper system; it is likely that other dynamics are contributing to the change in frequency, requiring further investigation. The larger amplitude data shows similar timing between the maximum amplitudes of the suspension for the three different damper settings. All three peaks occur at roughly 87 seconds into the data, corresponding to a frequency of 1.07 Hz, which is close to matching the frequency found for the minimum damper setting. Further analysis is required to understand why all of the suspension tests do not follow the same trend. A possible explanation based on the WAM-V longitudinal dynamics is detailed in Section 10.7.2.

Figure 10.19 shows the corresponding damper velocities calculated using the suspension displacement data from Figure 10.18. The motion ratio of the damper to the spherical joint of the suspension system is 0.356:1, so the damper velocity shown is actually significantly lower than the velocity of the spherical joint. Predictably, the minimum damper setting shows the greatest peak velocity during the tests. Due to the symmetrical ratio of compression to rebound damping, the peak damper velocities are similar in both directions. The maximum peak velocity achieved for each of three damper settings is listed in Table 10.2 for both directions.

Table 10.2 Maximum damper velocities for three suspension settings (negative = compression)

Suspension Setting:	Peak Velocities, Low-Displacement Test (in/sec):	Peak Velocities, High-displacement Test (in/sec):
Minimum	-8.2, 6.6	-19.6, 21.5
Middle	-6.1, 5.3	-14.9, 16.0
Maximum	-5.3, 5.6	-13.8, 14.3

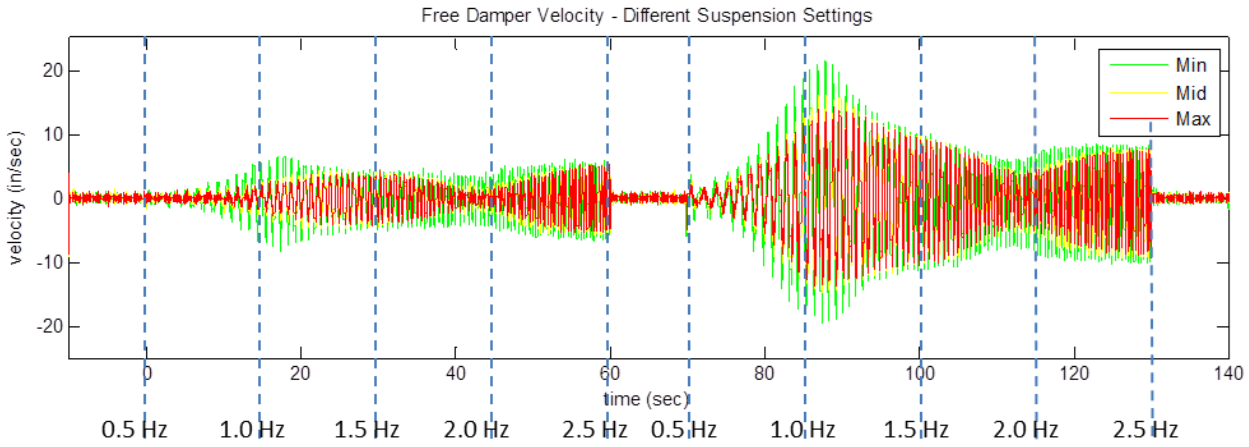

Figure 10.19 Damper velocities for three different suspension settings

10.6.3 Payload Acceleration Analysis

Figure 10.20 shows two plots with the vertical (a) and longitudinal (b) accelerations recorded on the superstructure near the base of the operator's seat. When comparing the two plots, the overall magnitudes between the vertical and longitudinal acceleration are similar, which is surprising given that there are no longitudinal actuators on the 2-post rig, only vertical inputs are applied.

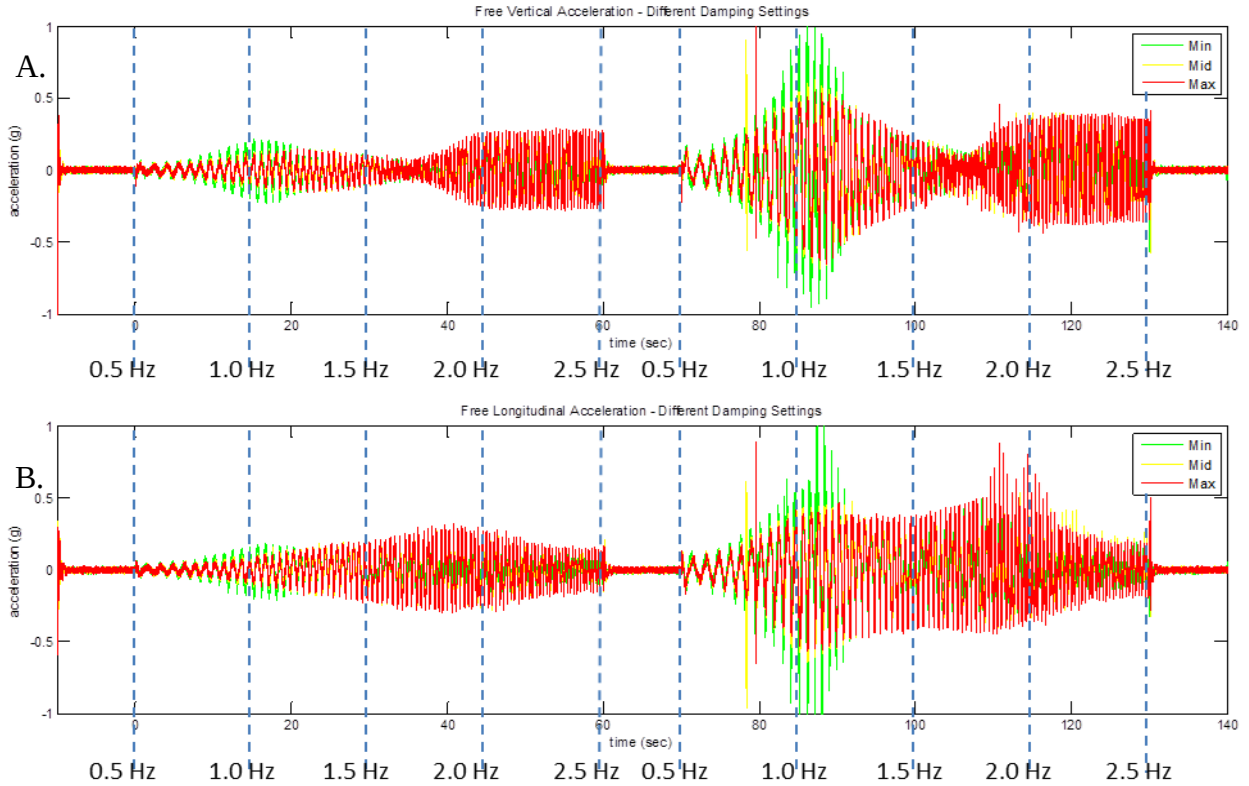

Figure 10.20 Vertical (a) and longitudinal (b) payload acceleration for three different damper settings

The vertical acceleration tests show nodes in the data at ~35 seconds into each test (at time = 35 and 105 seconds) for both testing amplitudes. The timing of these nodes also corresponds to nodes in the suspension displacement plots that were shown in Figure 10.20. This indicates that the suspension shows its best performance on the 2-post rig (in terms of attenuating vertical acceleration at the payload) at an input frequency of 1.67 Hz, or roughly two times the undamped natural frequency of the suspension system, as calculated in Chapter 6.

Interestingly though, at this same time the longitudinal acceleration of the payload is approaching a local maximum value. The local maximum values of longitudinal acceleration occur at 40 seconds into each test, corresponding to an input frequency of 1.83 Hz.

Qualitative observation of the 2-post rig during the tests showed an interesting phenomenon, which is also revealed in the data. For the first portion of the tests, corresponding from roughly 0.5 to 1.5 Hz, the motion of the payload appears to be vertical. Above 1.5 Hz, the dynamics seem to change and the dominant motion of the payload becomes horizontal. This is reflected in the acceleration data.

Figure 10.21 shows the payload acceleration data from Figure 10.20 divided by the pontoon acceleration data from Figure 10.17. The two plots show a transfer function between the vertical acceleration inputs at the pontoons and the vertical and longitudinal acceleration outputs at the payload tray.

For the plots shown in Figure 10.21, the range of values goes from 0 to infinity for positive accelerations, with a value of 1 indicating zero attenuation between the pontoons and payload. Numbers less than one indicate positive attenuation, numbers greater than one indicate negative attenuation. For negative accelerations, the plots go from 0 to negative infinity and value of -1 indicates zero attenuation between the pontoons and payload. Numbers greater than -1 indicate positive attenuation, numbers less than -1 indicate negative attenuation. The transfer functions can be used as a measure of the effectiveness of the suspension systems at attenuating vibrations.

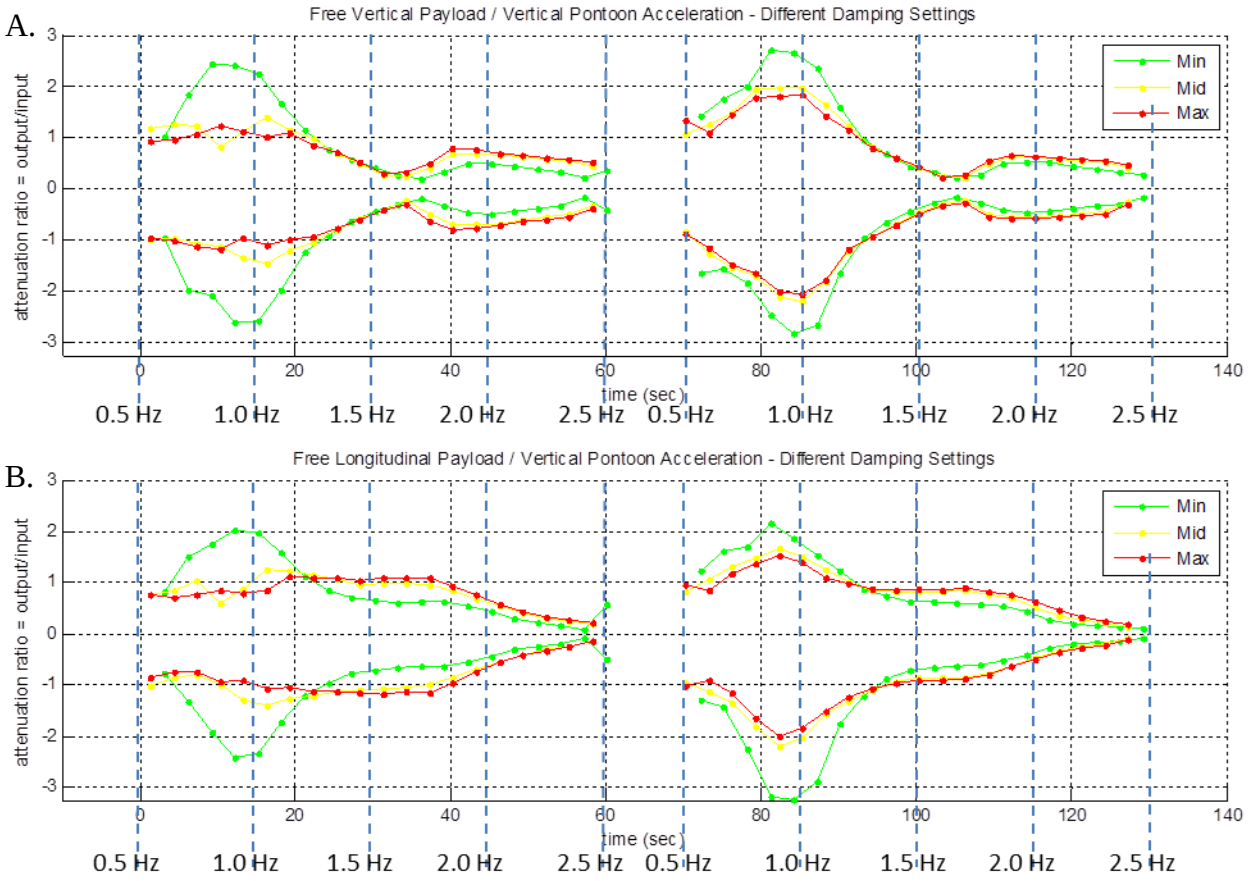

Figure 10.21 Transfer function of vertical (a) and longitudinal (b) payload acceleration over input vertical acceleration at the pontoons for three different damper settings

For both the longitudinal and vertical acceleration transfer function plots in Figure 10.21, the worst attenuation ratio comes at roughly 15 seconds into each test. The vertical transfer functions show good attenuation for all frequencies greater than 1.33 Hz.

The fact that the longitudinal values exceed attenuation ratios of one is very surprising, because the ratio shown in the plot is not a transfer function of longitudinal to longitudinal acceleration. The plot shown is the longitudinal acceleration output divided by vertical acceleration input. This makes the longitudinal plot not a measure, but an indication of amplification; the longitudinal attenuation ratio in equal to infinity since the output would be divided by a zero input.

A possible reason the longitudinal plots are greater than one may be due to the rear arch compliance, which is investigated in the next section. The unique longitudinal dynamics of the 33-ft WAM-V are investigated in further detail in Section 10.7.

10.6.4 Rear Arch Compliance Analysis

Figure 10.22 shows a plot of the data recorded from the longitudinal string potentiometer, shown in Figure 10.11, for the two different test amplitudes and the three different suspension settings. As with most of the other measurements, more longitudinal motion is found to occur with less damping in the suspension. The peak in longitudinal motion occurs at the same time as the suspension reaches its peak displacement, indicating a rigid body coupling is occurring at 15 seconds into the test. There is longitudinal motion at 35 seconds into the tests, while there is almost no suspension motion; this indicates a natural frequency for the compliance in the rear arch structure, which occurs at a frequency of 1.67 Hz.

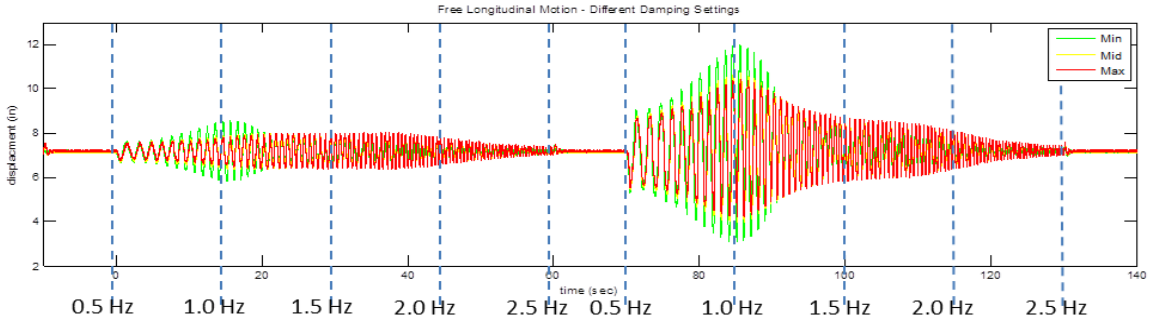

Figure 10.22 Longitudinal payload motion measured by string potentiometer

10.6.5 Dummy Acceleration Analysis

Figure 10.23 shows the level of acceleration recorded at the testing dummy for the vertical (a) and longitudinal (b) axes, divided by the corresponding acceleration along the same axis for each plot, recorded at the base of the operator's chair. In the vertical direction, the accelerometers at the payload and the dummy show roughly equal acceleration levels up to a frequency of 1.25 Hz, then the dummy shows worse acceleration performance from 1.25 to 1.75 Hz, and then the dummy shows better performance from 1.75 to 2.5 Hz. This is most likely due to the dynamics of the seat cushion, and the results would likely vary with a human operator.

In the longitudinal direction, the dummy always sees greater acceleration levels than does the payload tray. This is particularly concerning given the on-water testing results shown in Chapter 9, where longitudinal acceleration was found to be the WAM-V's biggest performance detriment. This conclusion were based on accelerations at the payload, not at the seat, so it is possible the operator experienced greater acceleration levels than recorded by the accelerometer. The poor acceleration results at the dummy could be attributed to a number of factors including:

compliance in the seat post, and the method of restraining the dummy. The accelerometer on the dummy is also located at a higher point than the payload accelerometer; since the WAM-V's rear arch moves on a pivot, the motion at the seat is amplified compared to the payload tray.

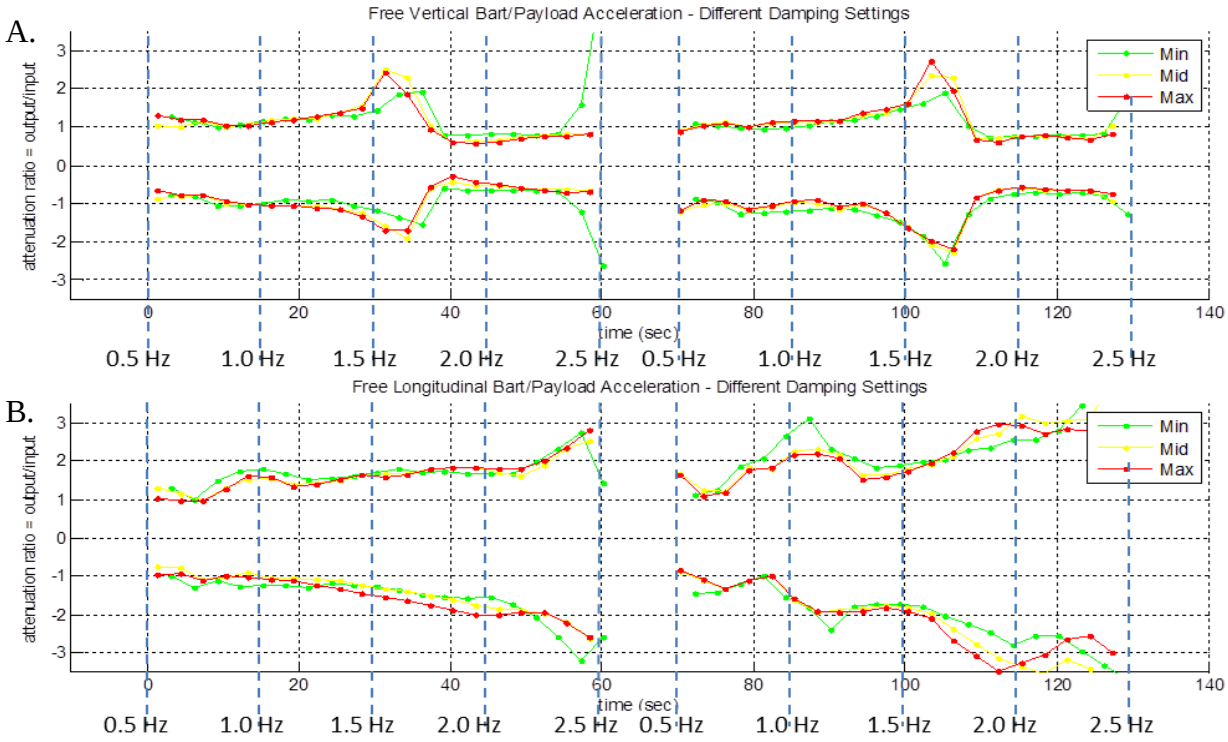

Figure 10.23 Bart vertical acceleration vs. payload vertical acceleration

10.6.6 Actuator Forces

Figure 10.24 shows the actuator force recorded during the tests. The forces are similar between the different damper settings; they are slightly greater for the maximum damper setting, except at resonance of the minimum damper setting. The maximum force recorded is ~1500 lbs; the actuators are rated for 5600 lbs, so a large factor of safety is available to test more severe inputs.

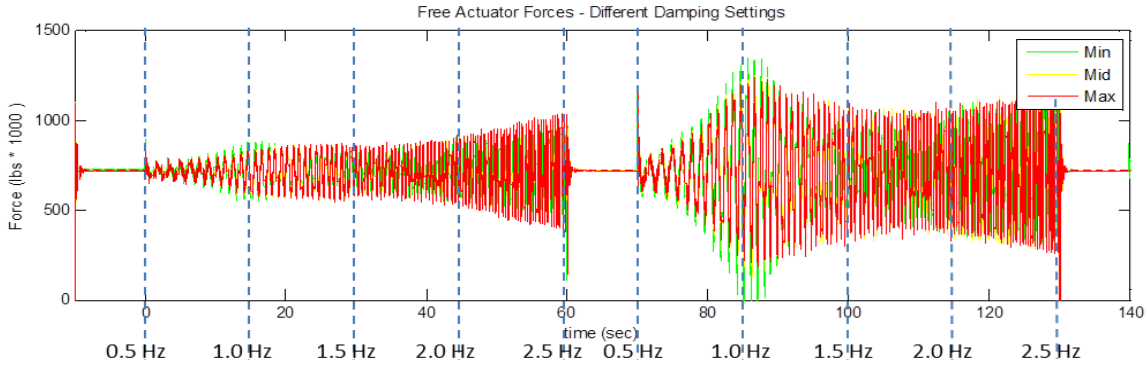

Figure 10.24 Actuator forces for three different damper settings

10.7 Longitudinal Stiffener Testing

The longitudinal compliance in the rear arch of the 33-ft WAM-V that was discussed in Chapter 9 has also been noticed during testing on the 2-post rig. The rear arch compliance is actually due to deadband in the joints that make up the rear arch's folding mechanism, rather than insufficient stiffness in the components of the rear arch. The compliance has also caused some correlation issues between the data from the 2-post rig and the 6-post model documented in Chapter 11, a linearized model of the rear arch compliance is presented in Section 11.4.

In order to reduce the effect of the rear arch compliance on the WAM-V's dynamics, two stiffening braces were constructed to tighten the connection between the payload tray and the rear arch. The braces run diagonally from the aft joints to the bottom of the payload tray. The braces are composed of a threaded rod and a turnbuckle, which are tightened to pull the WAM-V's arch to the end of its deadband travel, and hold it there by maintaining tension in the braces. The planned locations of the longitudinal braces on the 33-ft WAM-V are shown in Figure 10.25. It is also noteworthy that the braces as designed would need to be removed in order to fold the 33-ft WAM-V. For use on the water, it would be possible to design a solution that would not need to be removed, and also wouldn't impede folding operation; rather than to install the braces on the water each time the WAM-V was unfolded.

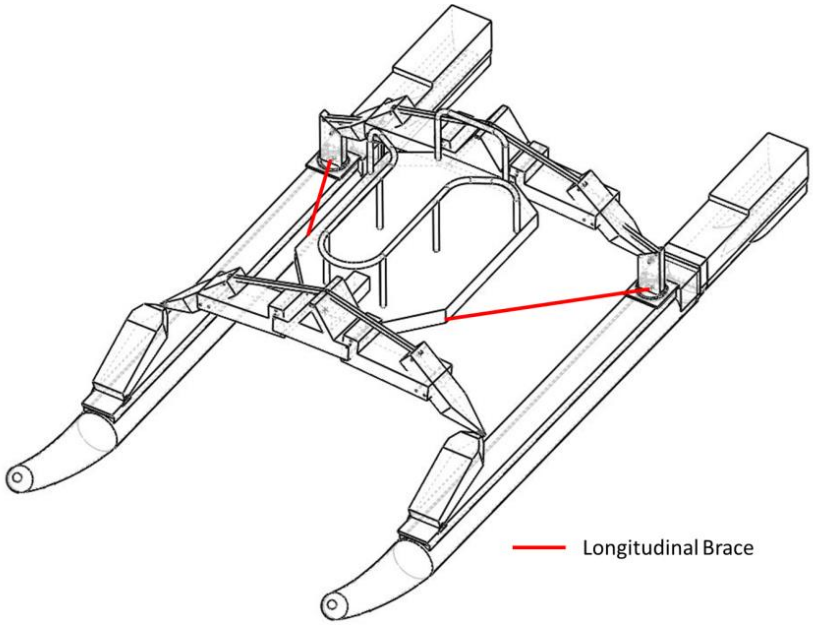

Figure 10.25 Longitudinal stiffening brace locations

The longitudinal braces were not designed to supplement the material strength of the rear arch. The braces are a turnbuckle design; the components of which are shown in Figure 10.26. The turnbuckle has left hand threads on one side and right hand threads on the other. Turning the turnbuckle in one direction causes the left hand and right hand threaded rods to pull together, pulling the aft joint and the payload tray toward each other. Thus, the braces are only effective when tension is maintained in the threaded rods, and the rods must be preloaded to maintain sufficient tension at all times. With the braces installed, the arches on the WAM-V can no longer be folded up properly, although it would be possible to design a brace for on-water use that did not impede the folding and unfolding operations.

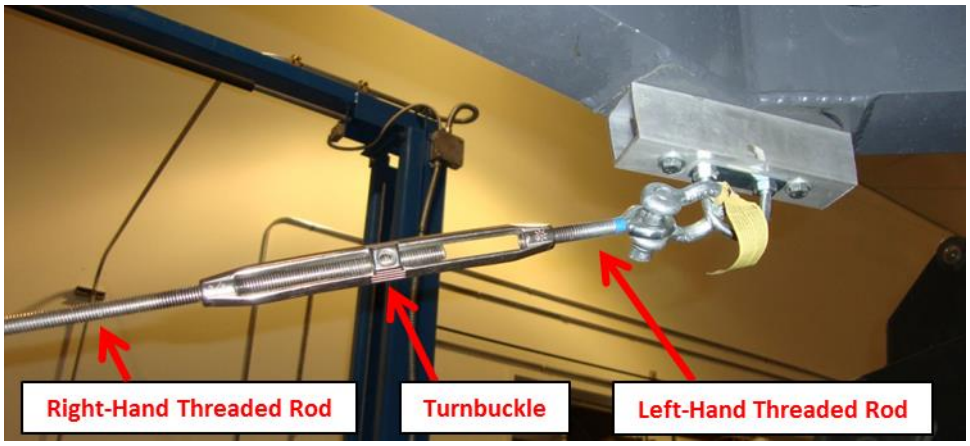

Figure 10.26 Turnbuckle adjustment of stiffening braces

The stiffening braces are attached to threaded shackles that allow the braces to be removed for back to back testing on the 2-post rig with and without the braces installed; it only takes a few minutes for the braces to be installed or removed. Figure 10.27 shows the longitudinal braces installed on the 33-ft WAM-V for testing on the 2-post rig. As shown in Figure 10.25, the braces are strategically located so as not to interfere with the suspension operation of the 33-ft WAM-V, which requires the payload tray to pivot about the aft joint hinge.

The longitudinal stiffening braces were evaluated using a series of sine wave chirp tests of the same type as in Section 10.5. The sweeps, which run from 0.5 - 2.5 Hz, were run at three suspension settings corresponding to the minimum, middle, and maximum settings of the dampers. The tests were then rerun without the stiffening braces for the same three suspension settings as a control.

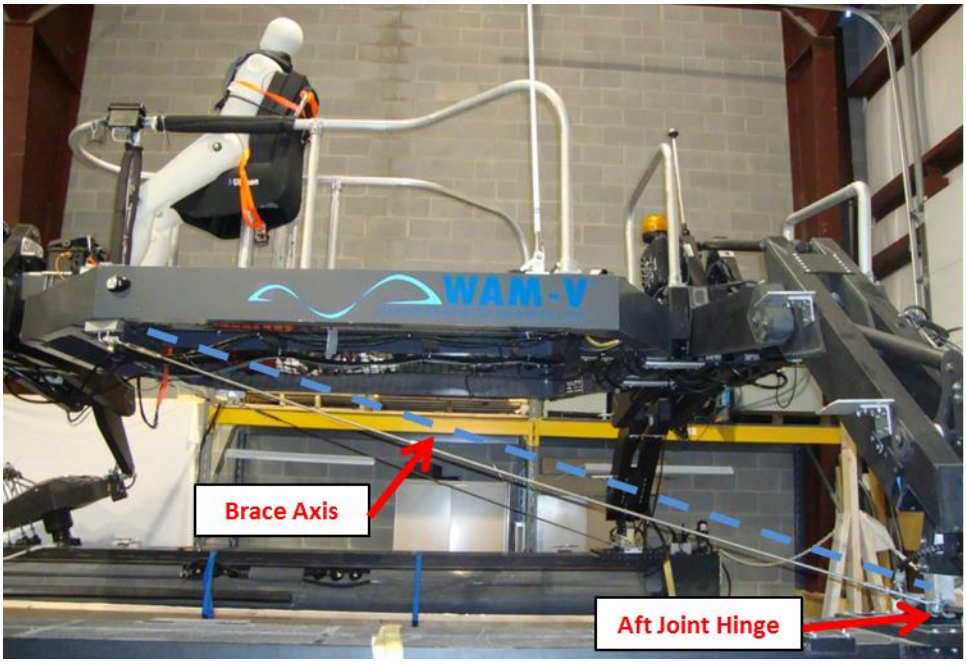

Figure 10.27 Longitudinal stiffening brace installation

10.7.1 Suspension Motion Analysis

Figure 10.28 contains three plots that show the change in suspension motion with and without the brace installed for each of the three damper settings. For all of the suspension motion plots, the static ride height of the suspension is changed when the longitudinal stiffening braces are installed. The heights of the spherical joints are raised up by ~0.5 inch each with the braces installed. The shift can be attributed to the stiffening brace pulling the payload tray to a slightly more rearward position, increasing the mass over the rear arch and decreasing the mass over the front arch. The change is subtle, based on the change in suspension heights, effectively 64 lbs shifts from the front to rear when the braces are installed. This decreases the sprung mass over each suspension system by 6%.

The most notable change in the suspension performance with the braces installed is the change in the node in the suspension displacement that was found to occur at 1.67 Hz in the previous section. The node has disappeared and the suspension has assumed a more uniform suspension travel at the higher frequencies of the chirp signal.

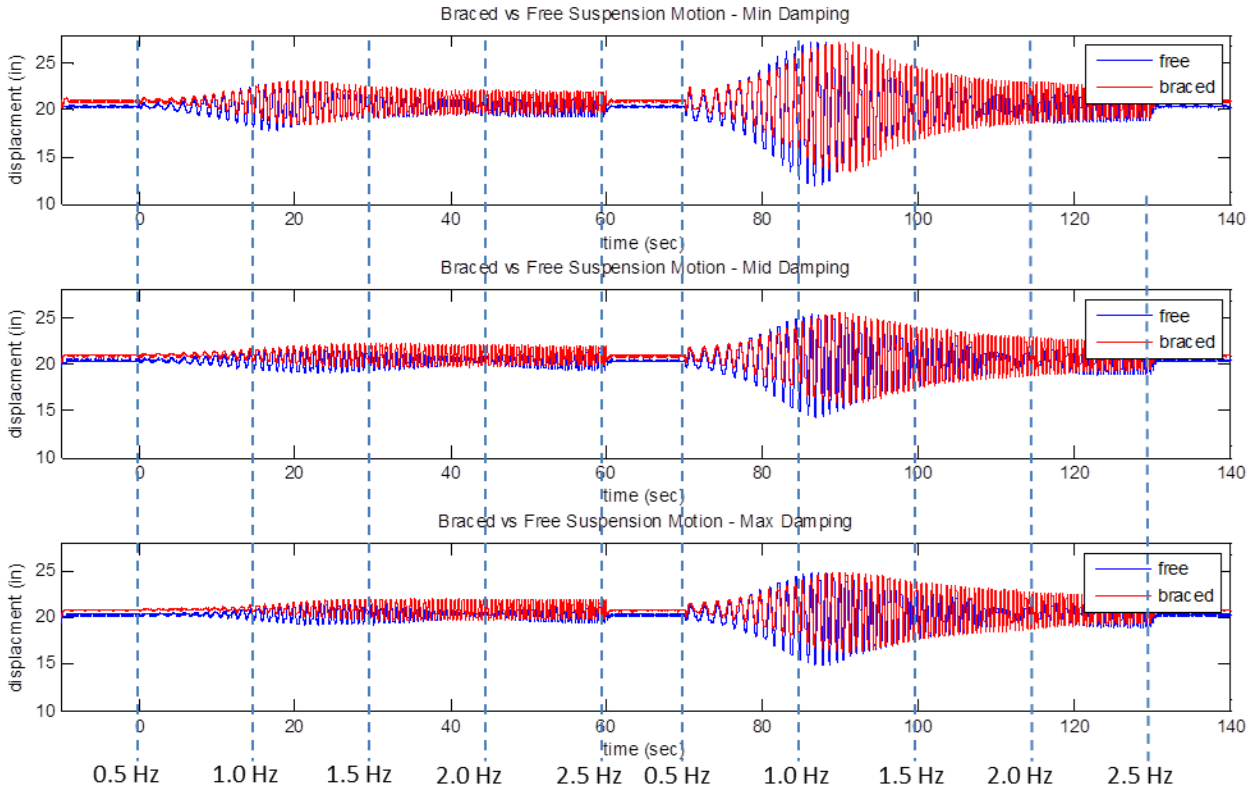

Figure 10.28 Suspension motion comparison with and without brace – three suspension settings

The suspension motion for all three damper setting shows a change in the resonant frequency with the braces installed. In Section 10.6.2, the resonant frequency of the suspension was found to be ~1 Hz without the longitudinal stiffening braces installed. The resonant frequency of the suspension with the braces installed occurs at ~1.22 Hz. The peak motion is smaller with the brace installed for all three suspension settings, as shown in Table 10.3 for the larger displacement tests; similar trends were recorded in the data for the smaller amplitude tests.

Table 10.3 Difference in peak suspension motion with and without longitudinal stiffening brace installed

Suspension Setting:	Peak Amplitudes, without Brace Installed (in):	Peak Amplitudes, with Brace Installed (in):
Minimum	11.9 - 27.1	13.4 – 27.2
Middle	14.4 - 25.4	15.8 - 25.5
Maximum	14.9 - 24.9	16.2 - 24.9

10.7.2 Vertical Payload Acceleration Analysis

Figure 10.29 shows three plots with comparisons of the vertical acceleration levels at the payload tray with and without the longitudinal stiffening braces installed, for the three damper settings.

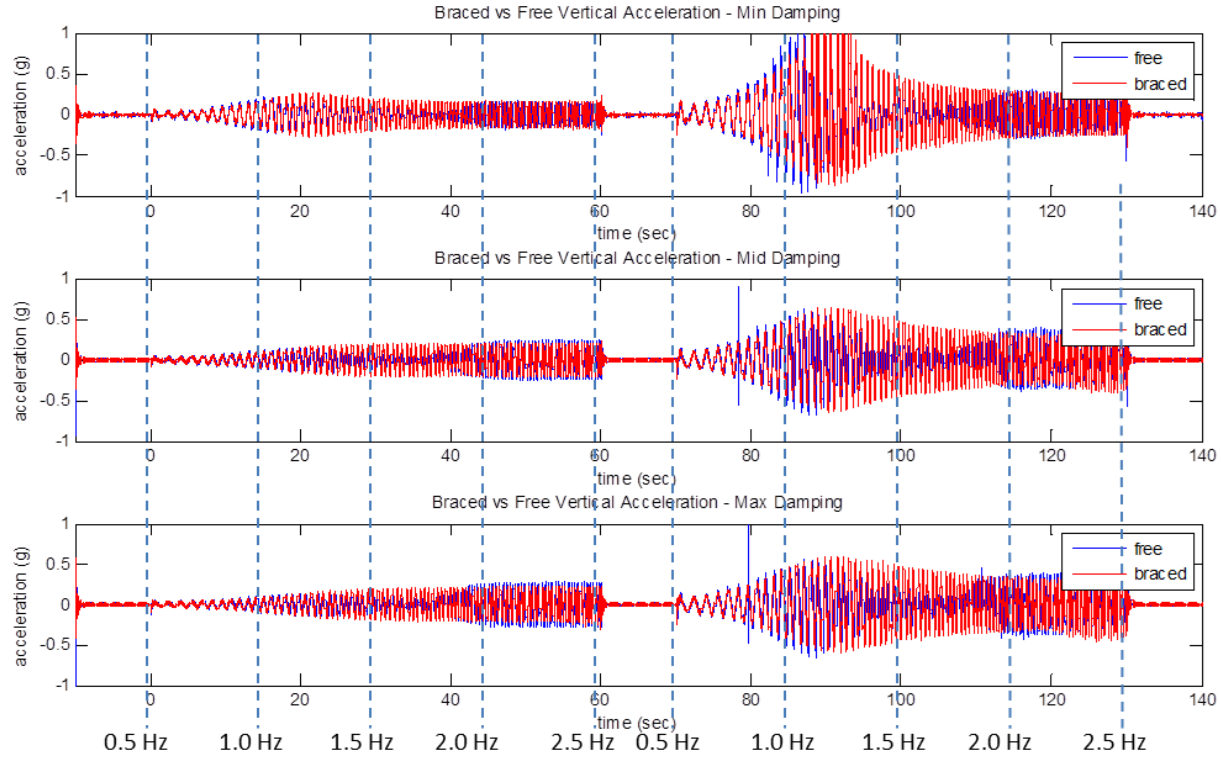

Figure 10.29 Vertical acceleration comparison with and without brace – three suspension settings

In the vertical direction, the longitudinal stiffening braces slightly improve the performance of the suspension at the lowest and highest frequencies of the test (from 0.5 - 1.0 Hz and 2.0 - 2.5 Hz), and degrade the performance for the middle range of frequencies (1.0 - 2.0 Hz). What is interesting is that the node at 1.67 Hz in the suspension performance discussed in Section 10.6.3 is no longer found in the data with the longitudinal stiffening brace installed. The node was likely due to a longitudinal resonance between the payload tray and the pitching motion of the front arch, coupled together to cause an anti-resonance point in the suspension data. This phenomenon would not likely have been found without testing the longitudinal stiffening brace.

The longitudinal stiffening brace was not found to consistently improve or impair the vertical acceleration attenuation of the WAM-V, so the longitudinal performance covered in the next section will determine whether a solution should be implemented on the 33-ft WAM-V for future on-water testing.

10.7.3 Longitudinal Payload Acceleration Analysis

Figure 10.30 shows three plots with comparisons of the longitudinal acceleration levels at the payload tray with and without the stiffening braces installed for the three damper settings.

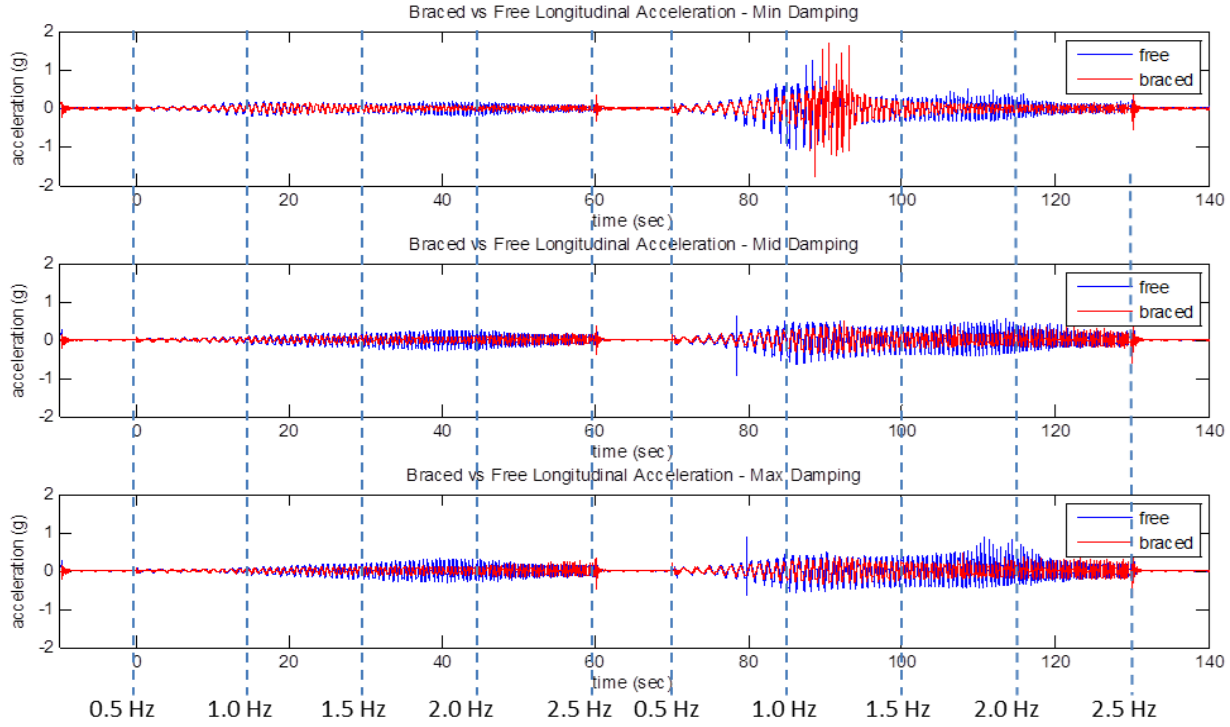

Figure 10.30 Longitudinal acceleration comparison with and without brace – three suspension settings

The longitudinal acceleration data shows improved performance with the braces installed throughout the entire frequency range for all three suspension settings. This differs from the vertical acceleration attenuation, which was highly dependent on frequency. There is one location in the data where the longitudinal acceleration levels are not an improvement compared to the acceleration levels without the brace. This point can found be at approximately 90 seconds into the data, and is only present for the damping at the minimum available damper setting. The spikes are due to the limit straps beginning to engage due to the suspension riding slightly higher in its travel with the braces installed. The bump stop located behind the front arch is rotating in pitch and may or may not be contacting its stop; pitch rotation of the front arch is not recorded in the data. This could be easily solved by lowering the spring perches on the suspension; it is not an issue related to the dynamics of the stiffening braces. It is recommended, based on the 2-post testing data, that a longitudinal stiffening brace be designed for future on-water use that would not impede the folding and unfolding of the arches.

10.7.4 Rear Arch Compliance Analysis

Figure 10.31 shows three plots with comparisons of the motion recorded by the longitudinal string potentiometer with and without the longitudinal stiffening braces installed, for the three different damper settings.

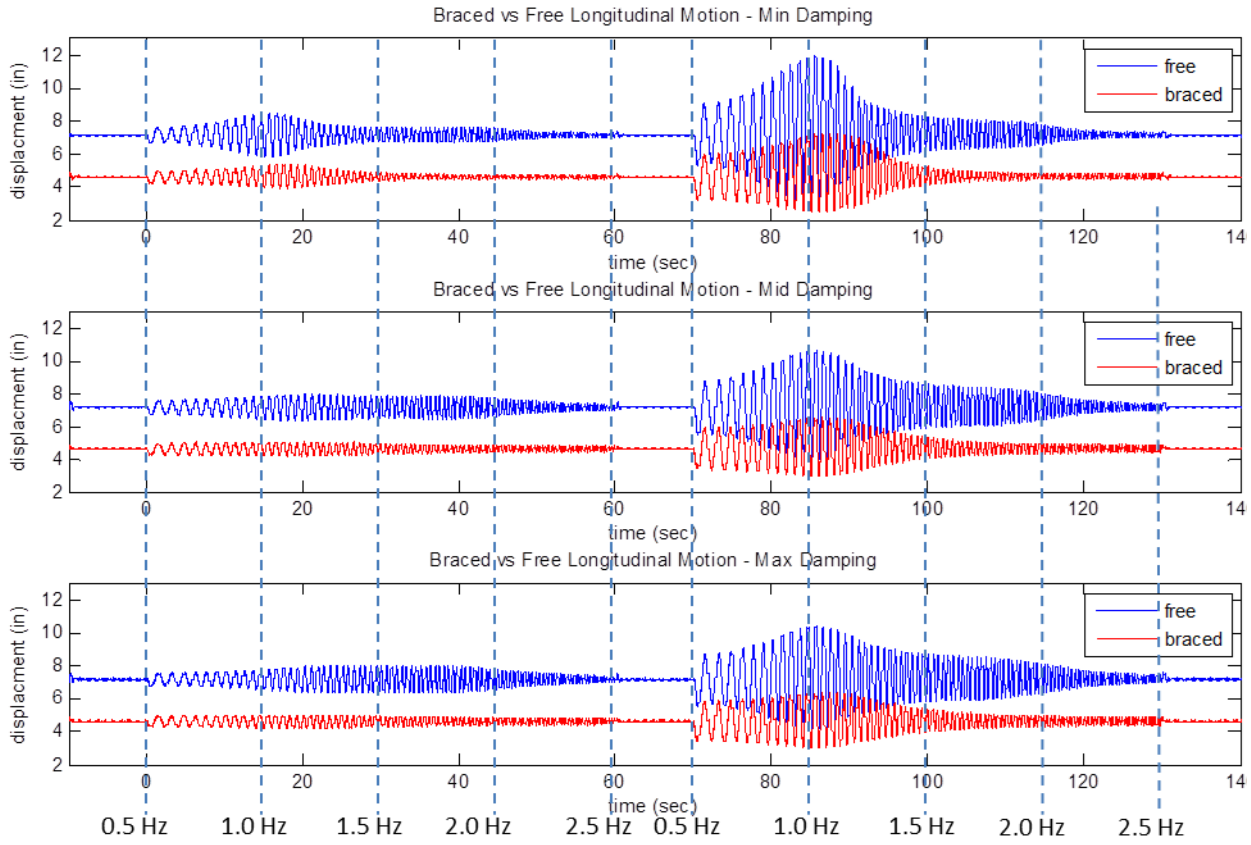

Figure 10.31 Longitudinal motion comparison with and without brace – three suspension settings

The plots in Figure 10.31 show that there is significantly less longitudinal motion with the braces installed. An ideal stiffening brace would not remove the motion entirely; as shown in the diagram of Figure 10.12, the longitudinal string potentiometer measures both the compliance and the rigid body motion required for the suspension to articulate.

It is also noteworthy that the data sets with and without the stiffening braces have different steady state values. The longitudinal stiffener effectively moves the payload tray rearward by 2.5 inches. This is consistent with the suspension motion analysis in the Section 10.7.1, which showed a 64 lb weight shift front to rear, based on changes in the height of the suspension systems.

10.8 Original vs. Second Generation Suspension Comparison Testing

A portion of the planned upgraded suspension on-water testing was meant to include a back to back comparison of the original and second generation suspension designs. The testing was not able to be completed due to powertrain reliability issues with the 33-ft WAM-V during testing. Also, it is the operator's opinion that the original suspension would not have been safe to test in the wave conditions that were available on the day of testing due to the original suspension's tendency to top out in rebound, thus causing the operator to experience excessive negative g loading and lose contact with the seat. The original suspension system had been previously tested in slightly less intense conditions and design flaws were found that affected its performance and would have been more apparent in more extreme conditions.

10.8.1 Second Generation Suspension Design Overview

Because a large percentage of the WAM-V's mass is unsprung, considerably more damping in compression was added in the damper's design to help control the motion of the unsprung mass. The new dampers have adjustable damping as well. The possible adjustment range of the new damper compared with the original dampers is shown in Figure 10.32. A more detailed analysis of the original and second generation damper can be found in Chapter 6.

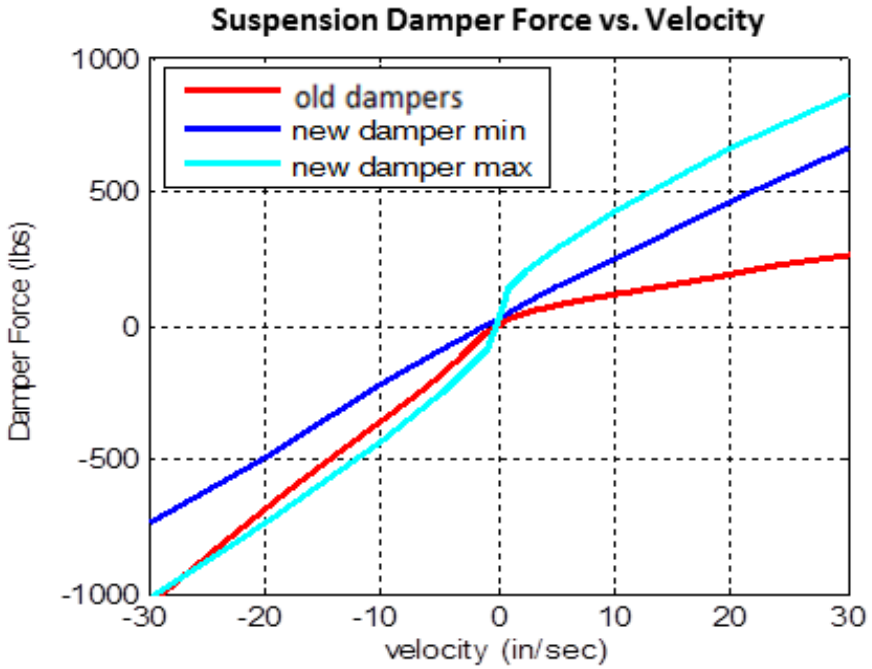

Figure 10.32 Original and second generation suspension damper rates

The Quarter-Boat model was used to help determine a spring rate that would not bottom out the suspension in compression, or require preloading of the spring. Both 400 lb/in and 500 lb/in springs were evaluated and compared with the original air spring design, as shown in Figure 10.33. A 500 lb/in spring was chosen as the best solution because the 400 lb/in spring required an inch of preload to achieve the required ride height, which would have been detrimental to the suspension's performance in rebound. A more detailed analysis of the Quarter-Boat model applied to simulate the 33-ft WAM-V can be found in Chapter 8.

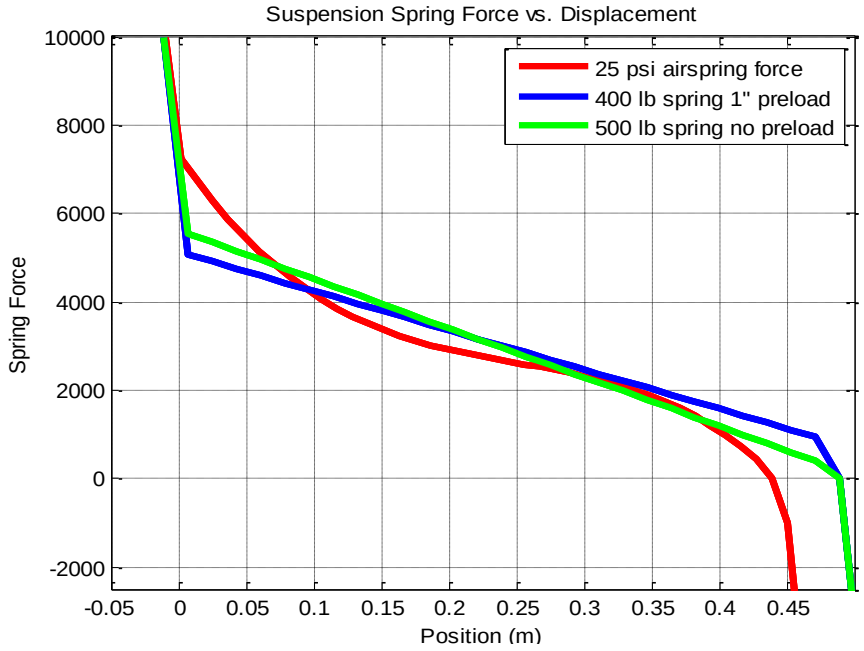

Figure 10.33 Original versus second generation suspension spring rate comparison

The 2-post rig allows for a controlled and safe environment for comparing the weaknesses and strengths of the two suspension types, as well as the possibly of further validating the choices made in the second generation suspension design.

10.8.2 Suspension Motion Analysis

Figure 10.34 shows a comparison of the suspension motion plots for the three new damper settings compared with the original dampers, with and without the longitudinal stiffening braces installed. When making a comparison between the two suspension setups, it is recommended that the middle and maximum damping settings be evaluated; the minimum adjustment of the damper produces a damping rate that is unlikely to be used outside of laboratory testing or testing in a low sea sate testing, due to the damper's limited energy absorbing capacity at this setting.

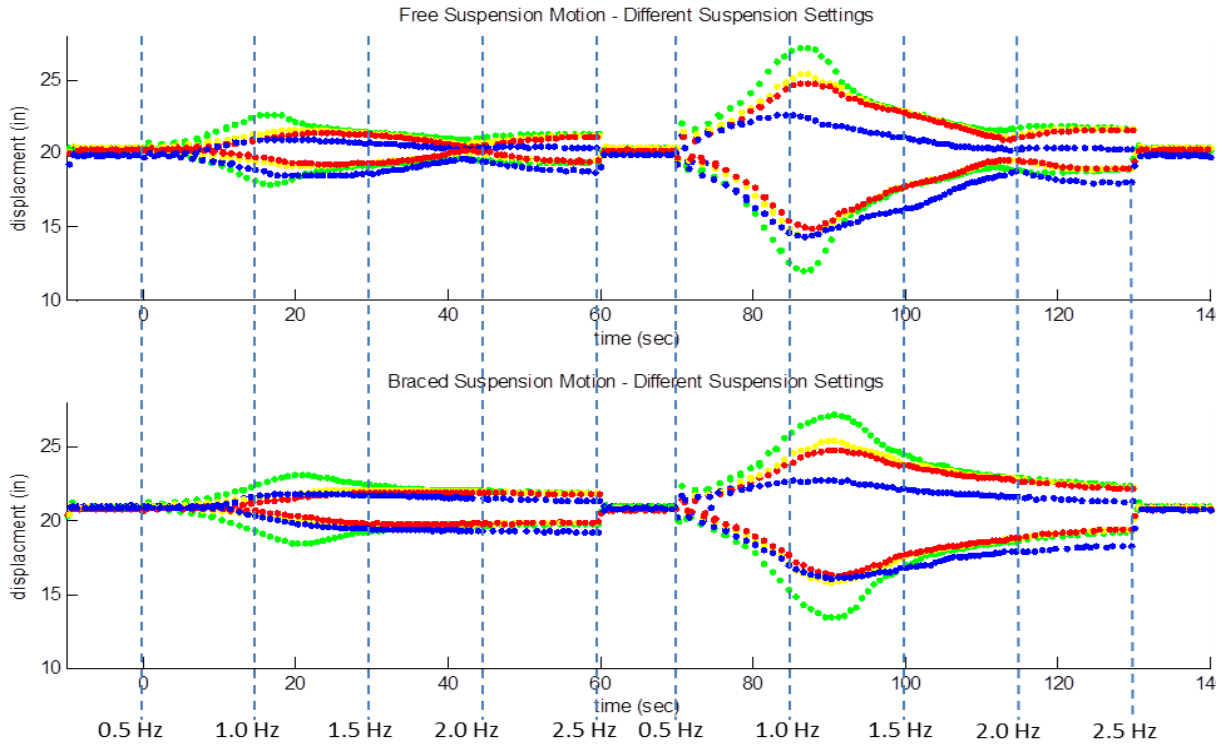

Figure 10.34 Suspension motion comparison between suspension settings with and without brace

It is also noteworthy when comparing the suspension systems, the original suspension has a maximum suspension height of 23 inches, while the second generation suspension has a maximum height of 28 inches. When comparing the curves from the different suspension systems, the two suspensions sit at similar static ride heights; however, at static ride height the original suspension is much closer to its rebound limits.

In Figure 10.34, the original dampers show a greater change in static ride height (~1 inch) due to the installation of the longitudinal stiffener braces. This can be attributed to the lower spring rate of the air springs at static ride height, as shown in Figure 10.33.

The plots of the original suspension system show motion that is less symmetrical between the rebound and compression directions than the plots of the second generation suspension. The original dampers have significantly more rebound than compression damping, so there is greater compression motion. Also, rebound motion is limited by the engagement of the suspension's straps at the end of its travel. The original suspension system also jacks down during each test, ending the test 0.75 inches lower than at the beginning. This is most evident in the rebound travel at the highest input frequencies of the tests, and is more apparent without the braces installed.

10.8.3 Payload Vertical Acceleration Analysis

Figure 10.35 shows a comparison of the vertical acceleration levels at the payload tray for the three new damper settings compared with the original dampers, shown with and without the longitudinal stiffening braces installed.

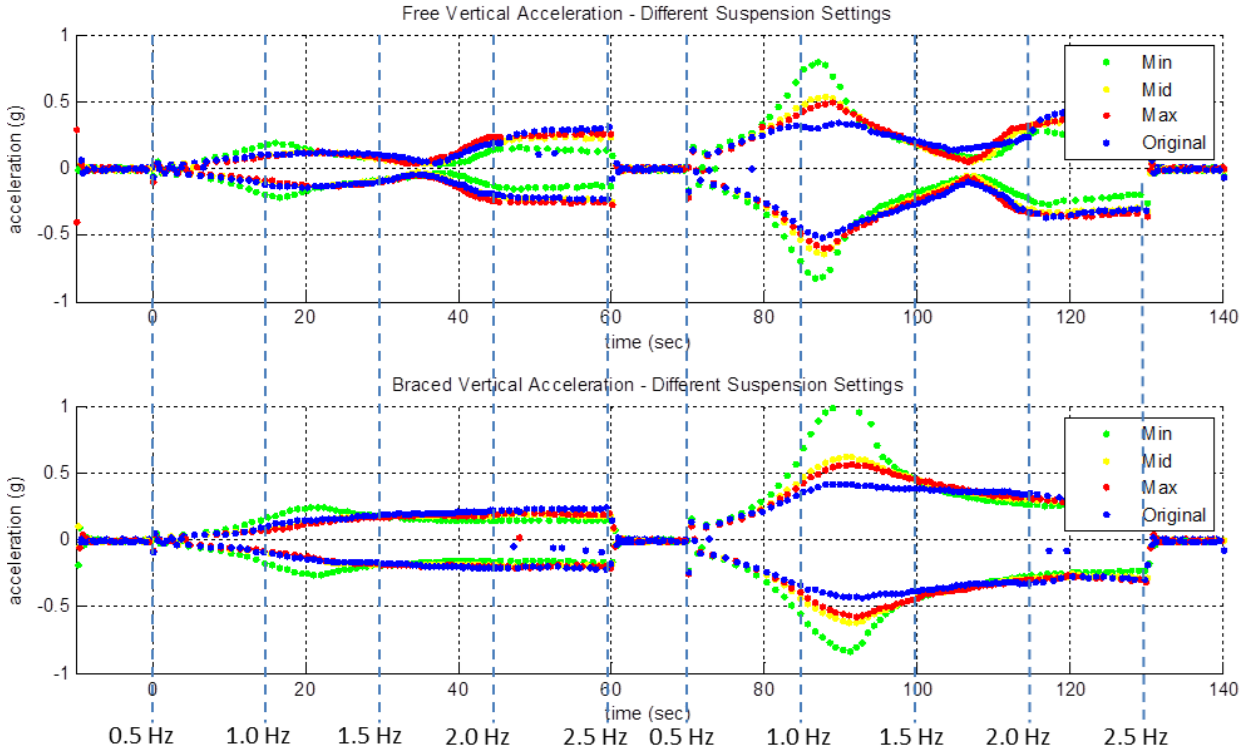

Figure 10.35 Vertical acceleration comparison between four suspension settings with and without brace

Without the braces installed, the original suspension shows similar performance to the middle and maximum damper settings for the smaller displacement tests. For the larger displacement tests, the original suspension shows marginally better performance for lower frequency inputs and equal to marginally worse performance for higher frequency inputs.

With the braces installed, the original suspension system shows marginally worse performance for the entire low displacement test. For the higher displacement tests, the original suspension once again shows better performance for lower frequencies and equal to marginally worse performance for higher frequencies.

Based on the vertical acceleration comparisons of the two suspension systems, there is little improvement shown by the second generation suspension system. This can largely be attributed to the 2-post rig not evaluating the unsprung dynamics of the WAM-V, and the inputs not being

as severe in nature compared to the on-water tests; both of which will favor the softer air springs over the higher energy absorbing capabilities of the second generation suspension system. It is believed that the 400 lb/in springs would also outperform the 500 lb/in springs and possibly the air springs; however, the 400 lb/in springs were not evaluated because they would likely be too soft for elevated sea state testing. This is a common problem with shaker rig testing, which often favors softer suspension settings than are practical for real world applications.

10.8.4 Payload Longitudinal Acceleration Analysis

Figure 10.36 shows a comparison of the longitudinal acceleration levels at the payload for the three new damper settings compared with the original dampers, with and without the longitudinal stiffening braces installed.

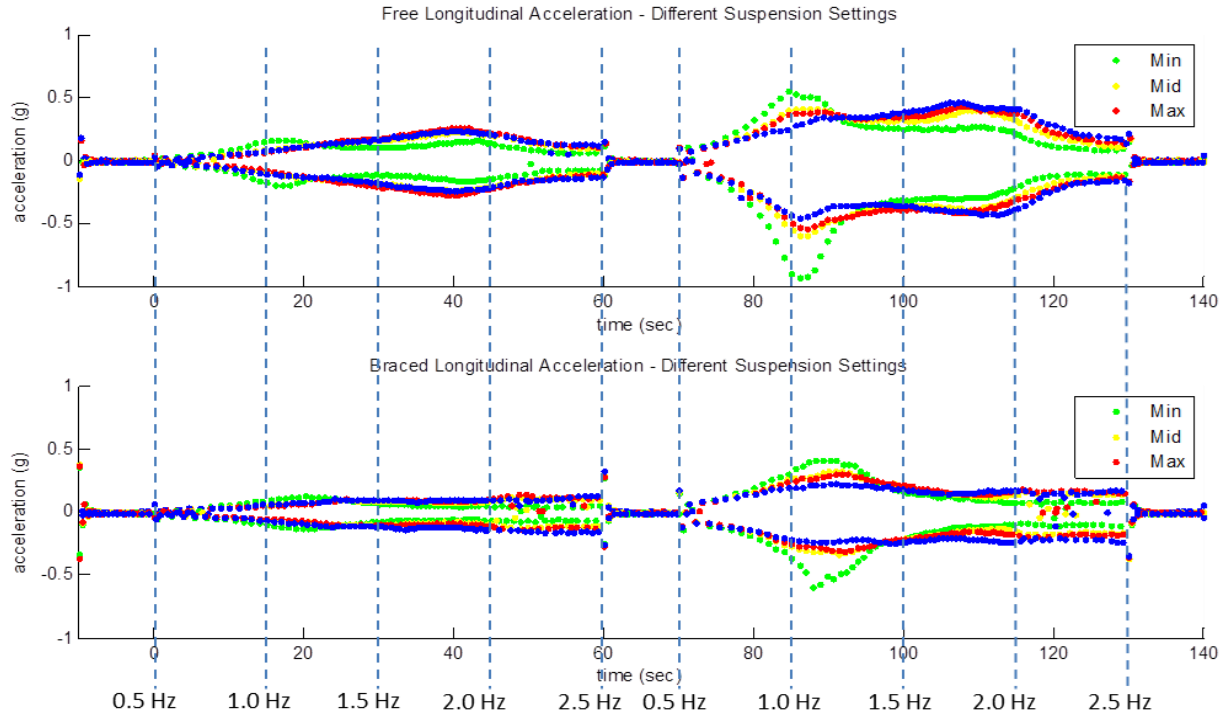

Figure 10.36 Longitudinal acceleration comparison between four suspension settings with and without brace

Based on the graphs shown in Figure 10.36, the original suspension shows equal performance for both of the low displacement tests. For the high displacement tests, the low frequency performance of the original suspension is marginally better and the high frequency performance is marginally worse. Much like the vertical acceleration results, the results on the 2-post rig do not show conclusive performance improvements for the second generation suspension system, as were found during the elevated sea state testing.

10.9 Whole-Body Vibration Analysis using the 2-Post Testing Rig

The Whole-Body Vibration analysis conducted in Chapter 9 with the Sea State 1 testing data can also be conducted using the 2-post rig. This section details the methodology for applying the ISO 2631-1 Whole-Body Vibration standard to the 2-post rig.

10.9.1 A Method for Applying the Standard to Short Time Series Events

For the Whole-Body Vibration analysis in Chapter 9, each test was treated as a single four minute dataset for computing the weighted accelerations. This meant that there was a single output weighted acceleration value from each test; however, there is no way to look at individual acceleration event sections within the tests.

For the 2-post rig, the same method of analysis could have also been carried out, leading to a single weighted acceleration value for each data channel for each test. As with the Sea State 1 data, comparison of different tests would be possible; however, there would be no way to compare the effects of the different frequencies of excitation that occur within each test, due to the chirp signal inputs. With this in mind, a method for analyzing the effects of the different frequencies individually was desired as part of the analysis.

10.9.2 Application of ISO-2631-1 to the Data from the 2-Post Rig

For applying ISO 2631-1 to the 2-post rig for short pieces of data, a five second time window was chosen for each data point; data points were analyzed in one second intervals. Figure 10.37 shows the input accelerations and the ISO 2631-1 weighted acceleration output for the starboard-side front pontoon accelerometer.

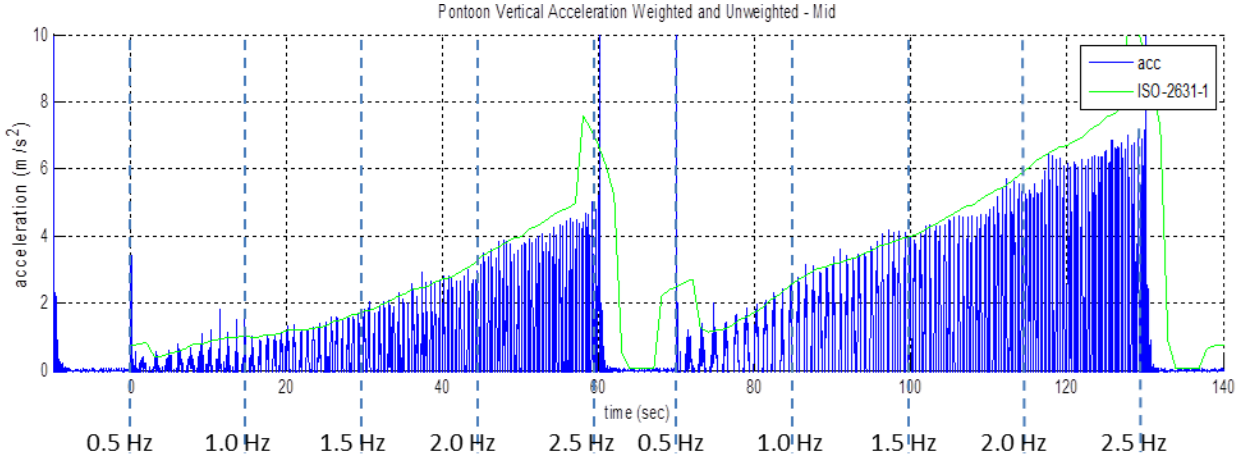

Figure 10.37 ISO 2631-1 weighted acceleration at 2-post rig pontoons

The spikes in the weighted acceleration values at the beginning and end of each test are due to a non-smooth transition at the start and end of the dSPACE input files. The data spikes are effectively amplified by the short, five second data windows used for analysis.

Figure 10.38 shows the ISO-2631-1 weighted vertical acceleration levels at the pontoons compared with weighted vertical acceleration values at the payload tray. The acceleration levels are shown for the middle damper setting, with and without the longitudinal stiffening brace installed.

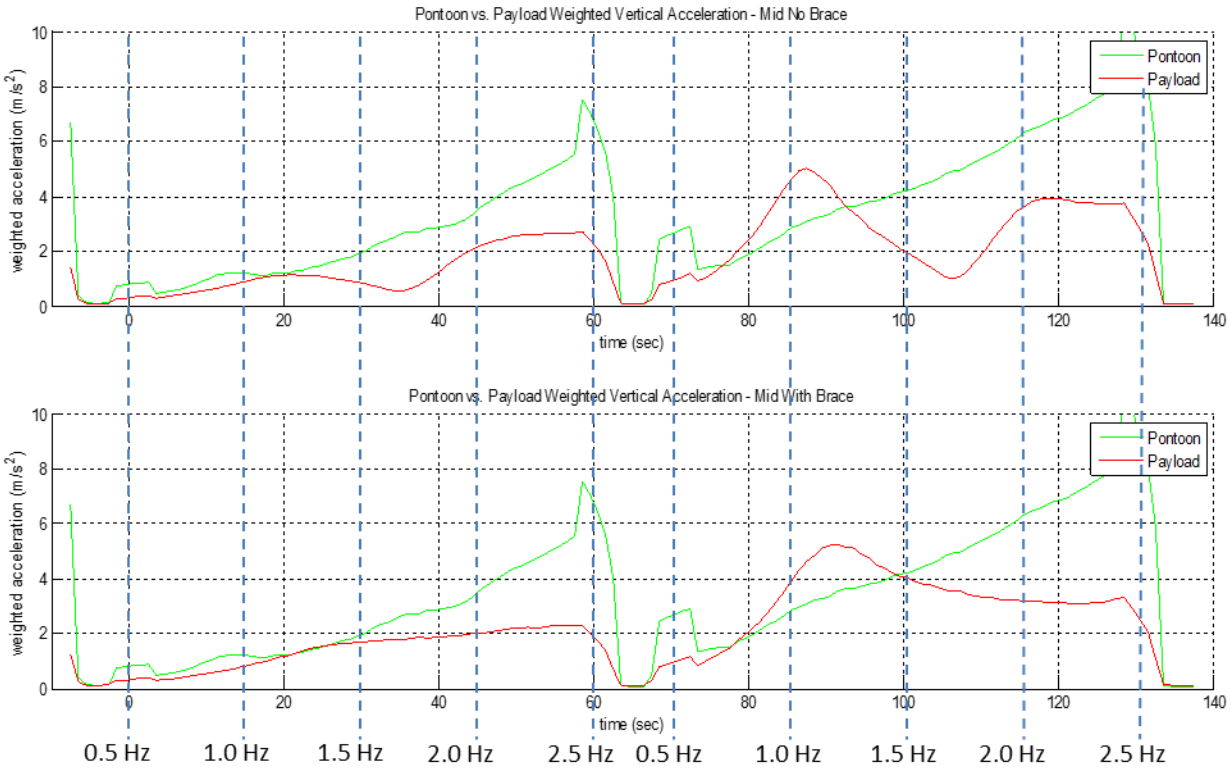

Figure 10.38 ISO 2631-1 weighted acceleration at 2-post rig pontoons compared with payload

It can be seen from Figure 10.38 that for the majority of the test, the payload sees lower weighted acceleration levels than do the pontoons. The only exception to this occurs at a frequency of 1.13 Hz (20 seconds into the test). This is also close to the location of the peaks in the unweighted acceleration data, which were shown in Figure 10.20 to occur at 1.0 Hz (15 seconds into the test). The difference can be attributed to the weighting of the vertical acceleration values. For frequencies of less than 4 Hz, the vertical weighting values increase with increases in frequency.

Figure 10.39 shows the weighted vertical acceleration level at the pontoons compared with the weighted longitudinal acceleration level at the payload to show the effectiveness of the suspension system for isolating the frequencies of greatest interest to human body dynamics, this time in the longitudinal direction. It is important to note when analyzing the data presented in Figure 10.39, that the longitudinal acceleration values receive different weighting values than do vertical acceleration values as per ISO 2631-1. The weighting values for the different axes are discussed in Section 2.6.2.

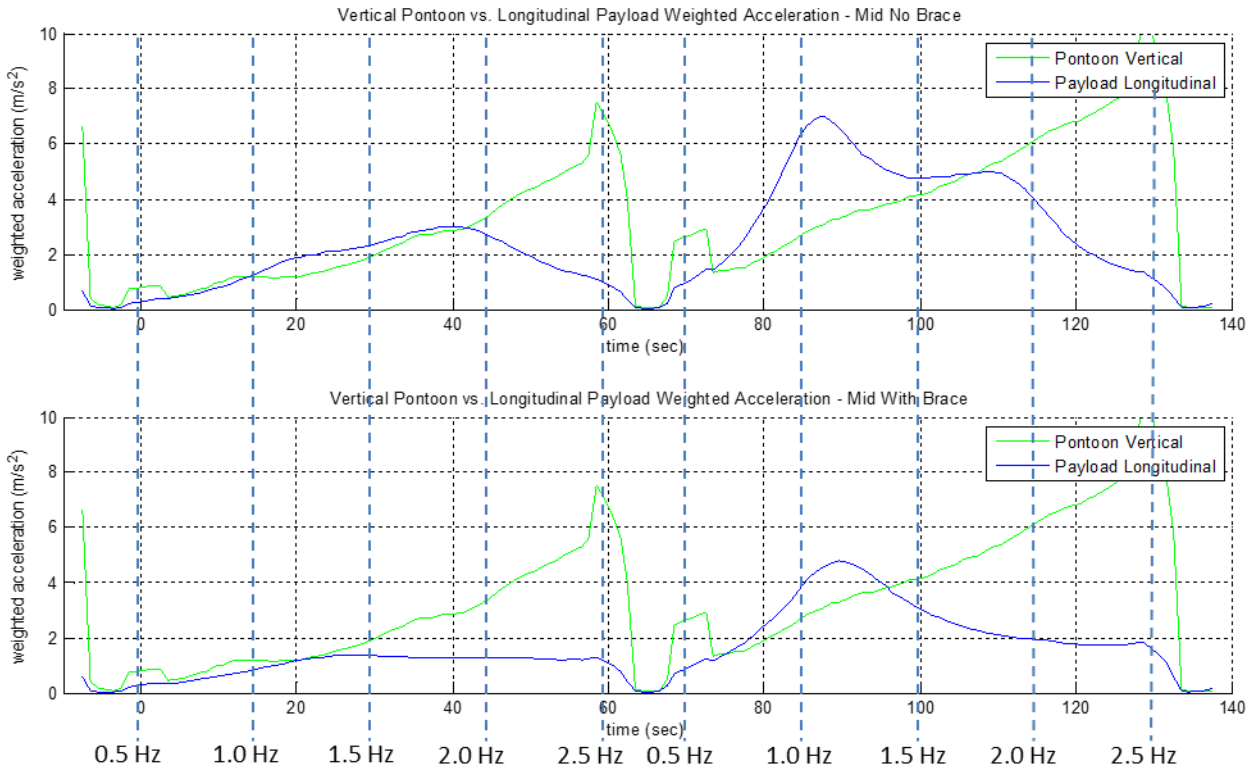

Figure 10.39 ISO 2631-1 weighted vertical acceleration at pontoons compared with weighted longitudinal payload acceleration

Figure 10.39 shows a marked reduction in the weighted acceleration values with the longitudinal brace installed. The reductions in acceleration are on average 50%, depending on frequency. When comparing the longitudinal acceleration values with the vertical acceleration inputs at the pontoons, the payload performs the best relative to the pontoons at higher frequencies. This is important because the upper limits of the chirp signal are the most sensitive frequencies in the human body to longitudinal acceleration.

Figure 10.40 shows a comparison between the vertical and longitudinal weighted acceleration values with and without the longitudinal stiffening brace installed for the middle damper setting. As with the comparison of the vertical pontoon acceleration and the longitudinal payload acceleration, when analyzing the data in Figure 10.40, the longitudinal acceleration values receive different weighting values than do vertical acceleration values as per ISO 2631-1. This needs to be factored into the resulting analysis.

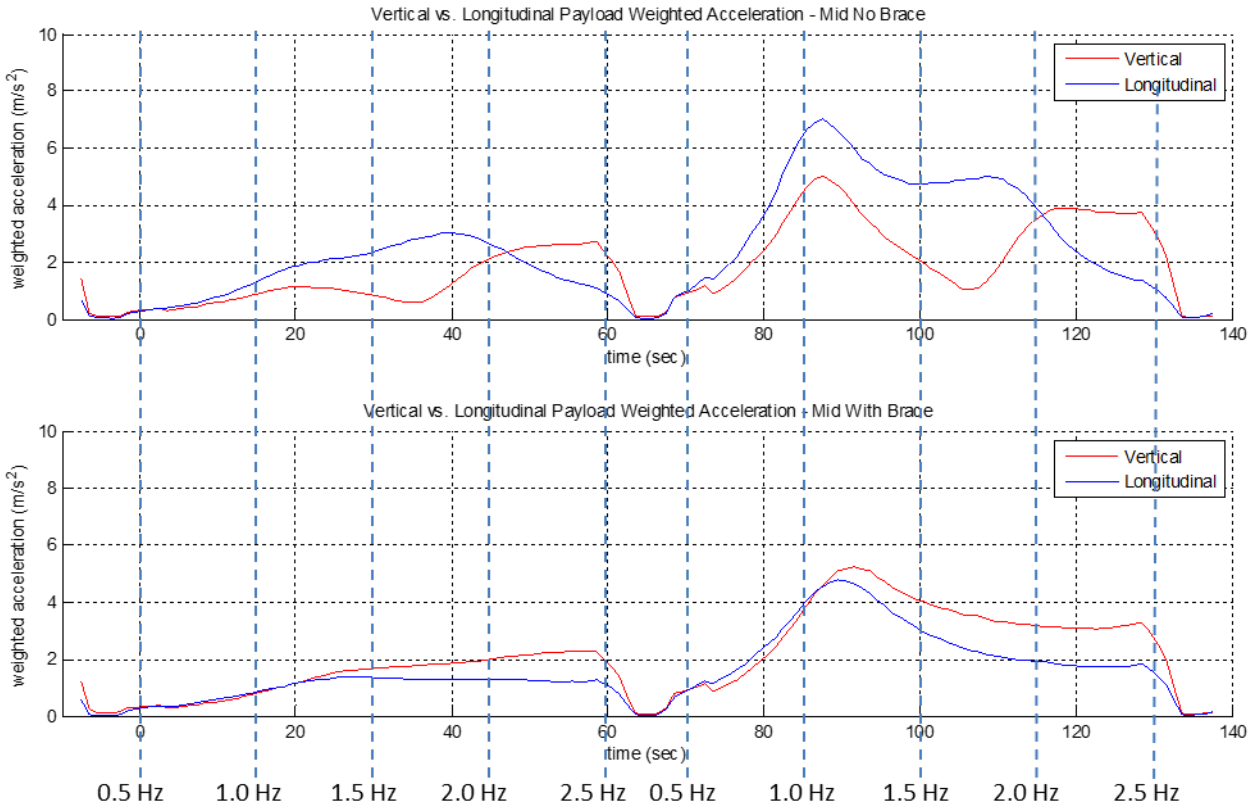

Figure 10.40 ISO 2631-1 weighted vertical vs. longitudinal payload acceleration

Figure 10.40 shows that without the brace installed, the weighted longitudinal acceleration is greater than the weighted vertical acceleration for the majority of the data. The only exceptions occur at frequencies greater than 2 Hz (after 45 second into each test). With the brace installed, the trend reverses itself, with the weighted vertical acceleration values greater than or equal to the weighted longitudinal acceleration values for the majority of the test. This confirms the results presented for the longitudinal stiffening brace.

10.10 Conclusions and Recommendations for Further Research

The results and information learned from the testing with the 2-post rig can be applied to improve the design of the 2-post rig, as well as the design of future WAM-Vs. The findings and conclusions from each round of testing are presented in this section.

10.10.1 Conclusions from 2-Post Rig Design, Construction, and Instrumentation

The design on the 2-post rig was able to produce good results in evaluating the WAM-V's dynamics. If the improvements are to be made to be to the rig, there are a number of possible upgrades which might be considered.

For improving the instrumentation setup, implementing a vertical string potentiometer on the front of the payload tray, similar in design and implementation to the longitudinal string potentiometer mounted at the rear of the payload tray, would generate an interesting data channel for directly measuring the motion of the payload. This would be a particularly interesting measurement because global vertical motion cannot be measured during on-water testing.

The methods of holding the pontoons with the cradle assemblies proved sufficient to restrain the pontoons without damaging the pontoons or the skis. However, the cradles added significant bending stiffness to the skis, so some of their dynamic properties were lost in testing.

The use of two active posts to be proved sufficient to excite the suspension and a great deal was learned about the properties of the WAM-V. For future testing, four active posts could be implemented; however, the number of required tests would increase dramatically. Four active posts would be useful for inputting on-water testing data to the rig. A second hydraulic pump would be required if two more posts are added, or a pump with a higher flow capacity could be installed.

The limited stroke of the actuators did prove to be limiting to the inputs that could be applied to the WAM-V. Actuators with a longer stroke would be a useful upgrade to the rig. The flow capacity of the rig would also have to be considered. A secondary option would be to put the actuators on a lever arm so that there would be an amplification of the motion at the pontoons, while the same actuators could be used. In Section 10.6.6 the actuators were found to be using only 1500 lbs of their 5600 lb force capacity. A motion ratio would have to be chosen within the force limits of the actuators.

10.10.2 Conclusions from Damper Testing

Based on the damper testing results, using a relatively high damping ratio (>0.5 critical) is recommended for on-water use. The testing results in Chapter 9 did not show proof of improved performance of lower damping settings in a less intense sea state. The 2-post rig favored higher damping levels, as would elevated sea state testing where energy absorption of the dampers is critical to keeping suspensions from bottoming out due to heavy impacts and to control the large unsprung mass of the pontoons.

10.10.3 Conclusions from Longitudinal Stiffener Testing

The longitudinal stiffening brace proved to be extremely effective at minimizing unwanted motions of the payload due to the rear arch folding mechanism. A brace should be designed that will allow for on-water use without interfering with the folding mechanism.

For instrumentation, the addition of a rotary potentiometer to the data acquisition setup to measure the angle of the rear arch could be implemented. A rotary potentiometer along with the longitudinal string potentiometer could to help quantify the difference between compliance and rigid body motion of the arch that are both currently being recorded by the string potentiometer. Adding this sensor is not critical for future testing.

10.10.4 Conclusions from Original vs. Second Generation Suspension Testing

Testing of the original suspension system did not show dramatic improvements with the second generation suspension system. This can most likely be attributed to the unsprung dynamics of the WAM-V, which were modeled extensively in Chapter 8 for the second generation suspension design, not being implemented on the 2-post rig. Two possible methods of implementing the pontoon dynamics onto the 2-post rig are discussed in Chapter 12 using the Quarter-Boat models from Chapter 5 and Chapter 8.

10.10.5 Conclusions from Whole-Body Vibrations Analysis

The ISO 2631-1 Whole-Body Vibration analysis of the 2-post rig data shows the frequencies of greatest interest to human body and WAM-V dynamics. The standards could be taken further to include exposure limits. The standards could also be further examined to include ride comfort and exposure limits for the different frequencies and the different tests.

Chapter 11 33-ft WAM-V Virtual Shaker Rig Modeling

The following chapter documents the design of a 6-post Multi-Body Dynamics (MBD) model, constructed based on the 33-ft WAM-V detailed in Chapter 6. The 6-post model builds upon the design of the 4-post model created for the 12-ft USV in Chapter 4. The majority of this chapter details a comparison of the 6-post model with the 2-post test rig data presented in Chapter 10. Other applications of the 6-post model are also discussed, including coupling the model with a Computation Fluid Dynamics (CFD) code for the 33-ft WAM-V developed in collaboration with the University of Iowa.

11.1 Chapter Overview

- Section 11.1 provides an overview of the chapter.
- Section 11.2 presents the parameters of the 6-post virtual model for the 33-ft WAM-V.
- Section 11.3 presents a comparison of the model with the data from the 2-post test rig.
- Section 11.4 details a method of modeling the compliance in the 33-ft WAM-V's rear arch and compares the linear compliance model with testing data from the 2-post rig.
- Section 11.5 details the coupling of the 6-post MBD model with a CFD code for simulating the 33-ft WAM-V with sea state inputs.
- Section 11.6 summarizes the results, conclusions, and recommendations from the chapter.

11.1.1 Significant Contributions

The virtual 6-post model is novel in that it allows for a three component comparison of the simulation environment, on-water testing data, and 2-post rig testing, to extend the field of knowledge for Wave-Adaptive Modular Vessels. The virtual 6-post model also represents a significant contribution from the WAM-V modeling efforts; the model is being used by researchers at Iowa who were not directly involved with creating the MBD model, although they are closely involved with WAM-V research efforts. One of the ultimate goals of the research into WAM-V suspension systems is to provide a set of tools for future WAM-V designers. The designers may be naval architects, researchers, or (in the case of Iowa) hydrodynamicists; for the tools to be successful, they must be usable by individuals not involved in creating the simulations. This chapter represents a significant step toward that goal.

11.2 6-Post Model Parameters

A 6-post virtual shaker rig was designed with similar model architecture to the virtual 4-post model for the 12-ft USV detailed in Chapter 4, to expand the testing capabilities of the 2-post shaker rig. The model is named after the six actuator posts under the WAM-V in the model; four actuators support the pontoons and two support the engine pods. The 6-post model serves an important function for improving the utility of testing with the 2-post shaker rig. The 2-post rig does an excellent job of testing the dynamics of WAM-Vs in the laboratory setting; the tests are highly repeatable and the cost of testing compared to an on-water test is extremely low. However, the 2-post rig is limited in its testing capabilities due to the limited number of live actuators (the 2-post rig only has two live actuators located at the front of the pontoons, the rear posts are stationary) and the limited stroke of the actuators. This presents a problem for inputting sea data into the 2-post rig because the sea data often contains displacements of greater magnitude than the 2-post rig is able to test.

A possible method of testing sea data using the 2-post rig is to scale the input data to fit within the actuator's stroke limits. A relationship then has to be defined between the scaled and the unscaled data. This is where the 6-post model can be utilized. Simulations using the 6-post model can be run for both the full scale sea displacement data and scaled data to compare the simulation results with the 2-post rig. The 6-post simulations can also be run with and without displacements inputs at the rear of the WAM-V or at the engine pods, to determine the effects of applying only front inputs on the model.

Before the 6-post virtual model can be used for analyzing sea data, the model must be correlated with the 2-post rig for known input types. Correlating the model and the testing data is the focus of the first part of this chapter.

11.2.1 Model Overview

The virtual 6-post model is similar to the 4-post model developed for the 12-ft USV in Chapter 4. Compared to the 4-post model, the 6-post model has been updated to include actuators under the rear of the engine pods, and to contain all of the parameters of the 33-ft WAM-V. The methodology for determining the parameters of the 6-post model based on the 33-ft is discussed in Section 6.6. A block diagram representation of the 6-post model constructed using SimMechanics is shown in Figure 11.1.

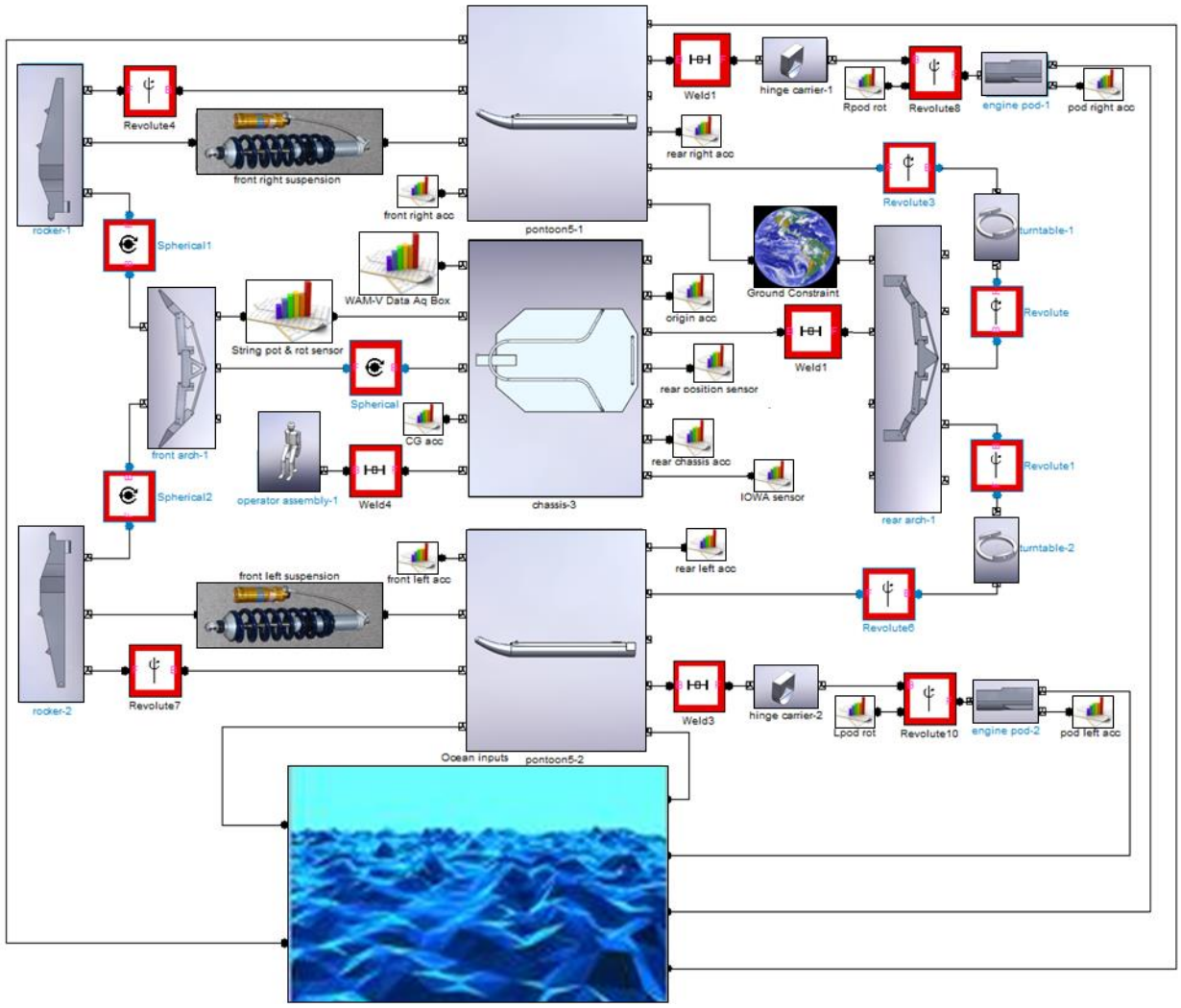

Figure 11.1 6-post model block diagram

11.2.2 Model Inputs

Compared to the 4-post model, the 6-post model features two additional actuators located at the rear of the engine pods, so the vertical engine pod dynamics can be included in the model. Compared to on-water testing data, applying vertical inputs under the engine pods cannot provide a complete picture of the pod's dynamics, since the model still does not consider the effects of the changing thrust vector of the propulsion units due to the changing angle of the pods. Only inputs from each of the six vertical actuators affect the model's dynamics. The location of each of the six actuators in the 6-post model is shown in Figure 11.2, along with the center of gravity location of each of the 14 components shown in Figure 11.1 and the total center of gravity of the WAM-V (shown in red).

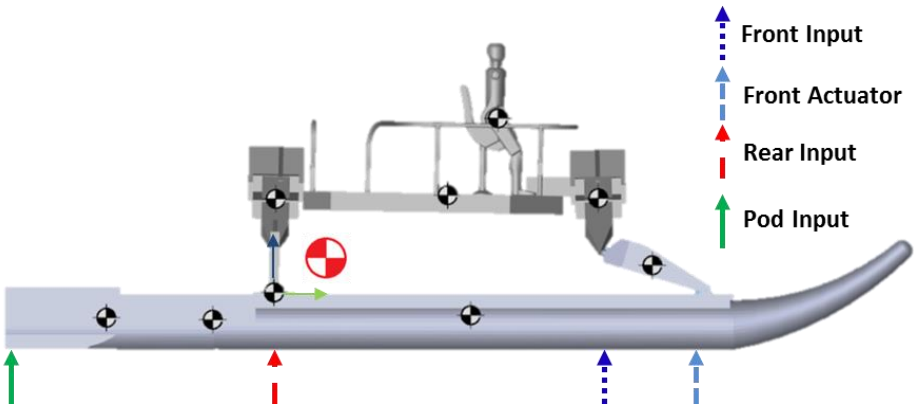

Figure 11.2 6-post rig setup with center of gravity locations of major components

In Figure 11.2, two different input locations are shown for the front actuators. This is due to the difference between the longitudinal positioning of the actuators on the 2-post rig and the vertical accelerometers on the skis. The actuators on the 2-post rig were placed at the far corners of the skis on the 33-ft WAM-V to make the rig as stable as possible; while the accelerometers on the 33-ft WAM-V were placed as close as possible to the spherical joints on the front suspension systems to record acceleration data at a location that was as close to directly under the front suspension systems as possible, to measure the differences in the acceleration across the suspension systems.

For applications where the 6-post model is being run with inputs from on-water testing data (using the method for filtering and integrating acceleration data to create displacement inputs detailed in Chapter 4), the front actuators will be placed directly under the spherical joints of the front suspension in the model. For applications where the 6-post model is being compared to test data from the 2-post shaker rig, the actuators will be placed under the hinges of the suspension rocker arms. Also, for comparison with the 2-post testing rig, the rear and engine pod actuators in the 6-post model will be set to zero displacement.

11.2.2.1 Model Degrees of Freedom

The degrees of freedom of the 6-post model are the same as the 4-post model except in the way the suspension and engine pods are modeled. The suspension systems were modeled in Chapter 4 as linear prismatic joints, the kinematics of the rocker arms were not included, only the vertical forces of the suspension systems were modeled. On the 6-post model, the suspension rocker arms are included in the model. The suspension is still modeled as a nonlinear vertical force between the skis and the spherical joints; however, the spherical joints are now constrained by the rocker

arms rather than by linear prismatic joints that are not present on the actual WAM-V. The mass of the rocker arms on the 33-ft WAM-V make up a significantly greater percentage of the 33-ft WAM-V's overall mass compared to the mass of the rocker arms relative to the overall mass of the 12-ft USV. The inertial effects of the rocker arms' mass are considered in the 6-post model.

For the 4-post USV model, the engine pods were modeled as though they were welded to the pontoons. This didn't affect the results because the 4-post model is a hub-coupled model, and since there is no rear suspension system on the 12-ft USV, displacement inputs at the pods do not affect the motion at the suspension systems. The 6-post model is also a hub-coupled model, and the 33-ft WAM-V also has no rear suspension system; however, for the 6-post model the vertical dynamics of the pods were incorporated into the model. The dynamics at the payload are still only affected by the front and rear input displacements, the reason for the difference in the models comes from how the two WAM-Vs were tested. The tests with the 33-ft WAM-V incorporated sensors on the engine pods, whereas the tests with the 12-ft USV did not, so the engine pods were modeled as hinged rather than rigid. Also, incorporating the vertical engine pod dynamics into the simulations will allow for the MBD model to be compared with the CFD coupled code in Section 11.5. For a hub-coupled model, actuators under the engine pods will affect the forces measured under the rear of the pontoons, which are used to compare the MBD and the CFD codes for the one-way coupling in Section 11.5. Also, for the two-way coupling of the MBD and CFD codes discussed in Section 11.6, movement of the engine pods is required. A diagram of the 6-post model is shown in Figure 11.3 with the degrees of freedom of each joint.

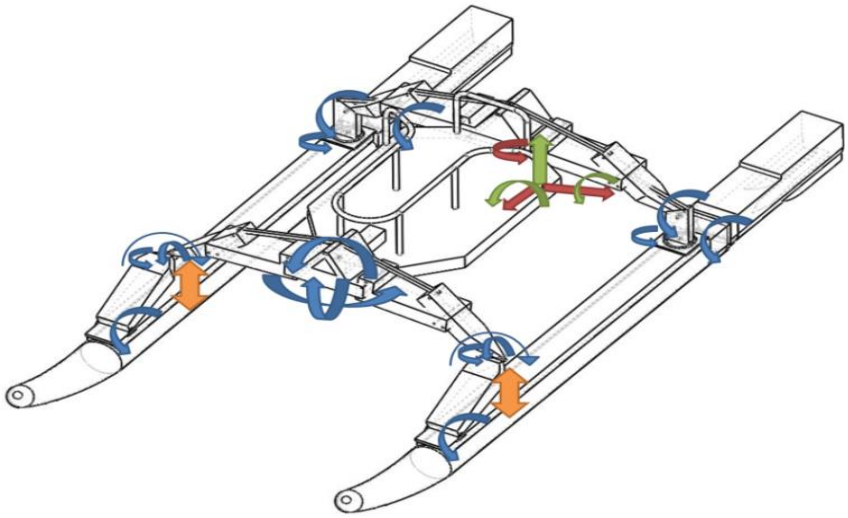

Figure 11.3 6-post model joint degrees of freedom and constraints

11.2.3 Model Constraints

Based on the experience from on-water testing, the WAM-V's longitudinal dynamics were found to have a large impact on its overall ride quality. Previous 4-post models discussed in Chapter 3 and Chapter 4 were focused on the WAM-V's vertical and suspension dynamics. This was reflected in the model's constraints; the models were pinned through the center of gravity using a three degree of freedom joint that allowed for vertical translation and rotation in pitch and roll of the payload. This meant that the longitudinal motion of the payload was also constrained.

The method of constraint was revised for the 33-ft WAM-V to better capture the vessel's longitudinal dynamics. Like the 4-post model, the joint still has three degrees of freedom that allow for vertical translation and for rotation in pitch and roll of the payload tray; however, the joint has been relocated to the bottom of the pontoons at the intersection of the rear arch and the boat's centerline. The location of the joint and its degrees of freedom are shown in Figure 11.4 along with the model's other degrees of freedom. The joint's location can also be seen in Figure 11.2 at the intersection of the arrows on the rear arch. It is noteworthy that the roll degree of freedom of the joint is not shown in Figure 11.4. Due to the WAM-V's architecture, the roll angle of the chassis is constrained by the aft inputs; it is not an independent degree of freedom.

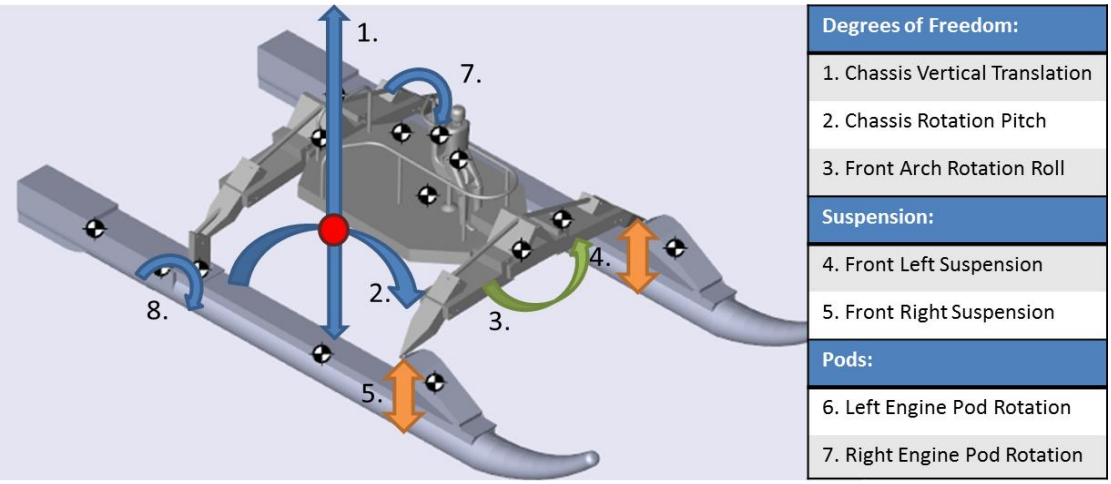

Figure 11.4 6-post testing rig model total degrees of freedom

The constraint method is functionally similar to how the WAM-V is constrained on the 2-post rig. The rear posts of the 2-post rig are stationary, and the cradles (which hold the pontoons) pivot on the rear posts as the front actuators articulate. Similar constraints will help to correlate the data from the 2-post rig with the simulations from the 6-post model.

11.2.3.1 Engine Pod Limit Strap Constraint

For the 6-post model to articulate correctly with actuators under the rear of the pontoons and the under the engine pods, the limit straps on the engine pods need to be removed in the model. On the 33-ft WAM-V, the engine pods are limited in rotation from to +5 to -15 degrees. Since the actuators in the model apply inputs directly to the pods and the rear pontoons, no extra constraint is necessary; otherwise the model would be over defined for certain inputs. With this in mind, inputs should be evaluated to avoid simulations outside the limitations of the WAM-V. In Section 11.5, the limit straps are modeled as part of the CFD code.

11.2.4 Model Output Data

The 6-post model is capable of outputting data from all the sensor locations from the on-water testing and 2-post testing setups detailed in Section 6.4 and Section 10.4.6, respectively. A number of additional sensors are also incorporated in the model which are not present on the WAM-V. Global position sensors record the motion of the payload tray, rotational sensors measure the rotation of the spherical joints, and accelerometers are mounted at different positions along different axes of measurement. An example sensor is an accelerometer located at the model's overall center of gravity; the center of gravity location is marked in Figure 11.2. This location would be difficult to mount an actual sensor on the 33-ft WAM-V, especially given that the WAM-V needs to fold and unfold.

The 6-post model is also equipped with a visualization package that runs through Simulink to provide qualitative comparisons of the simulation outputs. A screenshot of the visualization package is shown in Figure 11.5 for the 6-post model running a six component warp signal input.

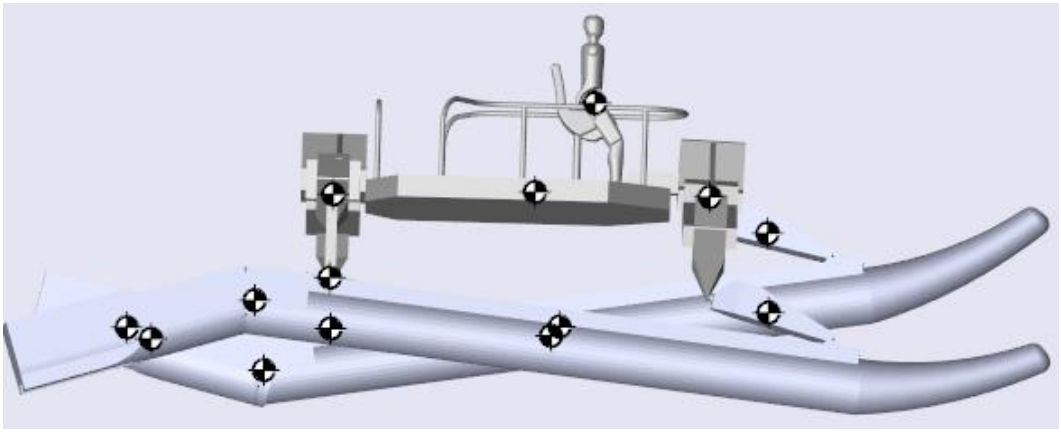

Figure 11.5 6-post model visualization (six component warp input shown)

11.3 Comparison of 6-Post Virtual Model and 2-post Testing Rig Data

In this section, the 6-post model will be compared with the 2-post testing data from Section 10.7, where the longitudinal stiffening brace was installed on the 33-ft WAM-V and tested with the second generation suspension system at different damper settings. A separate comparison of the 2-post rig without the longitudinal stiffening brace installed is detailed in Section 11.4. For the comparisons in this section, the adjustable dampers were set to their middle setting.

11.3.1 Acceleration Comparison

Figure 11.6 shows a comparison between the accelerometer data from the sensor located at the front of the payload tray on the 2-post test rig and for the same sensor in the model. Comparisons are shown for the longitudinal and vertical directions.

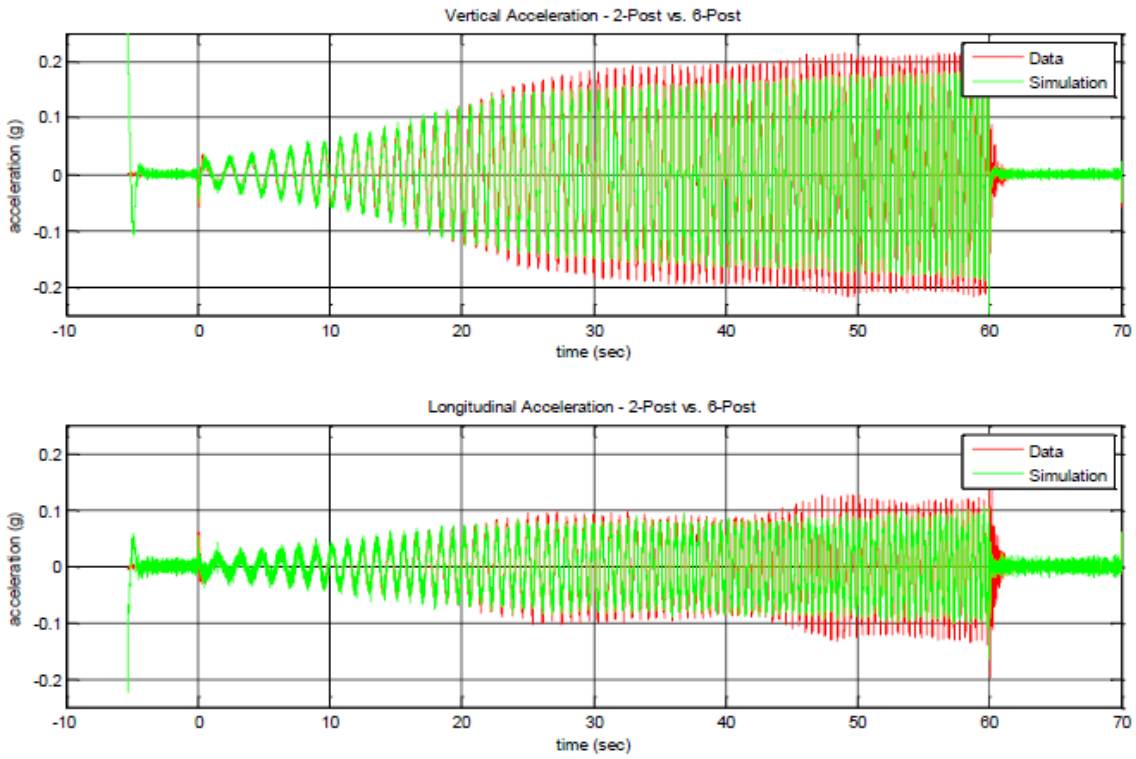

Figure 11.6 Payload accelerometer comparison

The simulations shows slightly lower acceleration levels in the vertical and longitudinal directions than does the testing data; however, the ratio of the peaks throughout the test is consistent. It is possible that there might be some high frequency content recorded in the test data due to localized structural vibrations and high frequency inputs from the control of the actuators that would not be present in the simulations; therefore the data and the simulation were both run

through a 20 Hz, fifth-order Butterworth filter and the results were compared. A 20 Hz cutoff frequency was chosen because the 2-post actuators are known from previous testing with other vehicles to exhibit frequency content at ~30 Hz. A comparison of the filtered test data with the filtered simulation data is shown in Figure 11.7. Dotted lines were also added to the acceleration peaks in Figure 11.7 to make the trends easier to view; dotted lines over the peaks of the data will be shown for the rest of the plots as well to better highlight the results.

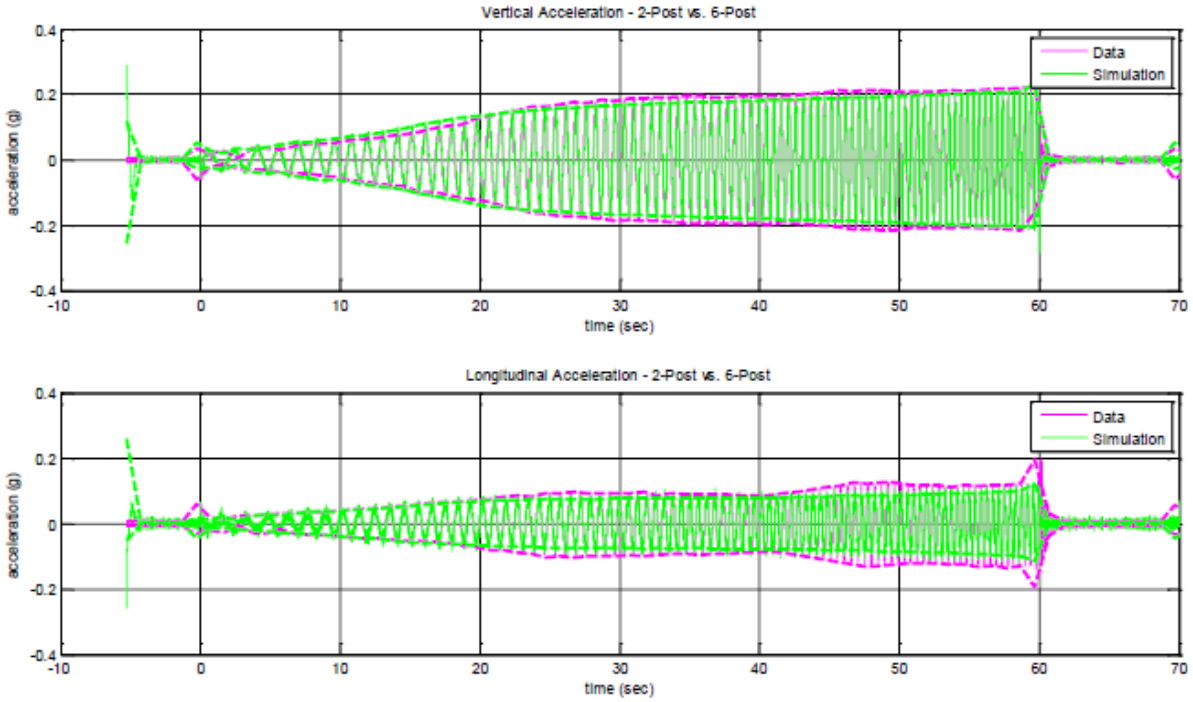

Figure 11.7 Filtered payload accelerometer comparison

Running the data and simulations through a filter improves their correlation. The acceleration levels in the data still slightly exceed the model; however, this is to be expected because the WAM-V has additional sources of friction and compliance not present in the 6-post model.

11.3.1.1 Suspension Comparison

Figure 11.8 shows a comparison of the suspension motion between the model and the 2-post rig for the starboard suspension system. The data and the simulation show good correlation; however, the simulation shows greater motion at the lower frequencies of the chirp signal and reduced motion at the higher frequencies when compared to the test data. Like the acceleration data, this could be explained by coulomb friction in the suspension affecting the results at low frequencies. At higher frequencies, the results either indicate the model is overdamped or

oversprung compared to the test data. It is difficult to determine whether either is true because the system doesn't appear to hit a resonant frequency during the test. The resonant points might become more apparent if the chirp signal was run for a longer time, or if tests were run at discrete frequencies.

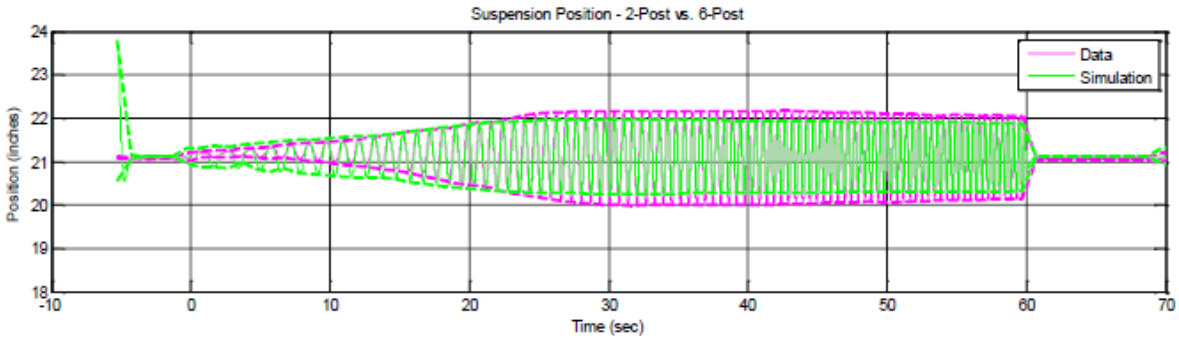

Figure 11.8 Suspension motion comparison

Another possible explanation for the change in suspension motion could have come from the addition of the longitudinal stiffening brace, which was shown in Section 10.7.4 to have an effect on the weight distribution of the payload tray between the front and rear arches. The longitudinal stiffening brace pulls the payload tray rearward, so there is less mass acting on the suspension system, leading to less motion as well.

11.3.1.2 Rear Arch Motion Comparison

Figure 11.9 shows a comparison of the motion of the rear arch for the 6-post model and the testing results. The results are fairly consistent for the different frequencies of the chirp signal, any differences are very small; however, the simulation shows slightly greater motion for low frequencies and lower motion at high frequencies. This could be explained by the same contributing factors as the suspension motion data.

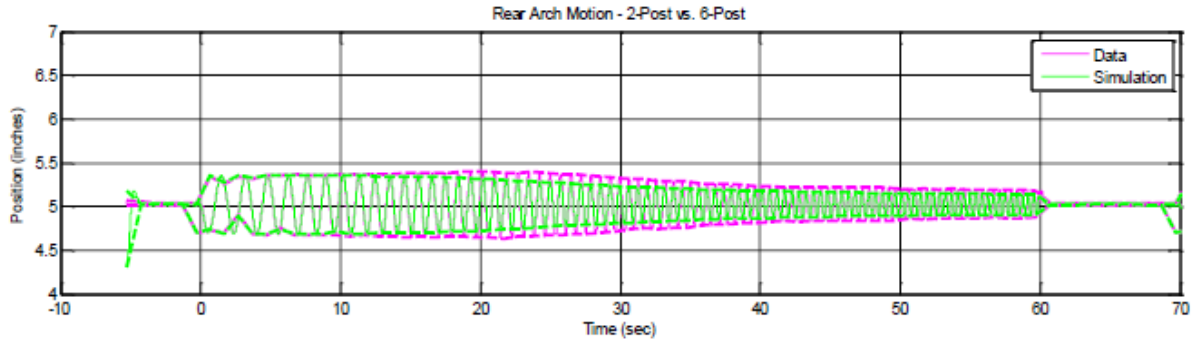

Figure 11.9 Rear arch longitudinal motion comparison

11.4 6-Post Modeling of 33-ft WAM-V Rear Arch Compliance

For the WAM-V testing performed on the 2-post rig, the compliance in the rear arch was shown to have a noticeable effect on the data. The longitudinal data changed dramatically in Section 10.7 when longitudinal stiffening braces were installed between the rear arch and the payload tray. In this chapter, the testing order is reversed compared to the 2-post rig testing; a 6-psot model with a rigid rear arch structure was compared with the 2-post test data collected with the longitudinal stiffening braces installed in Section 11.3. In this section, the 6-post model will be compared to the 2-post rig data with the longitudinal stiffening braces removed, which represents the on-water testing configuration. Prior to the comparisons, the 6-post model will need to be reconfigured to include a mechanism for incorporating the properties of the rear arch compliance into the simulations.

11.4.1 Linear Compliance Model Design

The compliance in the WAM-V's rear arch is due to the additional joints required for its folding mechanism to operate; the compliance is primarily due to deadband in the joints rather than insufficient material stiffness. To incorporate a degree of freedom to represent the compliance in the model, the weld joint between the rear arch and the payload tray shown in Figure 11.1 was replaced by a linear prismatic joint, separating the two masses and giving the chassis a fifth degree of freedom. For the initial compliance model, the compliance in the rear arch would be modeled by a linear spring and damper. The change in the block diagram model to provide a linearized representation of the rear arch compliance is shown in Figure 11.10.

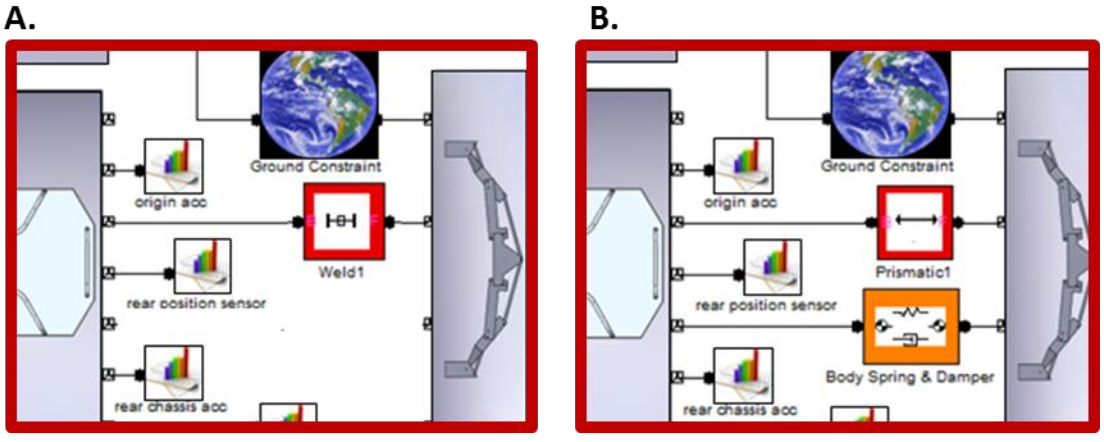

Figure 11.10 Additional blocks in the 6-post model to model the rear arch compliance

The properties of the linearized compliance model are most likely a major departure from the actual compliance mechanism in the WAM-V's rear arch. The rear arch is modeled as single lumped mass; however, the model is significantly different than the lumped mass approximations often used to linearize continuous deflections in beam elements as single degree of freedom systems. In those systems the mass of the beam is approximated as part of the overall lumped mass. For the linearized compliance model, the distribution of mass between the payload tray and the rear arch was unaltered. On the actual WAM-V, the oscillating mass of the rear arch would likely be split between the rear arch and the rear of the payload tray, with the majority of the mass on the payload tray due to the weight of the hydraulic actuator assemblies.

For the linear compliance model, the spring stiffness of the rear arch is modeled as linear; in reality the stiffness of the rear arch is likely very low through small displacements due to the deadband in the joints of the rear arch folding mechanism, and then the stiffness is very high once the joints are pushed to the ends of their deadband travel. The damping is modeled as viscous damping acting on a linear prismatic joint; damping in the WAM-V's rear arch can be attributed primarily to small amounts of coulomb friction in each of the individual joints. Future iterations of the 6-post model may be expanded to include nonlinearities in modeling the joint's compliance mechanism. The following section details the properties of the linearized system and provides comparisons between the modified 6-post model and the test data from the 2-post rig.

11.4.2 Compliance Model Coefficients

The spring stiffness and damping for the linearized compliance were determined by manually fitting coefficients to the model and comparing the results with the 2-post data. A method was also trialed by setting a cost function to each of the acceleration outputs and optimizing the model using the Simulink Design Optimization Toolbox. The following section will show comparisons for the 6-post model using the manually fitted model coefficients. Table 11.1 lists the coefficients chosen for the linear arch compliance model parameters.

Table 11.1 Linear rear arch compliance model coefficients

Rear Arch Parameter:	Model Value:
Spring Stiffness	60,000 N/m
Damping Constant	500 $N/\frac{m}{s}$

11.4.3 Linear Compliance Model Data Comparison

With a design for the linear compliance model incorporated into the 6-post model and values for the coefficients determined, the 6-post model can be compared with the data from the 2-post rig for the tests detailed in Section 10.6 without the longitudinal stiffening brace installed.

11.4.3.1 Acceleration Data Comparison

Figure 11.11 shows a comparison of the vertical and longitudinal accelerations at the accelerometer on the payload tray, near the operator's position for the 2-post rig tests compared with the 6-post model for the middle damping setting. Both sets of data have been run through a fifth order, low pass Butterworth filter with a cutoff frequency of 20 Hz.

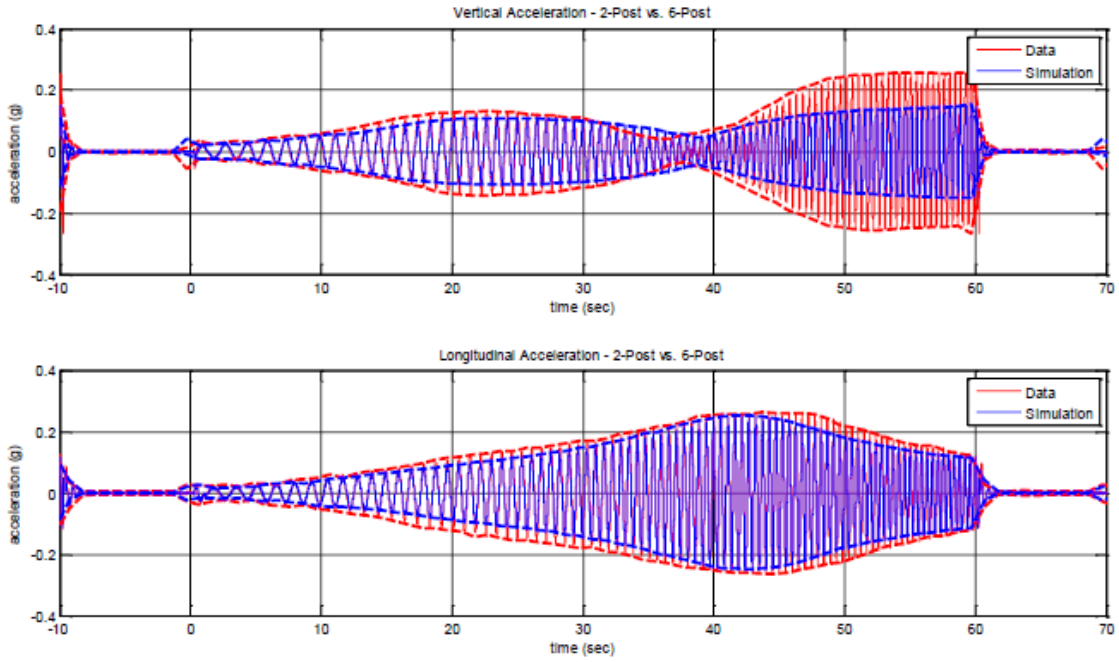

Figure 11.11 Linear compliance model vertical and longitudinal payload acceleration comparisons

The data in Figure 11.11 shows similar trends to the simulations. The data and the simulations both show very different results compared to the plots in Figure 11.6, which were tested and simulated with the longitudinal stiffening brace installed. The vertical acceleration data and simulations both show a similar node in the accelerations at approximately 37 seconds into the tests. The low frequency vertical acceleration data shows good correlation, while the simulation under-predicts the amplitudes of the higher frequency data. For the longitudinal accelerations, the data and simulation correlate well; the simulation slightly under-predicts the acceleration levels in a similar manner to the simulations with the longitudinal stiffening brace installed.

11.4.3.2 Suspension Motion Comparison

Figure 11.12 shows a comparison of suspension motion for the 2-post rig tests without the longitudinal stiffening brace installed compared with the 6-post model for the middle damping setting with the linearized model of the rear arch compliance.

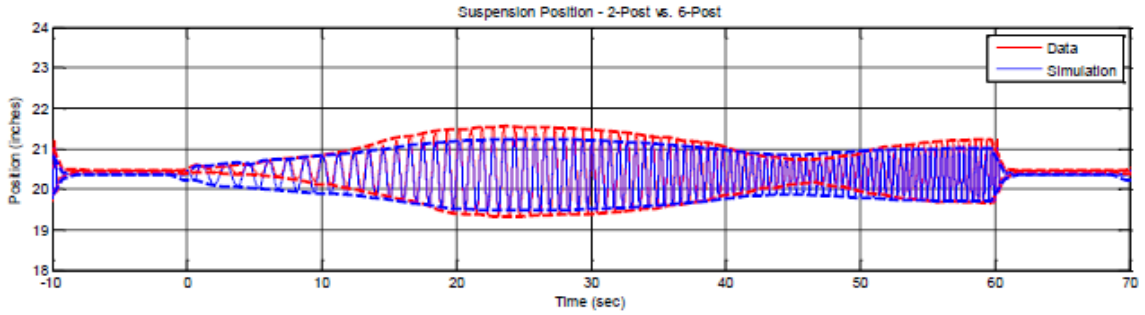

Figure 11.12 Rear arch compliance model suspension motion comparison

The motion of the suspension system in the simulation is slightly greater than the motion of the suspension system in the test data throughout the test. The attenuation is also greater in the data than the model for the node at ~45 seconds into the test. The plots show consistent correlation; it is likely that differences can be attributed to extra friction in the joints not present in the model.

11.4.4 Longitudinal Motion Comparison

Figure 11.13 shows a comparison of longitudinal motion of the rear arch for the 2-post rig tests compared with the 6-post model, measured by the longitudinal string potentiometer.

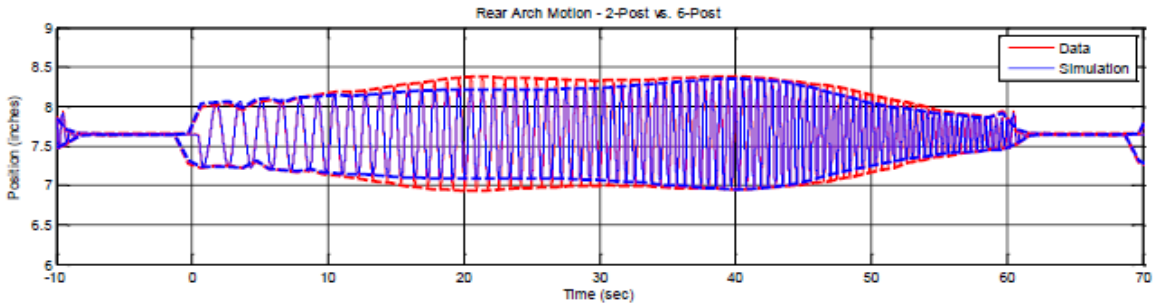

Figure 11.13 Linear compliance model rear arch longitudinal motion comparison

The results from the comparison of the compliance in the rear arch show good correlation, despite a linearized model being used. The data shows slightly more motion than the simulations, except at ~40 seconds into the data when the linearized system appears to resonate. For future simulations, it is recommended that the 6-post model with the longitudinal stiffening brace be used; however, for comparison with previous on-water tests the linearized compliance model should be implemented.

11.5 Coupling of Multi-Body Dynamics and Computation Fluid Dynamics codes

A collaboration to develop advanced simulation tools for the 33-ft WAM-V has begun as a joint effort between the Center for Vehicle Systems and Safety (CVeSS) at Virginia Tech and IIHR-Hydroscience & Engineering (IIHR) at the University of Iowa. The project will bring together the hydrodynamic modeling research at the University of Iowa using Computational Fluid Dynamics (CFD) and the Multi-Body Dynamics (MBD) research at Virginia Tech to create a CFD and MBD coupled code for evaluating the 33-ft WAM-V. The methodology and analysis involved in coupling the two codes is the subject of the remainder of this chapter, which covers the initial modeling and analysis from a one-way coupling between the two codes. A more advanced, two-way coupling of the codes is in progress and is discussed in the future work section.

11.5.1 Background on IIHR and CFDSHIP-Iowa

Researchers at the University of Iowa have developed a computer code for simulating the air and water flow around a virtual ship. CFDSHIP–IOWA is one of the most advanced computational fluid dynamics programs for ship hydrodynamics. The current version of the code (CFDSHIP – IOWA Version 4.5) uses a code developed for Unsteady Reynolds Averaged Navier-Stokes (URANS) equations. The code was previously validated against experimental tow tank data conducted with a scaled WAM-V prototype [77].

This section focuses on the research coupling the CFDSHIP-IOWA code with the 6-post virtual models of the 33-ft WAM-V. For further information on the inner workings of the CFDSHIP-IOWA code, the reader is directed to the publications below, full citations are listed in the references section.

1. “URANS Studies of WAM-V Multi-Body Dynamics in Calm Water and Waves” [77]
2. “Semi-Coupled Air/Water Immersed Boundary Approach for Curvilinear Dynamic Overset Grids with Application to Ship Hydrodynamics” [78]
3. “URANS Simulation and Validation of Added Resistance and Motions of the Modern Commercial Oil Carrier KVLCC2 with Fixed and Free Surge Conditions” [79]

11.5.2 Project Phases

Coupling the two codes is set out as a six-step process, and each process is documented in a separate subsection of this chapter:

1. The CFD and MBD models are synchronized with the properties of the 6-post model detailed in Section 6.6 and the exact hull and waterjet dimensions of the 33-ft WAM-V; the properties are nondimensionalized for use with the CFD code.
2. The CFD simulations are run for calm water conditions and validated against the calm water test data of the 33-ft WAM-V documented in Appendix B.
3. Wave inputs are created for the CFD model based on the on-water test data for the 33-ft WAM-V operating in Sea State 2 and Sea State 3 conditions, documented in Section 7.4.
4. CFD simulations are run for a rigid body model of the 33-ft WAM-V operating in regular waves with hinged engine pods. The CFD code outputs vertical and angular positions, velocities, and accelerations, as well as force and moment data at the center of gravity of the nondimensional WAM-V.
5. The outputs from the CFD code are dimensionalized and coordinate transforms are used to convert the data at the center of gravity into vertical inputs under the WAM-V's pontoons. The data is used as inputs to the 6-post model.
6. The results from the 6-post model are analyzed and the output forces at the actuators are compared with the forces and moments from the CFD simulations to analyze the suspension's impact on the force and moment data.

In addition to the six steps listed for the one-way coupling, two additional steps are necessary if the CFD simulations are to be compared with data from the 2-post rig. The CFD output data needs to be converted into input data that can be run on the 2-post rig. This requires the additional scaling of the data to fit within the limits of the 2-post rig (running the data for the front actuators only) and running the 6-post model for the scaled displacements to compare the results between the 6-post model and the 2-post data.

The initial six steps represent a one-way coupling of the CFD and MBD codes. A future step in the project will include a full two-way coupling of the codes, passing data between the codes at each time step of the simulation.

11.5.3 Simulation Properties

The initial model run in the CFD simulations had the same component properties as the 6-post model, except for non-functioning front suspension systems and a rigid front arch; making the pontoons, arches, and payload tray effectively one rigid body. The simulation conditions are collaboratively set up to match the on-water test conditions including the weights, centers of gravity, and radii of gyration of the major components; as well as the hinge axis for hinged pods, the jet nozzle locations and angles, and the hydrostatic sinkage, trim, and pod rotations. The engine pods are able to move through +5 to -15 degrees of travel in the CFD simulations.

Three types of modeling constraints were trialed:

- Model towed from the center of gravity, fixed engine pods.
- Model towed from the center of gravity, hinged engine pods.
- Thrust model, the location of the WAM-V's jet propulsion units.

11.5.4 Calm Water Validation

For the initial validation of the CFD simulations, the approach is to build upon previous WAM-V model testing conducted at the United States Naval Academy [80], while implementing a jet force model into the CFD code to be validated against on-water testing data of the 33-ft WAM-V. The calm water CFD results are validated against calm water testing measurements of the hinged pod angles. The calm water data taken on the 33-ft WAM-V does not contain some of the information required for validating the CFD code. Ideally, global angles of the WAM-V's pontoons and engine pods would be available for a number of different Froude numbers. On the 33-ft WAM-V, only the relative engine pod angle is measured in the data acquisition unit. Global angles can be estimated from a combination of video and sensor data; the estimation for the global angles and data for the relative pod angles are listed in Table 11.2.

Table 11.2 Calm water data to validate CFD simulations

WAM-V Speed (MPH):	Froude Number (Fr):	Estimated Absolute Pod Angle (Deg):	Estimated Relative Pod Angle (Deg):	Measured Engine Pod angle (Deg):
1	1.5	0	-1.5	-
6	2	2.5	0.5	1.3
17	1	5	4	4
23	0.5	6	5.5	5
23	0.5	5.5	5	4.5

Figure 11.14 shows a comparison of the coefficient of total resistance (ct, shown in plot a), sinkage (b), trim (c), and relative engine pod angles (d) for the calm water CFD simulations for each of the different model configurations. All of the plots are shown compared with the tow tank results from the scaled WAM-V prototype [80]. Figure 11.14(d) also shows the relative pod angle of the 33-ft WAM-V as measured in the calm water testing in Appendix B.

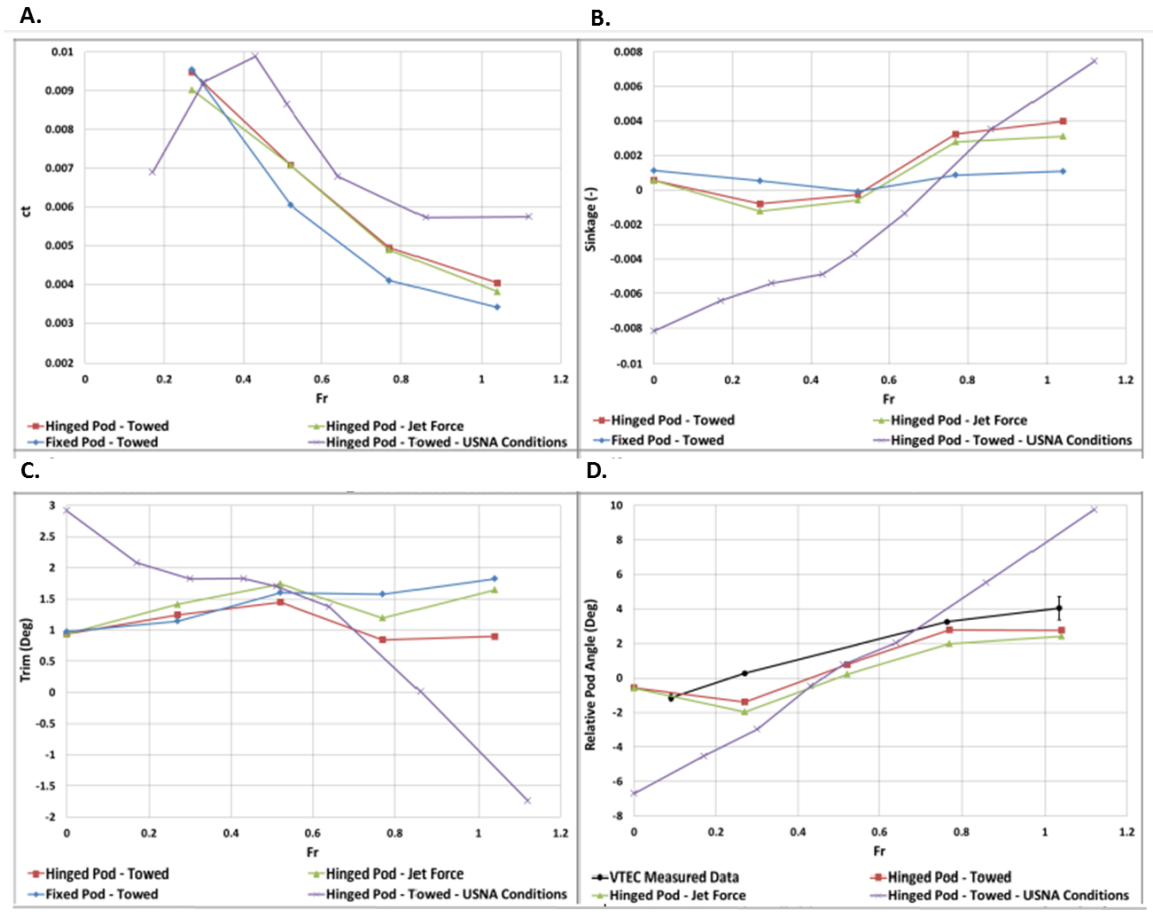

Figure 11.14 Calm water CFD simulation results (accompanying analysis from CFD perspective in [81])

The simulations in Figure 11.14(d) show a good correlation for the slopes of the relative pod angles between the simulations and the on-water test data. The absolute angles are not exact; the on-water data generally shows less angle throughout the tests. However, the trends are similar enough for the model to be considered valid for simulating the WAM-V's engine pods in a sea state. Other validations also were carried out for the WAM-V using fixed pod angles to validate the remainder of the code [77]. The CFD visualization results for the models with hinged engine pods towed from the center of gravity and the jet force model are shown in Figure 11.15.

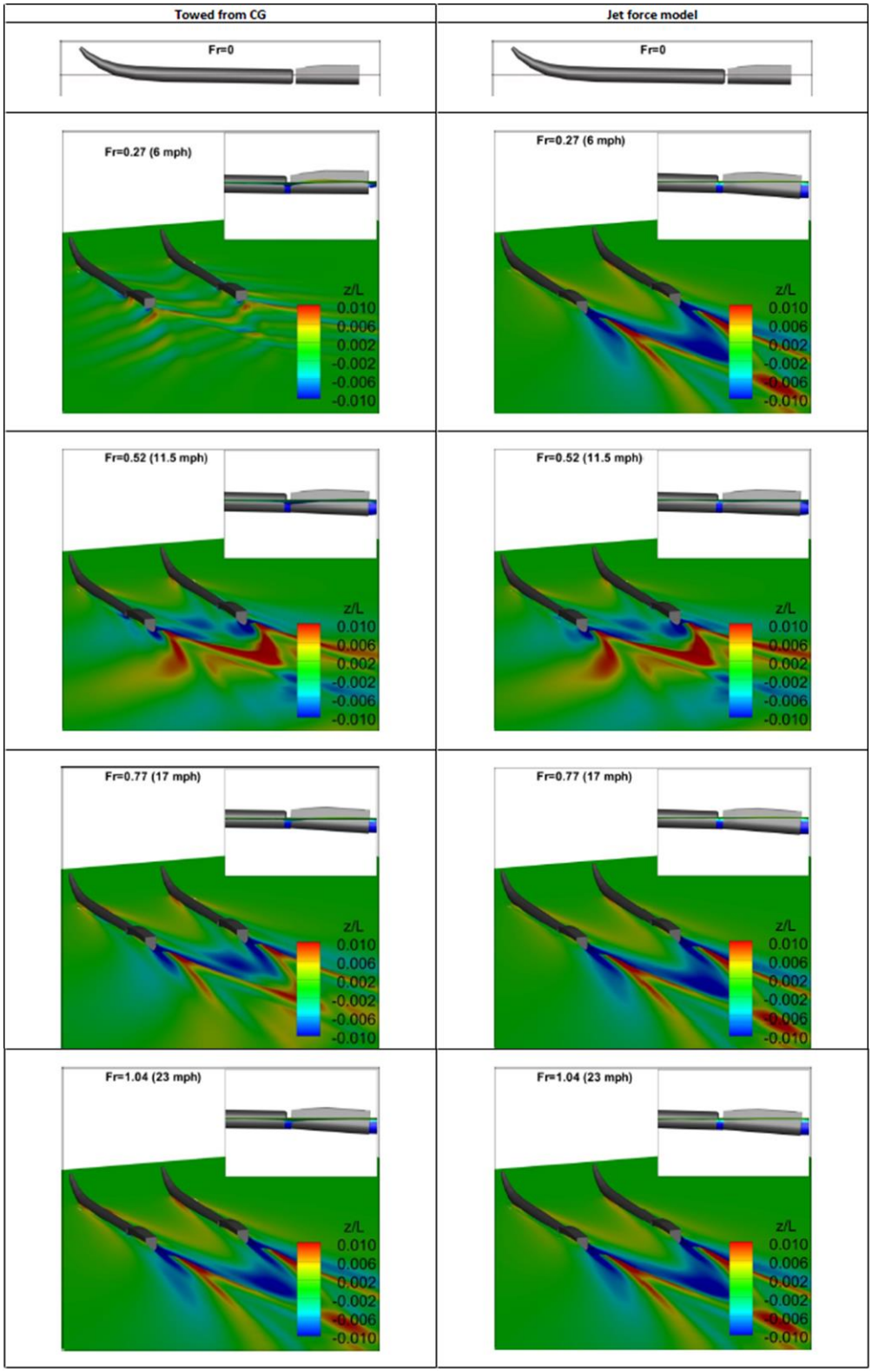

Figure 11.15 Free surface and hull motions for calm water simulations with jet force model and towed conditions (accompanying analysis from CFD perspective in [81])

11.5.5 Converting CFD Outputs to Run in 6-Post Model

To use the CFD results with the 6-post model, the outputs from the CFD need to be dimensioned to the 33-ft WAM-V and then coordinate transforms can be used to convert the data. Figure 11.16 shows the calculated vertical position, velocity, acceleration, and force (left column), as well as the angular position, velocity, acceleration, and torque (right column) for the 33-ft WAM-V operating at 10 knots in a simulated Sea State 3.

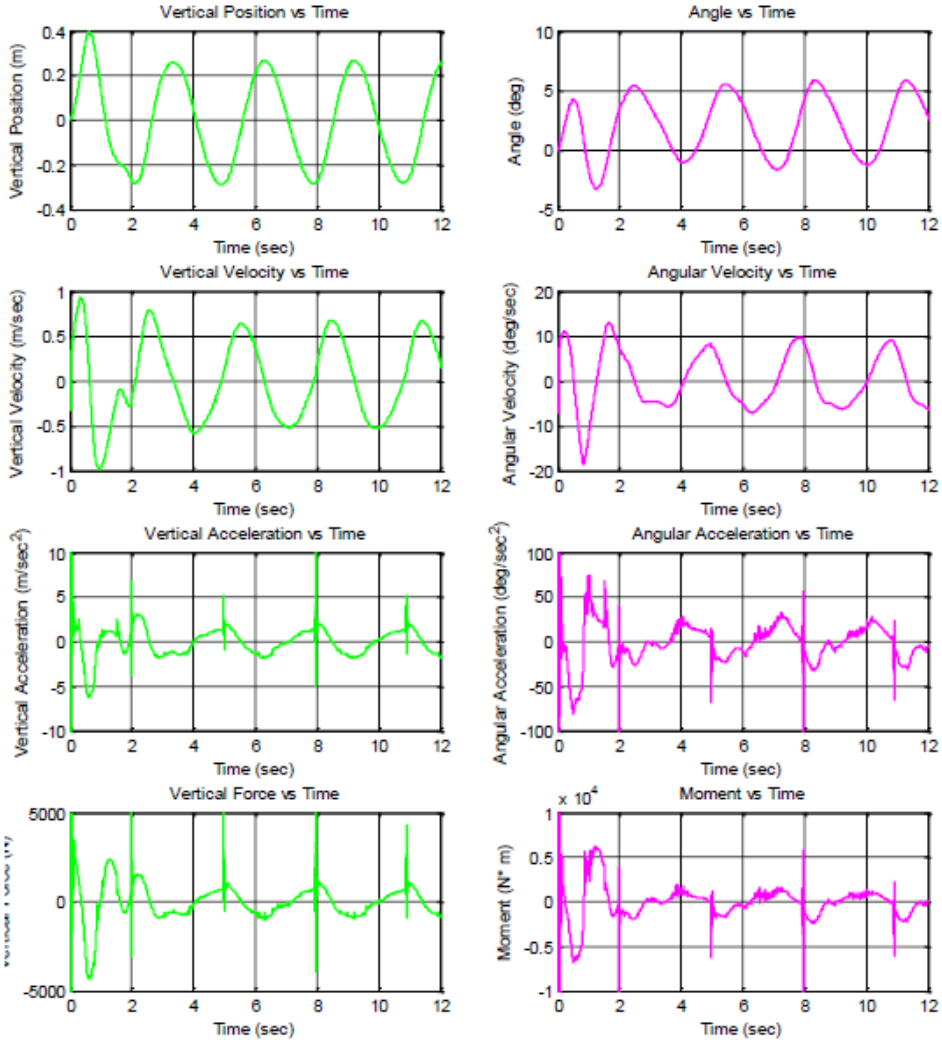

Figure 11.16 Dimensioned CFD output results at the model center of gravity

The sea state inputs were initially specified to the CFD code as 'regular' (sinusoidal) waves for Sea State 2 and Sea State 3 (shown in Figure 11.16) inputs. For a typical Sea State 3, wave height (H) / wave length (λ) value (H/λ) is 1/64, and the typical λ/L value is 3.72 (L is the overall length of the WAM-V, ~10 m). Running the CFD code at H/λ = 1/64, at a Froude number of 0.5

(corresponding to an operating speed of 10 knots for the WAM-V, matching the data in Section 7.4), produced the CFD displacement outputs for the WAM-V shown in Figure 11.17.

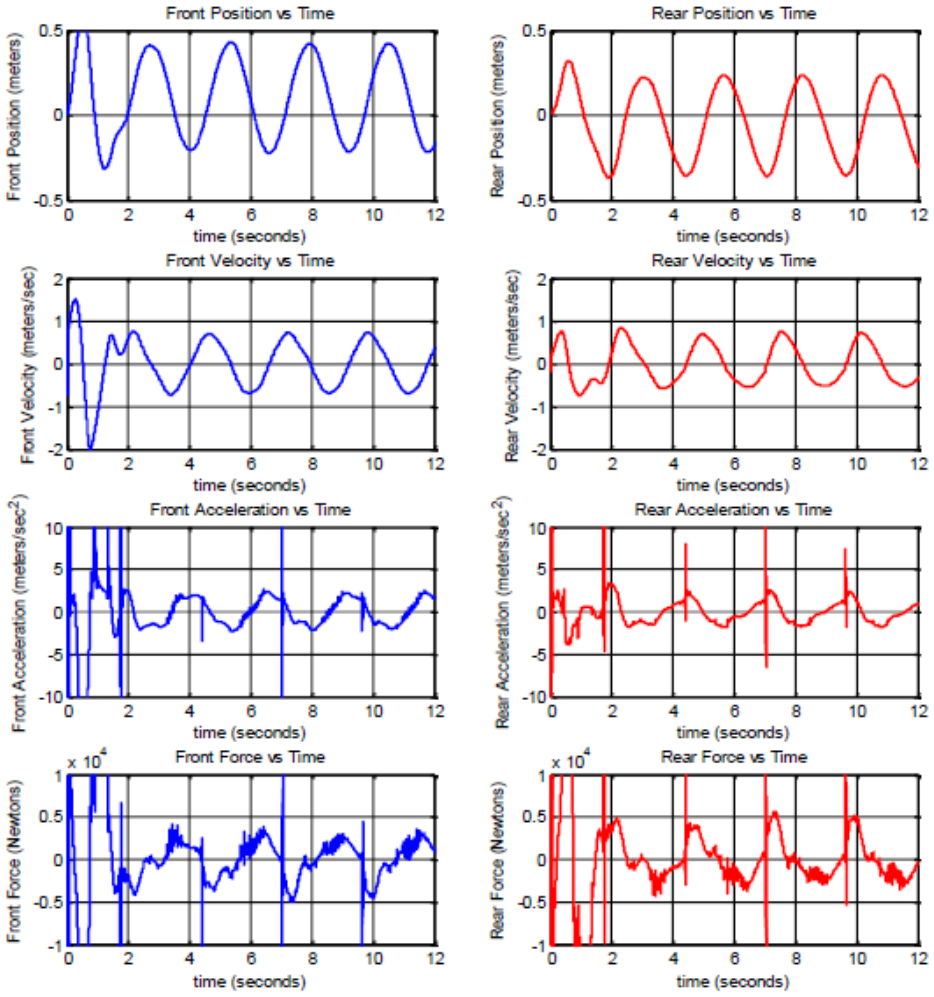

Figure 11.17 Front and rear inputs to 6-post model from CFD outputs

Looking at Figure 11.17, the rear inputs of the WAM-V are roughly equal in magnitude to the inputs at the front of the WAM-V. During on-water testing with the 33-ft WAM-V, the displacements at the front were 2-4 times greater than the displacements at the rear; during severe wave inputs, the actual WAM-V exhibits a pitching about the bottom of the rear arch. This is exemplified in the single-wave input analysis shown in Section 7.3, where the front of the pontoons come out of the water by an estimated 24 inches and the rear of the WAM-V only barely lifts out of the water as the WAM-V goes over the wave.

An explanation for the discrepancy in the ratio of the fore and aft inputs comes from the difference in the wavelength (λ) specified for the CFD simulations. The ratio of the λ/L of 3.72

indicates wavelengths 3.72 times greater than the overall length of the WAM-V. These values represent the waves that would be seen in open ocean, blue water conditions. Testing of the 33-ft WAM-V to this point has occurred exclusively in coastal, green water conditions. This makes for different λ/L values, which would lead to a change in the pitching motion of the WAM-V compared to the heave motion. The wave inputs are shown in Figure 11.16 to occur at a dominant frequency of 0.34 Hz. Shorter wavelengths will increase this frequency to a value closer to the conditions in Section 7.4. The H/λ = 1/64 corresponds to 0.6 meter wave heights, which is at the very extreme end of what has been tested on the water; however, on-water tests were run for smaller λ/L value waves.

11.5.6 Analysis of Sea State Data for Determining Wave Inputs

To determine more relevant wave input conditions for the CFD simulations, the data from the 33-ft WAM-V winter testing program was analyzed with a focus on the conditions in which the tests were conducted. The depth of the water around the test site was evaluated; Figure 11.18 shows a GPS trace of one leg of the testing, and the depth of the water versus position, based on nautical charts.

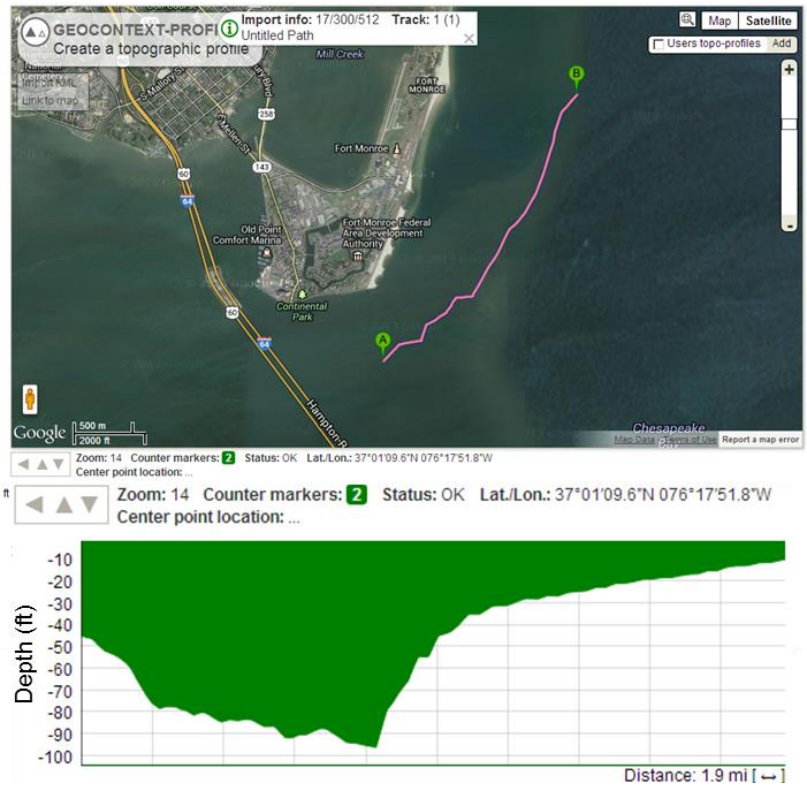

Figure 11.18 GPS trace of testing path and water depth during testing leg

Evaluating the depth trace shown in Figure 11.18, there is a section of the test that occurs at depths of 80-90 feet; however, the majority of the test is run in much shallower water depths ranging from 20-30 feet. The deeper section of the test occurred when the WAM-V crossed over the Chesapeake Bay Shipping Channel, where the ocean floor has been cut to accommodate the passage of large ships. The majority of the tests were run in close proximity to, but outside of, the shipping channel. Based on the depths shown, a depth of 26.4 feet was used to estimate a revised λ/L value for the green water CFD input parameters.

Statistical analysis of the sea trial data in waves was also conducted to provide an estimate of the dominant encounter frequency. During the testing leg shown in Figure 11.18, the dominant encounter frequency was found to occur at 0.73 Hz. The frequency was calculated by examining the time between peaks in the dataset, rather than using an FFT analysis. An FFT analysis was not performed due to the stochastic nature of the testing environment, which is better characterized as a series of discrete inputs occurring at semi-random intervals, rather than a sinusoidal input of a single frequency.

Figure 11.19 shows the revised CFD simulation results for the WAM-V in a shorter wavelength environment for the same Froude number and H/λ values. The wave profiles were specified based on the TMA shallow water spectrum using the significant wave height, wave modal frequency, and water depth as inputs to determine the wave profiles [82]. A λ/L value of 1.33 was calculated for the revised CFD input parameters. The results shown in Figure 11.19 are vertical forces and moments computed at the WAM-V's center of gravity, the four corner inputs results are shown in Figure 11.21.

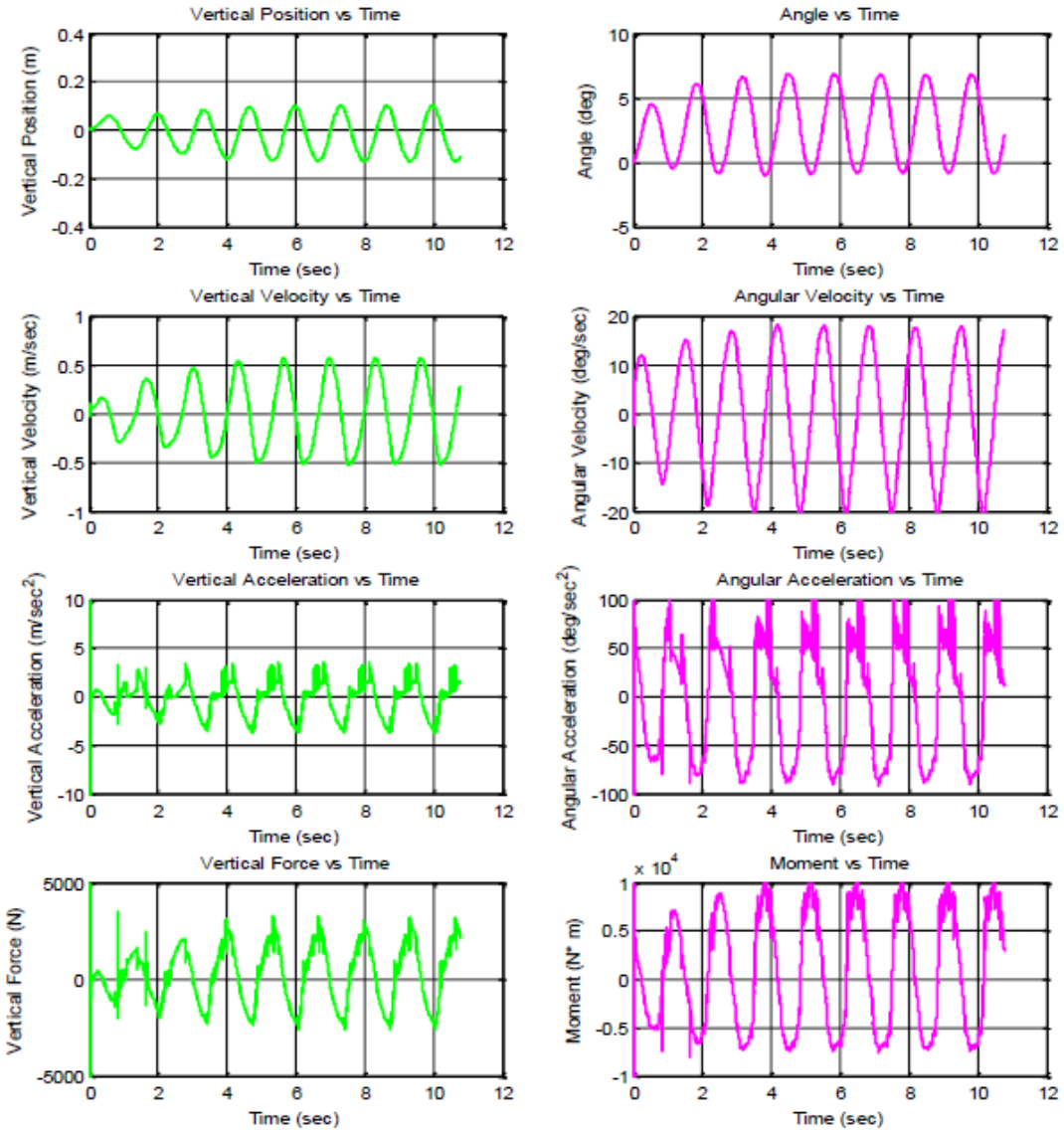

Figure 11.19 Shallow water CFD output results at the center of gravity

Compared to the CFD outputs shown in Figure 11.16, the outputs from the simulations in Figure 11.19 show higher frequencies in the position and angular data. The amplitude of the heave motion (vertical position) is reduced, and the amplitude of the pitch motion (angle) is roughly equivalent. For the velocity data, the vertical peaks are similar in magnitude; however, the angular peaks occur at more than double the magnitude than the blue water simulations. Similar trends occur in the acceleration and force/moment plots, with similar magnitudes in the vertical direction and increased magnitudes in the angular direction. Figure 11.20 shows the CFD visualization results for the shallow water CFD simulations.

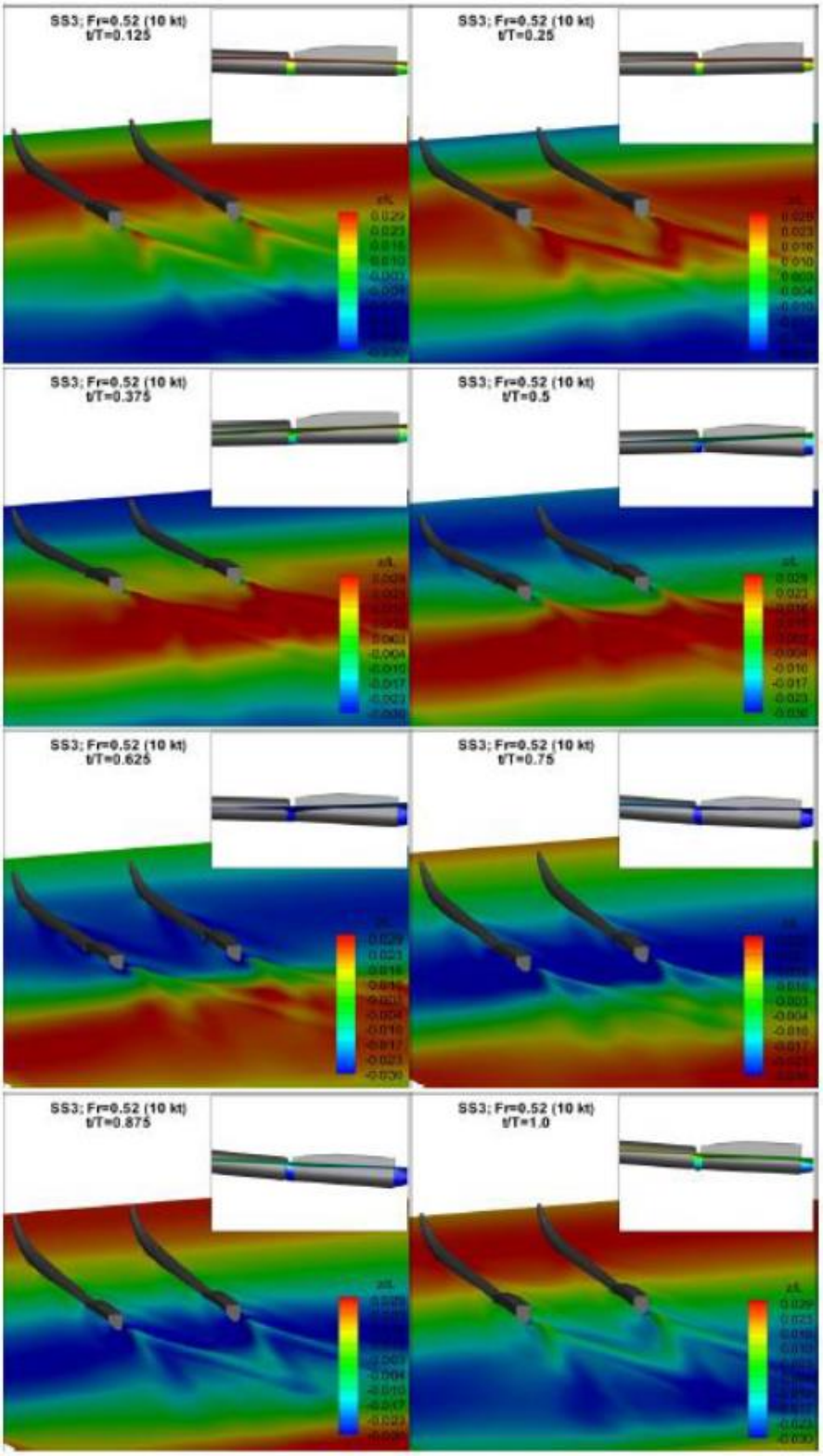

Figure 11.20 CFD results - free surface motions in a Sea State 3 (accompanying analysis from CFD perspective in [81])

11.5.7 Shallow Water CFD Output / MBD Input Analysis

Figure 11.21 shows the CFD output results converted to the vertical displacement inputs necessary to run on the 6-post model. Compared to the fore and aft inputs for blue water conditions shown in Figure 11.17, the values appear to be a much closer representation of the type of waves that were experienced during on-water testing. Figure 11.22 shows an overlaid comparison of the fore and aft pontoon input positions calculated from the CFD simulations.

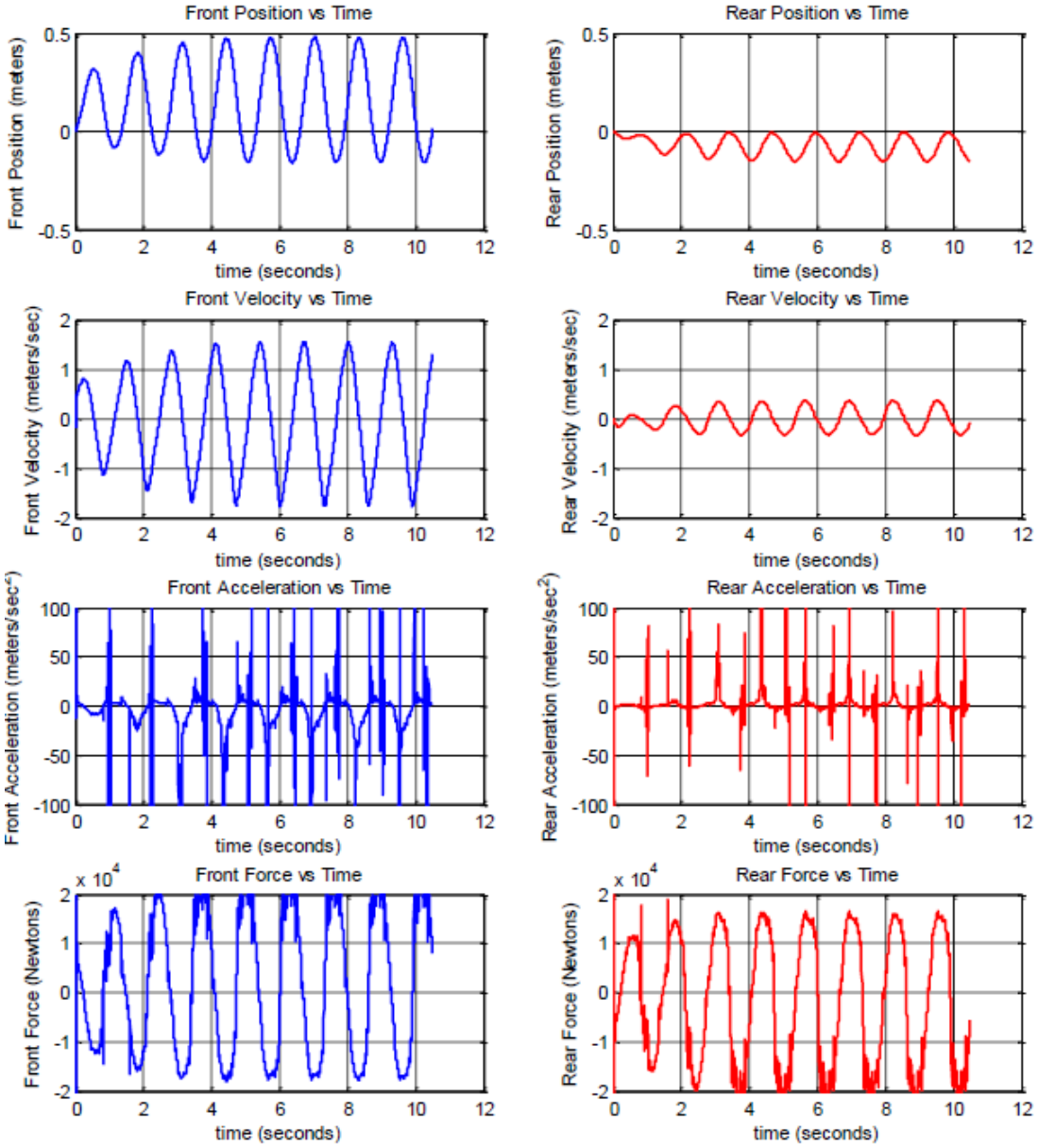

Figure 11.21 Shallow water front and rear inputs to 6-post model from CFD outputs

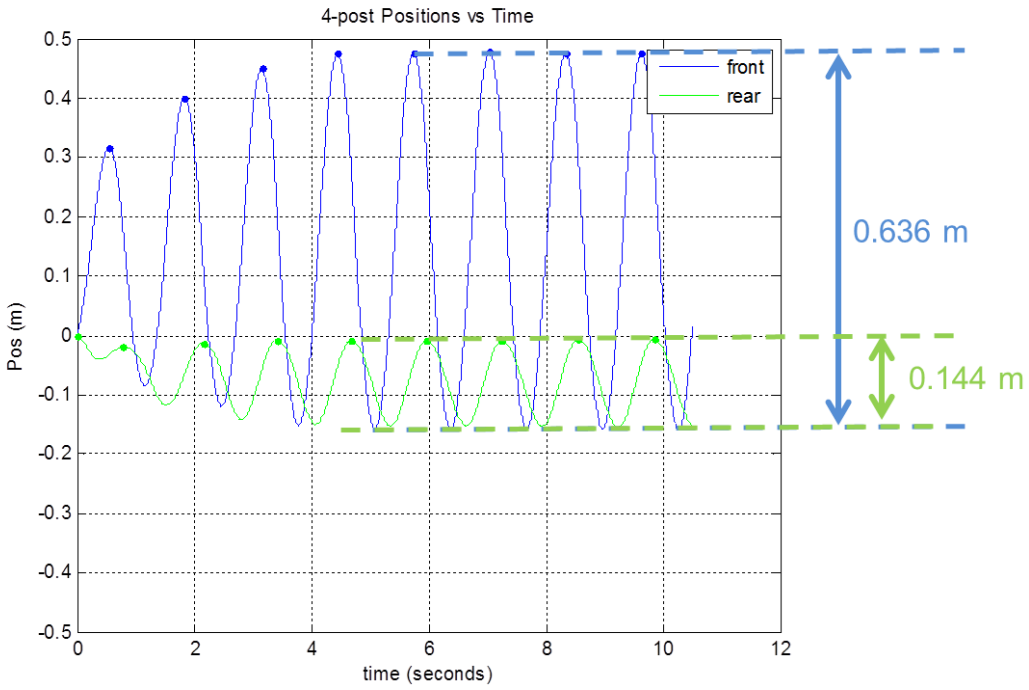

Figure 11.22 Comparison of front and rear displacement inputs

The comparisons of the displacement amplitudes in Figure 11.22 show displacement amplitudes of 0.636 meters at the front of the pontoons and 0.144 meters at the rear of the pontoons. This corresponds to an input displacement ratio of 4.4:1 front to rear. This is just outside the range observed during testing; however, since the inputs are also quite severe, it is plausible that this ratio is a good representation of the most extreme waves experienced during on-water testing. The front and rear input data is further analyzed in Table 11.3.

Table 11.3 Analysis of shallow water input peaks

Peak #	Time (front)	Time (rear)	Offset Time (sec, front-rear)	Phase (Deg, front leading rear)	Frequency Front (Hz):	Frequency Rear (Hz):
1	0.544	0.794	0.250	---	---	---
2	1.832	2.166	0.334	90.40	0.776	0.729
3	3.158	3.426	0.268	74.62	0.751	0.794
4	4.454	4.676	0.222	62.78	0.772	0.800
5	5.754	5.962	0.208	57.91	0.769	0.778
6	7.050	7.254	0.204	56.75	0.772	0.774
7	8.336	8.546	0.210	58.65	0.778	0.774
8	9.632	9.850	0.218	60.37	0.772	0.767

Based on the information listed, a mean time between peaks of 1.298 seconds was calculated for the CFD data. This corresponds to a dominant wave frequency of 0.77 Hz, which is very close to the 0.73 Hz wave period from on-water testing. The mean phase offset time between the front and rear inputs is 0.239 seconds, this gives a mean phase offset of 66.3 degrees (front inputs ahead of rear). The effects of different phase offsets on the simulation results were shown in Chapter 3 for the 100-ft WAM-V Proteus. Compared to the inputs tested for the Proteus, the data falls between the 0 degree and 90 offset pitch simulations conducted with 0 degrees roll phasing.

11.5.8 6-Post Simulation Analysis

With the CFD outputs converted, simulations with the 6-post model can be conducted using the calculated CFD displacements as inputs. The nature of the one-way coupling between the two codes makes the 6-post model effectively a hub-coupled simulation once the CFD code has been run, since changing the parameters of the MBD model does not affect the model inputs. This is one of the motivations for creating a two-way coupling between the two codes, as detailed in the future work section.

The simulations were run in two parts, each of which is discussed in this section. The two settings for the simulations correspond to the 33-ft WAM-V operating with and without a functioning suspension system. The primary purpose of running the 6-post model without a suspension system is to validate the successful transfer of the inputs between the CFD and the MBD codes. A secondary purpose of running two simulations is to analyze the suspension's impact on the vessel's performance by simulating the vessel as though the suspension system were not presented and the pontoons were rigidly connected to the superstructure.

Figure 11.23 shows a comparison between the results from the CFD output compared to the 6-post model with no suspension system using the CFD displacements as inputs. The results are shown for the longitudinal and vertical accelerations at the payload accelerometer. Longitudinal and vertical accelerations at the payload accelerometer were calculated from the CFD outputs by performing coordinate transforms on the rigid body. Acceleration outputs in the MBD model were recorded from sensor blocks at key locations.

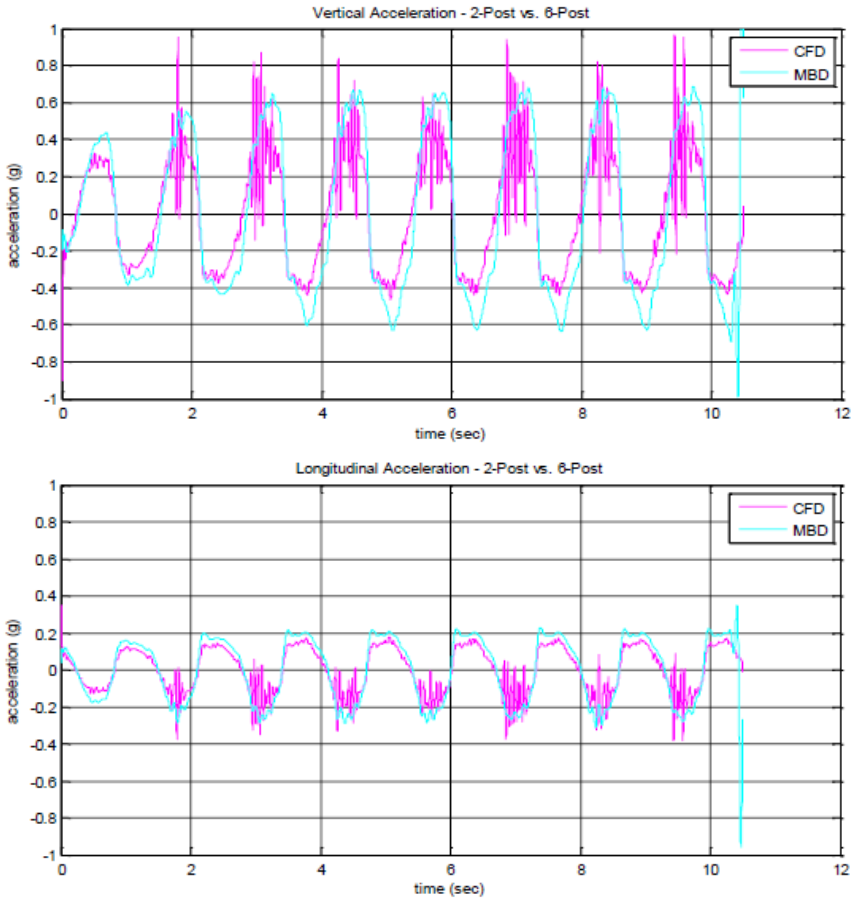

Figure 11.23 Rigid body comparison between CFD and 6-post model for shallow water inputs

The plots in Figure 11.23 show good correlation between the two codes. The MBD code applied to a rigid body seems to over-predict the acceleration values compared to the CFD results, but by a small percentage (<20%). The MBD code also seems to act as though it were a low-pass filter for the CFD output results; this could possibly be attributed to differences in the time steps that were used for the two simulations. The CFD simulations were run for a nondimensionalized time step proportional to the model's Froude scaling. For a vessel with the WAM-V's overall length, the sampling frequency is 394 Hz. The MBD code is run at 500 Hz to match the sampling frequency of the 33-ft WAM-V's data acquisition unit. A linear interpolation was used to convert the data between the two time steps; it is possible this had an effect on the high-frequency portions of the data. The small difference in the high-frequency data is unlikely to affect the results, particularly for the simulations with a functioning suspension system, which also acts like a low-pass filter. The affects will be most apparent when analyzing the results for the unsprung masses; this should be factored into any future analysis.

Figure 11.24 shows a comparison between the vertical and longitudinal acceleration outputs from the MBD code running the CFD shallow water inputs for two simulation scenarios. The first scenario is with a rigid suspension system. The second scenario is with the second generation suspension set to the middle damper setting. The middle damper setting was chosen to match the on-water testing data discussed in Section 7.4. It is also noteworthy that there is no suspension motion for the rigid simulations to compare with the suspended model.

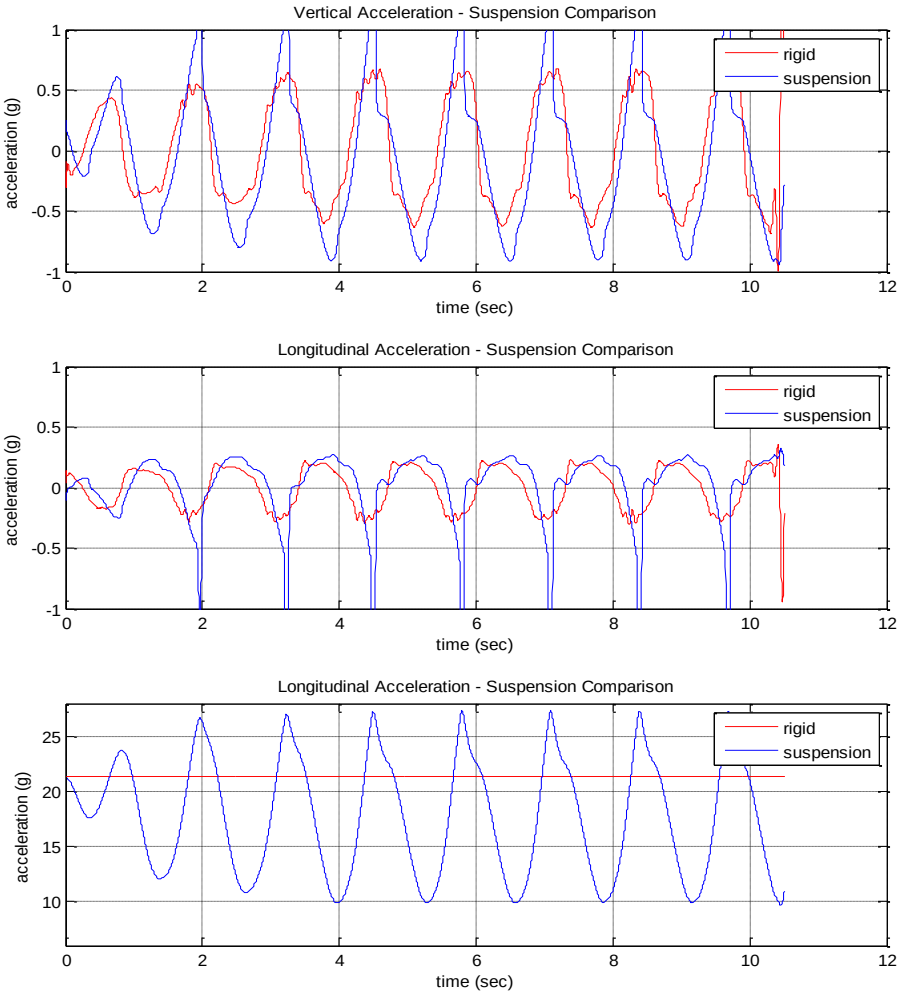

Figure 11.24 Suspension 6-post model data compared with rigid body data

The results in Figure 11.24 show diminished performance from the WAM-V with the suspension system compared to the rigid simulations. Analyzing the suspension plot, it is easy to determine the effect occurs because the suspension system has topped out on the limit straps. Interestingly, the suspension is not close to bottoming-out in compression in the simulations before it hits the limit straps in extension. The extension limit straps were never reached during on-water testing

with the second generation suspension system; although they were frequently engaged with the original suspension system which had less overall travel and a small percentage of its available travel in rebound.

To determine the effect of the suspension contacting the straps on the acceleration results, simulations were run with increased damping ratios. The maximum available damping setting was simulated (c_{crit} = 0.85); however, setting the dampers to their maximum setting was not enough to keep the suspension straps from engaging the limit straps. A damping ratio corresponding to two times the maximum available setting on the dampers was also simulated, corresponding to a damping ratio of 1.7; the results are shown in Figure 11.25.

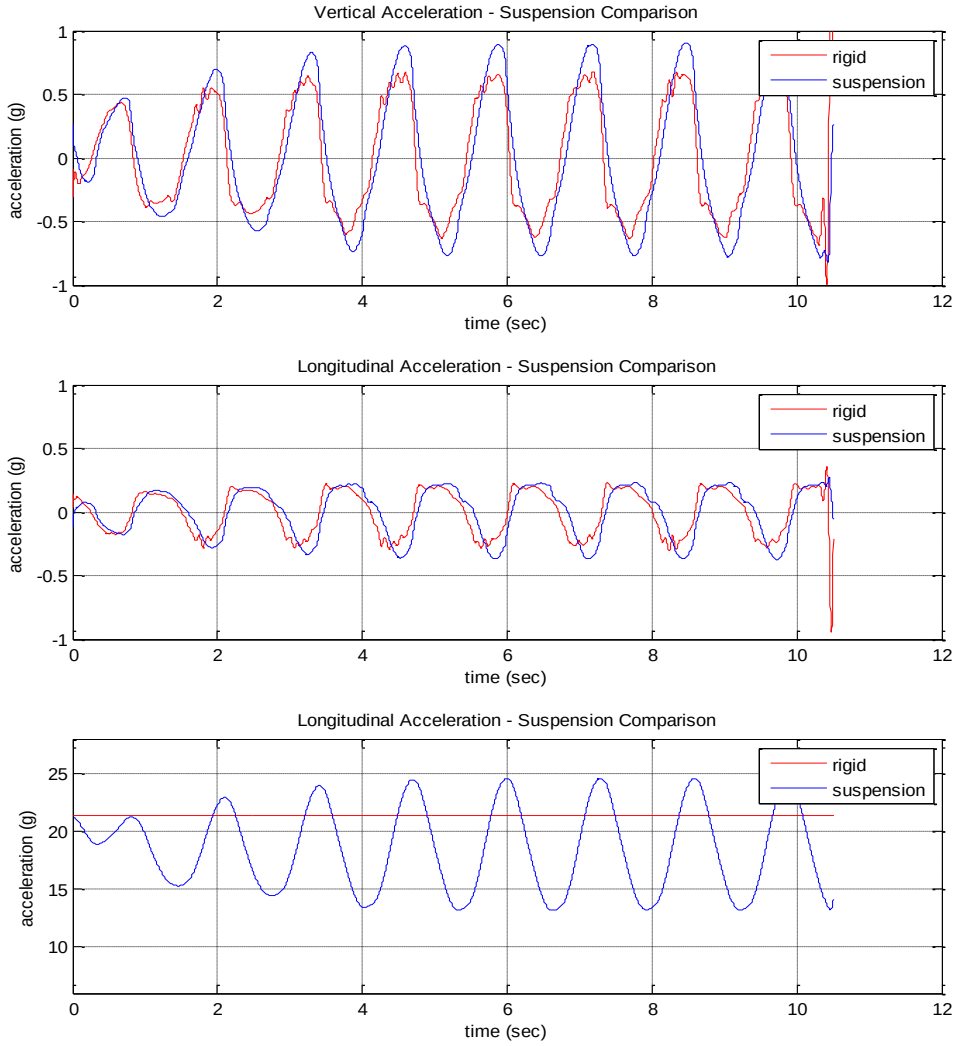

Figure 11.25 Shallow water simulation results at maximum damper setting

Setting the dampers to two times the maximum setting was found to be enough to keep the suspension straps from engaging the limit straps, as shown in the difference in the acceleration spikes between Figure 11.24 and Figure 11.25. Unfortunately, the suspension system still does not show improvements compared to the rigid body simulations. The suspension has an undamped natural frequency of ~0.8 Hz, which is very close to the 0.77 Hz wave period of the simulations. This is another reason why increased damping improved the simulation results, when the simulations were run near resonance. Despite the simulations being run so close to the suspension's natural frequency, there does not appear to be a cumulative effect or a beating effect to the displacement amplitudes over the eight peaks during the simulation. For the middle and maximum damper setting, this is explained by the suspension already reaching one of its limits; for data shown in Figure 11.25, it is likely the increased damping ratio (1.7 critical) mitigates any beating or cumulative effects. As with the simulations conducted in Chapters 3 and 4, changing the suspension design without adjusting the simulation inputs can have a misleading effect on the results. A future comparison between the results of the one-way coupling and two-way codes will determine just how important an effect this has on the overall simulation results.

11.5.9 2-Post Testing and Analysis with Scaled CFD Inputs

With the initial one-way coupling between the two codes complete, an experiment can be set up to test the inputs for the actual 33-ft WAM-V using the 2-post rig. For testing the inputs on the 2-post rig, the tests were run for three damper settings corresponding to the minimum, middle, and maximum available damper settings on the adjustable dampers, as detailed in Section 6.7. Since the effects of the both the dampers and the longitudinal stiffening brace were documented extensively, they are not repeated in this section. The comparisons will be shown for the middle damper setting with the longitudinal stiffening brace installed, to match the analysis in the previous section and the damper setting used during on-water test data.

11.5.9.1 2-Post Test Input Generation

The actuators on the 2-post rig have a 6 inch dynamic stroke limit, so the displacement inputs from the CFD simulations will have to be scaled to run on the rig. Also, since the rig has only two live actuators, the rear inputs will not be part of the test. As shown in Figure 11.22, the front inputs for the shallow water CFD simulations have a displacement magnitude of 0.636 meters (25.04 inches). Since the 2-post rig has a 6 inch dynamic stroke limit, the inputs are scaled by a

factor of 4.25 to fit within the stroke limitations with a small factor of safety. Also, the front input displacement is biased towards the positive (upward) direction, so the actuators must be moved downward prior to each test and raised up following the test. The scaled CFD data converted for testing on the 2-post rig is shown in Figure 11.26.

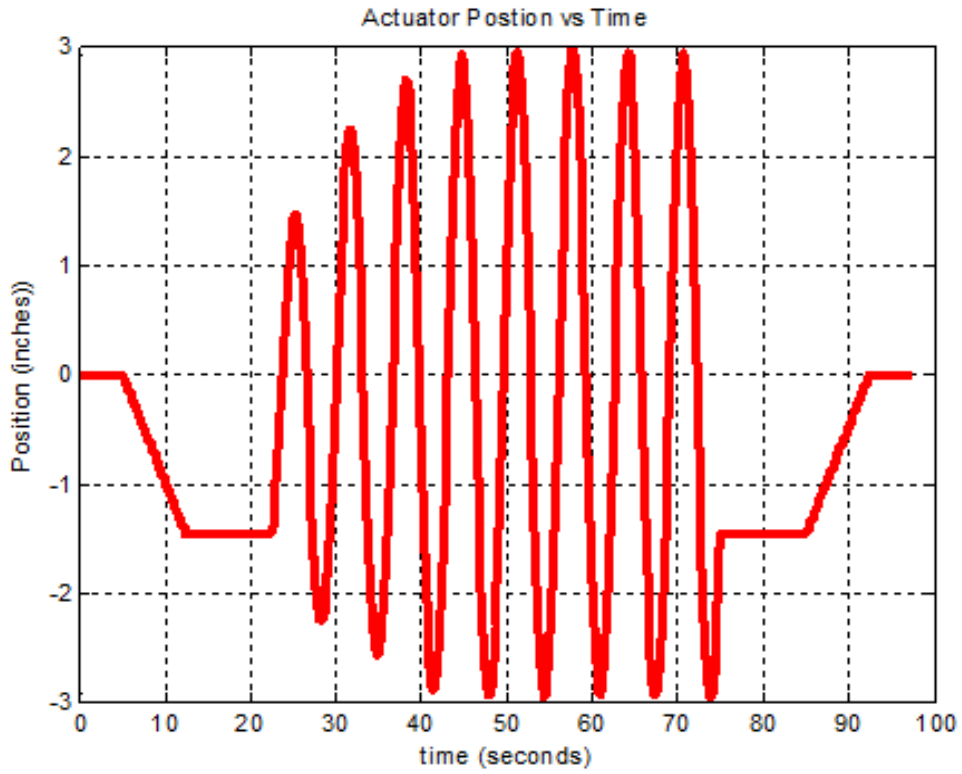

Figure 11.26 Scaled 2-post input displacements (4.25:1 scaling factor from CFD output)

The inputs shown in Figure 11.26 closely resemble a sine-wave input with a frequency of 0.77 Hz. For comparing the results of the scaled CFD data testing with the other tests conducted using the 2-post rig, the plots analyzed in Chapter 10 for the larger displacement tests contain very similar inputs in the data when the chirp signals are at approximately 8 seconds into each one minute test run. This is the point when the chirp signals pass through a frequency of 0.77 Hz.

11.5.9.2 Analysis of 2-Post and 6-Post Data Running Scaled CFD Inputs

Figure 11.27 shows plots comparing the vertical acceleration (a), longitudinal acceleration (b) and suspension motion (c) between the 2-post test rig and the 6-post model for the CFD shallow water inputs scaled to fit within the displacement limits of the 2-post rig, with no rear displacement inputs.

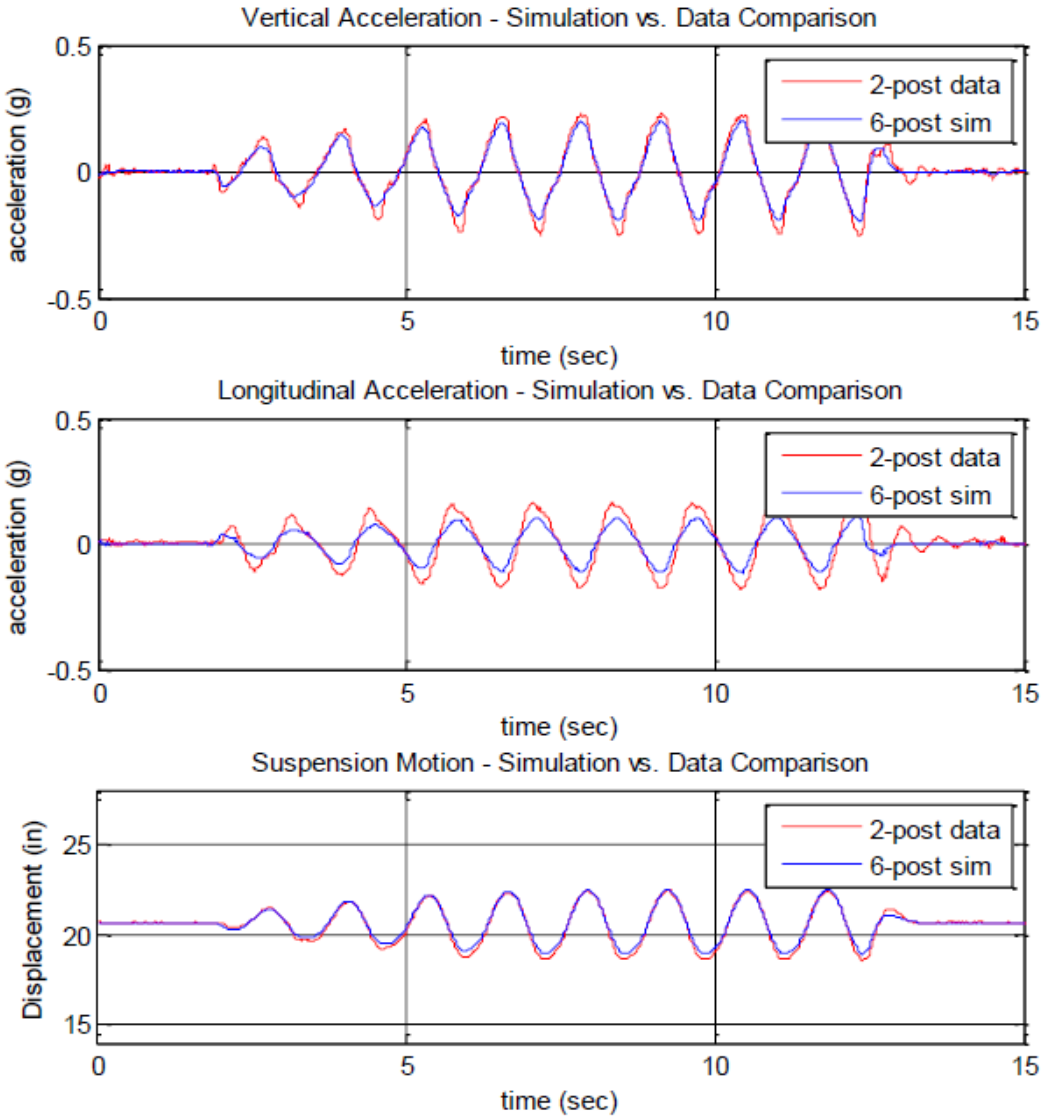

Figure 11.27 Comparison of 2-post and 6-post data for CFD shallow water inputs

The simulation seems to slightly underpredict the acceleration values in Figure 11.27 in a very similar way it did with the CFD input data shown in Figure 11.23. This is interesting because the 2-post testing data and the CFD simulations represent very different types of data to compare with the 2-post. The suspension position values correlate very well between the data and the simulation; the suspension uses very little of its travel compared to the simulations run for the CFD data run at full scale. As with the full scale data, no near resonant effects are observed in the data, despite the tests and the simulations being run close to the suspension's natural frequency.

11.6 Conclusions and Recommendations for Further Research

The 6-post model was able to be constructed using the 4-post model detailed in Chapter 4 as a blueprint. Like the 4-post model, the 6-post model was straightforward to validate, indicating that the modeling process is not sensitive to the size of the WAM-V being modeled. This is a good result, because the modeling methods are required to be applicable to future WAM-Vs of any size. The following section provides recommendations for improving the 6-post model, and opportunities for WAM-V future research based on the research documented in this chapter.

11.6.1 Recommendations for Improving the 6-Post Models for the 33-ft WAM-V

Prior to more in-depth studies using the 6-post model for the 33-ft WAM-V, the following recommendations should be considered:

- A nonlinear rear arch model might improve the modeling results. A full parameter estimation for the nonlinear parameters could be performed using Matlab. A more in-depth validation is required for modeling the compliance in the rear arch, particularly if on-water testing continues for the 33-ft WAM-V without a stiffening brace or modifications to the rear arch.
- Constraining the model at three joints at the bottom of the pontoons may improve the results. This would capture more of the transverse dynamics. The model could also be constrained about the engine pods. A study on the effects of different constraints might improve the quality of the modeling efforts.

11.6.2 Future Work for the CFD and MBD Code Coupling Research

The collaboration with the University of IOWA brings together an interesting opportunity for research into WAM-Vs. The simulations could be used to test a wide variety of configurations with the most advanced and complete WAM-V model to date. The next step in the research is to create a two-way coupling between the CFD and MBD codes. This will allow the motion of the suspension to impact the wave inputs in the same way the wave inputs affect the suspension system with the one-way coupling. The two simulations can be updated for each time step, improving the quality of the simulation output. The simulations will be able to accurately incorporate the effects of the unsprung dynamics on the suspension performance, which was not possible with the hub-coupled 6-post model or with the one-way CFD-MBD code coupling.

Chapter 12 Conclusions and Opportunities for Future Research

The following chapter provides a discussion of possible directions for future research into Wave-Adaptive Modular Vessels beyond the scope of this dissertation. The continuing research documented in earlier chapters, such as the development of the 6-post model for the MBD and CFD collaboration with the University of Iowa documented in Chapter 11, is not repeated here. This chapter will focus on future applications that may benefit from the research in this dissertation, with a focus on applications involving future Wave-Adaptive Modular Vessel designs.

12.1 Chapter Overview

- Section 12.1 provides an overview of the chapter.
- Section 12.2 discusses applications of the research beyond WAM-V technology.
- Section 12.3 discusses future suspension upgrades for the 33-ft WAM-V.
- Section 12.4 discusses control system upgrades on the 33-ft WAM-V for continued rough water testing.
- Section 12.5 discusses future applications of the Quarter-Boat models.
- Section 12.6 discusses design and testing improvements for the 2-post test rig.
- Section 12.7 provides concluding remarks regarding WAM-V technology.

12.2 Extended Applications of Research

While the current application of this research is to Wave-Adaptive Modular Vessels, beyond the immediate application towards improving future WAM-V platforms, the contributions presented in this dissertation are applicable to number of different areas of research. Within the marine domain, the research could be applied to improved shock mitigating seat technology, to improving the landing structures on seaplanes, to personal watercraft (which are beginning to incorporate suspension system designs), and to systems for improved launch and recovery of vessels. Some of the research could also be applied to catamarans without suspension systems. These applications would also benefit from the shaker rig testing techniques presented in this dissertation, which until now have not applied in the marine domain. Possible extensions of the research beyond the marine domain include: snowmobiles, off-road vehicle suspensions, and any suspension system with a large ratio of unsprung to sprung mass.

12.3 33-ft WAM-V Suspension Upgrades

Continued WAM-V testing is required for evaluating new and different suspension concepts. Regarding the 33-ft WAM-V, it is the author/WAM-V operator's opinion that the second generation suspension system performed at a fairly optimized level as far as the capabilities of a linear, passive, coil spring suspension system are concerned. The design could be marginally improved with more travel to handle larger impacts; the suspension used almost all of its available travel during the largest wave events. The suspension mounting points could be altered to make the suspension slightly progressive without replacing the major suspension components. This would increase the suspension's capacity to handle bigger impacts. Damping rates could be fine-tuned, a higher range of damping ratios could be tested by rebuilding the internals of the adjustable dampers, and nonlinear damping rates could also be evaluated. Given the limited testing time in rough conditions, the second generation suspension system performed quite well. Based on the damper testing results, using a higher damping ratio (>0.5 critical) is recommended for future suspensions. On-water testing in a Sea State 1 did not show improved performance at low damping levels. Test results from the 2-post rig favored high damping levels, as did Sea State 2-3 testing, where energy absorption of the dampers was found to be critical for keeping the suspensions from bottoming out during heavy impacts, and for controlling the motion of the substantial unsprung mass of the pontoons. The continued use of adjustable dampers for future suspension designs is recommended.

12.3.1 Applications for Advanced Suspension Technology

A logical next step for the research into improved suspension performance on the 33-ft WAM-V is to consider the application of more advanced, controllable suspension system designs. The information and the models presented in this dissertation can be leveraged to enhance the understanding of more advanced suspension designs. At the most basic level, the air spring on the original 33-ft WAM-V suspension design could be updated with load-leveling valves, providing adjustability to varying loads experienced by the WAM-V. More advanced solutions, such as interconnected hydraulic suspensions or semi-active suspensions could also be implemented, using the tools in this dissertation to determine their performance advantages. Incorporation of magnetorheological (MR) dampers would provide a wider range of adjustability than the current damper designs and changes could be made in real time. An example range of the available force outputs at different amperages for an MR damper is shown in Figure 12.1.

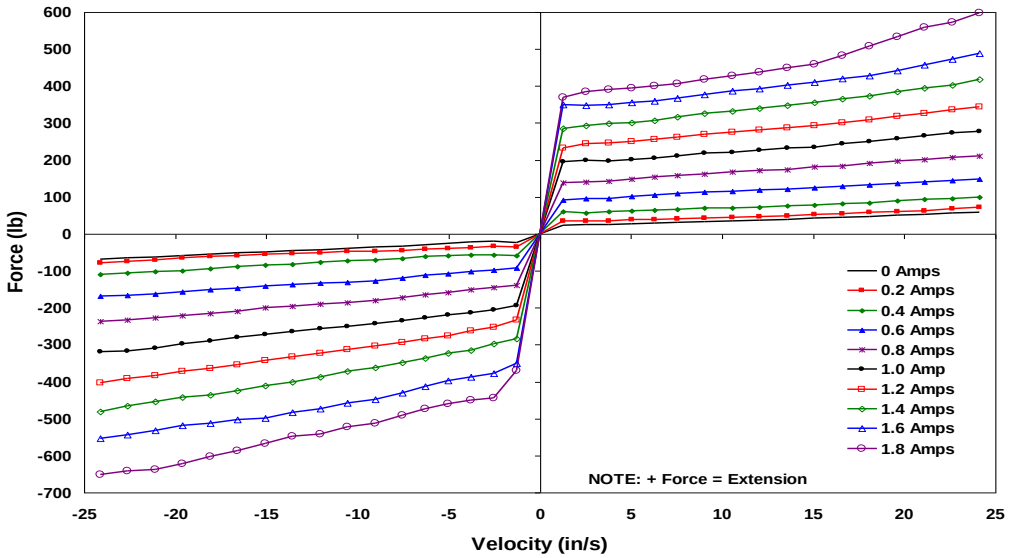

Figure 12.1 Example range of force adjustment for a magnetorheological damper [83]

12.3.2 Suspension Motion for Energy Harvesting

On future USV WAM-Vs, the suspension systems could serve as a platform for implementing advanced damper technology for energy harvesting. Within the CVeSS laboratory, a damper has already been developed that incorporates a vibration-based electromechanical energy harvesting system to provide electrical power in a freight car for rail applications. With a size and shape similar to conventional shock absorbers, energy harvesting dampers are designed to be placed in parallel with existing suspension elements [84]. The energy harvesting damper and a graph showing the power output test results are shown in Figure 12.2.

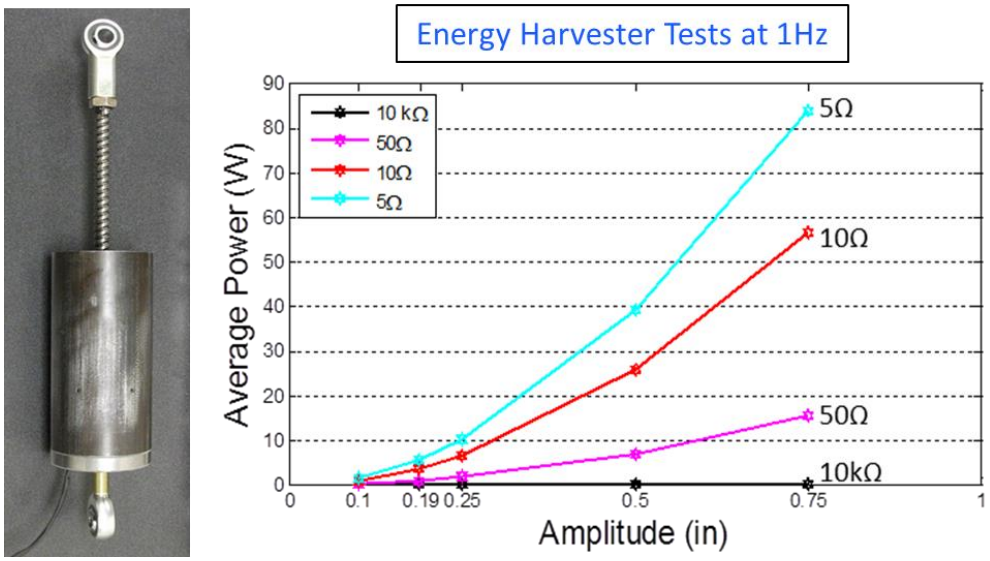

Figure 12.2 Energy harvesting damper in the CVeSS lab for rail applications [84]

Test results have indicated that the current energy harvester design is capable of generating up to 50 Watts at 22 Vrms, using a 10-Ohm resistor with sine wave inputs. Peaks of greater than 30 Watts are possible with replicated rail car suspension displacements, making them suitable to directly power on-board instruments or trickle charge a battery [84]. Wave inputs are considerably larger in magnitude, but with lower available force capacity.

For the application of energy harvesting dampers to WAM-Vs, the suspension systems might have to be redesigned with the goal of maximizing energy harvesting rather than minimizing accelerations at the payload. The two goals would likely require different suspension parameters, although they are not necessarily mutually exclusive. Energy harvesting would be particularly useful for USV WAM-Vs that utilize electric power plants, and for applications where mitigating accelerations at the payload is less critical to overall performance.

12.3.3 Improvement to Suspension and Platform Configurations

The direction of the suspension design for future WAM-Vs will depend largely on whether the WAM-V is designed for manned or unmanned applications. Future USVs may place less emphasis on how accelerations affect human operators and more emphasis on how they affect performance of sensitive equipment and the efficiency of the vessel. Future manned applications may investigate development paths that require departures from the architecture of current WAM-V platforms. Longitudinal dynamics are an important area of performance for future manned vessels. This should be reflected in research efforts; future WAM-Vs may benefit from incorporating both vertical and longitudinal suspension systems. The circular hulls could be replaced with a more advanced design that could be optimized in tandem with the suspension system. Advances in drop stitch fabrication and other manufacturing techniques may allow for non-circular hulls to be evaluated, while still utilizing an inflatable hull design.

The unsuspended rear arch design on the current generation of WAM-V platforms requires further investigation. It is possible that the current design architecture represents the best compromise for incorporating suspension systems onto a marine vessel; the 12-ft USV demonstrated improved dynamics compared to the 100-ft Proteus, despite utilizing only front suspensions. However, it is more likely that implementing suspensions on only the front corners represents an example of design optimization converging on a local minimum rather than the global minimum design, which would incorporate suspensions at all four corners of the vessel.

A more advanced design for shock mitigation might involve four fully independent suspensions, removing the unsprung connection between the front and rear suspensions. A quadramaran concept sketch with four independent suspension systems and four hulls is shown in Figure 12.3.

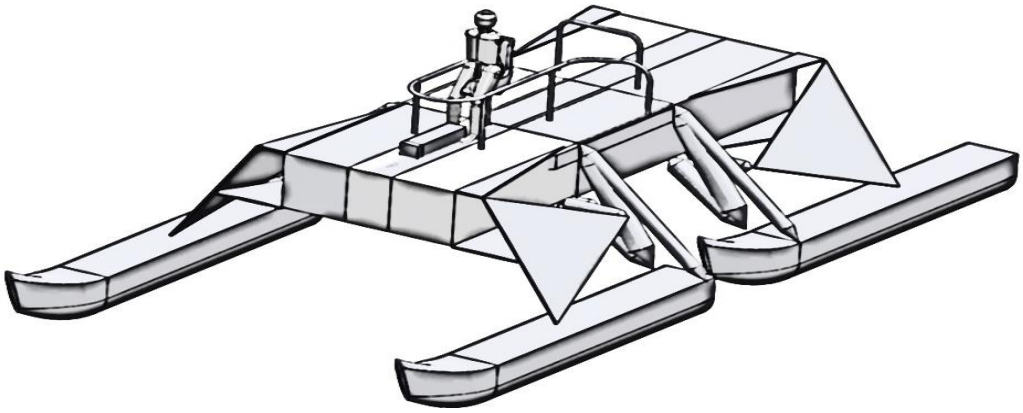

Figure 12.3 Future vessel concept incorporating four hulls and four independent suspensions

12.4 33-ft WAM-V Control System Improvements

Conducting the on-water suspension studies with the 33-ft WAM-V proved to be challenging due to a variety of reasons, most significant were powertrain reliability and vessel control difficulty related to propulsion system malfunctions. Motion Induced Interruptions (MII), operator controls inadequate for rough water use, and communication issues between the support craft and WAM-V all contributed to difficult rough water testing. A screenshot from testing, displaying an example of a Motion Induced Interruption due to a large wave where the operator had to remove both hands from the controls to brace for impact, is shown in Figure 12.4.

Figure 12.4 Motion induced interruption due to large wave impact

Significant changes to the operator controls, propulsion, and electrical systems are required in order to continue the on-water suspension testing of the 33ft WAM-V in a safe and reliable manner. The most notable upgrade is a rethinking of the radio control unit used by the operator onboard the WAM-V. The servos-operated control systems are set to be replaced with more robust, manual controls.

For steering the WAM-V's jet nozzles, a more conventional steering system should be implemented using standard steering wheel controls. Using a single steering wheel for steering both jet nozzles creates a problem for folding and unfolding the WAM-V, since the jet nozzles can no longer be steered independently to unfold the engine pods one at a time. A solution to this problem is diagramed in Figure 12.5 in the form of a dual helm control system.

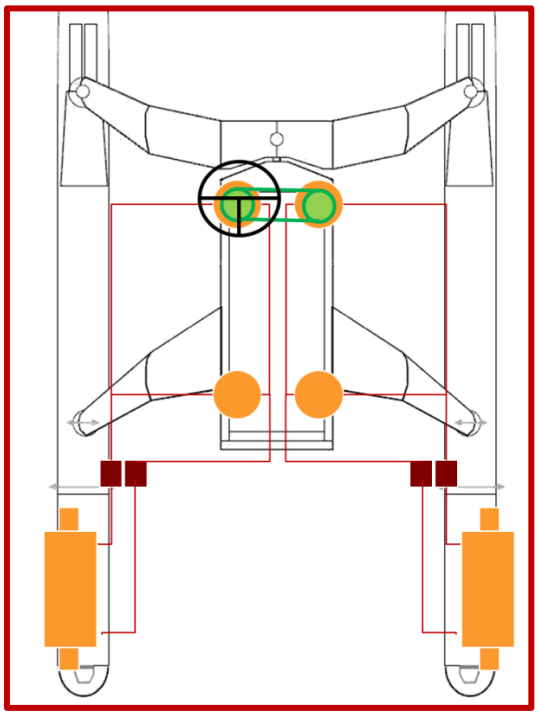

Figure 12.5 Schematic of dual helm control system for steering the 33-ft WAM-V

Four non-backdrivable hydraulic pumps are used for steering the two jet nozzles. Two pumps are located at the front helm; each pump controls a hydraulic steering actuator in one pod. The front pumps are mechanically linked together via a timing pulley, so turning the steering wheel causes both nozzles to be steered at the same rate. Two additional pumps are located at the rear of the WAM-V. The rear steering pumps are connected in parallel with the front helm pumps; however, the rear pumps are not mechanically linked together, so the jet nozzles can be steered

independently from the rear controls. The rear controls will be used during the folding and unfolding operations, and will not be operated once the WAM-V is underway.

The use of manual hydraulic controls will allow for hydraulic quick disconnects to be installed on the hydraulic lines, so the engine pods can still be removed from the WAM-V for maintenance purposes. Using hydraulics for controlling the buckets on the WAM-V is also advantageous for the same reason. For the throttle controls, the fly by wire throttle potentiometers located in the engine pods are to be relocated up to the operator control helm, where they will be operated by manual levers instead of by servos and radio control.

12.5 Applications of Quarter-Boat Models to WAM-V Research

The Quarter-Boat test rig proved highly effective for generating a dataset for analysis that led to the design of the Quarter-Boat model for simulating the surface interactions that occur below the WAM-V's pontoons. A number of possible future applications of the Quarter-Boat model are discussed in this section.

12.5.1 Integration of the Quarter-Boat and 6-Post Models for the 33-ft WAM-V

The 6-post model could be updated to incorporate the properties of the Quarter-Boat model between the actuators and the pontoons. This would allow the unsprung dynamics of the pontoons to be included in the model. It would also be possible to construct a mechanical version of the Quarter-Boat model for use on the 2-post test rig. It would be very interesting to see how the 6-post model with the Quarter-Boat parameters below the pontoons would compare to the MBD and CFD coupled codes for simulating the performance of the 33-ft WAM-V.

12.5.2 Application of the Quarter-Boat Model as a Plant Model for the 2-Post Rig

In Chapter 10, a function limitation of the 2-post rig was reached when comparing the original and the second generation suspension configurations. The unsprung dynamics of the pontoons are not currently being evaluated as part of the 2-post test rig. It would be possible to implement the Quarter-Boat model parameters within dSPACE, with the position and velocity measurements from the 2-post rig as inputs to the model and the force from the Quarter-Boat model as the output to the actuators on the rig. This would allow for some of the unsprung dynamics of the 33-ft WAM-V to be simulated on the 2-post rig, using the Quarter-Boat model as a plant. This is possibly one of the greatest advantages of the Quarter-Boat model relative to other hydrodynamics theories, its simplicity makes it easy to implement for controls applications.

12.5.3 Quarter-Boat Model as a Plant Model for the Semi-Active Suspensions

Creating a plant model that incorporates the Quarter-Boat modeling coefficients could also be used in the control design for future WAM-V suspension systems that incorporate semi-active control designs. Incorporating control strategies such as Skyhook, Groundhook, Hybrid Control, or any model-based control design could also implement the Quarter-Boat model as part of the plant model to estimate the forces and displacements occurring under the hulls that cannot be measured by sensors on the WAM-V. Control strategies could be evaluated prior to on-water testing via simulations using the Quarter-Boat model, the 6-post model, the coupled MBD and CFD code, or via laboratory testing using the 2-post test rig.

12.6 Improvements to Future Multi-Post Shaker Rigs for Testing WAM-Vs

The 2-post rig produced good results for evaluating the WAM-V's dynamics in the laboratory setting. For improving the 2-post rig, a number of possible upgrades might be considered that could improve the quality of the data. For future testing with the current rig setup, improved methods of scaling on-water testing data to fit within the actuator's stroke limitations should be researched so that sea data can be tested using the rig with better correlation to the on-water test data. This will likely result in the testing of irregular input types, as opposed to the sine wave inputs analyzed in Chapter 10.

The use of two active posts proved sufficient to excite the suspension and a great deal was learned about the WAM-V's dynamic properties. Four active posts would be useful for inputting on-water testing data to the rig. The actuator's six inch dynamic stroke range did prove to be limiting to the severity of inputs that could be tested, particularly for low frequency inputs. Longer stroke actuators would be a useful upgrade. For either upgrade, the flow capacity of the hydraulic pumps would have to be considered. A secondary solution would be to install a lever arm assembly between the current actuators and the pontoons, so the motion of the actuators would be amplified at the pontoons. The actuators have sufficient reserve force capacity for a lever arm with a reasonable motion ratio to be implemented; during testing the actuators only used approximately 1500 lbs of the available 5600 lb force capacity. Given the choice between upgrading to four actuators or upgrading to two actuators with a longer stroke capacity, two longer stroke actuators would be of greater benefit to future WAM-V testing.

12.7 Concluding Remarks

Wave-Adaptive Modular Vessels have an interesting place in the future naval shipyard. The concept of applying suspension systems to small, High Speed Craft is of significant interest to the U.S. Navy. Operators of High Speed Craft experience significant forces and accelerations during operation, often resulting in injuries, as well as damage to craft components. Improvements made in this area are of high value to the U.S. Navy.

In considering the usefulness of WAM-Vs for future missions, an analogy can be made to the field of aeronautics. In terms of their strengths and weaknesses, WAM-Vs can be considered the amphibious counterparts of helicopters; the choice between WAM-Vs and monohulls for future naval missions is not unlike the choice between helicopters and airplanes for aviation missions. WAM-Vs are not designed to replace existing technology, or to intrude upon the design space of more conventional hull forms. Rather, the technology was developed to push the boundaries of what is possible, by challenging the conventional brute force approach to ship building, and in doing so, provide the capability for future advancements.

Appendix

The following sections contain additional relevant material to WAM-V research program outside of the research relevant. Appendix A contains the results of a water inclining test for the 33-ft WAM-V. Appendix B contains the results of the calm water testing for the 33-ft WAM-V conducted prior to the rough water testing programs.

A 33-ft WAM-V Water Inclining Test

The purpose of an inclining test is to accurately determine a vessel's lightship weight and the coordinates of its center of gravity. In order to determine the center of gravity of an already constructed vessel, either an air or water inclining test is usually performed. An air inclining test involves suspending the vessel out of the water via multiple cables, and the determining the coordinates of the center of gravity by measuring the changing angles of inclination as ballast is moved across the vessel. A water inclining test also involves changing the angle of inclination of the vessel in order to determine its center of gravity. However, for a water inclining test, the center of gravity is determined from changes to the trim, draft, and heel of the vessel due to moving ballast between known locations on the vessel, producing a net roll moment.

A water inclining is performed in order to determine the metacentric height and the vertical center of gravity. Metacentric height is the distance between the center of gravity of a ship and its metacenter, and can be derived from the following formula:

$$GM = \frac{wd}{W \tan\theta}$$ [20]

Where:

w = inclining weight

D = distance weight moved

W = displacement of ship including inclining weight w

Θ = angle of heel

A vessel's metacenter is the point of intersection of an imaginary line drawn through the boat's centerline and a vertical line through the center of buoyancy [20], as shown in Figure A.1

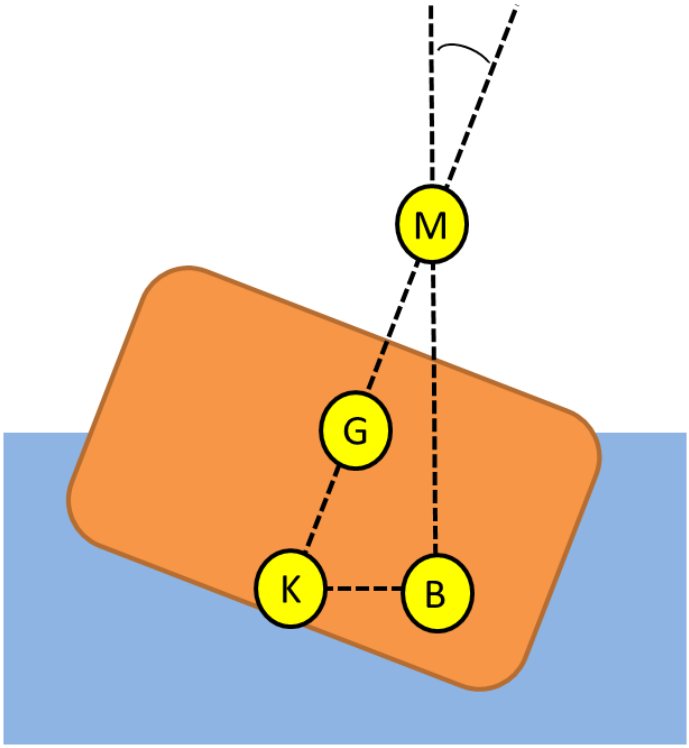

Figure A.1 Metacenter diagram for an inclining experiment

The metacentric height is the distance between the center of gravity of a ship and its metacenter. The metacenter (M) is defined as the point at the imaginary intersection of the boat's centerline (assuming the center of gravity is centered in the transverse plan) and a vertical plane through the new center of buoyancy [20]. The lateral change of the center of buoyancy of the vessel when heeled is determined from hydrostatic curves of the vessel, or from a CAD model of the hull if available. The distances KM and BM are defined from the following formulas:

$$KM = KB + BM$$

$$BM = \frac{KB}{\tan\theta} \qquad [20]$$

With the distance GM determined from the inclining test, and KB and KM determined from the hydrostatic curves or a CAD model of the hull, the location of the center of gravity of the vessel can be determined from the following formula:

$$CG_H \rightarrow KG = KM - GM \quad [20]$$

Stability curves for a vessel are determined from the roll frequency of the vessel. The roll frequency of the boat is determined by the amount of mass on the length of the swing arm. The equation for the period of roll is:

$$T = \frac{2\pi k}{\sqrt{gGM}} \text{ [20]}$$

Where:

T is the period of roll

K is the radius of gyration in the roll

A.1 Preparations to the WAM-V for a Water Inclining Test

Prior to the inclining test, the 33-ft WAM-V needs to be configured for the test. Any inclining test should be performed as near to the vessel's running configuration as possible; the standard for missing or different components should not exceed two percent of the vessel's weight [70]. Any items that may swing or move must be secured, this includes fuel; tanks should be empty or filled completely. For the WAM-V, the two smaller fuel tanks sit at the most forward location within the engine pods; the tanks each have a 15.9 gallon capacity. Additionally, two extended range tanks are housed inside the engine pod skis with a capacity of 40 gallons each. For the inclining test the two smaller fuel tanks were filled completely and the extended range tanks were left completely empty. No persons were onboard the WAM-V while measurements were being taken, nor was any ballast added to represent the weight of the operator. The mooring lines used to tether the WAM-V to the dock were set up to be relatively free of tension in the transverse direction to reduce external moments acting on the WAM-V. The 33-ft WAM-V being configured for the water inclining test is shown in Figure A.2.

Figure A.2 WAM-V being prepared for water inclining test

A.2 Movable Ballast for Inclining Test

The WAM-V was ballasted with 1400lbs of extra weight to provide approximately two degrees of heel in either direction when the weight was moved from one pontoon to the other. Individual lead bags were used to ballast the boat for the inclining test. The bags weighed 25lbs each, and were located at even increments along the port and starboard skis. Measurements for the location of each bag were taken for future inputs to the model. Figure A.3 shows the 56 lead bags in their starting locations prior to the test, as well as the small boat positioned under the WAM-V used as a place to take measurements from and a way to move the ballast back and forth between the port and starboard skis.

Figure A.3 Neutral location of ballast for water inclining test

A.3 Preparations to Suspension and Engine Pods

Compared to a standard vessel, the WAM-V has a few additional considerations that must be accounted for during the inclining test. The WAM-V's additional degrees of freedom due to the suspension systems, front arch, and engine pods may skew the results of testing if they are not accounted for.

In order to keep the suspension degree of freedom from impacting the results, the front suspension rocker arms were locked in place at their nominal ride height. The locked out air spring configuration is shown in Figure A.4. Ratchet straps were used to hold the suspensions from overextending, and the air pressure inside the springs was then increased to push hard against the straps.

The engine pods also have a degree of freedom with respect to the pontoons from the engine pod's hinge. The pod's degree of freedom with respect to the pontoons was removed for testing by pulling the engine pods to their forward stops against the bump stops with a ratchet strap; the port engine pod lock out strap location is shown in Figure A.4. The port and starboard pods were locked out at angles of 6.15 and 5.55 angles respectively.

The front arch was not locked out for the test; since the rear arch provides the 100% of the WAM-V's roll stiffness, locking out the front arch was not necessary. It would have also been possible to measure suspension and engine pod angles for each ballast configuration and factor them into the calculations rather than using the lockouts. However, this would have lengthened the time for the conducting the experiment significantly.

Figure A.4 Locked out suspension and engine pod for inclining tests

A.4 Initial Measurements

With the WAM-V ballasted and the lockouts in place, static draft readings were taken at three points along the hulls. The draft readings are taken so a waterline for the WAM-V could be established with the extra ballast onboard. Draft readings were taken at two locations along each of the skis and at one location on each of the engine pods, the locations are shown in Figure A.5; all measurements are defined from the centerline of the rear arch. Readings on the skis were taken at the front suspension and in front of the aft joint. Table A.1 contains the draft readings.

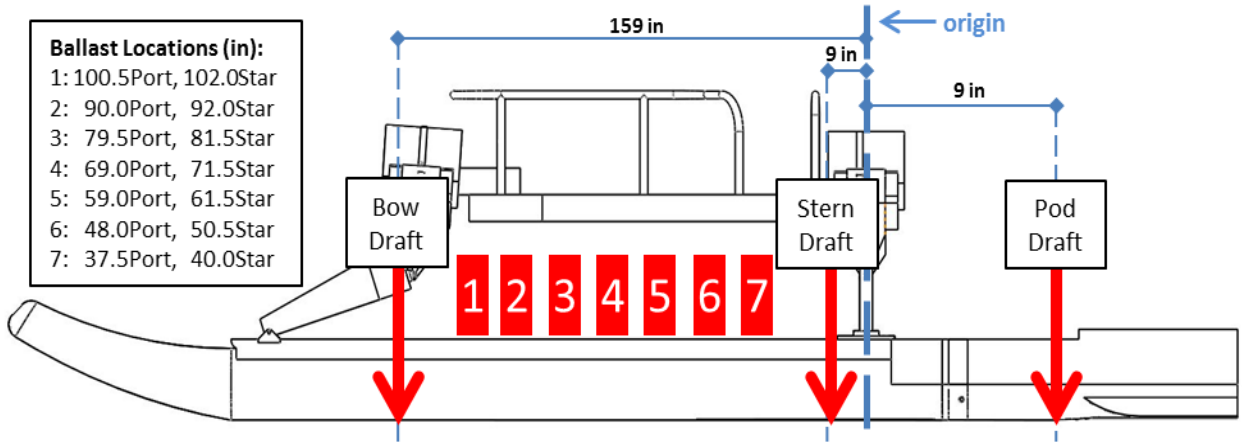

Figure A.5 Location of draft measurements and ballast

Table A.1 WAM-V inclining draft measurements

Location:	Port Draft (in):	Starboard Draft (in):
Fore	12.75	12.25
Aft	6.75	6.75
Pod	14.0	13.5

With the ballast in its neutral position as shown in Figure A.3, measurements were taken of the critical dimensions along the hulls. The dimensions were taken to be imported into a CAD model of the hulls used for determining the center of buoyancy. Table A.2 contains the measurements taken.

Draft readings were taken at the three locations on each of the skis for each ballast configuration. From the draft readings taken, a waterline was able to be established for each configuration. The CAD model of the portions of the pontoons and engine pods submerged below the waterline is shown in Figure A.6. The amount of ballast chosen for the test was based on the formula below,

where GM is estimated to be ~600 inches from the CAD model, W is the total weight, and d is equal to half the distance between the two hulls. Based on the formula below, 1400lbs of ballast should provide roughly two degrees of heel.

$$w = \frac{GM * W \tan\phi}{d} \text{ [20]}$$

Table A.2 WAM-V inclining measurements

Parameter:	Measurement:
Distance hull centerlines at front suspension	14 feet, 1 inch
Distance hull centerlines at rear joint	14 feet, 2inches
Port pontoon angle (taken at bow)	2.5 deg. bow up
Star pontoon angle (taken at bow)	2.1 deg. bow up
Port pontoon angle (taken at stern)	2.4 deg. bow up
Star pontoon angle (taken at stern)	2.6 deg. bow up
Port pontoon angle (taken at pod)	3.7 deg. bow down
Star pontoon angle (taken at pod)	3.2 deg. bow down
Port pontoon angle (taken at bow)	0.3 deg. toe in
Star pontoon angle (taken at bow)	2.2 deg. toe in
Water density	1.0145g/ml

Note: For the measurements listed in Table A.2, in the marine domain a toe measurement is analogous to measuring camber on an automobile (toe in = negative camber); whereas on an automobile, a toe measurement is used to indicate an angle in yaw, such as the relative steering angle between two tires.

A.5 Hydrostatic Curves Generated from CAD Model

The measurements from Table A.2 were added to the CAD model of the WAM-V's hulls. The volume submerged from the CAD model was found to be 158,000 cubic inches. This corresponds to a weight of 5,800lbs for the boat with the ballast installed and a weight of 4,400lbs without the ballast. From the CAD model, the center of buoyancy was also able to be determined. Figure A.6 shows a cut view of the portion of the hulls submerged below the waterline in the model. Figure A.7 shows the difference in submersion between the two hulls in the neutral position and at three degrees of heel.

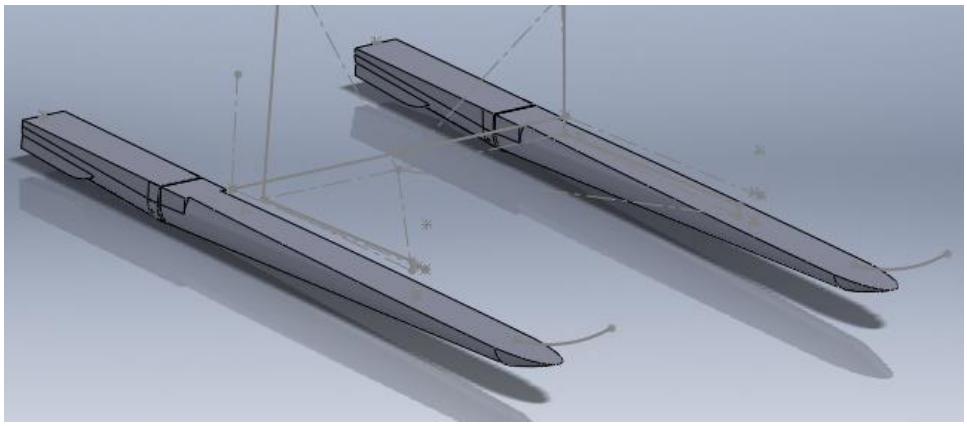

Figure A.6 Portion of the hulls below the waterline

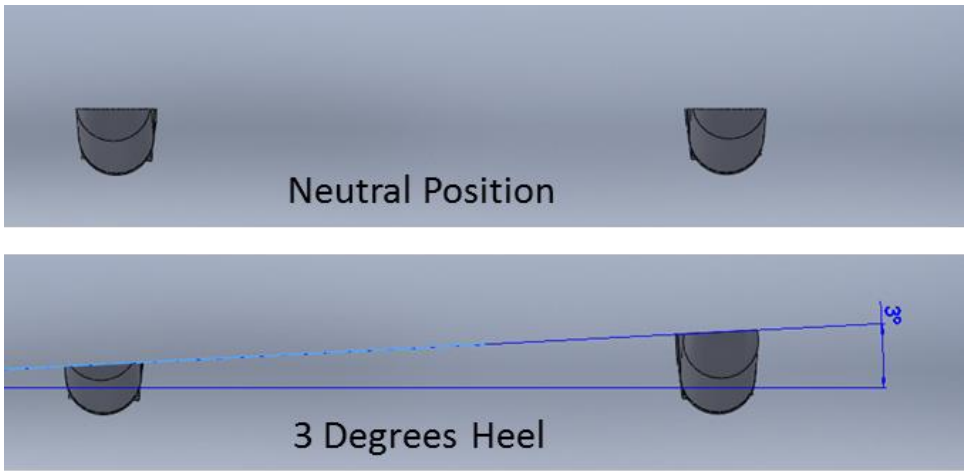

Figure A.7 Portion of the hulls below waterline at static equilibrium and at 3 degrees of heel

A.6 Inclining Test Procedure

For the water inclining, the ballast bags were moved between the port and starboard pontoons in seven different configurations. The different configurations are shown in Figure A.8. To get the necessary 1400 lbs of ballast, 56 bags were used in total. The bags were stacked 4 bags high in groups of 100lbs, and the bags were moved one stack at a time. This was done to keep the vertical center of gravity constant throughout the different configurations. A red square in the diagram shown in Figure A.8 indicates 100lbs of ballast at that location. For each configuration, the heel angle of the WAM-V was measured and recorded.

The goal of the seven different configurations in the test was to incrementally move the entire ballast from center, to starboard, and then to port. There were slight deviations in the testing procedure as run from a symmetrical testing procedure. In order for the ballast to have moved

symmetrically, twice as many bags have to be moved between tests 5 and 6 as between tests 1 and 2. The way the bags were placed on the inside or outside of the pontoon is not consistent; however, the vertical and lateral cg differences were maintained. An improved testing procedure would include more increments, and repeating of the test locations for consistency. Due to time constraints, the number of configurations that could be measured was limited. However, the number of configurations is still valid for all the calculations to be performed correctly.

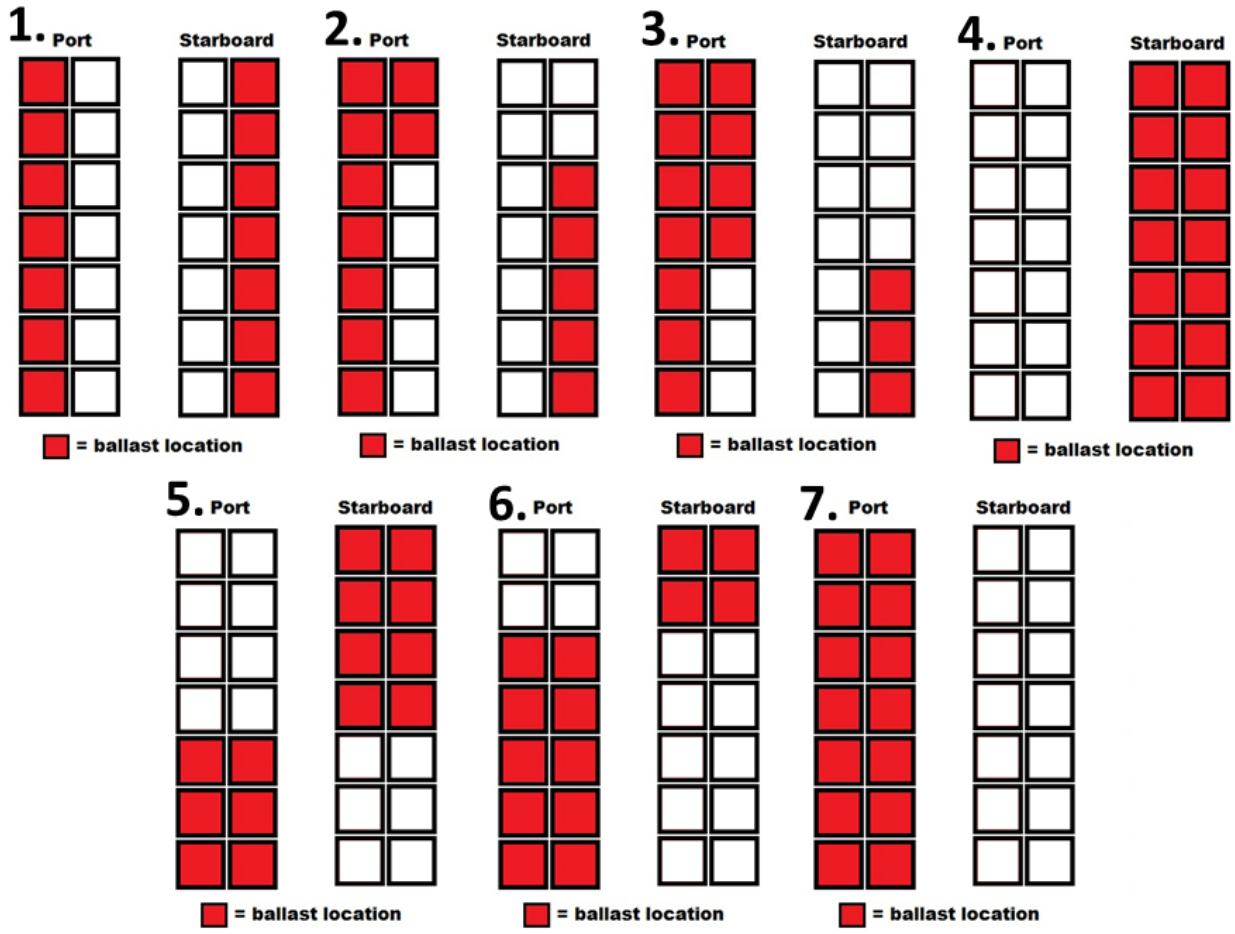

Figure A.8 Movement of ballast between the seven tests

A.7 Inclining Calculations

The volume submerged was found from the CAD model to be 158,000 cubic inches. This corresponds to a weight of 5800 lbs for the WAM-V with the ballast onboard, and a weight of 4400 lbs unballasted. This is known to be inaccurate, since the WAM-V was weighed at a later date for determining the model parameters in Section 6.7 and was found to be closer to 4100lbs without an operator onboard.

Using the CAD model, the center of buoyancy was also able to be determined. The longitudinal center of gravity can be taken directly from the center of buoyancy. The coordinates of the center of buoyancy coordinates measured with respect to the static waterline the rear arch (X), the centerline of the boat (Y), and the static waterline (Z) are:

X = 20.59 inches (to front)

Y = 1.60 inches (to right)

Z = 6.38 inches (down)

In order to determine the values of KB and MB, the waterline in the CAD model was set to different angles and the differences in the center of buoyancy were recorded. The model was set to seven different angles in one degree increments and the location of the center of buoyancy was recorded along with the change in mass of the water displaced. The coordinates of the center of buoyancy and the volume displaced are shown in Table A.3 for seven different angles of heel. Negative values equate to the starboard pontoon lifting out of the water. From the values in Table A.3, a correlation between the movement of the center of buoyancy and the angle of heel was determined. A graph of the center of buoyancy and the angle of heel is shown in Figure A.9, the center of buoyancy was found to change by 10.873 inches per degree of heel. The changes to the center of gravity at the different angles of heel are plotted in Figure A.9.

Table A.3 Changes in center of buoyancy with heel

Angle of Heel (Deg):	X:	Y:	Z:	Volume (in^3*10^3):
-3	-34.1	-.5.57	21.8	157.6
-2	-23.41	-6.02	21.16	157.9
-1	-12.54	-6.3	20.75	158.2
0	-1.6	-6.38	20.59	158.4
1	9.34	-6.29	20.66	158.3
2	20.23	-6.02	20.99	158.0
3	30.99	-5.56	21.54	157.7

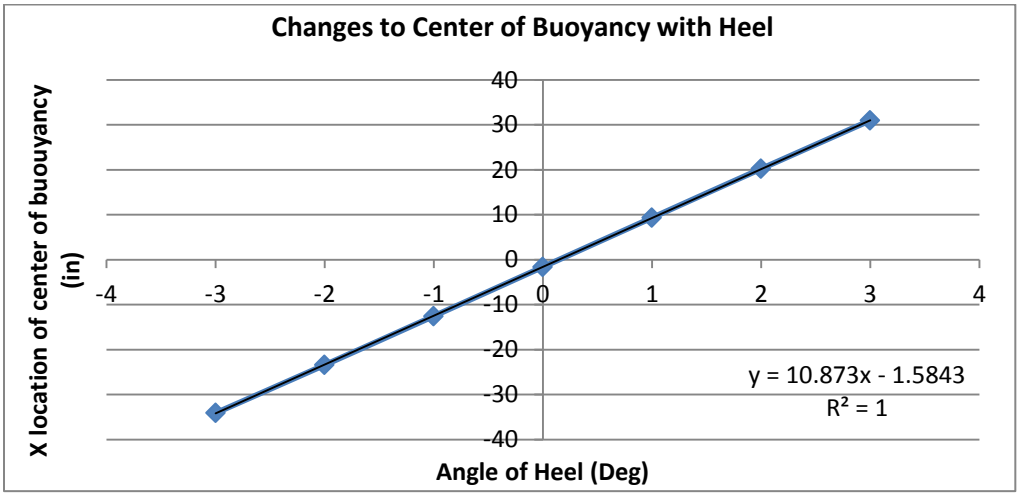

Figure A.9 Longitudinal center of buoyancy vs. angle of heel

With the inclining test performed and the changes to center of buoyancy determined, the vertical center of gravity of the WAM-V can be calculated for each angle of inclination. Table A.4 shows the distance GM and the vertical center of gravity calculated for each testing configuration. From the inclining calculations shown in Table A.4, it can be seen that the calculated center of gravity varies dramatically between each of the tests. Given the WAM-V's low draft hulls, this was a known possibility prior to the test. One method to attempt to reach a consensus center of gravity value for the data would be to plot the delta angle against the moved weight and draw a linear trendline, as shown in Figure A.9. Based on Table A.4, the center of gravity was best estimated to be at a height of 20.74 inches; however, it is unlikely that this value can be considered accurate.

Table A.4 33-ft WAM-V water inclining calculations

Test #	Port Ballast:	Star Ballast:	Delta Ballast:	Delta Angle (Deg):	Tan Angle:	GM (in):	CG Height (in):
1	700	700	0	0	0.0	(no angle)	N/A
2	900	500	400	-0.5	0.0	-663.9	-48.9
3	1100	300	800	-1.1	0.0	-603.5	11.6
4	1400	0	1400	-2.3	0.0	-504.9	110.2
5	1000	400	600	-1.3	0.0	-382.9	232.1
6	600	800	-200	-0.2	0.0	-829.9	-214.8
7	0	1400	-1400	2	0.0	580.7	34.4

A.8 Summary of Findings from Water Inclining Test

The water inclining test was not sufficient to determine the vertical center of gravity of the WAM-V to a sufficient degree of accuracy. For a vessel with a low draft such as the WAM-V, the sensitivity of the results to changes in draft readings is too high to produce good results. This was demonstrated by the difference in overall vessel weight from the inclining experiment to when the vessel was weighed. Using the CAD model of the hydrodynamics, the waterline was moved slightly to see how sensitive the calculations are, the results are shown in Table A.5.

Table A.5 Sensitivity of draft readings for inclining test

Waterline (change in inches):	Displaced Weight (lbs):	Sensitivity (lbs/in):
-2	5025	510
-1	5522	507
0	6015	---
1	6502	487
2	6985	485

The 300lb weight difference between the inclining test and the known weight of the WAM-V measured in Section 6.7 equates to roughly a 0.6 inch error in taking the static draft readings, given that the measurements changed by roughly 500lbs/in. This is plausible because even in calm water, it was not possible to achieve readings with an accuracy of better than 0.5 inch. Accuracy could possibly be improved by retaking trim measurements at each loading configuration tested, however, this would lengthen the time it takes to complete the inclining experiment.

In the future, an air inclining or a tilt test would be a better method to determine the vertical center of gravity for low draft, highly stable vehicles such as the WAM-V. The results from the inclining test could be used to generate stability curves based on the length of the righting arm; otherwise, the results are not useful for modeling purposes.

B Calm Water Testing Analysis

Prior to evaluating the dynamic properties of the 33-ft WAM-V in a rough water environment, a number of calm water trials were conducted with the WAM-V for a variety of reasons. The initial trials took place in parallel with reliability testing and upgrading the WAM-V and its data acquisition system in preparation for rough water operation. The calm water propulsion trials were conducted to characterize the WAM-V's performance and to determine what testing procedures should be used to characterize the WAM-V's dynamic properties. A number of different calm water trials were conducted; the results from the most relevant tests have been included. Most of the calm water testing data has little relevance to the WAM-V's suspension characteristics. However, the results may be relevant to other aspects of the WAM-V's dynamics and the calm water testing results are an important set of data to be used as part of future hydrodynamic and propulsion studies of Wave-Adaptive Modular Vessels.

Initial calm water trials were conducted in the San Francisco Bay using video acquisition for qualitative analysis. Instrumented trials using the data and video acquisition systems detailed in Section 6.4 were conducted at Claytor Lake in Radford, VA. The calm water trials in the San Francisco Bay were conducted with the WAM-V operated via radio control from the support craft for the purposes of evaluating if it would be preferable in rough seas to operate the WAM-V from onboard or from the support craft. The 33-ft WAM-V during calm water testing is shown in Figure B.1. For the remotely operated trials, a person was onboard WAM-V at all times with the ability to stop the WAM-V's engines in an emergency situation.

Figure B.1 Calm water testing in San Francisco, CA with WAM-V remotely operated from chase boat

For the calm water trials conducted at Claytor Lake, the operator was onboard the WAM-V for all of the tests. Remote operation was not deemed suitable for rough water operation due to regulations for testing procedures for unmanned surfaces vessels at U.S. Naval facilities. The 33-ft WAM-V testing in calm water at Claytor Lake with the operator onboard the WAM-V is shown in Figure B.2.

Figure B.2 WAM-V testing at Claytor Lake in Radford, VA with operator onboard the WAM-V

The instrumented calm water tests that were conducted for the 33-ft WAM-V can be broken down into three categories:

1. Constant radius, marine skidpad runs
2. Steady state runs at constant speed
3. Standing full acceleration and deceleration runs

Transient maneuvers such as the marine equivalents to automotive "J-turn" and slalom tests were initially considered to be conducted as part of the calm water tests. However, the WAM-V was found to be too directionally stable and to have a large yaw moment of inertia compared to the size of its propulsion and steering capabilities. Compared to an automobile, the WAM-V's transient dynamics are very slow. This is also important information for rough water testing. A rough water testing program was outlined for the 33-ft WAM-V similar in execution to the 12-ft USV testing documented in Chapter 4; with only in straight line testing at different headings and speeds, using the star pattern diagrams detailed in Section 4.5.

B.1 Steady State Marine Skidpad Maneuvers

The 33-ft WAM-V's steady state lateral acceleration capacity was evaluated by subjecting the WAM-V to a series of skidpad maneuvering tests. In the automotive domain, a skidpad test is a test of a car's lateral acceleration capability at a constant radius or steering angle. For the marine skidpad maneuvers, the tests were run in clockwise and counterclockwise directions with one engine at full throttle and one engine at idle.

For the first series of skidpad maneuvers, the tests were run using only throttle steering. For the second series of skidpad maneuvers, the tests were run with throttle steering and steering of the jet nozzles. On the 33-ft WAM-V, the jet nozzles are able to be steered by up to 30 degrees in either direction. The results from the first skidpad maneuver with no nozzle steering are shown in Figure B.3 for the counterclockwise direction.

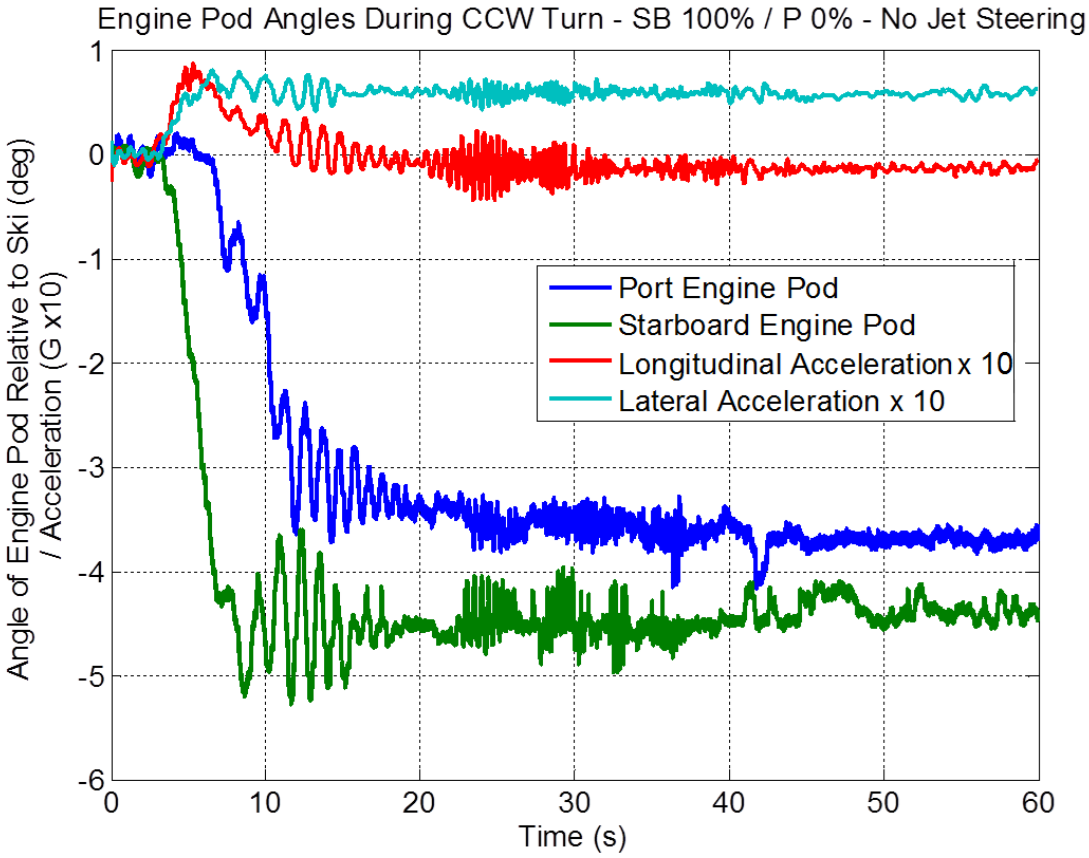

Figure B.3 Marine skidpad maneuver without jet nozzle steering

Figure B.3 shows the data collected from the lateral and longitudinal accelerometers on the superstructure, as well as the angle of the port and starboard engine pods. The first ten seconds of data are transient as the throttles are set to the correct positions. Once the WAM-V reaches a steady state condition, the longitudinal channel shows a lateral acceleration capacity of approximately 0.07g's for the test. The engine pods both show a change in angle from their position at idle to their positions during the skidpad maneuver. The starboard engine which is at full throttle in Figure B.3 changes to an angle of -4.5 degrees. The port engine which is idling during the test also changes to an angle of -3.5 degrees. The change in the starboard angle is to be expected from the thrust from the jet nozzle. The change in the port angle is less expected, as the changing angle is solely influenced the hydrodynamic forces acting on the engine pod.

Figure B.4 shows the results from the second series of skidpad maneuvers with one engine at full throttle and the other at idle with both of the nozzles steered to their maximum angle. The results are shown for the counterclockwise direction test.

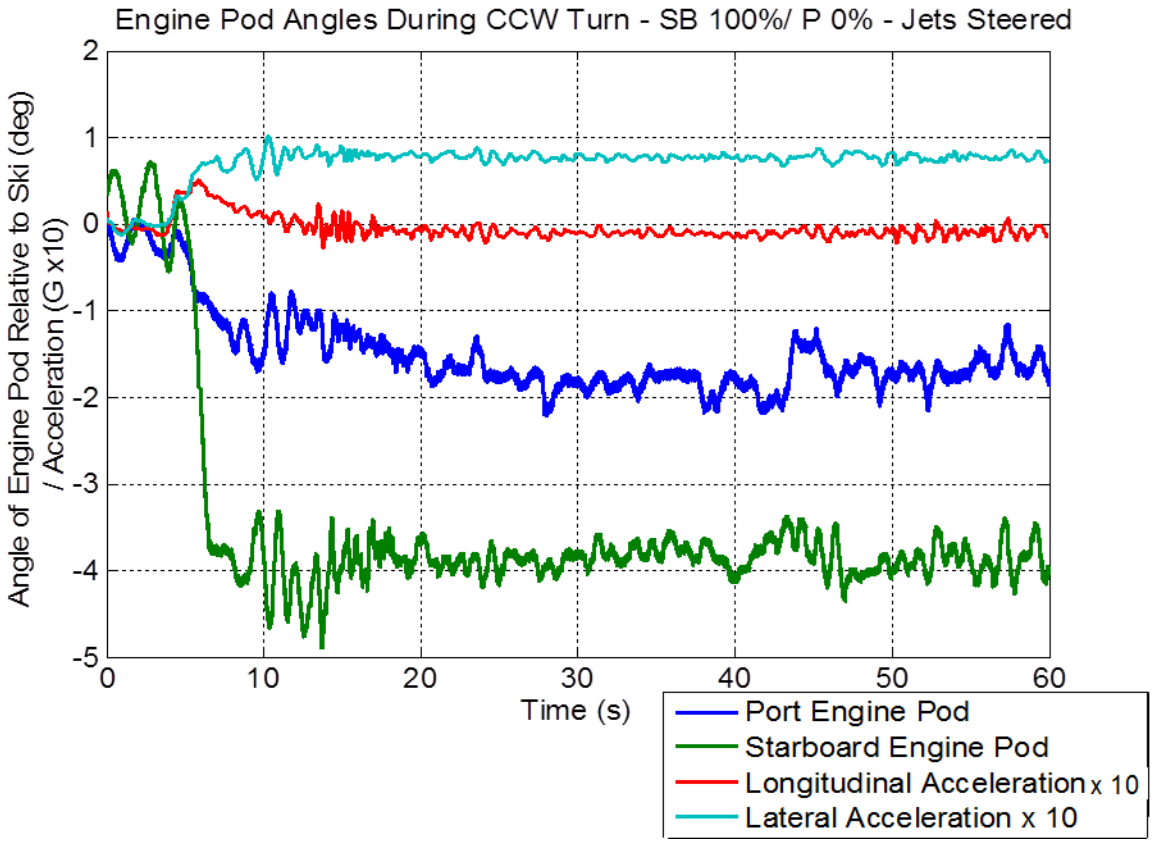

Figure B.4 Marine skidpad maneuver with jet nozzle steering

Steering the jet nozzles of the WAM-V while using differential throttle positions to turn, significantly lowered the WAM-V's steady state turning radius. The data from the marine skidpad maneuvers, however, shows that steering the jet nozzles during the turn did not significantly increase the WAM-V's lateral acceleration capacity. The WAM-V was able to achieve 0.07g's of lateral acceleration in first test and 0.08g's of lateral acceleration in the second test. The lack of change in lateral acceleration can most likely be attributed to partial cavitation of the jet nozzles during the test. Cavitation gets more severe as the nozzles are turned, which slows down the WAM-V's tangential velocity by limiting the engine's ability to generate thrust. The results of the cavitation can be observed in the change in the starboard engine pod angle during the second test. The angle changes less from its static position than during the first test.

An additional skidpad test was planned to be conducted with both engines at full throttle and only steering the nozzles to turn the WAM-V. This test was not completed because the turning radius in this configuration was excessively large, too large to be completed in the area of Claytor Lake the tests where tests were run. The acceleration performance is also very low in this configuration, far lower than for the other two skidpad maneuvers.

B.2 Steady State Speed Runs

During the calm water testing of the 33-ft WAM-V, a series of tests were performed at different throttle positions intervals corresponding to different constant forward speeds of the WAM-V. The tests were performed to characterize the WAM-V's operating position at different forward speeds, particularly to observe how the angle of the engine pods change as a function of forward speed. The tests were run by varying the throttle positions via the radio transmitter. The throttle positions do not have a linear correlation with engine rpm or engine power. Currently there are no sensors in the WAM-V's data acquisition system dedicated to recording engine rpm. The stepped throttle, constant forward speed tests were also conducted to aid with other WAM-V development programs focusing on the hydrodynamics and the propulsion system design. A graph showing the data from different channels during the test is shown in Figure B.5. Forward speed was measured using a GPS sensor independent of the data acquisition system. GPS measurements were added to the data acquisition system following the calm water tests.

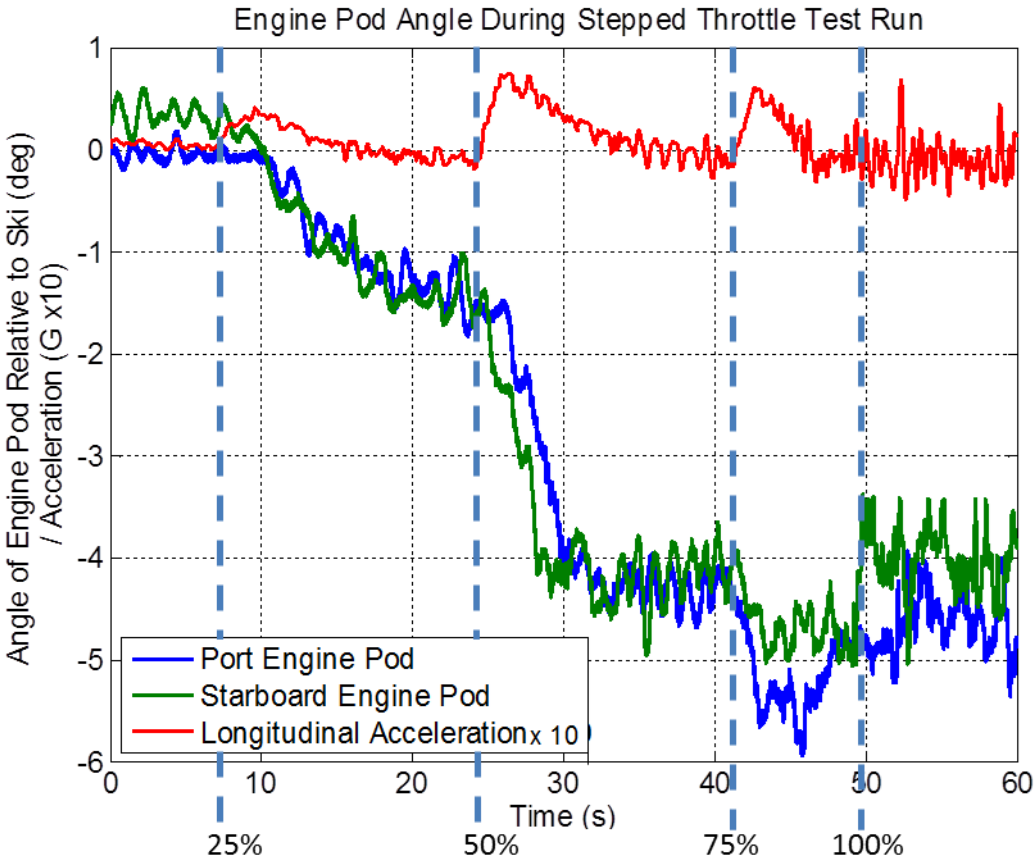

Figure B.5 Stepped throttle constant speed test runs

It can be seen from Figure B.5 that from 75% throttle to 100% throttle the WAM-V does not generate a noticeable increase in speed, as evidenced by the lack of positive longitudinal acceleration during the test. The angle of the engine pods, however, does change. The angles actually moved back toward the neutral position by 0.5 degrees for each engine pod. There is a noticeable increase in vibration as detected by the vertical accelerometers on top of the engine pods. It is also interesting that the engine pods move to different angles. This difference may be due to differing levels of cavitation or engine power.

B.3 Maximum Acceleration and Deceleration Testing

A test was conducted where the WAM-V was initially at rest with the engines at idle. The engines were then abruptly moved to full throttle. Full throttle was held until the WAM-V reached top speed. Once the WAM-V reached top speed, the engines were abruptly returned to idle, causing the WAM-V to decelerate. The data represents the maximum available acceleration of the WAM-V and the resistance of the WAM-V hulls from full speed. The acceleration performance is shown in Figure B.6, along with the motion of the engine pods during the test.

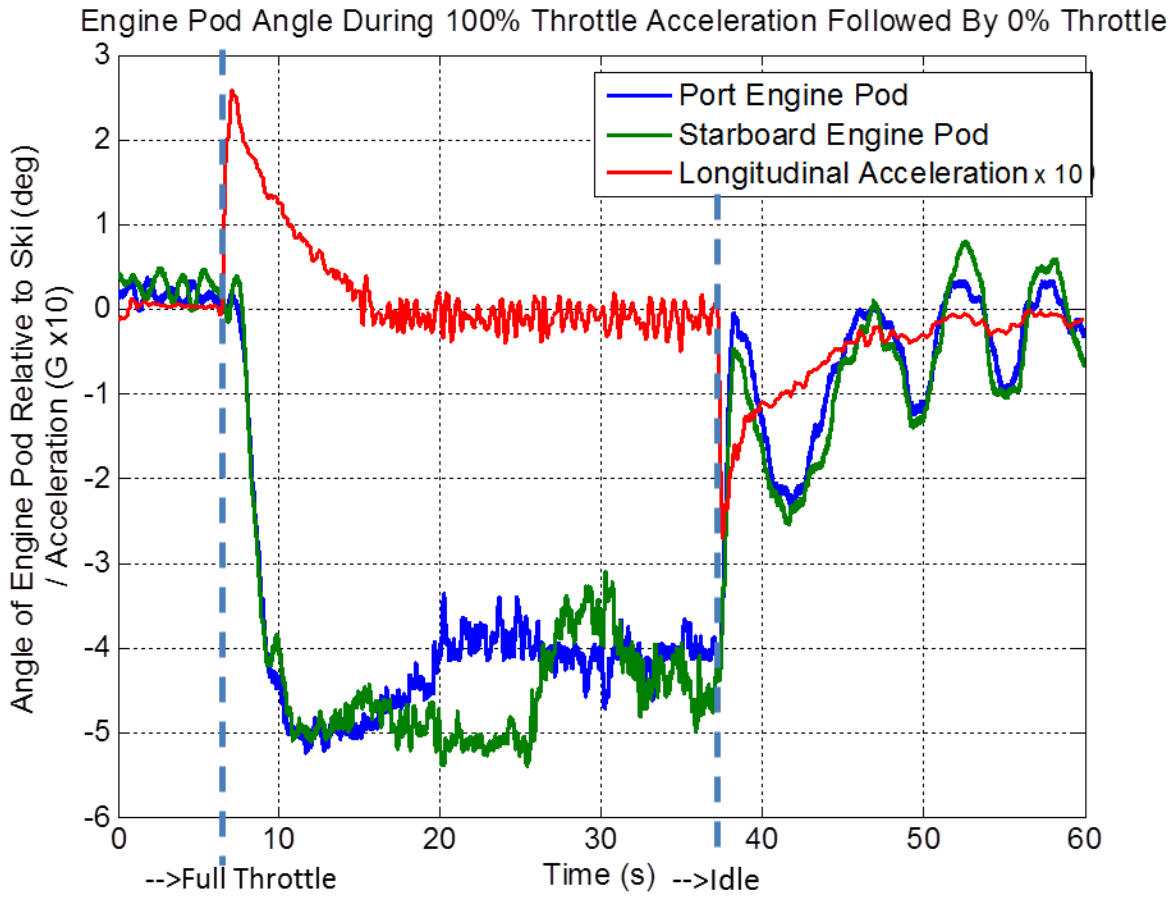

Figure B.6 Full acceleration and deceleration run data

The WAM-V is able to generate 0.25g's of positive acceleration and 0.25 g's of deceleration. It is noteworthy that for the deceleration portion of the test, the buckets were not lowered; based on the manufacturer's recommendation that lowering the buckets at full or partial throttle might strip the gears on the bucket servos. Lowering the buckets would have increased the stopping performance significantly; the current test only shows the deceleration due to drag of the WAM-V's hulls. The motion of the engine pods during the deceleration phase is noteworthy as well. The motion of the pods is highly undamped. The oscillation of the pods does not seem to generate significant changes in the longitudinal acceleration of the WAM-V; however, peaks in the acceleration at 49, 52 and 54 seconds also correlate with peaks in the motion of the pontoons, so some coupling is present between the parameters.

B.4 Conclusions Based on Calm Water Testing

The results from the marine skidpad testing showed that the 33-ft WAM-V is only able to generate roughly 0.07g's of lateral acceleration, which is an order of magnitude lower than the lateral acceleration capability of a standard automobile. As such, transient maneuvers should not be included as part of future testing programs. Also, the suspension showed little to no deflection during the skidpad maneuvers; since purpose of this study is to evaluate the suspension performance of the WAM-V, skidpad maneuvers are not considered to be an effective test.

From the calm water testing, the top speed of the WAM-V was found to be limited to ~20 knots. The WAM-V is a displacement type hull and cannot reach planning speed. Top speed would be increased if cavitation of the jet nozzles is able to be reduced. However, performance is sufficient for operating the WAM-V in elevated seas states, which were run at lower speeds. The full acceleration and deceleration runs were conducted both to better understand the WAM-V's performance and to understand the WAM-V's longitudinal dynamics; however, the tests showed little relevance to the suspension dynamics of the WAM-V. Due to the minimal transient performance capabilities of the 33-ft WAM-V, future tests should be straight line tests in an elevated sea state, maneuvering has little to no impact on suspension performance.

The waterjet design of the WAM-V is prone to cavitation at high speeds. Cavitation of the WAM-V's jet nozzles causes less than smooth running and noticeable vibrations at the operator's position. Change in vibration is qualitatively noticeable at operator location. Cavitation may become more severe in elevated sea states, even though it is less prevalent at lower test speeds.

References

[1] Thomas, G., Tomic, P., & Tuite, A. (2007). High-speed catamaran or monohull? How do you choose? *Ships and Offshore Structures*, 2(2), 137-147.

[2] Clark, D. J., Ellsworth W. M., & Meyer, J. R. (2004). The quest for speed at sea. *NSWC Carderock Division - Technical Digest*, 3-27.

[3] Dubrovsky, V., & Matveev, K. (2005). New types of sea-going multi-hull ships with superior comfort level and safety. *Passenger Vessels for the New Millenium: Joint Meeting of the Pacific Region Sections*, 1-12.

[4] Zouridakis, F. (2005). *A Preliminary Design Tool for Resistance and Powering Prediction of Catamaran Vessels* (Master's Thesis), Massachusetts Institute of Technology, Cambridge, MA.

[5] Kos, S., Brčić, D., & Frančić, V. (2009). Comparative analysis of conventional and SWATH passenger catamaran, *Proceedings of International Conference on Transport Science*, 1–11.

[6] Dyachkov, V., & Makov J. (2005). Seakeeping of a fast displacement catamaran. *Transport*, XX(1), 14-22.

[7] Fu, T. C., Fullerton, A. M., & Minnick, L. M. (2007, August). Characterization of sea fighter, fsf-1, wave slam events, *9th International Conference on Numerical Ship Hydrodynamics*. Ann Arbor, Michigan.

[8] Varyani, K. S., Gatiganti, R. M., & Gerigk, M. (2000). Motions and slamming impact on catamaran. *Ocean Engineering*, 27, 729-747.

[9] Tamotsu, N. (1987). Critical Review of SWATHs. *Research Reports of Ikutoku Technical University*, B-11, 1-21.

[10] Kitazaki, S., & Griffin, M. J. (1998). Resonance behaviour of the seated human body and effects of posture. *Journal of Biomechanics*, 31(2), 143-149.

[11] Riley, M.R., Coats T., Haupt, K., & Jacobson, D. (2011, September) Ride severity index – a new approach to quantifying the comparison of acceleration responses of high-speed craft, *11th International Conference on Fast Sea Transportation*, Honolulu, Hawaii.

[12] Payne, Peter R. (1976). On quantizing ride comfort and allowable acceleration, *Payne Incorporated – David Taylor Naval Ship Research and Development Center Paper,* 196-6, Bethesda, Maryland.

[13] ISO 2631-1:1997 Mechanical Vibration and Shock – Evaluation of Human Exposure to Whole-Body Vibration – Part 1: General Requirements.

[14] O'Hanlon, J. F., & McCauley, M. E. (1973). Motion sickness incidence as a function of the frequency and acceleration of vertical sinusoidal motion. *Human Factors Research, Inc. Technical Report,* 1733-1.

[15] Lawther, A., & Griffin, M. J. (1988). Motion sickness and motion characteristics of vessels at sea, *Ergonomics*, 31(10), 1373-1394.

[16] Bonnet, C. T., Faugloire, E., Riley, M. A., Bardy, B. G., & Stovregen, T. A. (2006). Motion sickness preceded by unstable displacements of the center of pressure. *Human Movement Science*, 25, 800–820.

[17] Piersol, A. G., Paez, T. L., & Harris, C. M. (2010). *Harris' shock and vibration handbook*. New York: McGraw-Hill.

[18] Wines, C. (2011, September). Stability and Safety Issues for High Speed Operation of Rigid Inflatable Boats, *11th International Conference on Fast Sea Transportation*, Honolulu, Hawaii.

[19] Randall, R. E. (2010). *Elements of ocean engineering*. College Station, TX: Society of Naval Architects.

[20] Lewis, E. V., & Society of Naval Architects and Marine Engineers (U.S.). (1988). *Principles of naval architecture*. Jersey City, N.J: Society of Naval Architects and Marine Engineers.

[21] Dobbins, T., Rowley, I., & Campbell, L. (2008). High speed craft human factors engineering design guide, *Human Sciences & Engineering Ltd.*, ABCD-TR-08-01 v1.0.

[22] Von Gierke, H. (1975). The iso standard guide for the evaluation of human exposure to whole-body vibration, *SAE Technical Paper,* 751009.

[23] Lee, R. A., & Pradko, F. (1968). Analytical analysis of human vibration, *SAE Technical Paper,* 680091.

[24] British Standard BS: 6841 (1987). *Measurement and Evaluation of Human Exposure to Whole-Body Mechanical Vibration and Repeated Shock*.

[25] Dupuis, H., & Zerlett, G. (1986). *The effects of whole-body vibration*. Berlin: Springer-Verlag.

[26] Griffin, M. J. (1996). *Handbook of Human Vibration*. London: Academic Press.

[27] Turan, O., Verveniotis, C., & Chirstos, K. H. (2009) Motion sickness onboard ships: Subjective vertical theory and its application to full-scale trials, *Journal of Marine Science and Technology*, 14(4), 409-416.

[28] McCauley, M. E., Royal, J. W., Wylie, C. D., O'Hanlon, J. F., & Mackie R. R. (1976). Motion sickness incidence: Exploratory studies of habituation, pitch and roll, and the refinement of a mathematical model, *Human Factors Research, Inc. Technical Report*, 1733-2.

[29] Stevens, S. C., & Parsons, M. G. (2002). Effects of motion at sea on crew performance: A survey. *Marine Technology*, 39(1), 29–47.

[30] Gahlinger, P. M. (2000). Cabin location and the likelihood of motion sickness in cruise ship passengers. *Journal of Travel Medicine*, 7, 120–124.

[31] Cheung, B. S. K., Money, K. E., & Jacobs, I. (1990). Motion sickness susceptibility and aerobic fitness: A longitudinal study. *Aviation, Space, and Environmental Medicine*, 3, 201-204.

[32] Boileau, P. E., Turcot, D., & Scory, H. (1989). Evaluation of whole-body vibration exposure using a fourth power method and comparison with ISO 2631, *Journal of Sound and Vibration*.

[33] Grimsley, J. S. (2010). *Methodology to Quantify Vertical Accelerations of Planing Craft in Irregular Waves* (Doctoral Dissertation). Old Dominion University, Norfolk, VA.

[34] Dobbins, T., & Schleicher, D. (2009). Impact count index for high speed craft motion assessment, *Multi-Agency Craft Conference*, Norfolk, Virginia.

[35] Riley, M. R., Haupt, K. D., & Jacobson, D. (2009). Analysis of response motions of an 11-meter planing hull in waves, *Naval Surface Warfare Center Carderock, Combatant Craft Division Report*, NSWCCD-23-TM-2009/29.

[36] Mansfield, N. J. (2005). *Human response to vibration*. Boca Raton, FL: CRC Press.

[37] (2011). Ride dynamics and evaluation of human exposure to whole body vibration, *Test Operations Procedure: Final Report*, 01-1-014A, Aberdeen Proving Ground, MD.

[38] Wolf, E. J. (2000). *Using the Absorbed Power Method to Evaluate Effectiveness of Selected Seat Cushions during Manual Wheelchair Propulsion* (Master's Thesis), University of Pittsburgh, Pittsburgh, PA.

[39] Murphy, N. R., & Ahmad, F. H. (1986). Comparison of measures of vibration affecting occupants of military vehicles. *Department of the Army, Technical Report*, GL-86-18.

[40] Stark, D. R. (1980). Ride quality characterization and evaluation in the low frequency regime, with applications to marine vehicles, *Human Factors in Transport Research*, 2, 140-148.

[41] Conti, U. (2009). A perfect body, *Multi-Agency Craft Conference*, Norfolk, Virginia.

[42] Bautista, J. Q., Riley, M. R., Kuehne, H. L., & Irvine, M. J. (2009). Marine advanced research WAM-V proteus propulsion, seakeeping, and miscellaneous trials, *Naval Surface Warfare Center Carderock Division*, Report NSWCCD-23-TM-2009/43.

[43] Conti, U., & Gundersen, M. (2011, September). Second generation design of wave adaptive modular vessels (WAM-V®): A technical discussion of design improvements, *11th International Conference on Fast Sea Transportation*, Honolulu, Hawaii.

[44] Lamb, T., & Society of Naval Architects and Marine Engineers (U.S.). (2003). *Ship design and construction*. Jersey City, NJ: Society of Naval Architects and Marine Engineers.

[45] Inman, D. J. (2008). *Engineering vibration*. Upper Saddle River, NJ: Pearson Prentice Hall.

[46] Goodyear Tire and Rubber Company. (2008). [PDF data file]. *#1S3-011*. Retrieved from www.goodyearep.com/WorkArea/DownloadAsset.aspx?id=15732

[47] Kowalczyk, H., (2002). Damper tuning with the use of a seven post shaker rig, *SAE Technical Paper Series*, 2002-01-0804.

[48] Applying motions and forces, (2011). *The Mathworks,* Retrieved from http://www.mathworks.com/help/physmod/sm/mech/ug/applying-motions-and-forces.html

[49] Blinchikoff, H. J., & Zverev, A. I. (1976). *Filtering in the time and frequency domains*. New York: Wiley.

[50] Robertson, D. G. E., & Dowling, J. J. (2003). Design and responses of butterworth and critically damped digital filters, *Journal of Electromyography and Kinesiology,* 13(6), 569–573.

[51] Mitra, S. K. (2011). *Digital signal processing: A computer-based approach*. New York, NY: McGraw-Hill.

[52] Virtual reality modeling language (vrml), (2011). *The Mathworks,* Retrieved from http://www.mathworks.com/help/sl3d/vrml.html

[53] Peterson, A. (2011). Simulation and testing of wave-adaptive modular vessels, *Multi-Agency Craft Conference*, Norfolk, Virginia.

[54] Peterson, A., & Ahmadian, M. (2011, September). Simulation and testing of wave-adaptive modular vessels, *11th International Conference on Fast Sea Transportation*, Honolulu, Hawaii.

[55] Rajamani, R. (2006). *Vehicle dynamics and control*. New York: Springer Science.

[56] Langdon, J. (2007). *Suspension Test Rig for the Accurate Re-creation of Vehicle Response* (Master's Thesis), Virginia Polytechnic and State University, Blacksburg, VA.

[57] Ellis, J. R. (1988). *Road vehicle dynamics*. Akron, OH: John R. Ellis Inc.

[58] Rawson, K. J., & Tupper, E. C. (2001). *Basic ship theory*. Boston: Butterworth-Heinemann.

[59] Vugts, J. H., (1968). The hydrodynamic coefficients for swaying, heaving and rolling cylinders on a free surface. Shipbuilding Laboratory, Technical University Delft, Report No. 112 S.

[60] Collins, S. (2012, January). J dampers in formula one. *Racecar Engineering Magazine.*

[61] Faltinsen, O. M. (2005). *Hydrodynamics of high-speed marine vehicles*. Cambridge: Cambridge University Press.

[62] Cummins, W. E. (1962). The impulse response function and ship motions. *Technical Report 1661, David Taylor Model Basin–DTNSRDC.*

[63] Perez, T., & Fossen, T. I. (2008). Time- vs. frequency-domain identification of parametric radiation force models for marine structures at zero speed. *Modeling, Identification and Control*, 29(1), 1–19.

[64] Sun, H., & Faltinsen, O. M. (2006). Water impact of horizontal circular cylinders and cylindrical shells, *Applied Ocean Research*, 28(5): 299-311.

[65] Bertram, V. (2000). *Practical ship hydrodynamics*. Oxford: Butterworth-Heinemann.

[66] Ogilvie, T. F., & Tuck, E. O. (1969). *A rational strip theory of ship motions: part I*. University of Michigan, Department of Naval Architecture and Marine Engineering. Report 013.

[67] Chen, W. F., & Duan, L. (2000). *Bridge engineering handbook*. Boca Raton, FL: CRC Press.

[68] McIver, P., & Evans, D. V. (1984). The occurrence of negative added mass in free-surface problems involving submerged oscillating bodies, *Journal of Engineering Mathematics*, 18, 7-22.

[69] Firestone Industrial Products. (2011). [PDF data file]. *#1T14C-3* Retrieved from http://fsip2.com/pdfs/industrial/datasheets/IMPERIAL_PDF/EMDG_1t14c-3.pdf

[70] Inclining test unified procedure, (2004). [PDF data file]. IACS. Retrieved from http://www.iacs.org.uk/document/public/Publications/Guidelines_and_recommendations/PDF/REC_31_pdf184.pdf

[71] Teng, C., & Liu, P. C. (2001). Estimating wave height distributions from wind speed measurements, *Coastal Engineering 2000*, 310-319.

[72] Hammond, L., & Saunders, D. (199). The applicability of scaling laws to underwater shock tests, *Maritime Platforms Division Aeronautical and Maritime Research Laboratory*, Tech. Report No. DSTO-GD-0162.

[73] Brennan, S. (1999). *Modeling and Control Issues Associated with Scale Vehicles* (Master's Thesis), University of Illinois at Urbana-Champaign, Urbana, IL.

[74] Daniels, Richard W. (1974). *Approximation Methods for Electronic Filter Design*. New York: McGraw-Hill.

[75] Kelly, J., Kowalczyk, H., & Oral, H. A. (2002). Track simulation and vehicle characterization with 7 post testing, *SAE Technical Paper Series*, 2002-01-0804.

[76] Boggs, C. M. (2009). *The use of simulation to expedite experimental investigations of the effect of high-performance shock absorbers* (Doctoral Dissertation), Virginia Polytechnic and State University, Blacksburg, VA.

[77] Mousaviraad, S.M., Bhushan, S., & Stern, F. (2013, June). URANS studies of wam-v multi-body dynamics in calm water and waves, *3rd International Conference on Ship Maneuvering in Shallow and Confined Water: Ship-to-Ship Interaction,* Ghent, Belgium.

[78] Sadat-Hosseini, H., Carrica, P., Kim, H., Yasuyuki, T., & Stern, F. (2010). URANS simulation and validation of added resistance and motions of the modern commercial oil carrier kvlcc2 with fixed and free surge conditions, *Gothenburg Workshop on CFD in Ship Hydrodynamics*.

[79] Huang, J., Carrica, P., & Stern, F. (2008). Semi-coupled air/water immersed boundary approach for curvilinear dynamic overset grids with application to ship hydrodynamics, *International Journal Numerical Methods Fluids*, 58, 591-624.

[80] Helsel, K. J., Pollara, A. S., & Rod, D. A. (2011). WAM-V (proteus) prototype model testing, *Naval Research Enterprise Intern Program Final Report*, Bethesda, MD.

[81] Mousaviraad, S.M., Conger, M., Peterson, A., Craft, M., Ahmadian, M., & Stern F. (2013, November). URANS cfd for two-body hydrodynamic simulation of wave adaptive modular (wam-v) vessels and validation against sea trials, *30th Symposium on Naval Hydrodynamics*, Hobart, Australia.

[82] Hughes, S. A. (1984). The tma shallow-water spectrum description and applications. *Department of the Army, Technical Report*, CERC-84-7.

[83] Marcu, F. (2009). *Semiactive cab suspension control for semitruck applications* (Doctoral Dissertation), Virginia Polytechnic and State University, Blacksburg, VA.

[84] Nagode, C. (2013). *Electromechanical suspension-based energy harvesting systems for railroad applications* (Doctoral Dissertation), Virginia Polytechnic and State University, Blacksburg, VA.